Geochemistry and mineralization of the Lundmark Akow area, North Caribou Greenstone belt, Ontario

Daniel Thomson

A thesis submitted in partial fulfillment of the requirements

of the degree of Master of Science

Department of Geology

Lakehead University

February 2024

Abstract

The Lundmark Akow area is located in the south-central portion of the South Rim assemblage of the North Caribou Greenstone Belt. The mineralization consists of several base metal-bearing massive sulphide horizons hosted in a sequence of garnetiferous staurolite mica schists in the southern portion of the study area, to a northern host rock sequence dominated by volcanic and intrusive mafic to felsic rocks. The igneous host rock portion of the study has been dated between 2973 to 2980 Ma through zircon U/Pb geochronology. The meta-sedimentary sequence which hosts the mineralization is built upon a basement of intrusive and volcanic rocks which formed in an oceanic plateau through plume magmatism before impinging upon a subduction zone. Negative high field strength element (HFSE) anomalies show that arc related magmatism built upon the oceanic plateau. Sm/Nd isotope values from the mafic to felsic volcanic and intrusive rocks show a spread in ε_{Nd} from -1.53 to 3.07 suggesting that melts were derived from both depleted mantle and plume sources, with some melts being contaminated by an older crustal basement.

The characteristics of the massive sulphide horizons, as well as the host meta-sedimentary rocks are consistent with them having formed through distal VMS processes including hydrothermal particulate fallout from buoyant plumes combined with pooling of dense sulphide-rich fluids in topographic lows on the sea floor. The garnet-rich meta-sedimentary rocks show Fe and Mn enrichment when normalized to immobile Al and Ti, consistent with addition through hydrothermal plume particulate processes. The characteristics of the garnet layers suggest they formed through metamorphism of a sediment derived from the intermixing of hydrothermal and terrigenous particulates. The garnet compositions show prograde growth with a Mn- and Ca-rich core to a Fe- and Mg-rich rim, supporting their formation as a result of metamorphic conditions post exhalative activity.

The massive sulphide horizons occur in lenses of 5 to 50 cm in width and do not show any clear alteration zonation leading up to the mineralization, suggesting they formed distal to the vent likely from

a dense bottom-hugging sulphide-rich brine. Tourmalinite occurrences associated with the massive sulphide horizons formed through metasomatic interactions between the plume fluids and the underlying seafloor sediments, forming continuous stratigraphic beds. The tourmaline composistions were very Fe-rich with base metal concentrations similar to the host massive sulphide, supporting the formation of the tourmaline coevally with the sulphides in an Fe rich hydrothermal plume.

The sedimentary nature of the host rocks to the mineralization did not allow for the evaluation of hydrothermal alteration through methods of Rb/Sr ratios or alteration index/ chlorite carbonate pyrite index alteration box plots. An evaluation of SWIR data on white micas showed the Al-OH band occurring at around 2200 nm, suggesting formation due to regional metamorphism rather than through a high heat and fluid/rock interaction associated with proximal VMS mineralization.

Efforts to vector to mineralization through mineral compositions were not successful. The presence of Mn-rich garnet was more dependent on host rock composition rather than proximity to massive sulphide. Zinc enrichment in staurolite was limited and no values greater than 2 wt.% were observed which suggests there is no massive sulphide mineralization in the vicinity of all tested staurolite. Evaluating a change in X_{Fe} in ferromagnesian silicates (garnet, biotite, staurolite, chlorite) in proximity to metamorphosed massive sulphide horizons due to the formation of a sulphidation oxidation halo showed that the composition of garnet, biotite, and chlorite were modified. However, the extent of this halo was limited to within a few meters of a metamorphosed massive sulphide horizon and as such the usefulness of this as a vector is limited.

Geothermometry using a Ti in biotite and garnet biotite composistion as well as a garnet, biotite, plagioclase muscovite barometer was applied to show an increasing metamorphic grade from the north to the south across the belt. Temperatures range from 573 ± 32.2° C in the north to 651 ± 32.6° C in the southern portion of the Lundmark Akow area. Pressure variation likewise varies from 3.0 Kbar in

the north to 5.3 Kbar in the southern most sample. Calculating peak metamorphic conditions based on calculated theoretical mineral assemblages from whole rock data through the use of a pseudosection is broadly consistent with the geothermobarometry, with a stable field for the coexistence of biotite garnet and staurolite occurs from between 510-600 °C and pressure between 2-5 Kbars.

Acknowledgments

Firstly, my gratitude is to my supervisor, Pete Hollings, whose academic mentoring and consistent feedback has helped me to expand my understanding and create a body of work far greater than anything I could have accomplished by myself. A similar thank you is extended to each of the faculty members at Lakehead, for your advice and counsel whenever I came to you.

Thank you to Romios Gold Resources for giving me the opportunity to take on this research on company property, and for the employment throughout this study period which has sustained me throughout the whole process. I am especially gracious to John Biczok, who's mentoring in the field has been an experience I will always cherish. You have made me a better geologist and I will always look up to your ability to retain knowledge and keep learning more.

My gratitude is extended to all the scholarship funding granted to me which made it possible to remain focused on my studies. In particular to the Ontario graduate scholarship, Bernie Schneiders memorial Reward, YMP equinox Scholarship, and the SEG Ronald E. Seavoy Student field trip.

To my fellow graduate students, hang in there you'll see the end of it soon enough. A special thank you to Vlad, Jordan, and Kevin. Honestly if you weren't around, I feel like I could have finished this thing months ago, but it would have been a whole lot less enjoyable. I truly owe you my sanity.

Finally, and most importantly a thank you to my family. To the patience and support of my wife, who always believed in me even when I didn't believe I could do it. To my two children, thank you for being the greatest reason to get up each day and for greeting me with joy each day I came home from school. I hope you can look at this and always know you can accomplish great things.

Table of Contents

Abstract.....i

Acknowledgements.....iv

Table of Contents.....v

List of Abbreviations.....viii

List of Figures.....ix

List of Tables.....xii

1. Introduction.....1
1.1 Project goals.....1
1.2 Volcanogenic Massive Sulphide Systems.....3
2. Regional Geology.....8
2.1 Superior Province.....8
2.2 North Caribou Terrane.....10
2.3 North Caribou Greenstone Belt.....11
2.4 Assemblage Descriptions.....13
2.5 Structural Deformation and Metamorphism.....18
2.6 Mineral Deposits.....19
3. Methodology.....22
3.1 Sample Collection.....22
3.2 Whole Rock Analysis.....22
3.3 Thin Section Petrography.....23
3.4 Scanning electron microscope/ energy dispersive X-ray spectroscopy.....24
3.5 Laser Ablation ICP MS.....25
3.6 Short Wave Infrared Spectroscopy.....26
3.7 Thermal ionization mass spectrometry Re-Os Geochronology of Molybdenite.....26
3.8 Laser ablation-Induced coupled plasma mass Spectrometry Garnet U-Pb Geochronology....27
3.9 Thermal ionization mass spectrometry Zircon U-Pb Geochronology 28
3.10 Sm-Nd isotopes.....28
3.11 Sulphur δ^{34} Isotopes.....29
4. Results.....30
4.1 Thin Section Description.....30
4.1.1 Metamorphosed pelite psammite schist.....30
4.1.2 Massive sulphide horizons.....37
4.1.3 Mafic rocks.....42
4.2 Geochemistry.....44
4.2.1 Mafic Rock Samples.....44
4.2.2 Felsic Volcanic and Intrusive Rocks.....48
4.2.3 Sedimentary Rocks.....50
4.3 Geochronology.....60

4.4 Isotopes....64
4.4.1 Sulfur δ^{34} Isotopes....64
4.4.2 Sm-Nd isotopes....65
4.5 Short Wave Infrared....65
4.6 Mineral Chemistry....66
4.7 Garnet Trace Element Data....70
4.8 Sulphide Laser Ablation Data....73
4.9 Tourmaline Laser Ablation Data....74
5. Disscussion....75
5.1 Tectonic Setting....75
5.2 Tectonic History....79
5.3 Mineralization at Lundmark Akow....83
5.4 Alteration and Major element behaviour....84
5.5 Garnet....91
5.6 Tourmaline....100
5.7 White Mica....105
5.8 Chlorite....106
5.9 Sulphides....107
5.10 Source of fluids and method of mineralization....113
5.11 Oxidation sulphidation state vectors to ore....117
5.12 Metamorphic Conditions....123
6. Conclusions....127
References....131
Appendix I....143
Appendix II....150
Appendix III....178
Appendix IV....212
Appendix V....234
Appendix VI....239
Appendix VII....250
Appendix VIII....257
Appendix IX....266
Appendix X....272
Appendix XI....276
Appendix XII....281
Appendix XIII....286
Appendix XIV....288

Appendix XV.....290

Appendix XVI.....292

Appendix XVII.....294

Appendix XVIII.....296

Appendix XIX.....303

Appendix XX.....306

Appendix XXI.....309

Appendix XXII.....311

List of Abbreviations

PPL	Plane-Polarized Light
RL	Reflected Light
XPL	Cross-Polarized Light
HFSE	High field strength element
AI	Alteration index
CCPI	Chlorite carbonate pyrite index

List of Figures

Figure 1.1: Overview of general model for VMS system……4
Figure 2.1: Superior province terrane and domain map……10
Figure 2.2: Northwest Superior Craton Map……11
Figure 2.3: North Caribou Greenstone Belt Map……12
Figure 2.4: Lundmark Akow Map……20
Figure 4.1: Photomicrographs of foliated schist……30
Figure 4.2: Photomicrographs of plagioclase feldspar……31
Figure 4.3: Photomicrographs of skeletal garnet and staurolite……31
Figure 4.4: Photomicrographs of garnet zonation and chlorite alteration……32
Figure 4.5: Photomicrograph of tourmaline……33
Figure 4.6: Photomicrograph of zircon, magnetite and ilmenite……34
Figure 4.7: Photomicrograph of sulphide textures……35
Figure 4.8: Photomicrograph of massive sulphide textures……36
Figure 4.9: Photomicrograph of arsenopyrite, galena, and sphalerite……38
Figure 4.10: Photomicrograph of amphibole and biotite in massive sulphide matrix……39
Figure 4.11: Photomicrograph of chlorite alteration of andalusite……40
Figure 4.12: Photomicrographs of tourmaline in massive sulphide horizons……41
Figure 4.13: Photomicrograph of amphibolite……42
Figure 4.14: Photomicrograph of biotite and garnet in amphibolite……43
Figure 4.15: Pearce trace element volcanic classification of mafic and felsic rock samples……44
Figure 4.16: Spider diagram of Mafic group 1……45
Figure 4.17: Spider diagram of Mafic group 2……46
Figure 4.18: Spider diagram of Mafic group 3……47
Figure 4.19: Spider diagram of Mafic group 4……47
Figure 4.20: Spider diagram of Mafic group 5……48
Figure 4.21: Spider diagram of Felsic group 1……49
Figure 4.22: Spider diagram of Felsic group 2……50
Figure 4.23: Photo of sample DT078……50

Figure 4.24: Photo of samples DT050 and DT049……51
Figure 4.25: Spider diagram of sedimentary group 1……52
Figure 4.26: Spider diagram of sedimentary group 2……53
Figure 4.27: Spider diagram of sedimentary group 3……54
Figure 4.28: Spider diagram of sedimentary group 4……55
Figure 4.29: Downhole diagram of all WRX sample locations……56
Figure 4.30: Concordia diagrams of zircon U/Pb of felsic volcanic samples……61
Figure 4.31: Concordia diagrams of garnets analyzed for U/Pb dating……63
Figure 4.32: Garnet ternary compositional diagram……66
Figure 4.33: Biotite discrimination diagram……68
Figure 4.34: Chlorite discrimination diagram……69
Figure 4.35: Tourmaline discrimination diagram……70
Figure 4.36: Garnet ternary minor oxide composition diagram……71
Figure 4.37: Garnet trace element spider diagrams……72
Figure 5.1: Sm/La vs. Th/La of mafic and felsic igneous rock groups……78
Figure 5.2: Sm/La vs. Th/La of sedimentary rocks……79
Figure 5.3: Composite stratigraphic section of Lundmark Akow……81
Figure 5.4: Tectonic history schematic of Lundmark Akow……82
Figure 5.5: AI/CCPI alteration box plot of felsic samples……85
Figure 5.6: Downhole plot of DDH 16-04 Oxide behaviour……87
Figure 5.7: Bivariate plots of Al, Ti, Fe……89
Figure 5.8: Al/(Al+Fe+Mn) vs. Fe/Ti hydrothermal sediments diagram……90
Figure 5.9: Garnet rich coticules of sample DT053, DT057, DT060……91
Figure 5.10: Garnet MnO, FeO Harker diagram……93
Figure 5.11: DT042 garnet line SEM-EDX line alanysis……94
Figure 5.12: DT058 SEM-EDX analysis points on garnet……95
Figure 5.13: P-T Pseudosection of garnet composition in metamorphic growth……97
Figure 5.14: Average of garnet trace element compositions……99
Figure 5.15: Locations of trace element analysis on garnet from sample DT074……100

Figure 5.16: Tourmaline in sulphide horizons……101
Figure 5.17: Tourmaline in inclusions within garnet from sample DT009 and DT017……102
Figure 5.18: Tourmaline Composition ternary……103
Figure 5.19: Tourmaline base metal content ternary diagram……104
Figure 5.20: White Mica Al-OH band location histogram……105
Figure 5.21: Photomicrograph of chlorite from sample DT120B……107
Figure 5.22: Photo of sample DT002 with garnet and sulphide horizon……108
Figure 5.23: Se/S ratio of sulphide samples……109
Figure 5.24: $\delta^{34}S$ of sulphide samples……111
Figure 5.25: Comparison of Se/S and $\delta^{34}S$ of sulphide samples……112
Figure 5.26: $\delta^{34}S$ values of sulphides from sedimentary hosted vs. igneous hosted massive sulphide….113
Figure 5.27: Contiguous downhole lithology plots……114
Figure 5.28: Schematic diagram of plume activity……115
Figure 5.29: Schematic diagram of the mixing of terrigenous and hydrothermal particulates……116
Figure 5.30: Schematic diagram of sulphide and tourmaline formation in pooling plume……117
Figure 5.31: Sulphidation oxidation halo ferromagnesium trends……118
Figure 5.32: Downhole plot of ferromagnesian composistions of DDH 17-01……119
Figure 5.33: Downhole plot of ferromagnesian composistions of DDH 16-04……121
Figure 5.34: Geothermobarometry intersection point graphs……124
Figure 5.35: P-T Psuedosection of sample DT050……125

List of Tables

Table 3.1: SEM-EDX sample standards……24

Table 3.3: Internal Standards for Iolite data reduction……25

Table 4.1: Re-Os geochronology results……62

Table 4.2: δ^{34} S values for sulphides from Lundmark Akow……64

Table 4.3: Sm-Nd isotope data……65

Table 5.1 Temperature and pressure data from Lundmark Akow……125

1. Introduction

1.1 Project Goals

To meet the needs of society as we transition to a green power supply and a digital economy, critical minerals such as copper will be needed (Government of Canada, 2022). The demand in copper is expected to more than double over the next ten years due to the integral role it plays in electrical circuity and current production rates do not appear to be increasing to meet that demand (S&P Global, 2022). Historically volcanogenic massive sulphide (VMS) deposits have accounted for 27% of Canada's Cu production, 49% of its Zn, 20% of its Pb, 40% of its Ag, and 3% of its Au (Galley et al., 2007). The polymetallic nature of VMS deposits has made them an attractive target. A growing demand for copper in the near future makes the need for exploration today even more pressing given the length of time to bring a deposit into production.

Lundmark Akow is located within the Southern Rim assemblage of the North Caribou Greenstone Belt located in northern Ontario. Located 20 km to the northwest of the Musselwhite mine, it is best accessed by means of a floatplane onto the nearby Lundmark Lake or Akow Lake. Exploration work undertaken in 1998 by Romios Gold Resources intersected a copper-gold zone within highly altered garnet staurolite biotite sericite schists termed the "Romios Shear Zone" (Biczok, 2016). A resumption in drilling in the area by Romios in 2016 identified copper-gold mineralization stretching several kilometers and the schists were described as the "hydrothermal pathway" of a VMS system (Biczok, 2016). This hydrothermal pathway, or semi-conformable alteration zone, represents the path of fluid flow of convecting VMS fluids and can potentially cause significant alteration many km away from significant massive sulphide mineralization (Franklin et al., 2005). Following the development of this VMS model, further drilling in 2017 and 2019 identified several lenses of massive sulphide mineralization including up to 1.5 m of 2.4% Cu and 1.4 g/t Au (Biczok, 2017, 2021).

The mineral assemblage associated with the alteration in Lundmark Akow is unusual in that it consists of horizons of quartz garnetite as well as massive biotite with coarse garnets up to 3-4 centimeters in width. Tourmaline is also a frequent occurrence within some portions of altered meta-sedimentary rocks, and especially within horizons of massive sulphide where it can form as agglomerate blebs of tourmalinite along a stratigraphic horizon. If the rocks at Lundmark Akow do represent a semi-conformable alteration zone of a VMS system, it is conceivable that more significant mineralization exists nearby. An in-depth study of Lundmark Akow will test the validity of the proposed model and the potential for a successful vector to mineralization.

The objectives of this study was to evaluate the tectonic setting of the Lundmark Akow area and to characterize the massive sulphide mineralization and the associated alteration mineral assemblage. The tectonic setting was evaluated through the use of trace element geochemistry and Sm-Nd isotopes on intrusive and volcanic rocks, in order to place the Lundmark Akow area within the larger context of the North Caribou greenstone belt. To characterize the mineralization a comparison between proximal vs. distal VMS mineralization was made to distinguish the source of the mineralization at Lundmark Akow. The garnet-staurolite-biotite schist which hosts a portion of the massive sulphide was previously proposed to have formed as a result of a semi-conformable fluid alteration, this was reconsidered using geochemical and petrological methods to reevaluate the method of formation. Various whole rock geochemical, mineral composition, and spectral methods were tested to gauge their effectiveness as a vectoring tool to locate mineralization. These goals were achieved through the use of whole rock major and trace element geochemistry, thin section petrography, scanning electron microscope/energy dispersive X-ray spectroscopy (SEM/EDS), laser ablation induced coupled plasma mass spectrometry (LA-ICP-MS), Shortwave infrared (SWIR), stable isotope mass spectrometry for $\delta^{34}S$, MC-ICP-MS of Sm-Nd isotopes, and Thermal ionization mass spectrometry (SIMS) of Re-Os and U-Pb. All together, these data were used to develop a more complete model for the evolution of the Lundmark Akow area.

1.2 VMS Systems

Volcanogenic massive sulphide systems form in subaqueous settings where a heat source is able to drive hydrothermal convection with downwelling of ocean water through volcanic rocks which are heated by subvolcanic intrusion(s) before subsequently ascending and leaching them of metals which are then deposited on or near the seafloor at venting discharge sites (Franklin et al., 1981; Gibson et al. 1999; Hannington et al., 2005). The hydrothermal fluid flow through volcanic rocks creates an alteration halo in the surrounding rocks, forming a semi-conformable alteration zone which can extend up to a hundred kilometers along strike and be several kilometers wide extending from the paleo seafloor down to the heat source of the subvolcanic intrusion (Franklin et al., 2005). Hydrothermal fluid flow through the country rock causes significant cation leaching, leaving residual TiO_2, Al_2O_3 and FeO (MacLean and Kranidiotis, 1987). The hydrothermal fluids also cause spilitization of mafic basalts, leaching Fe and other economic minerals and producing a greenschist assemblage of minerals such as chlorite, sericite, albite, epidote, and quartz (Franklin et al., 2005). Lateral fluid flow away from the heat source will create a zonation in alteration assemblages that will range from spilitization, silicification, epidote quartz, and carbonization to potassic alteration (Galley, 1993; Piercey, 2009). Alteration can be patchy and vary in the degree of gains or losses of Si, Ca, Fe, Na, and Mg throughout the various portions of the semi-conformable alteration zone (Galley, 1993; Piercey, 2009). In the upper regions of semi-conformable alteration zones some degree of sub seafloor replacement and deposition can occur leading to the formation of stringer sulphide mineralization (Maclean and Lawrence, 1991).

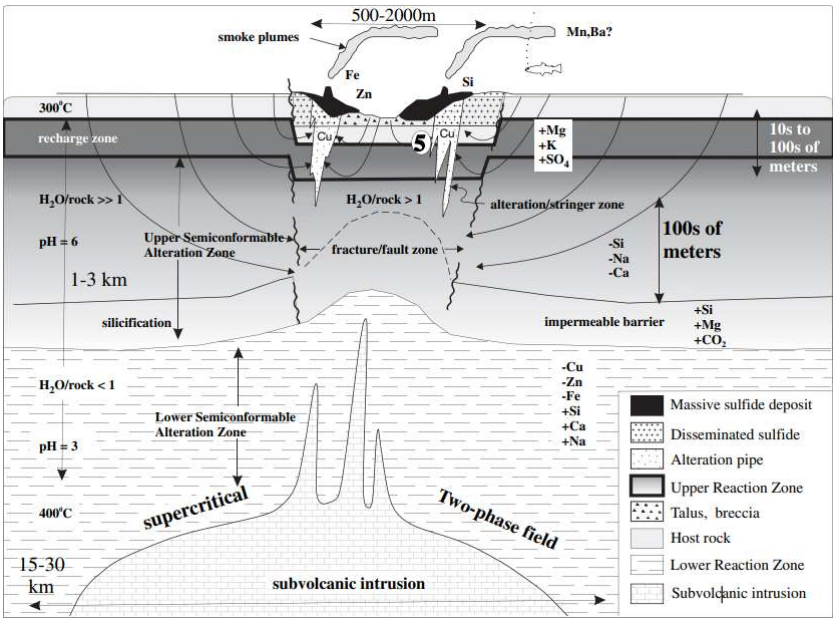

Figure 1.1. Overview of general model for VMS system. From Franklin et al. (1993)

Once the hydrothermal fluids reach a permeable structure such as a fault they can be channelled up to the surface (Galley et al., 2007). The fluid up-flow zone directly beneath the venting side is often referred to as the alteration pipe, as the early described examples from Noranda resembled pipe like structures (Franklin et al., 2005). The footwall alteration pipe is a zone of high temperature and high fluid/rock interactions producing an exterior sericite alteration halo and interior chlorite-rich zone with stringer chalcopyrite along with other base metal bearing sulfides (Hannington, 2014). Identifying the various types of alteration can be difficult in areas where greenschist to amphibolite facies metamorphism is present as these can create mineral assemblages which mimic hydrothermal alteration (Shanks, 2012). Metamorphism can also recrystalize a hydrothermal alteration zone into a new mineral assemblage which can make identification of the original fluid up-flow zones difficult (Petersen, 1984). For example, the chlorite-dominated spilitization and epidote altered portions of the semi-conformable alteration zone in the Chisel Lake deposit of Snow Lake consist of a garnet, biotite ± staurolite schist following greenschist metamorphism (Skirrow and Franklin, 1994).

Formation of massive sulphide lenses is typically dominated by chimney growth and collapse (Franklin et al., 2005). These sulphide chimneys and mounds are often capped and partially formed with a framework of anhydrite and amorphous silica (Franklin et al., 2005). Eventually the chimneys may grow large and unstable or undergo seismic fracturing causing the structures to break and crumble (Franklin et al., 2005). The retrograde solubilities of both anhydrite and quartz can cause periods of chimney growth and dissolution which aids the breakdown and formation of sulphide talus (Hannington et al., 2005; Hannington, 2014). The build up of sulphide talus acts as an insulator leading to thermal rezoning of the sulphides in the mound and also helps prevent the exhaling of metal bearing fluids to the water column (Franklin et al., 2005). Where the venting site has been effectively capped by the build-up of sulphides, anhydrite, quartz, and barite the fluids may then begin depositing sulphides by subsea-floor accumulation (Piercey et al., 2015).

The capping of the vent system can lead to fluid overpressure which can cause hydraulic jacking and fracturing parallel to bedding which can be infilled by massive sulphide (Gibson et al., 1999). The fluids can also infill the primary pore space in extrusive, autoclastic, and volcaniclastic to epiclastic rocks below the impermeable cap (Galley et al., 2007). Massive sulphide deposited within porous layers such as sediments or felsic volcaniclastic rocks are insulated from the loss of metals to a hydrothermal plume and lead to the formation of potentially very large VMS deposits (Hannington et al., 2005). Sub-seafloor replacement mineralization should contain relics of the host rock within the sulphide deposit and also have a recognizable replacement front between the sulphide deposit and the host rocks (Doyle and Allen, 2003; Franklin et al., 2005).

In some VMS systems, the lack of a sulphide mound means there is no effective blanket over the venting site. Consequently, much of the fluids are exhaled into the water column as a hydrothermal plume (Franklin et al., 1981; Hannington et al., 2005). This style of deposition is not conducive to the formation of very large VMS deposits due to the loss of metals to the water column, often spreading the

sulphides in a thin layer over a wide geographic area (Franklin et al., 2005; Hannington, 2005; Galley et al., 2007). These systems have been referred to in the past as “vent-distal” VMS deposits and are theorized to form in several different possible ways (Franklin et al., 1981). First, the deposit can be formed by particulate fallout from a buoyant hydrothermal plume (Franklin et al., 2005). This plume can rise several hundred meters above the sea floor and precipitate ferromanganese particles, clays, and sulphides up to five kilometers around a vent site (Peter, 2003; Hannington et al., 2005). These particulates intermix with terrigenous clastic material and form chemical sediments such as iron formations, bedded massive sulphide, and manganese and iron rich shales (Hannington, 2014). Although this method is not known to form significant deposits in the modern oceans due to the rapid dispersal and oxidation of plume particles, the more stagnant anoxic basins of the Archean may have been more suitable for this (Hannington, 2014). As these deposits form at a distance from the plumbing and vent sites they will often occur with no distinguishable hydrothermal alteration zones or feeder network (Franklin et al., 1981; 2005).

Another model for the formation of distal VMS deposits is as a product of a bottom-hugging brine which pool in topographic lows or depressions (Franklin et al., 1981; Hannington et al., 2005). The buoyancy of the plume is dependent upon temperature and composition of the exhaled fluids as well as the characteristics of the ocean waters (Hannington, 2014). Higher temperature fluids are generally more buoyant, but mixing with cooler ocean waters can increase their density and cause them to sink down into topographic lows (Franklin et al., 1981; Hannington, 2005). A high salinity also plays a major role in determining the buoyancy of a hydrothermal plume, with a salinity of 15 wt. % NaCl pooling at under 100°C, whereas at 25 wt. % NaCl pooling occurs regardless of temperature (Hannington, 2014). Data from a number of Archean to Paleoproterozoic VMS deposits show a range in salinities from 0.5 up to 38 wt. % NaCl, suggesting both buoyant to dense pooling plumes could have formed in ancient VMS systems (Hannington, 2014). High salinity and low pH of the fluids also allows for high concentrations of

metals in a brine pool even at lower temperatures (Hannington et al., 2005). As these pools are forming at a distance from the discharge vents they often lack strata bound alteration zones, or feeder zones, but may show a thin layer of metasomatic alteration at the boundary between the brine pool and the underlying sediments (Slack, 1996; Franklin et al., 2005). As the fluids are not widely dispersed, but concentrated in depressions, they can form significant deposits and display unique characteristics such as a strata-bound character, fine grained sulphides, bedding, and occasionally replacement textures (Hannington et al., 2005; Franklin et al., 2005).

Another method of forming a distal deposit is through the collapse of a sulphide mound on a stratigraphic high or steep slope (Franklin et al., 1981). The collapsing sulphide mound may move as a coherent slide sheet or as a turbulent mud and breccia flows (Franklin et al., 1981). Like other distal VMS deposits the spatial separation from the discharge site explains the lack of an alteration zonation, however, as the mound originally formed at the venting site, preservation of smoker chimneys structures is possible if they are not destroyed by transportation in which case a sulphide breccia may form (Franklin et al., 1981; 2005).

The spectrum of VMS deposits is large with varied methods of sulphide deposition, paths for fluid flow, host rock, and tectonic setting. The formation of a VMS deposit by proximal venting into sulphide chimney mounds; by sub-seafloor replacement or by distal hydrothermal plumes both buoyant or pooling will create unique characteristics both in alteration and mineralization. As the mineralization found at Lundmark Akow is believed to represent a VMS deposit, understanding the processes that led to its formation is essential in evaluating vectoring methods to the deposit. If the deposit formed in a vent proximal setting evidence of hydrothermal alteration such as the semi-conformable alteration zone or footwall alteration pipe should be distinguishable. If instead the mineralization represents a vent distal product evidence should support this with limited hydrothermal alteration being present, but with

evidence for plume particulate fallout and exhalative products. Such characteristics will be evaluated and discussed during this study.

2. Regional geology

2.1 Superior Province

The Lundmark Akow study area is a package of altered felsic and clastic rocks within the South Rim assemblage of the North Caribou Greenstone Belt of the Superior Province of the Laurentian Craton. Cratons are defined as large areas of continental lithosphere which have remained coherent and largely stable since the Precambrian. Laurentia, or the North American Craton, is one of the oldest and largest cratons on Earth (Hoffman, 1988). Laurentia consists of a framework of large Archean micro-continental crustal units stitched together by Proterozoic orogenic belts. The Superior Province is one of the largest blocks of North America and makes up more than 20% of all exposed Archean crust on Earth (Card and King, 1992). The Superior Province is a complex arrangement of east-west trending mafic to felsic volcanic greenstone belts, tonalite-trondhjemite-granodiorite (TTG) plutonic suites, sedimentary basins, and highly metamorphosed gneissic terranes (Stott, 1997). These varied terranes show the evidence of a long geological history stretching from 3.1 Ga to 2.6 Ga (Card, 1990) with major volcanic activity around 3.0 Ga and 2.7 Ga and the Kenoran orogeny at 2.71 to 2.67 Ga which amalgamated the many separate island arc chains and microcontinents into the Superior Province (Stott, 1997).

Various attempts have been made to subdivide the Superior into its component parts (Card and Ciesielski, 1986). Early attempts relied mostly on geographic positioning with Wilson (1939) dividing the Superior into northwest, southern, and eastern or Timiskaming sub-provinces as well as distinguishing a northern boundary from a separate Churchill province. As geological work in the area increased, attempts were made at dividing the Superior based on changes in structural trends or lithology (Stockwell, 1964; Douglas, 1973). The terms sub-provinces and assemblages (stratified volcanic and/or

sedimentary rock units built during a discrete interval of time in a common depositional or volcanic setting (Thurston, 1991) were adopted to divide the Superior into four lithotectonic types: volcano-plutonic, metasedimentary, plutonic, and high-grade gneiss (Card and Ciesielski, 1986). The volcano-plutonic sub-provinces are made of assemblages of metavolcanic supracrustal greenstone belts surrounded by voluminous felsic plutons (Card and Ciesielski, 1986). Meta-sedimentary sub-provinces are made of predominantly turbiditic psammites and pelites metamorphosed to greenschist to amphibolite facies(Card and Ciesielski, 1986). Plutonic sub-provinces consist of abundant intrusive plutonic bodies with limited supracrustal rock (Card and Ciesielski, 1986). High grade gneiss sub-provinces consist of upper amphibolite to granulite grade metamorphic intrusive and supracrustal rock commonly with layered gabbro-anorthosite bodies (Card and Ciesielski, 1986).

With increasing availability of age dates and quality seismic data in the 1980s there was a shift in the consensus as to how the Superior craton formed with more support for Phanerozoic-style horizontal tectonics (Card and King, 1992). Ages that show younging to the south and north of what was then called the Uchi-Sachigo and La Grande River sub-provinces suggested that these older protocontinents acted as the core of the Superior with subsequent belts being accreted to the south and north (Card, 1990). This change in the understanding of the formational processes of the Superior along with advancements in regional bedrock geology mapping, geophysical surveys, widespread geochronology, and geochemical and isotopic syntheses highlighted the need to adopt new terminology to better define the unique regions encompassed by the Superior Province. Stott (1997) (Stott et al., 2010) and Percival et al. (2006) devised a system of terranes and domains to subdivide the Superior (Fig. 2.1). A terrane is defined as a tectonically bounded region with internal characteristics distinct from those in adjacent regions prior to Neoarchean assembly of the Superior Province, whereas a domain is a typically younger, lithologically distinct part of a terrane, but with either juvenile crust or sharing a common basement (Stott et al., 2010).

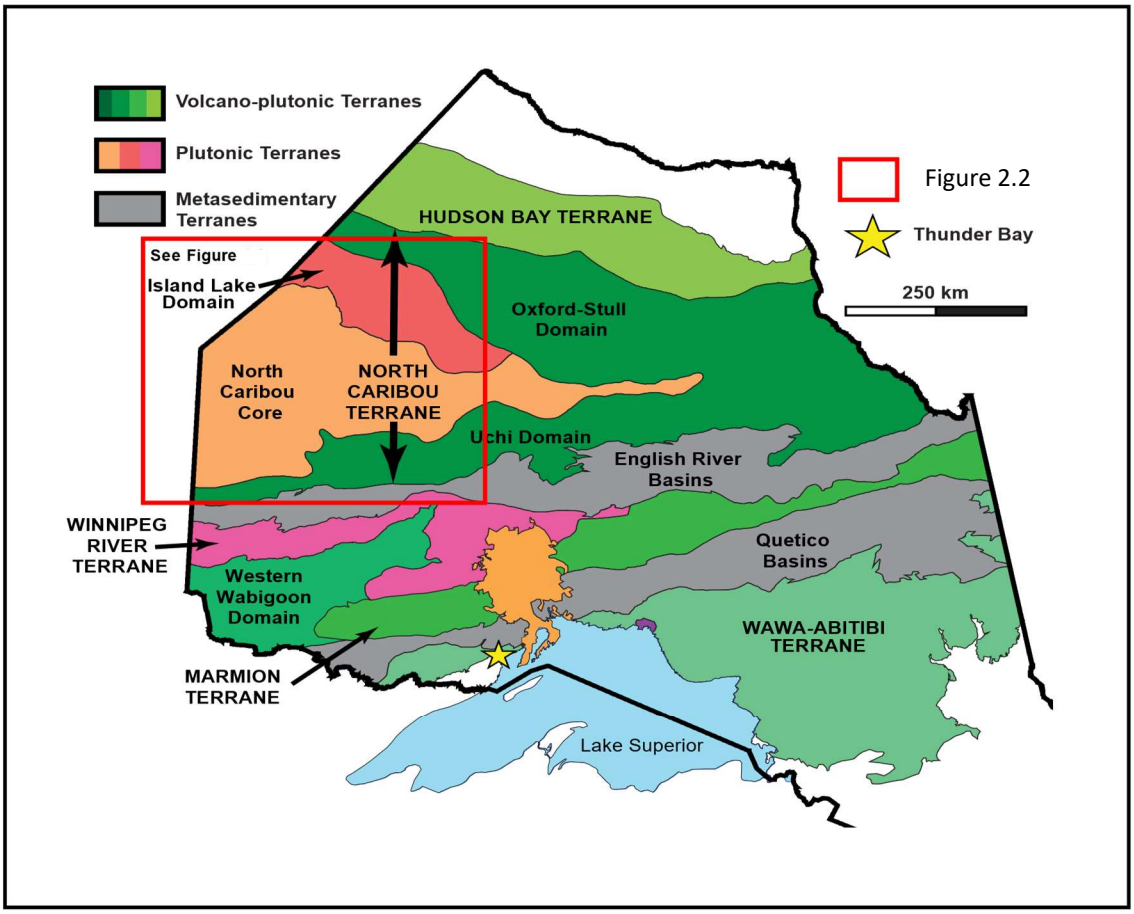

Fig. 2.1. Map showing the updated terrane and domains of the Superior Province. Modified after Stott (2010).

2.2 North Caribou Terrane

The area formally known as the Uchi-Sachigo-La Grande subprovinces has been grouped together and reorganized into what is now known as the North Caribou Terrane (NCT), consisting of the Uchi domain together with a North Caribou core and the Island Lake and Oxford-Stull domain (Fig. 2.2). The NCT is considered to be the nucleus for the Superior Province containing some of the oldest rocks in the belt with a 3.0 Ga basement of plutonic and minor volcanic rocks upon which early rift related (2.98-

2.85 Ga) and younger (2.85-2.71 Ga) arc related material were deposited (Percival, 2007). Much of the interior of the NCT is dominated by widespread tonalitic, dioritic, granodioritic, and granitic intrusive plutons that formed between 2.745 and 2.697 Ga (Corfu and Stone, 1998). Sandwiched between these larger intrusive plutons are remnants of the older volcanic derived greenstone belts of the Superior Province.

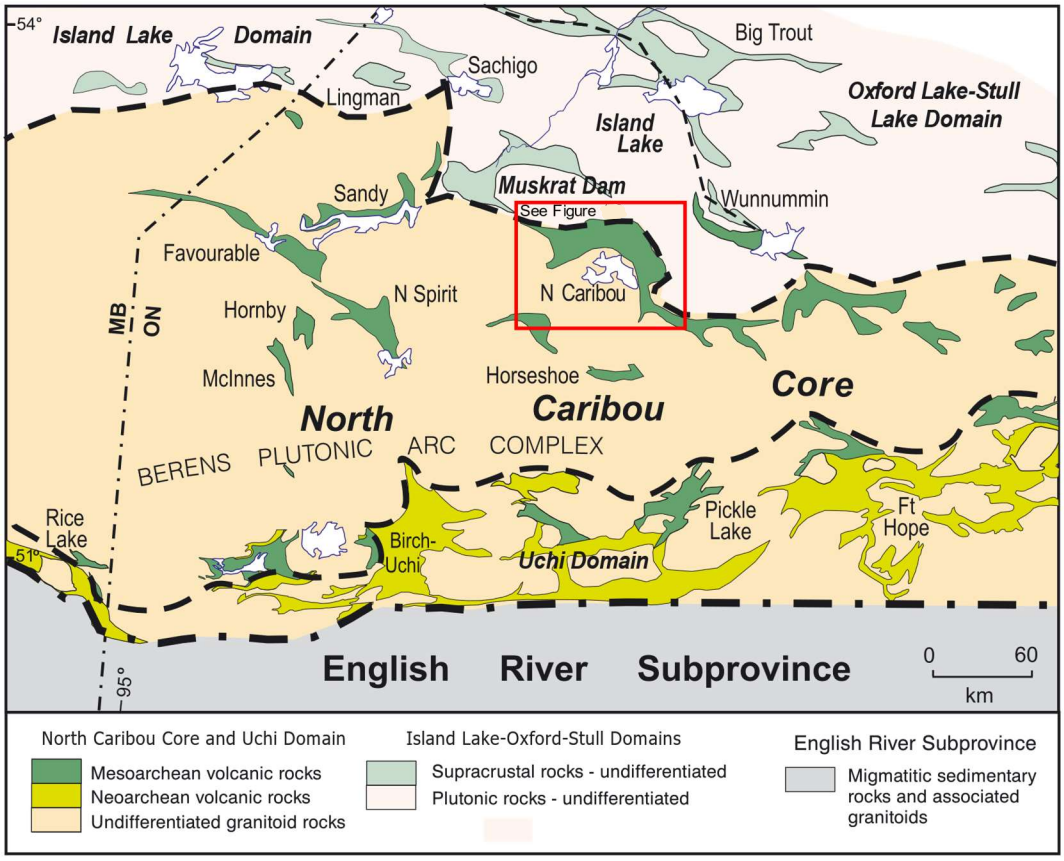

Fig. 2.2. Northwest of the Superior craton showing terranes and domains. Red box highlights North Caribou greenstone belt (Fig. 2.3).

2.3 North Caribou Greenstone Belt

The North Caribou Greenstone Belt (NCGB) is located near the center of the North Caribou terrane on the northern edge of the North Caribou core bordering the Island Lake domain (Fig. 2.3). The NCGB is a roughly Z shaped body 3-7 km wide with a total length of around 100 km (Oswald et al., 2015).

It is comprised of ultramafic to felsic volcanic units as well as sedimentary basin deposits from shales to conglomerates (Breaks et al., 2001). These metavolcanic and metasedimentary units are wrapped around the younger intrusive suites of the Island Lake gneissic complex to the north and east and the North Caribou pluton to the south and west of the greenstone belt (Oswald et al., 2015). Deformation of the belt is largely defined by regional, eastward compression of the volcano-sedimentary strata imposed by emplacement of the large crescent-shaped North Caribou pluton (Stott and Biczok, 2010). Geochronological work within the belt has highlighted three main episodes of volcanism/magmatism within the NCGB: (1) 2990–2959 Ma, (2) 2870–2856 Ma, and (3) 2729–2723 Ma (Biczok et al., 2012). These magmatic events coupled with related weathering and sedimentary processes formed the various assemblages of the NCGB.

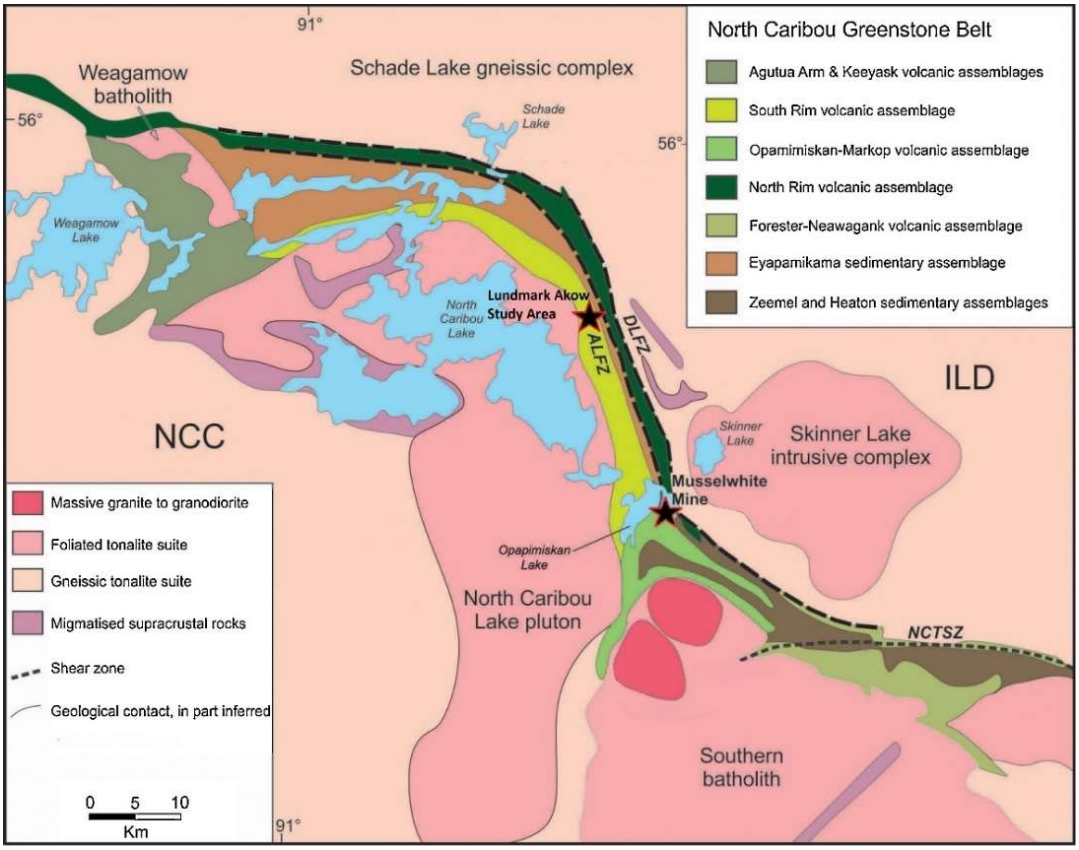

Fig. 2.3 Map of the North Caribou greenstone belt showing the various assemblages. The Lundmark Akow area of study highlighted by the star, as well as the nearby Musselwhite Mine. North caribou core (NCC), Island Lake domain (ILD). Modified from McNicoll et al. (2016)

2.4 Assemblage Descriptions

Based on mapping by the Ontario Geological Survey during a three year period from 1984 to 1986 as described by Breaks et al. (2001), the NCGB has been subdivided into eight lithotectonic supracrustal assemblages (Fig. 2.3): The Agutua Arm metavolcanic assemblage (AAV), Keeyask Lake metasedimentary assemblage (KLS), Keeyask Lake metavolcanic assemblage (KLV), South Rim metavolcanic assemblage (SRV), North Rim metavolcanic assemblage (NRV), Opapimiskan-Markop metavolcanic assemblage (OMU), Forester Lake metavolcanic assemblage (FLV), and Eyapamikama Lake metasedimentary assemblage (ELS).

The AAV assemblage is located in the extreme upper northwest corner of the NCGB, with an intrusive contact with the Round Lake batholith and with faulted contacts and spatial separation between the NRV and SRV (Breaks et al., 2001). Massive, fine-grained, equigranular mafic flows of normal to magnesium-tholeiitic composition predominate in the AAV along with intermediate to felsic flows and pyroclastic units (Breaks et al., 2001). A U-Pb zircon date of 2981±2 Ma (deKemp, 1987) from this unit make it potentially the oldest unit in the belt and it may have acted as a substrate for later supracrustal accumulations in the belt, especially the overlying Keeyask Lake assembalges (Breaks et al., 2001).

The KLV and KLS assemblage consists of a 20 m wide metasedimentary package topped by a 50-1700 m thick metavolcanic unit located from the northwest corner of Eyapamikama Lake to the south border of the North Caribou River (Breaks et al., 2001). The metasedimentary assemblage consists of up to 10 m of mature sandstones, 5 m of siltstones, and occasional banded iron formations (Breaks et al., 2001). Bed forms are visible within the coarser sediments dominated by planar and trough cross-beds, ripple cross-beds, and planar-stratified beds. Breccia texture is prominent towards the top of the assemblage, interpreted to represent seismic activity during rifting that initiated the major komatiitic

flows of the Keeyask Lake Metavolcanic assemblage (Breaks et al., 2001). The lowermost units of the KLV are dominated by spinifex-textured and polysutured ultramafic flows, intercalations of basaltic komatiite and minor peridotitic komatiitic rocks occur at the top of the sequence (Breaks et al., 2001)

The SRV forms the southern portion of the NCGB, it has been contact metamorphosed and folded into its present arcuate trace by intrusion of the crescent shaped 2871 Ma North Caribou Batholith to the south (Thurston et al., 1991). It stretches over 95 km and varies in width from 0.4 to 5 km (Breaks et al 2001). The SRU has yielded zircon U–Pb ages of 2981.9±0.8 Ma (Davis and Stott, 2001) from the Opapimiskan Lake Rhyolite Tuff. Further work in the vicinity of the Musselwhite mine by Biczok et al. (2012) and McNicoll et al. (2016) has correlated the rhyodacite ash tuff layer at the top of the mine sequence (Labelled Avol by mine terminology) with the SRV and obtained ages of 2972.4 ±1.6 Ma and 2978.7 ±1.0 Ma, respectively.

The SRV is dominated by mafic, pillowed and massive flows which are commonly normal to magnesium-tholeiitic in composition (Breaks et. al., 2001). These tholeiites are characterised by flat trace element patterns (La/Sm =0.9–1.0), comparable with modern day oceanic plateau, such as Ontong Java (Hollings and Kerrich, 1999). Felsic and intermediate units are also present within the assemblage, consisting of flows, pyroclastic units and hypabyssal equivalents, these comprise only a few percent of the supracrustal assemblage and occur mainly in thin localized units, typically less than 10 m in thickness (Breaks et al., 2001). These felsic units have been characterized as FI and FII rhyolites based on their Zr/Y of 3–19 and light rare earth element (LREE) enrichment in conjunction with weakly fractionated heavy rare earth element (HREE) (Hollings et al., 1999).

As the SRV and NRV progressively taper off towards Opapimiskan Lake in the southeast portion of the belt they are replaced by a distinct unit, the Opapimiskan Lake metavolcanic assemblage. The OLV varies in width between 0.1 to 1.5 km; it is dominated by ultramafic to mafic rocks of komatiitic to

tholeiitic composition (Breaks et al., 2001). Preserved volcanic structures of the mafic rocks of the OLV include pillows, pillow breccia, flow top breccias and varioles (Breaks et al., 2001). The spinifex texture and the geochemical signature of the komatiites from the OMU are characteristic of rock types related to the eruption of a hot mantle plume (Hollings and Kerrich, 1999). Geochemical studies of these komatiites and mafic tholeiites have shown evidence of LREE enrichment, which is evidence for crustal contamination, suggesting the plume interacted with TTG crust and incorporated it into the melt (Hollings and Kerrich, 1999). Intercalated within the mafic rocks of the OLV are chemical sedimentary rocks, mainly laminated oxide and silicate facies banded iron formations which act as host to the gold mineralization of the Musselwhite mine (Biczok et al., 2012). Geochronological dating of this unit has been attempted by McNicoll et al. (2016) using samples from mine units 6 and 4F within the Musselwhite mine. The sample consisted of Fe-rich garnet biotite schist, and contained both inherited and primary zircons; an age constraint of <2967 Ma was determined based on the youngest population of concordant data (McNicoll et al., 2016).

The NRV forms the northern extent of the NCGB (Fig. 2.3) stretching over 97 km, with a width varying between 0.4 and 2.6 km (Breaks et al., 2001). Once originally thought to correlate with the SRV as a possible opposite limb of a synform fold, age dating has shown this to be unlikely due to the significant difference in age between the units. Zircon U-Pb dating performed by Davis and Stott (2001) show a complex history of inherited zircons with some ages of 2980± 2 Ma, however, the age of eruption must be equal to or younger than the youngest datum of 2870 ± 2 Ma making it roughly 100 million years younger then the SRV.

The NRV consists mostly of tholeiitic mafic massive and pillowed flows, amygdules or vesicles are found in some pillowed flows but are rare in the nonpillowed flows (Breaks et al., 2001). There are also rare ultramafic and felsic tuffs intercalated within the common mafic units (Breaks et al., 2001). Their major and trace element compositions, in combination with Nd isotopic evidence of crustal recycling,

require substantial modification of parental magmas by a combination of crustal assimilation and hornblende-dominated fractional crystallization (Wyman et al., 2011). An environment of deep water oceanic volcanism may be represented by this assemblage due to the relative abundance of komatiitic flows and the scarcity of rhyolitic volcanism as well as the intercalations of laterally extensive sulphidic, argillite-oxide, and silicate-facies iron formation (Thurston et al., 1991).

The FLV assemblage occupies the southeast portion of the NCGB near Boyce Lake (Breaks et al., 2001). Metamorphic grades in this region reach amphibolite facies, but high MgO values up to 21.1% and low Al_2O_3 contents of 5.3%, suggest an originally komatiitic composition (Breaks et al., 2001). Pillow forms are distinguishable within the rocks, though exhibiting stretching, with pillow sizes ranging from 10 x 40 cm, 2 x 198 cm (Breaks et al., 2001).

The ELS unit is the youngest supracrustal rock unit within the NCGB, positioned between the NRV and SRV, and stratigraphically on top of the adjacent assemblages (Breaks et al., 2001). Generally, the ELS consists of fining upward sequences in which basal alluvium and fan delta conglomeratic cycles grade vertically and laterally into finer grained metasedimentary rocks (Breaks et al., 2001). The ELS is interpreted to be a submarine fan turbidite unit produced by erosion of older quartz-rich metasedimentary rocks. (Thurston et al., 1991). Relic zircons from a sandstone yielded an age of 2962.6 ± 1.3 Ma, however, these well-rounded zircons would have been scavenged from older units and the actual age of formation would be much younger (Davis and Stott, 2001). To the southeast of Eyapamikama Lake, approaching the study area of Lundmark Lake and Akow Lake, the ELS tapers to a width of 0.3 km. The rock types change into a mixed sedimentary sequence of laminated to thinly bedded wackes, feldspathic arenites, biotite-chlorite metapelites, and amphibole-rich wackes with local intercalated felsic metavolcanic rocks throughout (Breaks et al., 2001). Southeast of Opapimiskan Lake a very similar package of sedimentary rock was labelled the Zeemel-Heaton assemblage, Breaks et al. (2001) believed these rocks to be a continuation of the Eyapamikama metasediments, however, Biczok et

al. (2012) points out that this assemblage of sediments occurs at the bottom of the mine stratigraphy underneath what should be the older OLV and SRV, suggesting it must be a separate older package of rocks from the ELS. The work by McNicoll et al. (2016) has helped clear up the uncertainty between these units as the overturned nature of the mine stratigraphy would make the Zeemel-Heaton the youngest rock of the area, and thus likely is an extension of the ELS. If this is the case, then the zircon U-Pb age dates determined from the lower sediments of Musselwhite of < 2846 Ma (McNicoll et al., 2016) represent a much more likely age of formation for the ELS then the previous date of 2962.6 ± 1.3 Ma (Davis and Stott, 2001). The North Caribou Batholith consists predominantly of the tonalite–trondhjemite–granodiorite suite and range in composition from tonalite to granite (Breaks et al., 2001). Texturally they are massive, medium-grained, and equigranular. Approaching the contact with the SRV the rock becomes moderately foliated with an increase in biotite content (Breaks et al., 2001). It has been suggested that the diapiric emplacement of the intrusive body caused the pronounced flexure seen in the SRV (Breaks et al., 2001) with emplacement occurring around 2864 ± 1.1 Ma (Davis and Stott, 2001).

The North Caribou Batholith has seen late-stage periods of intrusion by volumetrically minor, brittle–ductile pegmatites which are predominantly granitic in composition (Wyman et al., 2011). The late-stage pegmatites commonly occur as centimetre- to metre-wide dykes, but some are locally larger intrusions that interfinger with the country rock (Van Lankvelt et al., 2016). The TTGs and later pegmatites exhibit a range of compositions that cannot be entirely accounted for by variable degrees of amphibolite melting alone (Wyman et al., 2011). It has been suggested that crystal fractionation of amphibole along with increasing amounts of assimilation of pre-existing crustal rock played a key role in the evolution of the of the intrusive rocks of the belt (Wyman et al., 2011).

2.5 Structural Deformation and Metamorphism

The deformational history of the NCGB consists of three ductile deformational events as well as more brittle faulting (Breaks et al., 2001). D1 has been rendered mostly unrecognizable due to later overprinting events, but the F1 folds are visible within the iron formation units of the Musselwhite mine, these folds are tight to isoclinal, asymmetrical with varied, but commonly relatively flat, axial plane attitudes (Breaks et al., 2001). It has been suggested that D1 represents the transpressive horizontal tectonic formation of the belt, forming overturned and nappe like structures (Oswald et al., 2015). D2 is the most pervasive deformation present in the belt, being distinguished by an F2 of close to open, asymmetric mesoscopic folds with axial planes that are near vertical and interlimb angles between 70 and 100°, and a moderate to strong S2 planer fabric (Breaks et al., 2001). The final deformation event D3 consists of locally pervasive, mesoscopic, open to gentle, asymmetric Z shaped F3 folds which represent an event of inhomogeneous strain (Breaks et al., 2001). Brittle ductile shear zones are present within the belt, commonly occurring along regions of competency contrasts between lithological units.

The NCGB shows a change in metamorphic grade, with greenschist grade assemblage dominated by chlorite and biotite in the northwest portion of the belt, gradually increasing to amphibolite metamorphic grade to the southeast, dominated by index minerals of garnet, staurolite, cordierite, grunerite, and sillimanite (Breaks et al., 2001). The increase in metamorphic grade away from the intrusive North Caribou Batholith suggests that the main regional metamorphic conditions in the belt occurred prior to 2870 Ma (Breaks et al., 2001) and are unrelated to possible contact metamorphic conditions during emplacement of the granites. Possible explanations for the change in metamorphic grade over the belt could be higher heat flow during regional metamorphism or exposure of a deeper crustal level in the southeastern portion of the NCGB (Breaks et al., 2001). A temperature range of 400 to 500°C at pressures of 3 kb or less has been suggested to be the peak metamorphic conditions of the amphibolite facies (Breaks et al., 2001).

2.6 Mineral deposits

The NCGB is host to Newmont's Musslewhite mine, a banded iron formation hosted orogenic gold deposit. The mine is located within the Opapimiskan-Markop unit on the south shore of Opapimiskan Lake (Fig. 2.3). The deposit comprises multiple orebodies within the South Iron Formation and North Iron Formation (Biczok et al., 2012). Gold mineralization is largely confined to subvertical high-strain zones in tightly folded areas, particularly where steeply dipping, isoclinal fold limbs transition into the crests or keels of antiformal and synformal structures (Biczok et al., 2012). Deposition of gold in the iron formations was due to sulfidation reactions between the Fe-rich rocks and the gold-bearing fluids with the gold occurring primarily within pyrrhotite-filled fractures in garnet grains and less so as scattered grains in green amphibole, feldspar, pyroxene, and quartz veins (Biczok et al., 2012). Starting production in 1997, the mine celebrated its 4 millionth ounce of gold produced on August 1st 2014. As of December 31^{st,} 2021, Musselwhite mine had a proven and probable reserve of 9.5 mt of ore at a grade of 5.77 g/tonne gold, and is expected to produce 1.79 M oz of gold through the remaining lifespan of the mine (Newmont, 2021).

Drilling undertaken by Romios Gold Resources since 2016 near Lundmark Lake and Akow Lake 20 km northwest of Musselwhite Mine has highlighted an extensive assemblage of intercalated fine-grained, clastic sedimentary rocks and felsic volcanic units up to 800 m thick and stretching at least 8 km (Fig. 2.4). These meta-sedimentary and felsic meta-volcanic-volcaniclastic rocks are exposed in only a few, small outcrops west of Akow Lake but make up a much larger percentage of the SRV than previously realised (Biczok, 2021). This drilling program has also highlighted the existence of an extensive package of felsic and clastic units, consisting of garnet-staurolite-biotite sericite schists. It has been suggested by Romios Gold Resources that these schistose rocks are the result of hydrothermal alteration in a lower semi conformable alteration zone, essentially a pathway for VMS forming fluids (Biczok, 2016). This

hydrothermal pathway and its proposed identity as a hydrothermal VMS system forms the basis of this MSc research project.

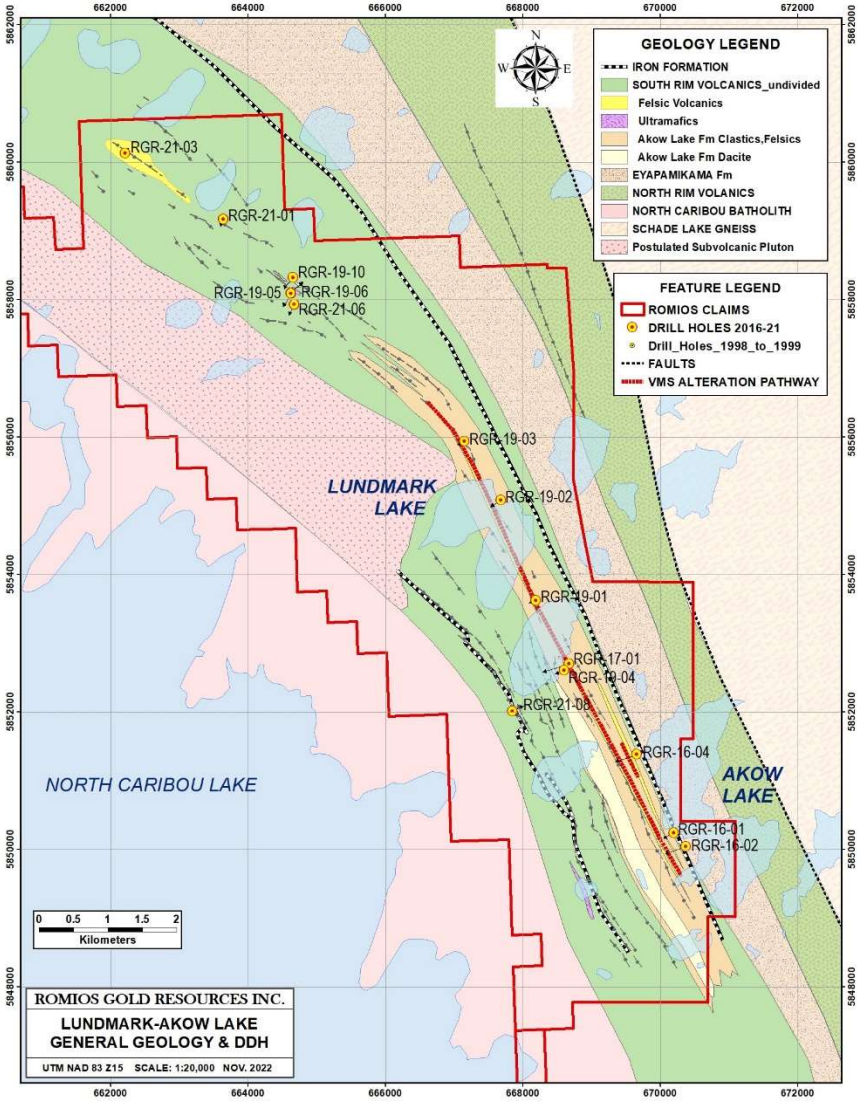

Figure 2.4. Map of Lundmark Akow showing the general geology as well as the location of the drill holes pertinent to this study. Basemap courtesy of Romios Gold Resources

The eight drill holes 16-01 through to 19-04 highlight the package of garnet-staurolite schistose meta-sedimentary and felsic volcanic-volcaniclastic being referred to as the hydrothermal pathway. Within this package of schistose rock are several small horizons of massive sulphide chalcopyrite-pyrrhotite mineralization raging from 10 cm to 1.5 m in width as well as widespread stringer sulphide mineralization. North of these eight drill holes the meta-sedimentary rock sequence is lost and instead

consists of mostly basalts with occasional felsic volcanic rhyolites and intrusive quartz-feldspar porphyry. This mafic and felsic dominated volcanic and intrusive sequence is highlighted in drill holes 19-05 to 19-20-03. VMS mineralization in this portion of the research area especially in drill hole 19-10 consists of chalcopyrite, sphalerite, galena, and pyrrhotite.

3. Methodology

3.1 Sample Collection

In the Fall of 2021, samples were selected from the stored core of the exploration programs conducted by Romios Gold Resources between 2016 and 2021. Samples were selected to give a comprehensive coverage of both downhole and inter-hole variation in lithology and alteration. Sampling was focused on the biotite-garnet-staurolite schist rocks that are believed to represent the metamorphic product of hydrothermally altered sedimentary rocks. Comparative samples were also taken from less altered meta-sedimentary rock in the stratigraphy. Representative samples were also taken of felsic volcanic rocks, basalts, ultramafic rocks, and lamprophyres that occur within the study area. In total 120 samples were collected for analysis (Appendix I).

3.2 Whole Rock Analysis

From the 120 core samples selected, a total of 56 samples were sent to ALS for whole rock analysis. This was combined with a data set of whole rock data on 49 samples that was performed by Activation Laboratories (ACTLabs) for Romios Gold Resources. Samples submitted to ALS and ACTLabs underwent a similar routine for analysis, starting with a fine crushing until 70% of the sample could pass through a 2mm mesh. The crushed fines were processed through a riffle splitter and a 250g sample of the crushed rock selected for further pulverisation until 85% of the sample could pass through a 75 micron mesh. A four-acid digestion was used for base metal content analysis. Whole rock analysis was performed using inductively coupled plasma atomic emission spectroscopy (ICP-AES). Loss on ignition was calculated by heating a 1g sample of the fines to a temperature of 1000°C and measuring weight loss to calculate percentage of volatile content of the rock such as water or CO_2. Trace elements were determined using inductively coupled plasma mass spectrometry (ICP-MS). To obtain values with lower detection limits the samples were also analyzed with ICP-MS after having undergone lithium borate

fusion. This process melts the sample into a lithium borate flux and chilled into a glass plate which allows for greater analytical accuracy as full sample decomposition is achieved (Zebedee et al. 2023). Finally, base metal content in the rock was obtained through a four-acid digestion and analysis using ICP-AES. QAQC for the samples was assured by inserting standards (Table 3.1), duplicates, and blank samples into the sampling sequence. All measured values of the standards and blanks matched the certified values and duplicates differed from original samples at values within instrumental error.

The 56 samples submitted to ALS were also analyzed for total sulfur and carbon content of the samples was determined using infrared spectroscopy. The process works as molecules will absorb frequencies that occur at resonant frequencies to their structural vibrations. The infrared spectrometer identifies characteristic wavelength absorptions to identify the absorbing molecule and the intensity of absorption determines the concentration. This analysis was not performed on the samples submitted to ACTLabs.

3.3 Thin Section Petrography

Polished thin sections were prepared at the lapidary laboratory at Lakehead University. In total 41 samples were selected with an emphasis on covering a wide area of the biotite-garnet schist and comparison with the less altered meta-siltstone. A few thin sections from basalt and ultramafic lamprophyre were selected to get coverage of all lithologies present. Polished thin sections were viewed in plane and cross polar transmitted light as well as reflected light using an Olympus BX 51 microscope at Lakehead University and photomicrographs taken using an Olympus SC180 Camera.

3.4 Scanning Electron Microscope/Energy Dispersive X-Ray Spectroscopy

Mineral compositional data from the thin section samples were obtained using a Hitachi Su-70 Schottky Field Emission scanning electron microscope (SEM) with an attached Oxford Aztec 80mm/124ev energy dispersive X-Ray spectroscopy (EDX). The beam was set to 20 kV, 300 pA, and a 15 mm working distance. A standards library was formed for calibrating the analysis using predetermined industry sample standards (Table 3.1).

Table 3.1 Listed standardized elements in the SEM with the standard used for calibration.

Element	Standard
Sodium	Jadeite
Magnesium	Periclase
Aluminum	Corundum
Silicon	Garnet-RHM
Potassium	LU-Ortho
Calcium	Wollastonite
Titanium	$SrTiO_3$
Chromium	Chromite-52n11
Manganese	MnSiO3
Iron	MnHort
Flourine	CaF_2

Before each analysis session the beam was calibrated to a nickel standard block as well as periodically updating the standards in the library as required. A trial run was performed on a sample of pyroxene with a known composition and the results were compared to ensure an accuracy of within 1% to the true value total for the pyroxene. Differences in values in each individual element were also monitored to insure values close to around 1%. Variations in element concentrations varying from the certified value of the pyroxene test sample were reduced by reanalyzing the standard for that element and updating the library.

3.5 Laser Ablation Induced Coupled Plasma Mass Spectrometry

A total of 49 sulphide grains consisting of pyrite, pyrrhotite, sphalerite, galena, chalcopyrite and arsenopyrite as well as 6 tourmalines from 16 thin sections were analysed in-situ ranging from samples from massive sulphide horizons to metasedimentary rocks. The analysis was performed using an Agilent 7900 inductively coupled plasma mass spectrometer coupled to a 193 nm excimer laser at the University of Windsor at the Element and Heavy Isotope Analytical Laboratory. The beam energy was set to 2.24 J/cm^2 at 20 Hz and a beam spot size of 20 µm. During sampling, an initial 30 s of background gas collection was performed, followed by 90 seconds of sample ablation and data acquisition. The ablated material is fed into a mass spectrometer via helium gas, and the signal intensity is recorded in counts pet second (CPS). CPS was converted into ppm data through the use of Iolite 4, where CPS data was imputed along with internal standards (Table 3.2) and an external iron reference standard gathered by SEM analysis of each spot.

Table 3.2 Analyzed elements with their internal standard used for Iolite data reduction.

Element	Li7	Be9	B11	Na23	Mg24	Al27	Si29	P31	S33	S34
Standard	G_GSD1G	NIST612	NIST612	NIST612	G_GSD1G	G_GSD1G	NIST612	G_GSD1G	FeS-1	FeS-1
Element	K39	Ca43	Sc45	Ti47	V51	Cr53	Mn55	Fe57	Co59	Ni60
Standard	G_GSD1G	NIST612	G_GSD1G	G_GSD1G	MASS-1	FeS-1	MASS-1	FeS-1	FeS-1	FeS-1
Element	Ni61	Cu63	Cu65	Zn66	Zn68	Ga69	As75	Se77	Se78	Se82
Standard	FeS-1	MASS-1	MASS-1	MASS-1	MASS-1	MASS-1	FeS-1	FeS-1	FeS-1	FeS-1
Element	Rb85	Sr88	Y89	Zr90	Nb93	Mo95	Ru101	Rh103	Pd105	Pd106
Standard	G_GSD1G	NIST612	NIST612	NIST612	NIST612	FeS-1	FeS-1	FeS-1	FeS-1	FeS-1
Element	Ag107	Pd108	Ag109	Cd111	Sn118	Sm147	Eu153	Gd157	Dy163	Er166
Standard	FeS-1	FeS-1	FeS-1	MASS-1	FeS-1	G_GSD1G	G_GSD1G	G_GSD1G	G_GSD1G	G_GSD1G
Element	Sn120	Sb121	Sb123	Te125	Cs133	Ba137	La139	Ce140	Pr141	Nd146
Standard	FeS-1	MASS-1	MASS-1	FeS-1	NIST612	FeS-1	G_GSD1G	G_GSD1G	NIST612	G_GSD1G
Element	Yb172	Hf178	Ta181	W182	Re185	Os189	Ir193	Pt194	Pt195	Au197
Standard	G_GSD1G	NIST612	NIST612	NIST612	FeS-1	FeS-1	MASS-1	MASS-1	MASS-1	MASS-1
Element	Tl205	Pb208	Bi209	Th232	U238					
Standard	MASS-1	FeS-1	FeS-1	NIST612	NIST612					

An additional eight offcuts from core samples were sent to School of Marine Sciences, Sun Yat-Sen University, China, for trace element analysis of garnet porphyroblasts hosted in schists with a focus on differentiating euhedral metamorphic garnet from more irregular potentially hydrothermally derived garnet grains. Analysis at Sun Yat-Sen was performed on iCAP™ RQ ICP-MS (Thermo Fisher Scientifc) with NewWave 193 UC. A 60 µm spot size was used with 5 J/cm^2 energy density and 5 Hz repetition rate with each analysis consisting of a 20s background measurement (laser-off) followed by 45s of data acquisition (Li et al., 2022). Trace element compositions were calibrated against the NIST610 standard with data reduction using iolite 4 (Paton et al., 2011).

3.6 Short Wave Infrared Spectroscopy

An analysis of white micas in the core samples was performed with a TerraSpec 4 Standard-Res mineral analyzer at Lakehead University. This instrument uses near-infrared (NIR)/short wave infrared (SWIR) with wavelengths from 350 to 2500 nm and a spatial resolution ranging from 3 to 6 nm. Analysis was performed on 42 core samples that displayed a significant sericite content. Samples were measured for 30 s individually, and between each analysis the instrument would be recalibrated against a standard diffuse white disk. The collected raw spectral data was evaluated using “The Spectral Geologist” (TSG) software version 8 to determine peak parameters such as wavelength, width, and depth of absorption features.

3.7 Thermal Ionization Mass Spectrometry Re-Os Geochronology of Molybdenite

One sample of a molybdenite-bearing quartz vein was sent for analysis at the Crustal Re-Os Geochronology Laboratory at the University of Alberta. Methods used for molybdenite analysis are described in detail by Selby & Creaser (2004). Areas of the sample with visible molybdenite were removed, and preparation of a molybdenite mineral separate was made by metal-free crushing and sieving followed by magnetic and gravity concentration methods. The ^{187}Re and ^{187}Os concentrations in

molybdenite were determined by isotope dilution mass spectrometry using carius-tube, solvent extraction, anion chromatography, and negative thermal ionization mass spectrometry techniques. A mixed double spike containing known amounts of isotopically enriched ^{185}Re, ^{190}Os, and ^{188}Os analysis was used (Markey et al., 2007). Isotopic analysis used a ThermoScientific Triton mass spectrometer by Faraday collector. Total procedural blanks for Re and Os are less than <3 picograms and 2 picograms, respectively, which were insignificant in comparison to the Re and Os concentrations in molybdenite. The Reference Material 8599 Henderson molybdenite (Markey et al., 2007) was routinely analyzed as a standard, and during the past 8 years returned an average Re-Os date of 27.78 ± 0.07 Ma (n=37), indistinguishable from the Reference Age Value of 27.66 ± 0.1 Ma (Wise and Watters, 2011). The 187Re decay constant used is 1.666e11.a-1 (Smoliar et al., 1996).

3.8 Laser Ablation Induced Coupled Plasma Mass Spectrometry Garnet U-Pb Geochronology

The LA-ICP-MS U–Pb age determination and trace element analyses of garnet were performed at the Key Laboratory of Marine Resources and Coastal Engineering, Sun Yat-Sen University, China. A 60 µm spot size was used with 5 J/cm^2 energy density and 5 Hz repetition rate with each analysis consisting of a 20s background measurement (laser-off) followed by 45s of data acquisition (Li et al., 2022). Data reduction was performed using iolite 4 (Paton et al., 2011), 'U–Pb Geochronology' was chosen as the data reduction scheme with 'gaps between samples' selected as the 'beam second method'. Garnet standards PL57 and GRT-Mali were used to calibrate the results. A correction in the data was performed by measuring the ^{204}Pb, which is not produced by radioactive decay, normalizing the decay equation with ^{204}Pb helps to compensate for common lead in the garnet. IsoplotR software (Ludwig, 2003) was used for the construction of the concordia/intercept diagram, isochrons, weighted mean calculations and final error calculations.

3.9 Thermal Ionization Mass Spectrometry Zircon U-Pb Geochronology

TIMS U-Pb zircon grain analysis was undertaken at the Pacific Centre for Isotopic and Geochemical Research at the University of British Columbia. Three felsic samples from rhyolitic flows and intrusive feldspar quartz porphyry units were sent to obtain an age of formation of these units. Zircons were removed from the sample using a Rhino jaw crusher, a Bico disk grinder equipped with ceramic grinding plates, and a Wilfley wet shaker table equipped with a machined plexiglass top. This was followed by conventional heavy liquid and magnetic separation using a Frantz magnetic separator after which the zircon grains were then picked out by hand using a binocular microscope. Zircons were analyzed through the use of chemical abrasion thermal ionization mass spectrometry (CA-TIMS) using a VG54R TIMS instrument which employs an analogue single daly collector. U and Pb were loaded together on an outgassed zone-refined Re filament and run separately in peak-hopping mode. The elements were spiked with a UBC ^{205}Pb-$^{233\text{-}235}U$ isotopic tracer. Data reduction was done with U-Pbr, an Excel-based routine based on the error estimate algorithms published by Schmitz and Shoene (2007). Concordia diagrams were constructed from the $^{206}Pb/^{238}U$ and $^{207}Pb/^{235}U$ data through the use of IsoplotR software developed by Ludwig (2003).

3.10 Sm-Nd isotopes

Nine samples were analyzed for Sm-Nd isotope values selected from a range of lithologies showing unique REE patterns. Two samples from the felsic volcanic and intrusive rocks, three mafic basalts, and four ultramafic samples were analyzed. Samples were prepared in the clean lab of the Isotope Geochronology and Geochemistry Research Centre (IGGRC) at Carleton University. Rock powders were doped with a ^{148}Nd-^{149}Sm mixed spike before being dissolved in a mixture of concentrated HF and HNO_3. Sample solutions were then dried down and the residues were sequentially dissolved in 7 M HNO_3 and in 6 M HCl and were finally dried. The sample residues were dissolved in 1.5 ml of 2.5 M HCl and

were loaded onto 14 ml Bio-Rad borosilicate glass chromatography columns containing 3 ml of Bio-Rad AG50W-X8 cation exchange resin. Columns were washed with 16 ml of 2.5 M HCl before Sr was eluted in 7 ml of 2.5 M HCl. The columns were then washed with 3.5 ml of 6M HCl before REE were eluted using 9 ml of 6 M HCl. REE fractions were dissolved in 0.26 M HCl and were loaded onto 2 ml prepacked Ln resin columns. Neodymium was eluted using 0.26M HCl, followed by Sm elution using 0.5 M HCl. Neodymium isotope ratios were measured using IGGRC's Thermo-Finnigan Neptune MC-ICP-MS and were normalized against $^{146}Nd/^{144}Nd=0.7219$. $^{143}Nd/^{144}Nd$ ratios were normalized for offsets using bracketing JNdi-1 average values against an average JNdi-1 value 0.512100 of IGGRC's Thermo-Finnigan Triton TIMS (Tanaka et al., 2000). The resulting epsilon Nd values were recalculated using the revised age of formation of 2980 Ma for the felsic volcanic and intrusive rocks determined by zircon U-Pb geochronology.

3.11 Sulphur δ^{34} Isotopes

Sulphur isotope analysis was performed at the Facility for Isotope Research at Queen's University. Seventeen core samples were selected that had large visible sulphide grains on them that could be individually drilled. The sample was placed over a foil collection sheet and a small Dremel was used to extract powders from individual sulphides. The Dremel was cleaned between each use with ethanol and a new foil sheet was used with each sample. Twenty-three different sulphide powders were sampled with four pyrite, 11 pyrrhotite, seven chalcopyrite, and one arsenopyrite powder sample analyzed. The powders were then sent to the facility at Queen's where they were weighed into tin capsules and the sulfur isotopic composition measured using a MAT 253 Stable Isotope Ratio Mass Spectrometer coupled to a Costech ECS 4010 Elemental Analyzer. $\delta^{34}S$ values were calculated by normalizing the $^{34}S/^{32}S$ ratios in the sample to that in the Vienna Canyon Diablo Troilite (VCDT) international standard. Values are reported using the delta (δ) notation in units of per mil (‰) and were reproducible to within 0.2‰ of the original reading.

4. Results

4.1 Thin Section Descriptions

4.1.1 Metamorphosed pelite psammite schist

The majority of samples consist of schistose biotite-muscovite-garnet-rich rocks. Biotite and muscovite lamellae are interbedded with quartz and occasionally feldspars. The micas occur in foliated bands, often wispy and anastomosing through the quartz dominated lamellae (Fig. 4.1A). Interstitial isolated biotite or muscovite grains occur with the quartz grains and are orientated sub-parallel to oblique to the general trend of the lamellae foliation. The micas in the sample range from biotite to muscovite and make up as little as 15% to over 50% of the sample and range in size between 100-500 µm. The interstitial grains are commonly finer than those occurring within lamellae. These lamellae often display deformed textures, as well as foliation that bends around porphryoblastic phenocrysts in the sample (Fig. 4.1 B, C, D).

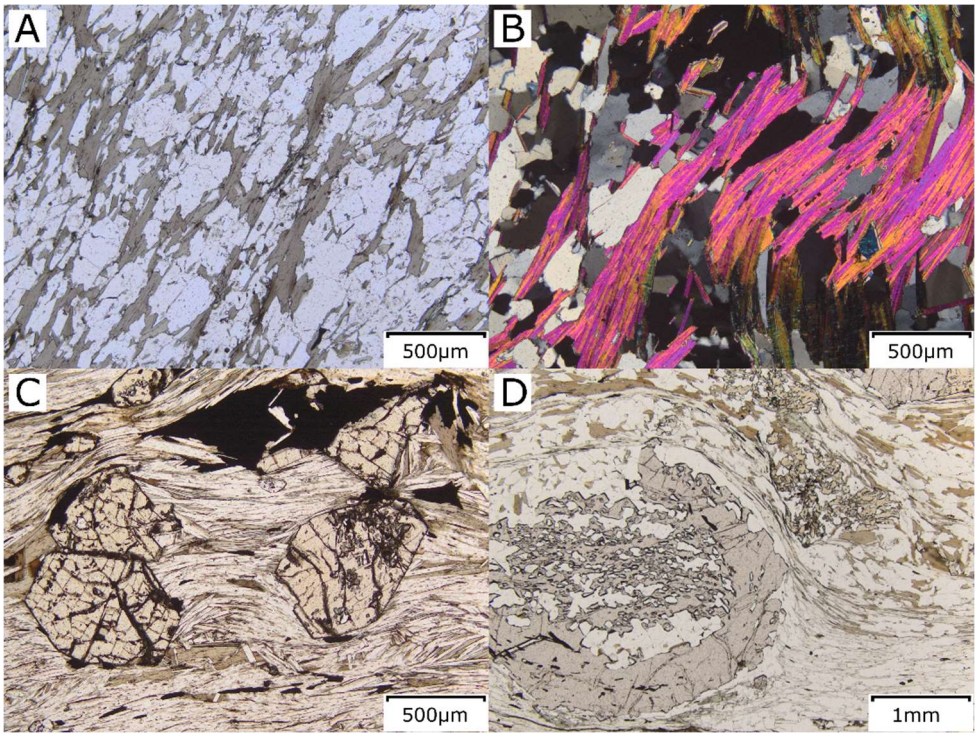

Figure 4.1. (A) Anastomosing biotite lamellae around quartz (PPL, DT058). (B) Folded muscovite lamellae (XPL, DT022). (C) Biotite muscovite lamellae folding around staurolite phenocrysts (PPL, DT024). (D) Muscovite lamellae folding around a garnet phenocryst (PPL, DT099).

The quartz grain boundaries vary from irregular bulging grains to straight edges meeting at triple points. Feldspar grains occur intermittently alongside the quartz, occasionally showing polysynthetic or tartan twinning, but often displaying no twinning at all (Fig. 4.2). When no twinning was visible the feldspars are distinguishable from the quartz grains only due to the dusty surface of the feldspar grains caused by sericite alteration.

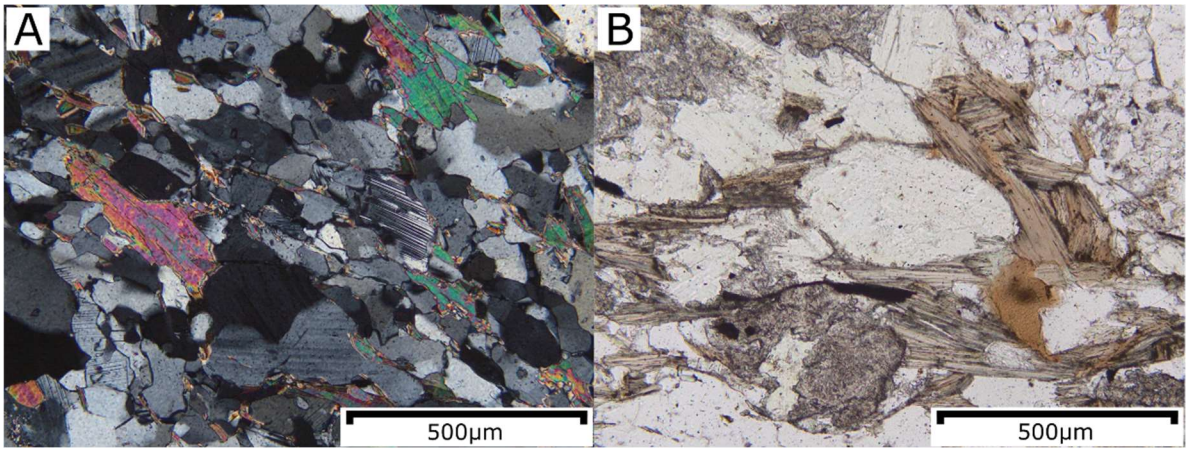

Figure 4.2. (A) Polysynthetic twinning visible in plagioclase grains present alongside quartz in the schist (XPL, DT042). (B) Altered dusty appearance of feldspar grains (PPL, DT039)

Porphryoblastic grains of garnet and staurolite occur within many of the samples. The garnets range in size from 50 µm to over 2 cm and make up as little as 1% to just over 50% of the samples. Staurolite is generally smaller than the garnets ranging in size from 50 µm to 1 cm in size and comprise up to 30% of the content of the samples. The garnet and staurolite crystals are often skeletal and highly fractured, with the general form of the original grains being discernable from the remaining fragments (Fig. 4.3).

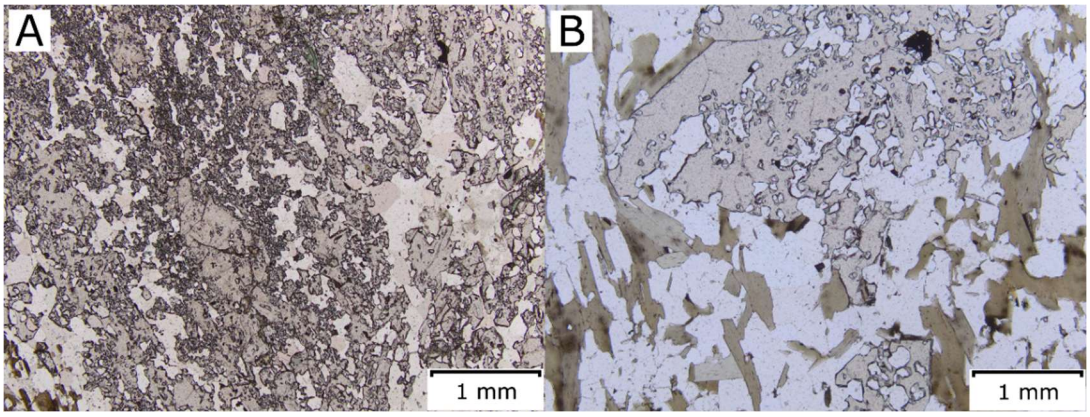

Figure 4.3. (A) Skeletal fragmented garnet (PPL, DT054). (B) Skeletal fragmented staurolite (PPL, DT056).

The garnets often display zoning with a darker red etched interior surrounded by a clearer rim (Fig. 4.4A). The garnet and staurolite grains are fractured and, in some instances, have been replaced by chlorite (Fig. 4.4B). Chlorite is ubiquitous throughout all the samples, consisting of between 2% up to 16% of the sample. Chlorite always appears to be late in occurrence, as a pseudomorph replacement of biotite, especially when located adjacent to staurolite (Fig. 4.4 B,C,D).

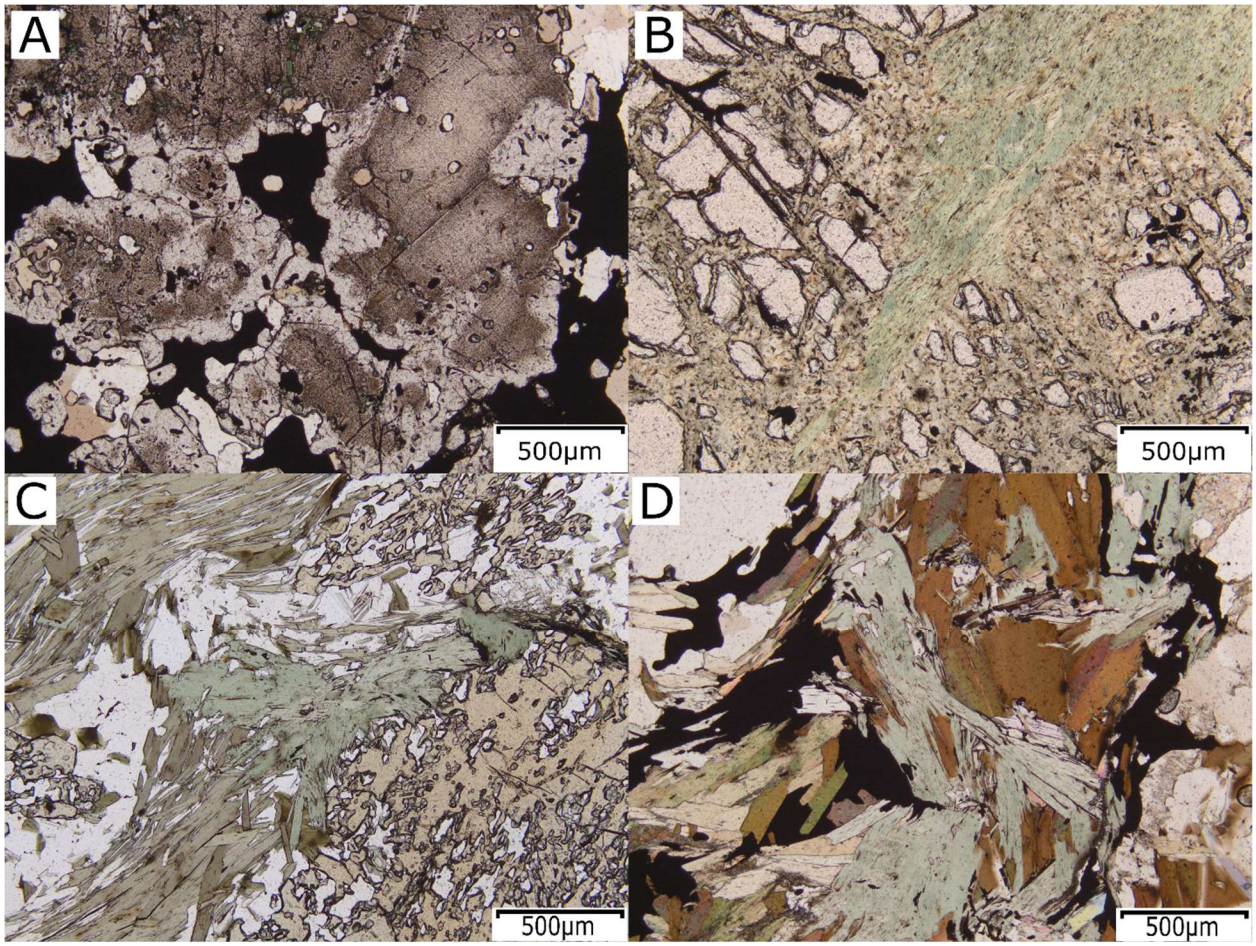

Figure 4.4. (A) Garnet zonation showing the darker etched interior and lighter rim (PPL DT023). (B) Fragmented garnet infilled and replaced by chlorite (PPL DT003). (C) Biotite altered to chlorite around the rim of staurolite (PPL DT050B). (D) Biotite replaced by chlorite (PPL DT022).

Tourmaline is found in many of the schist samples, often as a trace mineral with a few isolated euhedral crystals of 20-200 µm in size. When viewed down the C axis the tourmaline displays zonation with colouration from light to dark green and brown (Fig. 4.5A). In some samples the tourmaline can

make up as much as 16% of the sample, forming masses of tourmaline radiating out from a central point that are up to 1000 µm in size (Fig. 4.5B).

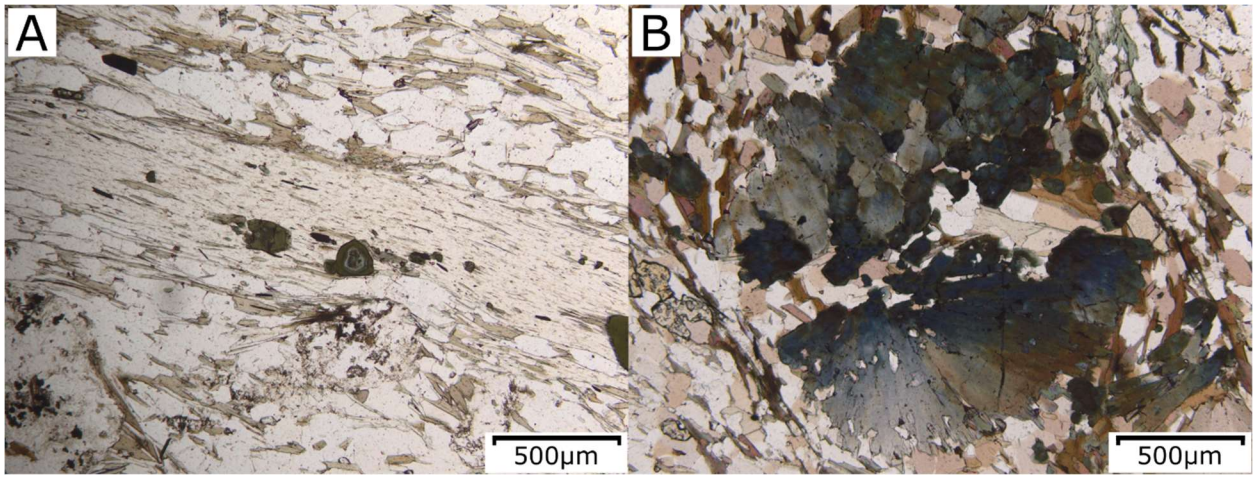

Figure 4.5. (A) Euhedral tourmaline with zoning within a biotite muscovite schist (PPL DT024). (B) Radiating coarse tourmaline in a biotite quartz schist (PPL DT088).

The schist samples contain other minor to trace minerals, including zircon. The zircon makes up less than 1% of the samples and occur as small grains of 1-25 µm in size. The zircons are small but most easily identifiable by the destruction halo formed in the micas containing zircons (Fig. 4.6 A). Oxides are common, but in small quantities, from trace to up to 5% of the sample. Minor magnetite is found in five of the samples as subhedral grains of 50-500 µm in size and forming rough square to triangular shapes with eroded edges (Fig. 4.6B). Minor ilmenite was found in 24 samples, as 10-200 µm irregular lath shaped grains most commonly occurring within chlorite crystals, often trending along foliation and within the interface between biotite and chlorite (Fig. 4.6B, D). Ilmenite also occurs as small inclusions or exsolutions within staurolite grains.

Sulphides in the Lundmark Akow area range from minor fine-grained diagenetic pyrite up to semi-massive to massive chalcopyrite, sphalerite, pyrrhotite horizons. Almost all of the analysed schists contain some sulphide, most often as fine-grained subhedral pyrite or pyrrhotite grains disseminated throughout the rock. The sulphide is interpreted to be diagenetic in nature due to its textural

characteristics and shape and the dominance of Fe sulphide over any other base metal sulphides. However, in samples with high garnet and staurolite contents, stringer mineralization is present with chalcopyrite veinlets occurring along with pyrrhotite. Sulphides in the schists consist of pyrrhotite, pyrite, chalcopyrite, and arsenopyrite as discrete grains and small veinlets. Sulphide grains are irregular, occasionally subrounded to lath shaped to fit interstitially between micas and quartz grains of the schist (Fig. 4.7A, B). Pyrrhotite is the most common sulphide that occurs in the rocks, making up 1-4% of most of the schists and occurs as small 20-100 µm sized grains or as coarser 200-500 µm crystals in veinlets.

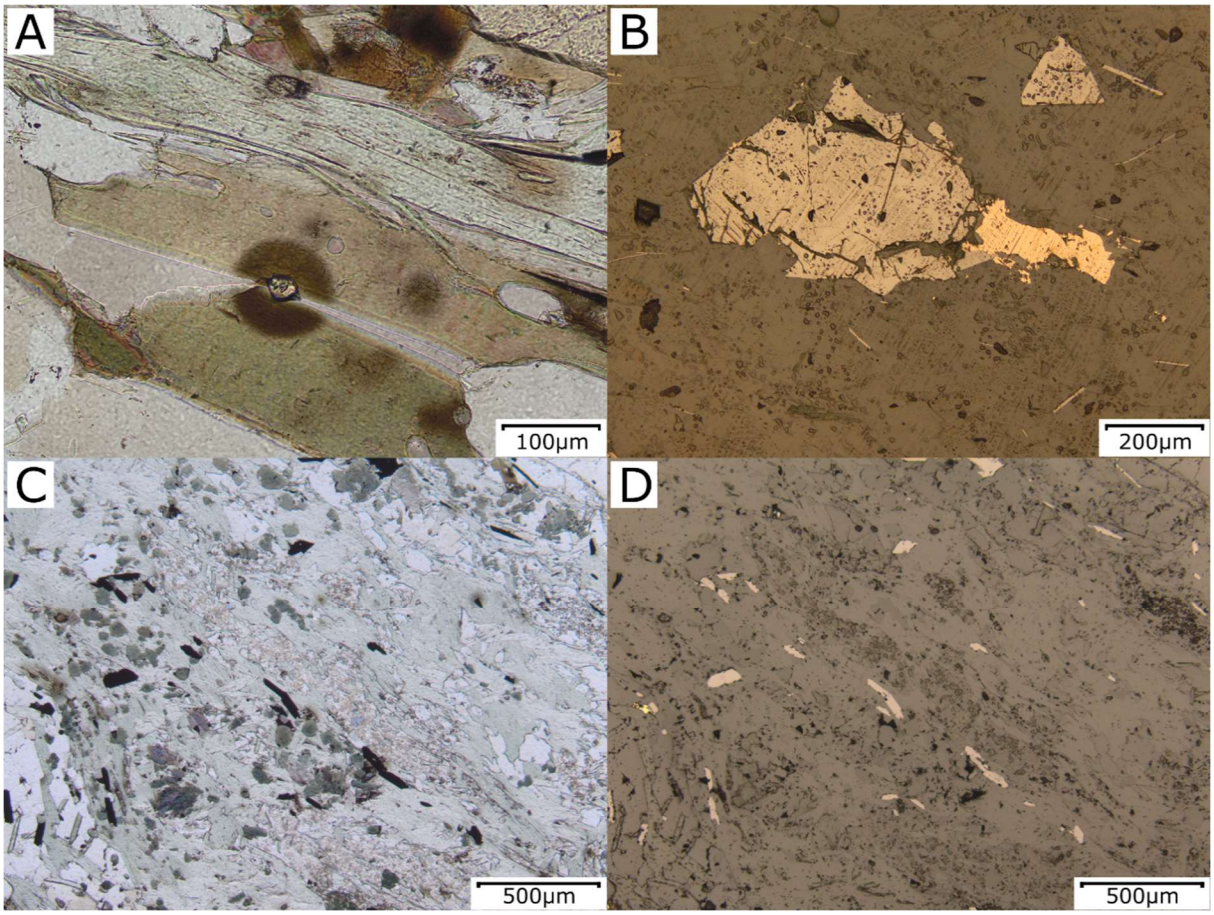

Figure 4.6. (A) Zircon with destructive halo in biotite (PPL, DT001). (B) Magnetite grain alongside pyrrhotite (RL, DT120A). (C) Ilmenite laths in a chlorite biotite schist (PPL, DT017). (D) Ilmenite laths in a chlorite biotite schist (RL, DT017).

Pyrrhotite often occurs with chalcopyrite, usually with irregular rounded blebs of chalcopyrite hosted within the pyrrhotite or vice versa (Fig. 4.7C). Chalcopyrite is the second most common sulphide

making up 1-3% of most of the samples. Pyrrhotite and chalcopyrite both show exsolution with troilite from pyrrhotite and cubanite from chalcopyrite (Fig. 4.7C, D). Pyrite frequently occurs in trace quantities but can make up to 2% of some samples. Late pyrite grains are often euhedral to subhedral. Whereas early irregular pyrite is altered to pyrrhotite leaving only small patches of remnant pyrite.

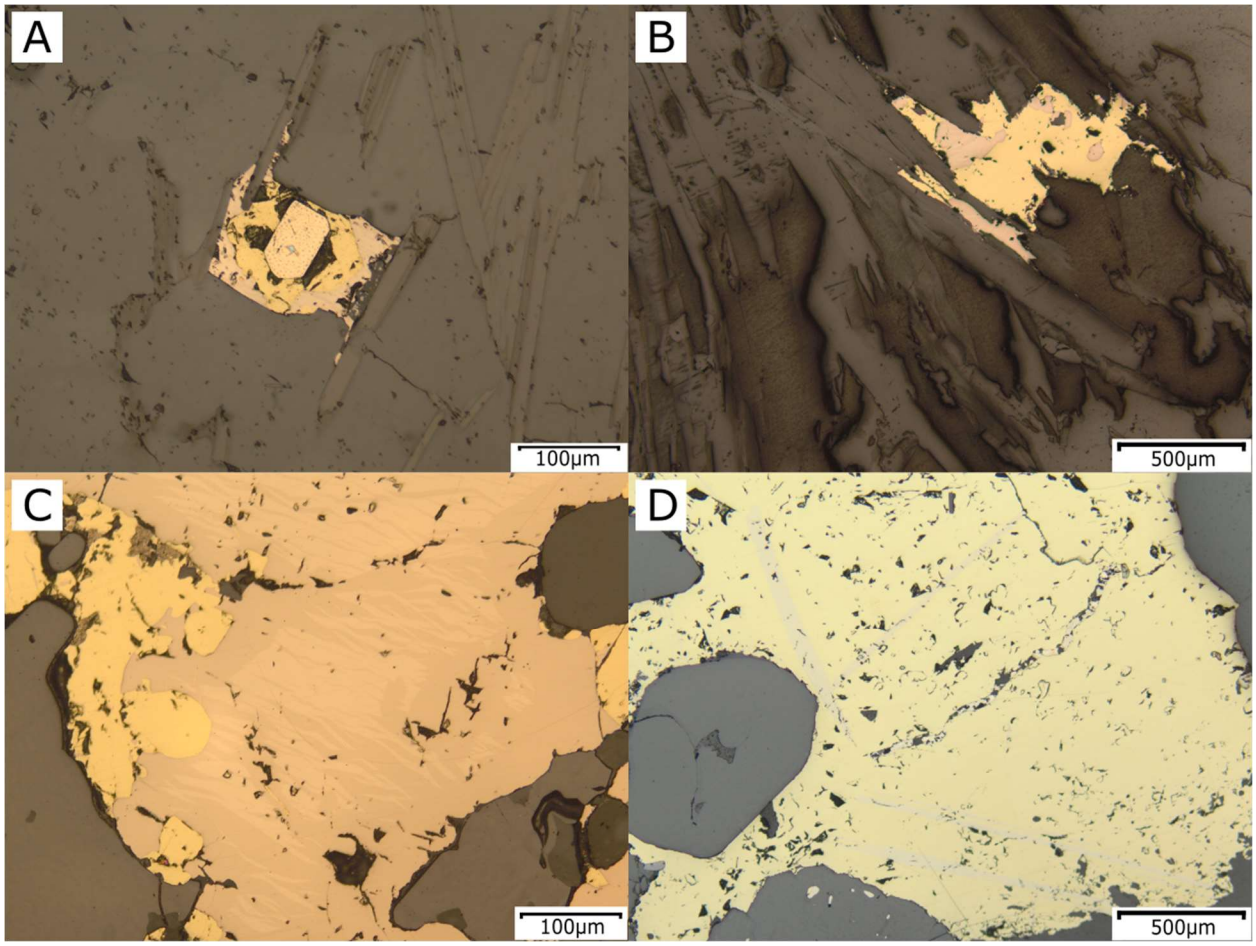

Figure 4.7. (A) Grain of pyrite within chalcopyrite within pyrrhotite in a schist (RL, DT028). (B) Chalcopyrite with pyrrhotite (RL, DT069). (C) Rounded irregular contact between pyrrhotite and chalcopyrite, pyrrhotite also displays flame like exsolutions of troilite (RL, DT050). (D) Tan coloured lath shaped exsolutions of cubanite within a large chalcopyrite (RL, DT003).

In samples with veinlets of chalcopyrite and pyrrhotite there is often a net texture infilling fractures and surrounding fragments of garnet (Fig. 4.8A, B, C, D). In some instances, the sulphides occur as small blebs possibly representing inclusions within garnet (Fig. 4.8E, F). Several unique minerals are found in minor quantities in some of the schist samples. Cobaltite

was found in sample DT017, forming euhedral to subhedral grains of 40-250 µm. Arsenopyrite also occurs in a few samples, often as individual euhedral to subhedral grains of 200-800 µm in size.

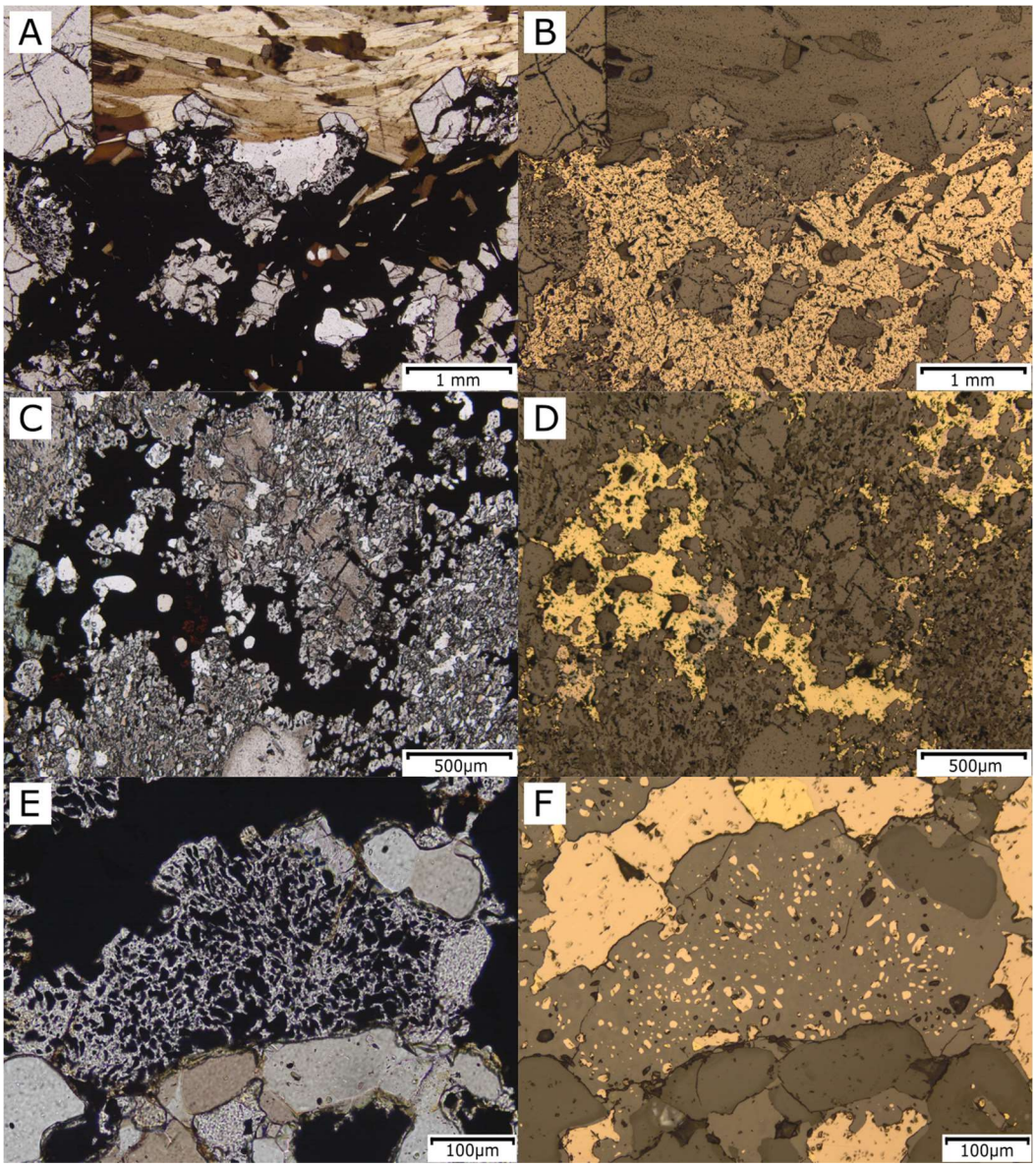

Figure 4.8. (A) Pyrrhotite veinlet in garnet biotite schist (PPL, DT050A). (B) Pyrrhotite veinlet in garnet biotite schist (RL, DT050A). (C) Chalcopyrite, pyrrhotite, sphalerite veinlets in altered garnet with green gahnite (PPL, DT053). (D) Chalcopyrite, pyrrhotite, sphalerite veinlets in altered garnet with green gahnite (RL, DT053). (E) Garnet with pyrrhotite, chalcopyrite inclusions (PPL, DT050B). (F) Garnet with pyrrhotite, chalcopyrite inclusions (RL, DT050B)

4.1.2 Massive sulphide horizons

Massive sulphide horizons also occur within the schist, with widths ranging from 5 to 50 cm and consisting predominantly of chalcopyrite and pyrrhotite with sphalerite and minor quantities of galena and pyrite. The massive sulphide horizons are not associated with any significant alteration halos and no obvious feeder zone was observed. Six individual massive to semi-massive sulphide horizons occur within the study area. Two of the horizons are pyrite-dominated (DT117 and DT118 from drill hole 19-10). Whereas the other four are pyrrhotite-dominated (DT119 from drill 17-01, DT102 and DT034 from drill hole 19-04, and DT009 from drill hole 16-02).

The pyrite dominated sulphide horizons occur within a host rock sequence consisting of a muscovite biotite schist rich in quartz and feldspar. The feldspar has a weathered appearance with sericite alteration of the feldspar grains. The schistose nature of the host rocks is difficult to discern due to fracturing and replacement of host rock fabric by sulphide (Fig. 4.9B, C, E, G). Quartz rich blebs 1-3 cm in size are hosted within the matrix of sulphide.

Sulphides are diverse with an average of 25% pyrite, 8-10% pyrrhotite, 5-15% chalcopyrite, 5% sphalerite. Sample DT118 has 5% arsenopyrite while sample DT117 has up to 1% galena. Pyrite and arsenopyrite occur as euhedral to subhedral isolated grains suspended in a groundmass of pyrrhotite and chalcopyrite (Fig. 4.9A, D, H). Pyrite grains vary in size from 50 µm up to 3 mm whereas arsenopyrite ranges from 200-500 µm. The chalcopyrite, pyrrhotite, sphalerite, and galena appear to have formed coevally with irregular rounded boundaries (Fig. 4.9A, D, F). The chalcopyrite forms a net textured groundmass in which it is difficult to discern any individual grains, but masses of chalcopyrite are between 50 µm up to 15 mm in size. Pyrrhotite ranges in size from 100 µm up to 3 mm, and individual grains can only be discerned by differing anisotropy under cross polars. Sphalerite forms irregular rounded grains in the net textured sulfide matrix, with size ranging from 50-800 µm. Chalcopyrite disease is present in some of the sphalerite samples showing blebs of chalcopyrite hosted in the

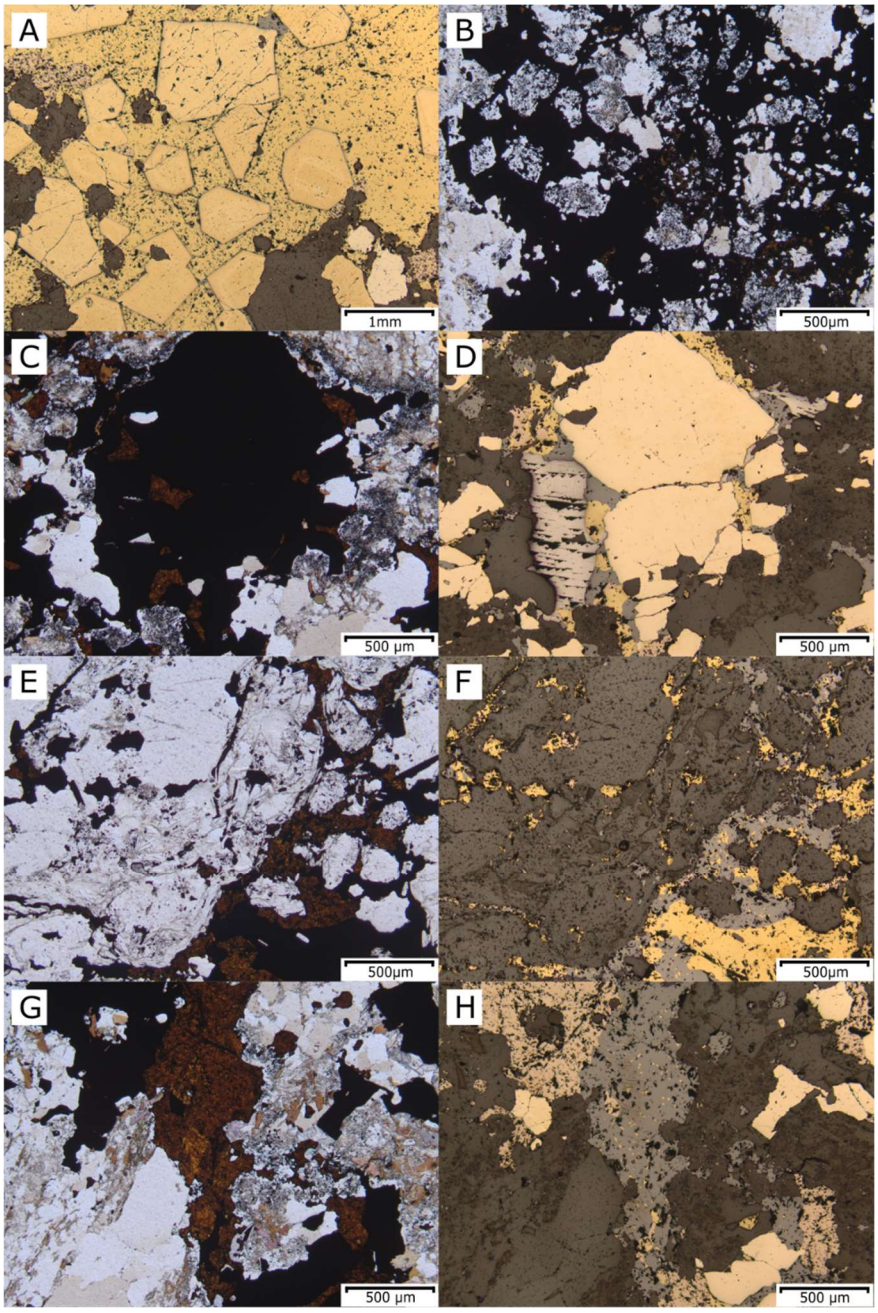

Figure 4.9. (A) Euhedral pyrite and minor arsenopyrite in a matrix of chalcopyrite and pyrrhotite (RL, DT118A). (B) Sulphides occurring alongside a host rock matrix of quartz and sericite altered feldspar (PPL, DT118B). (C) Sulphides occurring alongside the host rock matrix of quartz and sericite altered feldspar (PPL, DT117). (D) Subhedral pyrite occurring within a matrix of chalcopyrite, pyrrhotite, sphalerite, and galena (RL, DT117). (E) Sulphides occurring alongside the host rock matrix of quartz and sericite altered feldspar (PPL, 118B). (F) Chalcopyrite and sphalerite with rounded irregular boundaries within a quartz and sericite altered feldspar host rock (RL, 118B). (G) Sulphides occurring alongside the host rock matrix of quartz, sericite altered feldspar, and biotite (PPL, DT117). (H) Sphalerite and pyrrhotite occurring alongside each other with chalcopyrite exsolutions occurring in the sphalerite due to chalcopyrite disease. Subhedral pyrite grains occur suspended in the sphalerite chalcopyrite matrix as well as within the quartz feldspar host rock matrix (RL, DT117).

sphalerite (Fig. 4.9G, H). Galena forms a few small grains from 50-300 µm with distinctive triangular pitting visible (Fig. 4.9C, D).

In the pyrrhotite dominated horizons found in drill holes 19-04, 17-01, and 16-02 the sulphides consist of 28-60% pyrrhotite, 2-19% chalcopyrite, and up to 4% pyrite. Where chalcopyrite and pyrrhotite occur together they show irregular rounded grain boundaries suggesting coeval emplacement. The pyrrhotite grains range in size from 200 µm up to 3 mm whereas chalcopyrite ranges from 50-1000 µm. Pyrite occurs as euhedral to subhedral crystals suspended in the sulphide matrix ranging in size from 100-700 µm. The sulphide horizons occur within schistose host rocks and appear to have replaced the host rock with suspended host rock fragments such as biotite and amphibole occurring within the sulphide matrix (Fig. 4.10).

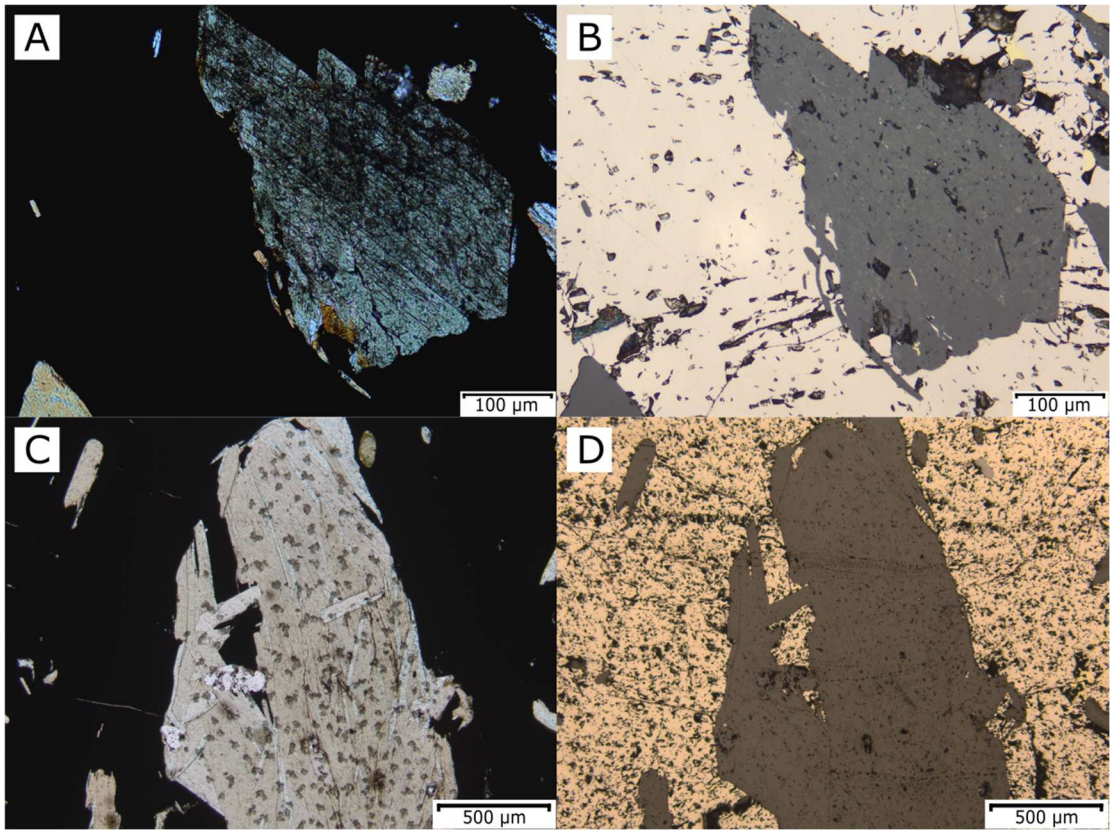

Figure 4.10. (A) Amphibole crystal suspended in pyrrhotite matrix (PPL, DT102). (B) Amphibole crystal suspended in pyrrhotite matrix (RL, DT102). (C) Host rock fragment of biotite suspended in pyrrhotite matrix (PPL, DT102). (D) Host rock fragment of biotite suspended in pyrrhotite matrix (RL, DT102).

Other minerals occur alongside the sulphides that display evidence of the alteration fluids in the system. Sample DT119 contains up to 8% andalusite which are rimmed by chlorite (Fig. 4.11). Tourmaline is present in samples DT119, DT034, DT009 and makes up between 27-40% of these samples.

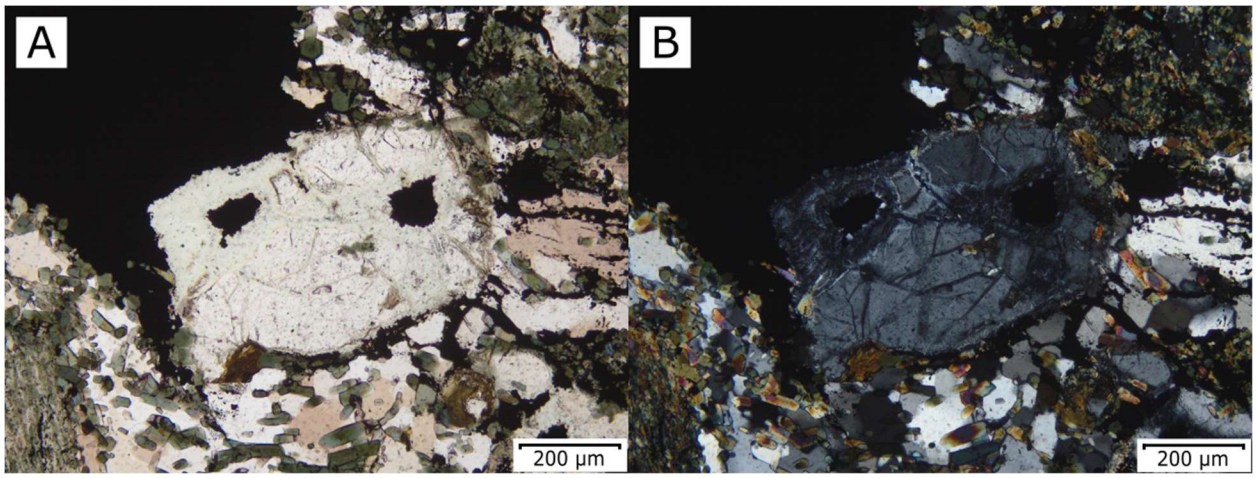

Figure 4.11. (A) Andalusite rimmed by chlorite adjacent to sulphide, quartz, tourmaline (PPL, DT119). (B) Andalusite rimmed by chlorite adjacent to sulphide groundmass, quartz, tourmaline (XPL, DT119).

The tourmaline occurs as subhedral to euhedral crystals, as isolated coarse crystals ranging in size from 100-400 µm, or as very fine 5-20 µm tourmaline that form amalgamated blebs which can be up to 8mm in size (Fig. 4.12 A). The tourmaline crystals are suspended in a sulphide matrix of chalcopyrite pyrrhotite and occasional pyrite (Fig. 4.12 B). The tourmaline occasionally forms radiating structures which were infilled by sulphides interstitially between the tourmaline (Fig. 4.12 C, D). Evidence for later remobilization of sulphides is presented in Figure 4.12 E, F where a tourmalinite bleb suspended in sulphides has been fractured and then infilled by chalcopyrite and pyrrhotite, suggesting a complex history of tourmaline and sulphide deposition.

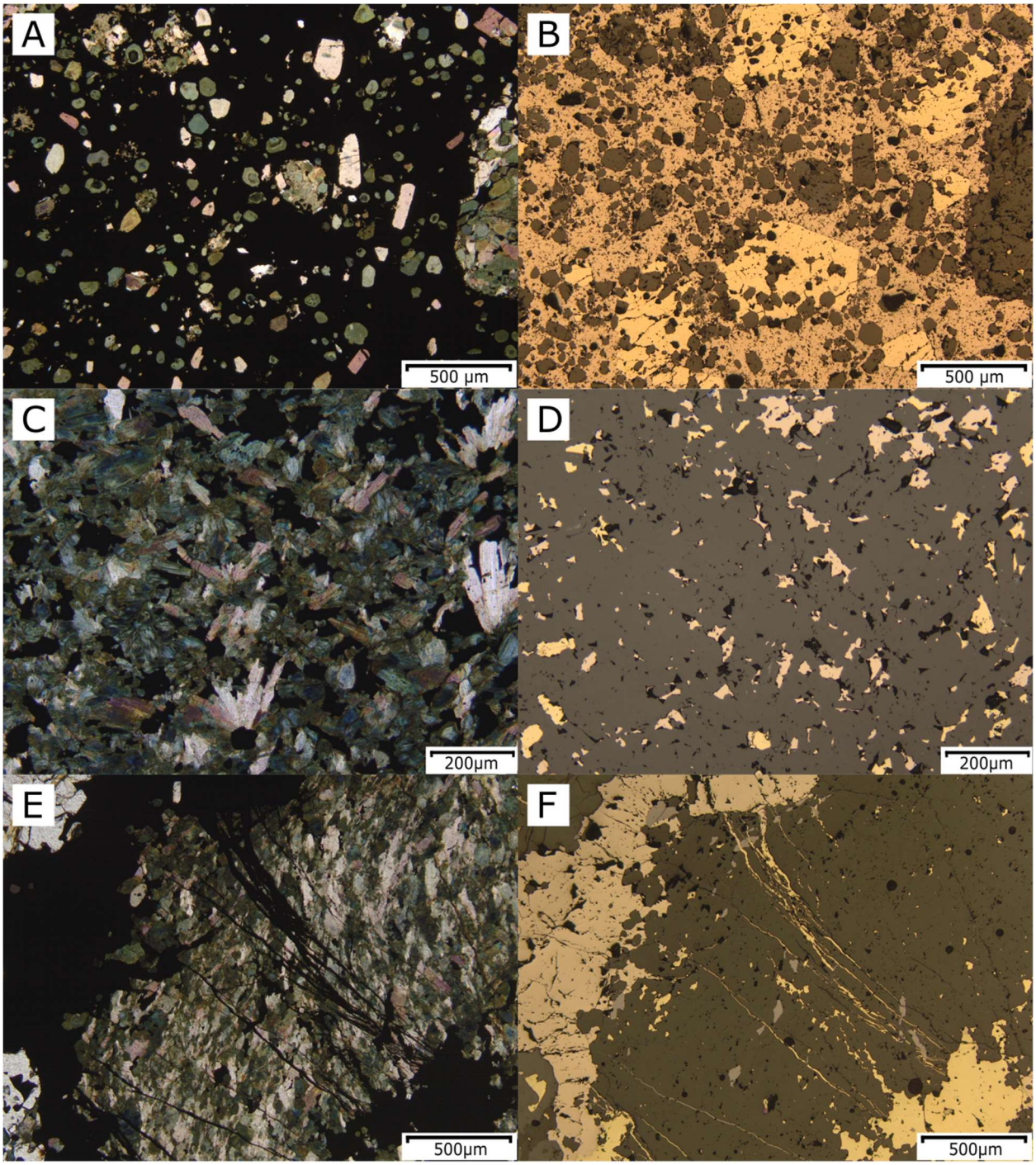

Figure 4.12. (A) Tourmaline crystals suspended in a pyrrhotite, pyrite matrix (PPL, DT034). (B) Tourmaline crystals suspended in pyrrhotite, pyrite matrix (RL, DT034). (C) Radiating tourmaline growths infilled by interstitial pyrrhotite and chalcopyrite (PPL, DT009). (D) Radiating tourmaline growths infilled by interstitial pyrrhotite and chalcopyrite (RL, DT009). (E) Fractured tourmaline blebs infilled by chalcopyrite and pyrrhotite (PPL, DT009). (F) Fractured Tourmaline blebs infilled by chalcopyrite and pyrrhotite (RL, DT009).

4.1.3 Mafic rocks

Three mafic thin sections were analysed and display an amphibolite grade metamorphic assemblage. Amphiboles make up the bulk of the samples ranging from 40-92%. The amphiboles range in size from as small as 20 µm up to 600 µm, have a green to brown colour, and in well developed grains displays a diagnostic 56-124° cleavage. In samples DT113 and DT076 the amphibole occurs as foliated overlapping layers of interwoven amphibole separated only by the occasional calcite grain which make up between 2-10% of the samples or rarely quartz in DT076 (Fig. 4.13 A, B). In sample DT111 most of the amphibole ranges from 50-200 µm except for a coarse amphibole veinlet across the sample where the width of the amphibole reached 600 µm. This sample also consists of around 25% plagioclase feldspar that occur interstitial to the amphibole (Fig. 4.13 C).

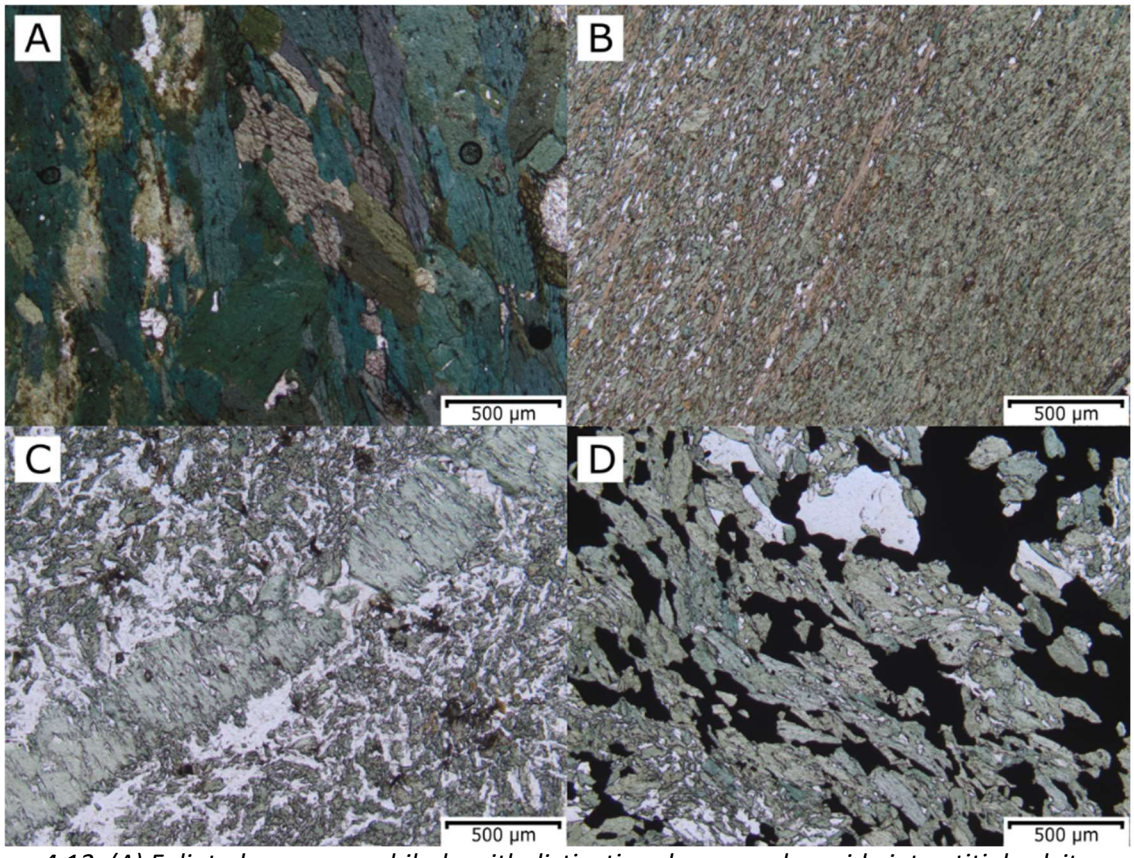

Figure 4.13. (A) Foliated coarse amphibole with distinctive cleavage alongside interstitial calcite grains (PPL, DT113). (B) Fine-grained amphibolite matrix with calcite and lesser quartz grains (PPL, DT076). (C) Amphibole as fine-grained irregular grains and within a coarse amphibole veinlet, occurring with interstitial plagioclase (PPL, DT111). (D) Amphibole with quartz and a chalcopyrite, pyrrhotite veinlet (PPL, DT076).

Quartz is rare within the mafic samples, only occurring in sample DT076 and comprising up to 5% of the sample and occurring likely as a secondary product. It occurs primarily as very small 20-50 µm grains in the amphibole matrix or as a few 200-300 µm grains located next to a sulphide vein (Fig. 4.13D). Biotite is uncommon but does make up to 5% of sample DT111 with biotite grains interstitial to the amphibole, and especially common surrounding a pyrrhotite bleb (Fig. 4.14A). The calcite found in sample DT076 is especially prominent adjacent to the sulphide veinlet, forming crystals up to 500 µm in size (Fig. 4.14B).

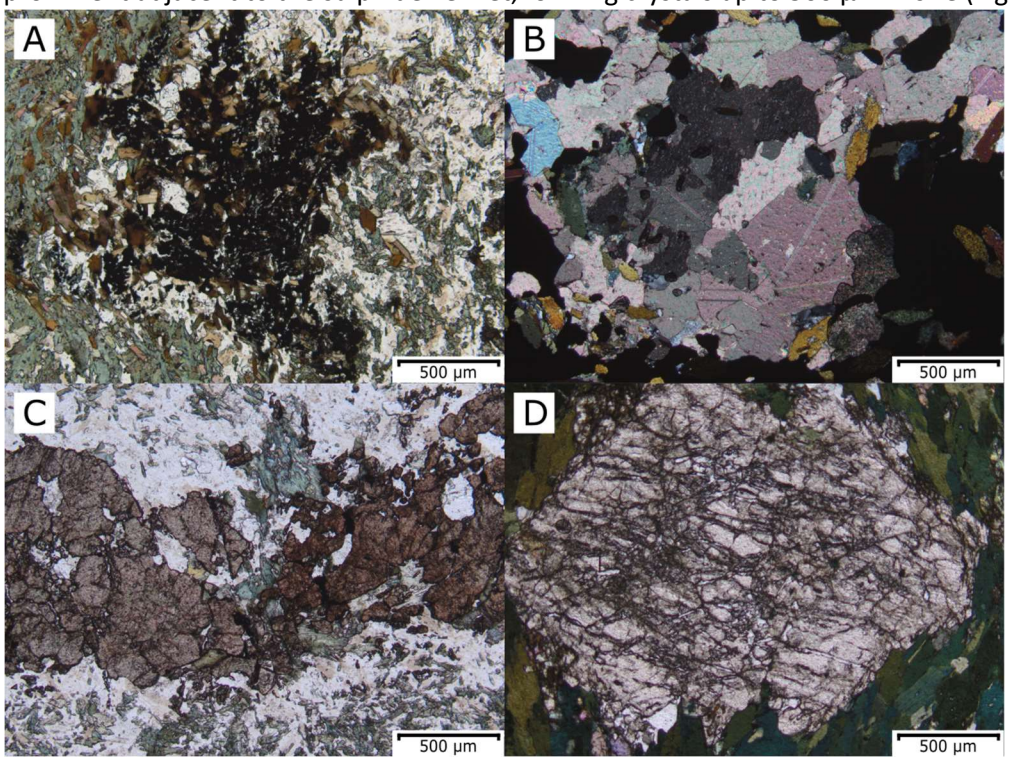

Figure 4.14. (A) Biotite interstitial to amphibole plagioclase matrix near pyrrhotite blebs (PPL, DT111). (B) Calcite within a chalcopyrite, pyrrhotite sulphide vein in amphibolite (XPL, DT076). (C) Garnet within an amphibole plagioclase rich matrix (PPL, DT111). (D) Garnet within a foliated amphibolite (PPL, DT113).

Samples DT111 and DT113 contain porphyroblastic garnets which occur within the amphibolite matrix (Fig. 4.14 C, D). The garnet makes up 3-5% of the samples and range in size from 500 µm to 4 mm. The garnet is often heavily fractured and pitted and the open space is infilled by calcite. The foliation of the amphibole appears to wrap around the porphyroblastic garnet grains.

4.2 Geochemistry

4.2.1 Mafic Rock Samples

Major element geochemistry can be used to subdivide the mafic samples into mafic, ultramafic and lamprophyre samples. The lamprophyre samples are considered ultrapotassic low silica rocks and are thus distinguished by rocks containing greater than 2% K_2O and less than 50% SiO_2. Three samples are classified as lamprophyres under these criteria with K_2O ranging from 2.3-3.4% and SiO_2 between 31.0 to 47.3%. Ultramafic rocks are defined by a Mg# greater than 0.6 and less than 46% silica, two samples fall into this category with Mg# from 0.65 to 0.68 and SiO_2% of 46.3%. The remaining 17 samples are classified as mafic with Mg# ranging from 0.31 to 0.56 and SiO_2 from 44.8 to 53.8%. Plotting the samples in a trace element discrimination diagram shows a spread from sub alkaline to ultra-alkaline with the mafic and ultramafic samples occurring as basalts to alkali basalts and the lamprophyres as foidite (Fig. 4.15).

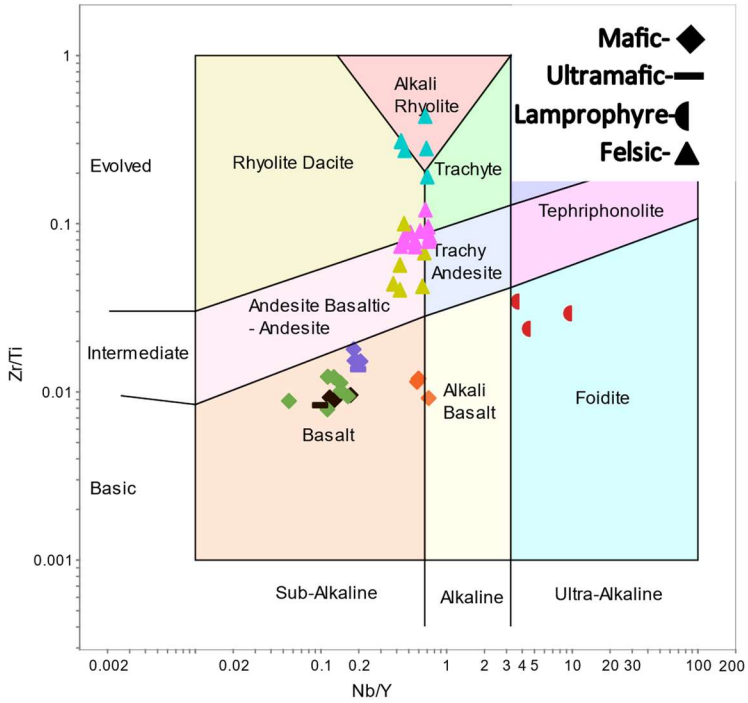

Figure 4.15. Trace element volcanic classification diagram plot of the mafic and felsic rock samples adapted from Pearce (1996). Samples are colour coded to match groups defined by trace element spider diagrams.

Trace element concentrations and behaviour of the mafic samples is displayed through the use of spider diagrams normalized to the primitive mantle values of Sun and McDonough (1989). Five distinct groups of mafic rocks were distinguished. Mafic Group 1 contains three samples that are defined by high LREE enrichment and a very steep LREE trend. The major element content of these samples consists of 31.0-47.3% SiO_2, 5.9-10.2% Al_2O_3, 9.8-14.0% Fe_2O_3, 7.8-21.6% MgO, 2.3-3.4% K_2O, 1.4-1.7% TiO_2, and a LOI of 7-14.55%. The samples have a steep LREE trend with La/Sm_N values between 4.49 to 6.46 (Fig. 4.16). HREE are moderately enriched with Gd/Yb_N values between 6.27 to 10.21. A minor negative Nb anomaly is present with Nb/Nb* values between 0.66 to 0.72. A significant Zr and Hf negative anomaly is present with Zr/Zr* values between 0.35 to 0.52 and Hf/Hf* values of 0.29 to 0.39. A large negative Ti anomaly is present with a Ti/Ti* ranging from 0.21 to 0.24.

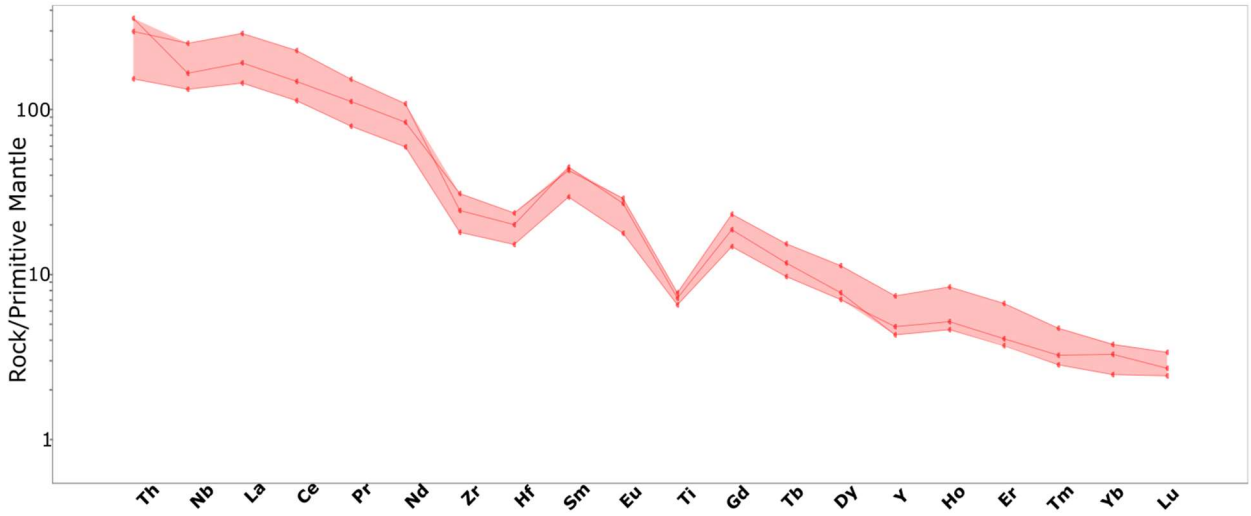

Figure 4.16. Spider diagram of Mafic group 1. Normalized to primitive mantle values of Sun and McDonough (1989).

Mafic group 2 is comprised of three samples (Fig. 4.17). The major element content of these samples consists of 47.7-49.2% SiO_2, 6.6-7.7% Al_2O_3, 15.6-16.0% Fe_2O_3, 13.5-16.7% MgO, 0.1-0.5% K_2O, 0.9-1.0% TiO_2, and a LOI of 1.0-1.5%. This group is characterized by moderately enriched LREE with

La/Sm_N values from 1.86 to 2.07 and weakly fractionated HREE with Gd/Yb_N values between 1.99 and 2.02.

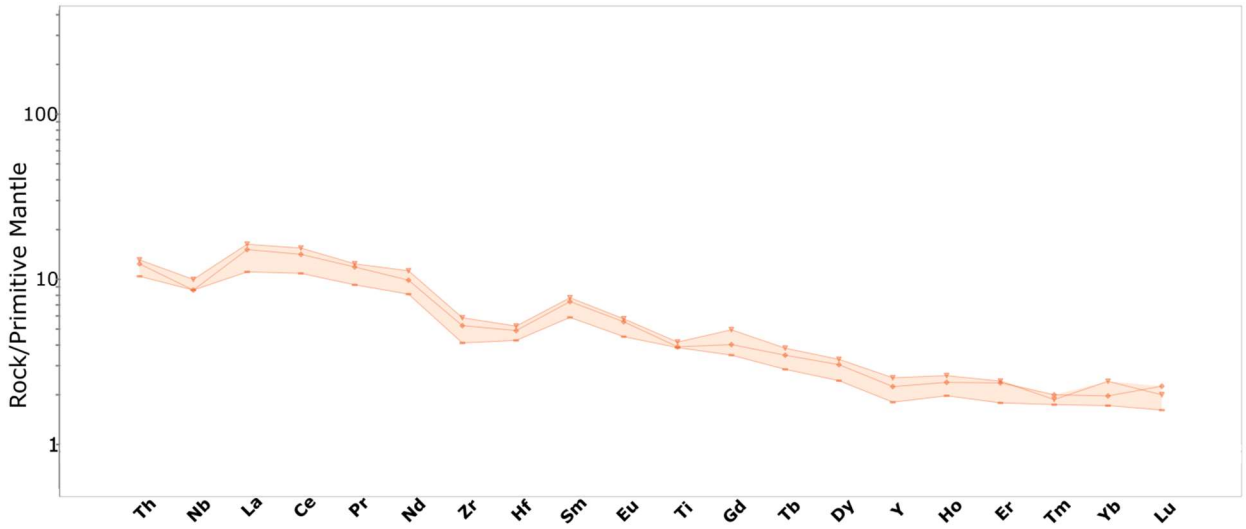

Figure 4.17. Spider diagram of the Mafic group 2 samples. Normalized to primitive mantle values of Sun and McDonough (1989).

A weak negative Nb anomaly is present with Nb/Nb* values ranging between 0.54 and 0.76. A moderate negative Zr and Hf anomaly is present with Zr/Zr* values between 0.60 and 0.63 and Hf/Hf* values between 0.56 and 0.62. A minor negative Ti anomaly is present with Ti/Ti* values between 0.68 and 0.86.

Five samples comprise mafic group 3 (Fig. 4.18) with major element content of these samples consisting of 46.3-51.7% SiO_2, 6.3-11.3% Al_2O_3, 11.2-12.6% Fe_2O_3, 10.4-21.1% MgO, 0.2-0.4% K_2O, 0.3-0.6% TiO_2, and a LOI of 1.1-4.8%. This group is characterized by a moderate LREE enrichment defined by La/Sm_N values between 1.93 to 2.62 and with a nearly flat HREE with Gd/Yb_N values between 1.08 to 1.24. A large negative Nb anomaly is present with Nb/Nb* values between 0.21 to 0.34. A minor negative Ti anomaly is present with Ti/Ti* values between 0.66 to 0.78.

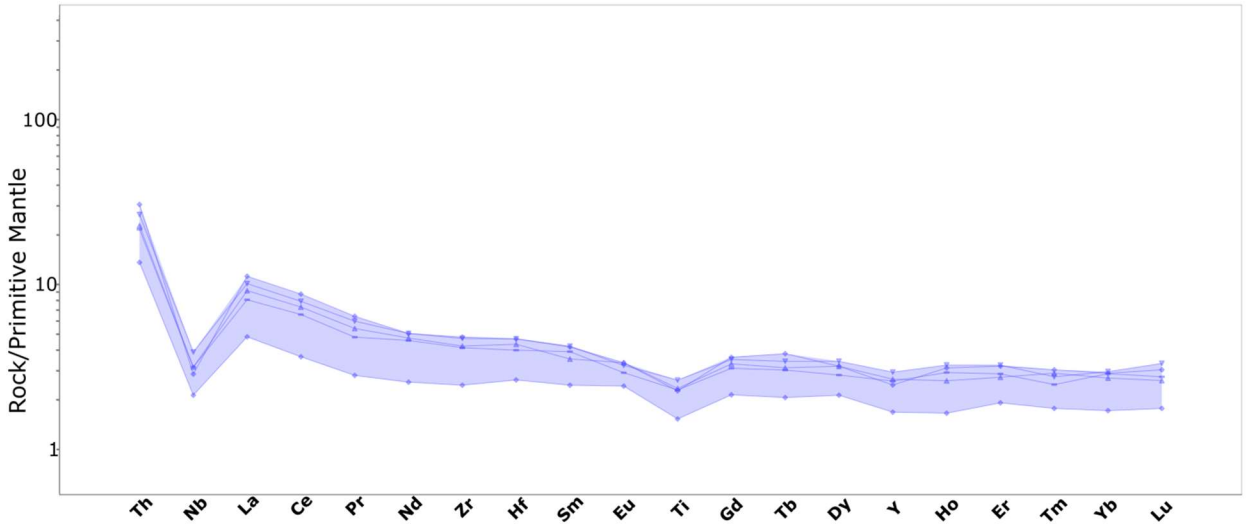

Figure 4.18. Spider diagram of the Mafic group 3 samples. Normalized to primitive mantle values of Sun and McDonough (1989).

Seven mafic samples comprise Mafic group 4 (Fig. 4.19) with the major element content of these samples consisting of 44.8-53.9% SiO_2, 11.4-15.1% Al_2O_3, 12.3-20.9% Fe_2O_3, 6.7-9.4% MgO, 0.2-1.2% K_2O, 0.4-1.1% TiO_2, and a LOI of 0.5-1.0%. The samples have weakly enriched LREE with La/Sm_N values between 1.03 to 1.66. HREE have a flat to mildly positive slope with Gd/Yb_N values ranging from 0.68 to 1.13. A moderate negative Nb anomaly is present with Nb/Nb* values between 0.36 to 0.73. A minor Ti anomaly is present with a Ti/Ti* value between 0.76 to 1.06.

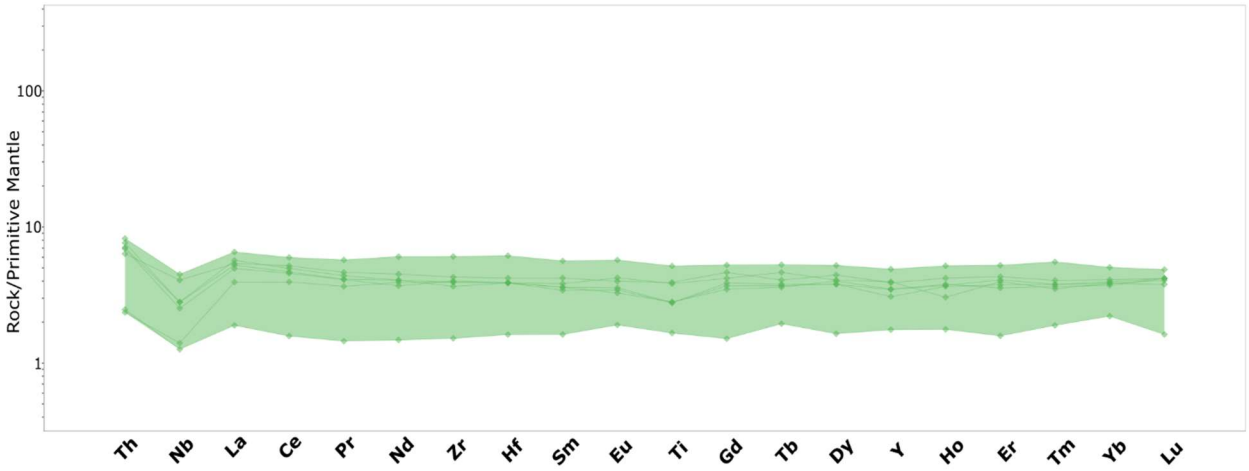

Figure 4.19. Spider diagram of the Mafic group 4 samples. Normalized to primitive mantle values of Sun and McDonough (1989).

The final four samples are placed into mafic group 5 (Fig. 4.20), the major element content of these samples consists of 48.6-49.8% SiO_2, 7.42-16.15% Al_2O_3, 11.3-13.6% Fe_2O_3, 7.2-21.4% MgO, 0.0-1.1% K_2O, 0.3-0.9% TiO_2, and a LOI of 0.7-4.7%. The trace element pattern of the group is defined by broadly flat LREE and HREE. The LREE has a slightly positive slope with La/Sm_N values between 0.45 to 0.95. The HREE are flat with Gb/Yb_N values between 0.91 to 1.20.

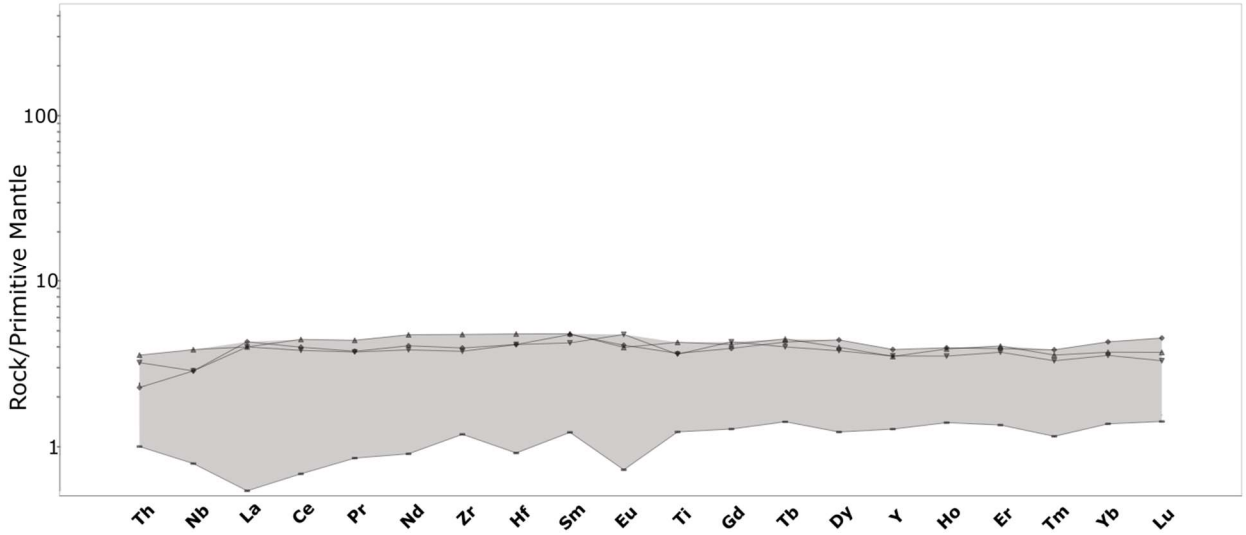

Figure 4.20. Spider diagram of the Mafic group 5 samples. Normalized to primitive mantle values of Sun and McDonough (1989).

4.2.2 Felsic Volcanic and Intrusive Rocks

A total of 24 samples were collected from felsic volcanic and intrusive rocks in the study area ranging from volcanic dacites to rhyolitic flows and quartz feldspar porphyritic intrusions. These samples have been separated into two groups based on their trace element characteristics in spider diagrams. Felsic group 1 consists of 18 samples and is defined by highly enriched LREE with a La/Sm_N value from 4.73 to 7.67 (Fig 3.21). The HREE are moderately enriched with Gd/Yb_N ranging from 1.26 to 2.75. A very large negative Nb anomaly is present with Nb/Nb* values of 0.11 to 0.24. A positive Zr and Hf anomaly is present within these samples with Zr/Zr* values between 0.92 to 1.73 and Hf/Hf* value ranging between 0.81 to 1.60. A significant negative Ti anomaly is present with Ti/Ti* values ranging from 0.15 to 0.40.

The major element content of these samples consists of 63.1-74.7% SiO_2, 13.5-17.7% Al_2O_3, 1.7-7.9% Fe_2O_3, 0.4-7.0% Na_2O, 0.7-4.7% K_2O, 0.2-0.6% TiO_2, and a LOI of 0.7-5.6%.

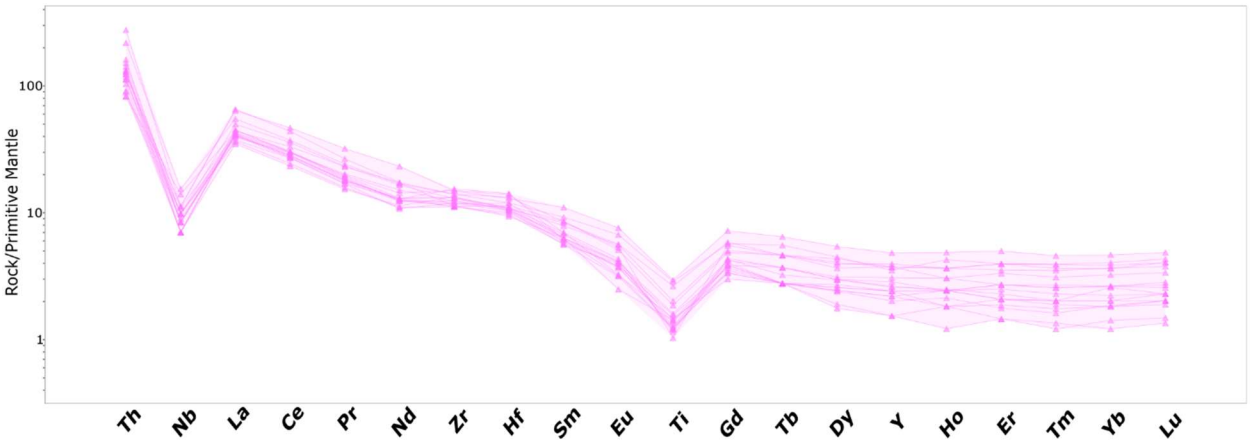

Figure 4.21 Spider diagram of Felsic group 1 samples. Normalized to primitive mantle values of Sun and McDonough (1989).

Felsic group 2 contains six samples and is best separated from the previous groups based on its significant positive Hf anomaly and very large negative Ti anomaly (Fig. 3.22). LREE are moderately enriched with La/Sm_N values between 3.73 to 4.62. The HREE are moderately fractionated with Gd/Yb_N values between 0.90 to 1.02. A moderate negative Nb anomaly is present with Nb/Nb* values between 0.35 to 0.65. A significant positive Hf anomaly is present with Hf/Hf* values between 0.86 to 1.46. A large negative Ti anomaly is present with values between 0.03 to 0.06. The major element content of these samples consists of 73.5-77.0% SiO_2, 12.8-13.1% Al_2O_3, 1.1-2.1% Fe_2O_3, 0.2-3.9% Na_2O, 3.8-4.3% K_2O, 0.0-0.1% TiO_2, and a LOI of 0.8-2.0%.

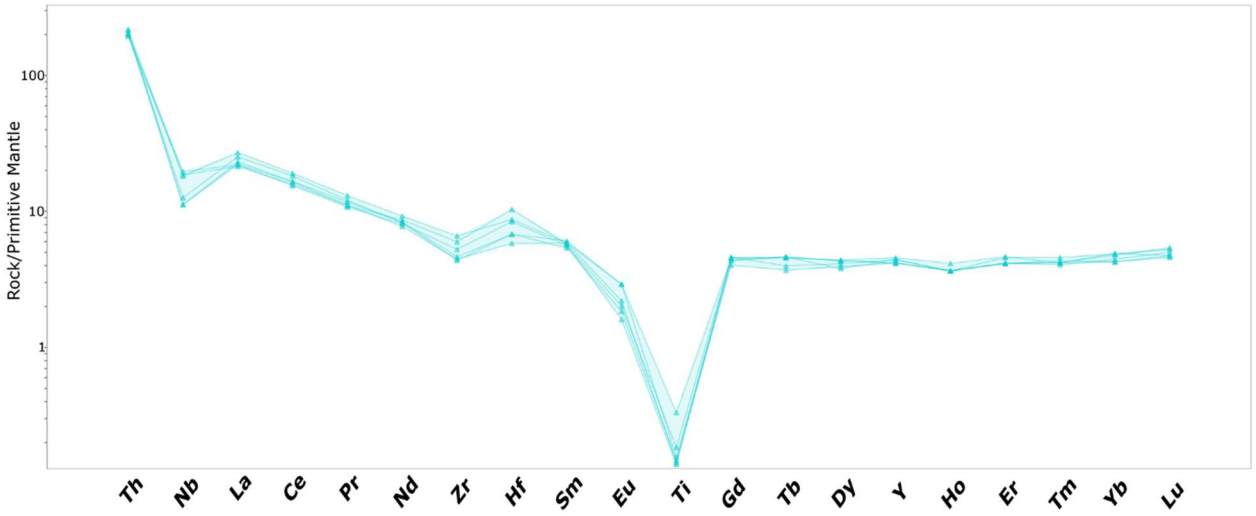

Figure 4.22 Spider diagram of Felsic group 2 samples. Normalized to primitive mantle values of Sun and McDonough (1989).

4.2.3 Sedimentary Rocks

A total of 59 samples were collected from sedimentary units, with siltstones and sandstones protoliths metamorphosed to mica-rich schists. Some samples were relatively unaltered sedimentary rocks with banding visible as biotite-rich to sericite-rich portions in the rock (Fig 4.23). The sequence of systematic patterns of mudstone to sandstone lithologies suggests formation through turbidites.

Fig 4.23 Photo of sample DT078, showing the schistose nature of the rock consisting of interbedded biotite and muscovite rich lamellae.

A portion of samples contain coarse porphyroblastic garnets and staurolite with massive biotite and sulphide veinlets (Fig. 4.24). The sedimentary samples are divided into four unique groups. Sedimentary group 1 consists of 20 samples defined by highly enriched LREE with La/Sm_N values ranging from 3.11 to

6.44 (Fig. 4.25). HREE are fractionated with Gd/Yb_N values between 1.37 to 1.94. A large negative Nb anomaly is present with Nb/Nb* values between 0.11 to 0.29. A small positive Hf anomaly is present defined by Hf/Hf* values between 0.79 to 1.21. A significant negative Ti anomaly is present defined by Ti/Ti* values ranging from 0.14 to 0.39. The major element content of these samples consists of 58.2-76.8% SiO_2, 13.7-21.0% Al_2O_3, 1.2-18.2% Fe_2O_3, 0.1-1.5% Na_2O, 0.9-6.1% K_2O, 0.2-0.7% TiO_2, and a LOI of 0.0-3.9%.

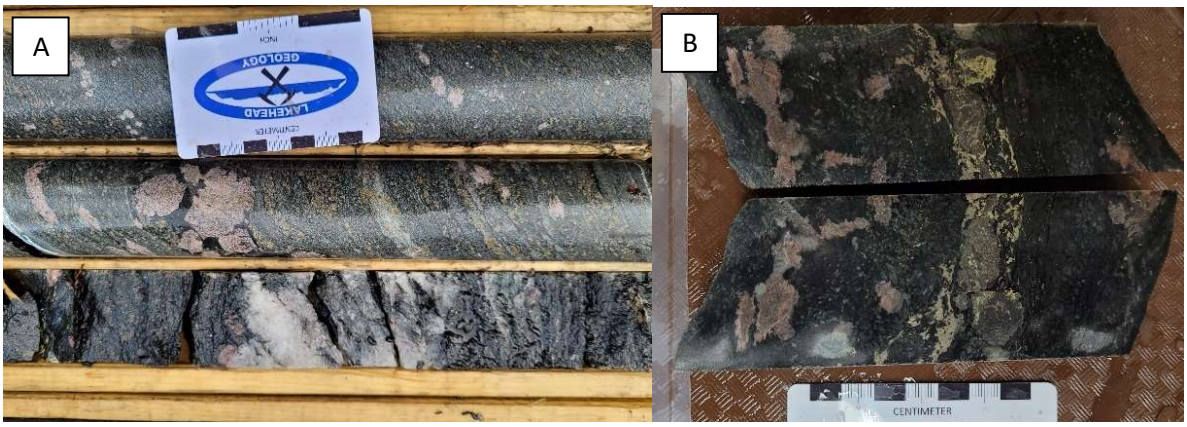

Figure 4.24 Coarse schist samples. (A) Sample DT050 contains massive biotite vein with coarse garnets as well as significant staurolite content. (B) Vein consisting of coarse garnet with chalcopyrite and pyrrhotite (sample DT049).

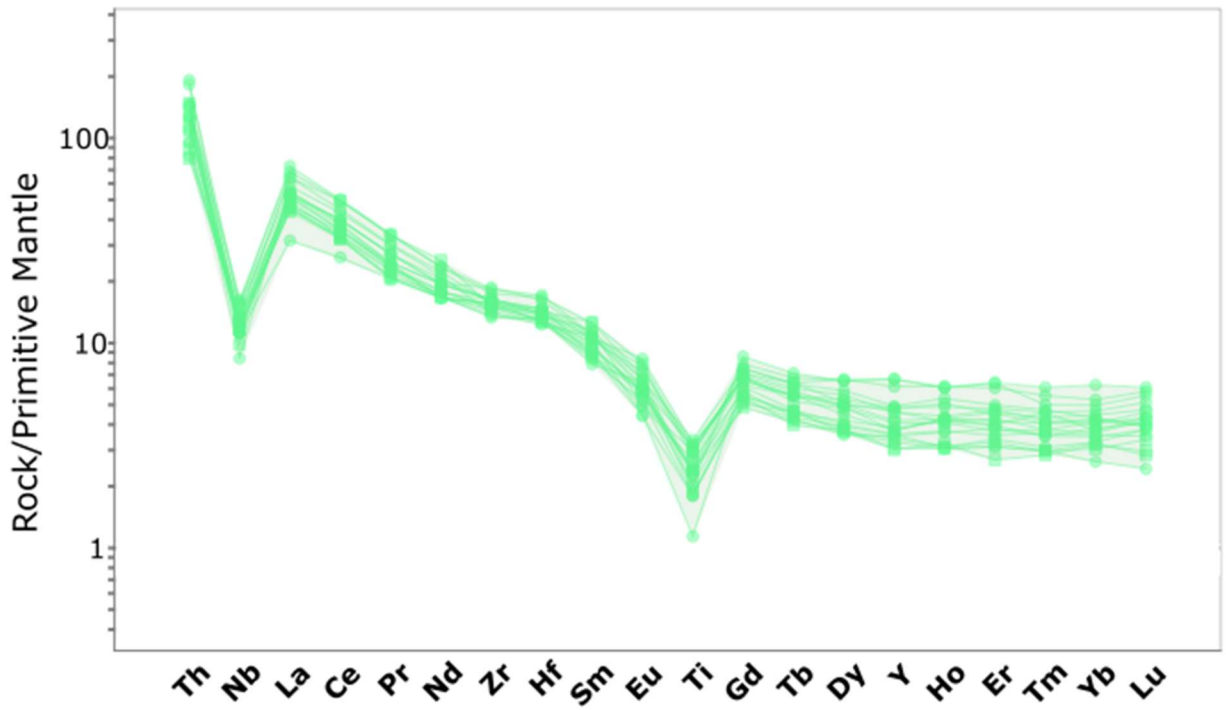

Figure 4.25 Spider diagram of sedimentary group 1 samples. Normalized to primitive mantle values of Sun and McDonough (1989).

Sedimentary group 2 consists of 32 samples and appears very similar to group 1 but is distinguished by a larger positive Zr and Hf anomaly (Fig 4.26). The LREE are enriched with La/Sm_N values between 3.03-6.95. HREE are moderately fractionated with Gd/Yb_N values between 1.22 to 2.48. A large negative Nb anomaly is present with Nb/Nb* values of 0.12 to 0.31. A moderate positive Zr anomaly is present with Zr/Zr* between 1.11 to 2.30. A moderate positive Hf anomaly is present with Hf/Hf^*_N values between 0.91 to 2.17. A large negative Ti anomaly is present with Ti/Ti* values between 0.27 to 0.53. The major element content of these samples consists of 59.3-77.3% SiO_2, 12.4-18.4% Al_2O_3, 1.8-21.3% Fe_2O_3, 0.1-2.0% Na_2O, 1.2-4.7% K_2O, 0.1-0.8% TiO_2, and a LOI of 0-2.2%

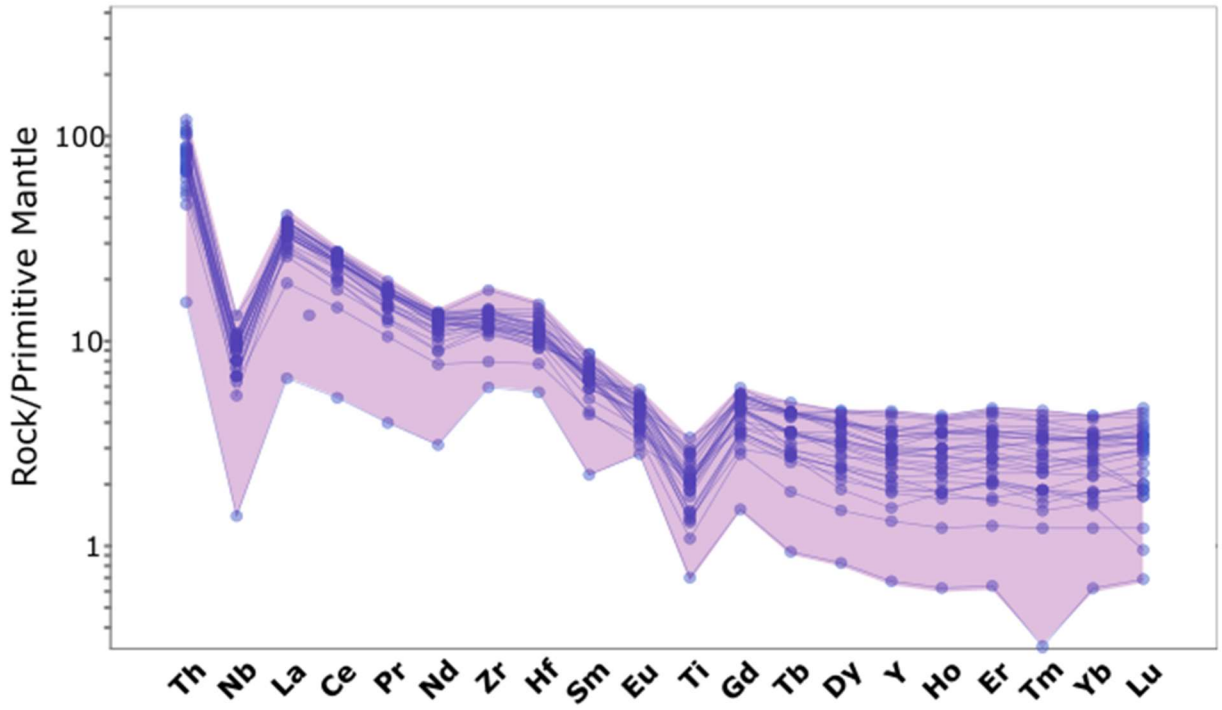

Figure 4.26. Spider diagram of sedimentary group 2 samples. Normalized to primitive mantle values of Sun and McDonough (1989).

Sedimentary group 3 is differentiated by its flat to negative anomalies which are unlike any of the other groups (Fig. 4.27). It has enriched LREE with La/Sm_N values between 5.0 and 7.3. HREE are enriched with Gd/Yb_N values between 1.5 to 3.2. A large negative Nb anomaly is present with Nb/Nb* values between 0.07 to 0.15. A negative zircon anomaly is present with Zr/Zr* values between 0.38 to 1.09. A large negative Ti anomaly is present with Ti/Ti* values between 0.08 to 0.32. The major element content of these samples consists of 11.4-76.2% SiO_2, 5.0-15.6% Al_2O_3, 2.3-43.2% Fe_2O_3, 0.1-1.2% Na_2O, 0.6-3.9% K_2O, 0.1-0.5% TiO_2, and a LOI of 1.2-10.7.

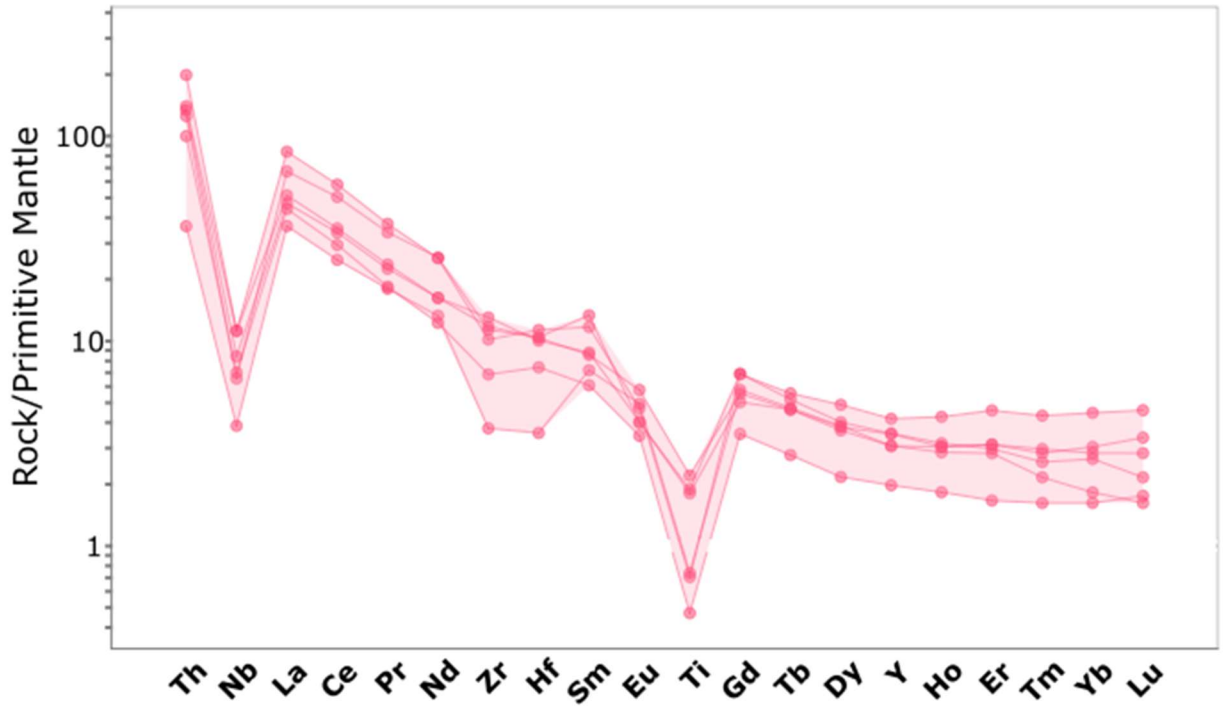

Figure 4.27. Spider diagram of sedimentary group 3 samples. Normalized to primitive mantle values of Sun and McDonough (1989).

Sedimentary group 4 consists of one outlier sample (DT078) which does not fit with any previously defined groups and is characterized by a positive Nb and Ti anomaly (Fig. 4.28). The LREE is slightly enriched with a La/Sm_N value of 1.75. The HREE are defined by a Gd/Yb_N value of 0.65. A minor positive Nb anomaly is present with a Nb/Nb* value of 1.25. A moderate negative Zr and Hf anomaly is present with a Zr/Zr* value of 2.03 and Hf/Hf* value of 2.18. A positive Ti anomaly is present with a Ti/Ti* value of 2.37. The major element content of this sample consists of 67.6% SiO_2, 19.85% Al_2O_3, 1.61% Fe_2O_3, 0.21% Na_2O, 6.77% K_2O, 1.09% TiO_2, and a LOI of 2.71%.

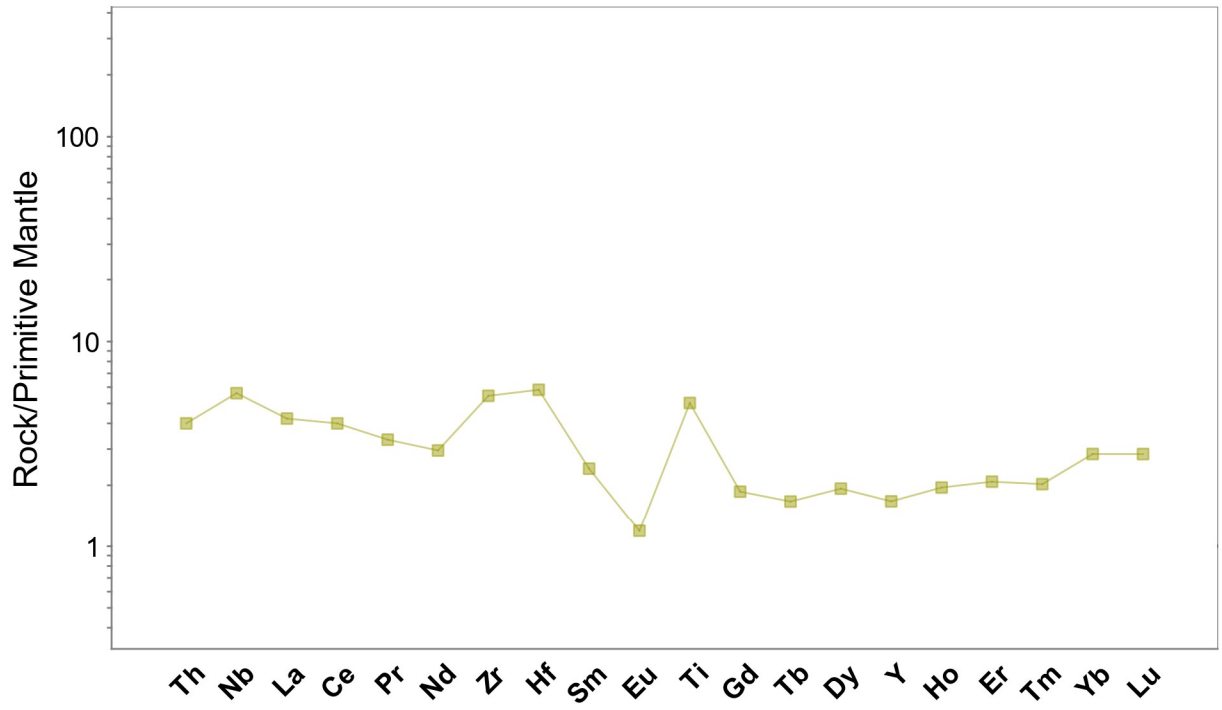

Figure 4.28. Spider diagram of sedimentary group 4 sample normalized to primitive mantle values of Sun and McDonough (1989).

The full Whole rock (WRX) data on all samples is presented in appendix II. The spatial position of all the mafic, felsic, and sedimentary samples is presented in Figure 4.29 with the samples colour coded to match the previously assigned groups.

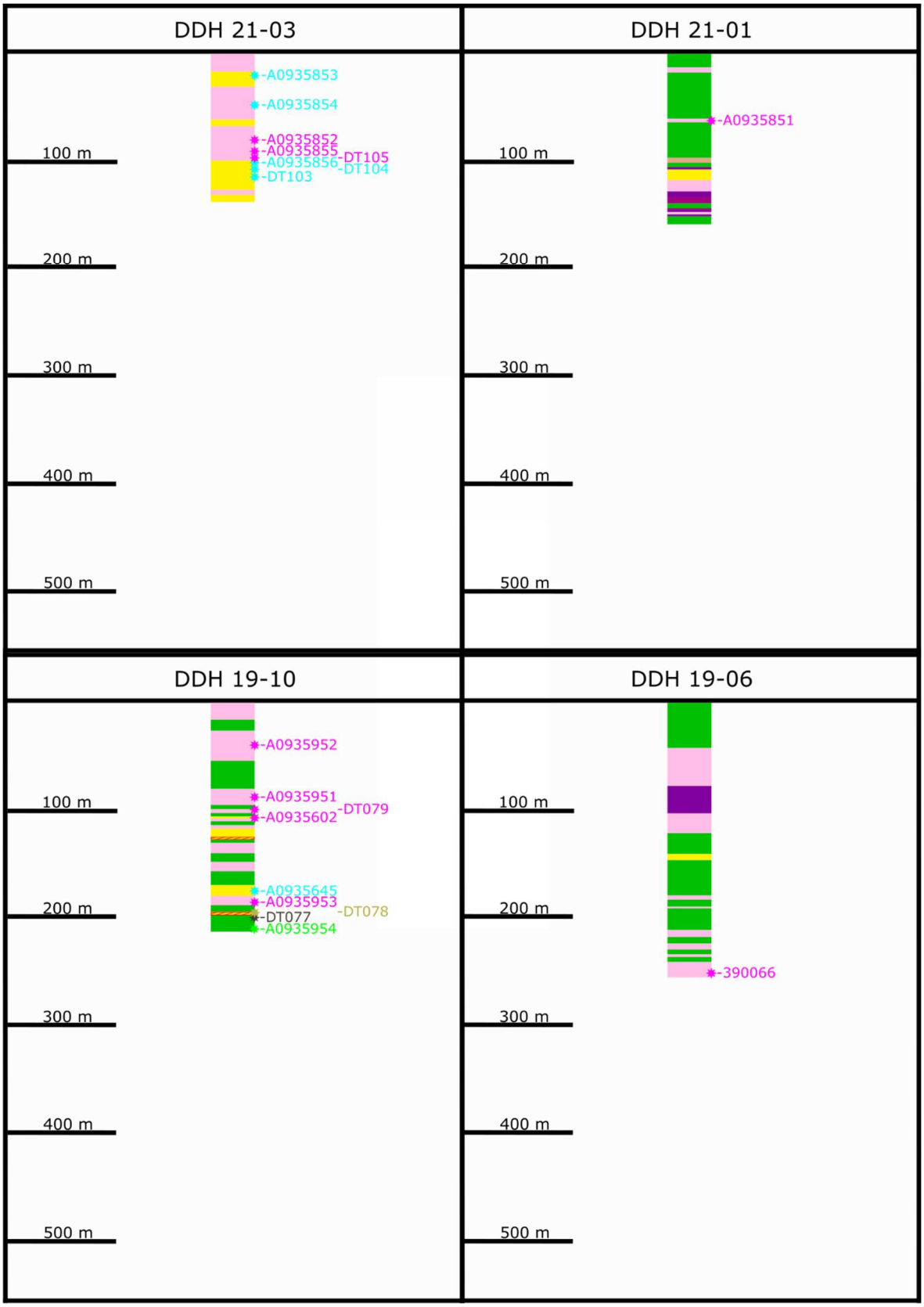

Figure 4.29 Spatial Organization of all whole rock samples. Coloured to match defined groups

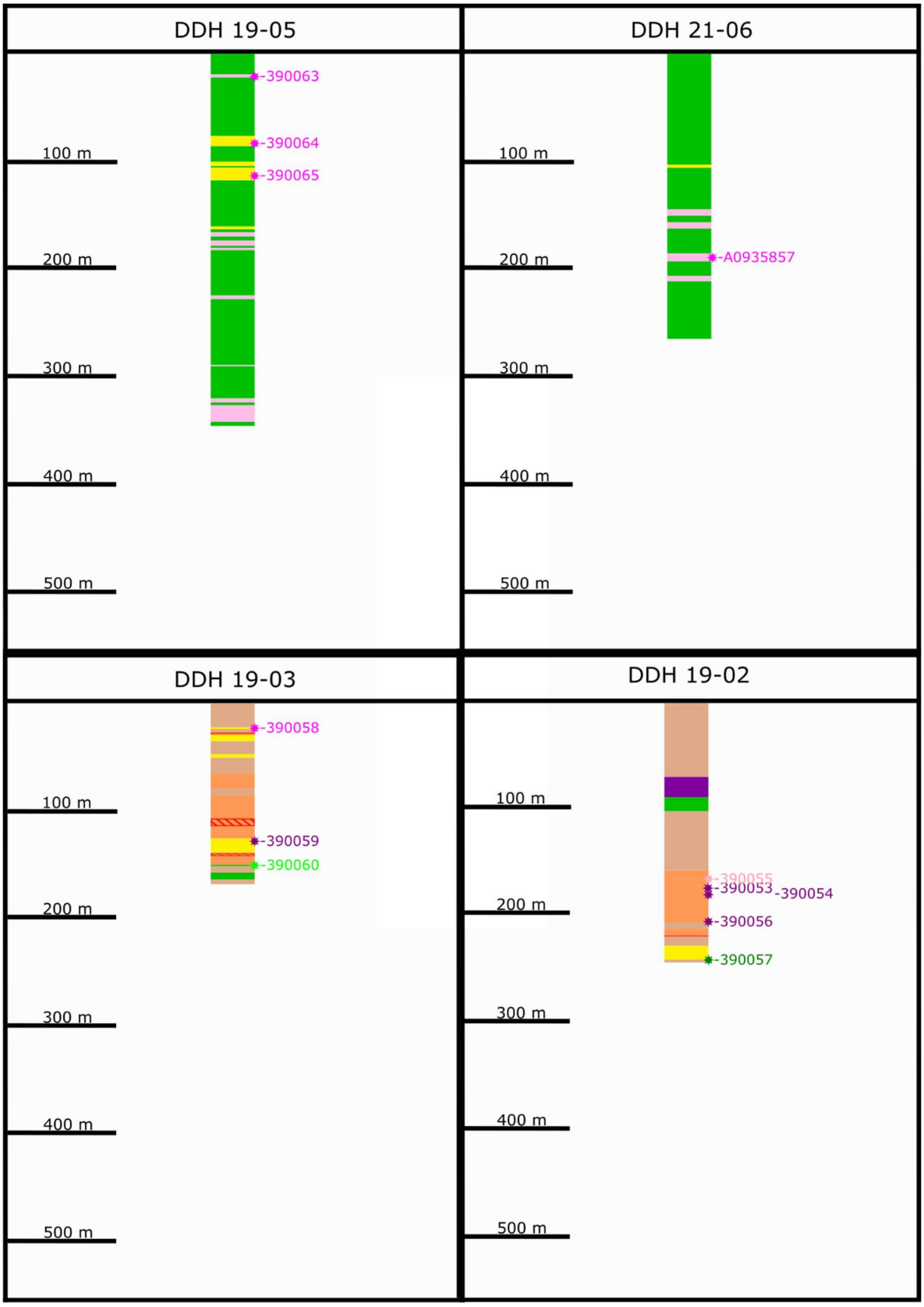

Figure 4.29 continued

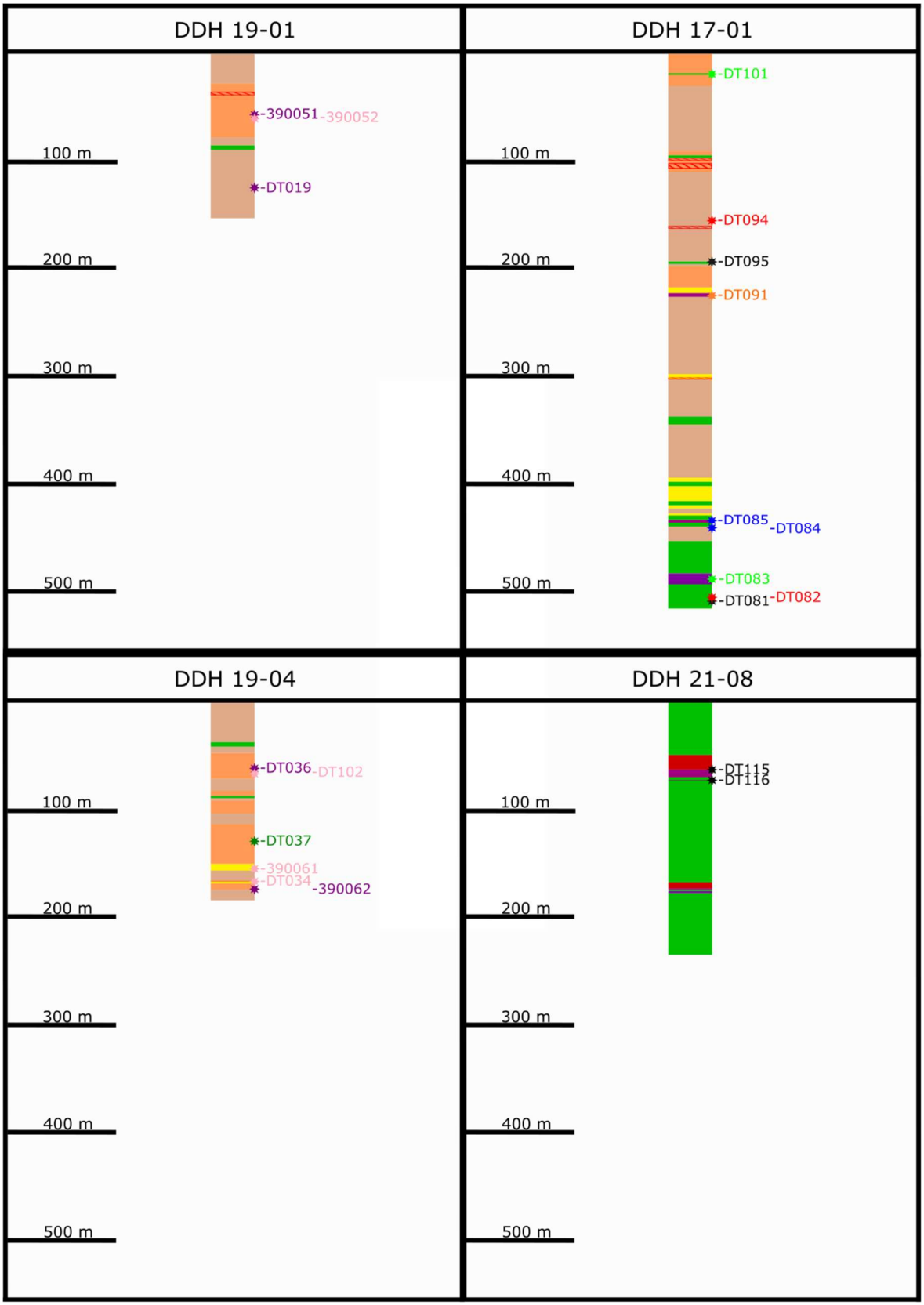

Figure 4.29 continued

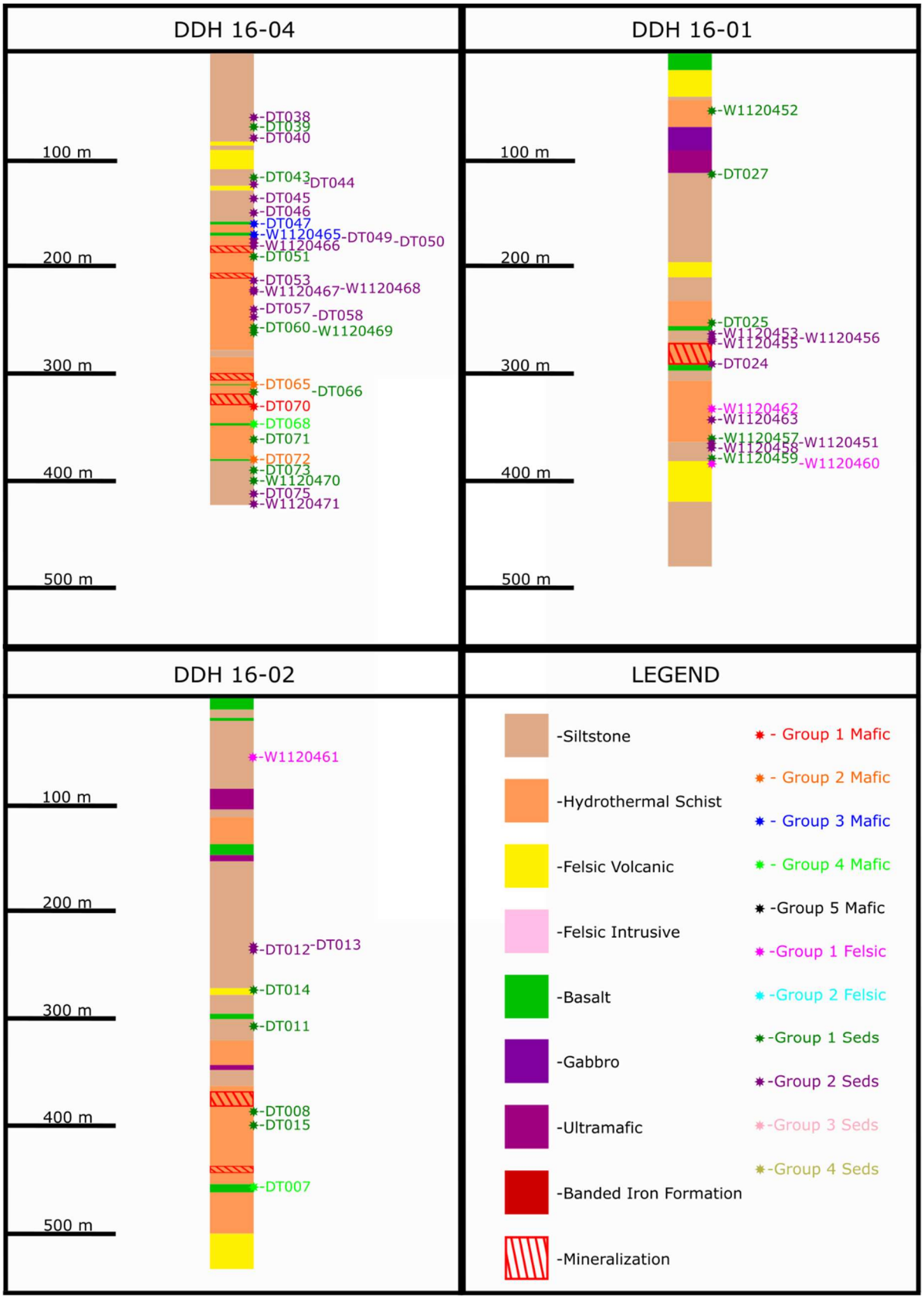

Figure 4.29. continued

4.3 Geochronology

Three felsic volcanic samples were analyzed for zircon U/Pb age dates. Sample DT079 consisted of a quartz feldspar porphyritic felsic intrusive rock. A total of 141 zircon grains were extracted from this sample, subjected to 41 LA-ICP-MS analysis of which five were selected for TIMS to calculate a Concordia age date of 2973.96 +- 0.42 Ma (Figure 4.30). Sample DT103 consisted of a felsic volcanic rhyolite. Thirty nine zircon grains were extracted from the sample and underwent 37 LA-ICP-MS point analysis of which five where selected for TIMS to produce a Concordia age of 2980.02 ± 0.77 Ma. Sample DT105 consisted of a quartz feldspar porphyritic rhyolite. 138 zircon grains were extracted from the sample and subjected to 58 LA-ICP-MS analyses of which five where analyzed by TIMS to generate a Concordia age of 2972.99 ± 0.42 Ma (Fig. 4.30). Samples DT079 and DT105 both belong to the previously defined felsic group 1 sharing similar geochemical characteristics as well as close to overlapping age dates. DT103 belongs to the geochemically distinct felsic group 3. Full geochronological data and zircon photos are presented in Appendix XVIII.

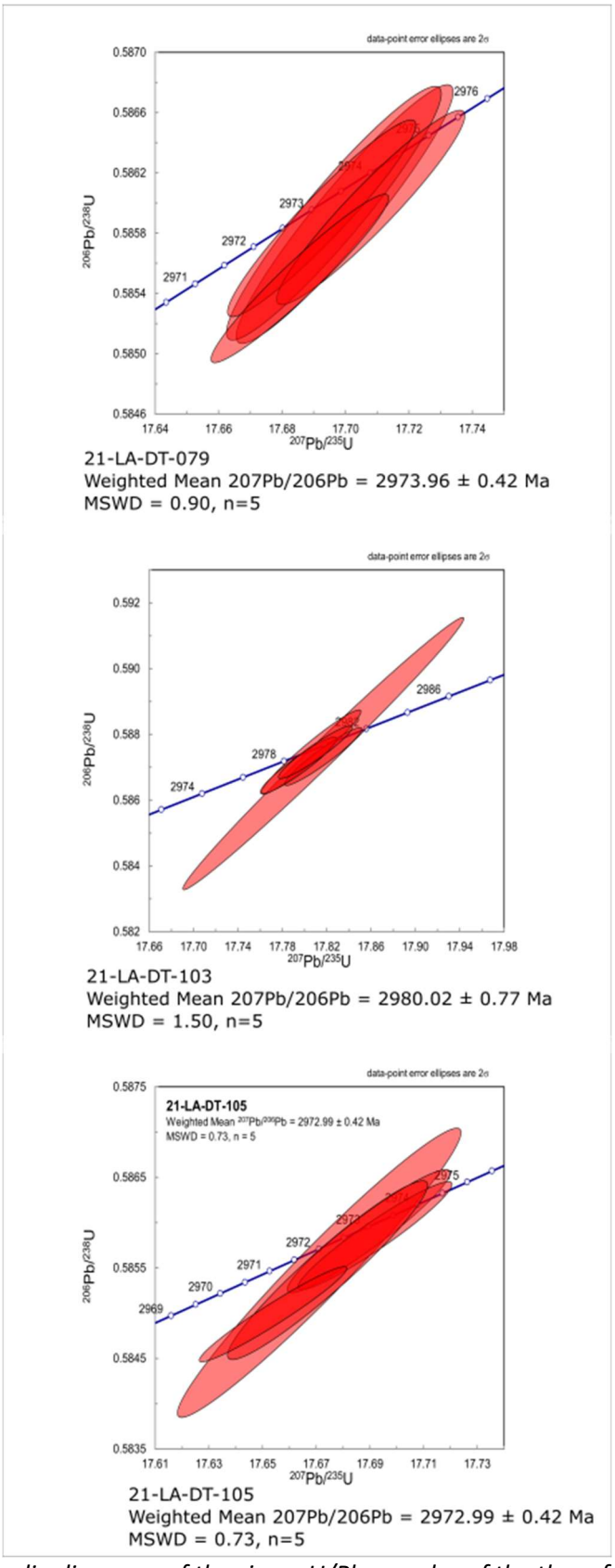

Figure 4.30. Concordia diagrams of the zircon U/Pb samples of the three felsic volcanic samples.

Sample DT112 was analyzed for a Re/Os age date from molybdenite within a quartz vein that crosscuts the host rock basalt. This sample returned an age of 2976 ± 13 Ma. The full results of the Re and Os analysis on the sample is presented in Table 4.1.

Table 4.1 Analytical results of Re/Os age date sample

Sample	Re ppm	± 2σ	^{187}Re ppm	± 2σ	^{187}Os ppb	± 2σ	Modal Age (Ma)	± 2σ (with λ) Ma
LA21-DT112	22.83	0.06	14.35	0.04	729.3	0.08	2976	13
Replicate	23.07	0.06	14.5	0.04	737.3	0.17	2976	13

Two samples of garnets from garnet biotite schist rocks were analysed with LA-ICP-MS for U/Pb geochronology (Fig. 4.31). A garnet grain hosted within sample LA-21-DT-017 was analyzed using a 60 um spot size on 57 spots on one individual garnet grain which returned an age date of 2523.42± 9.06 Ma. A garnet grain hosted within sample LA-21-DT-096 showed a visual zonation between the core and rim. A laser spot size of 60 um was utilized on 34 spots and returned an age date for the core at 2960.1±18.7 Ma. The rim of the garnet was analyzed with a 160um size laser on 54 spots and dated the rim for 2424.1±2.87 Ma.

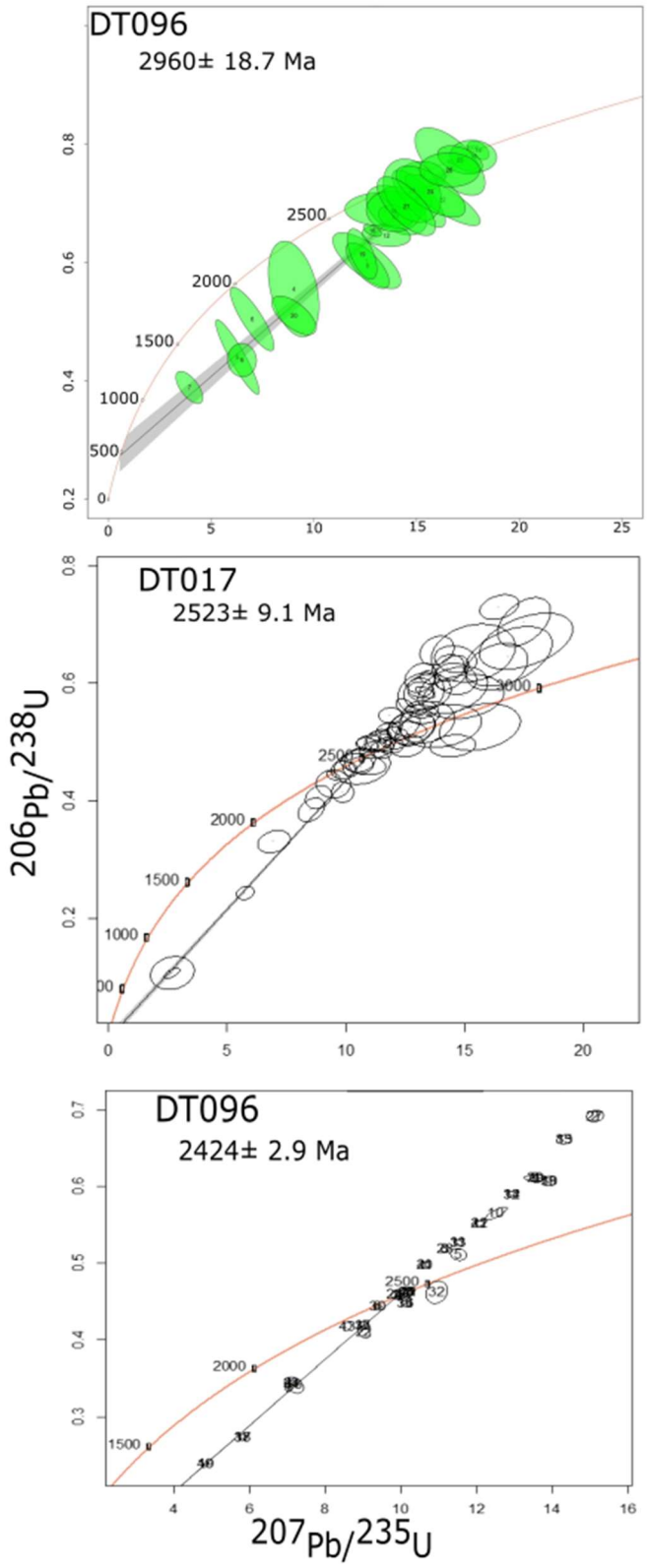

Figure 4.31 Concordia diagrams of garnets analyzed for U/Pb dating.

4.4 Isotopes

4.4.1 Sulfur δ^{34} isotopes

A total of 23 δ^{34} sulfur analysis were performed from 17 samples from massive sulphide to minor sulphide occurrences within the meta-sedimentary schist and felsic volcanic host rock , 11 were on pyrrhotite grains, seven on chalcopyrite, four on pyrite, and one on arsenopyrite standardized to VCDT (Table 4.2). The pyrrhotite samples returned values between 1.7 and 3.0‰ with an average of 2.4‰ δ^{34}S. The chalcopyrite samples returned values between 1.8 and 3.4‰ with an average of 2.4‰ δ^{34}S. The pyrite samples returned values between 1.5 and 3.0‰ with an average of 2.4‰ δ^{34}S. The arsenopyrite sample returned the value of 3.7‰ δ^{34}S. The analysis is accurate to within an error of 0.2‰ for each value and two duplicate analyses were performed in the sequence which returned values within the 0.2‰ error.

Table 4.2 δ^{34} S values for LA Lake area.

Sample Number	Host Rock	Sulphide type	δ^{34}S ‰
LA-21-DT-009	Schist	Pyrrhotite	2.9
LA-21-DT-009	Schist	Chalcopyrite	3.4
LA-21-DT-010	Schist	Chalcopyrite	2.1
LA-21-DT-017	Schist	Chalcopyrite	1.8
LA-21-DT-022	Schist	Pyrrhotite	2.9
LA-21-DT-023	Schist	Pyrrhotite	2.3
LA-21-DT-034	Schist	Pyrrhotite	2.0
LA-21-DT-034	Schist	Pyrite	1.5
LA-21-DT-049	Schist	Pyrite	3.0
LA-21-DT-055	Schist	Pyrrhotite	3.0
LA-21-DT-057	Schist	Arsenopyrite	3.7
LA-21-DT-069	Schist	Pyrrhotite	2.6
LA-21-DT-102	Schist	Pyrrhotite	2.3
LA-21-DT-106	Felsic Volcanic	Pyrrhotite	1.7
LA-21-DT-106	Felsic Volcanic	Chalcopyrite	1.8
LA-21-DT-107	Felsic Volcanic	Pyrrhotite	2.4
LA-21-DT-108	Felsic Volcanic	Chalcopyrite	2.1
LA-21-DT-117	Felsic Volcanic	Pyrite	2.2
LA-21-DT-118	Felsic Volcanic	Chalcopyrite	2.9
LA-21-DT-118	Felsic Volcanic	Pyrite	3.0
LA-21-DT-118	Felsic Volcanic	Pyrrhotite	1.8
LA-21-DT-119	Schist	Pyrrhotite	2.6
LA-21-DT-119	Schist	Chalcopyrite	2.4

4.4.2 Sm-Nd isotopes

The nine samples selected for Sm-Nd isotope analysis were taken from a range of ultramafic to felsic rocks with focus on the trace element defined groups (Table 4.3). ε_{Nd} values were calculated from the Sm-Nd isotope data using the zircon U/Pb age for sample DT-103 of 2980.02 Ma. Sample DT079 was calculated using the younger age of 2973.96 Ma determined from zircon U/Pb dating on this younger intrusive felsic sample. An ultramafic rock sample from Mafic group 1 yielded the ε_{Nd} value of 3.07 whereas an ultramafic sample from Mafic group 2 yielded an ε_{Nd} value of -1.53 and a mafic sample from Mafic group 3 returned the ε_{Nd} value of 1.07. Two ultramafic and two mafic samples from Mafic group 4 yielded ε_{Nd} values of 0.39, 0.71, 0.97, and 2.61. One felsic sample from Felsic group 1 yielded an ε_{Nd} value of 1.16. One felsic sample from Felsic group 2 returned the ε_{Nd} value of 0.07.

Table 4.3. Sm-Nd Isotope data with calculated ε_{Nd} Values

Sample Name	Nd (ppm)	Sm (ppm)	Age (Ma)	143Nd/144Nd (Current)	Sm147/Nd144	Nd143/Nd144 (initial)	εNd	Rock Type	Group
LA-21-DT-077	6.11	2.00	2980	0.51270	0.19796	0.50880	0.71	Mafic	Mafic 5
LA-21-DT-079	19.52	3.39	2974	0.51089	0.10484	0.50883	1.16	Felsic	Felsic 1
LA-21-DT-081	7.43	2.38	2980	0.51259	0.19349	0.50879	0.39	Mafic	Mafic 5
LA-21-DT-084	6.93	1.79	2980	0.51177	0.15659	0.50869	-1.53	Ultramafic	Mafic 3
LA-21-DT-091	13.99	3.13	2980	0.51159	0.13539	0.50892	3.07	Ultramafic	Mafic 2
LA-21-DT-101	9.26	2.83	2980	0.51246	0.18505	0.50882	1.07	Mafic	Mafic 4
LA-21-DT-103	7.44	1.77	2980	0.51161	0.14406	0.50877	0.07	Felsic	Felsic 2
LA-21-DT-115	1.98	0.72	2980	0.51321	0.21888	0.50890	2.61	Ultramafic	Mafic 4
LA-21-DT-116	1.86	0.70	2980	0.51333	0.22918	0.50882	0.97	Ultramafic	Mafic 5

4.5 SWIR

Forty-two samples were analyzed with short wave infrared and yielded 86 unique spectra (Appendices XIX, XX, XXI). Of the 86 spectra, 44 were of a high enough resolution to distinguish a mineral phase, while the remaining 42 returned low signals and were ambiguous. One sample returned two kaolinite spectrums with the 1900 nm position from 1912.0-1914.0 with a trough magnitude from 0.12 to 0.18. The 2200nm position occurs at 2207.7 with a magnitude of 0.15 to 0.17. Twenty of the spectra represent a mixture of muscovite and an Fe-rich phase such as biotite or chlorite. Seven samples have no 1900 nm position whereas the remainder vary from 1907.2 to 1943.0 with a magnitude ranging from

0.01 to 0.09. The position of the 2200 nm trough ranges from 2196.9 to 2206.5 with a magnitude of 0.02 to 0.10. The position of the 2250 nm trough ranges from 2246.8 to 2259.4 with a magnitude ranging from 0.001 to 0.008. Twenty two of the spectra represented pure muscovite samples with 1900 nm position ranging from 1895.9 to 1938.9 with a magnitude ranging from 0.001 to 0.084. The 2200 position ranges from 2196.8 to 2207.7 with a magnitude from 0.03 to 0.19.

4.6 Mineral Chemistry

Forty-one polished thin sections were analyzed under the SEM SU-70 to evaluate mineral compositional variations throughout the deposit with an emphasis on garnet, staurolite, biotite, chlorite, and muscovite. Two hundred and nine analyses of garnet grains were performed on 32 separate thin sections (Appendix VI). There is a variation in garnet types with four spessartine, four grossular, and the remaining 201 analysis consisting of almandine (Fig. 4.32).

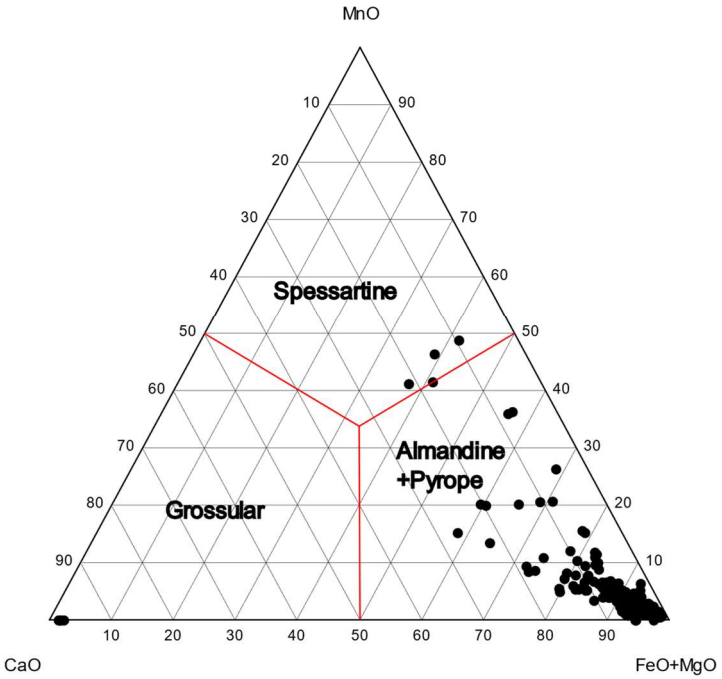

Figure 4.32. Compositional discrimination of the garnets analysed in the research area. After Wright (1938).

The four reported grossular garnets contain between 0.8-1.8% Al_2O_3, 30.1-31.2% SiO_2, 29.2-29.9% CaO, 37.5-38.4% TiO_2, and 0.3-0.6% FeO. The very high TiO_2 values along with the CaO suggest this garnet is a schorlomite rather than a true grossular garnet. The spessartine garnets contain between 20.3-21.0% Al_2O_3, 36.0-36.5% SiO_2, 1.3-1.8% MgO, 4.1-9.3% CaO, 17.6-21.4% MnO, and 14.6-16.6% FeO. The almandine garnets contain between 19.9-21.6% Al_2O_3, 34.7-36.9% SiO_2, 0.3-2.8% MgO, 0.4-11.5% CaO, 0-15.8% MnO, 0-0.4% TiO_2, and 22.2-42.3% FeO.

A total of 87 analyses of staurolite grains were performed on 23 separate thin sections (Appendix VII). This yielded a tightly clustered grouping of similar compositions. The staurolite have a composistion ranging from 51.2-58.5% Al_2O_3, 23.9-28.8% SiO_2, 0.4-1.9% MgO, 0- 0.6% TiO_2, 0-0.6 % MnO, 12.73-16.89% FeO, and 0-1.64% ZnO. Only nine of the samples contains MnO and a separate nine samples contains ZnO with the rest of the samples returning null values for those oxides.

A total of 141 analysis of biotite grains was performed on 41 separate thin sections (Appendix VIII). The biotite was classified as annite to phlogopite based on its iron versus magnesium content (Fig. 4.33). Eight of the analysed biotite crystals can be classified as phlogopite and have compositions ranging from 36.6-45.3% SiO_2, 8.4-18.7% Al_2O_3, 15.0-22.0% MgO, 8.0-10.2% K_2O, 0.6-2.2% TiO_2, and 6.3-14.3% FeO. The phlogopite analysis were all from three thin sections, one from a lamprophyre dyke, one from a massive biotite quartz vein in a basalt, and a biotite vein in a massive sulphide horizon. The 133 annite samples have compositions ranging from 26.1-42.8% SiO_2, 15.2-23.2% Al_2O_3, 4.9-13.9% MgO, 2.5-10.2% K_2O, 0-3.29% CaO, 0-3.1% TiO_2, and 11.32-34.23% FeO.

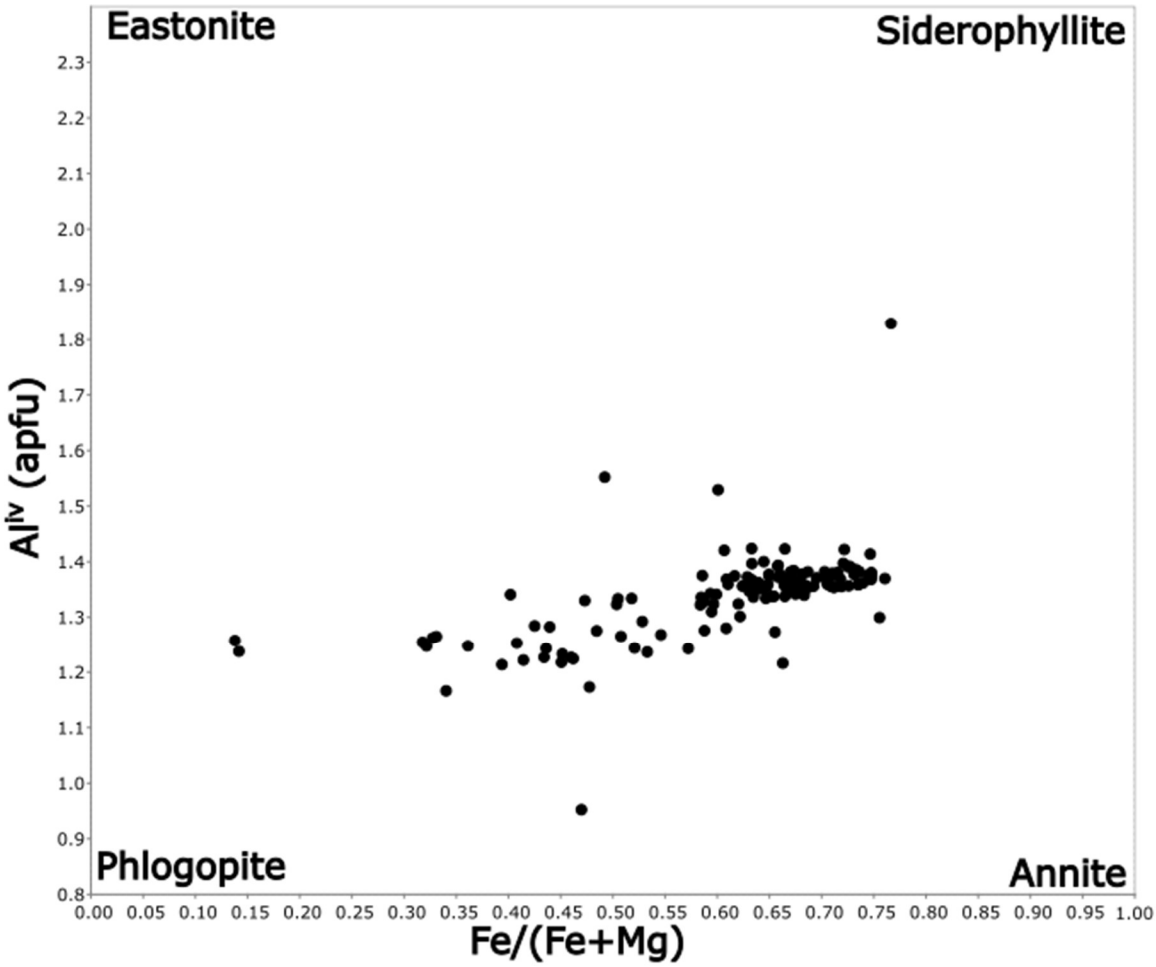

Figure 4.33. Biotite discrimination diagram for iron rich annite and magnesium rich phlogopite. From Rieder et al. 1999.

A total of 129 analysis of chlorite grains were performed on 39 separate thin section samples (Appendix IX). The chlorite was divided into two separate groups, chlorite with an Fe/Mg# greater than 0.83 was defined as the iron rich chlorite chamosite (Fig. 4.34). Thirty four of the samples are classified as chamosite with a compositional range from 11.8-24.0% Al_2O_3, 19.8-28.6% SiO_2, 0.5-7.3% MgO, and 34.4-46.5% FeO. The 95 remaining chlorite samples have compositional ranges from 16.5-24.3% Al_2O_3, 21.5-29.1% SiO_2, 7.4-19.6% MgO, and 18.9-36.3% FeO.

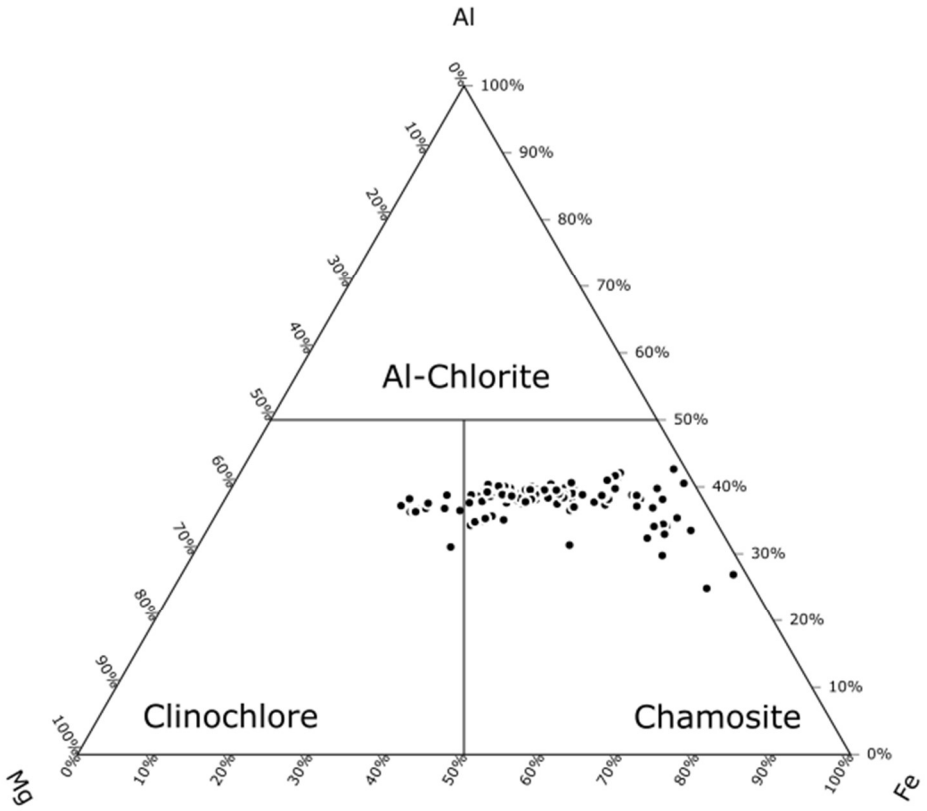

Figure 4.34. Chlorite discrimination ternary diagram between chlorite endmembers clinochlore and chamosite. From Zane and Wiess (1999).

Analysis of muscovite grains were performed on 50 grains from 22 separate thin sections (Appendix X). The muscovite varied in composition with 0-1.8% Na_20, 0-1.9% MgO, 30.6-36.8% Al_2O_3, 42.0-46.6% SiO_2, 7.5-11.3% K_2O, 0-1.3% TiO_2, and 0.6-3.2% FeO. Analysis was performed on 58 grains of tourmaline from 19 thin sections (Appendix XI). All tourmaline samples are Fe-rich and plot almost entirely as schorl with three samples plotting as feruvite. The tourmaline present in the samples plot into two separate groups when displayed on a Fe# vs Na# tourmaline discrimination diagram (Fig. 4.35) with the group displayed in blue being the Na rich schorl and the samples in orange grouping as the Ca rich schorl or feruvite.

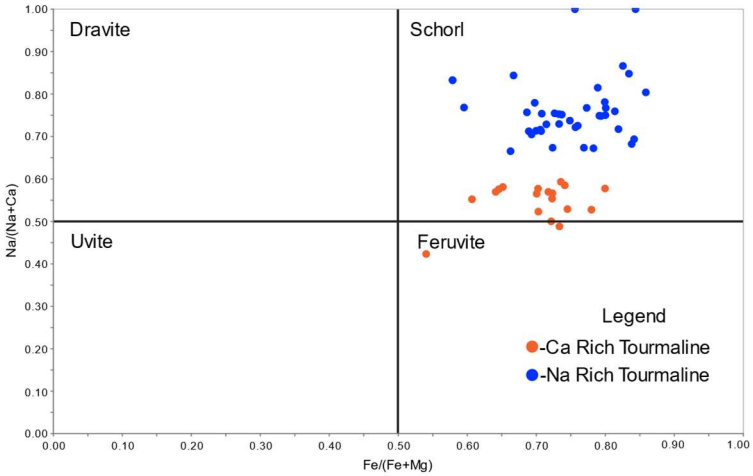

Figure 4.35. Discrimination diagram of tourmalines based on the Fe# vs Na# displaying two distinct groups of tourmaline compositions. After Dietrich (1985).

The Na rich group ranges from 1.15-2.14 wt. % Na_2O, 2.96-6.73 wt. % MgO, 30.62-34.21 wt. % Al_2O_3, 32.41-36.18 wt. % $Si0_2$, 0-0.88 wt. % CaO, 0-0.74 wt. % TiO_2, and 7.13-13.97 wt.% FeO. The Ca rich schorl and feruvite group contains a range of major element compositions of 1.16-1.71 wt. % Na_2O, 3.9-7.52 wt. % MgO, 28.83-33.91 wt. % Al_2O_3, 32.85-35.86 wt. % $Si0_2$, 1.09-1.64 wt. % CaO, 0.21-0.78 wt. % TiO_2, and 6.86-12.08 wt.% FeO.

4.7 Garnet Trace Element Data

Five garnet grains were analysed by laser ablation ICP-MS for a total of 142 analysis (appendix III). The variations in minor and major oxide content of the five grains range with sample LA-21-DT-017 having between 1.09-2.05% MgO, 20.0-20.2% Al_2O_3, 36.1-36.7% SiO_2, 1.4-2.3% CaO, 0.01-0.03% TiO_2, 0.1-1.2% MnO, and 15.5-29.1% FeO. Sample LA-21-DT-021 has minor and major oxide compositions of between 1.1-1.4% MgO, 19.4-20.1% Al_2O_3, 35.8-36.0% SiO_2, 2.7-4.3% CaO, 0.1-0.6% TiO_2, 12.2-14.9% MnO, and 13.5-16.8% FeO. Sample LA-21-DT-049 has compositional variation of 1.1-1.2% MgO, 20.9-21.5% Al_2O_3, 38.7-39.8% SiO_2, 2.6-3.3% CaO, 0.1-0.3% TiO_2, 2.7-3.1% MnO, and 21.3-23.1% FeO. Sample LA-21-DT-074 has compositional variation of 1.4-1.8% MgO, 19.5-20.2% Al_2O_3, 35.4-36.1% SiO_2, 1.6-2.9%

CaO, 0.03-0.08% TiO_2, 2.6-5.5% MnO, and 24.1-27.8% FeO. Sample LA-DT-21-096 has a range from 0.5-0.9% MgO, 19.2-19.8% Al_2O_3, 34.3-35.5% SiO_2, 1.2-2.3% CaO, 0.01-0.4% TiO_2, 0.4-3.3% MnO, and 20.6-31.0% FeO. Plotting the minor oxides MgO, MnO, and CaO, shows a trend in composition with a consistent MgO and CaO percent but show variation in MnO compositions both between samples and within sample analysis (Fig. 4.36)

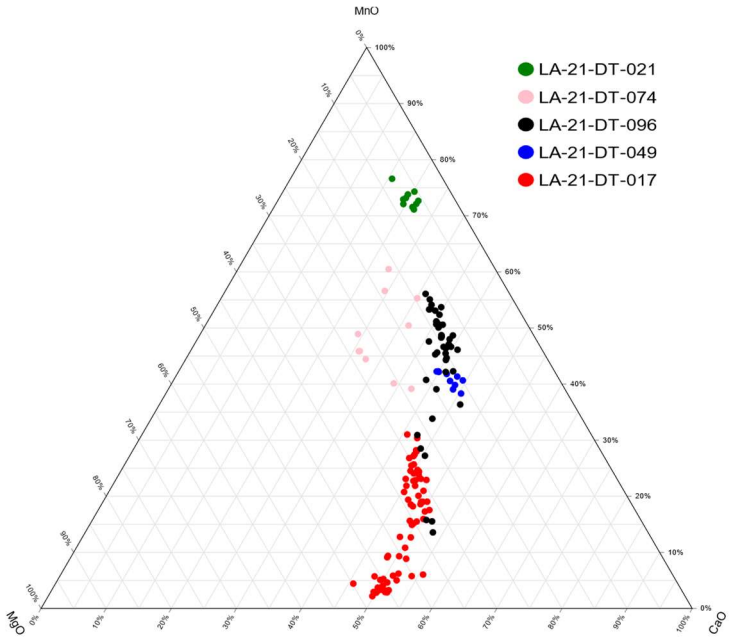

Figure 4.36. Ternary diagram of minor oxide composition of the five garnet samples analysed by laser ablation ICP-MS.

Trace element compositions of the samples are shown in Figure 4.37 as a spider diagram normalized to chondrite from Sun and Mcdonough (1989). Sample LA-21-DT-021 has depleted LREE with a positive slope defined by La/Sm_n values ranging from 0.00014 to 1.61. HREE are moderately enriched with a weak positive slope defined by Gd/Yb_n of 0.17 to 2.21.

Sample LA-21-DT-074 shows a diverse spread in LREE from enriched to depleted values, and has an overall negative slope with La/Sm_n value ranging from 0.0034 to 6.60. The HREE elements are moderately enriched and with a flat trend with Gd/Yb_n value ranging 0.072 to 3.47. A positive Eu anomaly is present with a Eu* value ranging from 1.13 to 4.69.

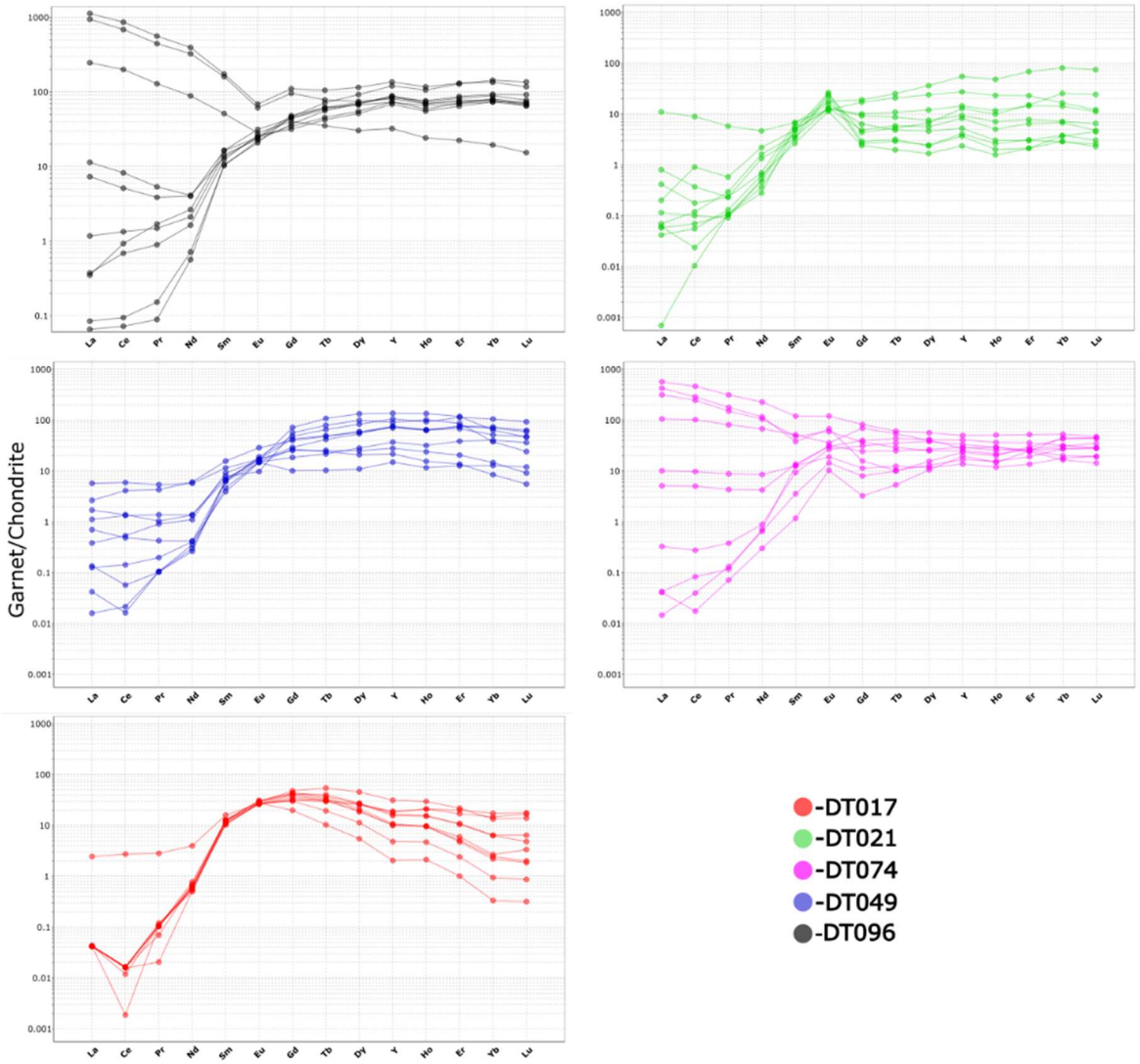

Figure 4.37. Spider diagram of trace elements of each garnet grain normalized to Chondrite (chondrite values from Sun and McDonough, 1989)

Sample LA-21-DT-096 shows a diverse spread in enriched and depleted LREE. The majority of samples are LREE depleted and have a positive slope defined by La/Sm_n values between 0.0062 to 6.47. The HREE are enriched and have a minor positive slope defined by Gd/Yb_n values between 0.32 to 2.06. A negative Eu anomaly is present with Eu* values between 0.48 to 1.21.

Sample LA-21-DT-017 has depleted LREE with a positive slope defined by La/Sm_n values between 0.0033 to 0.15. The HREE are moderately enriched and have a significant negative slope defined by Gd/Yb_n values between 1.86 to 59.28.

Sample LA-21-DT-049 is depleted in LREE with a positive slope defined by a La/Sm_n values between 0.0034 to 0.50. The HREE elements are enriched and with a minor negative slope defined by Gd/Yb_n values of 0.40 to 3.15.

4.8 Sulphide Laser Ablation Data

A total of 16 thin sections containing 49 unique sulphide samples sites were analysed with laser ablation ICP-MS yielding results from eight different sulphide mineral types (appendix IV). The 15 chalcopyrite samples contain between 34.3-35.5 wt.% S, 29.1-30.6 wt.% Fe, and 34.1-36.1wt% Cu, 2.70-332.57 ppm Se, 2.29-38.91 ppm Cd, 0.35-1068.51 ppm Ag, and 0-1.05 ppm Au. The 16 pyrrhotite samples contain between 36.9-40.3 wt.% S and 60.0-63.3 wt.% Fe, 7.94-205.17 ppm Se, 0-3.35 ppm Cd, 0-28.83 ppm Ag, and 0-1.68 ppm Au. The eight pyrite samples contain between 52.7-54.3 wt.% S and 45.4-46.7 wt.% Fe, 7.89-295.08 ppm Se, 0-342.84 ppm Cd, 0.02-118.92 ppm Ag, and 0-0.40 ppm Au. Two samples of sphalerite were analysed with between 33.4-33.5 wt.% S, 6.0-6.9 wt.% Fe, and 58.8-59.3 wt.% Zn, 15.87-86.44 ppm Se, 16155.04-29162.64 Cd, 15.22-1788.37 ppm Ag, and 2.96-12.35 ppm Au. Three samples of arsenopyrite contain between 17.2-21.2 wt.% S, 25.42-34.37 wt.% Fe, 0-7.9% Co, and 44.9-49.6 wt.% As, 21.20-265.82 ppm Se, 0.27-0.66 ppm Cd, 0-0.13 ppm Ag, and 0.11-3.71 ppm Au. Two samples of cobaltite contain between 19.4-22.2 wt.% S, 3.3-5.5 wt.% Fe, 28.64-30.81 wt.% Co, and 41.79-44.85 wt.% As, 517.47-577.77 ppm Se, 0-1.06 ppm Cd, 0-1.54 ppm Ag, and 0.12-6.46 ppm Au. Two samples of cubanite were analysed and return values of between 34.6-35.6 wt.% S, 39.7-40.5 wt.% Fe, and 24.3-25.7 wt. % Cu, as well as 105.68-282.80 ppm Se, 98.86-112.72 ppm Cd, and 108.56-267.60 ppm

Ag. One sample of galena was analysed and returned values of 14.06 wt.% S and 86.3 wt.% Pb, as well as 15.86-86.44 ppm Se, 10.91 ppm Cd, 3611.86 ppm Ag, and 0.14 ppm Au.

4.9 Tourmaline Laser Ablation Data

Six individual tourmalines were analyzed by laser ablation with one tourmaline grain displaying zonation being separated into three distinct analyses, one on each zone for a total of nine analysis. Of six tourmalines, five fall within the Na schorl group based on their major element composition, the sixth sample with zonation bands belongs to the Ca schorl group. The Na schorl group contain between 135.3-319.7 ppm Mn, 16.9-120.6 ppm Ni, 0.1-24.3 ppm Cu, 12.3-28.7 ppm Zn, 35.4-83.8 Ga, 0-1930.8 ppm Sr, 0.4-2.1 ppm Ba, and 0.7-9.7 ppm Pb. The Ca schorl and feruvite samples contain between 823.8-918.2 ppm Mn, 25.4-104.7 ppm Ni, 1.41-3.6 ppm Cu, 125.8-143.8 ppm Zn, 75.7-104.1 Ga, 155.9-276.7 ppm Sr, 1.7-3.4 ppm Ba, and 8.6-22.7 ppm Pb.

5. Discussion

5.1 Tectonic Setting

The first goal of this research was to evaluate the tectonic setting and history of the Lundmark Akow area. This was accomplished by an analysis of the geochemistry of mafic and felsic volcanic and intrusive rocks from Lundmark Akow.

Mafic rocks from Lundmark Akow have been divided into five distinct groups based on their trace element chemistry. The five groups show varying degrees of REE fractionation, LREE/HREE enrichment, as well as variable negative HFSE anomalies. Factors effecting the trace element geochemistry include the source of the parent magma, melting processes, and contamination (Murphy, 2007). Mafic group 1 consists of three lamprophyre samples, which show very enriched LREE vs HREE and have a pronounced negative Zr, Hf, and Ti anomaly as well as minor negative Nb anomalies (Fig. 4.16). Lamprophyres are typically derived from a very volatile rich magma from deep mantle sources (Mitchell, 1994). Mafic group 1 was likely derived from a hydrous magma that was sourced from an undepleted mantle explaining the LREE enrichment but flat HREE.

Mafic group 2 shows moderate enrichment of LREE over HREE with negative anomalies of Nb, Zr, Hf, and Ti (Fig. 4.17) consistent with them having formed in an arc setting or having been contaminated by crustal rocks (Murphy, 2007). In an arc setting the subducted slab undergoes dehydration which releases volatiles into the mantle wedge promoting melting and producing a hydrous melt (Murphy, 2007). However, the insolubility of HFSE in water rich solutions compared to that of large ion lithophile elements (LILE), results in enrichment of LILE and relative negative HFSE anomalies in arc magmas. It is possible that the melt was not formed in an arc, but rather inherited these anomalies by incorporating a contaminate crustal material that was arc derived. The addition of enough crustal material will cause the new melt to inherit the HFSE anomalies (Murphy, 2007). The source of this anomaly can be determined

by Sm/Nd isotopes as contamination by older crustal material will lead to negative ε_{Nd} values. The ε_{Nd} of the one analyzed sample from this group is 3.07. The average ε_{Nd} for the depleted mantle at 2.67-3.02 Ga in the Superior Province is estimated to be +3.0 ±0.5 (Henry et al., 2000). Given the minimum age of the unit at 2980 Ma based on a cross cutting relationship with a dated rhyolite intrusion, the ε_{Nd} value of 3.07 suggests a depleted mantle source, with no evidence for crustal contamination.

Mafic group 3 shows a moderate enrichment in LREE compared to HREE and has negative Nb and Ti anomalies (Fig. 4.18). An arc setting could account for both the LREE enrichment and the decrease in both Nb and Ti. However, one sample from this group yields an ε_{Nd} value of -1.53, which suggests that this melt has assimilated older crustal rock. Because Sm is preferentially enriched over Nd in partial melts, crustal rock will have increased levels of Nd/Sm versus the depleted mantle, resulting in negative ε_{Nd} values. The negative ε_{Nd} value of this sample suggests the existence of an older crustal basement to the North Caribou Greenstone belt. The only age date for a rock which predates the 2982 Ma age for the South Rim rhyolites of Davis and Stott (2001) or the 2980 Ma age from this study, is from the base of a rhyolite unit which returned a U/Pb date of 3053 ± 0.8 Ma (McNicoll et al., 2016). This rhyolite unit is located in the extreme south of the South Rim Volcanic Assemblage and is separated from the basalts of that assemblage by an unconformity or fault zone (McNicoll et al., 2016). The rhyolites are the only known evidence for any volcanic activity predating the bulk of early belt formation from 2.98 to 2.93 Ga (Biczok et al., 2012), but suggests that an early proto-continent may have been present and buried by further volcanic activity and could explain the negative value in Mafic group 3. Mafic groups 2 and 3 represent arc magmatism, most likely in a continental arc setting due to the existence of older basement crust.

Mafic groups 4 and 5 have very flat trace element patterns with no LREE or HREE fractionation. Mafic group 4 has very minor Nb anomalies but no other HFSE anomaly. An analysis of Sm-Nd isotopes of two sample from group 4 returned an ε_{Nd} value of 1.07, and 2.61. three samples taken from mafic

group 5 yielded ε_{Nd} values of 0.39, 0.71 and 0.97. Somewhat enriched ε_{Nd} values of around 1 have previously been interpreted in the Western Superior Province to represent a less depleted mantle source such as from a mantle plume (Tomlinson et al., 2004). A mantle plume source for these rocks is consistent with Hollings and Kerrich (1999) interpretation for the source of the tholeiitic basalts of the South Rim assemblage. The flat trace element pattern displayed by both mafic groups 4 and 5 are diagnostic of plume volcanism, similar to what is seen in modern oceanic plateaus of Ontong java or Nauru (Hollings and Kerrich, 1999). The one higher ε_{Nd} value of 2.61 from mafic group 4 is from a sample high in the stratigraphic sequence and may represent a later event of an interplay between a plume and depleted mantle source.

Ages of 2973 ± 0.42 Ma for felsic group 1 and 2980 ± 0.77 Ma for felsic group 2 were yielded from U/Pb analysis of zircons. Felsic groups 1 and 2 are characterized by highly enriched LREE compared to HREE, negative Nb and Ti anomalies as well as minor positive Zr and Hf anomalies. The negative Nb and Ti as well as the LREE enrichment suggests these felsic rocks were formed in an arc environment (Murphy, 2007). The positive Zr and Hf anomalies may be a result of fractionation and zircon accumulation (Hollings and Kerrich, 1999). Felsic group 1 yields an ε_{Nd} value of 1.16 whereas felsic group 2 has an ε_{Nd} value of 0.07. The felsic rocks could represent separate partial melt events, or alternatively could represent the result of melt evolution and fractionation from an originally mafic melt. Fractionation of a mafic melt will raise the total REE but (barring a few specific minerals) will not alter the trend on a spider diagram, likewise ε_{Nd} values of igneous rocks are not altered by fractionation thus are maintained through early mafic melt all the way to the later felsic fractionated products of the original melt (Tomlinson et al., 2004; Murphy, 2007). Similarities in the spider diagrams suggest that mafic group 3 could be a potential mafic equivalent from which the felsic groups evolved. However, ε_{Nd} values suggest that felsic group 1 is not derived from Mafic group 3 as ε_{Nd} value of 1.16 of felsic group 1

is distinct from mafic group 3 at -1.53. Felsic group 2 has an ε_{Nd} value of 0.07 approaching the values of mafic group 3 which does support the possibility of a genetic link.

Hollings and Kerrich (1999) previously noted that the felsic rocks from the South Rim assemblage of the North Caribou greenstone belt had elevated Th/La ratios (0.26-0.31) compared to similar rocks of the Abitibi greenstone belt (0.17-0.22). Such findings are replicated in this study, with felsic group 1 having Th/La values between 0.23 to 0.52 and felsic group 2 showing even more elevated values with a range between 0.99 and 1.19. Elevated Th/La ratios may represent contributions from sediments derived from continental crust or contamination by a highly evolved basement crust (Hollings and Kerrich, 1999; Plank, 2005). The suggestion that high Th/La ratios is indicative of crustal contamination is supported by the negative ε_{Nd} values of the groups showing the highest Th/La values (Fig. 5.1). In contrast, the groups which have a mantle or depleted mantle ε_{Nd} value such as groups 2, 4 and 5 also show the lowest Th/La ratios as they have not undergone any crustal contamination. The differences in Sm/La and Th/La between the felsic and mafic samples suggests that the felsic volcanic rocks did not evolve from any of the identified mafic groups and instead represent a unique sequence of magmatism.

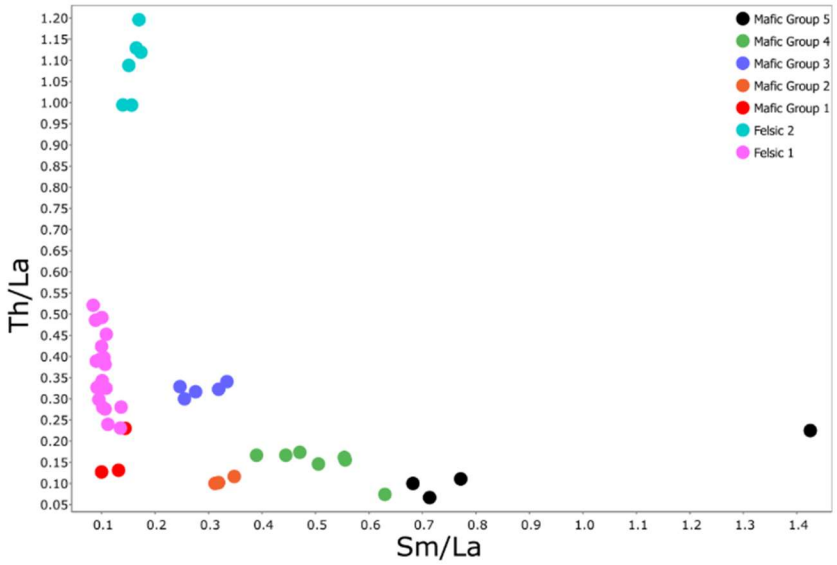

Figure 5.1. Sm/La vs Th/La of each of the mafic and felsic igneous rock groups

When sediments form by the erosion of other rocks, the trace element trends and content of the sediments will match that of the parent rock (Fralick, 2003). The trace element characteristics of the meta-sedimentary rocks from this study show arc signatures with prominent negative Nb and Ti anomalies as well as a LREE enrichment over HREE (Figs. 4.25, 4.26, 4.27). These trends match those of arc derived magmatism such as felsic group 1 or mafic group 3 which could have been the source for the sediments. A comparison of Sm/La vs. Th/La of the sedimentary rock groups shows overlap and a possible mixing trend between felsic group 1 and mafic group 3 as possible parent rocks to the sedimentary assemblages in the Lundmark Akow area (Fig. 5.2).

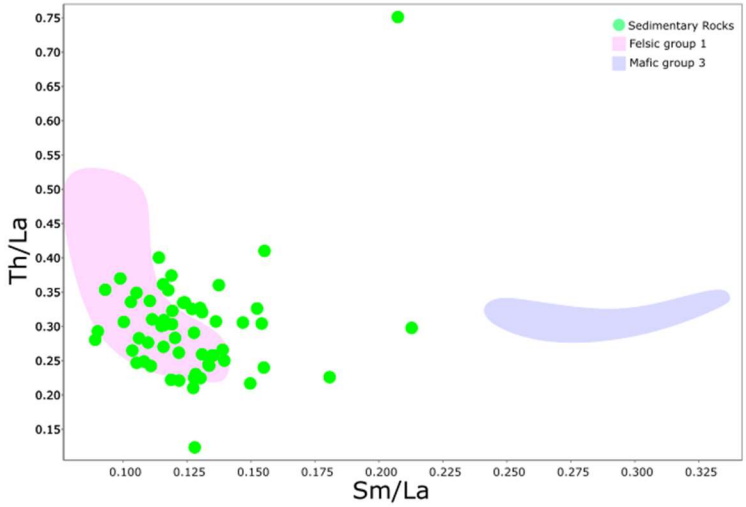

Figure 5.2. Sm/La vs Th/La plot of the meta-sedimentary rocks, with the spread in values for felsic group 1 and mafic group 3 drawn in.

5.2 Tectonic History

The earliest dated assemblage from the project is from felsic group 2 with sample DT103 yielding an age of 2980.02 ± 0.77 Ma. This sample was a rhyolite flow from drill hole 21-03 and is intruded by sample DT105 which is a quartz feldspar porphyry unit from felsic group 1 with an age date of 2972.99 ± 0.42. Sample DT079 from felsic group 1 yielded an age of 2973.96 ± 0.42 and occurs in drillhole 19-10. The ages of these volcanic rocks is consistent with the previously determined periods of volcanic activity in the belt of around 2.98-2.93 (Biczok et al., 2012; McNicoll et al., 2016). No mafic rocks in the study

area were dated, but cross cutting relationships and the uphole younging direction implied by the dated felsic rocks suggest that mafic groups 4 and 5 predate the felsic volcanism in the area. A molybdenite-bearing quartz vein hosted in the massive basalts of drill hole 21-06 which returned an age date of 2976 ± 13 Ma supports a minimum age for these mafic rocks that is at least as old if not older than the felsic volcanic rocks in the area.

The meta-sedimentary rocks in this study have not been directly dated, however, some constraints on the relative age can be made based on their association with the felsic and mafic rocks. When drill holes were deep enough to intersect the mafic assemblage beneath the meta-sedimentary package it consisted of mafic groups 4-5 which have been interpreted to represent an early oceanic plateau which predates the felsic volcanism occurring at around 2980 Ma. The sedimentary rocks have been intruded by felsic volcanic rocks belonging to felsic group 1. The felsic intrusive units have not been dated but match the geochemistry of felsic group 1 in which two other samples were dated to 2972 Ma, suggesting that the sediments formed earlier than that.

A possible tectonic history for the South Rim assemblage of the North Caribou Greenstone belt is as follows. Mafic group 4 and 5 occur early in the history of the belt, as a plume generated plateau on oceanic crust (Fig. 5.4A). The high heat of the plume in a deep sea environment could explain the banded iron formations present with these mafic rocks. Mafic groups 4 and 5 are found predominantly at the bottom of drill holes 19-10, 17-01 and 21-08, where a transition is seen from the upper portion of the drill holes that is sediment dominated with intermittent felsic volcaniclastic layers and mafic intrusions to massive basalts and gabbroic units (Fig. 5.3). Thus, mafic group 4 and 5 are interpreted to represent a plume generated oceanic plateau consistent with Hollings and Kerrich (1999) which formed the basement for later volcanic and sedimentary deposistion in an arc setting. The presence of banded iron formations and lack of significant volcaniclastic material associated with the mafic tholeiites is consistent with a subaqueous setting for volcanism in this early stage (Hollings and Kerrich, 1999).

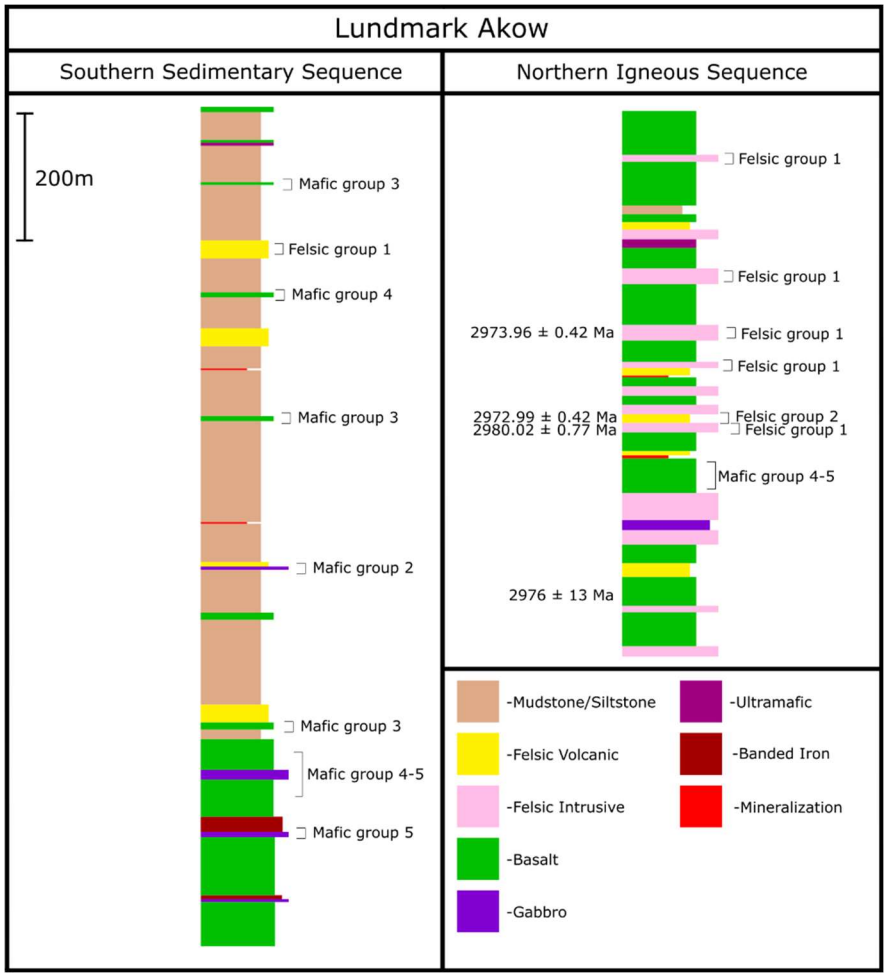

Figure 5.3. Composite stratigraphic section of Lundmark Akow of both the southern sedimentary sequence and the northern igneous sequence. This section includes data from multiple drill holes that are not directly contiguous, as such this represents the best efforts of the author to approximate the full stratigraphy of Lundmark Akow.

The only challenge to this interpretation is samples DT101 and DT095 from drill hole 17-01, which belong to mafic group 4 and 5 but occur as meter wide intrusions with sharp contacts within the sedimentary-dominated upper portions of the drill hole. These two intercepts of unevolved plume generated melt are emplaced into mafic, felsic, and sedimentary rocks with arc signatures and are interpreted to have formed after the plume generated magmas of mafic group 4 and 5. Potentially this could be evidence that the plume remained present and interacted with the subducting arc as suggested by Hollings and Kerrich (1999) and these two units could represent a later pulse of plume magmatism

that was able to remain uncontaminated by arc magmas and sediments on its way to the surface suggesting a long lived plume event that preceded and interacted with arc magmatism.

After the formation of the oceanic plateau, deep sea sediments then began to accumulate on top of it. Eventually, shortly before 2980, Ma this oceanic plateau collided into a subduction arc environment with some older protocontinent (Fig. 5.4B). When a semi-buoyant oceanic plateau enters a subduction zone it can impact the rate of subduction, cause a subduction jump, or decrease the overall angle of the subducting slab (Yan et al., 2022). It is possible a portion of the plateau was thrust over the protocontinent within the arc due to the higher buoyancy of the plateau versus the rest of the oceanic crust. This formed the basement to further arc related volcanic activity seen throughout the North Caribou greenstone belt from 2980 to 2972 Ma. The arc related volcanic activity led to increased erosion and sedimentation into the adjacent ocean. The sedimentary rock assemblages within the study area are interspersed with occasional basaltic and intrusive to volcaniclastic material formed as a result of coeval arc and plume related magmatism (Fig. 5.4C).

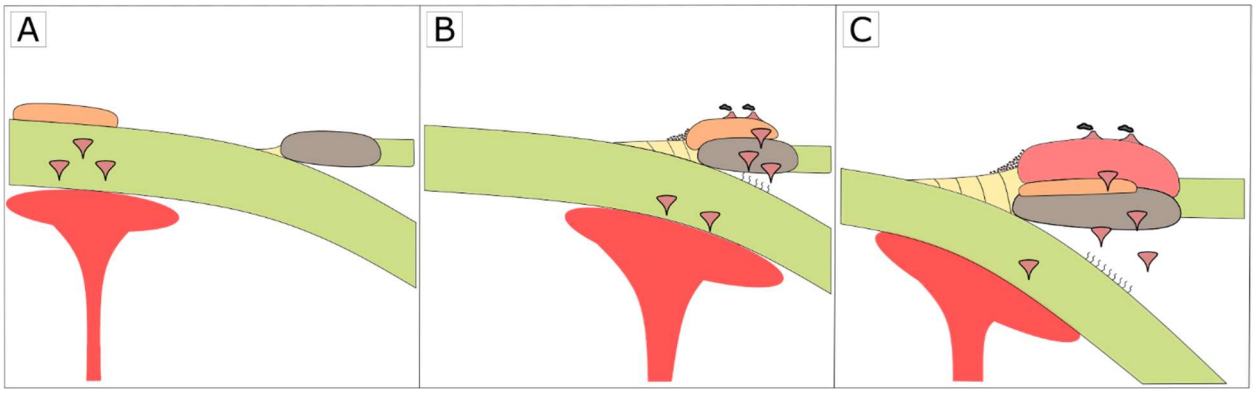

Figure 5.4. Tectonic history of the Lundmark Akow area. (A) Formation of an oceanic plateau (orange)from plume generated magmatism, represented by mafic groups 4 and 5. (B). The oceanic plateau is obducted onto older basement crust, arc magmatism (pink) begins to build on top of the oceanic plateau and erosion takes material from the plateau and builds it up on the oceanic shelf. Plume derived magmatism continues with volcanism containing both plume and arc signatures forming on top of the plateau. This magmatic activity is represented by mafic groups 2 and 3 as well as felsic groups 1 and 2. (C) Arc and plume magmatism is built up on top of the plateau, continued erosion leads to the build up of a large sedimentary package along the margins of this Archean protocontinent. The erosion of material from both the oceanic plateau and the later arc magmatism leads to the formation of the sedimentary rock sequences found in Lundmark Akow.

5.3 Mineralization at Lundmark Akow

The second goal of the project was to characterize the mineralization present in Lundmark Akow and determine how it formed. The focus of this project was a 300-400 meters thick assemblage of meta-sedimentary rock with significant portions of the assemblage consisting of garnetiferous biotite sericite schist with a variable content of staurolite containing horizons of semi-massive to massive sulphide mineralization.

The meta-sedimentary assemblage consist of fine clay to siltstone particles deposited in alternating sequences consistent with deposition by turbiditic flows. Some portions of the assemblage consist of massive biotite, interpreted to be the metamorphic product of pelagic sediments. Petrographic analysis of these samples show that they consist predominantly of very fine-grained quartz crystals separated by thin bands of biotite or muscovite. This suggests that the mudstones to sandstones underwent regional metamorphism reaching greenstone to amphibolite grade (Bucher and Frey, 2002). Garnet and eventually staurolite porphyroblasts formed within the schists as regional metamorphism reached a peak at amphibolite grade conditions (Breaks et al., 2001). The garnet content varies throughout the assemblage, in some portions the garnet makes up only a few percent of the rock, whereas some beds are very garnetiferous, consisting of up to 70-80 percent garnets along with quartz and biotite.

Petrographic analysis of the tuffaceous units shows that plagioclase content comprises 10 to 30% of the sample, often occurring as somewhat rounded and heavily sericite altered. The tuffs also consist of fine-grained quartz and muscovite with lesser amounts of biotite. This is consistent with the beds of tuffaceous felsic volcanics rocks which were interpreted to be water lain tuffs by Biczok (2016).

Overall given the arc setting suggested by the geochemistry and combined with the subaqueous low energy environment suggested by the mudstones and siltstone layers; the sequence of sedimentary

rocks likely represents an ocean floor basin where felsic volcanic activity deposited water lain tuffs that were later buried by subsequent deep-sea sediments.

Given the subaqueous setting, in a high heat environment associated with plume and arc magmatism, a volcanogenic massive sulphide model may be appropriate for the mineralization in Lundmark Akow (e.g. Franklin et al., 1981). The Cu-rich mineralization with associated Zn and to a lesser extent Pb mineralization is consistent with the metal endowment found in volcanogenic massive sulphide systems around the world (Franklin et al., 1981; Large, 1992). If the mineralization present at Lundmark Akow was formed in a VMS system than that should be reflected in the rocks of the area. A proximal VMS system should show evidence of significant water/rock interactions which would create an alteration halo below sulphide mineralization (Franklin et al., 2005). In contrast vent distal mineralization will be distinguished by the lack of an alteration feeder zone to the massive sulphides, as well as the presence of other exhalative products such as iron enriched sediments, quartz garnitites, or tourmalinites (Spry et al., 1999; Franklin et al., 2005).

5.4 Alteration and major element behaviour

If the mineralization present in Lundmark Akow represents a proximal VMS system than there should be evidence for hydrothermal alteration of the local rock. Previous work at Lundmark Akow argued that the garnet-staurolite-rich schists formed as a result of hydrothermal alteration that leached out mobile elements and caused a residual increase in Fe (Biczok, 2016). Biczok (2016) proposed that Rb/Sr ratios could be a potential proxy for hydrothermal alteration intensity in Lundmark Akow as they have been used in the past to assess hydrothermal alteration (Plimer and Elliot, 1979) and recently applied at Myra Falls VMS in British Columbia (McNulty et al., 2020). Due to the similar ionic radii, electronegativity, and ionization potential between Rb and Sr with K and Ca, respectively, they are able to substitute into the lattice of K and Ca bearing minerals (Taylor, 1965). The sericitization of plagioclase

feldspars by hydrothermal alteration will cause a decrease in Sr values in whole rock (Shanks, 2010). The formation of white micas of which K is a major component will cause an increase in Rb. Both of these effects will result in an increase in Rb/Sr ratios. Rocks containing no plagioclase and a high biotite content (most of the analysed rocks at Lundmark Akow) will have high Rb content contained within the K site of biotite and low Sr and Na due to the lack of plagioclase. Therefore, these elements are not appropriate to be used to test for hydrothermal alteration within Lundmark Akow.

Another method of evaluating the occurrence of hydrothermal alteration within VMS systems is the AI/CCPI boxplot created by Large et al. (2001). This method combines the Ishikawa alteration index (AI) (Ishikawa et al., 1976) with the chlorite carbonate-pyrite index (CCPI). The AI evaluates increasing K and Mg content contrasted with decreasing Na and Ca levels using the equation AI= (100*(K_2O+MgO)) /(K_2O+MgO+Na_2O+CaO), essentially quantifying the breakdown of plagioclase by sericite alteration. The CCPI index tracks increasing Mg and Fe contents against decreasing K and Na to test if the rock has undergone chloritization using the equation CCPI= (100*(MgO+FeO)) /(MgO+FeO+Na_2O+K_2O). This method is designed to evaluate felsic volcanics rather than sedimentary rocks. The trends highlighted in Figure 5.5 do show possible alteration in the sericite, chlorite-sericite, and chlorite-pyrite directions moving out from the cluster of least altered samples.

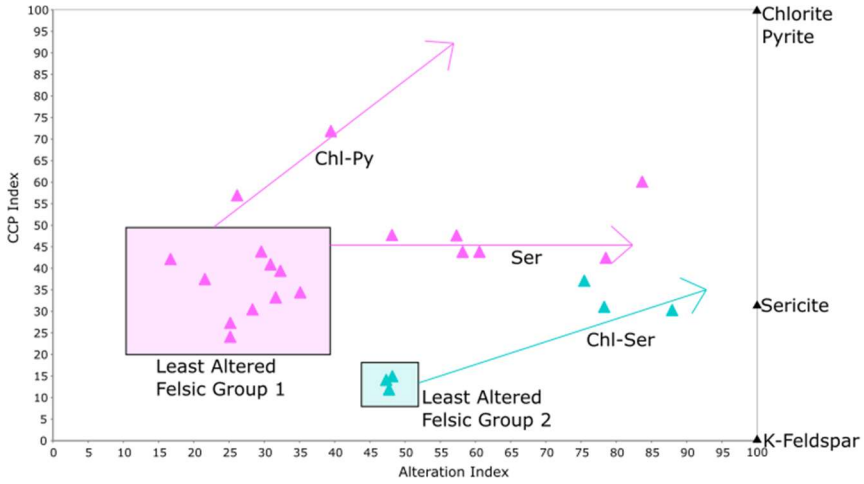

Figure 5.5. AI/ CCPI alteration box plot diagram of felsic volcanic and intrusive samples.

Most felsic volcanic samples in this study were from drill holes 19-10 and 21-3 which occur roughly 5 kilometres north of the proposed “hydrothermal pathway”. These northern drillholes have a much more volcanic and intrusive dominated stratigraphy with limited clastic input compared to the southern drill holes and may represent a more vent proximal setting. This is supported by the more significant mineralization with meter wide massive sulphide, as well as the presence of Cu, Zn and Pb bearing sulphides with typical VMS features such as chalcopyrite disease. However the distance between this northern mineralization and the southern lithologies, and the sparsity of drill hole data prevent a definitive connection between the two, they may occur at different stratigraphic levels or represent an entirely separate mineralization event.

Only three felsic volcanic samples were taken from within the “hydrothermal alteration pathway” two of which returned altered values. The three samples were interpreted as felsic volcanic tuffs due to an overall higher sericite content than in the surrounding biotite dominated metapelite, suggestive of a higher primary feldspar content (Biczok, 2016). However, alternating biotite-muscovite layering is also recognized in the area and is a result of turbiditic banding creating coarser siltstone units which form muscovite rich layers after metamorphism. Thus, a sericite-rich rock is not necessarily derived from a felsic volcanic parent and may have some degree of terrigenous input into the protolith sediment. A mixed source would effect the geochemistry of the sample, and lead to a false positive for hydrothermal alteration. Indeed, both altered samples occur within sequences of metapelite and psammite and contain no visible feldspar grains whereas the unaltered sample is described as containing over 1% plagioclase feldspar phenocrysts which explains its higher Na and Ca values (Biczok, 2016).

Given the limited sample numbers it is difficult to suggest that this assemblage represents the upper semi-conformable region of a VMS system and the geochemical methods to trace hydrothermal alteration is more applicable to felsic and mafic igneous rocks than the sedimentary assemblage found in Lundmark Akow. A more effective means of evaluating the potential for hydrothermal alteration is by

evaluating the behaviour of elements within the meta-sedimentary rocks. An overview of the behaviour of several major oxides in the sedimentary rocks is presented in Figure 5.6.

The content of both Fe and Mn behave very similarly downhole showing compositional increases and decreases at the same time throughout the drill hole (Fig. 5.6A). Figure 5.6 B and C compares Fe_2O_3 with Al_2O_3 and Na_2O respectively and show an inverse relationship between the oxides, in that when Fe increases Al and Na decrease. Figure 5.6 D shows that Na and Al behave very similarly through most of the down hole plot. The only exception to this is sample DT058 at a depth of 245m where Na shows a significant jump with no increase in Al. Thin section analysis of this sample revealed the presence of up to 16% plagioclase feldspar likely due to the input of some felsic volcanic material in this interval. Thus, the high Na content at this point is likely related to the composition of the sediments and not alteration.

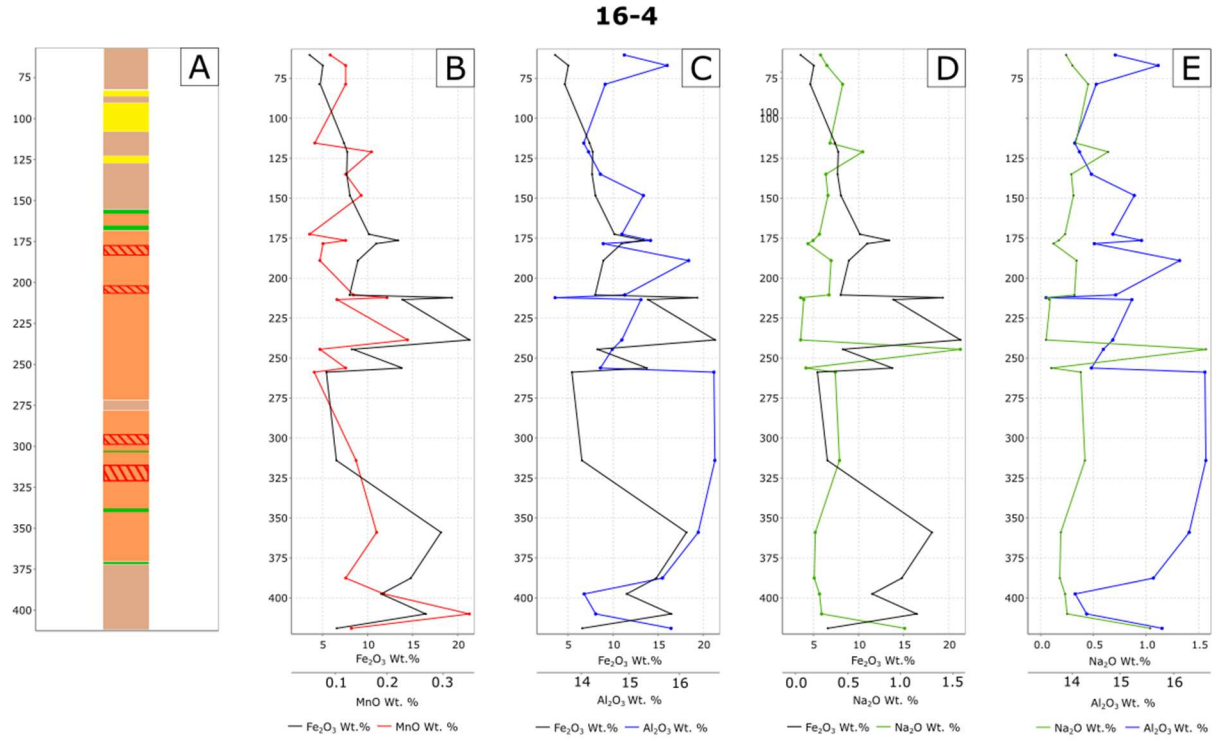

Figure 5.6 Downhole plot of drill hole 16-4 comparing contents of Fe_2O_3, Na_2O, and Al_2O_3 in meta-sedimentary rock samples. A. Downhole lithology of drill hole 16-04. Brown is biotite muscovite schist, orange is biotite muscovite garnet schist, yellow is felsic volcanoclastic, green is basalt, red hatch is massive sulphide mineralization.

Overall, these trends show that Fe and Mn are being added to the sediments in a process which does not cause a similar enrichment of Al or Na. If this enrichment was caused by a hydrothermal process which leached mobile cations and left a relative enrichment in the immobile elements, then each immobile element should show similar trends in the graph. As Fe and Al do not behave similarly this suggests they are effected by different processes (Fralick, 2003). Mobile elements such as Na should also be leached in hydrothermal alteration which would cause relative enrichment in Al, so an inverse behaviour would be expected, however, the graph does not show this relationship, instead suggesting similar behaviour between Na and Al. As the behaviour of these elements are not consistent with hydrothermal alteration associated with a semi-conformable alteration zone another possible source must be considered. If the deposits at Lundmark Akow were formed as a vent distal deposit through a hydrothermal plume then the effect on the local rocks would be different than what would form through hydrothermal alteration.

Distinguishing a sedimentary rock that has incorporated a hydrothermal plume component can be accomplished by an evaluation of major element behaviour in the formation of sediments (Fralick, 2003). Figure 5.7 illustrates the behaviour of Al, Ti, and Fe in the sedimentary rock samples. The graph of Al and Ti show a linear trend, suggesting both are enriched by similar sedimentary transportation processes. The graphs of Fe vs. Al and Fe vs. Ti show two distinct trends in the data. The first half show a linear relationship between the data points in black with the trend highlighted by the black arrow. This trend represents Fe in the rock derived from a parent source as it correlates with the immobile Ti and Al. The samples highlighted in blue show a decoupling in Fe content vs Al or Ti where Fe is being added to the rock without any addition of Ti or Al. This Fe addition could be from particulate fallout from hydrothermal plumes as it would not increase Al or Ti contents in the way that sedimentary processes would (Fralick, 2003). Therefore, the highlighted blue samples may have undergone hydrothermal particulate enrichment. The term hydrothermal particulates is being used to refer to the Fe-oxides and

oxy-hydroxides as well as potential sulphide particles which precipitate out of hydrothermal plumes and settle along the sea floor (German and Seyfried, 2014).

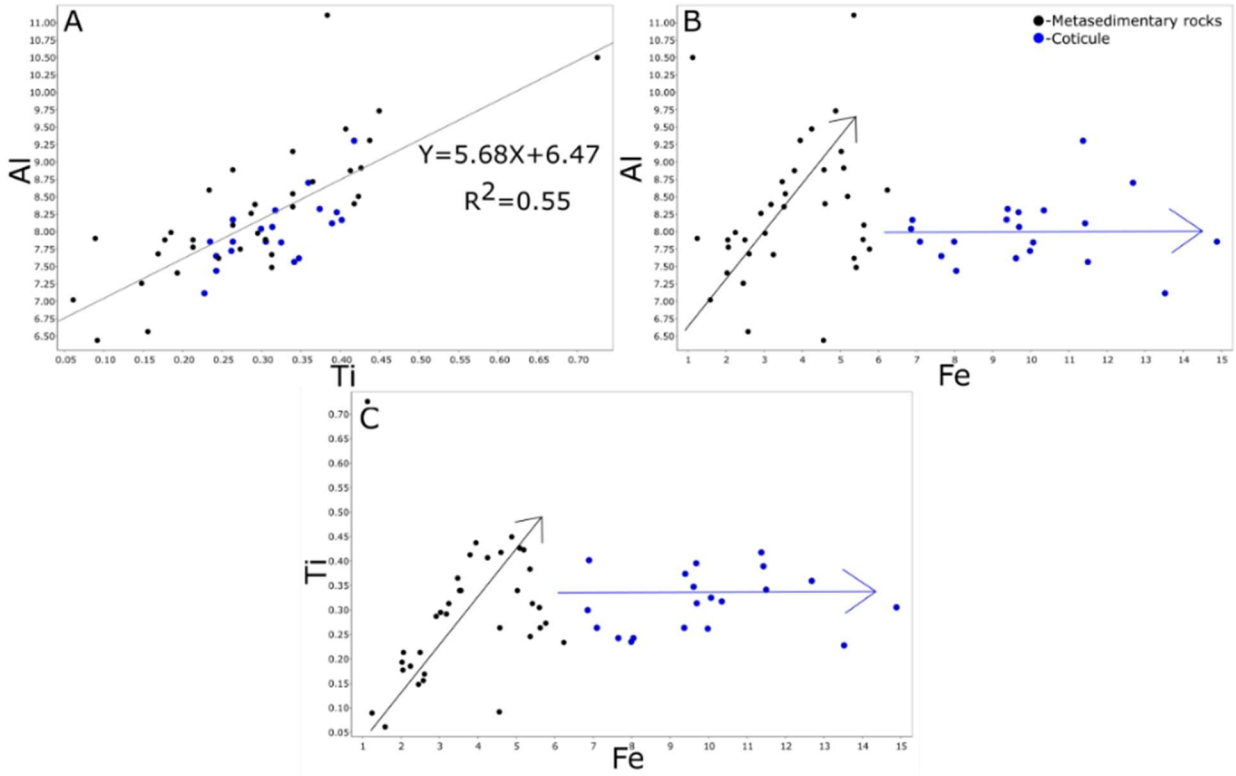

Figure 5.7 Bivariate plots between Al, Ti, and Fe showing interactions between the various elements. All data is whole rock analysis of schistose rocks. Samples highlighted in blue represent an iron enrichment in the samples unrelated to sedimentary processes.

Evaluation of hydrothermal input into sediments around the hydrothermal massive sulphide deposit of Broken Hill, Australia, by Heimann et al. (2009) defined hydrothermal vs non hydrothermal metasediments based on a theoretical mixing diagram shown in Figure 5.8. Hydrothermal input is estimated by plotting a mixing line between the composition of modern sediments in the Red Sea (a modern exhalative hydrothermally dominated regime) with those of the average continental crust. The samples which did not show the Fe enrichment trend in Figure 5.7 plot largely within or below the highlighted region defined by metasediments from Broken Hill, Australia. The blue coloured hydrothermal samples plot on the margins of the metasedimentary rock field towards the field for hydrothermal sediments from Broken Hill. Based on the mixing line the blue samples would be

composed of between 10% to 30% hydrothermal plume particulates with a few outliers reaching up to a maximum of 50% particles mixed with a remainder of terrigenous derived pelagic metasediment. The samples plot to the right of the hydrothermal sediment field for Broken Hill suggesting that the Lundmark Akow samples are more distal to the vent or are formed by a regional diffuse plume which is slowly raining down particles but not as quickly as the build up of terrigenous material. Being closer to the source would cause a greater input in of hydrothermal particulates over terrigenous and plot farther to the left on the diagram.

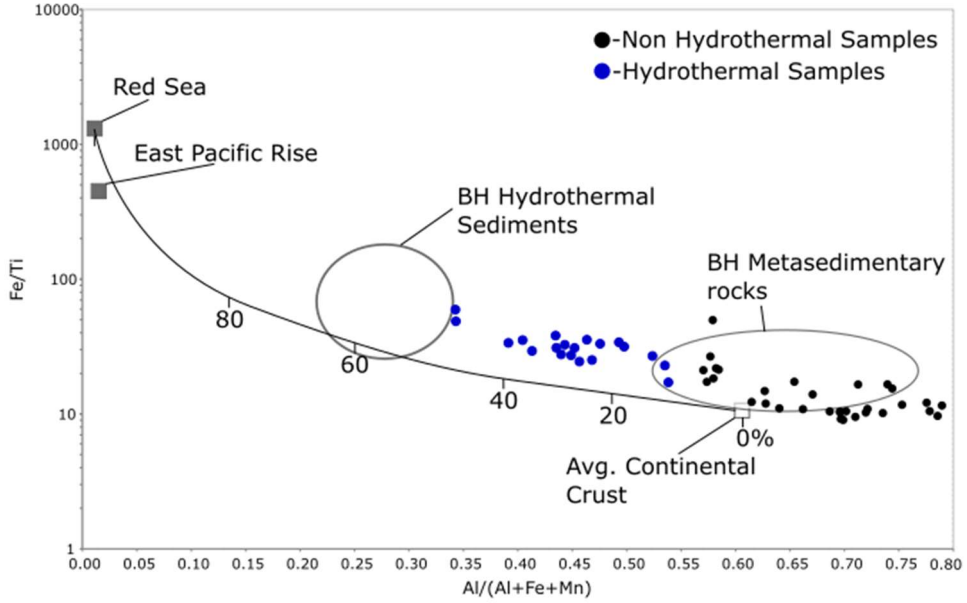

Figure 5.8 Al/(Al+Fe+Mn) vs. Fe/Ti diagram, showing compositions of Lundmark Akow sedimentary rock compared to Broken Hill, Australia mine coticule and metasedimentary rocks. Blue coloured samples are those previously determined to undergo Fe enrichment. Curve represents a mixing line between compositions of hydrothermal sediments from the Red Sea and East Pacific Rise with an average continental crust composition. Tick marks and numbers along the mixing line represent approximate mixing proportions in percent. Adapted from Böstrom (1973) with data fields from Heimann et al. (2009).

Overall, the behaviour of elements, in particular the enrichment of Fe and Mn in the sediments is more indicative of distal VMS mineralization formed by hydrothermal plume particulate fallout. No method of detecting hydrothermal alteration of the sediments was successful. The loss of mobile Na occurs in tandem with a loss in Al which does not suggest sodium being removed by hydrothermal

alteration, but rather is a result of an increasing plume particulate input at the expense of the terrigenous input (the source for both Al and Na in the rock).

5.5 Garnet

At Lundmark Akow there are frequent occurrences of garnet rich rock consisting of 20 to 50% garnet porphyroblasts. These often occur as thin beds dominated by coarse quartz and garnet with accessory muscovite and biotite. Figure 5.9 shows typical garnet textures from Lundmark Akow, characterized by coarse garnet dominated bands.

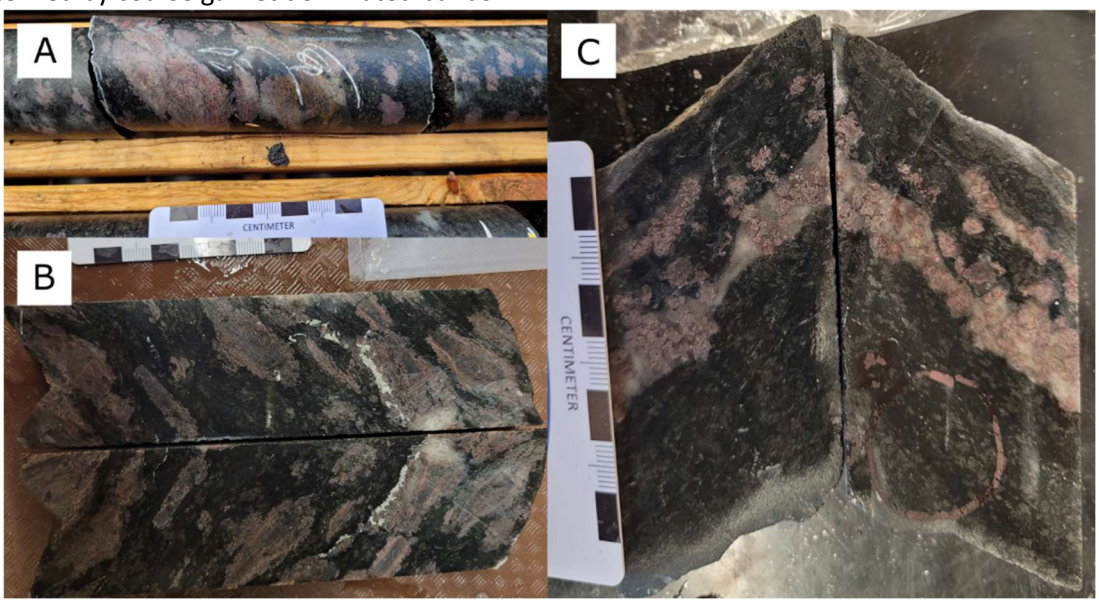

Figure 5.9 Hand sample photos of garnet rich beds or horizons within the biotite muscovite schist. A. DT053, B. DT057, C. DT060.

The occurrence of garnets within a meta-pelitic rock is a common and expected mineral from greenschist to amphibolite grade metamorphism (Sturt, 1962; Caddick et al., 2010). The required elements for the formation of almandine (Fe, Al, Si) can all be found in terrigenous derived meta-pelites (Forshaw and Pattison, 2022). However, difference in the texture of the garnet forming in distinct bedded horizons of predominantly only garnet is suggestive of unique conditions for formation defined in the literature as an exhalite product referred to as a coticule (Spry et al., 1998).

The term “coticule” is defined as a garnet-quartz rock regardless of garnet composition (Spry et al., 1998). Coticules occur as discontinuous stratiform units above, below, or along strike of massive sulphide horizons and can extend over several kilometers (Spry et al., 1998). Coticules form layers of less then a centimeter to up to 2 meters in width with the individual garnets being less than 1 mm up to greater than 1 cm in diameter depending on the metamorphic conditions reached (Spry et al., 1998). The minerology of a coticule consists primarily of quartz and garnet and may have accompanying biotite, muscovite, chlorite, and other aluminosilicates and ferromagnesian silicates (Spry et al., 1998). Although commonly described as consisting predominantly of quartz and garnet, coticules with a variety of minerals (apatite, gahnite, tourmaline, biotite, feldspar) are commonly associated with the largest deposits such as Broken Hill, Australia and Gamsberg, South Africa (Spry et al., 1998).

The mineralogy in samples from Lundmark Akow match the suite described by Spry et al. (1998). The garnet-rich samples were also identified as having a high input of hydrothermal particulate fallout in Figure 5.9, consistent with the proposed mechanism of formation for coticules. Hydrothermal particulate fallout mixing with terrigenous sediments has also been proposed as the method of formation of the garnet-biotite schists present in the nearby Musselwhite mine (Moran, 2008).

Manganese enrichment in garnet can suggest proximity to vent sites as Mn is a component of the exhaled fluids (Franklin et al., 2005; Spry et al., 2000). Major element compositions of the garnets in the Lundmark Akow property as displayed in Figure 4.32 show a trend between almandine and spessartine endmembers. A comparison of MnO vs. FeO Wt. % of garnets in a Harker diagram shows a clear trend line between MnO and FeO composistions suggesting direct substitution between the two (Fig. 5.10).

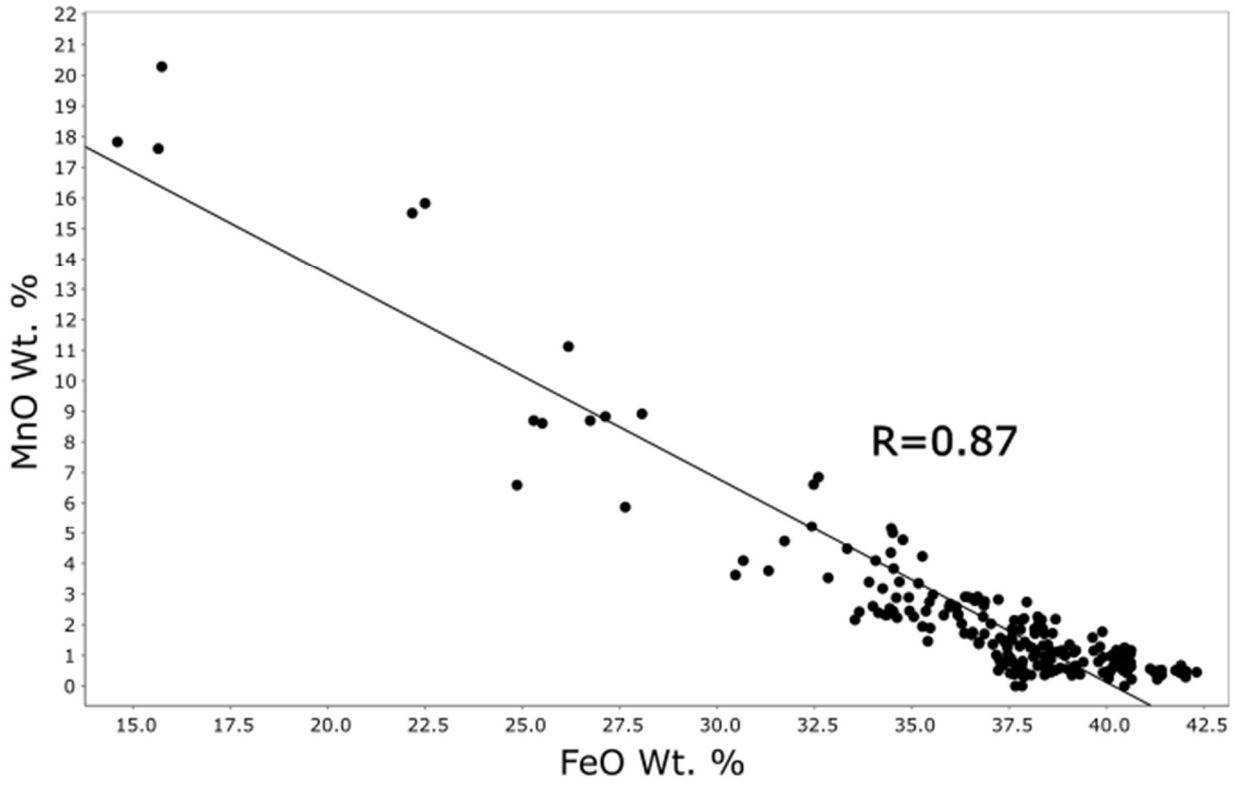

Figure 5.10 Harker diagram showing trendline between MnO and FeO composistions of garnet

Despite both Fe and Mn representing a hydrothermal component, fractionation occurs between the solubilities of Fe and Mn as the pH and oxidation state changes with intermixing between hydrothermal plume fluids and seawater (Spry et al., 2000). Evaluating if Mn enrichment is related to mineralization requires discrimination of proximity of the garnets to identified mineralization. The highest MnO contents in any garnet analyzed were four spessartine garnets from sample DT006 containing up to 22% wt. % MnO, followed by sample DT042 which contains up to 15% wt. % MnO. Both of these samples occur within layers of felsic volcaniclastic rock and do not appear to be located near any known massive sulphide mineralization. Sample DT058 has garnets with MnO values which are moderately high, up to 7 Wt. %; however, it occurs in a rock which was not considered to have a hydrothermal component based on Figure 5.9. Overall the data suggests that Mn enrichment in garnets is more a factor of the parent rock than any input by hydrothermal particulates. This is also supported by

the behaviour of Fe and Mn displayed in Figure 5.7 which shows an increase in Fe and Mn jointly with the Mn component being much smaller than Fe. Thus, Mn enrichment in garnets does not appear to be an effective vector to sulphide mineralization in Lundmark Akow.

Evaluation of the major element compositions of garnets also revealed significant variation in composition within a single mineral. Garnets throughout the research area show a general trend in compositional variation with a core containing higher concentrations of MnO and CaO, and a rim with higher concentrations of MgO and FeO (Fig. 5.11). The total magnitude of CaO, or MnO is unique to each sample, but the general trend remains constant with MnO and CaO decreasing from core to rim.

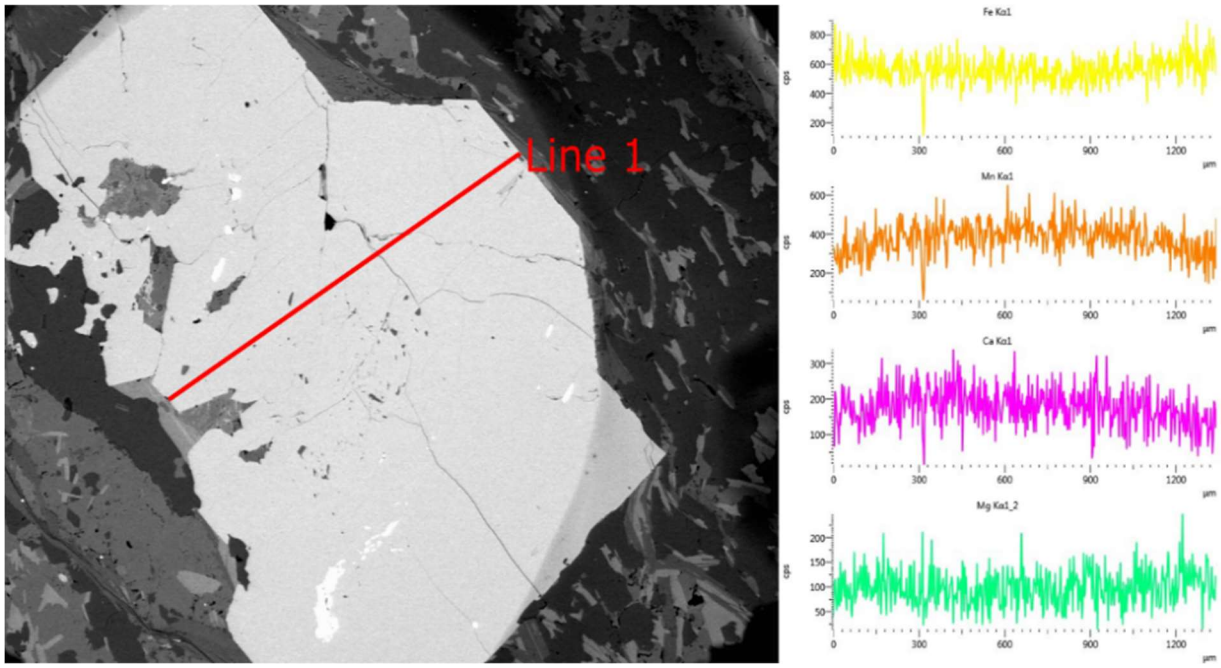

Figure 5.11. SEM-EDX line analysis across a garnet grain from sample DT042 showing a convex trend in Mn and Ca from rim to interior to rim. Fe content, and to a lesser degree Mg display a concave trend with higher concentrations in the exterior rims vs. the core of the garnet.

Point analysis on a garnet from sample DT058 yielded core values of 8.7 wt. % MnO, 6.1 wt. % CaO, 1.5 wt. % MgO, and 26.7 wt. % FeO at sample site labeled Garnet 1 (Fig. 5.12). Analysis of the garnet at rim sample sites labelled garnet 2-3 yielded values of 6.6 to 6.9 wt. % MnO, 2.6 to 2.7 wt. % CaO, 1.7 to 1.8 wt. % MgO, and 32.5 to 32.5 wt. % FeO respectively. This represents a change in

composition from core to rim of 24.1% decrease in MnO, 57.4% decrease in CaO, 20% increase in MgO, and a 17.8% increase in FeO.

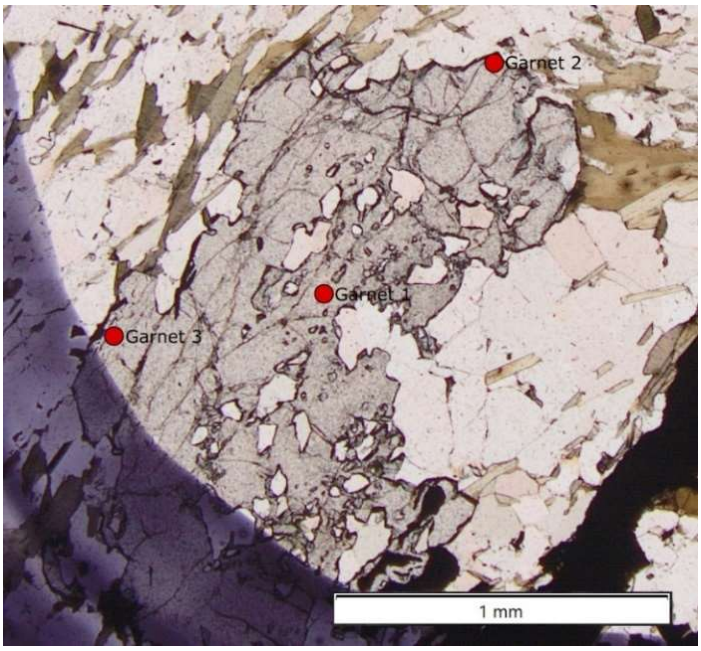

Figure. 5.12 SEM-EDX analysis points on a garnet. The results show a Mn and Ca rich core replaced with high Mg and Fe to the rim (DT058, PPL).

The cause of this compositional variation is debatable, but it could suggest two independent periods of garnet growth. Biczok (2016) suggested that garnet mineralization was coeval with sulphide deposition as a product of fluid alteration in a semi-conformable alteration zone. This was supported by a 1 cm wide ptygmatic folded garnet vein with associated pyrrhotite and chalcopyrite. The folding of an already formed garnet vein suggests an early genesis for this garnet that predates regional deformation and folding, or alternatively could be a result of several different metamorphic and deformation events. The difference in composition in the core compared to the rim of the garnet may also support the idea of an early garnet genesis associated with VMS fluids to form the core, and later growth under regional metamorphic conditions that forms the rim of the garnet. One garnet from drill hole 17-01 returned two separate U/Pb ages, the core of the garnet was dated at 2960.1± 18.7 Ma with the rim of the same mineral grain dating 2424.1 ± 2.87 Ma. A separate garnet grain returned an age date of 2523.42 ± 9.06 Ma. Previous work using Sm/Nd dating of garnets from the Musselwhite mine returned an age of garnet

formation of 2690 ± 9 Ma which was interpreted to indicate syngenetic to the orogenic gold mineralization during peak to post peak metamorphism (Biczok et al., 2012). Uplift and cooling in the belt was dated to around 2.5 Ga based on Ar diffusion in biotite (Biczok et al., 2012).

The younger garnet ages yielded from the two samples in this study occur around or after the time reported as uplift and cooling post metamorphism by Biczok et al. (2012) and may represent cooling past the closure temperature for the garnet grains during this period of uplift. The garnet core age of 2960 million years ago would suggest it formed several hundred million years prior to peak metamorphism when regional temperature and pressure conditions would have been too low to crystallize garnet and as such could represent the formation of garnet through hydrothermal processes unrelated to regional metamorphism. Although U/Pb age dating of garnet was first applied in 1989 (Mezger et al. 1989) the technique has since fallen out of favour in comparison to Sm-Nd and Lu-Hf techniques (Baxter and Scherer, 2013). The susceptibility of garnet to the complexities of local mineral-scale equilibrium and to the mobility of parent and daughter elements in crustal fluids and the common occurrence of mineral inclusions has created scepticism in regard to age dates garnered through U/Pb (Romer and Xiao, 2004; Baxter and Scherer, 2013; Sousa et al., 2013). The scatter in the Concordia diagrams also suggests that U concentrations may have been effected by alteration, with many of the points falling above the Concordia curve (Fig. 3.31). If the cores of the garnets were truly formed as a result of VMS fluids then this would support the mineralization being formed by a proximal VMS system but the single age us not definitive proof and should be treated with caution.

Compositional zoning in metamorphic garnet has long been recognized and indeed characterized by decreasing Mn content out from the center (Hollister, 1966). Concentric zoning in Mn and Ca reflects a depletion of a reservoir of available Mn and Ca to the growing garnet porphyroblast (Ague and Carlson, 2013). Major cations of Mg, Fe, Ca, and Mn form the dodecahedral sublattice of the garnet and are a multicomponent system requiring substitution of one element for another to maintain stoichiometry

(Ague and Carlson, 2013). Zoning formed during metamorphism is preserved even during later higher temperature or pressure conditions up to the staurolite isograd so long as the porphyroblast is greater than 0.4mm in size (Florence and Spear, 1991). The large grain size of porphyroblasts at Lundmark Akow suggests they have not been altered by metamorphic resetting and thus display primary growth zoning.

Caddic et al. (2010) calculated mineral assemblages at various conditions for an average pelitic protolith to correlate the assemblages with the expected composition of a growing garnet porphryoblast (Fig. 5.13). The expected trend in the calculated examples matches what was observed in analyzed samples at Lundmark Akow. This suggests that the change in garnet composition does not require different fluid sources, such as an early VMS hydrothermal fluid forming the core and the rim forming from a later metamorphic fluid, the garnet composition variation can be entirely explained by prograde metamorphic growth. This supports a model where sulfide mineralization formed from a distal VMS system as the garnet rich horizons would have formed by metamorphism of a iron enriched hydrothermal sediment.

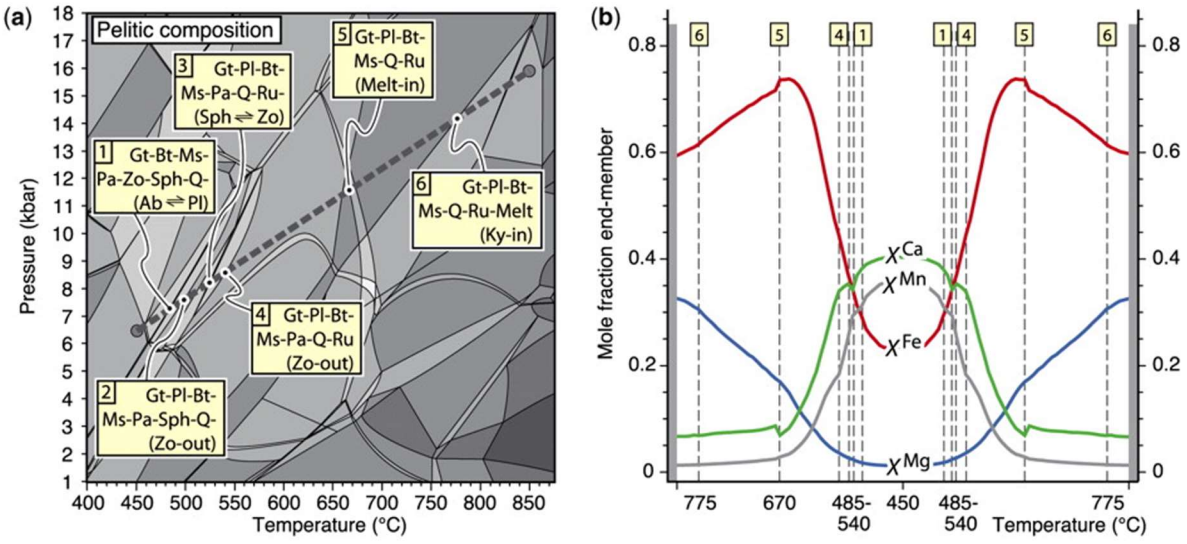

Figure 5.13 A. P-T psuedosection with a modeled heating path labelled for key mineral reaction assemblages. B. Profile through the core of model garnet crystal grown in metamorphic conditions up to 850℃. Graphs from Caddick et al. (2010). Gt = garnet, Bt = biotite, Chl = chlorite, Pl = plagioclase, Ms = muscovite, Pa = paragonite, Crd = cordierite, Opx = orthopyroxene, Omp = omphacite, Law = lawsonite, Ab = albite, Ilm = ilmenite, Ru = rutile, Sph = sphene, Zo = zoisite, Sil = sillimanite, Ky = kyanite, And = andalusite.

Garnet trace element compositions have been used to evaluate prospectivity for massive sulphide mineralization. For example garnets analyzed from the Gamsberg deposit of South Africa show a trend in HREE enrichment relative to LREE and the presence of a positive Eu anomaly approaching mineralization (Stalder and Rozendaal, 2005). Lottermoser (1989) suggested Eu anomalies in meta-exhalite at Broken Hill, Australia are dictated by redox conditions, pH, and temperature and that a positive Eu anomaly was characteristic of proximity to a hydrothermal vent and sulfide mineralization whereas negative Eu anomalies suggest meta-exhalite forming distal to ore. These findings were supported by Spry et al. (2007) who identified positive Eu anomalies within garnet in proximity to ore, but also highlighted the complexities as the REE concentrations in garnet are dependent on several variables such as the partitioning of elements among coexisting minerals, bulk-rock composition, crystal chemistry, aqueous speciation of REE in the metamorphic fluid phase in equilibrium with garnet, metamorphic P-T regime, and fO_2 conditions. Eu anomalies develop from several possible sources. Stalder and Rozendall (2005) suggested that the reduction of Eu^{3+} to Eu^{2+} by hot hydrothermal fluids altering the host rock at temperatures greater than 200°C allows the Eu to better incorporate into the garnet structure. Alternatively, the Eu anomaly occurs due to the ease at which Eu^{2+} can be leached by acidic hydrothermal fluids at temperatures around 250°C. The Eu can then be transported through the VMS system and deposited with Fe and sulphide particles at the seafloor (Honarvar et al., 2006).

Garnet trace elements composistions from Lundmark Akow show distinct trends in their spider diagrams. Samples DT074 and DT096 show enriched LREE and HREE contents whereas samples DT021, DT017, and DT049 show depleted LREE and enriched HREE (Fig. 5.14). Samples DT074 and DT021 have a prominent positive Eu anomaly whereas sample DT096 has a minor negative Eu anomaly. Both samples with prominent Eu anomalies come from a siltstone host rock that does not have hydrothermal additive characteristics such as coticules, and thus do not appear to be prospective for massive sulphide mineralization. Whole rock chemistry of sample DT049 suggest it contains a minor hydrothermal

component of up 10-20% particulates (Fig. 5.8). A potential reason for why Eu anomalies in garnet are not always successful for vectoring to VMS mineralization is the limited amount of hydrothermal particulates vs. terrigenous input (Peter, 2003). Peter (2003) showed that in weakly hydrothermal sediments the REE contributions of the hydrothermal sediments will be swamped by the terrigenous input and lead to patterns that more closely resemble the source rock than any VMS hydrothermal signature. As the garnets in Lundmark Akow are believed to represent the metamorphic product of these weakly hydrothermal sediments, they would inherit their geochemical trends from the sediments.

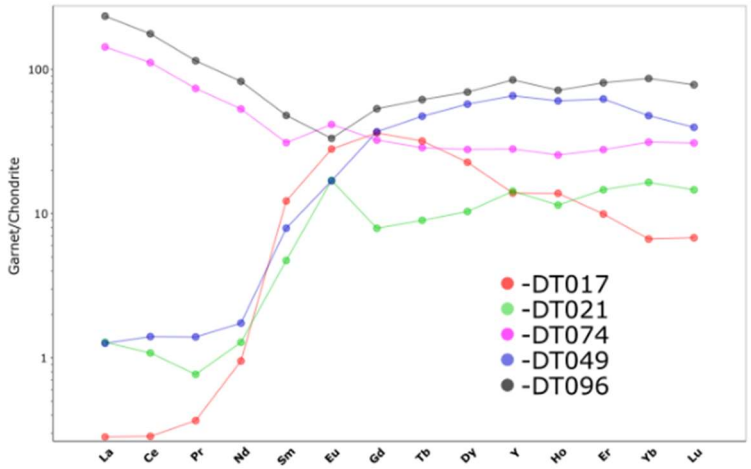

Figure 5.14. Garnet trace element spider diagram plotting the average values of each garnet sample analyzed, normalized to chondrite values from Sun and McDonough, 1989.

Before discarding the effectiveness of this vector, it is important to note the limited sample size with only five samples none of which come from highly mineralized regions of the study area or from samples that were identified as containing a large portion of hydrothermal particles as defined on Figure 5.8. The variation in results from within the same sample are also worth evaluating (Fig. 4.37). There are significant variations in LREE contents within the same sample especially in DT074 and DT096 with no clear zonation of REE abundances (Fig. 5.15). The distinct zonation suggests that the variation in LREE may be a result of inclusions or alteration. The very pitted and weathered appearance of the garnet is also supportive of alteration and may explain the lack of reliability of the garnet trace element data from Lundmark Akow.

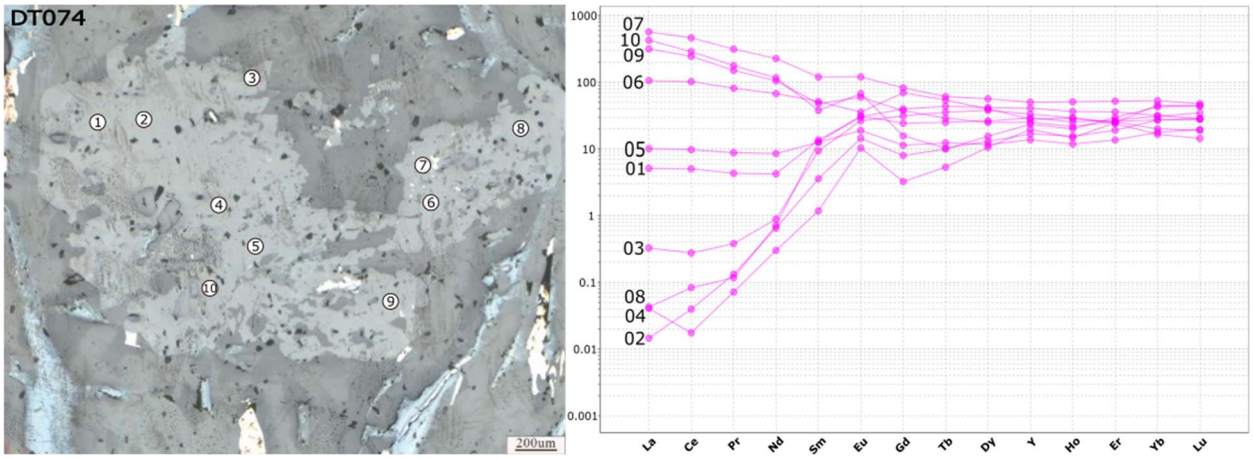

Figure 5.15 Locations of each trace element analysis on garnet grain from sample DT074

The erratic trace element behaviour in the garnets also suggest the U/Pb ages for the garnets from Lundmark Akow should be treated with caution. If the behaviour in REE is erratic, it is possible that the U and Pb concentrations could also have been influenced by alteration. All together this suggests that the garnet age dates and variation in REE concentrations cannot be relied upon as evidence for early garnet formation as a result of VMS fluid interaction with the host rock. Regional metamorphism of an iron enriched sediment is the simplest explanation for the trends in all collected garnet data.

5.6 Tourmaline

At Lundmark Akow tourmaline frequently occurs within the sediments and sulphide horizons (Figs. 4.5 B, 4.12, 5.16). The tourmaline occurs with the sulphides both as individual grains in a sulphide matrix or with sulphides infilling open space around radiating tourmaline structures (Fig. 5.16 B, D). The tourmaline often occurs as an agglomerate of very fine-grained tourmalines into much larger blebs. Tourmaline occurrences, especially in clastic dominated strata bound settings, represent an integral product of local hydrothermal systems (Slack, 1996). For example, in modern siliciclastic hydrothermal settings boron concentration in the exhalative fluids from the Guaymas basin, Escanaba trough, and Middle Valley are five to ten times greater than in sediment free settings such as the southern Juan de Fuca ridge or Atlantic mid ocean ridge (Palmer, 1991). The boron concentration in these fluids is derived

from the leaching of continentally derived sediments by convecting hydrothermal fluids driven by the heat of an underlying magma (Slack, 1996). As Lundmark Akow is also a sediment dominated basin it is possible that a hydrothermal fluid system in the area would also be boron-rich. In order to precipitate tourmaline from these hydrothermal fluids, it must concentrate in topographic lows in brine pools to facilitate the concentration and preservation of boron without dilution by seawater (Turner, 1992). Metasomatic interactions between these boron-rich fluids and aluminous sediments cause the precipitation of tourmaline (Slack, 1996). Iron, Mn, and P may also be enriched through syngenetic precipitation in saline brine pools which together with boron caused diagenetic replacement of detrital clay, feldspar, and/or chlorite on or near the sea floor (Spry et al., 1998). Such a model for tourmalinite formation has been put forward for the deposits of the Sullivan mine in B.C., Broken Hill in Australia, Bleikvassli in Norway, and Zawar in India (Slack, 1996).

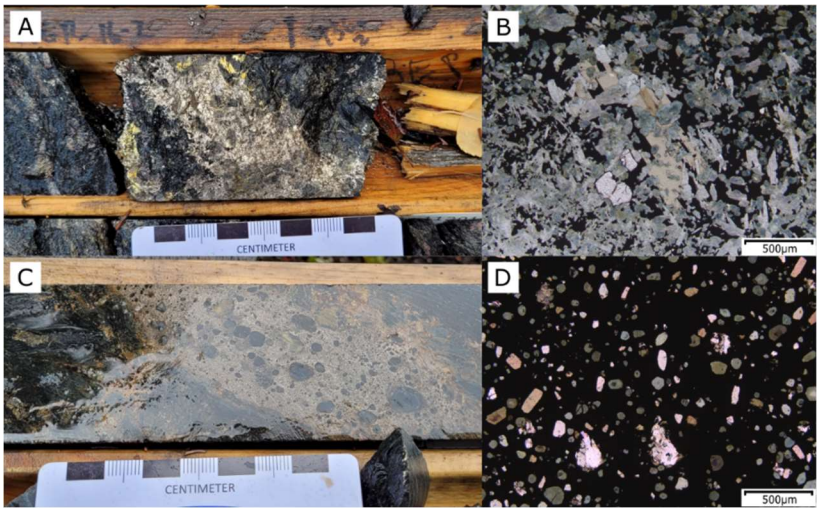

Figure 5.16 A-B Radiating tourmaline crystals occurring within a five-centimeter sulphide horizon of pyrrhotite and chalcopyrite (DT009, Photo micrograph in PPL). C-D Tourmaline blebs in a 7 cm wide pyrrhotite chalcopyrite sulphide horizon (DT034, photo micrograph in PPL).

Tourmalinites can occur in stratiform layers that can vary in thickness from the centimeter to meter scale and in some locations have been traced along strike for several kilometers (Slack, 1996). They can be interbedded with other exhalative rocks such as iron formations or coticules and can occur in contact with massive sulfide or in its adjacent metavolcanic and metasedimentary rocks (Slack, 2022).

Tourmalinites are known to occur from the Archean to the Permian predominantly in siliciclastic dominated domains (Slack, 1996). Textures of tourmaline within tourmalinites vary widely, often larger agglomerate masses are made up of small tourmalines 5-200 µm in diameter although with increasing metamorphic grade the tourmalines can be coarser and occur in optically zoned and aligned prisms (Slack, 2022).

The presence of tourmaline-bearing massive sulphide horizons and tourmalinites act as stratigraphic markers suggesting a location at or near the paleo-seafloor surface (Slack, 2022). Because the tourmaline from hydrothermal sediment metasomatism occurs as a pre-metamorphic product its interaction with the metamorphic products such as garnet can be informative (Slack, 2022). Tourmalines occur as inclusions within the garnet and form a matrix which is infilled by sulphides and later garnet (Fig. 5.17). The inclusion of sulphides and tourmaline in garnet suggests they formed before garnet, possibly from premetamorphic diagenesis in saline brine pools as the fluids must have interacted with an aluminous sediment to form tourmaline and the lack of a alteration halo suggests the tourmaline was not due to fluid flow through the sediment.

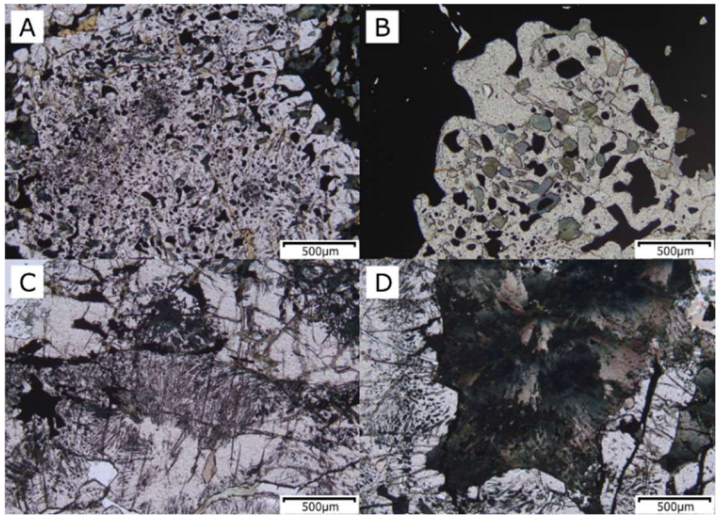

Fig. 5.17 A-B Tourmaline and sulphide inclusions within the garnet (DT009 PPL). C-D Radial tourmaline growth as inclusions within garnet (DT017 PPL).

Compositions of the tourmaline are plotted in Figure 5.18 and compared to other tourmaline-rich massive sulphide deposits. The tourmaline from Lundmark Akow is iron rich similar to volcanic dominated deposits such as Kidd Creek which is believed to have been precipitated in a major felsic volcanic center where high heat production in the VMS system prevented influx of Mg-rich

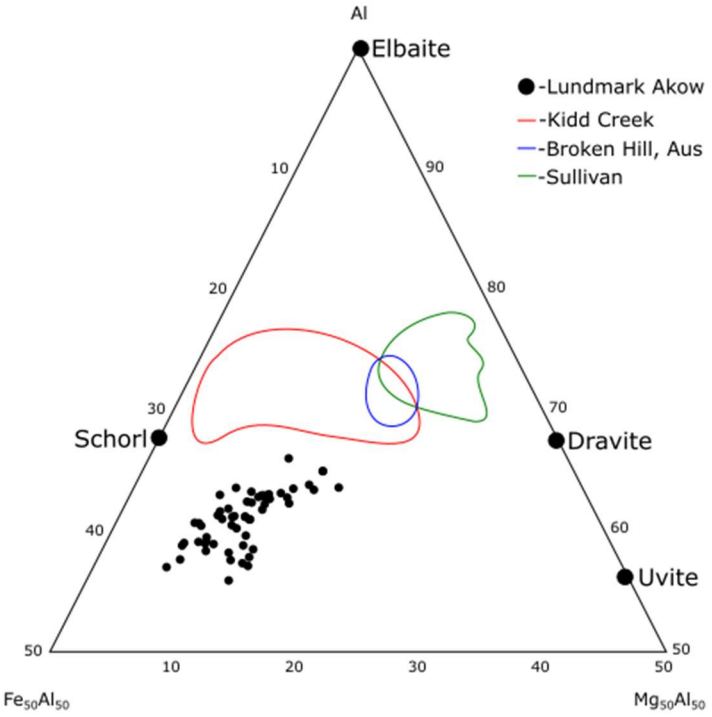

Figure 5.18. Tourmalines from Lundmark Akow plotted onto the top corner of a Al, Fe, Mg diagram with fields for the compositions of tourmalines from several tourmaline rich massive sulphide deposits. Graph adapted from Slack (1996), with data for the composistion fields of tourmaline taken from Slack and Coad (1989), Slack et al. (1993), and Ethier and Campbell (1977) for Kidd Creek, Broken Hill, and Sullivan respectively.

seawater during mineralization (Slack, 1996). However, the samples taken at Lundmark Akow are in a siliciclastic dominated setting with no known nearby volcanic center. Iron-rich tourmaline may also form in Fe-rich brine pools where mixing with Mg-rich seawater was limited (Slack 1996). The composition of the tourmaline will also depend on the composition of the altered aluminous sediments they form from (Slack, 1996). In Lundmark Akow the pelagic sediments, iron enriched or not, have a mean average FeO content of 8.7 wt. % vs a MgO content of 1.5 wt. % which would also be a factor in producing Fe-rich

tourmaline as there is less available Mg for the growing crystals. Overall, the tourmaline composition is not definitive evidence, but does suggest that they formed in a dense Fe-rich pool consistent with the textural characteristics of the tourmaline.

Trace element compositions of tourmaline can be used as a potential vector to ore or to show the trace element compositions of the tourmaline-forming fluid (Spry et al. 1998). Work by Griffin et al. (1996) showed that base metal proportions within tourmaline will match the metallogeny of the massive sulfide deposit. The majority of the tourmaline samples from Lundmark Akow plot within the overlap of barren to Broken Hill fields (Fig. 5.19). The samples from Lundmark Akow occur as tourmalinites in metasediments with limited sulphides or as tourmalinite within massive Fe sulphide that has little to no base metal content. Such samples although indicative of hydrothermal activity, suggest limited base metal contents in the tourmaline forming fluids.

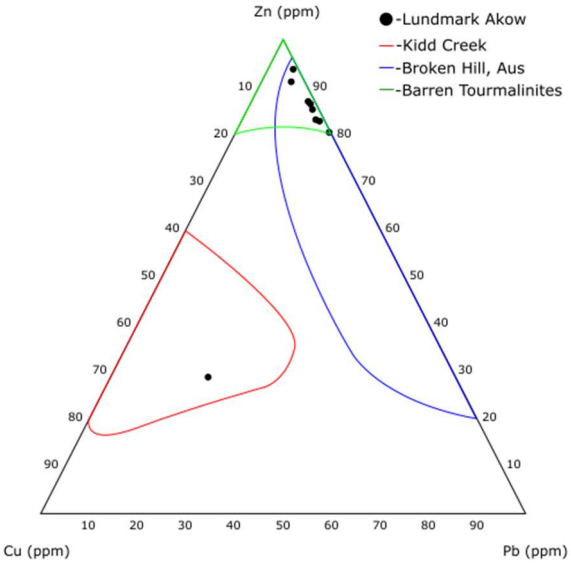

Figure 5.19. Tourmaline base metal content ternary diagram with deposit fields taken from Griffen et al. (1996).

The one tourmaline which does plot within the Kidd Creek field is from a tourmalinite sample DT119 which is base metal rich containing up to 20% chalcopyrite and 30% pyrrhotite in a 40cm wide massive sulphide lens. As the base metal contents of all the tourmaline resembles those of the sulphides

contained within the horizon this supports the idea that the massive sulphide horizons and tourmalines formed from the same localized dense hydrothermal pools. The lack of base metals in the other tourmalinite bearing massive Fe sulphide horizons suggests they do not represent strong targets for future exploration along strike.

5.7 White Mica

SWIR data collected from white micas from Lundmark Akow show a variation in the Al-OH band wavelength from 2196 to 2204 nm. The Al-OH band in the analysis occurred on the lower range below 2200 nm for the majority of analysis performed (Fig. 5.20). The shift in location of the Al-OH band represents the amount of octahedral Al occurring within the white mica (Yang et al., 2011). A value around or below 2200 nm represent aluminous muscovite samples with 3.9 Al^{IV} (based on 4 octahedral cation per formula unit) whereas a shift to a higher wavelength suggests increasing Fe and Mg substitution for Al and thus a more phengitic to celadonite composition (Jones et al., 2005). The composition of white mica is a function of physical and chemical conditions, mainly temperature, pressure, and bulk chemical composition (Massonne and Schreyer, 1987; Yang et al., 2011).

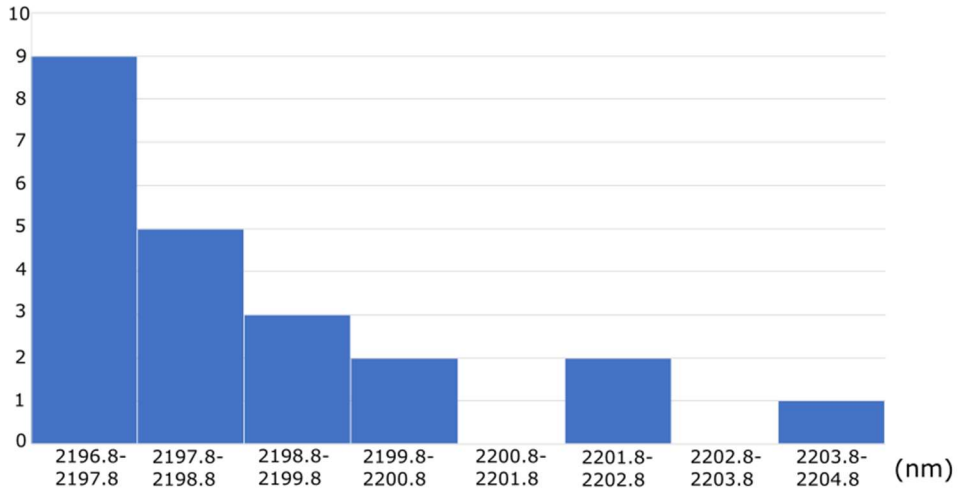

Figure 5.20. Histogram displaying the range in the 2200nm trough of SWIR analysis of white micas from Lundmark Akow.

Studies of other VMS deposits show a shift to higher wavelengths for the Al-OH band proximal to mineralization with lower distal values (Jones et al., 2005). This trend has been identified in several deposits such as Myra falls in British Columbia, Hellyer in Tasmania and Rio Tinto in Spain (Leistel et al., 1998; Jones et al., 2005; Yang et al., 2011). Studies at Myra Falls proposed that a shift to a wavelength greater than 2206 nm represented a product of proximal alteration with values as high as 2215, similarly the Hellyer deposit had a shift to as large as 2222 nm (Jones et al., 2005; Yang et al., 2011).

The values obtained from Lundmark Akow suggest a white mica composition closer to muscovite rather than phengite. The low values around 2200 nm are not consistent with formation by proximal alteration in a VMS system. The highest value analysed in Lundmark Akow of 2204 was from sample DT006, a felsic volcanic unit rather than the pelitic protolith of the other samples. This suggests that the bulk composition of the host rock has a strong influence on the composition of the resulting white mica as was also consistent with the case at Myra Falls (Jones et al., 2005). Overall, the white mica SWIR values are more supportive of their formation as a result of regional metamorphism rather than hydrothermal activity proximal to a VMS system.

5.8 Chlorite

Chlorite is a major component of VMS hydrothermal alteration, usually being indicative of the highest fluid flow in the central alteration pipe below the massive sulphide (Franklin et al., 1981). Chlorite at Lundmark Akow generally occurs around the rims of garnet and staurolite as well as pseudomorphs of biotite suggesting it formed late, likely post-peak metamorphism, and possibly as a result of retrograde metamorphism. Consequently, it is unlikely to have formed as a result of VMS alteration which would occur pre-peak metamorphism. It is possible that chlorite could have formed early but replaced by the garnet staurolite schist in subsequent metamorphism as occurred in the chlorite pipe in the Chisel Lake deposit (Skirrow and Franklin, 1994).

If the chlorite was formed as a result of hydrothermal alteration of volcanic rocks linked to a VMS system then proximal chlorite would be iron-rich, whereas chlorite found in the semi-conformable alteration zone would be Mg-rich chlorite (Piercey, 2009). The composistions of chlorite in Lundmark Akow vary from Fe-rich chamosite to a solid solution Fe-Mg chlorite. The chamosite appears to form as an alteration product of magnetite or garnet whereas the Fe and Mg solid solution chlorite is a replacement alteration of interstitial biotite in the matrix to chlorite (Fig. 5.21). Among the solid solution Fe-Mg chlorite, all samples had Fe greater than Mg and thus do not match the expected composition of a semi-conformable alteration zone (Piercey, 2009). Although Fe-rich chamosite would be an expected product of proximal vent alteration in a VMS system, that the chamosite in Lundmark is found only as an alteration product of magnetite or later regional metamorphic minerals such as garnet suggests that this chamosite did not form syngenetic to a VMS system. Overall the chlorite in Lundmark Akow is not evidence of VMS hydrothermal alteration based on their compositions and their late timing.

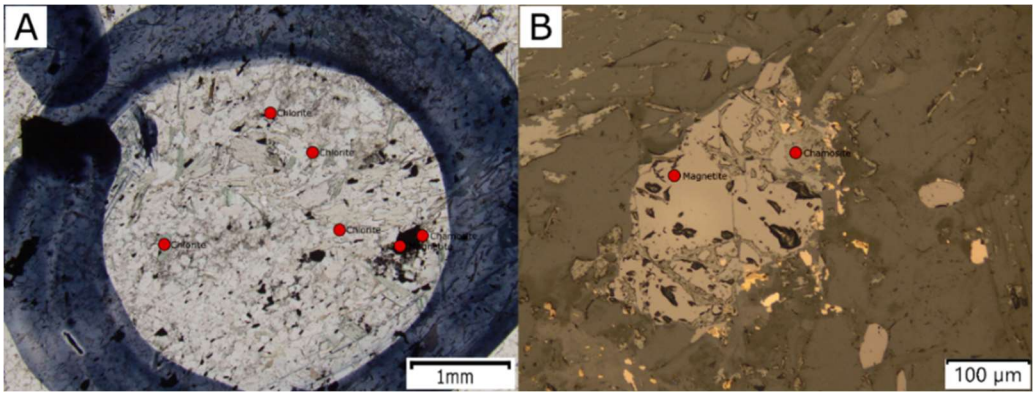

Figure 5.21 A. Sample of chlorite and Fe rich chlorite chamosite occurring alongside each other with the chlorite forming as interstitial laths in the mica schist possibly as retrograde alteration of biotite. The chamosite forms as an alteration product of magnetite (PPL, DT120B). B. Close up of magnetite altering to an Fe rich chamosite (RL, DT120B).

5.9 Sulphides

At Lundmark Akow the massive sulphides occur as thin lenses of 5-30cm width. Most are pyrrhotite dominated with lesser chalcopyrite. Chalcopyrite is the most common economic base metal sulphide, however, the occurrence of gahnite in sample DT053 suggests the presence of sphalerite

within a coticule as gahnite forms from the metamorphism and desulfidation of sphalerite (Spry, 1998). Smaller lenses of sulphide often occur with quartz garnet coticules, forming a matrix around garnet grains and as inclusions within garnet phenocrysts (Fig. 5.22).

The presence of massive sulphide mineralization can occur in both proximal and distal VMS systems. Sulfide facies meta-exhalite can form by hydrothermal plume fallout or as a bottom-hugging brine which may flow along the undersea topography settling into depressions or brine pools (Franklin, 2005).

Figure 5.22. Sample DT002, sulphide horizon occurrence with a quartz granitite/coticule.

Distal VMS mineralization may produce appreciable levels of base metal bearing minerals such as chalcopyrite or sphalerite up to several hundred meters from a vent and may form distal pyrite and pyrrhotite-rich horizons much further from the vent due to the formation of sulfidic-rich bottom waters forming from the input of hydrothermal fluids into the water column (Slack, 2012). Sulphides deposited in such a way may show no distinct alteration in the hanging or footwall sedimentary rocks surrounding the sulphides (Franklin, 2005). Hydrothermal plume particulate fallout or pooling of dense sulfur-rich fluids could explain the thin lenses of massive sulphide found in Lundmark Akow and is consistent with the lack of a feeder pipe or alteration zone leading up to the sulphides. The presence of both chalcopyrite-bearing massive sulphide as well as some lenses of only massive pyrrhotite also matches

the description of exhalative sulphide facies by Slack (2012), suggesting that the iron sulphide horizons are more distal to the vent.

The major and trace element content of sulphides can also help distinguish the type of VMS deposit. Selenium contents in sulphide minerals have been considered a valuable tool in evaluating massive sulphide deposits due to their ability to reflect the source of the fluids and Se content within a hydrothermal fluid (Huston et al., 1995). The variability in Se/S values at Lundmark Akow ranges from $6.19X10^{-6}$ with 2.7 ppm Se in chalcopyrite from DT117 to $7.19X10^{-4}$ with 181.2 ppm Se in pyrrhotite from sample DT034 (Fig. 5.23). The Lundmark Akow samples generally have higher Se values from massive sulphide horizons hosted within the sedimentary sequence which are postulated to be the product of dense sulphide-rich hydrothermal pools and plume fallout rather than being local to a vent. Samples such as DT119, DT034, DT009, and DT050 have the characteristics of a meta-exhalite, with Fe enrichment leading to garnet formation, and tourmalinite formed from the metasomatism of boron-rich sediments. The lowest Se/S ratios are from samples DT117 and DT119 which are hosted within a volcanic sequence and appear to be a more localized vent system. Temperature variation may be a potential reason for the variance in Se seen throughout the system.

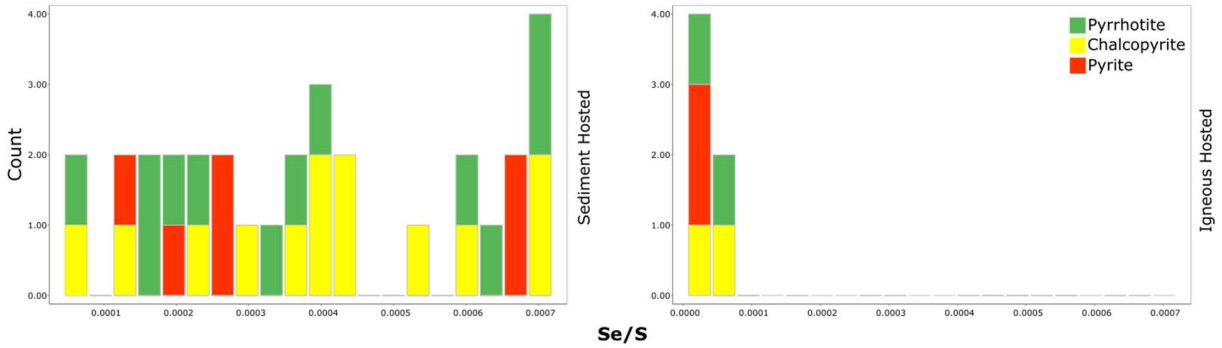

Figure 5.23. Se/S ratios of all analyzed pyrrhotite, pyrite and chalcopyrite minerals from sediment and igneous hosted massive sulphide horizons

Within VMS related hydrothermal fluids S and Se will be transported as H_2S and H_2Se, respectively (Yamamoto, 1976). The uptake of Se into sulphide phases is inversely related to temperature with higher fluid temperatures associated with lower Se contents. (Huston et al., 1995). Oxygen fugacity

conditions also effect Se incorporation, with reduced fluids having lower Se contents (Huston et al., 1995). Fluid mixing between magmatic and seawater sources can effect Se uptake with magmatic fluids containing higher H_2Se content than seawater, but the decrease in temperature and potential increase in oxygen fugacity from seawater leads to an overall increase in Se contents in sulphides (Huston et al., 1995).

If sedimentary-hosted massive sulphide formed as a result of a hydrothermal plume it could explain the higher Se content as the plume would cool when in contact with seawater even if mixing is limited due to the subsurface pooling of dense fluids (Hannington et al., 2005). This cooler fluid would allow for greater substitution of Se for S in the precipitating sulphides. Fluids precipitating sulphides in a vent proximal setting in DT117 and DT118 would likely be much warmer and thus limit the substitution of Se for S. Other possible reasons for the high Se values include more magmatic input to the fluids which precipated into the sedimentary sequences, as the Se/S ratios of magmatic rocks are around 5-20 X 10^{-5} whereas present day ocean water ratios are much lower around 2-10 X 10^{-8} (Huston et al., 1995).

Evaluating the potential for magmatic fluid sources in Lundmark Akow can better accomplished by considering both Se/S and $\delta^{34}S$ values together. $\delta^{34}S$ has traditionally been used to evaluated sulfur sources in VMS systems (Leybourne et al., 2022) due to its ability to highlight the input of biologically reduced sulfur from seawater and sedimentary rocks by the mass dependent fractionation of ^{34}S by sulfate reducing bacteria (Canfield, 2004). Proterozoic to Archean VMS deposits generally have a restricted range of 1.0±2.6‰ $\delta^{34}S$ suggesting either a sulfur source dominated by leaching of volcanic rocks or direct magmatic sulfur input (Huston et al., 2011). This is in contrast to Phanerozoic values which are often much higher and more variable (Huston et al., 2011). The difference is a result of low sulphur (2 ppm) and sulphate (80ppm) content in seawater in the Archean (Huston, 1999, Jamieson et al.,2012) compared to modern ocean water.

The majority of samples from Lundmark Akow plot just outside of a typical mantle range of -2 to 2‰ $\delta^{34}S$, with 73% of pyrrhotite, 71% of chalcopyrite, 75% of pyrite, and the one arsenopyrite grain having values greater than 2‰ $\delta^{34}S$ (Fig. 5.24). These values are slightly elevated compared to the mantle value of 0‰ and may indicate the presence of seawater sulfide raising the overall $\delta^{34}S$ value, however, such an effect is uncommon in Archean deposits due to the limited quantity of sea water sulphate (Huston et al., 2011). Sulphide $\delta^{34}S$ is not directly equivalent to the $\delta^{34}S$ of the H_2S of the fluid it

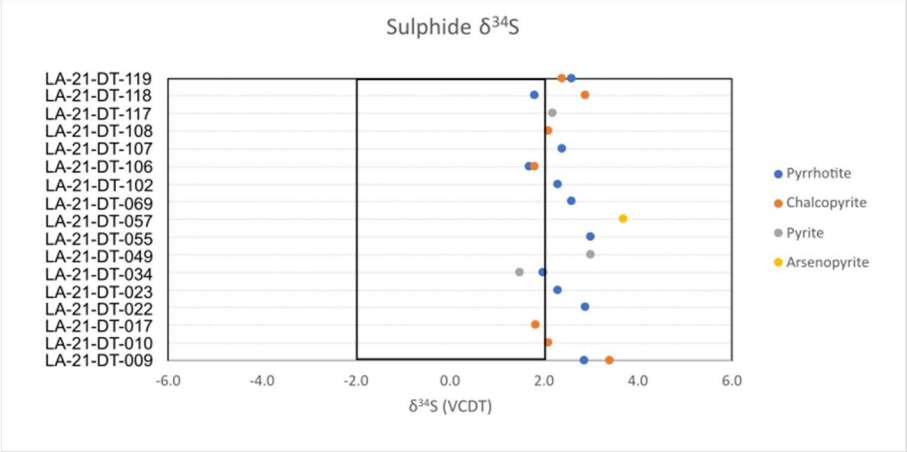

Figure 5.24. Y axis lists the hand sample from which the sulphide grains were extracted. Points are colour coded for each type of sulphide analyzed. Black box from -2 to 2 ‰ represents mantle sulphur values (Huston et al., 2010).

formed from (Ohmoto and Rye, 1979). Compensating for the temperature dependent fractionation at 300°C would yield a $\delta^{34}S$ of H_2S of 1‰ lower than the values of pyrite and pyrrhotite which in Lundmark Akow would be a $\delta^{34}S$ value of around 1.5 (Ohmoto and Rye, 1979). This suggests the $\delta^{34}S$ of H_2S in the fluids that formed sulphides in Lundmark Akow are within the mantle range. However, $\delta^{34}S$ of the chalcopyrite would be elevated about 0.2‰ from the H_2S, which would still suggest a value slightly above the mantle range for some of the chalcopyrite samples (Li and Liu, 2006).

Comparing both Se/S and $\delta^{34}S$ together allows for a more accurate analysis of the sulphur source in the samples. The data points for Lundmark Akow are scattered and do not show a clear trend (Fig. 5.25). However, the samples showing the highest Se and $\delta^{34}S$ are from massive sulphide horizons within

the sedimentary sequences which are proposed to have formed as a product of precipitation from dense hydrothermal pools. As previously stated, the high Se can be explained as a result of the cooler temperatures of the fluids after exposure to seawater. The higher $\delta^{34}S$ values support this theory suggesting an increased level of sulphur from seawater or sedimentary sources. Samples DT117 and DT118 are from within a sequence of volcanic intrusive and extrusive rocks and have the lowest Se values and lower $\delta^{34}S$ values for pyrrhotite and chalcopyrite suggesting higher temperatures possibly due to proximity to the vent source, and a mantle $\delta^{34}S$ signature likely sourced from leaching of local volcanic rocks or magmatic input.

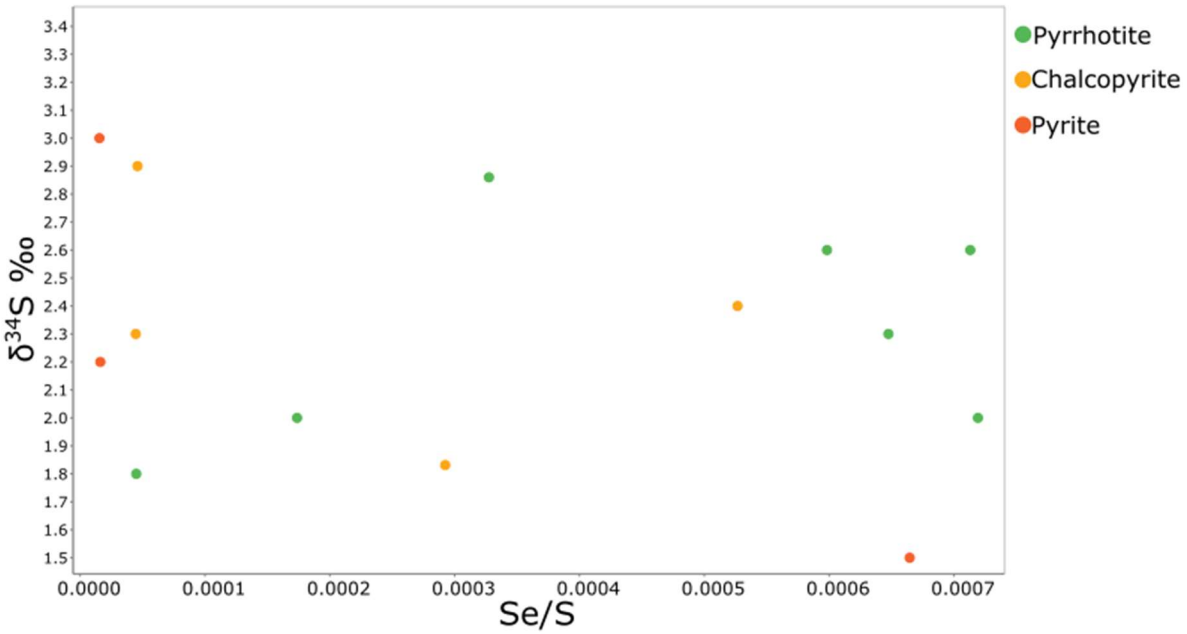

Figure 5.25. Comparison between Se/S ratios and $\delta^{34}S$ of sulphides from Lundmark Akow.

The data for pyrite is not consistent with that of pyrrhotite and chalcopyrite with the highest $\delta^{34}S$ values occurring in the volcanic hosted massive sulphide horizons and decreasing to the lowest value in a sediment hosted horizon (Fig. 5.26). Only three data points are available for pyrite, but the textural characteristic of the pyrite suggests it formed late in the paragenesis. The later timing of the pyrite in this

deposit may mean it was sourced from different fluids or influenced by later metamorphic events which may explain the different trend in Se/S and $\delta^{34}S$ value.

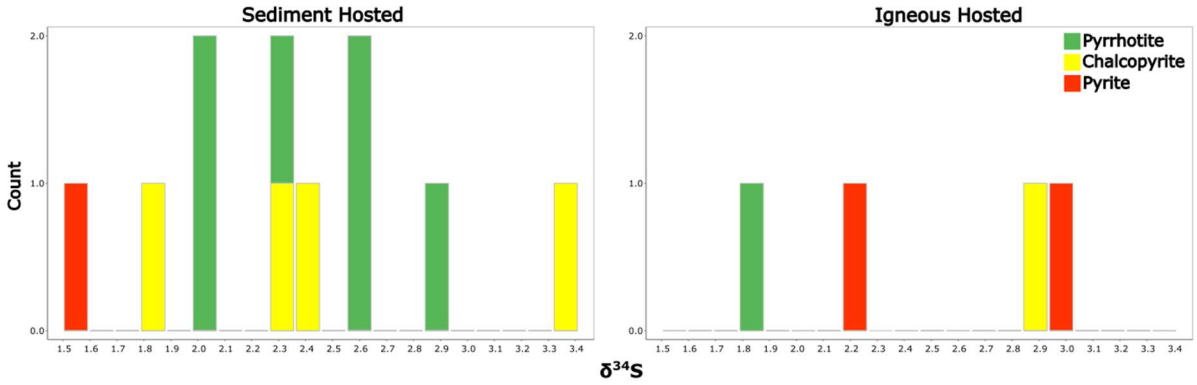

Figure 5.26 $\delta^{34}S$ values of sulphides from massive sulphide horizons hosted in sediments vs Igneous rocks from Lundmark Akow.

Overall, the sulphide trace element data does not provide definitive evidence for a setting or method of deposition but are broadly consistent with the pooling of sulphide-rich brine pools at lower temperatures due to the intermixing of hydrothermal fluids and seawater. Lower fluid temperatures that generate elevated Se contents and the slightly elevated $\delta^{34}S$ values of the sulphides also support the formation of these deposits in a distal setting from the vent source potentially dominated by sulphur sources in the seawater and clastic host rocks.

5.10 Source of fluids and mode of mineralization

As the mineralogical data is broadly consistent with formation by venting of dense to buoyant hydrothermal fluids the question remains where could these vents be located? Locating the source of venting for these various exhalative products is challenging. The drill hole density in the area is limited and staggered at distances of over a kilometer between holes. An attempt to align stratigraphy between the southernmost holes is made in Figure 5.27. A felsic volcanic marker bed was assumed to be contiguous across drill holes and allowed for a possible comparison between units. A clear iron enriched region is visible across the three drill holes representing a period of regional hydrothermal activity.

However, there is not a clear direction of increasing iron abundance across drill holes. Closer spacing between holes and a higher sampling density would be necessary to make any claims in regard to direction to the source of the hydrothermal material.

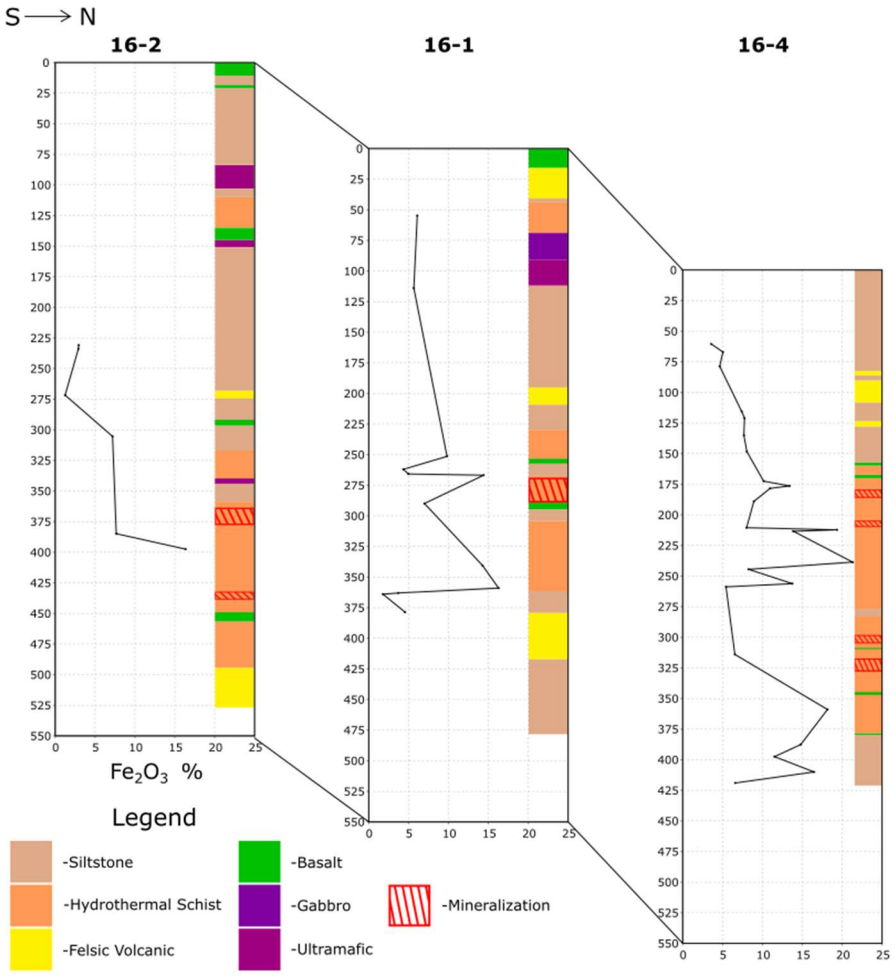

Figure 5.27 Downhole lithology plots moving from south to north with drill holes 16-2, 16-1, and 16-4. The downhole plots are staggered to line up potentially contiguous units.

It is likely that the Fe-enrichment leading to the formation of the coticules was caused by separate but potentially related hydrothermal activity to the more localized tourmalinite and massive sulphide horizons (Fig. 5.28). Iron enrichment in sea floor sediments is dependent both on the quantity of Fe particulate downfall and the rates of mass accumulation of terrigenous material (Barrett and Jarvis, 1988). If the rate of accumulation of Fe particulates was very rapid it would overwhelm the terrigenous sediments and produce banded iron formations (Peter, 2003). Given that the hydrous particulates make

up only between 20-40% of the sedimentary rocks, terrigenous input exceeded that of hydrothermal particulates. Sedimentation rates in deep sea settings are very slow with shelf zones around continents and islands averaging around 0.1-1 cm/year (Restreppo et al., 2020). This suggests that the iron is sourced from diffuse regional plumes rather than a local bottom-hugging brine as the iron build up is gradual (Fig. 5.29). Chert magnetite iron formations are generally the products of distal or widespread unfocused low temperature hydrothermal discharge (Gross, 1995; Franklin et al., 2005). These may potentially be from a similar source to the iron formations of the Musselwhite mine as magnetic surveys show iron formations continuous from the Opapimiskan up through the South Rim (Ontario Geological Survey, 2003).

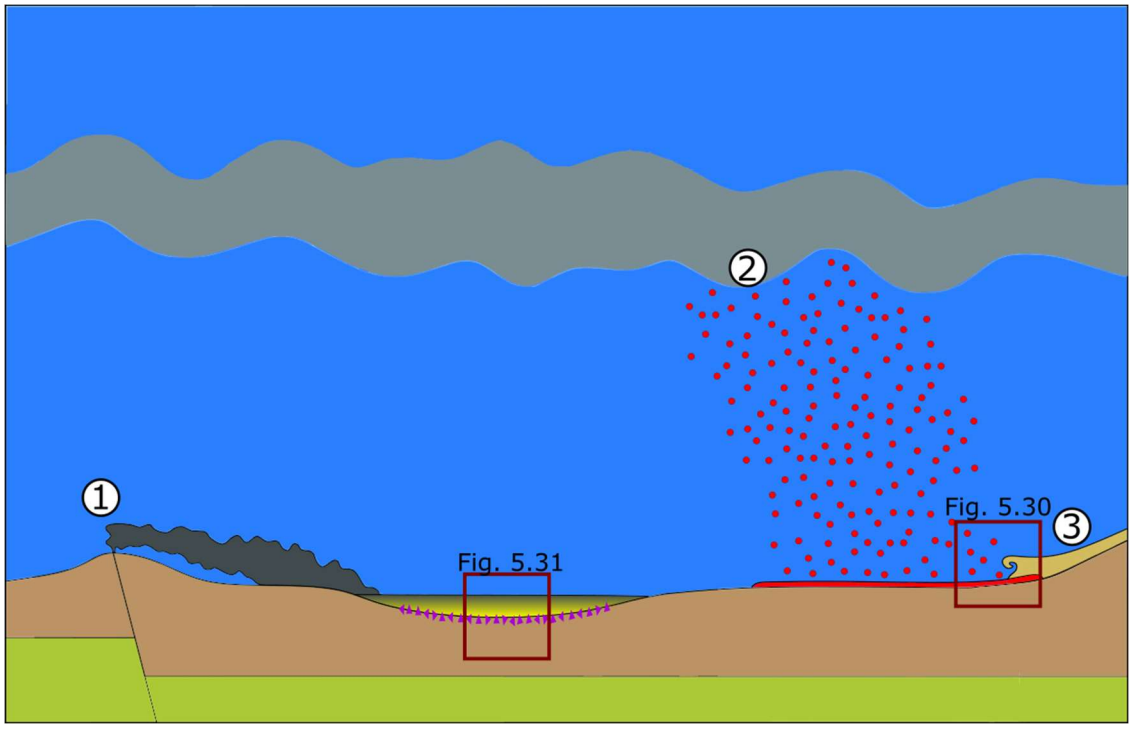

Figure 5.28. Schematic diagram of theorized plume activity in Lundmark Akow. (1). Localized vents of dense sulphide rich hydrothermal plume, the density of the plume causes it to be bottom-hugging, pooling into topographic lows. In the pools the interaction between the hydrothermal fluids and seafloor sediments leads to mineralization of tourmalinite as well as massive sulphides as described in detail in Figure 5.31. (2). Diffuse regional iron-rich plumes which slowly rain down iron rich particulates onto the sea floor, the source of this plume may be located tens of kilometers away (Peter, 2003). (3). Turbiditic flows bring down terrigenous sediments which intermix with the hydrothermal iron particulates as described in detail in Figure 5.30.

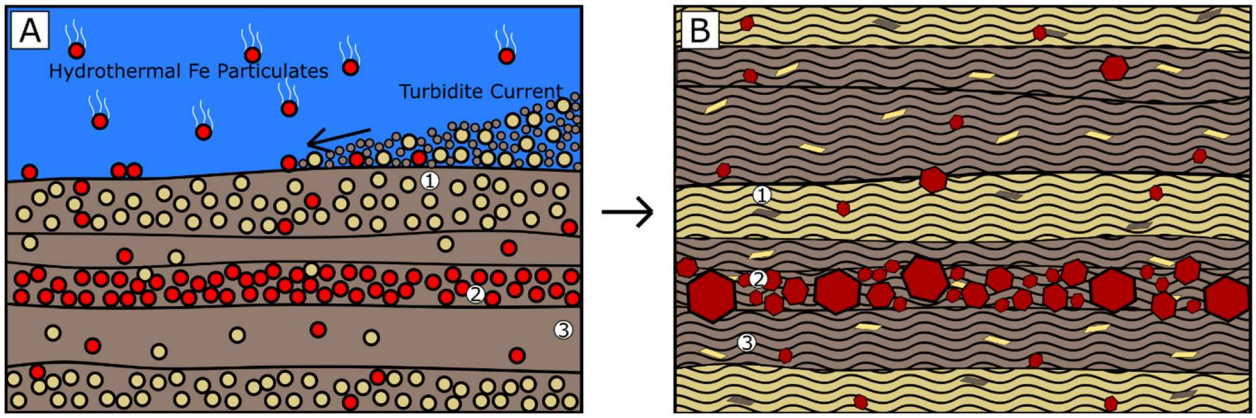

Figure 5.29. A. The sedimentation of hydrothermal iron particulates with terrigenous turbidite derived sediments. The rate of input from terrigenous and hydrothermal sources impacts the level of iron enrichment in each sedimentary layer. Periods of limited turbidite activity or alternatively increased hydrothermal activity would lead to very iron rich layers, vice versa increased terrigenous input will decrease the level of iron enrichment. B. Regional amphibolite metamorphism of the hydrothermal and terrigenous sediments leads to the formation of interbedded biotite muscovite schists containing porphyroblastic garnet. (1). fine sandstone to siltstone sediments become muscovite schist. (2). Iron particulate layer is metamorphosed into a coticule/ quartz garnetite. (3) mudstone-rich sediments are metamorphosed into biotite schist containing porphyroblastic garnet.

The massive sulphides and tourmalinites are likely the products of a local hydrothermal source as significant quantities of sulphides would need to be deposited in a short time period to create a massive sulphide horizon between 5-20 cm in width without being overwhelmed by terrigenous input (Peter, 2003). Slow particulate fallout from a diffuse plume would not be conducive to the formation of massive sulphide horizons, and it is more likely they represent a dense sulphur-rich vent fluid that pools within topographic lows. This is also supported by the presence of tourmalinites within massive sulphide horizons as the boron-rich fluids need to remain concentrated and in contact with aluminum-rich sediments that metasomatize into tourmaline (Fig. 5.30).

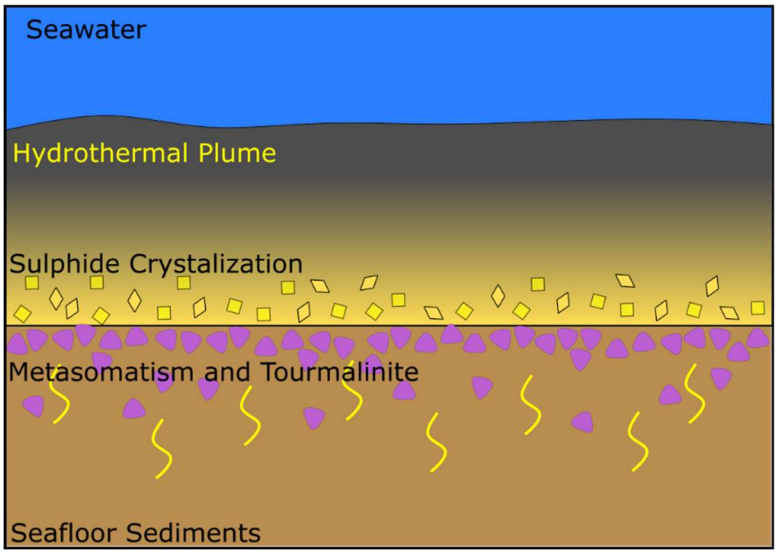

Figure 5.30. Schematic diagram of a bottom-hugging brine which has pooled at the seafloor. The interaction between hydrothermal fluids and the seafloor sediments causes metasomatic alteration and the formation of tourmaline due to the boron content of the fluids and the aluminum rich seafloor sediments. This tourmaline forms a stratigraphic layer at the interface of these two phases. The cooling of the plume liquids leads to the crystallization of sulphides which settle in alongside the tourmalinite leading to tourmaline rich massive sulphide deposits found at Lundmark Akow.

5.11 Oxidation and Sulphidation State vectors to Ore

The third goal of this project was to determine if more significant mineralization could be located in the Lundmark Akow area through the use of vectors. Mineral composition variations as a vector to massive sulphide deposits have been attempted in a variety of locations and with varying degrees of success (Fullagar et al., 1967; Staten, 1976; Nesbitt, 1982; Petersen, 1984; Pollock et al., 2018). The basic underlying premise for ferromagnesian silicate mineral variation relies on the buffering capacity of sulphides during metamorphism (Spry, 1998). Under regional metamorphic conditions from greenschist to amphibolite facies, pyrite will be altered to pyrrhotite (Marmo, 1957). This chemical alteration can be expressed as an empirical change from an average Fe content in pyrite of 46.55% to that of pyrrhotite of 63.33%, thus Fe is required for this reaction. The presence of increasing sulphide content, especially pyrite, in country rock from stringer sulphides to massive sulphide horizons will change the equilibrium state of ferromagnesian silicates nearby and cause a relative enrichment in Mg content of those minerals (Spry, 1998).

Attempts have been made to map out this “sulphidation halo” using compositional data from ferromagnesian silicates such as biotite, garnet, and staurolite (Spry et al., 1998). Fullagar et al. (1967) used three drill holes through the Ore Knob sulfide deposit, North Carolina and mapped the variation in biotite Fe content several hundred feet from the massive sulphide horizon. Similarly, Nesbitt (1982) used systematic increases in Mg over Fe content of biotite, chlorite, and staurolite at the Ducktown deposit to define a halo 50 meters out from the massive sulphide body. In contrast, work on the Great Gossan Lead deposit by Staten (1976) identified variations in ferromagnesian silicates but only within two meters of the sulphide body. Investigations into the Geco mine in Ontario reveled systematic trends in ferromagnesian silicate compositions, however, the diverse suite of metavolcanic rocks in both the hanging wall and footwall of the deposit resulted in an asymmetric halo around the deposit (Petersen, 1984). A summary of trends in ferromagnesian silicates composistions near metamorphosed massive deposits created by Nesbitt (1986) is presented in Figure 5.31.

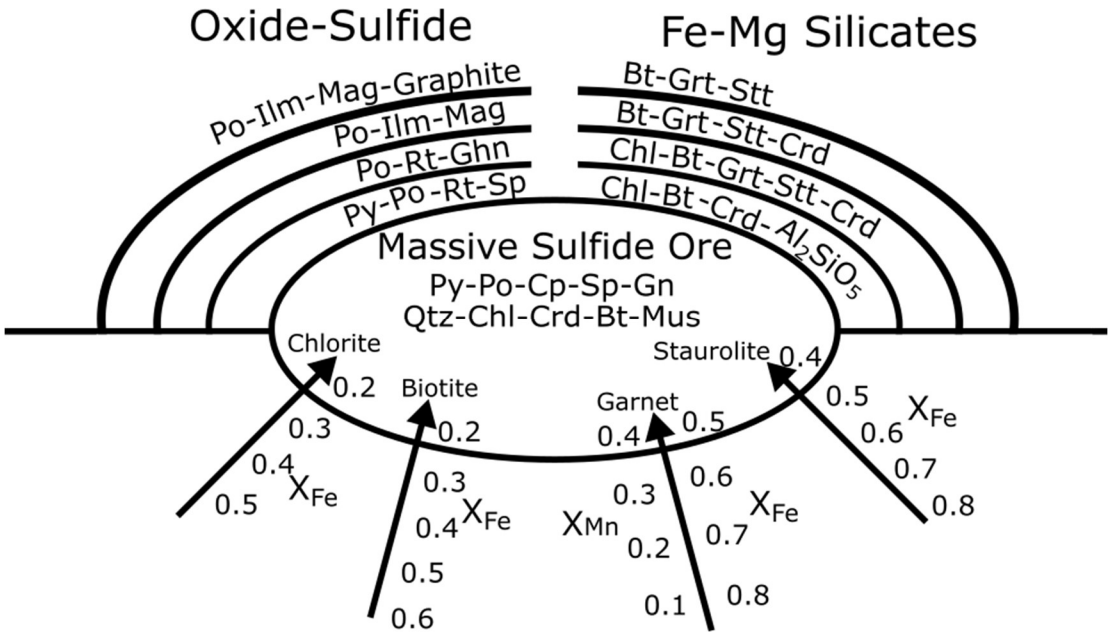

Figure 5.31 Ferromagnesian mineral composition trends summary, adapted from Nesbitt (1986). Abbreviations Po: Pyrrhotite, Py: Pyrite, Mag: Magnetite, Bt: Biotite, Stt: Staurolite, Grt: Garnet, Ilm: Ilmenite, Rt: Rutile, Ghn: Gahnite, Crd: Cordierite, Chl: Chlorite, Sp: Sphalerite.

Compositional ranges in ferromagnesian silicates at Lundmark Akow are presented as $X_{Fe,}$ calculated as FeO/(FeO+CaO+MnO+MgO) for garnets and as FeO/(FeO+MgO) for biotite, chlorite, and staurolite (Figs. 5.33, 5.34). Plotting up variations in X_{Fe} of ferromagnesian minerals in drill hole 17-01 shows a mean average for garnet of 0.85, 0.71 for biotite, 0.73 for chlorite, and 0.93 for staurolite (Fig. 5.32). There is a distinct drop in X_{Fe} at a depth of 302.7m in sample DT120 for garnet, biotite, and chlorite with an average X_{Fe} of 0.64, 0.60, and 0.63, respectively. This represents a drop in X_{Fe} of 0.21 for garnet, 0.11 for biotite, and 0.1 for chlorite. This compositional change across multiple mineral phases at the same location suggests a change in sulfur fugacity conditions that would use up available Fe. Sample DT120 were taken two meters below a 1.4-meter-wide massive sulphide horizon. The extent of this sulphidation halo around the sulfide horizon can be tested by looking at samples located eight meters below the massive sulphides which are hosted in the same pelagic schists. The mineral phases at that location record a X_{Fe} of 0.84 for garnet, 0.76 for biotite, and 0.81 for chlorite. All these values are at or above the average value for X_{Fe} suggesting that at Lundmark Akow the effective range of sulphidation around a meter wide sulphide horizon is less than 8 meters. Thus, for Lundmark Akow using mineral composistions as a vector to ore is not an effective exploration tool.

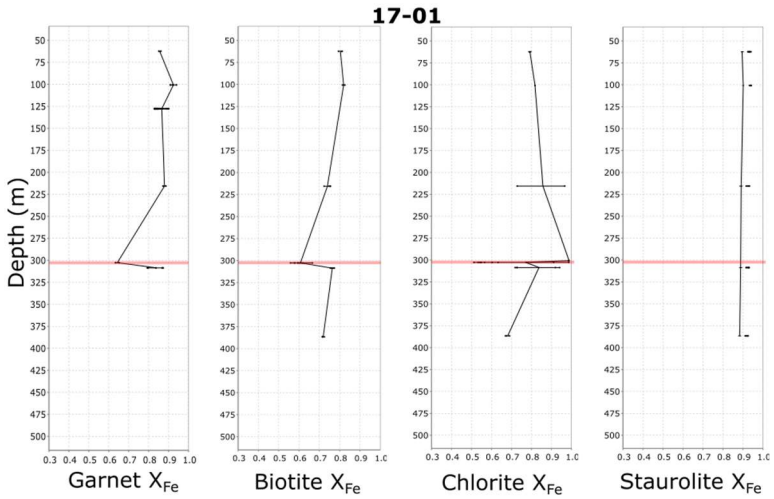

Figure 5.32 Downhole plots of the compositions of ferromagnesian minerals garnet, biotite, chlorite, and staurolite in drill hole 17-01. Expressed as X_{Fe} calculated as FeO/(FeO+MgO+MnO+CaO) for garnet, and FeO/(FeO+ MgO) for biotite, chlorite, and staurolite.

Manganese enrichment has also been used as a vector to massive sulphide mineralization (Nesbitt, 1982). Manganese enrichment is the driving force behind the changes to garnet X_{Fe}. In drill hole 17-01 the mean average MgO, MnO, and CaO in garnet was 1.01, 2.09, and 1.86 respectively. Near the mineralized zone in sample DT120, the average values of each oxide increased to 2.40, 8.90, and 4.10 for MgO, MnO, and CaO. This represents an increase by a factor of 2 for MgO, 4 for MnO, and 2 for CaO thus Mn addition is the most significant change in the garnet.

Drill hole 16-04 was sampled with sufficient density to show trends in ferromagnesian silicate compositions (Fig. 5.33). The mean average X_{Fe} for garnet is 0.83, 0.78 for biotite, 0.77 for chlorite, and 0.93 for staurolite. Several areas show distinct X_{Fe} drops first at a depth of 67 meters in sample DT039. Biotite has an average X_{Fe} of 0.63, 0.65 for chlorite, and 0.89 for staurolite. This represents a decrease in X_{Fe} of 0.14 for biotite, 0.12 for chlorite, and 0.04 for staurolite. Likewise, in sample DT042 at a depth of 112.4 meters we see a drop in X_{Fe} with an average of 0.55 for garnet and 0.54 for chlorite. This represents a drop in X_{Fe} of 0.28 for garnet and 0.23 for chlorite suggesting a possible sulfidation halo nearby. These two samples do not occur near any known occurrence of massive sulphide horizon. It is possible that they represent a blind target for VMS mineralization, however, lithological variation may also explain the decreased values. Both samples were logged as a meta-arkosic rock with possible intermixed felsic volcanic tuff. They contain up to 25% anorthitic plagioclase feldspar which occur as subhedral subrounded grains 50-600 μm in diameter. These plagioclase grains occur in distinct five-millimeter-wide lamellae and may represent a component of volcaniclastic debris in the sedimentary sequence. Heterolithic country rocks create unique conditions for oxygen and sulfur fugacity and may cause ferromagnesian minerals to reach equilibrium with varied composition (Nesbitt, 1986). Heterolithic host rocks at Geco prevented the clear distinction between country rock and sulphide hosting wall rock which rendered the vectoring capacity of the mineral phases less definitive (Petersen,

1984). This highlights a possible hazard in applying this vector to all portions of the drillhole in Lundmark Akow irrespective of possible parent lithology.

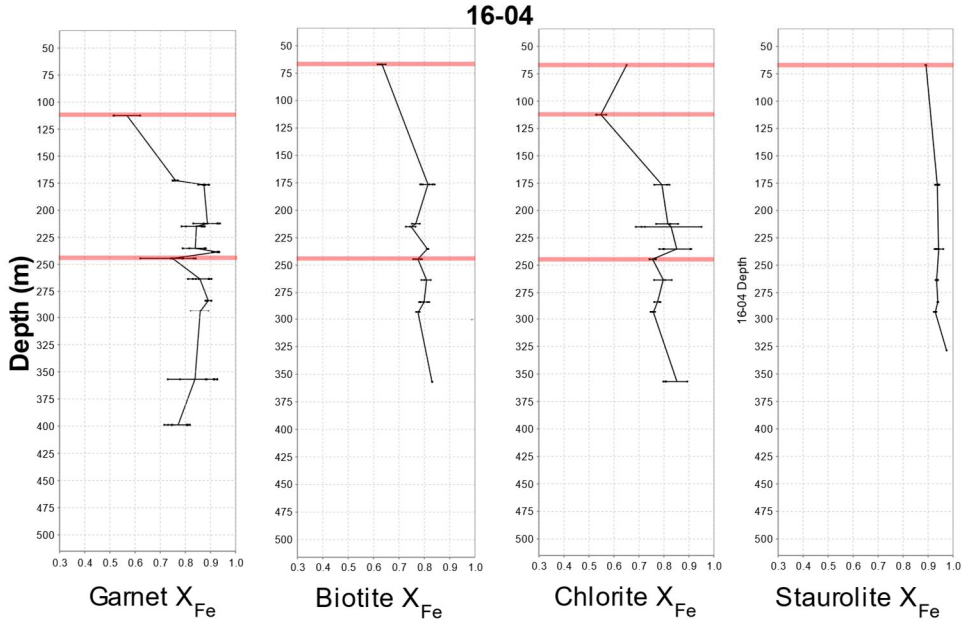

Figure 5.33. *Downhole plots of the compositions of ferromagnesian minerals garnet, biotite, chlorite, and staurolite in drill hole 16-04. Expressed as X_{Fe} calculated as FeO/(FeO+MgO+MnO+CaO) for garnet and FeO/(FeO+ MgO) for biotite, chlorite, and staurolite.*

In sample DT058 at a depth of 244.5 meters there is a small dip in X_{Fe} values with averages of 0.76 and 0.75 for garnet and chlorite respectively (Fig. 5.33). This is a small drop of 0.07 for garnet and only 0.02 for chlorite. This small change may be small enough to be considered within the average for the country rock in the area, however, the drop in values may be as a result of a minor sulphide content as stringer veinlets of up to 2% pyrrhotite and 1% chalcopyrite are contained in the sample. It is possible that even a small sulphide content in the rocks is enough to create localized halos. However, if this is the case it would be expected that all samples containing sulphide veinlets would show a localized decrease in X_{Fe} values. Sample DT050 which occurs at a depth of 176.4 meters in drill hole 16-04 contains pyrrhotite and chalcopyrite inclusions in garnet as well as infilling in garnet fractures, the pyrrhotite make up 3% of the sample and chalcopyrite up to 1%. Given the sulphide content in the sample it would be expected that the X_{Fe} content of the ferromagnesian silicates should be below the average for the drill hole. The X_{Fe} for garnet, biotite, and chlorite was 0.87, 0.83, and 0.79 respectively. This is a slight increase

over the drill hole average and suggests small quantities of sulphides up to a few percent of the rock is not enough to cause drastic differences in indicator mineral composition.

Staurolite has been used in VMS exploration partly due to its ability to incorporate zinc into its structure (Spry and Stott, 1986). Zincian staurolite forms during metamorphism of a massive sulphide deposit, where desulfidation and deoxidation mechanisms involving sphalerite, pyrrhotite and pyrite, where staurolite becomes the most stable receptacle for zinc in the system (Spry, 1998). Thus, the presence of zincian staurolite acts as a vector to proximal massive sulphides. Of the 87 staurolites analyzed from Lundmark Akow, zinc was detected in only nine samples with values of 0.2 to 1.64 wt. % ZnO. Staurolite is known to incorporate up to 9 wt. % ZnO near Zn-rich massive sulphide deposits, and at Geco would be considered zinc-rich above 4 wt. % ZnO (Petersen, 1984). None of the analyzed staurolites from Lundmark Akow would be considered high zinc content in other deposits that have been evaluated for staurolite zinc content (Spry and Stott, 1987; Spry et al., 1998).

The staurolite which returned the highest zinc value was from sample DT035, which occurs 2 meters below a 6cm wide sulphide horizon of chalcopyrite, pyrrhotite, and tourmalinite. As amphibolite metamorphic conditions were reached, the presence of this massive sulphide horizon changed the equilibrium state of Zn within sphalerite and led to the formation of zincian staurolite. This was however the only staurolite with a ZnO value greater than 1 wt. %, suggesting that the other analysed staurolite grains are not close to mineralization.

Overall the results show that mineral composition vectors have limited usefulness in Lundmark Akow, only showing a response if the massive sulphide is located within a few meters of the analyzed mineral. There is no indication based on mineral compositions that there remains an untested massive sulphide horizon within the Lundmark Akow area. However, the lack of an indication for mineralization

based on mineral composition does not signify that such mineralization does not exist, as the range of this vector is limited and the drilling performed is limited.

5.12 Metamorphic Conditions

Metamorphic conditions played an important role in altering the protolith hydrothermal particles and sediments into the mineral assemblage observed at Lundmark Akow. Previous attempts at constraining the metamorphic conditions in the North Caribou Greenstone Belt have focused on the Musselwhite mine. Arsenopyrite-iron sulphide geothermometry of the metapelites in Musselwhite mine vicinity by Hall and Rigg (1986) constrained peak metamorphic temperatures between 530°C – 570°C. Otto (2002) conducted garnet-biotite geothermometry on lithologies at Musselwhite mine and determined that peak metamorphic temperatures occurred between 540°C – 600°C at 5 to 7 kilobars.

Constraining the pressure temperature conditions of metamorphism in Lundmark Akow can be accomplished through the use of mineral composition geothermometers and barometers. Two separate geothermometers were utilized; a Ti in biotite method (Wu and Chen, 2015) with a random error of no greater than 65°C, and a biotite-garnet composition method (Holdaway, 2000), with an absolute error of 25°C. The Hoisch (1990) mineral compositional barometer for an assemblage of garnet, biotite, muscovite, and plagioclase was utilized to constrain the pressure for the samples. This barometer has an error of up to a maximum of 0.3Kbar. Four samples from the project area contain the full suite of elements necessary to calculate both a geothermometry and barometry point (Fig. 5.34). The two outlier points in sample DT024 are a result of variable Ti content in biotite in the schist matrix combined with indirect contact with the garnet phenocrysts. Generally, minerals in the immediate vicinity of one another are more likely to represent samples in equilibrium. If only geothermometer values from minerals in contact are used, the average temperature would be 596.9 °C with a standard deviation of 5.8 °C and an average pressure of 3.6 Kbar with a standard deviation of 0.2 Kbar.

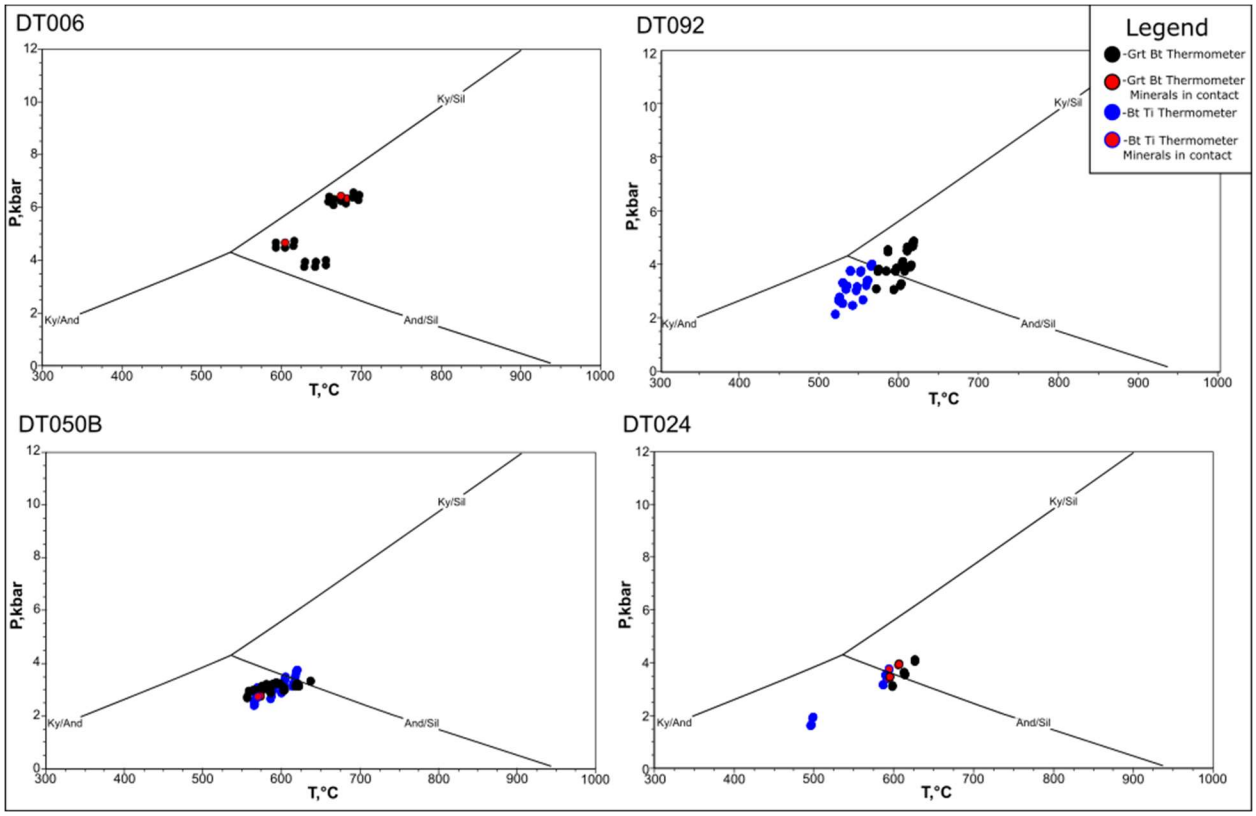

Figure 5.34. Geothermobarometer intersection points plotted in P-T space. Points in black were calculated using a garnet biotite geothermometer while those in blue used a Ti in biotite geothermometer. Points with a red interior represent samples taken only on mineral phases in direct contact with one another.

The results are consistent with previous interpretations on the belt (Breaks et al., 2001), showing increasing metamorphic grade from the north to the south of the belt (Table. 5.1). The temperature conditions are 573°C for the northernmost sample and increase to 651°C in the southernmost sample. Although the standard deviations for these samples are up to 30°C, they are smaller than the temperature variation. Pressure likewise varies from 3.0 Kbar in the north to 5.3 Kbar in the southern most sample.

Table 5.1. All temperature and pressure data calculated from the four samples with their standard deviation.

Sample	Analysis	Temperature (°C)	St. Dev (°C)	Pressure (Kbar)	St. Dev. (Kbar)
DT006	24	651.2	32.6	5.3	1.1
DT092	96	573.0	32.2	3.6	0.6
DT050	120	589.9	19.8	3.0	0.3
DT024	48	584.7	40.3	3.3	0.7

Pseudo-sections are another method of analysing potential metamorphic conditions of the sample based on calculating theoretical mineral assemblages from whole rock data. Computations of mineral phase equations have been performed to create dividing lines which can then highlight stability fields for various mineral phases. Sample DT050 contains15% staurolite and 15% garnet in equilibrium with each other in a matrix of biotite, muscovite, and quartz. The presence of both garnet and staurolite together occurs only within the staurolite field highlighted in purple (Fig. 5.35). This field constrains the conditions of peak metamorphism for this sample to between 510-600 °C and pressure between 2-5 Kbars. Plotted in light blue is the field for the previously determined conditions based on the mineral composition geothermometers. The black point shows the mean average of all geothermobarometers with the cross showing the region contained within the first standard deviation of the values.

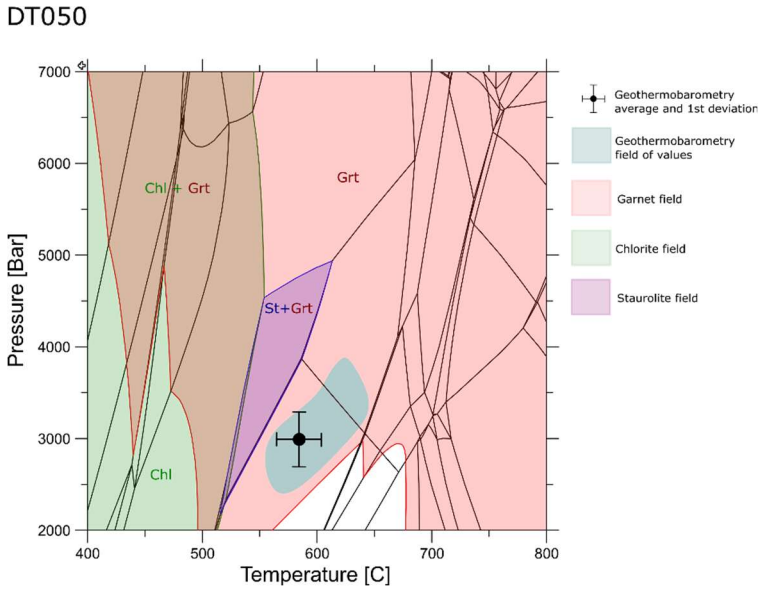

Figure 5.35. Pseudo section calculated from whole rock data for sample DT050. In blue is plotted the field of geothermometery values displayed in 5.35. Pseudo section created using Theriak Domino

The conditions calculated from mineral compositional data do not plot directly within the staurolite field as would be expected from the mineral assemblage in the sample. This suggests that the geothermobarometer values used may be calculating conditions slightly hotter and lower pressures than actually occurred. This could be a result of the imprecision in calculating mineral compositions through the use of scanning electron microscope with energy dispersive X-ray spectroscopy (SEM-EDX). The use of an electron microprobe may have produced more precise compositional data which would have refined the calculated temperature and pressure data. However, despite the difference in values, both methods still return a pressure temperature value in generally similar conditions of lower amphibolite metamorphic grade and broadly consistent with previous work.

6. Conclusions

The objectives of the study were to evaluate the tectonic setting of the Lundmark Akow and characterize the massive sulphide mineralization and associated alteration assemblage. The regional tectonic setting, local geology, and method of sulphide deposition were evaluated to better understand the mineralization. Various whole rock geochemical, mineral composition, and spectral vectoring methods were evaluated to gauge their effectiveness and potential to locate more significant mineralization in the area. A variety of data was collected through the use of whole rock major and trace element geochemistry, thin section petrography, SEM/EDS, laser ablation ICP MS, SWIR, $\delta^{34}S$ isotopes, Sm-Nd isotopes, and Re-Os and U-Pb geochronology. This data was used to develop a more complete model of the mineralization in the area.

The flat trace element patterns and CHUR-like Sm-Nd values of mafic group 4 and 5 suggest a period of early sea floor plume generated mafic magmatism associated with the development of an oceanic plateau. This plateau eventually collided with older crustal material in an arc setting where subsequent magmatism generated arc like magmas with elevated LREE, negative Nb and Ti anomalies and Sm-Nd values ranging from +3 suggesting an uncontaminated mantle derived magma down to a value of -1.5 which suggests contamination by older crust. This arc related mafic magmatism had to have occurred by 2976 ± 13 Ma based on a cross cutting relationship with a dated molybdenite bearing quartz vein. Felsic volcanism in the Lundmark Akow area occurred in a period around 2980.02 ± 0.77 to 2972.99 ± 0.42 Ma based on U-Pb dating of zircons. A sequence of sedimentary mudstones and siltstones was deposited on these plateau and arc magmas to form the sedimentary basin found in Lundmark Akow.

The lack of felsic volcanic rock within the biotite garnet staurolite schists mean that alteration plots such as Rb/Sr vs. Na_2O or the AI/CCPI box plot diagram are not effective for evaluating the potential of hydrothermal alteration in Lundmark Akow. The behaviour of Fe and Mn vs. immobile elements such

as Ti and Al show that some sedimentary rocks have undergone Fe enrichment that was the result of mixing between 15-50% particulate fallout from hydrothermal plumes and terrigenous sediments.

The textural characteristics of the garnet in garnet and quartz rich bands are typical of these having formed by metamorphism of hydrothermal plume particulate fallout. The garnets ranged from almandine to spessartine garnets, with the composition more strongly influenced by host rock chemistry than the proximity to massive sulphide mineralisation. Variations in major oxide compositions from core to rim likely represent prograde metamorphic growth, consistent with their formation as the metamorphic product of iron hydroxide plume particulates rather than representing an earlier syngenetic garnet formation rimmed by later metamorphic garnet. The U/Pb date of the core of the garnet at 2960 ± 19 Ma and the rim dated to 2424 ± 3 Ma could suggest that the core and rim were formed by separate events, an earlier formation by VMS fluids, and a regional metamorphic formed rim. However, garnet trace element data was scattered, suggesting that extensive alteration and inclusions make the trace element data unreliable and suggest that caution may be necessary when interpreting the U-Pb age dates of garnets gathered in this study.

The formation of tourmaline as radiating growths and agglomerate blebs along stratigraphic horizons is consistent with them having formed as exhalative tourmalinite. This tourmalinite would form by metasomatic interactions between a bottom hugging boron rich hydrothermal plume and aluminous terrigenous sediments. The Fe-rich composition of the tourmaline is consistent with formation in an Fe-rich plume which did not significantly intermix with Mg-rich seawater before sinking into topographic lows. Petrographic analysis shows that the tourmaline predates the garnet and biotite, which supports there syngenetic formation by the metasomatic interactions between hydrothermal plumes and sediments with the garnets forming later as a result of regional metamorphism.

Staurolite composistions throughout the Lundmark Akow area showed little to no zinc enrichment. This suggests that the staurolite is more likely to have formed as a result of metamorphism of hydrothermal plume particulate fallout rather than by alteration by VMS fluids as the latter would have caused an enrichment in Zn which would be incorporated into staurolite (Spry et al., 1998).

SWIR data from white micas in Lundmark Akow show the Al-OH band occurring at a low wavelength of 2196 to 2200 nm, indicating a high Al^{Iv} content with limited Fe and Mg substitution. This is not consistent with formation proximal to a high temperature setting like a VMS system and may either be the product of distal alteration or metamorphism.

The textural characteristics of the sulphides at Lundmark Akow are consistent with formation in a bottom hugging brine given the lack of associated alteration in the surrounding host rock, as well as the presence of tourmalinite. The high Se/S ratios of massive sulphide hosted within the sedimentary sequences are indicative of cooler temperatures of formation which would be expected in a hydrothermal plume which is cooled by the surrounding seawater. The slight elevation of $\delta^{34}S$ above mantle values may suggest that some sulfur may have been sourced from the ocean water or sediments although the age of the deposit and the limited amount of sulphate reducing bacteria in the Archean makes this distinction uncertain.

The usefulness of garnet, biotite, chlorite, and staurolite compositions as a vector to a metamorphosed massive sulphide deposit through the formation of a sulfidation oxidation halo was evaluated. A decrease in iron content within the mineral species adjacent to massive sulphide mineralization in drill hole 17-01 was detected, consistent with the development of a sulphidation oxidation halo. However, the extent of this halo was limited to within a few meters of massive sulphide mineralization. The mineral compositions were more effected by host rock lithology than proximity to

mineralization and thus mineral chemistry was not found to be an effective vector to locate further mineralization in Lundmark Akow.

Geothermobarometric data was derived by evaluating Ti in biotite and garnet biotite geothermometry with intersection points formed with a garnet, biotite, muscovite, plagioclase geobarometer. The general trend suggested a peak metamorphic grade of amphibolite facies with temperatures around 550° to 650°C and 2.5 to 4 Kbar. A pseudo section analysis confirmed a stability field for garnet occurring alongside staurolite would occur at around 500 to 600°C and 2 to 5 Kbar.

In summary, the bulk of the data suggest that the host rock volcanic and intrusive rocks were formed on top of a plume derived oceanic plateau which was obducted onto crustal material in an arc setting. The mineralization at Lundmark Akow formed distal to a hydrothermal vent as a product of a bottom-hugging brine. The mineral assemblage of garnet staurolite biotite schist is consistent with an Fe enriched sediment formed by hydrothermal particulate fallout from diffuse Fe rich plumes. Fluid rock alteration indices and mineral compositions were not successfully employed as an effective vector to more significant mineralization.

References

Ague, J., W. D. Carson. (2013). Metamorphism as Garnet Sees It: The Kinetics of Nucleation and Growth, Equilibration, and Diffusional Relaxation. Elements. v. 9, p. 439-445.

Barrett T.J. and I. Jarvis, (1988). Rare-Earth Element Geochemistry of Metalliferous Sediments from DSDP Leg 92: The East Pacific Rise Transect. Chemical Geology, v. 67, p. 243-259.

Basori M.B.I., Gilbert SE, Zaw K and Large RR (2021) Geochemistry of sphalerite from the Permian volcanic-hosted massive sulphide (VHMS) deposits in the Tasik Chini area, Peninsular Malaysia: constraints for ore genesis. Minerals, v. 11, p. 728.

Baxter, Ethan F., Erik E. Scherer. (2013). Garnet Geochronology: Timekeeper of Tectonometamorphic Processes. Elements, v. 9, p. 433–438.

Bédard J. H. (2006). A catalytic delamination-driven model for coupled genesis of Archaean crust and sub-continental lithospheric mantle. Geochimica et Cosmochimica Acta, v. 70, p. 1188–1214.

Biczok J. (2016). Report on The 2016 Diamond Drilling Program At The Lundmark-Akow Lake Property Of Romios Gold Resources INC. Ontario Geological Survey Assessment File Database.

Biczok, J. (2021). Report On The 2019 Diamond Drilling, Geological and Geochemical Exploration Program At The Lundmark-Akow Lake Property Of Romios Gold Resources INC. Ontario Geological Survey Assessment File Database.

Biczok, J. P. Hollings, P Klipfel, L. Heaman, R. Maas, M. Hamilton, S. Kamo, R. Friedman. (2012). Geochronology of the North Caribou greenstone belt, Superior Province Canada: Implications for tectonic history and gold mineralization at the Musselwhite mine. Precambrian Research v. 192–195, p. 209–230.

Bostrom, K. (1973). The Origin and Fate of Ferromanganoan Active Ridge Sediments. Stockholm Contributions in Geology, v. 27, p. 149-243.

Breaks, F.W., Osmani, I.A. and deKemp, E.A. (2001). Geology of the North Caribou Lake area, northwestern Ontario; Ontario Geological Survey, Open File Report 6023.

Bucher, K., and M. Frey. (2002). Petrogenesis of Metamorphic Rocks. Springer-Verlag. Berlin. Chapter 7.

Caddick, Mark J., Jiri Konopasek, Alan B. Thompson. (2010). Preservation of Garnet Growth Zoning and the Duration of Prograde Metamorphism. Journal of Petrology. v. 51, p. 2327-2347

Canfield D. E. (2004). The Evolution of the Earth Surface Sulfur Reservoir. American Journal of Science, v. 304, p. 839-861.

Card, K. D. (1990). A review of the Superior Province of the Canadian Shield, a product of Archean accretion. Precambrian Research, v. 48: p. 99-156.

Card, K. D. and J. E. King. (1992). The tectonic evolution of the Superior and Slave provinces of the Canadian Shield: introduction. Can. J. Earth Sci, v. 29, p. 2059-2065.

Card, K. D. and A. Ciesielski. (1986). Subdivisions of the Superior Province of the Canadian Shield. Geoscience Canada. v. 13, p. 5-9.

Cave B, Lilly R. and Barovich K. (2020) Textural and geochemical analysis of chalcopyrite, galena, and sphalerite across the Mount Isa Cu to Pb-Zn transition: implications for a zoned Cu-Pb-Zn system. Ore Geology Reviews, v. 124, 103647.

Corfu, F. and D. Stone. (1998). Age structure and orogenic significance of the Berens River composite batholiths, western Superior Province. Can. J. Earth Sci. v. 35, p. 1089–1109.

Davis, D.W., Stott, G.M. (2001). Geochronology of several greenstone belts in the Sachigo Subprovince, northwestern Ontario, #18 Project Unit 89-7. In: Baker, C.L., Kelly, R.I., Parker, J.R. (Eds.), Summary of Field Work and Other Activities 2001: Ontario Geological Survey, Open File Report 6070, p. 18-1-13.

DeKemp, E.A. (1987). Stratigraphy, Provenance and Geochronology of Archean supracrustal rocks of western Eyapamikama Lake area, northwestern Ontario; unpublished MSc thesis, Carleton University, Ottawa, Ontario, 98p.

DePaolo, D.J. (1981). Neodymium isotopes in the Colorado Front Range and crust-mantle evolution in the Proterozoic. Nature, v. 291, p. 193-196.

Dietrich, R.V. (1985). The Tourmaline Group. Van Nostrand Reinhold Company, p. 300.

Douglas, R.J.W. (1973). Geological Provinces. Map 27-28, National Atlas of Canada, 4th Edition: Surveys and Mapping Branch, Department of Energy, Mines and resources, Ottawa.

Doyle, M.G., and Allen, R.L. (2003), Sub- Sea floor replacement in volcanic hosted massive sulfide deposits: Ore Geology Reviews, v. 23, p. 183–222.

Ethier V.G., Campbell F.A. (1977). Tourmaline concentrations in proterozoic sediments of the southern cordillera of Canada and their economic significance. Canadian Journal of Earth Sciences, v. 14, p. 2348-2363.

Florence, Frank P., Frank S. Spear. (1991). Effects of diffusional modification of garnet growth zoning on P- T path calculations. Contributions to Mineralogy and Petrology, v. 107, p. 487-500.

Forshaw Jacob B., David R.M. Pattison. (2022). Major-element geochemistry of pelites. *Geology* ; 51 (1): 39–43.

Fralick, P.W., (2003), Geochemistry of clastic sedimentary rocks: ratio techniques, in lentz, D.R. ed., Geochemistry of Sedimentary Rocks: Evolutionary Considerations to Mineral Deposit- Forming Environments. Geological Association of Canada, GeoText v. 4, p. 85-103.

Franklin, J., J. Lydon, D. Sangster. (1981). Volcanic-Associated Massive Sulfide Deposits. Economic Geology. 75h anniversary volume. p. 485-627.

Franklin, J., H. Gibson, I. Jonasson, A. Galley. (2005). Volcanogenic Massive Sulfide deposits. Economic Geology 100th anniversary volume, p. 523-560.

Fullagar, P.D., Brown, H.S., and Hagner, A.F., (1967), Geochemistry of wall rock alteration and the role of sulfurization in the formation of the Ore Knob sulfide deposit: Economic Geology, v. 62, p. 798–825.

Gagnon, E., D. Schneider, T. Kalbfleisch, G. Habler, J. Biczok. (2016). Characterization of transpressive deformation in shear zones of the Archean North Caribou greenstone belt (NW Superior

Province) and the relationship with regional metamorphism. Tectonophysics, v. 693, p. 261–276.

Galley, A.G. (1993), Characteristics of semi-conformable alteration zones associated with volcanogenic massive sulphide districts. Journal of geochemical Exploration, v. 28, p. 175-200.

Galley, A. & Hannington, M.D. & Jonasson, Ian. (2007). Volcanogenic massive sulphide deposits, in mineral deposits of Canada: A synthesis of major deposit types. Earth Sciences Sector. P. 141-162.

German, C.R., W.E. Seyfried (2014). Hydrothermal Processes. In Treatise on Geochemistry. Ed. H. Holland, K. Turekian. v. 8 p. 191-233.

Gibson, H.L., Morton, R.L., and Hudak, G.J. (1999). Submarine volcanic processes, deposits, and environments favorable for the location of volcanic-associated massive sulfide deposits: Reviews in Economic Geology, v. 8, p. 13–51.

Government of Canada, 2022, The Canadian Critical Minerals Strategy: Ottawa, Natural Resources Canada. 58 p.

Griffin, W., L. John F. Slack, Anthony R. Ramsden, Tin Tin Win, Chris G. Ryan. (1996). Trace Elements in Tourmalines from Massive Sulfide Deposits and Tourmalinites: Geochemical Controls and Exploration Applications, Economic Geology, v. 91, p. 657-675.

Gross, G.A. (1995). Stratiform iron: Geological Survey of Canada, Geology of Canada, no. 8, p. 41–54.

Hall, R.S. and Rigg, D.M. (1986). Geology of the West Anticline Zone, Musselwhite Prospect, Opapimiskan Lake, Ontario, Canada; in Proceedings, Gold ’86 Symposium; Toronto, Ontario, September 28–October 1, p. 124–136.

Hannington, M. (2014). Volcanogenic Massive Sulfide Deposits, Treatise on Geochemistry (Second Edition), Ed. Heinrich D. Holland, Karl K. Turekian. p. 463-488.

Hannington, M.D., de Ronde, C.E.J., and Petersen, S. (2005). Sea-floor tectonics and submarine hydrothermal systems: Economic Geology 100TH Anniversary Volume, p. 111-141.

Heimann, A., Paul G. Spry, Graham S. Teale, Colin H.H. Conor, and Wolfgang R. Leyh. (2009). Geochemistry of Garnet-Rich Rocks in the Southern Curnamona Province, Australia, and Their Genetic Relationship to Broken Hill-Type Pb-Zn-Ag Mineralization. Economic Geology, v. 104, 687-712.

Henry, P., Ross K. Stevenson, Youcef Larbi, Clément Gariépy. (2000). Nd isotopic evidence for Early to Late Archean (3.4-2.7 Ga) crustal growth in the Western Superior Province (Ontario, Canada). Tectonophysics, v. 322, p. 135-151.

Hoisch, T.D. (1990). Empirical calibration of six geobarometers for the mineral assemblage quartz + muscovite + biotite + plagioclase + garnet. Contributions to Mineral Petrology, v. 104, p.225-234.

Hoffman, P. F. (1988). United Plates of America, The Birth of a Craton: Early Proterozoic Assembly and Growth of Laurentia. Ann. Rev. Earth Planet. Sci, v. 16, p. 543-603.

Holdaway, M.J. (2000). Application of new experimental and garnet Margules data to the garnet-biotite geothermometer. American Mineralogist, v. 85, p. 881-892.

Hollings, P., Kerrich R. (1999). Trace element systematics of ultramafic and mafic volcanic rocks from the 3 Ga North Caribou greenstone belt, northwestern Superior Province. Precambrian Research, v. 93, p. 257–279.

Hollings, P., D.A. Wyman. (1999). Trace element and Sm–Nd systematics of volcanic and intrusive rocks from the 3 Lumby Lake greenstone belt, Superior Province: evidence for Archæan plume-arc interactions. Lithos v.46, p. 189–213.

Hollings, P., R. Kerrich, D.A. Wyman. (1999). Komatiite–basalt–rhyolite volcanic associations in Northern Superior Province greenstone belts: significance of plume-arc interaction in the generation of the proto continental Superior Province. Lithos, v. 46, p. 137–161.

Hollister, L. S. (1966), Garnet Zoning: An interpretation based on the Rayleigh Fractionation Model. Science, V. 154, p. 1647-1651.

Honarvar, P. Barrie C.T., Harris J.R. (2006). Initial Results of Weights-of-Evidence Modelling to Assess the Mineral Potential of the Lucas-Crawford Area, Timmins, Ontario. In: GIS for the earth sciences, Harris J.R. (Ed). Geological Association of Canada, Special Paper 44, 616 p.

Huston D.L. (1999). Stable isotopes and their significance for understanding the genesis of volcanic-hosted massive sulfide deposits: a review. Rev Econ Geol. V. 10, p. 151–180.

Huston D.L., Sie SH, Suter GF, Cooke DR, Both RA. (1995). Trace elements in sulfide minerals from eastern Australian volcanic hosted massive sulfide deposits 1. Proton microprobe analyses of pyrite, chalcopyrite, and sphalerite, and 2. Selenium levels in pyrite: Comparison with delta S-34 values and implications for the source of sulfur in volcanogenic hydrothermal systems: Economic Geology, v. 90, p. 1167-1196.

Huston DL, Pehrsson S, Eglington BM, Zaw K (2010) The geology and metallogeny of volcanic-hosted massive sulfide deposits: variations through geologic time and with tectonic setting. Economic Geology, v. 105, p. 571-591.

Huston, D.L., Jorge M. R. S. Relvas, J. Bruce Gemmell, Susan Drieberg. (2011). The role of granites in volcanic-hosted massive sulphide ore-forming systems: an assessment of magmatic–hydrothermal contributions. Mineralium Deposita, v. 46, p. 473-507.

Ioannou, S. E., Spooner E. T. C., Barrie C. T. (2007). Fluid Temperature and Salinity Characteristics of the Matagami Volcanogenic Massive Sulfide District, Quebec. *Economic Geology,* v. 102, p. 691–715.

Jamieson, J.W., Wing, B.A., Farquhar, J., & Hannington, M.D. (2012) Neoarchaean seawater sulphate concentrations from sulphur isotopes in massive sulphide ore. Nature Geoscience, v. 6, p. 61–64.

Jones, S., Herrmann W., Gemmell J. B. (2005). Short Wavelength Infrared Spectral Characteristics of the HW Horizon: Implications for Exploration in the Myra Falls Volcanic-Hosted Massive Sulfide Camp, Vancouver Island, British Columbia, Canada. Economic Geology, v. 100, p. 273-294.

Large, R.R., (1992), Australian volcanic-hosted massive sulphide deposits: features, styles, and genetic models: Economic Geology, v. 87, p. 471-510.

Laurent, O., H. Martin, J.F. Moyen, R. Doucelance. (2014). The diversity and evolution of late-Archean granitoids: Evidence for the onset of “modern-style” plate tectonics between 3.0 and 2.5 Ga. Lithos, v. 205, p. 208-235.

Layton-Matthews, D., Jan M. Peter, Steven D. Scott, Matthew I. Leybourne. (2008). Distribution, Mineralogy, and Geochemistry of Selenium in Felsic Volcanic-Hosted Massive Sulfide Deposits of the Finlayson Lake District, Yukon Territory, Canada. Economic Geology. V. 103, p. 61-88.

Layton-Matthews, D., Matthew I. Leybourne, Jan M. Peter, Steven D. Scott, Brian Cousens, Bruce M. Eglington. (2013). Multiple sources of selenium in ancient seafloor hydrothermal systems: Compositional and Se, S, and Pb isotopic evidence from volcanic-hosted and volcanic-sediment-hosted massive sulfide deposits of the Finlayson Lake District, Yukon, Canada. Geochimica et Cosmochimica Acta, v. 113, p. 312-331.

Le Bas, M. J., Le Maitre, R. W., Streckeisen, A. and Zanettin, B. (1986). A chemical classification of volcanic rocks based on the total alkali-silica diagram. Journal of Petrology, v. 27, p. 745-750.

Leistel, J.M., Marcoux, E., Thieblemont, D., Quesada C., Sanchez, A., Alomdovar, G.R., Pascual, E., and Saez, R. (1998). The volcanic hosted massive sulfide deposits of the Iberian Pyrite Belt: Mineralium Deposita, v. 33, p. 2–30.

Leybourne, Matthew I., Jan M. Peter, James A. Kidder, Daniel Layton-Matthews, Joseph A. Petrus, Clinton F.W. Rissmann, Alexandre Voinot, Robert Bowell, T. Kurt Kyser. (2022). Stable and Radiogenic Isotopes in the Exploration for Volcanogenic Massive Sulfide Deposits. The Canadian Mineralogist, v. 60, p. 433-468.

Li, Dengfeng, Fu Y, Hollings P, Mitchell RH, Zurevinski S, Kamo S, Zhang R, Zhang Y, Liu Q, Liao J, et al. (2022). PL57 garnet as a new natural reference material for in situ U–Pb isotope analysis and its perspective for geological applications. Contributions to Mineralogy and Petrology. v. 177:19.

Li M-L, Liu S-A, Xue C-J and Li D. (2019). Zinc, cadmium and sulfur isotope fractionation in a supergiant MVT deposit with bacteria. Geochimica et Cosmochimica Acta, v. 265, p. 1–19.

Li, Yongbing, Jianming Liu. (2006). Calculation of sulfur isotope fractionation in sulfides. Geochimica et Cosmochimica Acta, .v. 70, p. 1789-1795.

Lottermoser. B.G. (1989). Rare earth elements study of exhalites within the Willyama Supergroup, Broken Hill Block, Australia: Mineralium Deposita, v. 24, p. 92–99.

Lydon J.W. and Reardon N.C. (2000). Sphalerite compositions of the Sullivan deposit and their implications for its metamorphic history. In The Geological Environment of the Sullivan Deposit, British Columbia (eds JW Lydon, T Höy, JF Slack and ME Knapp), Geological Association of Canada, Mineral Deposits Division, Special Publication 1. p. 281–301.

Maclean, W.H., Lawrence D. Hoy. (1991). Geochemistry of Hydrothermally Altered rocks at the Horne mine, Noranda, Quebec. Economic Geology, v. 86, p. 506-528.

MacLean W.H. and P. Kranidiotis. (1987). Immobile Elements as Monitors of Mass Transfer in Hydrothermal Alteration: Phelps Dodge Massive Sulfide Deposit, Matagami, Quebec. Economic Geology, v. 82, p. 951-962.

Markey, R., Stein H.J., Hannah J.L., Selby D., and Creaser R.A. (2007). Standardizing Re-Os geochronology: A new molybdenite Reference Material (Henderson, USA) and the stoichiometry of Os salts. Chemical Geology, v. 244, p. 74-87.

Marmo, V. (1957). Geology of the Nokia region, south-west Finland: Finland Geological Society Bulletin, v. 176, p. 1–3.

Martin, H. (1987). Petrogenesis of Archaean trondhjemites, tonalites and granodiorites from eastern Finland: Major and trace element geochemistry: Journal of Petrology, v. 28, p. 921–953.

Massonne, H.J., Schreyer, W., (1987). Phengite geobarometry based on the limiting assemblage with K-feldspar, phlogopite, and quartz. Contributions to Mineralogy and Petrology. v. 96, p. 212–224.

McLennen, Scott. M, Barbara Bock, Sidney R. Hemming, Joal A. Hurowitz, Steven M. Lev, Diane K. McDaniel (2003). The roles of provenance and sedimentary processes in the geochemistry of sedimentary rocks, in Lentz, D.R. Ed., Geochemistry of sediments and sedimentary rocks: evolutionary considerations to Mineral Deposit- Forming Environments: Geological Association of Canada, Geotext 4, p. 7-38.

McNicoll, V., B. Dube, S. Castonguay, W. Oswald, J. Biczok, P. Mercier-Langevin, T. Skulski, M. Malo. (2016). The world-class Musselwhite BIF-hosted gold deposit, Superior Province, Canada: New high-precision U–Pb geochronology and implications for the geological setting of the deposit and gold exploration. Precambrian Research v. 272, p. 133-149.

McNulty, B.A., Fox N., Gemmell J. B. (2020). Assessing hydrothermal alteration intensity in Volcanic-Hosted massive sulphide systems using portable X-Ray Fluorescence analysis of Drill Core: An example from Myra Falls, Canada. Economic Geology, v. 115, p.443–453.

Mishra B.P., Patia P., Dora M.L., Baswani S.R., Meshram T, Shareef M, Pattanayak R.S., Suryavanshi H, Mishra M and Raza M.A. (2021). Trace element systematics and isotopic characteristics of sphalerite-pyrite from volcanogenic massive sulfide deposits of Betul belt, central Indian Tectonic Zone: insight of ore genesis to exploration. Ore Geology Reviews, v. 134, 104149.

Mitchell, R. (1994). The Lamprophyre Facies. Minerology and Petrology, v. 51. p. 137-146.

Moran, Patrick Cowen. (2008). Lithogeochemistry of the sedimentary stratigraphy and metasomatic alteration in the Musselwhite gold deposit, North Caribou Lake belt, Superior province, Canada : implications for deposition and mineralization. MSc Thesis, Lakehead Knowledge Commons.

Moyen J.F., Martin H. (2012). Forty years of TTG research, Lithos, V. 148, p. 312-336.

Murphy, J. (2007). Igneous Rock Associations 8. Arc Magmatism II: Geochemical and Isotopic Characteristics. Geoscience Canada. v 34. p. 7-35.

Nesbitt, B.E. (1982). Metamorphic sulfide-silicate equilibria in the massive sulfide deposits at Ducktown, Tennessee: Economic Geology, v. 77, p. 364–378.

Nesbitt, B. E. (1986). Oxide-Sulfide-Silicate Equilibria Associated with Metamorphosed Ore Deposits. Part II: Pelitic and Felsic Volcanic Terrains. Economic Geology, v. 81, p. 841-856.

O'Brien J.J., Spry P.G., Teale G.S., Jackson S.E., Koenig A.E. (2015). Gahnite composition as a means to fingerprint metamorphosed massive sulfide and non-sulfide zinc deposits. Journal of geochemical exploration, v. 159, p. 48–61.

Ohls K, Bogdain B. (2016). History of inductively coupled plasma atomic emission spectral analysis: from the beginning up to its coupling with mass spectrometry, Journal of analytical atomic spectrometry, v. 31, p. 22–31.

Ohmoto, H., Rye, R.O. (1979). Isotopes of sulfur and carbon. In: Barnes, H.L. (Ed.), Geochemistry of Hydrothermal Ore Deposits, 2nd ed. Wiley, New York, p. 509 – 567.

Ontario Geological Survey. (2003). Ontario airborne geophysical Surveys, magnetic and electromagnetic data, grid and profile data, ASCII format, Opapimiskan Lake area; Ontario Geological Survey, Geophysical Data Set 1011a.

Oswald w., S. Castonguay, B. Dube, M. Malo, P. Mercier-Langevin, J. Biczok. (2015). New insights on the geological and structural settings of the Musselwhite banded iron formation–hosted gold deposit, North Caribou greenstone belt, Superior Province, Ontario. Geological Survey of Canada, Current Research 2015-3, 19.

Otto, A., (2002). Ore forming processes in the BIF-hosted gold deposit Musselwhite mine, Ontario, Canada; M.Sc. thesis Freiberg University of Mining and Technology, Freiberg, Germany, 86 p.

Palmer, M.R. (1991). Boron isotope systematics of hydrothermal fluids and tourmalines: A synthesis, Chemical Geology: Isotope Geoscience section, v. 94, p. 111-121.

Paton, C., Hellstrom, J., Paul, B.,Woodhead, J. and Hergt, J. (2011). Iolite: Freeware for the visualisation and processing of mass spectrometric data. Journal of Analytical Atomic Spectrometry.

Pearce, J.A. (1996). A User's Guide to Basalt Discrimination Diagrams. In: Wyman, D.A., Ed., Trace Element Geochemistry of Volcanic Rocks: Applications for Massive Sulphide Exploration, Geological Association of Canada, Short Course Notes, v. 12, p. 79-113.

Percival J.A, Sanborn-barrie M., T. Skulski, G.M. Stott, H. Helmstaedt, D.J. White. (2006). Tectonic Evolution of the Western Superior Province from NATMAP and Lithoprobe Studies. Can. J. Earth Sci, v. 43, p. 1085- 1117.

Percival, J.A., (2007). Geology and Metallogeny of the Superior Province, Canada, in Goodfellow, W.D., ed., Mineral Deposits of Canada: A Synthesis of Major Deposit-Types, District Metallogeny, the Evolution of Geological Provinces, and Exploration Methods: Geological Association of Canada, Mineral Deposits Division, Special Publication.

Peter, J. M. (2003). Ancient iron-rich metalliferous sediments (iron formations): their genesis and use in the exploration for stratiform base metal sulphide deposits, with examples from the Bathurst Mining Camp, in Lentz, D.R., ed., Geochemistry of Sediments and Sedimentary Rocks: Secular Evolutionary Considerations to Mineral Deposit-Forming Environments, GEOtext 4.: St. John's, Geological Association of Canada, p. 145-173.

Petersen, E.U. (1984). Metamorphism and geochemistry of the Geco massive sulfide deposit and its enclosing wall-rocks: Unpublished Ph.D. dissertation, Ann Arbor, University of Michigan.

Petrus, J.A. and Kamber, B.S. (2012). VizualAge: A novel approach to laser ablation ICP-MS U-Pb geochronology data reduction. Geostandards and Geoanalytical Research, v. 36, p. 247-270.

Piercey, S.J. (2009). Lithogeochemistry of volcanic rocks associated with volcanogenic massive sulfide deposits and applications to exploration. *In* Submarine volcanism and mineralization: modern through ancient. *Edited* by B. Cousens and S.J. Piercey. Geological Association of Canada. p. 15-38.

Piercey, S. J. (2015); A Semipermeable Interface Model For The Genesis Of Subseafloor Replacement-Type Volcanogenic Massive Sulfide (VMS) Deposits. *Economic Geology*; v. 110 (7), p. 1655–1660.

Plank, T. (2005). Constraints from Thorium/Lanthanum on Sediment Recycling at Subduction Zones and the Evolution of the Continents. Journal of Petrology. v. 46. p. 921-944.

Plimer, I.R., and Elliott, S.M. (1979). The use of Rb/Sr ratios as a guide to mineralization: Journal of Geochemical Exploration, v. 12, p. 21–34.

Pollock, M.V., Spry P.G., Tott K. A., Koenig A., R. A. Both, J. Ogierman. (2018). The origin of the sediment-hosted Kanmantoo Cu-Au deposit, South Australia: Mineralogical considerations: Ore Geology Reviews, v. 95, p. 94-117.

Restreppo, G.A., Wood W.T., Phrampus B.J. (2020). Oceanic sediment accumulation rates predicted via machine learning algorithm: towards sediment characterization on a global scale. Geo-Marine Letters, v. 40, p. 755–763.

Revan MK, Genç Y, Maslennikov VV, Maslennikova SP, Large RR and Danyushevsky LV. (2014). Mineralogy and trace-element geochemistry of sulfide minerals in hydrothermal chimneys from the Upper-Cretaceous VMS deposits of the eastern Pontide orogenic belt (NE Turkey). Ore Geology Reviews v. 63, p. 129–49.

Ridley, W.I. (2012). Geochemical Characteristics. In: volcanogenic massive sulfide occurrence model. Ed. (W.C. Pat Shanks III and Roland Thurston). US Geological Survey Scientific Investigations Report 2010-5070-C. p. 207-225.

Rieder, Milan, G. Cavazzini, Yakonov, V. Frank-Kamenetskii, G. Gottardi, S. Guggenheim, P. Koval, G. Müller, A. Neiva, E. Radoslovich, J.L. Robert, F. Sassi, H. Takeda, Z. Weiss, D. Wones, (1999). Nomenclature of the micas. Mineralogical Magazine.v. 63, p. 267-279.

Romer R.L., Xiao Y. (2004). Initial Pb–Sr (– Nd) isotopic heterogeneity in a single allanite–epidote crystal: implications of reaction history for the dating of minerals with low parent-to-daughter ratios. Contributions to Mineralogy and Petrology, v. 148, p. 662-674.

Schmitz, M.D. and Schoene, B. (2007). Derivation of isotope ratios, errors, and error correlations for U-Pb geochronology using ^{205}Pb-^{235}U-(^{233}U)-spiked isotope dilution thermal ionization mass spectrometric data. Geochemistry Geophysics Geosystems 8. issn: 1525-2027.

Schwartz, Micheal O. (2000). Cadmium in Zinc Deposits: Economic Geology of a Polluting Element. International Geology Review. Vol. 42. P 445-469.

Selby D. and R.A. Creaser. (2004). Macroscale NTIMS and microscale LA-MC-ICP-MS Re-Os isotopic analysis of molybdenite: Testing spatial restrictions for reliable Re-Os age determinations, and implications for the decoupling of Re and Os within molybdenite". Geochimica et Cosmochimica Acta, v. 68, p. 3897-3908.

Shanks, Wayne. (2012). Hydrothermal alteration. In: volcanogenic massive sulfide occurrence model. Ed. (W.C. Pat Shanks III and Roland Thurston). US Geological Survey Scientific Investigations Report 2010-5070-C. p. 165-180.

Shen, Y., Roger Buick, Donald e. Canfield. (2001). Isotopic evidence for microbial sulphate reduction in the early Archaean era. Nature. v. 410, p. 77-81.

Skirrow R.G., Franklin J.M. (1994). Silicification and metal leaching in semi-conformable alteration beneath the Chisel Lake massive sulfide deposit, Snow Lake, Manitoba. *Economic Geology*, v. 89, v. 31–50.

Slack, J.F. (1996). Tourmaline Associations with Hydrothermal Ore Deposits, Reviews in Mineralogy, v. 33, p. 559-644.

Slack, J.F. (2012). Exhalites in volcanogenic massive sulfide occurrence model: U.S. Geological Survey Scientific Investigations Report 2010–5070 –C, chap. 10, 6 p.

Slack, J.F. (2022). Perspectives on premetamorphic stratabound tourmalinites, Journal of Geosciences, v. 67, p. 73-102.

Slack J.F., Coad P.R., (1989). Multiple hydrothermal and metamorphic events in the Kidd Creek Volcanogenic massive sulphide deposit, Timmins, Ontario: Evidence from tourmalines and chlorites. Canadian Journal Earth Sciences, v. 26, p. 694-715.

Slack J.F., Ramsden A.R., Griffin W.L., Win T.T., French D.H., Ryan C.G. (1996). Trace elements in tourmalines from the Kidd creek massive sulphide deposit and vicinity, Timmins, Ontario- A proton microprobe study. In: M.D. Hannington, C.T. Barrie, W. Bleeker (eds) The Kidd Creek volcanic-associated massive sulphide deposit, Abitibi subprovince, Canada. Economic Geology Monograph 10.

Smoliar, M., Richard Walker, John Morgan. (1996). Re-Os ages of group IIA, IIIA, IVA, IVB iron meteorites, Science, v. 271, p. 1099-1102.

Sousa J, M. Kohn, M. Schmitz, C. Northrup, F. Spear. (2013). Strontium isotope zoning in garnet: implications for metamorphic matrix equilibration, geochronology, and phase equilibrium modelling. Journal of Metamorphic Geology, v. 31, p. 437-452.

Spry, P.G., Jan M. Peter, John F. Slack. (1998). Meta-Exhalites as Exploration Guides to Ore, Reviews in Economic Geology, v. 11, p. 167-204.

Spry, P.G. (1998). Sulfidation and Oxidation Haloes as Guides in the Exploration for Metamorphosed Massive Sulfide Ores. Reviews in Economic Geology, v. 11, p. 153-166.

Spry, P.G., and Scott, S.D., 1986, The stability of zincian spinels in sulfide systems and their potential as exploration guides for metamorphosed massive sulfide deposits: Economic Geology, v. 81, p. 1146–1463.

Spry P.G., Mathur R.D., Teale G.S., and Godfrey L.V. (2022). Zinc, sulfur and cadmium isotopes and Zn/Cd ratios as indicators of the origin of the supergiant Broken Hill Pb–Zn–Ag deposit and other Broken Hill-type deposits, New South Wales, Australia. Geological Magazine, v. 159, p. 1787–1808.

Stalder, M., Rozendaal, A. (2005). Trace and rare earth element chemistry of garnet and apatite as discriminant for Broken Hill-Type mineralization, Namaqua Province, South Africa. In: Mao, J., Bierlein, F.P. (eds) Mineral Deposit Research: Meeting the Global Challenge. Springer, Berlin, Heidelberg.

Staten, W.T. (1976). A chemical study of the silicate minerals of the Great Gossan Lead and surrounding rocks in southwestern Virginia: Unpublished M.S. thesis, Blacksburg, Virginia Polytechnic Institute and State University.

Stockwell, C. H. (1964). Fourth report on structural provinces. Orogenies and time-classification of rocks of the Canadian Precambrian Shield. Part 11. Geological Studies, Geological Survey of Canada, v. 64-17, p. 1-7.

Stott, G. The superior province, Canada. (1997). In deWit, M.J. Ashwal, L.D. Eds., The Tectonic Evolution of Greenstone Belts. Oxford Univ. Press, p. 480–507.

Stott, G. M. and J. Biczok. (2010). Project Unit 03-011. North Caribou Greenstone Belt: Gold and Its Possible Relation to the North Caribou Pluton Emplacement—A Belt-wide Contact-Strain Aureole? Summary of Field Work and Other Activities 2010, Ontario Geological Survey, Open File Report 6260, p. 1-12.

Stott, G.M., Corkery, M.T., Percival, J.A., Simard, M. and Goutier, J. (2010). A revised terrane subdivision of the Superior Province; in Summary of Field Work and Other Activities 2010, Ontario Geological Survey, Open File Report 6260, p. 1-10.

Sturt, B. (1962). The composition of Garnets from Pelitic Schists in relation to the Grade of Regional Metamorphism, Journal of Petrology. v. 3, p. 181-191.

Sun, S.S. and McDonough, W.F. (1989). Chemical and Isotopic Systematics of Oceanic Basalts: Implications for Mantle Composition and Processes. In: Saunders, A.D., Norry, M.J., Eds., Magmatism in the Ocean Basins, Geological Society, London, Special Publications, v. 42, p. 313-345.

Sylvester, P. and Jackson, Simon. (2016). A Brief History of Laser Ablation Inductively Coupled Plasma Mass Spectrometry (LA–ICP–MS). Elements, v. 12, p. 307-310.

S&P Global. (2022). The future of Copper: Will the looming supply gap short-circuit the energy transition? https://cdn.ihsmarkit.com/www/pdf/0722/The-Future-of-Copper_Full-Report_14July2022.pdf

Tagirov, B. R. & Seward, T. M. (2010). Hydrosulfide/sulfide complexes of zinc to 250 °C and the thermodynamic properties of sphalerite. Chem. Geol. V. 269, p. 301–311.

Tanaka, T., Togashi, S., Kamioka, H., Amakawa, H., Kagami H., Hamamoto, T., Yuhara, M., Orihashi, Y., Yoneda, S., Shimizu, H., Kunimaru, T., Takahashi, K., Yanagi, T., Nakano, T., Fujimaki, H., Shinjo, R., Asahara, Y., Tanimizu, M., Dragusanu, C., (2000). JNdi-1: a neodymium isotopic reference in consistency with LaJolla neodymium. Chemical Geology, vol. 168, p. 279-281.

Taylor, S.R., (1965), The application of trace element data to problems in petrology: Physics and Chemistry of the Earth, v. 6, p. 133–213.

Thurston, P.C., (1991). Archean Geology of Ontario: introduction. In: Thurston, P.C., Williams, H.R., Sutcliffe, R.H., Stott, G.M. (Eds.), Geology of Ontario, Ontario Geological Survey Special Volume 4, Pt. 1, p. 73–80.

Thurston, P.C. (2015). Igneous Rock Associations 19. Greenstone Belts and Granite−Greenstone Terranes: Constraints on the Nature of the Archean World. Geoscience Canada, v. 42, p. 437–484.

Thurston, P.C., I. Osmani, D. Stone. (1991). Northwestern Superior Province: Review and Terrane Analysis. Geology of Ontario, Ontario Geological Survey, Special Volume 4, Part 1, p. 26-57.

Tomlinson, K. Y., Stott, G.M., Percival, J.A., Stone, D., (2004). Basement terrane correlations and crustal recycling in the wester Superior Province: Nd isotopic character of granitoid and felsic volcanic rocks in the Wabigoon subprovince, N. Ontario, Canada. Precambrian Research, v. 132, p. 245-274.

Turner R.J.W. Formation of phanerozoic stratiform sediment-hosted zinc-lead deposits, Evidence for the critical role of ocean anoxia, Chem Geol, v. 99, p. 165-188.

Van Lankvelt, A., D. Schneider, J. Biczok, C. McFarlane, K. Hattori. (2016). Decoding Zircon Geochronology of Igneous and Alteration Events Based on Chemical and Microstructural Features: A Study from the Western Superior Province, Canada Journal of Petrology, v. 57, p. 1309–1334.

Wen H., Zhu C., Zhang Y., Cloquet C., Fan H. and Fu S. (2016) Zn/Cd ratios and cadmium isotope evidence for the classification of lead-zinc deposits. Nature Scientific Reports, v. 6, 25273.

Wilschefski, S.C., M.R. Baxter. (2019). Inductively Coupled Plasma Mass Spectrometry: Introduction to Analytical Aspects. Clin Biochem Rev, v. 40, 115-133.

Wilson, M, E. (1939). The Canadian Shield: Geology des Erde, Geology of North America 1.

Wise S.A. and R.L. Watters. (2011). Reference Material 8599 Henderson Molybdenite. National Institute of Standards and Technology Report of Investigation.

Woodhead, Jon D., John Hellstrom, Janet M. Hergt, Alan Greig, Roland Maas. (2007). Isotopic and Elemental Imaging of Geological Materials by Laser Ablation Inductively Coupled Plasma-Mass Spectrometry. Geostand Geoanalytical Res, v. 31, p. 331-343.

Wright, W. (1938). The composition and occurrence of garnets, American Mineralogist, v. 23, p. 436-449

Wu C.M., Chen H.X. (2015). Revised Ti-in-biotite geothermometer for ilmenite- or rutile-bearing crustal metapelites. Science Bulletin, v. 60, p.116-121.

Wyman, D., P. Hollings, J. Biczok. (2011). Crustal evolution in a Cratonic nucleus: Granitoids and felsic volcanic rocks of the North Caribou Terrane, Superior Province Canada. Lithos, v. 123, v. 37-49.

Yamamoto M. (1976). Relationship between Se/S and sulfur isotope ratios, hydrothermal sulfide minerals: Mineralium Deposita, v. 11, p. 197-209.

Yan, Zhiyong, Lin Chen, Andrew Zuza, Jiaxuan Tang, Bo Wan, Qingren Meng. (2022). The fate of oceanic plateaus: subduction versus accretion. Geophysical Journal International, v. 231, p. 1349-1362.

Yang, K., J.F. Huntington, J.B. Gemmell, K.M. Scott. (2011). Variations in composition and abundance of white mica in the hydrothermal alteration system at Hellyer, Tasmania, as revealed by infrared reflectance spectroscopy. Journal of Geochemical Exploration, v. 108, p. 143-156.

Yi, Wen, Alex Halliday, Jeffrey Alt, Der-Chuen Lee, Mark Rehkämper, Michael Garcia, Yongjun Su,. (2000). Cadmium, indium, tin, tellurium, and sulfur in oceanic basalts: Implications for chalcophile element fractionation in the Earth. Journal of Geophysical Research, v. 105, 18927-18948.

Zane, A., Z. Wiess. (1999). A procedure for classifying rock-forming chlorites based on microprobe data. Rendiconti Lincei Scienze Fisiche e Naturali. v. 9, p. 51-56.

Zhu, Chuanwei, Hanjie Wen, Yuxu Zhang, Zhilong Huang, Christophe Cloquet, Beatrice Luais, Tao Yang,. (2021). Cadmium isotopic constraints on metal sources in the Huize Zn-Pb deposit, SW China, Geoscience Frontiers, v. 12, 101241.

Zivkovic, Zebedee, Leonid Danyushevsky, Scott Halley, Shaun Barker, Michael Baker. (2023). Comparison of lithium borate fusion and four acid digestions for the determination of whole rock chemistry – implications for lithogeochemistry and mineral exploration. *Geochemistry: Exploration, Environment, Analysis*, v. 23

Appendix I

Drill core samples

Term definitions:

SWIR- Short wave infrared

SEM- Scanning electron microscope with energy dispersive X-ray spectroscopy

WRX- Whole rock analysis

LA-ICP-MS- Laser ablation induced coupled plasma mass spectrometer

Sulphur δ^{34}- Sulphur δ^{34} isotope analysis

Sm/Nd MC-ICP-MS- Multicollector Inductively Coupled Plasma Mass Spectrometer analysis of samarium neodymium isotopes

Sample ID	Hole ID	Lithology	From (m)	To (m)	Methods
LA-21-DT-001	19-3	Staurolite, garnet, biotite schist	69.2	69.4	Petrography, SEM
LA-21-DT-002	19-3	Mineralized garnet, staurolite schist	65.65	65.78	SWIR
LA-21-DT-003	19-3	Mineralized garnet, Staurolite schist	88.1	88.2	Petrography, SEM
LA-21-DT-004	19-3	Sericite garnet schist	99.65	99.75	SWIR
LA-21-DT-005	19-3	Staurolite, garnet, biotite schist with milky quartz vein	124.7	124.9	Petrography, SEM
LA-21-DT-006	16-2	Siltstone with minor Garnets	515.1	515.15	Petrography, SEM, SWIR
LA-21-DT-007	16-2	Basalt	452.7	453	WRX
LA-21-DT-008	16-2	Sericite garnet staurolite schist	384.9	385	WRX, SWIR
LA-21-DT-009	16-2	Pyrrhotite, Chalcopyrite with massive biotite and small garnets	436.15	436.25	Petrography, SEM, LA-ICP-MS, Sulphur δ^{34}
LA-21-DT-010	16-2	Garnet, biotite schist with pyrrhotite and chalcopyrite	435.15	435.25	Sulphur δ^{34}, SWIR
LA-21-DT-011	16-2	Siltstone with minor Garnets	305.4	305.5	WRX, SWIR
LA-21-DT-012	16-2	Siltstone with minor Garnets	234	234.1	WRX, SWIR
LA-21-DT-013	16-2	Siltstone, unaltered	230.8	230.9	WRX
LA-21-DT-014	16-2	Sericite schist with minor garnets	271.7	272.2	WRX, Geochronology, SWIR
LA-21-DT-015	16-2	Garnet, staurolite, biotite schist	397.5	397.6	WRX
LA-21-DT-017	19-1	Garnet, staurolite, biotite schist, with chalcopyrite	65	65.2	Petrography, SEM, LA-ICP-MS, Sulphur δ^{34}

LA-21-DT-018	19-1	Siltstone with minor garnets	125.7	125.8	SWIR
LA-21-DT-019	19-1	Siltstone, unaltered	123.8	124	WRX
LA-21-DT-020	19-1	Large garnets in bio schist	34.4	34.6	Petrography, SEM, LA-ICP-MS
LA-21-DT-021	16-1	Siltstone with minor garnets	452.9	452.95	LA-ICP-MS, SWIR
LA-21-DT-022	16-1	Sericite schist with biotite, garnet, pyrite, pyrrhotite	401.3	401.4	Petrography, SEM, Sulphur δ^{34}, SWIR
LA-21-DT-023	16-1	Garnet, staurolite, bio schist with chalcopyrite, pyrrhotite	321.65	321.75	Petrography, SEM, LA-ICP-MS, Sulphur δ^{34}
LA-21-DT-024	16-1	Massive biotite, garnet, staurolite sericite schist	289.9	290	Petrography, SEM, WRX, SWIR
LA-21-DT-025	16-1	Garnet, biotite schist	251.4	251.5	WRX, SWIR
LA-21-DT-026	16-1	Basalt	257.4	257.6	WRX
LA-21-DT-027	16-1	Garnet, staurolite, biotite schist	114	114.2	WRX, SWIR
LA-21-DT-028	16-2	Garnet schist with tourmalinite spots	433.8	433.85	Petrography, SEM, LA-ICP-MS
LA-21-DT-029	19-2	Garnet sericite schist	221	221.1	SWIR
LA-21-DT-030	19-2	Garnet, staurolite, schist with trace Chalcopyrite	204.6	204.7	Petrography, SEM
LA-21-DT-032	19-2	Garnet staurolite schist with Po+ mag veinlets	166.8	166.9	Petrography, SEM, SWIR
LA-21-DT-034	19-4	Pyrrhotite, chalcopyrite vein 6 cm wide with tourmalinite spots	165.1	165.4	Petrography, SEM, LA-ICP-MS, WRX, Sulphur δ^{34}
LA-21-DT-035	19-4	Garnet schist with 2mm chalcopyrite veinlets	167.1	167.15	Petrography
LA-21-DT-036	19-4	Garnet, staurolite, biotite schist	61.1	61.3	WRX, SWIR
LA-21-DT-037	19-4	Siltstone with minor garnets	128	128.2	WRX
LA-21-DT-038	16-4	Meta arkose with minor garnets	60.4	60.5	WRX, SWIR
LA-21-DT-039	16-4	Meta arkose with minor garnets and staurolite	67	67.1	Petrography, SEM, WRX, SWIR
LA-21-DT-040	16-4	Meta arkose with minor garnets	78.7	78.8	WRX
LA-21-DT-041	16-4	Sericite schist with pyrite	102.6	102.7	SWIR
LA-21-DT-042	16-4	sericite schist with garnet and staurolite	112.4	112.5	Petrography, SEM, SWIR
LA-21-DT-043	16-4	Sericite schist with minor garnets and pyrite	115.5	115.6	WRX, SWIR
LA-21-DT-044	16-4	Siltstone	121	121.2	WRX
LA-21-DT-045	16-4	Sericite schist with minor garnets and staurolite	135	135.1	WRX, SWIR
LA-21-DT-046	16-4	Garnet staurolite schist	148.3	148.4	WRX, SWIR
LA-21-DT-047	16-4	Basalt	158.5	158.7	WRX

LA-21-DT-049	16-4	Garnet staurolite schist with pyrrhotite	172.5	172.7	WRX, LA-ICP-MS, Sulphur δ^{34}
LA-21-DT-050	16-4	large garnets and staurolite in massive bio schist	176.4	176.6	Petrography, SEM, LA-ICP-MS, WRX, SWIR
LA-21-DT-051	16-4	Biotite, garnet, staurolite schist	189	189.2	WRX, SWIR
LA-21-DT-052	16-4	Garnet staurolite schist	197.5	197.6	SWIR
LA-21-DT-053	16-4	Large garnets, staurolite, chalcopyrite veinlet	212.2	212.3	Petrography, SEM, WRX
LA-21-DT-054	16-4	Large garnets in massive biotite, pyrrhotite and chalcopyrite veinlets	214.9	215	Petrography, SEM
LA-21-DT-055	16-4	Garnet bio schist with po veins	223.6	223.7	Sulphur δ^{34}
LA-21-DT-056	16-4	Garnet sericite schist with chalcopyrite, pyrrhotite, arsenopyrite	235.2	235.3	Petrography, SEM
LA-21-DT-057	16-4	Large garnets in schist with pyrite, chalcopyrite	238.6	238.7	WRX, Sulphur δ^{34}
LA-21-DT-058	16-4	Siltstone with minor garnets	244.5	244.6	Petrography, WRX
LA-21-DT-059	16-4	Sericite, biotite, garnet, staurolite schist	248.7	248.8	SWIR
LA-21-DT-060	16-4	biotite, garnet, staurolite schist with quartz vein	256.2	256.3	WRX, SWIR
LA-21-DT-061	16-4	Garnet, staurolite sericite vein	263.5	263.6	Petrography, SEM, SWIR
LA-21-DT-063	16-4	Garnet staurolite, bio schist with trace pyrite	283.6	283.7	Petrography, SEM, LA-ICP-MS
LA-21-DT-064	16-4	Garnet, staurolite, massive bio schist	293.5	293.6	Petrography, SEM, SWIR
LA-21-DT-065	16-4	Basalt	308.4	308.7	WRX
LA-21-DT-066	16-4	Garnet, staurolite, sericite schist	314	314.2	WRX, SWIR
LA-21-DT-067	16-4	Garnet biotite sericite schist	329.5	329.6	SWIR
LA-21-DT-068	16-4	Basalt	345	345.3	WRX
LA-21-DT-069	16-4	Garnet, Biotite schist with chalcopyrite veinlets	356.9	356.95	Petrography, SEM, LA-ICP-MS, Sulphur δ^{34}, SWIR
LA-21-DT-070	16-4	Lamprophyre Dyke	328.6	329.1	SEM, WRX
LA-21-DT-071	16-4	Garnet staurolite biotite schist	359	359.2	WRX, SWIR
LA-21-DT-072	16-4	Basalt	378	378.3	WRX
LA-21-DT-073	16-4	Garnet, biotite, sericite schist	387.6	387.7	WRX, SWIR
LA-21-DT-074	16-4	Garnet siltstone	398.8	398.9	LA-ICP-MS, SWIR
LA-21-DT-075	16-4	Garnet biotite schist	410	410.2	WRX, SWIR
LA-21-DT-076	19-10	Pyrrhotite, chalcopyrite vein in basalt	204.9	205	Petrography, SEM
LA-21-DT-077	19-10	Basalt	199.8	200	WRX, Sm/Nd MC-ICP-MS

LA-21-DT-078	19-10	Siltstone	193.7	193.9	WRX
LA-21-DT-079	19-10	Quartz feldspar porphyry	99.8	100.2	WRX, Geochronology, Sm/Nd MC-ICP-MS
LA-21-DT-081	17-1	Basalt	506.8	506.9	Petrography, SEM, WRX, Sm/Nd MC-ICP-MS
LA-21-DT-082	17-1	Lamprophyre dyke	503.4	503.6	Petrography, SEM, WRX
LA-21-DT-083	17-1	Gabbro	486.5	486.7	WRX
LA-21-DT-084	17-1	Ultramafic	439.5	439.8	WRX, Sm/Nd, MC-ICP-MS
LA-21-DT-085	17-1	Ultramafic	431.5	431.8	WRX
LA-21-DT-087	17-1	Metasiltstone with staurolite	386.6	386.7	Petrography, SEM
LA-21-DT-088	17-1	Siltstone with tourmalinite and garnets	308.6	308.7	Petrography, SEM, LA-ICP-MS
LA-21-DT-089	17-1	Siltstone with tourmalinite and garnets	308	308.1	SWIR
LA-21-DT-091	17-1	Ultramafic	223.4	223.6	WRX, Sm/Nd MC-ICP-MS
LA-21-DT-092	17-1	Biotite, staurolite, garnet schist	215.6	215.8	Petrography, SEM
LA-21-DT-093	17-1	Staurolite, garnet schist	176.7	176.9	SWIR
LA-21-DT-094	17-1	Lamprophyre dyke	154.2	154.4	Petrography, SEM, WRX
LA-21-DT-095	17-1	Basalt	192.5	192.6	WRX
LA-21-DT-096	17-1	Garnet, staurolite schist	127.7	127.8	LA-ICP-MS, SWIR
LA-21-DT-098	17-1	Garnet vein and quartz vein with pyrite	100.7	100.8	Petrography, SEM, LA-ICP-MS
LA-21-DT-099	17-1	Biotite, staurolite, garnet schist	62.3	62.4	Petrography, SEM, LA-ICP-MS
LA-21-DT-100	17-1	Biotite, garnet, staurolite schist	37.1	37.3	SWIR
LA-21-DT-101	17-1	Basalt	22.4	22.5	WRX, Sm/Nd MC-ICP-MS
LA-21-DT-102	19-4	Pyrrhotite massive sulphide in garnet schist	64.7	64.9	Petrography, SEM, LA-ICP-MS, WRX, Sulphur δ^{34}
LA-21-DT-103	21-3	Rhyolite flow	113.9	114.5	WRX, Geochronology, Sm/Nd MC-ICP-MS
LA-21-DT-104	21-3	Rhyolite flow	113.75	113.9	WRX
LA-21-DT-105	21-3	Rhyolite porphyry	95.8	96.5	WRX, Geochronology
LA-21-DT-106	21-2	Pyrrhotite, chalcopyrite, pyrite in quartz veinlet	154.25	154.35	Sulphur δ^{34}
LA-21-DT-107	21-1	Po veinlets in felsic volcanic	109.7	109.8	Sulphur δ^{34}
LA-21-DT-108	21-1	Chalcopyrite, quartz vein in feldspar porphyry	148.1	148.2	Sulphur δ^{34}
LA-21-DT-109	21-6	Massive biotite adjacent to quartz vein	146.9	147.1	Petrography, SEM

LA-21-DT-111	21-6	Garnets within basalt	236.7	236.9	Petrography, SEM
LA-21-DT-112	21-6	Molybdenite within quartz vein	238.75	238.9	Geochronology
LA-21-DT-113	21-8	Garnet amphibolite	58	58.25	Petrography, SEM
LA-21-DT-115	21-8	Ultramafic	61.9	62	WRX, Sm/Nd MC-ICP-MS
LA-21-DT-116	21-8	Ultramafic	71.7	71.9	WRX, Sm/Nd MC-ICP-MS
LA-21-DT-117	19-10	Pyrite, chalcopyrite, pyrrhotite, and galena VMS zone	126.5	126.6	Petrography, SEM, LA-ICP-MS, Sulphur δ^{34}
LA-21-DT-118	19-10	Pyrite, chalcopyrite, pyrrhotite vein with quartz fragments	195.3	195.5	Petrography, SEM, LA-ICP-MS, Sulphur δ^{34}
LA-21-DT-119	17-1	Pyrrhotite, chalcopyrite in siltstone schist	300.7	300.9	Petrography, SEM, LA-ICP-MS, Sulphur δ^{34}
LA-21-DT-120	17-1	Tourmalinite spots in siltstone	302.7	302.9	Petrography, SEM
W1120452	16-1	Staurolite rich schist	54.7	54.9	WRX
W1120453	16-1	Siltstone	262	262.2	WRX
W1120455	16-1	Staurolite, garnet siltstone	265.8	266	WRX
W1120456	16-1	Garnet, staurolite siltsone	266.8	267	WRX
W1120462	16-1	Dacite	331.5	331.7	WRX
W1120463	16-1	Staurolite, biotite, garnet, schist	340.7	340.9	WRX
W1120457	16-1	Staurolite, garnet, biotite schist	359	359.2	WRX
W1120458	16-1	Staurolite siltstone	363	363.2	WRX
W1120451	16-1	Felsic volcaniclastic	364	364.2	WRX
W1120459	16-1	Staurolite siltstone	378.7	378.9	WRX
W1120460	16-1	Sericite schist	382.4	382.6	WRX
W1120461	16-2	Andesite	57.7	57.9	WRX
W1120464	16-3	Garnet, sericite, staurolite schist	106.5	106.7	WRX
W1120465	16-4	Basalt	166.8	167	WRX
W1120466	16-4	Biotite, staurolite, biotite schist	178.4	178.6	WRX
W1120467	16-4	Siltstone	210.5	210.7	WRX
W1120468	16-4	Garnet, staurolite siltstone	213.4	213.6	WRX
W1120469	16-4	Sericite, garnet schist	258.8	259	WRX
W1120470	16-4	Sericite garnet, biotite schist	397.5	397.7	WRX

W1120471	16-4	Sericite siltstone	419	419.2	WRX
390051	19-1	Sericite, biotite, garnet Schist	56.85	57.05	WRX
390052	19-1	Sericite, garnet schist	59.1	59.3	WRX
390053	19-2	Siltstone	171.5	171.7	WRX
390054	19-2	Staurolite, biotite, quartz flooded alteration zone	173.4	173.6	WRX
390055	19-2	Garnet sericite Schist	163.8	164	WRX
390056	19-2	Sericite, staurolite, garnet schist	202	202.2	WRX
390057	19-2	Sericite, staurolite, garnet schist	237.4	237.6	WRX
390058	19-3	Dacite	22.9	23.1	WRX
390059	19-3	Sericite schist	129	129.2	WRX
390060	19-3	Basalt	150	150.2	WRX
390061	19-4	Sericite schist	153.8	154	WRX
390062	19-4	Tourmalinite spots in siltstone	172.2	172.4	WRX
390063	19-5	Feldspar porphyritic dyke	21.45	21.65	WRX
390064	19-5	Quartz phyric rhyolite dyke	82.8	83	WRX
390065	19-5	Rhyolite dyke	112.4	112.6	WRX
390066	19-6	Quartz feldspar porphyry	250	250.2	WRX
A0935602	19-10	Felsic Volcanic	105.5	105.7	WRX
A0935645	19-10	Felsic Volcanic	174.5	174.7	WRX
A0935951	19-10	Feldspar porphyry dyke	87.5	87.7	WRX
A0935952	19-10	Quartz feldspar porphyry	39.5	39.7	WRX
A0935953	19-10	Feldspar porphyry dyke	184.8	185	WRX
A0935954	19-10	Basalt	210.5	210.7	WRX
A0935851	21-1	Felsic volcanic	63.8	64	WRX
A0935852	21-3	Quartz feldspar porphyry dyke	90	90.2	WRX
A0935853	21-3	Ash felsic tuff	20	20.2	WRX
A0935854	21-3	Feldspar quartz phyric rhyolite	47.5	47.7	WRX
A0935855	21-3	Quartz feldspar porphyry rhyolite	96.7	96.9	WRX
A0935856	21-3	Ash Felsic Tuff	100.8	101	WRX
A0935857	21-6	Quartz feldspar porphyry dyke	188.5	188.7	WRX

Appendix II

Whole Rock Analysis

Element	SiO2	Al2O3	Fe2O3	CaO	MgO	Na2O	K2O	Cr2O3	TiO2	MnO	P2O5
Unit	%	%	%	%	%	%	%	%	%	%	%
LOD	0.01	0.01	0.01	0.01	0.01	0.01	0.01	0.002	0.01	0.01	0.01
Element	SrO	BaO	LOI	Total	C	S	Ba	Ce	Cr	Cs	Dy
Unit	%	%	%	%	%	%	ppm	ppm	ppm	ppm	ppm
LOD	0.01	0.01	0.01	0.01	0.01	0.01	0.5	0.1	5	0.01	0.05
Element	Er	Eu	Ga	Gd	Ge	Hf	Ho	La	Lu	Nb	Nd
Unit	ppm	ppm	ppm	ppm	ppm	ppm	ppm	ppm	ppm	ppm	ppm
LOD	0.03	0.02	0.1	0.05	0.5	0.05	0.01	0.1	0.01	0.05	0.1
Element	Pr	Rb	Sm	Sn	Sr	Ta	Tb	Th	Tm	U	V
Unit	ppm	ppm	ppm	ppm	ppm	ppm	ppm	ppm	ppm	ppm	ppm
LOD	0.02	0.2	0.03	0.5	0.1	0.1	0.01	0.05	0.01	0.05	5
Element	W	Y	Yb	Zr	As	Bi	Hg	In	Re	Sb	Se
Unit	ppm	ppm	ppm	ppm	ppm	ppm	ppm	ppm	ppm	ppm	ppm
LOD	0.5	0.1	0.03	1	0.1	0.01	0.005	0.005	0.001	0.05	0.2
Element	Te	Tl	Ag	Cd	Co	Cu	Li	Mo	Ni	Pb	Sc	Zn
Unit	ppm	ppm	ppm	ppm	ppm	ppm	ppm	ppm	ppm	ppm	ppm	ppm
LOD	0.01	0.02	0.5	0.5	1	1	10	1	1	2	1	2

Sample ID	LA-21-DT-007	LA-21-DT-008	LA-21-DT-011	LA-21-DT-012	LA-21-DT-013	LA-21-DT-014	LA-21-DT-015	LA-21-DT-019	LA-21-DT-024	LA-21-DT-025	LA-21-DT-026	LA-21-DT-027
SiO_2	53.2	58.2	62.2	73.0	73.9	76.8	61.6	65.7	63.2	65.8	50.8	69.8
Al_2O_3	14.05	21.00	17.30	14.00	14.70	14.85	15.35	16.15	18.40	15.20	10.65	17.6
Fe_2O_3	12.30	7.66	7.19	2.90	2.95	1.24	16.35	5.09	6.98	9.81	12.55	5.65
CaO	11.15	0.57	4.06	3.97	3.14	0.35	0.56	4.56	1.12	1.62	8.95	0.40
MgO	6.81	0.83	2.17	1.60	1.46	0.26	1.69	2.05	1.14	1.33	14.15	0.53
Na_2O	0.85	0.51	0.38	0.31	0.29	0.26	0.11	1.65	0.54	0.54	0.39	0.36
K_2O	0.17	6.07	2.87	1.82	1.97	2.96	3.00	3.53	4.74	3.68	0.17	2.98
Cr_2O_3	0.014	0.009	0.006	0.002	0.002	0.005	0.006	0.003	0.007	0.002	0.205	0.007
TiO_2	0.61	0.64	0.51	0.29	0.32	0.52	0.65	0.51	0.75	0.50	0.56	0.73
MnO	0.20	0.09	0.52	0.08	0.05	0.01	0.15	0.07	0.09	0.15	0.23	0.05
P_2O_5	0.05	0.17	0.13	0.11	0.13	0.19	0.18	0.12	0.19	0.12	0.05	0.3
SrO	0.02	0.005	0.01	0.01	-	0.01	0.005	0.01	0.005	0.005	0.03	0.005
BaO	-	0.05	0.03	0.01	0.01	0.03	0.04	0.05	0.06	0.06	-	0.02
LOI	0.53	2.76	1.45	0.88	1.31	3.38	0.18	0.96	2.04	0.95	2.17	1.29
Total	99.95	98.56	98.83	98.98	100.23	100.86	99.87	100.45	99.26	99.76	100.91	99.72

Sample ID	LA-21-DT-034	LA-21-DT-036	LA-21-DT-037	LA-21-DT-038	LA-21-DT-039	LA-21-DT-040	LA-21-DT-043	LA-21-DT-044	LA-21-DT-045	LA-21-DT-046	LA-21-DT-047	LA-21-DT-049
SiO_2	40.7	62.8	61.5	73.2	68.5	68.1	67.9	61.7	68.2	67.4	49.0	68.4
Al_2O_3	13.45	15.65	16.85	14.90	15.80	14.50	14.05	14.15	14.40	15.30	10.30	14.85
Fe_2O_3	24.30	13.85	7.28	3.57	5.04	4.64	7.39	7.75	7.67	8.04	12.20	10.15
CaO	0.44	0.27	4.93	3.07	3.57	5.40	1.10	7.95	2.49	1.78	10.20	0.85
MgO	2.01	1.57	2.93	1.56	2.02	2.41	1.18	4.80	2.21	2.21	13.80	1.42
Na_2O	0.65	0.24	1.47	0.24	0.30	0.45	0.33	0.64	0.29	0.31	0.24	0.23
K_2O	0.59	3.29	2.91	1.66	1.74	1.21	3.45	1.32	2.73	2.95	0.18	3.11
Cr_2O_3	0.005	0.007	0.006	0.004	0.004	0.003	0.003	0.027	0.004	0.005	0.203	0.005
TiO_2	0.41	0.66	0.64	0.32	0.51	0.47	0.39	0.47	0.41	0.44	0.5	0.44
MnO	0.04	0.22	0.23	0.09	0.12	0.12	0.06	0.17	0.12	0.15	0.23	0.05
P_2O_5	0.14	0.19	0.23	0.12	0.16	0.17	0.14	0.09	0.12	0.09	0.05	0.12
SrO	0.01	0.005	0.01	0.01	0.01	0.01	0.005	0.01	0.005	0.005	0.01	0.005

BaO	0.01	0.05	0.06	0.02	0.02	0.01	0.04	0.03	0.04	0.04	-	0.05
LOI	5.21	0.51	0.90	0.93	1.78	1.16	3.92	0.61	1.39	1.08	1.68	0.92
Total	87.97	99.31	99.95	99.69	99.57	98.65	99.95	99.72	100.07	99.8	98.59	100.60

Sample ID	LA-21-DT-050	LA-21-DT-051	LA-21-DT-053	LA-21-DT-057	LA-21-DT-058	LA-21-DT-060	LA-21-DT-065	LA-21-DT-066	LA-21-DT-068	LA-21-DT-070	LA-21-DT-071	LA-21-DT-072
SiO_2	65.5	66.7	62.3	59.3	65.8	65.9	49.2	70.2	52.9	47.3	59.2	47.7
Al_2O_3	15.45	16.25	13.45	14.85	14.65	14.40	7.73	16.8	14.00	10.25	16.45	7.17
Fe_2O_3	13.40	8.92	19.35	21.30	8.25	13.75	15.55	6.54	12.65	14.00	18.15	15.55
CaO	0.32	0.19	0.47	0.75	2.97	0.42	10.25	0.47	10.40	6.46	0.41	9.94
MgO	1.41	1.06	2.02	1.92	1.64	1.00	13.45	0.87	6.93	7.82	1.42	14.75
Na_2O	0.17	0.34	0.05	0.05	1.57	0.10	0.65	0.42	1.55	1.79	0.19	0.48
K_2O	3.12	4.30	1.99	1.34	2.75	2.02	0.17	3.14	0.33	2.71	2.60	0.13
Cr_2O_3	0.005	0.005	0.007	0.009	0.004	0.006	0.117	0.003	0.015	0.056	0.006	0.137
TiO_2	0.44	0.39	0.38	0.51	0.41	0.58	0.96	0.44	0.60	1.42	0.60	0.90
MnO	0.12	0.07	0.20	0.24	0.07	0.12	0.23	0.14	0.21	0.16	0.18	0.34
P_2O_5	0.11	0.12	0.11	0.15	0.12	0.17	0.14	0.13	0.07	0.53	0.14	0.08
SrO	0.005	0.005	0.005	0.005	0.01	0.005	0.01	0.005	0.02	0.09	0.005	-
BaO	0.05	0.07	0.03	0.02	0.05	0.05	-	0.03	-	0.12	0.03	-
LOI	1.08	1.89	-0.17	-0.52	0.72	0.07	1.42	1.48	0.47	7.00	0.03	0.98
Total	101.18	100.31	100.19	99.92	99.01	98.59	99.88	100.66	100.15	99.71	99.41	98.16

Sample ID	LA-21-DT-073	LA-21-DT-075	LA-21-DT-077	LA-21-DT-078	LA-21-DT-079	LA-21-DT-081	LA-21-DT-082	LA-21-DT-083	LA-21-DT-084	LA-21-DT-085	LA-21-DT-091	LA-21-DT-094
SiO_2	61.6	62.0	48.6	67.6	72.2	49.8	31.0	49.4	49.0	46.3	48.4	34.8
Al_2O_3	15.70	14.30	14.60	19.85	14.30	14.15	5.97	14.90	9.53	6.29	6.58	6.07
Fe_2O_3	14.80	16.45	13.60	1.61	2.26	12.90	9.82	12.35	11.95	11.35	15.95	13.45
CaO	0.49	0.92	9.74	0.18	2.49	10.30	10.95	10.90	8.61	8.64	9.60	11.15
MgO	1.42	2.18	7.19	0.87	0.71	7.77	21.60	7.48	15.10	21.10	16.70	13.70
Na_2O	0.18	0.25	2.50	0.21	4.29	2.21	0.67	1.83	1.27	0.07	0.50	0.80
K_2O	2.59	2.80	1.42	6.77	1.97	0.64	3.44	0.37	0.42	0.01	0.48	2.27

Cr_2O_3	0.004	0.005	0.042	0.053	0.001	0.020	0.176	0.031	0.236	0.398	0.145	0.058
TiO_2	0.53	0.57	0.81	1.09	0.25	0.94	1.56	0.85	0.49	0.33	0.89	1.68
MnO	0.12	0.36	0.10	0.01	0.01	0.17	0.18	0.20	0.21	0.16	0.26	0.20
P_2O_5	0.18	0.14	0.07	0.07	0.07	0.08	0.70	0.07	0.05	0.04	0.09	0.93
SrO	0.005	0.005	0.01	0	0.01	0.01	0.15	0.01	0.02	-	-	0.08
BaO	0.03	0.04	0.02	0.12	0.04	-	0.28	-	0.01	-	0.01	0.13
LOI	1.02	0.43	0.91	2.71	1.15	0.96	12.25	0.83	1.92	4.79	1.51	14.55
Total	98.66	100.45	99.61	101.14	99.75	99.95	98.75	99.22	98.82	99.48	101.12	99.87

Sample ID	LA-21-DT-095	LA-21-DT-101	LA-21-DT-102	LA-21-DT-103	LA-21-DT-104	LA-21-DT-105	LA-21-DT-115	LA-21-DT-116	W1120451	W1120452	W1120453
SiO_2	49.2	49.1	11.4	77.0	73.5	68.5	44.8	46.3	72.4	70.0	67.4
Al_2O_3	16.15	14.85	4.97	13.10	12.80	14.40	11.40	7.42	14.94	17.91	15.08
Fe_2O_3	12.25	14.35	43.20	1.10	1.34	3.13	20.90	11.25	1.78	6.08	4.33
CaO	11.00	10.85	0.75	0.99	1.10	2.42	10.35	8.45	5.20	0.37	5.06
MgO	8.76	7.16	2.16	0.11	0.17	0.87	9.38	21.40	0.62	0.70	1.51
Na_2O	1.62	0.68	0.10	3.84	3.61	4.27	0.91	0.09	1.69	0.60	2.01
K_2O	0.63	1.03	0.98	4.30	4.21	2.75	1.06	0.01	1.20	0.85	2.49
Cr_2O_3	0.051	0.033	0.001	0.001	0.003	0.001	0.345	0.254			
TiO_2	0.8	1.12	0.16	0.03	0.04	0.32	0.36	0.28	0.149	0.679	0.443
MnO	0.18	0.22	0.12	0.04	0.04	0.01	0.32	0.17	0.089	0.068	0.077
P_2O_5	0.05	0.09	0.09	0.005	0.01	0.08	0.03	0.01	0.04	0.26	0.15
SrO	0.03	0.01	0.005	0.01	0.01	0.02	-	-			
BaO	0	0.02	0.01	0.06	0.06	0.13	0.04	-			
LOI	0.72	0.51	10.70	1.27	1.30	1.54	1.04	4.47	0.86	1.05	1.34
Total	101.44	100.02	74.64	101.85	98.19	98.44	100.94	100.10	98.93	98.56	99.89

Sample ID	W1120455	W1120456	W1120457	W1120458	W1120459	W1120460	W1120461	W1120462	W1120463	W1120464
SiO_2	69.3	64.0	60.2	77.3	71.0	63.5	63.6	69.15	65.2	67.1
Al_2O_3	16.48	14.83	17.59	12.41	15.86	15.59	15.18	14.97	14.60	14.85

Fe_2O_3	4.97	14.40	16.27	3.69	4.55	7.88	5.87	3.60	14.28	11.43
CaO	0.57	0.35	0.30	0.69	0.27	0.66	6.18	3.82	0.34	0.35
MgO	0.94	1.49	1.64	0.79	0.84	0.57	2.67	1.02	1.38	0.82
Na_2O	0.65	0.21	0.09	0.26	0.22	0.37	1.06	3.42	0.12	0.24
K_2O	3.13	2.77	2.51	2.85	3.82	4.71	2.05	2.02	2.63	3.29
Cr_2O_3										
TiO_2	0.548	0.488	0.697	0.234	0.438	0.642	0.573	0.348	0.437	0.392
MnO	0.082	0.143	0.063	0.067	0.052	0.032	0.096	0.058	0.084	0.11
P_2O_5	0.15	0.14	0.18	0.07	0.13	0.18	0.15	0.10	0.13	0.11
SrO										
BaO										
LOI	1.93	0.80	0.88	1.76	2.10	5.55	1.74	2.31	0.73	1.36
Total	98.75	99.65	100.40	100.10	99.36	99.71	99.2	100.8	99.93	100.10

Sample ID	W1120465	W1120466	W1120467	W1120468	W1120469	W1120470	W1120471	390051	390052	390053
SiO_2	51.7	68.2	64.8	62.8	67.9	65.5	63.2	71.3	73.7	63.5
Al_2O_3	11.30	14.46	14.91	15.25	16.78	14.06	15.88	14.52	12.17	16.08
Fe_2O_3	11.23	10.95	8.01	13.87	5.43	11.51	6.58	3.73	6.52	7.43
CaO	11.30	0.34	3.84	0.29	0.30	0.41	5.47	3.58	0.12	6.00
MgO	10.41	1.43	1.75	1.89	0.57	1.33	2.58	1.52	0.81	2.67
Na_2O	0.43	0.12	0.32	0.08	0.38	0.23	1.04	0.72	0.25	0.49
K_2O	0.39	2.64	3.22	2.67	4.02	3.54	2.39	2.53	3.25	2.40
Cr_2O_3										
TiO_2	0.484	0.405	0.458	0.471	0.689	0.405	0.627	0.282	0.153	0.635
MnO	0.212	0.076	0.135	0.103	0.059	0.194	0.131	0.021	0.142	0.151
P_2O_5	0.05	0.14	0.11	0.11	0.18	0.14	0.16	0.09	0.04	0.15
SrO										
BaO										
LOI	1.09	0.91	1.12	0.74	2.05	2.28	0.95	1.42	1.29	0.99
Total	98.79	100.20	100.20	98.60	98.59	99.63	100.70	99.75	98.48	100.50

Sample ID	390054	390055	390056	390057	390058	390059	390060	390061	390062	390063	390064	390065
SiO_2	62.96	70.95	73.49	75.72	70.73	72.28	53.85	76.18	65.73	64.07	71.56	73.26
Al_2O_3	15.74	15.62	14.9	13.72	14.12	15.1	13.84	13.27	15.44	17.74	14.83	14.42
Fe_2O_3	13.44	4.17	2.93	3.51	3.14	3.21	12.35	2.27	9.86	4.45	1.80	1.84
CaO	0.24	0.24	0.17	0.09	3.73	0.23	11.27	1.80	1.62	4.01	3.80	3.03
MgO	2.07	0.56	0.50	0.65	0.82	0.61	6.70	0.89	2.37	1.55	2.21	1.82
Na_2O	0.11	0.55	0.37	0.49	3.05	0.59	0.89	1.19	0.52	6.97	1.49	0.86
K_2O	2.89	3.90	3.79	2.28	2.21	3.82	0.16	2.78	2.41	0.65	2.70	3.59
Cr_2O_3												
TiO_2	0.624	0.479	0.296	0.247	0.309	0.309	0.604	0.102	0.603	0.405	0.267	0.262
MnO	0.078	0.049	0.040	0.107	0.043	0.060	0.198	0.060	0.130	0.033	0.027	0.037
P_2O_5	0.14	0.12	0.08	0.05	0.10	0.09	0.06	0.04	0.17	0.12	0.07	0.08
SrO												
BaO												
LOI	0.99	2.38	2.11	1.66	0.68	2.24	0.60	1.26	0.77	0.65	1.21	1.35
Total	99.28	99.01	98.68	98.51	98.95	98.54	100.50	99.83	99.61	100.7	99.95	100.60

Sample ID	390066	A0935602	A0935645	A0935951	A0935952	A0935953	A0935954	A0935851	A0935852	A0935853
SiO_2	70.06	74.73	75.79	70.58	69.64	66.98	48.98	63.08	70.88	76.71
Al_2O_3	14.48	13.54	12.90	14.41	15.03	14.94	15.14	14.92	14.52	12.97
Fe_2O_3	3.17	2.97	2.10	3.28	4.55	4.09	12.75	5.76	1.71	1.43
CaO	3.72	0.73	0.77	2.52	1.27	2.48	10.76	5.41	2.30	0.45
MgO	1.59	0.84	0.78	0.76	1.05	1.36	7.53	2.64	0.79	0.65
Na_2O	0.63	0.63	0.72	4.9	2.24	5.36	2.41	4.90	5.49	0.22
K_2O	4.25	4.13	3.8	1.28	4.34	2.38	1.17	1.01	1.83	4.23
Cr_2O_3										
TiO_2	0.278	0.224	0.034	0.270	0.298	0.438	0.831	0.623	0.307	0.031
MnO	0.061	0.023	0.027	0.019	0.040	0.021	0.108	0.052	0.020	0.020
P_2O_5	0.09	0.07	0.01	0.08	0.11	0.14	0.07	0.22	0.10	0.02
SrO										

BaO										
LOI	1.43	2.19	1.97	1.15	1.53	1.57	0.95	0.81	1.55	1.85
Total	99.76	100.10	98.91	99.24	100.10	99.77	100.70	99.43	99.49	98.57

Sample ID	A0935854	A0935855	A0935856	A0935857
SiO_2	77.02	69.17	75.34	71.65
Al_2O_3	12.82	14.96	13.10	14.43
Fe_2O_3	1.70	2.82	1.41	1.73
CaO	0.65	2.84	0.81	3.35
MgO	0.66	0.93	0.06	0.68
Na_2O	0.69	4.49	3.91	4.11
K_2O	4.17	2.46	4.18	1.83
Cr_2O_3				
TiO_2	0.072	0.338	0.032	0.262
MnO	0.019	0.018	0.03	0.018
P_2O_5	0.01	0.09	0.01	0.07
SrO				
BaO				
LOI	1.07	2.04	0.83	1.86
Total	98.89	100.20	99.72	99.99

Sample ID	LA-21-DT-007	LA-21-DT-008	LA-21-DT-011	LA-21-DT-012	LA-21-DT-013	LA-21-DT-014	LA-21-DT-015	LA-21-DT-019	LA-21-DT-024	LA-21-DT-025	LA-21-DT-026	LA-21-DT-027
C	0.03	0.08	0.04	0.03	0.04	0.01	0.03	0.08	0.04	0.04	0.05	0.03
S	0.03	0.39	0.03	0.04	0.12	0.38	0.04	0.05	0.43	0.1	0.02	0.02
Ba	7.9	438.0	263.0	81.6	118.0	276.0	301.0	432.0	524.0	495.0	18.1	142.0
Ce	8.1	67.5	57.5	44.3	51.3	58.8	71.2	46.2	46.4	58.0	13.4	62.9
Cr	110	59	38	13	10	50	39	30	47	12	1490	47
Cs	0.01	1.2	1.44	1.77	1.29	0.74	0.87	1.94	1.52	1.15	0.05	1.10
Dy	2.95	4.11	3.77	1.66	1.77	2.75	3.64	2.27	3.10	2.96	2.46	4.32
Er	1.71	2.27	2.05	0.83	0.97	1.29	2.17	1.20	1.74	1.70	1.52	2.39
Eu	0.55	0.85	0.96	0.72	0.71	1.00	1.11	0.82	0.8	0.98	0.53	1.12
Ga	18.7	23.2	19.5	18.0	22.8	20.1	20.5	23.0	21.7	20.0	16.0	22.6
Gd	2.08	4.21	4.23	2.04	2.18	3.27	4.07	2.29	3.09	3.64	2.04	4.47
Ge	0.3	1.3	1.1	0.8	0.3	0.3	1.2	0.3	1.1	1.0	0.3	1.4
Hf	1.20	4.55	4.32	3.65	3.80	4.00	4.20	3.20	4.97	4.01	1.40	5.00

Sample ID	LA-21-DT-034	LA-21-DT-036	LA-21-DT-037	LA-21-DT-038	LA-21-DT-039	LA-21-DT-040	LA-21-DT-043	LA-21-DT-044	LA-21-DT-045	LA-21-DT-046	LA-21-DT-047	LA-21-DT-049
C	0.04	0.03	0.05	0.03	0.03	0.02	0.03	0.05	0.02	0.03	0.04	0.03
S	10.85	0.14	0.06	0.10	0.07	0.03	2.71	0.18	0.63	0.01	0.04	0.26
Ba	45.3	400.0	498.0	173.0	191.5	104.5	408.0	248.0	365.0	377.0	23.2	506.0
Ce	89.6	43.0	87.7	45.6	57.0	49.7	63.3	27.5	50.1	50.1	12.4	50.5
Cr	40	44	30	21	21	22	18	190	33	36	1520	40
Cs	0.13	1.80	1.56	1.34	1.44	2.29	1.03	0.88	2.66	2.80	0.11	1.34
Dy	2.96	3.04	3.55	1.56	2.74	2.42	2.62	2.49	2.32	2.98	2.30	1.87
Er	1.43	2.13	1.79	0.96	1.57	1.22	1.84	1.52	1.48	1.64	1.29	1.02
Eu	0.67	0.91	1.33	0.79	0.98	0.90	0.88	0.53	0.80	0.84	0.55	0.85
Ga	19.0	19.5	22.7	17.6	20.5	18.6	17.2	18.8	18.2	19.5	16.1	17.6
Gd	4.13	3.66	4.11	2.18	2.89	2.89	3.12	2.31	2.75	3.40	1.92	2.95
Ge	0.6	1.1	0.3	0.7	1	0.8	0.8	0.3	1.0	1.1	0.3	1.0
Hf	3.23	3.77	4.40	3.85	3.93	3.64	4.07	2.50	4.03	4.72	1.30	4.34

Sample ID	LA-21-DT-050	LA-21-DT-051	LA-21-DT-053	LA-21-DT-057	LA-21-DT-058	LA-21-DT-060	LA-21-DT-065	LA-21-DT-066	LA-21-DT-068	LA-21-DT-070	LA-21-DT-071	LA-21-DT-072
C	0.03	0.03	0.02	0.04	0.02	0.02	0.10	0.04	0.05	1.75	0.03	0.02
S	0.98	0.62	0.66	0.41	0.28	0.05	0.03	0.27	0.07	0.08	0.06	0.04
Ba	497.0	611.0	247.0	168.0	462.0	427.0	24.2	285.0	23.2	1085.0	282.0	2.9
Ce	52.6	59.0	38.5	45.8	47.4	60.4	28.2	89.3	8.8	201.0	79.5	25.9
Cr	42	39	56	74	32	47	880	26	100	380	45	1000
Cs	1.32	1.94	0.89	1.03	1.26	0.94	0.10	0.76	0.06	1.46	1.42	0.02
Dy	2.95	3.08	2.03	3.42	2.41	2.88	2.58	4.80	2.79	5.20	4.89	2.40
Er	1.76	1.91	1.31	2.33	1.30	1.63	1.25	3.08	1.96	1.96	3.06	1.22
Eu	0.74	0.74	0.65	0.62	0.82	0.83	1.02	1.15	0.58	2.99	1.3	0.98
Ga	19.4	20.0	15.2	16.2	17.4	17.8	16.9	21.3	18.6	20.0	18.4	14.9
Gd	3.27	3.29	2.60	3.34	2.94	3.46	3.12	5.12	2.31	8.80	4.48	2.55
Ge	1.1	0.7	1.5	1.3	0.9	1.3	0.3	1.5	0.3	0.3	1.5	0.3
Hf	4.49	4.57	3.43	3.97	4.27	4.26	1.70	5.15	1.20	4.70	4.36	1.60

Sample ID	LA-21-DT-073	LA-21-DT-075	LA-21-DT-077	LA-21-DT-078	LA-21-DT-079	LA-21-DT-081	LA-21-DT-082	LA-21-DT-083	LA-21-DT-084	LA-21-DT-085	LA-21-DT-091	LA-21-DT-094
C	0.02	0.03	0.14	0.03	0.17	0.15	2.63	0.06	0.09	0.29	0.05	3.52
S	0.24	0.67	-	0.12	0.02	0.04	0.06	0.1	0.05	0.01	0.09	0.06
Ba	261.0	328.0	137.5	1055.0	328.0	42.8	2620.0	40.1	54.8	-	48.9	1040.0
Ce	88.0	33.7	7.2	7.1	52.7	8.0	405	9.2	11.2	6.3	20.0	263.0
Cr	36	41	290	380	10	140	1270	210	1710	2850	890	410
Cs	0.74	2.32	3.78	0.98	0.91	0.43	6.77	0.24	0.86	0.02	0.62	1.95
Dy	4.89	3.49	3.30	1.42	2.18	2.99	5.72	3.27	2.04	1.55	1.93	8.35
Er	2.9	2.26	1.91	1.00	1.1	1.98	1.78	2.07	1.35	0.91	0.93	3.21
Eu	1.04	1.01	0.7	0.2	0.73	0.68	4.54	0.67	0.48	0.40	0.80	4.87
Ga	18.5	14.2	19.9	21.1	17.9	21	14.9	21.1	16	10.8	12.7	14.1
Gd	4.70	3.20	2.38	1.11	2.55	2.51	11.15	2.76	1.81	1.26	2.21	13.85
Ge	1.4	1.4	0.3	0.3	0.3	0.3	0.3	0.3	0.3	0.3	0.3	0.3
Hf	5.29	3.46	1.30	1.80	4.30	1.50	6.20	1.30	1.20	0.80	1.40	7.30

Sample ID	LA-21-DT-095	LA-21-DT-101	LA-21-DT-102	LA-21-DT-103	LA-21-DT-104	LA-21-DT-105	LA-21-DT-115	LA-21-DT-116	W1120451	W1120452	W1120453
C	0.04	0.03	0.04	0.23	0.26	0.3	0.11	0.03			
S	0.03	0.06	27.8	0.02	0.03	0.34	0.05	0.17			
Ba	22.4	140.5	64.0	517.0	519.0	1185.0	280.0	1.6	227.0	51.0	490.0
Ce	6.9	10.6	44.2	28.2	27.5	48.0	2.8	1.3	9.7	70.7	52.2
Cr	360	220	8	20	10	10	2340	1860	40	60	40
Cs	0.39	0.76	1.43	0.90	1.08	1.30	7.07	0.16	0.8	0.25	1.40
Dy	2.85	3.85	2.84	3.04	3.24	1.77	1.21	0.95	0.60	3.60	2.50
Er	1.82	2.51	1.36	1.98	2.23	0.85	0.76	0.68	0.30	1.90	1.40
Eu	0.81	0.96	0.83	0.27	0.34	0.54	0.32	0.13	0.48	1.22	0.92
Ga	17.5	20.2	6.8	18.6	18.8	18.5	12.9	9.4	18.0	22.0	18.0
Gd	2.60	3.13	3.44	2.75	2.73	1.79	0.90	0.80	0.90	4.00	2.80
Ge	0.3	0.3	0.3	0.3	0.3	0.3	0.3	0.3	0.5	1.0	0.5
Hf	1.3	1.9	1.1	3.2	2.6	4.4	0.5	0.3	1.8	4.3	3.6

Sample ID	W1120455	W1120456	W1120457	W1120458	W1120459	W1120460	W1120461	W1120462	W1120463	W1120464
C										
S										
Ba	499	399	250	388	517	538	350	472	239	429
Ce	52.3	49.6	70.5	37.1	66.6	83.0	52.9	50.2	50.9	62.9
Cr	40	40	50	20	30	50	80	30	50	10
Cs	0.8	2.2	1.4	0.6	0.9	0.7	1.0	1.1	1.3	0.8
Dy	2.8	2.3	3.7	1.1	2.8	4.0	3.2	2.2	3.1	2.8
Er	1.6	1.3	2.2	0.6	1.5	2.4	1.9	1.3	1.8	1.5
Eu	0.93	0.60	1.41	0.58	0.96	1.28	0.95	0.69	0.64	0.68
Ga	19	18	21	16	20	19	17	18	16	17
Gd	3.4	2.8	3.9	1.7	3.3	4.3	3.5	2.5	2.9	3.0
Ge	1.0	1.0	1.0	0.5	0.5	0.5	1.0	0.5	1.0	0.5
Hf	3.9	3.7	4.5	3.0	3.9	4.0	3.3	3.2	3.2	3.1

Sample ID	W1120465	W1120466	W1120467	W1120468	W1120469	W1120470	W1120471	390051	390052	390053
C										
S										
Ba	171	302	581	331	670	359	291	616	423	567
Ce	14.8	47.7	47.3	47.5	76.8	63.8	39.5	46.5	103	47.7
Cr	850	40	70	70	70	40	40	30	20	80
Cs	0.3	1.0	0.7	0.9	0.6	0.3	1.7	0.8	0.6	1.7
Dy	2.3	2.1	2.7	2.7	3.3	2.7	3.2	1.8	3.6	3.0
Er	1.5	1.1	1.5	1.7	2.0	1.5	1.9	1	2.2	1.7
Eu	0.55	0.75	0.89	0.66	1.00	1.08	0.96	0.76	0.79	0.90
Ga	11	14	16	17	17	19	17	17	13	18
Gd	2.1	2.5	2.9	2.9	3.7	3.0	3.1	2.2	4.1	3.3
Ge	0.5	0.5	0.5	1.0	0.5	1.0	0.5	0.5	1.0	0.5
Hf	1.4	3.6	3.3	3.5	3.8	4.0	3.5	3.5	3.5	3.4

Sample ID	390054	390055	390056	390057	390058	390059	390060	390061	390062	390063	390064	390065
C												
S												
Ba	407	615	509	267	415	561	13	444	273	94	316	650
Ce	47.0	60.1	37.2	46.5	48.8	42.9	8.3	52.3	46.2	66.2	49.8	53.0
Cr	80	60	20	20	30	20	120	20	90	30	30	30
Cs	1.9	0.7	0.3	0.8	1.1	1	0.3	0.5	0.8	2.3	1.3	0.9
Dy	3.0	2.7	1.4	3.9	2.0	1.8	2.8	1.6	3.4	3.0	2.3	2.2
Er	1.8	1.5	0.8	2.3	1.2	1.0	1.8	0.8	2.2	1.9	1.3	1.3
Eu	0.81	0.97	0.65	0.75	0.70	0.78	0.60	0.58	0.84	0.86	0.55	0.68
Ga	18	19	18	17	17	18	13	16	17	18	17	17
Gd	3.3	3.3	1.8	3.9	2.4	2.1	2.2	2.1	3.4	2.9	2.6	2.3
Ge	1.0	0.5	1.0	2.0	0.5	0.5	2.0	0.5	1.0	3.0	1.0	1.0
Hf	3.1	3.2	3.2	4.0	3.3	3.4	1.2	2.3	3.0	4.1	3.4	3.7

Sample ID	390066	A0935602	A0935645	A0935951	A0935952	A0935953	A0935954	A0935851	A0935852	A0935853
C										
S										
Ba	479	628	759	384	1341	977	91	122	307	316
Ce	43.4	78.1	32.4	54.0	50.7	63.7	7.0	58.9	54.2	29.3
Cr	30	20	10	20	10	30	270	80	10	10
Cs	1.5	0.8	0.7	0.7	1.4	2.8	2.1	1.8	1.3	1.0
Dy	1.8	2.9	2.8	1.3	1.9	2.7	3.0	3.3	1.4	3.2
Er	1.0	1.7	2.0	0.7	0.9	1.6	1.9	1.9	0.7	2.2
Eu	0.67	0.90	0.49	0.63	0.62	0.94	0.71	1.13	0.42	0.37
Ga	16	15	12	17	16	17	14	17	18	16
Gd	2.3	3.3	2.6	2.0	2.3	3.0	2.5	3.4	2.0	2.6
Ge	1.0	2.0	2.0	1.0	2.0	2.0	3.0	1.0	0.5	0.5
Hf	3.0	3.5	2.1	2.9	3.1	3.4	1.2	3.7	3.4	1.8

Sample ID	A0935854	A0935855	A0935856	A0935857
C				
S				
Ba	420	842	512	589
Ce	33.9	41.5	29.5	48.3
Cr	10	10	10	10
Cs	1.0	1.1	0.7	0.7
Dy	3.2	1.9	2.9	1.8
Er	2.0	1.0	2.0	1.0
Eu	0.49	0.64	0.31	0.53
Ga	16	17	15	16
Gd	2.7	2.2	2.4	2.1
Ge	1.0	0.5	1.0	1.0
Hf	2.7	3.3	2.1	3.2

Sample ID	LA-21-DT-007	LA-21-DT-008	LA-21-DT-011	LA-21-DT-012	LA-21-DT-013	LA-21-DT-014	LA-21-DT-015	LA-21-DT-019	LA-21-DT-024	LA-21-DT-025	LA-21-DT-026	LA-21-DT-027
Ho	0.62	0.72	0.68	0.28	0.34	0.53	0.83	0.37	0.67	0.61	0.52	0.88
La	3.4	38.2	31.7	24.3	28.3	30.9	36.9	24.3	23.7	31.2	6.6	32.0
Lu	0.31	0.29	0.31	0.07	0.14	0.22	0.30	0.21	0.26	0.26	0.24	0.29
Nb	1.80	11.30	8.31	7.04	7.50	8.90	8.53	5.50	10.10	8.08	2.70	11.05
Nd	5.0	26.1	23.7	16.4	18.0	24.3	27.9	18.2	19.6	22.4	6.6	26.5
Pr	1.13	6.82	5.83	4.22	5.17	6.32	7.50	4.88	5.15	5.78	1.59	6.80
Rb	1.6	149.5	102.0	54.0	49.7	90.8	104.0	130.5	148.5	106.0	5.7	64.2
Sm	1.60	5.00	4.32	2.96	2.98	4.13	5.15	3.18	3.68	4.22	1.82	4.79
Sn	0.3	1.7	2.7	1.0	1.0	1.0	12.4	1.0	2.3	5.4	0.3	2.0
Sr	212.0	19.6	63.5	68	65.4	23.8	8.8	108.0	23.2	30.9	241.0	36.8
Ta	0.2	1.0	0.8	0.6	0.5	0.6	0.7	0.4	0.8	0.7	0.2	0.8
Tb	0.39	0.65	0.69	0.28	0.31	0.43	0.63	0.40	0.47	0.51	0.36	0.68
Th	0.59	12.25	9.74	6.36	6.99	7.50	9.23	6.30	9.72	8.04	2.09	6.94

Sample ID	LA-21-DT-034	LA-21-DT-036	LA-21-DT-037	LA-21-DT-038	LA-21-DT-039	LA-21-DT-040	LA-21-DT-043	LA-21-DT-044	LA-21-DT-045	LA-21-DT-046	LA-21-DT-047	LA-21-DT-049
Ho	0.52	0.69	0.67	0.31	0.51	0.46	0.60	0.50	0.45	0.56	0.42	0.37
La	46.2	22.3	44.1	25.6	30.1	26.7	35.6	14.1	28.6	28.6	6.0	28.6
Lu	0.16	0.29	0.34	0.13	0.21	0.14	0.28	0.24	0.23	0.24	0.19	0.17
Nb	4.68	7.30	9.70	7.54	9.39	8.26	9.55	4.70	7.65	7.79	2.20	8.16
Nd	34.6	17.8	34.4	16.5	22.6	20.0	22.9	10.9	18.5	19.2	6.20	19.4
Pr	9.36	4.42	9.27	4.44	5.66	4.97	6.51	3.06	5.22	5.33	1.44	5.43
Rb	12.1	108.5	105.5	66.5	64.5	46.4	104.5	54.9	133.0	140.0	6.6	108.0
Sm	5.93	4.03	5.62	2.72	3.92	2.96	3.67	2.07	3.26	3.40	1.53	3.55
Sn	4.4	8.4	1.0	1.0	0.9	0.7	1.9	1.0	2.3	1.2	1.0	9.6
Sr	68.1	31.3	126.5	89.2	79.7	101.0	21.8	81.9	28.8	38.8	112.5	25.3
Ta	0.4	0.5	0.6	0.6	0.6	0.6	0.8	0.4	0.7	0.8	0.2	0.7
Tb	0.56	0.50	0.56	0.31	0.45	0.39	0.46	0.35	0.39	0.48	0.33	0.33
Th	10.65	5.04	9.27	7.24	6.76	6.47	11.95	4.31	11.45	10.70	1.80	9.58

Sample ID	LA-21-DT-050	LA-21-DT-051	LA-21-DT-053	LA-21-DT-057	LA-21-DT-058	LA-21-DT-060	LA-21-DT-065	LA-21-DT-066	LA-21-DT-068	LA-21-DT-070	LA-21-DT-071	LA-21-DT-072
Ho	0.62	0.68	0.42	0.73	0.45	0.51	0.46	0.99	0.61	0.85	1.00	0.42
La	30.9	33.9	21.9	24.2	26.7	32.7	11.5	50.1	3.9	99.5	44.2	10.7
Lu	0.25	0.32	0.22	0.32	0.14	0.28	0.16	0.45	0.31	0.20	0.41	0.18
Nb	7.71	8.00	6.69	7.18	7.30	8.40	7.40	11.05	2.00	94.70	9.77	6.40
Nd	19.6	22.5	15.0	18.4	18.6	24.3	15.8	31.6	5.5	80.4	30.2	13.9
Pr	5.78	6.18	4.24	5.15	4.95	6.58	3.54	9.43	1.21	21.9	8.35	3.39
Rb	109.5	126.5	75.5	60.3	112.0	66.0	3.9	113.5	6.7	103.0	119.0	2.3
Sm	4.02	3.92	3.01	2.95	3.07	3.90	3.59	5.58	1.52	13.10	4.78	3.41
Sn	7.9	6.8	10.8	6.1	2.8	9.0	4.0	9.6	1.0	9.0	11.0	3.0
Sr	12.3	39.0	1.3	2.7	82.7	15.3	72.6	22.3	187.5	807.0	15.6	30.6
Ta	0.7	0.8	0.6	0.6	0.6	0.7	0.5	1.1	0.1	4.2	0.7	0.4
Tb	0.50	0.49	0.32	0.56	0.38	0.47	0.44	0.77	0.41	1.05	0.69	0.40
Th	10.10	12.25	7.89	5.35	8.03	10.55	1.15	15.55	0.65	13.05	11.00	1.09

Sample ID	LA-21-DT-073	LA-21-DT-075	LA-21-DT-077	LA-21-DT-078	LA-21-DT-079	LA-21-DT-081	LA-21-DT-082	LA-21-DT-083	LA-21-DT-084	LA-21-DT-085	LA-21-DT-091	LA-21-DT-094
Ho	1.01	0.71	0.66	0.32	0.41	0.65	0.76	0.69	0.47	0.27	0.35	1.38
La	47.0	19.1	3.0	2.9	29.1	2.8	199.0	3.7	5.3	3.2	7.9	132.0
Lu	0.43	0.36	0.34	0.21	0.17	0.28	0.18	0.31	0.20	0.13	0.13	0.25
Nb	11.65	6.74	2.10	4.00	7.80	2.80	180.00	2.90	2.20	1.50	6.40	118.50
Nd	31.9	14.0	5.6	4.0	19.4	6.5	147.0	6.1	6.0	3.4	11.5	113.5
Pr	9.25	3.75	1.06	0.92	5.45	1.23	42.20	1.28	1.28	0.76	2.66	30.90
Rb	101.0	133.0	118.0	192.5	82.1	27.6	182.5	17.0	16.7	0.4	13.1	100.5
Sm	4.87	2.91	2.14	1.07	3.10	2.16	19.90	1.87	1.69	1.07	2.75	19.00
Sn	11.0	4.7	3.0	5.0	1.0	1.0	2.0	0.3	0.3	1.0	1.0	4.0
Sr	9.3	25.1	100.5	8.8	96.9	114.0	1255.0	121.5	197.5	7.4	45.2	700.0
Ta	0.9	0.5	0.1	0.2	0.8	0.1	8.0	0.2	0.2	0.1	0.4	5.6
Tb	0.73	0.48	0.47	0.18	0.35	0.49	1.27	0.44	0.32	0.22	0.33	1.66
Th	12.45	6.23	0.20	0.34	11.10	0.31	25.30	0.54	1.71	1.09	0.92	30.40

Sample ID	LA-21-DT-095	LA-21-DT-101	LA-21-DT-102	LA-21-DT-103	LA-21-DT-104	LA-21-DT-105	LA-21-DT-115	LA-21-DT-116	W1120451	W1120452	W1120453
Ho	0.59	0.85	0.47	0.60	0.68	0.35	0.29	0.24	0.10	0.70	0.50
La	2.8	4.5	25.0	14.7	15.1	25.7	1.3	0.4	4.7	36.0	28.5
Lu	0.25	0.36	0.12	0.35	0.40	0.15	0.12	0.11	0.05	0.30	0.22
Nb	2.10	3.20	2.75	13.30	14.00	6.40	0.90	0.60	1.00	9.00	7.00
Nd	5.3	8.2	18.0	11.7	11.0	17.4	2.0	1.3	4.3	26.2	18.9
Pr	1.05	1.58	4.97	3.05	2.97	4.71	0.40	0.25	1.13	7.54	5.42
Rb	18.6	44.1	57.9	138	144	68.5	62.9	0.6	43	16	95
Sm	1.91	2.50	3.20	2.55	2.49	2.74	0.72	0.57	1.0	4.6	3.3
Sn	0.3	1.0	1.1	3.0	2.0	1.0	1.0	0.3	0.5	0.5	0.5
Sr	278.0	80.6	11.9	53.0	60.2	137.0	13.2	1.7	122	29	94
Ta	0.1	0.2	0.2	1.9	2.0	0.5	0.1	0.1	0.1	0.8	0.7
Tb	0.44	0.57	0.51	0.43	0.49	0.30	0.21	0.16	0.1	0.6	0.4
Th	0.28	0.7	3.09	16.45	17.05	7.09	0.21	0.09	1.4	8.1	7.7

Sample ID	W1120455	W1120456	W1120457	W1120458	W1120459	W1120460	W1120461	W1120462	W1120463	W1120464
Ho	0.5	0.4	0.7	0.2	0.5	0.8	0.6	0.4	0.6	0.5
La	27	26.1	36.8	21.5	36.1	43.8	27.1	28.7	27.7	35.3
Lu	0.24	0.23	0.35	0.09	0.25	0.36	0.32	0.21	0.26	0.25
Nb	7	6	9	4	7	8	7	5	8	8
Nd	19.5	18.3	26.5	12.6	22.8	31.5	20.5	17.6	17.7	22.0
Pr	5.38	5.08	7.49	3.61	6.68	8.87	5.59	4.95	5.17	6.52
Rb	91	116	114	93	132	144	59	63	117	96
Sm	3.6	3.1	4.7	2.0	3.8	4.9	3.7	3.0	3.3	3.9
Sn	2.0	5.0	15.0	1.0	1.0	1.0	0.5	0.5	13.0	11.0
Sr	47	22	7	15	21	29	145	162	11	14
Ta	0.7	0.6	0.8	0.5	0.9	0.7	0.7	0.8	0.7	0.7
Tb	0.5	0.4	0.6	0.2	0.5	0.7	0.5	0.4	0.5	0.5
Th	6.6	5.8	10.7	7.6	12.6	10.5	7.6	11.4	8.4	11.9

Sample ID	W1120465	W1120466	W1120467	W1120468	W1120469	W1120470	W1120471	390051	390052	390053
Ho	0.5	0.4	0.5	0.6	0.7	0.5	0.6	0.3	0.7	0.6
La	7.3	25.8	25.2	25.1	39.9	34.9	20	27.3	57.7	25.2
Lu	0.22	0.19	0.26	0.26	0.32	0.18	0.3	0.15	0.34	0.28
Nb	2	6	5	5	6	8	6	6	8	7
Nd	6.6	17	17.4	17.2	28.8	22.5	15.9	16	34.3	19.1
Pr	1.7	4.99	4.92	4.99	8.26	6.48	4.23	4.62	10.3	5.05
Rb	12	91	117	103	106	85	108	69	97	107
Sm	1.8	3	3.2	3.1	4.8	3.5	3.1	2.7	5.2	3.5
Sn	0.5	5	2	7	11	5	1	3	5	1
Sr	52	10	32	3	36	12	85	66	16	107
Ta	0.2	0.6	0.6	0.6	0.6	0.7	0.4	0.8	1	0.6
Tb	0.4	0.4	0.4	0.5	0.6	0.5	0.5	0.3	0.6	0.5
Th	2.4	7.8	8.2	8.4	11.3	10.7	4.8	10.1	16.9	6.7

Sample ID	390054	390055	390056	390057	390058	390059	390060	390061	390062	390063	390064	390065
Ho	0.6	0.5	0.3	0.8	0.4	0.3	0.6	0.3	0.7	0.6	0.5	0.4
La	25.2	32.3	20.7	21.7	27.7	24.6	3.6	30.3	24	37.8	28.5	31.1
Lu	0.27	0.21	0.13	0.38	0.17	0.15	0.28	0.13	0.34	0.30	0.19	0.20
Nb	6	6	5	8	6	5	2	5	8	11	7	6
Nd	18.8	22.0	12.8	22.6	16.7	15.1	5.5	16.6	18.5	22.9	17.3	16.9
Pr	5.11	6.22	3.76	5.67	4.89	4.37	1.14	5.09	5.04	6.67	5.01	5.13
Rb	123	114	99	82	97	123	2	88	85	50	80	94
Sm	3.4	3.8	2.4	4.5	2.8	2.7	1.6	2.7	3.7	3.8	3.1	2.8
Sn	6	2	1	3	1	2	1	1	7	8	2	2
Sr	10	62	35	23	146	25	164	104	57	94	62	46
Ta	0.6	0.7	0.6	1.1	0.7	0.6	0.1	0.6	0.7	1.3	0.9	0.9
Tb	0.5	0.5	0.3	0.6	0.3	0.3	0.4	0.3	0.5	0.5	0.4	0.4
Th	6.5	11.4	6.4	16.3	9.5	6.8	0.6	8.5	7.3	18.6	12.9	12.1

Sample ID	390066	A0935602	A0935645	A0935951	A0935952	A0935953	A0935954	A0935851	A0935852	A0935853
Ho	0.4	0.6	0.6	0.2	0.3	0.5	0.5	0.7	0.3	0.6
La	25	45.1	17.3	29.5	28.0	34.3	2.7	30.3	30.6	15.3
Lu	0.17	0.30	0.34	0.11	0.14	0.25	0.30	0.28	0.10	0.39
Nb	7	8	9	5	6	7	1	10	5	8
Nd	15.0	23.5	11.2	16.9	17.2	22.4	5.3	23.4	17.7	10.5
Pr	4.38	7.35	3.33	5.23	5.01	6.41	1.01	6.39	5.37	3.07
Rb	130	130	86	58	111	86	95	56	62	135
Sm	2.5	3.8	2.7	2.8	2.7	3.5	1.7	4.1	2.8	2.6
Sn	1	4	2	1	2	2	1	1	0.5	1
Sr	73	22	23	175	96	182	97	186	105	21
Ta	0.9	1.3	2.0	0.6	0.9	0.8	0.1	0.6	0.5	2
Tb	0.3	0.5	0.5	0.3	0.3	0.5	0.5	0.6	0.3	0.5
Th	10.6	23.5	17.2	8.8	11.0	9.6	0.2	7.0	10.0	18.3

Sample ID	A0935854	A0935855	A0935856	A0935857
Ho	0.6	0.4	0.6	0.3
La	18.6	24	15.9	28.2
Lu	0.37	0.15	0.35	0.15
Nb	13	5	8	6
Nd	12.5	15.4	11.3	14.6
Pr	3.61	4.24	3.23	4.67
Rb	127	68	136	54
Sm	2.6	2.6	2.4	2.5
Sn	1	1	2	1
Sr	50	180	63	140
Ta	2	0.7	1.9	0.8
Tb	0.5	0.3	0.4	0.3
Th	18.5	7.8	17.3	13.7

Sample ID	LA-21-DT-007	LA-21-DT-008	LA-21-DT-011	LA-21-DT-012	LA-21-DT-013	LA-21-DT-014	LA-21-DT-015	LA-21-DT-019	LA-21-DT-024	LA-21-DT-025	LA-21-DT-026	LA-21-DT-027
Tm	0.27	0.31	0.28	0.14	0.12	0.21	0.3	0.17	0.27	0.27	0.20	0.35
U	0.15	4.19	2.96	2.48	2.11	1.98	2.59	1.74	3.53	2.25	0.59	1.88
V	280	90	83	36	42	69	116	92	122	72	217	96
W	0.3	15.2	29.7	0.8	1.0	6.0	9.0	2.0	12.5	5.9	1.0	1.6
Y	15.9	21.0	21.0	8.3	9.3	13.7	21.8	11.4	16.8	16.4	13.1	22.4
Yb	1.84	2.06	1.80	0.78	0.92	1.57	2.10	1.25	1.65	1.75	1.43	2.12
Zr	45	182	183	152	161	168	179	125	212	175	51	209
As	250.0	250.0	69.1	0.6	2.9	20.6	63.7	12.0	214.0	20.5	250.0	0.9
Bi	0.12	1.05	0.08	0.02	0.02	0.19	2.64	0.12	2.31	6.12	0.06	0.06
Hg	0.009	0.009	0.003	0.003	0.003	0.026	0.007	0.003	0.020	0.003	0.009	0.003
In	0.011	0.001	0.023	0.008	0.007	0.012	0.139	0.013	0.164	0.054	0.003	0.007
Re	0.001	0.001	0.001	0.0005	0.001	0.001	0.001	0.001	0.001	0.001	0.001	0.001
Sb	0.19	0.22	0.16	0.03	0.05	0.18	0.16	0.11	0.15	0.15	0.46	0.07

Sample ID	LA-21-DT-034	LA-21-DT-036	LA-21-DT-037	LA-21-DT-038	LA-21-DT-039	LA-21-DT-040	LA-21-DT-043	LA-21-DT-044	LA-21-DT-045	LA-21-DT-046	LA-21-DT-047	LA-21-DT-049
Tm	0.19	0.31	0.28	0.14	0.22	0.18	0.26	0.21	0.25	0.26	0.21	0.14
U	3.04	1.46	2.17	1.21	1.88	1.68	3.32	1.2	3.69	2.8	0.49	2.6
V	116	129	108	39	66	69	52	173	64	71	202	70
W	3.5	5.3	2.0	0.7	3.0	0.6	3.3	2.0	1.4	1.7	0.3	3.3
Y	16.1	16.8	18.5	8.5	15.6	12.9	16.0	13.3	13	16.2	11.9	10.0
Yb	1.31	1.84	2.01	0.85	1.60	1.31	1.72	1.57	1.72	1.56	1.31	1.09
Zr	127	153	169	164	176	171	149	93	154	169	46	159
As	36.3	36.7	2.1	0.6	0.7	0.3	8.0	69.8	57.3	10.1	250.0	28.1
Bi	25.4	2.01	0.16	0.27	0.06	0.03	0.74	0.06	0.31	0.06	0.17	1.21
Hg	0.138	0.003	0.003	0.003	0.003	0.003	0.005	0.006	0.003	0.003	0.005	0.005
In	3.370	0.056	0.035	0.028	0.016	0.017	0.011	0.008	0.017	0.013	0.003	0.189
Re	0.003	0.001	0.001	0.001	0.001	0.001	0.001	0.001	0.001	0.001	0.001	0.001
Sb	1.08	0.11	0.05	0.025	0.025	0.05	0.35	0.38	0.46	0.14	0.44	0.11

Sample ID	LA-21-DT-050	LA-21-DT-051	LA-21-DT-053	LA-21-DT-057	LA-21-DT-058	LA-21-DT-060	LA-21-DT-065	LA-21-DT-066	LA-21-DT-068	LA-21-DT-070	LA-21-DT-071	LA-21-DT-072
Tm	0.28	0.34	0.18	0.35	0.21	0.23	0.15	0.45	0.28	0.24	0.37	0.16
U	2.59	3.62	2.11	1.22	2.02	2.68	0.45	4.15	0.18	3.00	2.96	0.35
V	72	66	63	86	59	92	190	57	275	125	99	171
W	2.9	4.3	1.5	0.6	2.7	3.2	1.0	30.7	2.0	13.0	6.4	0.3
Y	17.8	17.6	12.2	21.4	13.7	16.2	12.4	30.3	15.8	22.0	30.5	11.0
Yb	1.78	1.84	1.36	2.19	1.20	1.62	1.28	3.08	1.95	1.62	2.45	1.05
Zr	166	175	138	160	163	167	69	196	44	202	175	62
As	9.8	3.7	250.0	250.0	29.2	15.1	250.0	5.5	250.0	4.8	240.0	250.0
Bi	0.74	0.50	14.90	11.55	11.20	1.43	4.14	0.35	0.30	3.38	29.90	15.75
Hg	0.003	0.003	0.034	0.015	0.003	0.003	0.011	0.003	0.005	0.007	0.006	0.016
In	0.039	0.163	2.190	0.205	0.054	0.073	0.006	0.024	0.010	0.065	0.081	0.001
Re	0.001	0.001	0.001	0.001	0.001	0.001	0.001	0.001	0.001	0.001	0.001	0.001
Sb	0.09	0.18	0.41	1.40	0.22	0.18	0.71	0.09	0.21	0.06	0.31	0.20

Sample ID	LA-21-DT-073	LA-21-DT-075	LA-21-DT-077	LA-21-DT-078	LA-21-DT-079	LA-21-DT-081	LA-21-DT-082	LA-21-DT-083	LA-21-DT-084	LA-21-DT-085	LA-21-DT-091	LA-21-DT-094
Tm	0.41	0.31	0.29	0.15	0.15	0.27	0.21	0.30	0.18	0.13	0.14	0.35
U	3.35	1.78	0.09	0.15	3.28	0.11	3.64	0.12	0.51	0.32	0.26	7.08
V	73	104	277	288	23	307	140	288	192	135	143	148
W	7.8	2.6	1.0	32.0	1.0	1.0	3.0	0.1	0.1	0.1	0.1	5.0
Y	27.9	20.8	17.9	7.6	11.8	16.3	19.6	17.7	11.6	7.6	8.9	33.8
Yb	2.61	2.11	2.15	1.40	1.27	1.87	1.22	2.02	1.39	0.84	0.92	1.86
Zr	205	137	45	61	168	54	274	48	45	27	49	347
As	250.0	250.0	5.6	250.0	4.6	4.9	2.6	9.8	10.8	85.4	84.5	14.2
Bi	2.05	1.44	0.19	0.21	0.01	0.18	0.09	0.06	0.04	0.03	1.33	0.38
Hg	0.003	0.006	0.005	0.007	0.003	0.005	0.012	0.007	0.001	0.001	0.007	0.006
In	0.019	0.097	0.01	0.01	0.0025	0.012	0.037	0.007	0.001	0.001	0.005	0.079
Re	0.001	0.001	0.001	0.003	0.0005	0.001	0.001	0.001	0.001	0.001	0.001	0.001
Sb	0.24	0.30	0.45	3.70	0.17	0.47	0.08	0.24	0.12	0.16	0.07	0.12

Sample ID	LA-21-DT-095	LA-21-DT-101	LA-21-DT-102	LA-21-DT-103	LA-21-DT-104	LA-21-DT-105	LA-21-DT-115	LA-21-DT-116	W1120451	W1120452	W1120453
Tm	0.25	0.41	0.16	0.31	0.31	0.12	0.14	0.09	0.03	0.26	0.19
U	0.07	0.20	1.01	8.56	8.51	2.10	0.09	0.03	0.60	2.50	2.30
V	280	335	41	2.5	5	42	189	150	23	91	59
W	2.0	1.0	74.1	2.0	2.0	6.0	1.0	1.0	1.0	0.5	1.0
Y	16.4	22.3	14.0	20.2	20.8	9.2	8.0	6.1	3.0	17.0	13.0
Yb	1.79	2.49	0.90	2.43	2.36	0.92	1.09	0.71	0.3	1.9	1.4
Zr	43	68	42	67	59	173	17	14	69	184	153
As	250	250	15.5	0.4	2.9	1.3	2.8	6.5	2.5	2.5	16
Bi	2.4	0.48	10.05	0.04	0.07	0.2	0.13	0.15	0.2	0.2	0.2
Hg	0.005	0.009	0.011	0.0025	0.005	0.0025	0.006	0.005			
In	0.007	0.011	0.054	0.0025	0	0.021	0.012	0	0.1	0.1	0.1
Re	0.001	0.001	0.001	0.0005	0	0.0005	0	0			
Sb	0.42	0.22	0.13	0.12	0.14	0.09	0	0	0.25	0.25	0.25

Sample ID	W1120455	W1120456	W1120457	W1120458	W1120459	W1120460	W1120461	W1120462	W1120463	W1120464
Tm	0.22	0.2	0.32	0.09	0.22	0.34	0.29	0.19	0.26	0.21
U	1.8	1.5	2.8	2.1	3.9	3	2.2	3.8	2.5	3.7
V	85	72	113	26	63	106	90	40	66	50
W	2	3	3	5	3	8	0.5	0.5	5	10
Y	14	12	19	6	14	22	17	12	16	16
Yb	1.5	1.3	2.2	0.6	1.5	2.3	2	1.3	1.6	1.5
Zr	169	154	182	130	160	167	138	147	137	146
As	6	3	3	172	40	63	3	16	151	10
Bi	0.2	0.2	0.5	0.7	0.2	0.9	0.2	0.2	1.9	0.5
Hg										
In	0.1	0.1	0.1	0.1	0.1	0.1	0.1	0.1	0.1	0.1
Re										
Sb	0.3	0.3	0.3	0.3	0.3	1.0	0.3	0.6	0.3	0.3

Sample ID	W1120465	W1120466	W1120467	W1120468	W1120469	W1120470	W1120471	390051	390052	390053
Tm	0.22	0.17	0.24	0.25	0.30	0.22	0.29	0.14	0.32	0.25
U	0.7	2.4	2.3	2.5	2.9	3	1.3	3.1	5	1.7
V	189	48	73	77	111	57	113	30	2.5	120
W	1	1	2	1	7	11	1	10	9	5
Y	11	11	14	14	17	15	16	9	19	15
Yb	1.4	1.1	1.7	1.7	2.0	1.3	1.8	0.9	2.2	1.7
Zr	52	148	136	146	156	153	142	142	114	141
As	167	3	3	16	94	792	18	6	17	3
Bi	0.8	0.8	0.2	1.5	0.2	0.6	0.2	0.2	41.6	0.4
Hg										
In	0.1	0.1	0.1	0.1	0.1	0.1	0.1	0.1	0.1	0.1
Re										
Sb	1.7	0.3	0.3	0.3	0.3	0.3	0.3	0.3	0.3	0.3

Sample ID	390054	390055	390056	390057	390058	390059	390060	390061	390062	390063	390064	390065
Tm	0.26	0.22	0.11	0.34	0.17	0.13	0.28	0.12	0.33	0.29	0.2	0.19
U	1.6	3.4	1.9	3.8	2.5	2.0	0.2	2.1	2.3	4.0	4.2	4.2
V	119	76	28	10	34	28	276	3	97	57	27	27
W	2	3	7	4	0.5	4	1	1	4	6	5	8
Y	17	14	7	22	11	10	14	9	20	17	14	13
Yb	1.7	1.4	0.8	2.3	1.1	0.9	1.9	0.8	2.2	1.9	1.3	1.3
Zr	136	132	140	166	139	150	41	77	133	157	134	131
As	3	3	3	35	12	2.5	40	7	6	3	3	3
Bi	0.2	0.2	0.2	1.8	0.2	0.2	0.2	0.2	6.5	0.2	0.2	0.2
Hg												
In	0.1	0.1	0.1	0.1	0.1	0.1	0.1	0.1	0.1	0.1	0.1	0.1
Re												
Sb	0.25	0.25	0.25	0.25	0.25	0.25	0.25	0.25	0.25	0.25	0.25	0.25

Sample ID	390066	A0935602	A0935645	A0935951	A0935952	A0935953	A0935954	A0935851	A0935852	A0935853
Tm	0.15	0.26	0.31	0.09	0.13	0.23	0.26	0.27	0.10	0.34
U	3.9	6.7	8.1	2.7	4.3	2.7	0.05	1.8	2.6	9.8
V	30	22	2.5	26	30	58	280	94	28	2.5
W	5	8	5	1	4	3	1	1	5	3
Y	10	18	20	7	11	17	18	16	7	19
Yb	1.0	1.8	2.1	0.7	0.9	1.6	1.9	1.8	0.6	2.4
Zr	125	126	49	127	125	145	44	157	148	50
As	3	3	3	5	3	9	3	3	3	14
Bi	0.2	0.2	0.2	0.2	0.2	0.2	0.2	0.2	0.2	0.2
Hg										
In	0.1	0.1	0.1	0.1	0.1	0.1	0.1	0.1	0.1	0.1
Re										
Sb	0.25	0.25	0.25	0.25	0.25	0.25	1.00	2.50	0.60	1.10

Sample ID	A0935854	A0935855	A0935856	A0935857
Tm	0.30	0.15	0.32	0.14
U	9.0	2.4	9.1	4.4
V	5	39	3	25
W	10	1	5	3
Y	19	11	19	10
Yb	2.2	1.0	2.1	0.9
Zr	74	150	52	134
As	20	3	3	3
Bi	0.2	0.2	0.2	0.2
Hg				
In	0.1	0.1	0.1	0.1
Re				
Sb	1.2	2.5	2.5	2.5

Sample ID	LA-21-DT-007	LA-21-DT-008	LA-21-DT-011	LA-21-DT-012	LA-21-DT-013	LA-21-DT-014	LA-21-DT-015	LA-21-DT-019	LA-21-DT-024	LA-21-DT-025	LA-21-DT-026	LA-21-DT-027
Se	0.1	0.6	0.1	0.1	0.1	0.1	0.3	0.1	3.5	1.1	0.4	0.1
Te	0.02	0.08	0.01	0.01	0.01	0.01	0.05	0.01	0.24	0.08	0.02	0.01
Tl	0.01	0.33	0.60	0.20	0.17	0.04	0.52	0.70	0.45	0.52	0.01	0.15
Ag	0.3	0.3	0.3	0.3	0.3	0.3	1.0	0.3	6.9	0.3	0.3	0.3
Cd	0.7	0.3	0.7	0.3	0.3	1.4	0.3	0.3	2.2	0.3	0.7	0.3
Co	48	31	12	6	8	16	22	12	64	11	70	8
Cu	82	228	15	20	49	35	308	7	3150	226	64	26
Li	10	10	10	40	30	10	10	10	10	10	10	20
Mo	1	1	2	1	1	1	1	1	1	1	1	1
Ni	108	19	18	10	5	20	23	18	26	5	434	14
Pb	11	19	11	8	8	22	8	7	16	7	9	7
Sc	45	12	9	3	5	7	12	9	10	7	32	10
Zn	95	86	25	39	36	191	27	23	51	31	84	15

Sample ID	LA-21-DT-034	LA-21-DT-036	LA-21-DT-037	LA-21-DT-038	LA-21-DT-039	LA-21-DT-040	LA-21-DT-043	LA-21-DT-044	LA-21-DT-045	LA-21-DT-046	LA-21-DT-047	LA-21-DT-049
Se	80.2	0.2	0.3	0.7	0.3	0.1	0.2	0.4	0.3	0.1	0.3	1.7
Te	2.24	0.01	0.01	0.02	0.01	0.01	0.01	0.02	0.01	0.01	0.02	0.01
Tl	0.03	0.55	0.59	0.28	0.18	0.26	0.28	0.36	0.79	0.79	0.03	0.62
Ag	49.3	0.03	0.03	0.03	0.03	0.03	0.80	0.03	0.03	0.03	0.03	2.70
Cd	2.3	0.3	0.3	0.3	0.3	0.3	0.3	0.9	0.6	0.3	0.8	1.4
Co	114	17	14	5	8	9	13	26	22	12	74	18
Cu	20600	83	3	61	41	12	363	31	83	8	127	1280
Li	5	10	10	20	20	10	10	10	20	20	10	10
Mo	1	1	1	1	1	1	2	2	1	1	2	1
Ni	47	29	25	13	10	10	21	35	24	17	473	18
Pb	9	10	7	11	10	16	16	21	15	13	12	13
Sc	6	14	11	4	7	6	6	31	8	10	29	9
Zn	52	14	40	42	42	62	45	134	61	29	97	53

Sample ID	LA-21-DT-050	LA-21-DT-051	LA-21-DT-053	LA-21-DT-057	LA-21-DT-058	LA-21-DT-060	LA-21-DT-065	LA-21-DT-066	LA-21-DT-068	LA-21-DT-070	LA-21-DT-071	LA-21-DT-072
Se	2.9	1.6	5.2	1.4	1.1	0.3	0.3	0.3	0.4	0.3	0.5	0.2
Te	0.005	0.01	0.01	0.01	0.02	0.005	0.04	0.005	0.04	0.02	0.12	0.08
Tl	0.57	0.56	0.46	0.43	0.67	0.4	0.02	0.35	0.02	0.33	0.55	0.02
Ag	0.025	0.025	8.4	0.5	0.025	0.025	0	0.025	0	0.5	0.5	1.3
Cd	0.025	0.5	55.6	0.9	0.025	0.025	1	0.025	0.5	0.7	0.025	1
Co	22	6	28	46	13	17	88	9	48	38	36	99
Cu	515	481	2580	330	288	45	91	217	184	236	323	161
Li	10	10	10	10	10	10	10	10	0	20	10	10
Mo	1	0.5	1	0.5	2	0.5	1	2	2	3	1	1
Ni	29	11	25	35	15	18	807	11	107	196	31	994
Pb	8	22	5	2	6	18	6	10	11	13	7	7
Sc	9	9	9	13	7	12	23	7	44	15	12	22
Zn	25	76	1205	44	63	20	100	12	94	66	14	107

Sample ID	LA-21-DT-073	LA-21-DT-075	LA-21-DT-077	LA-21-DT-078	LA-21-DT-079	LA-21-DT-081	LA-21-DT-082	LA-21-DT-083	LA-21-DT-084	LA-21-DT-085	LA-21-DT-091	LA-21-DT-094
Se	1.1	0.8	0.1	0.4	0.1	0.2	0.1	0.4	0.3	0.2	0.2	0.4
Te	0.08	0.02	0.02	0.07	0.01	0.02	0.02	0.02	0.02	0.02	0.01	0.01
Tl	0.27	0.74	0.32	0.02	0.21	0.13	0.27	0.07	0.17	0.01	0.10	0.46
Ag	0.03	1.1	0.03	1.4	0.25	0.03	0.03	0.03	0.03	0.03	0.03	0.03
Cd	0.3	0.7	0.5	0.7	0.3	0.5	0.7	0.6	0.6	0.6	1.4	0.6
Co	46	59	50	55	7	38	68	48	70	89	97	69
Cu	71	542	11	610	2	25	88	149	93	10	249	241
Li	10	10	10	10	10	10	30	10	10	0	10	30
Mo	1	2	1	1	1	2	3	1	1	1	1	3
Ni	17	30	150	113	4	98	678	129	493	868	1070	466
Pb	10	8	2	7	6	3	23	4	10	6	7	16
Sc	10	13	38	14	3	37	23	40	30	22	24	18
Zn	18	25	32	40	10	74	79	89	82	86	127	77

Sample ID	LA-21-DT-095	LA-21-DT-101	LA-21-DT-102	LA-21-DT-103	LA-21-DT-104	LA-21-DT-105	LA-21-DT-115	LA-21-DT-116	W1120451	W1120452	W1120453
Se	0.3	0.3	11.8	0.1	0.1	0.5	0.2	0.4			
Te	0.01	0.02	0.10	0.01	0.01	0.09	0.05	0.04			
Tl	0.08	0.19	0.32	0.03	0.04	0.17	0.52	0.01	0.1	0.05	0.4
Ag	1.0	0.3	2.1	0.3	0.3	0.3	0.3	0.3	0.3	0.3	0.3
Cd	0.9	0.6	0.3	0.3	0.3	0.3	0.6	0.5			
Co	49	52	223	1	1	14	51	88	2	19	10
Cu	175	177	741	4	20	566	16	93	10	40	30
Li	10	10	10	5	0	10	30	10			
Mo	1	1	3	1	2	1	1	1	1	1	1
Ni	175	124	193	0.5	6	6	451	635	10	30	10
Pb	9	3	9	15	15	3	4	5	11	6	10
Sc	37	40	5	1	1	4	35	28	2	16	8
Zn	104	94	10	13	23	7	119	70	15	15	15

Sample ID	W1120455	W1120456	W1120457	W1120458	W1120459	W1120460	W1120461	W1120462	W1120463	W1120464
Se										
Te										
Tl	0.4	0.6	0.5	0.4	0.6	0.5	0.3	0.3	0.6	0.5
Ag	0.3	0.3	0.3	0.3	0.3	0.3	0.3	0.3	0.3	0.3
Cd										
Co	12	15	26	5	9	21	15	7	51	17
Cu	60	70	80	5	30	30	20	20	130	330
Li										
Mo	1	1	1	1	1	1	1	1	1	1
Ni	10	10	10	10	10	30	30	10	20	10
Pb	12	9	8	7	10	9	18	14	6	7
Sc	11	9	14	4	8	12	12	5	8	6
Zn	80	70	70	15	15	15	100	70	40	15

Sample ID	W1120465	W1120466	W1120467	W1120468	W1120469	W1120470	W1120471	390051	390052	390053
Se										
Te										
Tl	0.1	0.4	0.7	0.7	0.6	0.2	0.6	0.3	0.5	0.6
Ag	0.3	0.3	0.3	0.3	0.3	0.3	0.3	0.5	1.8	0.7
Cd										
Co	40	12	13	16	11	129	16	5	19	22
Cu	60	400	60	90	20	120	40	10	130	50
Li										
Mo	1	1	1	1	1	1	1	6	4	1
Ni	210	10	30	30	10	10	30	10	10	40
Pb	6	6	7	6	23	15	7	13	12	12
Sc	34	6	10	10	14	7	15	4	4	15
Zn	90	70	30	240	60	40	40	15	15	50

Sample ID	390054	390055	390056	390057	390058	390059	390060	390061	390062	390063	390064	390065
Se												
Te												
Tl	0.6	0.5	0.5	0.4	0.5	0.6	0.1	0.4	0.7	0.2	0.2	0.2
Ag	0.6	0.6	0.5	0.8	0.6	0.6	0.3	0.3	0.7	0.6	0.5	0.5
Cd												
Co	24	11	5	4	6	3	48	2	9	16	3	3
Cu	60	50	20	70	40	20	120	5	50	300	5	5
Li												
Mo	1	1	1	3	2	1	1	5	1	10	3	7
Ni	40	10	10	10	10	10	90	10	30	30	10	10
Pb	9	9	7	9	7	2.5	5	8	9	8	8	9
Sc	15	9	4	5	4	4	46	2	13	7	4	4
Zn	50	15	15	15	15	15	100	40	90	15	15	15

Sample ID	390066	A0935602	A0935645	A0935951	A0935952	A0935953	A0935954	A0935851	A0935852	A0935853
Se										
Te										
Tl	0.4	0.2	0.1	0.1	0.2	0.1	0.1	0.2	0.3	0.6
Ag	0.6	0.5	0.3	0.3	0.3	0.3	0.3	0.3	0.3	0.3
Cd										
Co	8	5	2	8	10	14	46	17	3	1
Cu	250	440	170	130	180	5	60	20	5	5
Li										
Mo	3	2	2	1	1	1	1	1	1	2
Ni	10	10	10	10	10	20	150	30	10	10
Pb	16	12	17	7	8	6	2.5	2.5	5	15
Sc	4	4	1	3	4	7	39	12	3	1
Zn	50	15	15	15	15	15	15	15	15	15

Sample ID	A0935854	A0935855	A0935856	A0935857
Se				
Te				
Tl	0.5	0.3	0.6	0.1
Ag	0.3	0.3	0.3	0.25
Cd				
Co	2	5	1	4
Cu	5	10	20	5
Li				
Mo	2	1	2	3
Ni	10	10	10	10
Pb	18	8	26	9
Sc	2	5	1	3
Zn	15	15	15	15

Appendix III

Garnet LA-ICP-MS

Sample Mean (ppm)	LA-21-DT-017-1	LA-21-DT-017-2	LA-21-DT-017-3	LA-21-DT-017-4	LA-21-DT-017-5	LA-21-DT-017-6	LA-21-DT-017-7	LA-21-DT-017-8	LA-21-DT-017-9
Na^{23}	16.24	12.35	19.24	18.72	20.80	14.49	19.20	14.79	38.59
Mg^{24}	8881.3	8558.3	8603.6	8242.1	8689.9	8430.6	7955.5	7913.0	7538.4
Al^{27}	76764	78165	77570	74251	76937	78663	77622	76714	76661
Si^{29}									
P^{31}	39.70	60.17	61.92	48.30	75.36	74.66	68.58	65.51	59.40
K^{39}	-	-	-	-	2.28	-	-	0.93	-
Ca^{43}	11680	12501	12116	13132	12511	14512	12331	11698	11973
Sc^{45}	10.36	18.94	15.49	19.65	18.46	21.46	49.72	46.06	71.22
Ti^{47}	135.35	203.69	195.28	170.39	163.71	216.51	213.50	196.11	203.67
Mn^{55}	1021.4	1625.2	1503.6	1519.7	1308.7	1708.7	2291.7	2345.2	5940.5
Fe^{57}	122464	124361	125585	120260	127114	128420	136366	137864	142352
Ga^{69}									
Ga^{71}	3.24	3.60	3.51	3.38	3.52	3.72	3.79	3.41	4.35
Rb^{85}	-	-	0.03	-	0.02	-	-	-	0.02
Sr^{88}	0.01	0.01	0.06	0.11	-	-	-0.01	-	0.06

Sample Mean (ppm)	LA-21-DT-017-10	LA-21-DT-017-11	LA-21-DT-017-12	LA-21-DT-017-13	LA-21-DT-017-14	LA-21-DT-017-15	LA-21-DT-017-16	LA-21-DT-017-17	LA-21-DT-017-18
Na^{23}	15.96	22.42	26.49	29.34	22.51	19.84	16.86	11.04	17.98
Mg^{24}	7726.1	6926.1	6885.3	6953.7	7434.0	9164.6	9406.6	9554.1	7467.5
Al^{27}	77502	77625	78298	77036	78093	77694	77762	78083	77222
Si^{29}									
P^{31}	72.96	50.99	70.66	89.33	75.76	78.87	61.38	44.47	69.74
K^{39}	-	-	0.54	-	-	3.23	-	0.76	-
Ca^{43}	12526	11777	12436	12916	13419	11866	11972	12033	12785
Sc^{45}	37.54	70.36	75.75	67.58	64.45	25.53	16.68	15.75	34.33

Ti^{47}	227.76	182.49	218.19	205.52	179.03	175.49	154.91	125.80	209.20
Mn^{55}	3410.7	7039.2	7321.2	6085.1	4570.3	1321.9	969.64	734.97	4298.8
Fe^{57}	157957	168597	169951	169038	168766	169351	168294	168005	169806
Ga^{69}									
Ga^{71}	3.76	3.93	4.17	3.99	3.72	3.51	3.61	3.36	3.87
Rb^{85}	0.01	0.01	-	0.02	-	-	-	0.02	0.02
Sr^{88}	0.01	0.02	-	-	0.01	0.03	0.02	-	-

Sample Mean (ppm)	LA-21-DT-017-19	LA-21-DT-017-20	LA-21-DT-017-22	LA-21-DT-017-23	LA-21-DT-017-24	LA-21-DT-017-25	LA-21-DT-017-26	LA-21-DT-017-27	LA-21-DT-017-28
Na^{23}	19.73	14.17	32.08	16.55	20.99	18.15	13.67	18.23	19.58
Mg^{24}	7119.3	8723.3	6696.8	8351.6	8212.5	9509.2	7606.1	7730.4	7542.3
Al^{27}	78515	74299.	78635	77843	73261	78281	77665	78388	77713
Si^{29}									
P^{31}	80.67	63.15	67.50	74.58	79.68	75.63	86.85	85.93	70.19
K^{39}	4.93	0.06	0.85	1.52	-	0.33	1.51	-	2.84
Ca^{43}	13472	10888	11443	12924	11188	10343	12691	12818	12302
Sc^{45}	44.24	19.88	67.31	16.28	14.83	5.08	23.89	32.59	25.57
Ti^{47}	196.21	147.55	196.46	226.41	189.71	86.06	175.26	212.56	194.08
Mn^{55}	5583.4	1397.1	9440.5	3001.4	2278.3	1087.1	4202.2	5420.6	5533.0
Fe^{57}	168359	161341	170625	171380	162920	176008	172120	172391	171462
Ga^{69}									
Ga^{71}	3.89	3.05	3.93	3.78	3.60	3.14	3.60	3.98	3.95
Rb^{85}	0.01	0.04	-	-	-	-	0.02	0.01	0.01
Sr^{88}	-	0.01	-	0.07	0.03	-	0.01	0.01	0.63

Sample Mean (ppm)	LA-21-DT-017-29	LA-21-DT-017-30	LA-21-DT-017-31	LA-21-DT-017-32	LA-21-DT-017-34	LA-21-DT-017-35	LA-21-DT-017-36	LA-21-DT-017-37	LA-21-DT-017-38
Na^{23}	21.02	17.31	19.87	36.62	11.57	27.15	16.71	16.66	21.68
Mg^{24}	8064.4	7038.0	7498.3	7254.5	7084.3	7469.8	6965.1	6945.7	6716.1
Al^{27}	78849.6	74016.2	78970.5	79076.4	79392.2	79924.9	77671.1	78442.7	78078.0
Si^{29}									
P^{31}	62.15	75.01	70.91	71.30	60.42	59.48	67.26	72.02	65.42
K^{39}	4.88	0.40	0.02	18.17	0.14	2.10	0.77	-	-
Ca^{43}	13122	12876	12183	12519	13043	13023	12139	12680	12019
Sc^{45}	33.88	38.44	31.43	33.45	38.76	28.25	34.88	42.88	44.68
Ti^{47}	203.60	232.18	164.49	167.24	191.00	185.63	160.98	205.85	221.18
Mn^{55}	4551.7	5396.4	6392.2	6737.6	6985.8	6636.1	7009.2	7322.5	8197.5
Fe^{57}	172097	163136	173521	171661	174321	176156	168939	171008	170873
Ga^{69}									
Ga^{71}	3.91	3.97	3.75	3.90	3.97	3.88	4.02	4.17	4.20
Rb^{85}	0.02	-	0.01	0.02	0.01	0.03	-	0.01	0.01
Sr^{88}	-	0.01	0.01	0.05	0.01	0.09	0.10	0.02	0.01

Sample Mean (ppm)	LA-21-DT-017-39	LA-21-DT-017-40	LA-21-DT-017-41	LA-21-DT-017-42	LA-21-DT-017-43	LA-21-DT-017-44	LA-21-DT-017-45	LA-21-DT-017-46	LA-21-DT-017-47
Na^{23}	18.42	24.14	25.32	27.33	15.70	31.99	31.70	13.37	16.71
Mg^{24}	6739.1	6682.8	6866.2	6618.7	6788.2	6863.6	6985.6	7417.0	7505.7
Al^{27}	78608	78290	78007	74718	76375	78183	78215	77088	79375
Si^{29}									
P^{31}	61.39	61.91	80.09	85.56	68.74	77.36	75.39	66.85	64.10
K^{39}	-	1.08	-	5.44	-	3.79	-	1.00	-
Ca^{43}	12313	12184	11684	11647	12324	13227	12277	13644	14322

Sc^{45}	39.34	47.16	41.75	34.04	27.32	31.48	27.31	24.64	32.17
Ti^{47}	189.44	201.50	236.81	194.17	161.47	178.75	197.02	176.27	186.39
Mn^{55}	8558.1	8563.1	7867.6	7301.1	6919.7	6880.9	6606.5	5080.9	5352.9
Fe^{57}	171118	170182	171570	166963	169335	171291	173249	173724	178258
Ga^{69}									
Ga^{71}	3.99	4.02	4.28	4.30	4.09	3.99	4.03	3.58	3.77
Rb^{85}	0.01	-	-	-	0.01	0.02	0.03	0.02	0.04
Sr^{88}	0.01	0.01	0.10	0.15	0.02	0.31	0.16	0.02	0.02

Sample Mean (ppm)	LA-21-DT-017-48	LA-21-DT-017-49	LA-21-DT-017-50	LA-21-DT-017-51	LA-21-DT-017-52	LA-21-DT-017-53	LA-21-DT-017-54	LA-21-DT-017-55	LA-21-DT-017-56
Na^{23}	17.61	36.80	24.65	26.72	32.46	19.50	32.63	32.04	11.94
Mg^{24}	7262.3	7486.7	6613.7	6880.9	6926.9	7289.6	7255.9	7654.5	8049.0
Al^{27}	77006	79470	79262	78296	78616	78458	78304	79536	79434
Si^{29}									
P^{31}	89.51	89.57	69.04	109.13	90.67	79.46	62.93	73.80	62.99
K^{39}	5.22	2.01	0.48	-	-	2.33	10.09	8.28	3.66
Ca^{43}	12997	13496	12344	11842	12246	11834	12875	12889	13267
Sc^{45}	20.18	30.20	42.29	42.66	59.94	33.91	42.70	52.95	15.98
Ti^{47}	175.19	217.01	182.04	218.65	218.10	192.78	205.93	216.83	176.94
Mn^{55}	5343.7	5685.3	9538.4	7408.1	8263.7	6662.6	5850.9	5298.0	4329.4
Fe^{57}	175744	178885	178809	180172	181530	181228	175554	182142	182211
Ga^{69}									
Ga^{71}	3.89	3.96	3.88	4.01	4.47	3.91	5.36	3.68	3.32
Rb^{85}	0.05	0.10	0.02	0.01	-	-	-	-	-
Sr^{88}	0.10	0.34	-	-	-	0.02	4.14	0.07	0.02

Sample Mean (ppm)	LA-21-DT-017-57	LA-21-DT-017-58	LA-21-DT-017-59	LA-21-DT-017-60	LA-21-DT-017J-01	LA-21-DT-017J-02	LA-21-DT-017J-03	LA-21-DT-017J-04	LA-21-DT-017J-05
Na^{23}	16.36	12.80	12.53	15.12	24.13	20.85	20.21	20.36	24.20
Mg^{24}	8817.9	8013.0	9513.0	9333.9	12231	11976	11940	12074	12229
Al^{27}	75917	75169	80920	79716	106726	106469	106341	107152	106136
Si^{29}					171637	170167	170936	168823	169787
P^{31}	74.42	69.61	73.65	69.05	54.66	79.46	92.81	60.35	64.59
K^{39}	-	-	3.40	0.15	0.92	1.09	-	-	-
Ca^{43}	12085	12020	12883	12336	16314	16164	16288	16294	15395
Sc^{45}	20.02	15.86	23.07	23.68	16.86	24.89	24.56	15.90	14.74
Ti^{47}	198.65	158.52	150.43	154.38	186.19	194.97	176.11	162.01	118.28
Mn^{55}	2528.6	3410.9	1272.5	1407.5	1000.8	1083.1	1112.8	982.72	957.31
Fe^{57}	176451	174730	180464	179749	219453	222940	222110	224353	225175
Ga^{69}					4.20	4.66	4.64	4.68	4.05
Ga^{71}	3.59	3.45	3.61	3.44					
Rb^{85}	-	-	-	0.02	-	-	-	-	-
Sr^{88}	-	-	0.05	0.01	0.13	-	-	0.01	-

Sample Mean (ppm)	LA-21-DT-017J-06	LA-21-DT-017J-07	LA-21-DT-017J-08	LA-21-DT-017J-09	LA-21-DT-017J-10	LA-21-DT-021-01	LA-21-DT-021-02	LA-21-DT-021-03	LA-21-DT-021-04
Na^{23}	22.75	22.64	13.24	16.13	15.18	72.75	85.82	80.32	96.07
Mg^{24}	11926	11791	12386	11925	12035	6877.8	7668.7	6688.7	7358.1
Al^{27}	106367	105946	106760	106907	106819	102947	102460	103326	104657
Si^{29}	169767	169825	169803	169239	169632	167874	168272	168318	167505

P^{31}	75.28	69.06	83.48	87.71	85.77	81.18	81.35	64.95	53.39
K^{39}	-	-	-	-	-	68.40	1135.8	54.51	56.39
Ca^{43}	15702	1528	15216	15268	14909	30747	26108	29020	29740
Sc^{45}	14.82	13.69	10.87	25.03	24.95	32.75	18.77	20.66	14.45
Ti^{47}	155.93	155.03	129.33	161.26	132.27	3257.8	3883.6	3142.4	1864.7
Mn^{55}	1093.7	1213.3	727.8	1066.6	961.17	112042	107481	115772	107780
Fe^{57}	224597	225941	224692	225584	225523	107562	114225	104942	112366
Ga^{69}	4.49	4.55	4.17	4.44	4.08	10.55	8.99	10.32	9.05
Ga^{71}									
Rb^{85}	0.01	0.04	-	-	0.01	0.23	6.72	0.48	0.28
Sr^{88}	-0.01	0.01	-	0.01	0.01	-	0.01	0.04	0.14

Sample Mean (ppm)	LA-21-DT-021-05	LA-21-DT-021-06	LA-21-DT-021-07	LA-21-DT-021-08	LA-21-DT-021-09	LA-21-DT-021-10	LA-21-DT-049-01	LA-21-DT-049-02	LA-21-DT-049-03
Na^{23}	55.70	74.79	47.10	73.43	57.50	41.78	36.50	36.34	47.49
Mg^{24}	8305.1	7817.7	8462.5	7797.9	7888.1	8242.6	7414.0	7325.1	7162.9
Al^{27}	105160	104798	105639	105438	105340	106344	113223	114091	113627
Si^{29}	168177	168471	167984	167542	167853	167304	185842	185886	184990
P^{31}	58.41	56.83	72.22	82.78	85.07	50.30	75.94	60.64	263.44
K^{39}	-	-	1.93	3.29	-	-	11.67	5.13	24.94
Ca^{43}	23845	27404	23649	27943	24576	19562	22344	19463	18572
Sc^{45}	16.38	14.17	6.18	22.92	13.21	10.30	22.17	19.27	16.92
Ti^{47}	833.80	1102.7	747.47	1089.1	819.72	411.03	110.20	196.37	243.08
Mn^{55}	98301	99950	94291	99293	100276	104042	21620	22241	21454
Fe^{57}	126722	121679	130290	122284	124573	126047	165832	166203	170174
Ga^{69}	6.62	7.38	6.61	7.60	6.32	5.50	7.59	7.56	8.29
Ga^{71}									

Rb^{85}	-	0.01	-	0.02	0.03	-	0.24	0.17	0.39
Sr^{88}	-	0.58	0.03	0.17	-	0.02	3.33	0.02	0.15

Sample Mean (ppm)	LA-21-DT-049-04	LA-21-DT-049-05	LA-21-DT-049-06	LA-21-DT-049-07	LA-21-DT-049-08	LA-21-DT-049-09	LA-21-DT-049-10	LA-21-DT-074-01	LA-21-DT-074-02
Na^{23}	57.22	66.81	58.89	52.89	75.53	68.47	81.81	43.02	80.05
Mg^{24}	7069.4	7122.0	7086.4	7184.9	6868.7	6635.2	6894.7	10843.4	9022.9
Al^{27}	111612	112883	112991	112929	110935	110729	111157	104309	106323
Si^{29}	183882	183100	182838	182465	182047	181645	180800	166487	165531
P^{31}	1791.9	47.27	43.00	66.35	88.19	87.53	43.69	91.78	83.77
K^{39}	64.36	1.92	5.12	11.59	0.27	-	6.25	12.38	24.94
Ca^{43}	23252	20800	21132	19008	22830	23453	21606	11580	15100
Sc^{45}	16.24	14.90	15.57	27.19	33.45	22.79	15.90	31.21	20.70
Ti^{47}	295.03	335.26	377.64	254.82	537.28	653.93	488.66	210.91	281.39
Mn^{55}	21292	22767	21836	21841	23652	23257	21368	25351	42784
Fe^{57}	167071	169463	172124	175056	173161	174294	179221	213487	193193
Ga^{69}	8.77	8.84	8.08	6.74	7.91	8.67	7.59	3.65	5.74
Ga^{71}									
Rb^{85}	2.23	0.10	-	0.12	-	0.05	0.19	0.09	0.10
Sr^{88}	0.92	0.02	-	0.16	-	-	0.06	0.08	1.54

Sample Mean (ppm)	LA-21-DT-074-03	LA-21-DT-074-04	LA-21-DT-074-05	LA-21-DT-074-06	LA-21-DT-074-07	LA-21-DT-074-08	LA-21-DT-074-09	LA-21-DT-074-10	LA-21-DT-096-1
Na^{23}	31.90	107.27	130.75	42.40	25.06	40.04	38.98	31.07	31.48
Mg^{24}	10573.6	8388.6	9588.3	10181	9422.3	10825	10474	9734.6	5303.9

Al^{27}	103865	107048	105976	103592	103202	103352	103894	103360	81878
Si^{29}	168580	166682	167201	167221	165951	168392	167555	166060	
P^{31}	85.34	53.52	60.59	71.87	109.61	107.58	80.06	142.47	106.41
K^{39}	-	288.30	1011.2	1219.1	76.81	32.55	-	1.65	23.91
Ca^{43}	11464	20529	14711	15971	17678	12706	11476	19640	9786.9
Sc^{45}	13.68	15.25	18.17	17.67	23.77	56.18	24.20	66.31	19.13
Ti^{47}	165.87	473.88	263.90	187.08	188.44	221.90	338.88	315.00	139.19
Mn^{55}	22013	40847	36863	20358	20127	22138	21943	34394	3262.1
Fe^{57}	215000	187119	195226	213579	216291	214156	216401	199476	184777
Ga^{69}	3.00	6.85	4.96	4.77	4.29	3.77	3.30	4.34	
Ga^{71}									3.21
Rb^{85}	-	0.94	3.50	9.22	0.91	0.09	0.01	0.01	0.14
Sr^{88}	0.01	2.85	1.22	0.22	0.19	0.02	0.05	0.10	1.56

Sample Mean (ppm)	LA-21-DT-096-9	LA-21-DT-096-11	LA-21-DT-096-12	LA-21-DT-096-13	LA-21-DT-096-14	LA-21-DT-096-21	LA-21-DT-096-23	LA-21-DT-096-26	LA-21-DT-096-28
Na^{23}	21.82	20.12	13.32	15.62	22.19	19.46	9.83	17.56	20.50
Mg^{24}	5289.6	5056.4	4644.5	4670.9	4648.1	3256.4	3333.4	3535.8	3452.9
Al^{27}	82334	79030	76911	77513	77010	71259	73985	77561	76047
Si^{29}									
P^{31}	112.47	115.46	113.34	103.00	115.53	79.89	92.65	114.27	102.30
K^{39}	-	1.51	-	1.13	-0.66	0.86	-	-	0.48
Ca^{43}	10131	9733.1	9097.6	8884.6	8715.9	9277.0	9959.5	10625	10767
Sc^{45}	21.46	22.29	30.56	30.02	29.63	24.50	21.55	29.41	35.41
Ti^{47}	85.78	110.48	179.87	200.98	259.09	275.31	1251.0	249.08	182.89
Mn^{55}	2789.0	3133.9	5920.7	6230.0	6897.4	18180	18491	18941	18223
Fe^{57}	184732	180906	180280	178941	181098	160339	164628	169217	166687

Ga^{69}									
Ga^{71}	3.23	3.13	3.71	3.86	4.14	3.89	3.78	4.11	4.10
Rb^{85}	0.01	0.01	-	-	0.01	0.01	0.02	-	0.04
Sr^{88}	0.01	0.04	-	0.02	-	-	0.02	-	0.53

Sample Mean (ppm)	LA-21-DT-096-37	LA-21-DT-096-38	LA-21-DT-096-39	LA-21-DT-096-40	LA-21-DT-096-41	LA-21-DT-096-42	LA-21-DT-096-43	LA-21-DT-096-44	LA-21-DT-096-45
Na^{23}	12.19	17.10	18.64	9.80	12.09	23.42	21.34	24.05	6.87
Mg^{24}	3660.5	3594.1	3736.7	3594.7	3627.2	3664.4	3730.1	3716.9	3687.3
Al^{27}	78694	77801	79659	77909	78220	79100	80058	80437	79958
Si^{29}									
P^{31}	73.97	85.55	88.62	89.26	79.79	73.50	79.15	83.11	81.93
K^{39}	-	3.56	11.99	2.45	1.90	3.39	0.51	0.45	1.21
Ca^{43}	10401	11539	11207	10917	10592	11247	11427	11460	12765
Sc^{45}	30.86	35.87	38.51	30.04	39.12	29.03	30.53	35.98	29.42
Ti^{47}	640.63	529.17	209.98	1386.9	214.47	183.35	300.71	205.16	352.75
Mn^{55}	18230	17476	17399	17243	18509	17468	17231	17445	17134
Fe^{57}	170006	167384	170463	168411	176820	178289	183314	184970	184520
Ga^{69}									
Ga^{71}	4.16	4.06	4.35	4.25	4.08	4.09	3.90	4.36	4.62
Rb^{85}	-	0.04	0.09	0.01	0.03	0.05	0.03	0.03	0.03
Sr^{88}	0.02	0.39	0.47	0.01	0.03	0.11	0.22	0.05	0.05

Sample Mean (ppm)	LA-21-DT-096-46	LA-21-DT-096-47	LA-21-DT-096-48	LA-21-DT-096-49	LA-21-DT-096-50	LA-21-DT-096-51	LA-21-DT-096-52	LA-21-DT-096-53	LA-21-DT-096-54
Na^{23}	11.16	24.66	44.81	18.35	17.01	105.53	38.86	32.56	25.28

Mg^{24}	3728.6	3741.9	3950.2	3948.0	3880.9	3824.8	3868.4	4153.4	4152.4
Al^{27}	78738	79108	82961	82422	83194	77943	77688	81887	81363
Si^{29}									
P^{31}	91.56	85.07	79.07	74.65	69.32	80.91	70.98	80.37	76.39
K^{39}	-	-	3.35	0.57	-	22.83	4.91	-	0.86
Ca^{43}	11585	12518	12440	12118	11778	12262	9854.9	11092	12045
Sc^{45}	32.39	26.65	25.22	30.49	30.34	23.87	21.90	27.72	24.35
Ti^{47}	217.72	215.41	740.53	180.60	270.89	127.85	128.42	180.05	195.56
Mn^{55}	16478	16344	16034	15908	18508	13330	14210	14367	13400
Fe^{57}	189286	188758	195933	195939	200852	191219	196835	208370	205681
Ga^{69}									
Ga^{71}	4.04	4.18	3.96	3.89	4.25	15.35	3.83	4.09	4.48
Rb^{85}	0.03	0.01	0.04	-	0.01	0.23	0.03	0.04	0.04
Sr^{88}	0.02	0.02	0.90	0.01	-	20.14	0.67	0.02	0.01

Sample Mean (ppm)	LA-21-DT-096-55	LA-21-DT-096-56	LA-21-DT-096-57	LA-21-DT-096-58	LA-21-DT-096-59	LA-21-DT-096-60	LA-21-DT-096J-01	LA-21-DT-096J-02	LA-21-DT-096J-03
Na^{23}	30.51	27.36	18.82	16.38	15.07	19.15	33.89	44.97	38.20
Mg^{24}	4069.1	4025.6	4319.7	3748.4	3877.0	4413.2	4544.1	4422.5	5260.5
Al^{27}	82233	82716	79283	79410	82553	80680	104635	103230	103585
Si^{29}							161204	161390	160473
P^{31}	63.69	53.61	76.17	61.44	60.10	118.16	76.44	82.78	1129.24
K^{39}	1.16	1.86	-0.12	1.89	-	0.40	4.53	38.07	1.58
Ca^{43}	11205	12411	9685.1	11658	11914	9822.6	15052	16421	16501
Sc^{45}	25.36	19.10	19.98	26.52	29.19	20.87	30.15	34.20	39.38
Ti^{47}	185.14	783.81	206.10	418.98	250.03	382.39	544.14	1046.0	408.65
Mn^{55}	14575	15515	11032	16451	16706	8341.1	22668	22258	14074

Fe^{57}	206489	206016	203067	197663	203448	205146	231358	230955	238193
Ga^{69}							6.12	5.67	5.32
Ga^{71}	4.02	3.79	3.71	4.10	3.84	4.39			
Rb^{85}	0.03	0.05	0.04	0.03	0.03	-	0.03	0.27	0.02
Sr^{88}	-	-	-	0.01	0.01	0.01	0.06	0.51	0.70

Sample Mean (ppm)	LA-21-DT-096J-04	LA-21-DT-096J-05	LA-21-DT-096J-06	LA-21-DT-096J-07	LA-21-DT-096J-08	LA-21-DT-096J-09	LA-21-DT-096J-10
Na^{23}	30.11	44.21	69.20	27.48	33.06	34.14	35.27
Mg^{24}	5342.4	4357.4	4303.2	4367.4	4474.9	4512.8	5074.9
Al^{27}	103792	102640	102393	101716	101940	101409	102682
Si^{29}	161854	162416	160624	164996	165059	165747	161921
P^{31}	103.44	73.86	72.82	64.70	68.71	64.37	71.82
K^{39}	3.42	63.29	36.52	11.09	8.83	11.73	21.90
Ca^{43}	13203	16269	15090	14342	13538	15456	15628
Sc^{45}	32.01	33.25	17.21	39.77	33.41	30.71	30.75
Ti^{47}	612.52	245.03	2492.3	288.61	189.17	361.33	394.89
Mn^{55}	13581	19881	25381	23251	16242	19714	18935
Fe^{57}	241149	233052	230390	229991	237265	230492	234438
Ga^{69}	5.09	5.74	6.03	5.29	5.09	4.97	6.09
Ga^{71}							
Rb^{85}	0.02	0.49	0.07	0.09	0.06	0.09	0.18
Sr^{88}	0.09	3.58	0.91	0.09	0.03	0.02	2.29

Sample Mean (ppm)	LA-21-DT-017-1	LA-21-DT-017-2	LA-21-DT-017-3	LA-21-DT-017-4	LA-21-DT-017-5	LA-21-DT-017-6	LA-21-DT-017-7	LA-21-DT-017-8	LA-21-DT-017-9
Y^{89}	16.55	8.73	8.14	7.28	9.87	11.01	20.71	15.68	116.76
Zr^{90}	179.69	446.48	489.28	253.39	665.11	994.66	431.91	50.69	386.13
Zr^{91}	178.60	447.95	487.83	252.11	659.27	977.16	432.91	50.15	391.72
Nb^{93}	-	0.01	0.01	0.01	0.02	0.04	0.03	0.01	0.03
Cs^{133}	-	-	0.01	-	0.01	-	-	0.01	-
Ba^{137}	-	-	-	0.05	-	-	-	-	-
La^{139}	-	-	0.20	0.13	-	-	-	-	0.08
Ce^{140}	0.01	0.01	0.50	0.31	0.01	0.01	0.01	0.01	0.32
Pr^{141}	0.01	0.01	0.07	0.06	0.01	0.01	0.01	0.01	0.06
Nd^{146}	0.25	0.27	0.52	0.55	0.25	0.44	0.26	0.20	0.48
Sm^{147}	1.16	1.05	1.00	1.09	1.08	1.23	0.90	0.86	0.95
Eu^{153}	1.01	1.03	1.44	1.20	1.05	1.30	0.90	0.85	1.09
Gd^{157}	3.63	1.98	1.96	2.08	2.16	2.26	2.47	1.97	4.93
Tb^{159}	0.60	0.30	0.29	0.29	0.33	0.35	0.47	0.41	1.37
Dy^{163}	3.69	1.62	1.68	1.42	1.85	1.98	3.29	2.89	14.19

Sample Mean (ppm)	LA-21-DT-017-10	LA-21-DT-017-11	LA-21-DT-017-12	LA-21-DT-017-13	LA-21-DT-017-14	LA-21-DT-017-15	LA-21-DT-017-16	LA-21-DT-017-17	LA-21-DT-017-18
Y^{89}	15.79	74.04	97.58	67.70	35.62	16.18	25.59	14.39	13.47
Zr^{90}	93.81	78.53	544.25	619.57	110.84	170.28	106.54	558.59	56.72
Zr^{91}	93.58	79.70	538.03	610.38	111.16	171.80	106.60	557.63	57.04
Nb^{93}	0.02	-	0.03	0.04	-	0.01	-	0.01	0.01
Cs^{133}	-	-	-	-	-	-	-	0.01	0.01
Ba^{137}	-	-	-	-	-	-	-	-	-
La^{139}	-	0.01	-	-	-	0.11	0.01	0.05	-

Ce^{140}	0.01	0.05	0.01	0.01	0.01	0.16	0.02	0.14	-
Pr^{141}	0.01	0.01	0.01	0.01	0.01	0.03	0.01	0.03	0.01
Nd^{146}	0.30	0.23	0.17	0.26	0.29	0.36	0.29	0.30	0.25
Sm^{147}	1.03	0.85	1.10	1.07	1.01	1.05	1.43	1.44	1.04
Eu^{153}	1.15	0.96	1.17	1.16	1.08	0.99	1.29	1.33	1.21
Gd^{157}	2.88	4.24	4.93	4.76	3.74	3.21	5.79	6.05	2.56
Tb^{159}	0.45	1.10	1.31	1.11	0.81	0.63	1.01	0.86	0.40
Dy^{163}	3.04	10.68	13.51	10.02	6.28	3.69	6.38	3.91	2.40

Sample Mean (ppm)	LA-21-DT-017-19	LA-21-DT-017-20	LA-21-DT-017-22	LA-21-DT-017-23	LA-21-DT-017-24	LA-21-DT-017-25	LA-21-DT-017-26	LA-21-DT-017-27	LA-21-DT-017-28
Y^{89}	19.55	9.40	46.71	12.20	10.18	3.73	8.43	21.74	12.92
Zr^{90}	279.91	1379.20	209.65	759.69	369.49	724.75	77.05	229.08	138.66
Zr^{91}	281.92	1350.25	213.46	734.50	370.98	714.72	77.25	228.97	140.14
Nb^{93}	0.02	0.01	0.01	0.03	0.03	0.01	0.02	0.01	0.02
Cs^{133}	0.01	0.01	0.01	0.01	0.01	0.01	0.01	0.02	0.02
Ba^{137}	-	-	-	-	-	-	-	-	0.05
La^{139}	-	-	-	0.02	0.10	-	-	-	13.76
Ce^{140}	0.01	0.01	0.01	0.08	0.39	0.02	0.01	0.01	18.60
Pr^{141}	-	0.01	0.01	0.02	0.08	0.01	-	0.01	1.53
Nd^{146}	0.31	0.22	0.19	0.33	0.83	0.17	0.28	0.25	4.43
Sm^{147}	1.18	0.84	0.76	1.16	1.02	1.05	0.95	1.01	1.32
Eu^{153}	1.28	0.80	0.93	1.13	1.16	1.06	1.20	1.20	1.48
Gd^{157}	3.17	2.23	3.21	2.08	2.16	2.54	1.72	2.91	2.74
Tb^{159}	0.52	0.36	0.71	0.31	0.30	0.24	0.24	0.49	0.39
Dy^{163}	3.39	2.05	6.32	2.14	1.70	0.88	1.51	3.35	2.42

Sample Mean (ppm)	LA-21-DT-017-29	LA-21-DT-017-30	LA-21-DT-017-31	LA-21-DT-017-32	LA-21-DT-017-34	LA-21-DT-017-35	LA-21-DT-017-36	LA-21-DT-017-37	LA-21-DT-017-38
Y^{89}	22.81	24.87	10.03	15.64	20.22	15.35	20.84	35.20	32.15
Zr^{90}	368.32	3736.0	176.09	986.62	372.07	32.38	690.90	680.43	1192.6
Zr^{91}	367.85	3550.3	175.12	938.72	375.77	33.35	674.06	662.32	1149.3
Nb^{93}	0.02	0.05	0.02	0.03	0.02	0.04	0.05	0.03	0.03
Cs^{133}	0.01	0.02	0.01	0.01	-	0.01	0.01	0.01	0.01
Ba^{137}	-	-	-	0.07	-	0.05	0.05	-	-
La^{139}	-	0.01	-	0.01	-	0.39	0.27	-	0.01
Ce^{140}	0.01	0.03	0.01	0.02	0.02	1.25	1.02	0.01	0.02
Pr^{141}	-	0.01	0.01	0.01	-	0.22	0.20	0.01	0.01
Nd^{146}	0.29	0.31	0.21	0.21	0.26	1.60	1.34	0.27	0.27
Sm^{147}	1.10	1.16	1.00	0.94	1.16	1.91	1.59	1.04	1.09
Eu^{153}	1.20	1.27	1.29	1.31	1.30	1.38	1.55	1.21	1.31
Gd^{157}	2.74	2.66	2.20	2.30	2.90	3.67	3.51	3.15	3.23
Tb^{159}	0.46	0.46	0.29	0.36	0.48	0.50	0.52	0.63	0.63
Dy^{163}	3.29	3.48	1.77	2.36	3.41	2.90	3.40	5.12	4.86

Sample Mean (ppm)	LA-21-DT-017-39	LA-21-DT-017-40	LA-21-DT-017-41	LA-21-DT-017-42	LA-21-DT-017-43	LA-21-DT-017-44	LA-21-DT-017-45	LA-21-DT-017-46	LA-21-DT-017-47
Y^{89}	23.63	23.24	33.50	35.42	14.04	28.26	20.43	8.69	13.24
Zr^{90}	305.44	441.35	303.86	374.65	632.05	924.52	576.65	1139.2	1312.2
Zr^{91}	306.60	439.68	305.83	385.18	616.13	889.69	570.10	1088.9	1245.4
Nb^{93}	0.02	0.03	0.03	0.06	0.02	0.02	0.02	0.03	0.02
Cs^{133}	0.01	0.01	0.01	0.01	0.01	0.01	0.01	-	0.01
Ba^{137}	-	-	0.01	0.04	-	0.09	-	-	-
La^{139}	-	-	0.17	0.73	0.02	1.42	0.87	-	-

Ce^{140}	0.01	0.01	0.34	2.23	0.06	6.25	3.26	0.02	0.01
Pr^{141}	-	-	0.05	0.40	0.02	1.32	0.62	0.01	0.01
Nd^{146}	0.21	0.23	0.39	2.63	0.23	9.52	4.92	0.28	0.35
Sm^{147}	0.96	1.02	1.08	1.93	1.02	3.68	2.47	1.10	1.21
Eu^{153}	1.27	1.27	1.22	1.84	1.13	3.31	2.37	1.35	1.36
Gd^{157}	3.03	3.23	3.69	4.15	2.60	5.34	4.13	1.86	2.52
Tb^{159}	0.52	0.53	0.67	0.71	0.40	0.69	0.55	0.25	0.39
Dy^{163}	3.69	3.65	5.32	5.36	2.42	4.61	3.47	1.43	2.13

Sample Mean (ppm)	LA-21-DT-017-48	LA-21-DT-017-49	LA-21-DT-017-50	LA-21-DT-017-51	LA-21-DT-017-52	LA-21-DT-017-53	LA-21-DT-017-54	LA-21-DT-017-55	LA-21-DT-017-56
Y^{89}	5.54	13.18	20.60	31.28	43.94	23.96	42.33	25.39	5.62
Zr^{90}	835.62	1978.81	431.28	260.37	626.08	501.82	969.13	2371.8	257.82
Zr^{91}	808.06	1860.1	431.64	263.62	620.29	503.88	946.16	2228.0	256.07
Nb^{93}	0.03	0.11	0.02	0.03	0.04	0.04	0.03	0.06	0.02
Cs^{133}	0.02	0.02	-	0.01	-	-	0.02	-	0.01
Ba^{137}	0.02	0.14	-	-	-	-	0.54	0.07	-
La^{139}	0.32	1.21	-	-	-	0.06	54.07	0.01	-
Ce^{140}	0.60	3.70	0.01	0.01	0.01	0.19	120.16	0.05	0.02
Pr^{141}	0.07	0.51	-	-	0.01	0.04	13.00	0.01	0.01
Nd^{146}	0.52	3.42	0.24	0.24	0.23	0.42	51.70	0.31	0.30
Sm^{147}	1.03	1.88	1.01	1.13	1.14	1.02	9.81	1.08	0.96
Eu^{153}	1.50	3.11	1.18	1.29	1.21	1.18	3.67	1.24	1.23
Gd^{157}	1.79	2.69	2.86	3.75	3.66	3.26	9.26	2.95	1.77
Tb^{159}	0.19	0.34	0.50	0.64	0.73	0.53	1.30	0.52	0.22
Dy^{163}	0.91	2.09	3.32	5.03	6.08	3.93	8.18	3.79	1.15

Sample Mean (ppm)	LA-21-DT-017-57	LA-21-DT-017-58	LA-21-DT-017-59	LA-21-DT-017-60	LA-21-DT-017J-01	LA-21-DT-017J-02	LA-21-DT-017J-03	LA-21-DT-017J-04	LA-21-DT-017J-05
Y^{89}	9.53	5.08	24.02	16.79	16.12	17.06	49.15	24.43	15.65
Zr^{90}	542.89	212.32	21.21	1511.5					
Zr^{91}	540.55	207.18	20.40	1408.9	42.61	10.96	8.83	7.36	42.74
Nb^{93}	0.02	0.01	0.01	0.01	0.14	-	-	-	-
Cs^{133}	-	-	-	-	-	0.01	-	-	-
Ba^{137}	-	-	-	-	-	-	-	-	-
La^{139}	-	0.02	0.20	-	0.58	-	-	-	-
Ce^{140}	0.01	0.04	0.70	0.01	1.67	0.01	-	-	-
Pr^{141}	0.01	0.01	0.14	0.01	0.27	-	-	0.01	-
Nd^{146}	0.22	0.28	1.21	0.30	1.86	0.24	0.36	0.32	0.32
Sm^{147}	0.87	0.86	1.64	1.17	2.45	1.97	1.92	1.90	1.89
Eu^{153}	0.99	1.10	1.20	1.02	1.56	1.68	1.69	1.73	1.51
Gd^{157}	1.75	1.62	4.81	3.17	8.07	8.42	9.90	9.01	7.30
Tb^{159}	0.25	0.18	0.81	0.52	1.16	1.27	2.04	1.38	1.15
Dy^{163}	1.67	1.14	5.26	3.46	4.74	5.38	11.57	6.76	4.90

Sample Mean (ppm)	LA-21-DT-017J-06	LA-21-DT-017J-07	LA-21-DT-017J-08	LA-21-DT-017J-09	LA-21-DT-017J-10	LA-21-DT-021-01	LA-21-DT-021-02	LA-21-DT-021-03	LA-21-DT-021-04
Y^{89}	26.22	7.52	3.21	29.65	28.81	20.27	3.73	5.80	6.38
Zr^{90}									
Zr^{91}	6.60	7.97	6.44	7.41	6.28	6.86	75.04	7.66	6.51
Nb^{93}	-	-	-	-	-	4.88	4.28	4.17	1.62
Cs^{133}	-	-	-	-	-	-	0.09	-	-
Ba^{137}	-	-	0.01	-	-	1.04	4.92	0.65	0.35
La^{139}	-	-	-	-	-	0.02	0.01	0.05	0.19

Ce^{140}	-	-	-	0.01	-	0.07	0.03	0.56	0.23
Pr^{141}	0.01	-	-	0.01	0.01	0.03	0.01	0.05	0.02
Nd^{146}	0.28	0.26	0.26	0.30	0.24	0.76	0.30	1.03	0.62
Sm^{147}	1.94	1.57	1.70	1.61	1.77	0.59	0.41	0.74	0.51
Eu^{153}	1.80	1.56	1.60	1.58	1.54	1.42	0.66	1.54	1.31
Gd^{157}	8.62	6.20	4.07	6.61	6.39	0.90	0.50	0.60	0.54
Tb^{159}	1.51	0.73	0.38	1.19	1.11	0.20	0.07	0.12	0.11
Dy^{163}	6.97	2.88	1.39	6.58	6.50	1.70	0.43	0.60	0.63

Sample Mean (ppm)	LA-21-DT-021-05	LA-21-DT-021-06	LA-21-DT-021-07	LA-21-DT-021-08	LA-21-DT-021-09	LA-21-DT-021-10	LA-21-DT-049-01	LA-21-DT-049-02	LA-21-DT-049-03
Y^{89}	12.99	8.24	14.75	86.52	22.72	43.04	43.88	34.07	141.98
Zr^{90}									
Zr^{91}	63.80	44.46	19.53	7.97	2.58	2.63	23.68	14.48	4.38
Nb^{93}	0.56	1.78	0.24	0.63	0.11	0.03	0.07	0.44	0.28
Cs^{133}	-	-	-	0.01	-	-	0.05	0.03	0.06
Ba^{137}	-	-	-	-	-	-	0.13	0.03	0.11
La^{139}	0.01	0.03	0.01	0.10	2.62	-	0.40	0.17	0.26
Ce^{140}	0.01	0.06	0.04	0.11	5.49	0.01	0.84	0.30	0.82
Pr^{141}	-	0.01	0.01	0.02	0.55	-	0.10	0.04	0.13
Nd^{146}	0.17	0.25	0.22	0.33	2.18	0.13	0.63	0.20	0.64
Sm^{147}	0.53	0.86	0.76	1.01	1.05	0.78	1.05	0.96	1.21
Eu^{153}	0.76	0.93	0.76	1.03	0.73	0.71	0.99	0.86	0.57
Gd^{157}	1.00	1.31	1.90	3.92	2.07	3.52	5.21	5.52	11.62
Tb^{159}	0.22	0.18	0.33	0.94	0.41	0.78	0.95	0.90	2.97
Dy^{163}	1.42	1.17	1.91	9.22	3.06	6.10	6.38	5.32	25.33

Sample Mean (ppm)	LA-21-DT-049-04	LA-21-DT-049-05	LA-21-DT-049-06	LA-21-DT-049-07	LA-21-DT-049-08	LA-21-DT-049-09	LA-21-DT-049-10	LA-21-DT-074-01	LA-21-DT-074-02
Y^{89}	110.44	214.41	58.17	166.24	118.67	23.47	119.15	64.06	36.78
Zr^{90}									
Zr^{91}	393.46	141.70	147.36	45.10	76.73	232.47	166.34	100.07	7.73
Nb^{93}	0.72	0.11	0.43	0.19	0.29	1.34	0.46	1.23	0.15
Cs^{133}	0.42	-	0.01	0.02	-	0.01	0.01	-	0.01
Ba^{137}	0.13	-	-	-	-	-	-	0.10	0.64
La^{139}	1.36	0.09	-	0.03	-	0.03	0.63	1.21	-
Ce^{140}	3.63	0.33	0.01	0.03	-	0.09	2.53	3.08	0.02
Pr^{141}	0.51	0.09	-	0.01	-	0.02	0.41	0.41	0.01
Nd^{146}	2.67	0.52	0.17	0.12	0.14	0.19	2.85	1.98	0.30
Sm^{147}	1.76	1.41	0.72	0.96	1.06	0.60	2.40	2.09	0.55
Eu^{153}	0.99	0.94	0.87	1.10	0.94	0.85	1.67	1.76	0.84
Gd^{157}	8.81	14.76	3.80	9.91	6.01	2.08	8.21	8.19	1.64
Tb^{159}	1.84	4.05	0.81	2.45	1.56	0.39	1.79	1.64	0.37
Dy^{163}	15.07	33.90	7.19	21.25	13.77	2.79	14.85	10.64	3.95

Sample Mean (ppm)	LA-21-DT-074-03	LA-21-DT-074-04	LA-21-DT-074-05	LA-21-DT-074-06	LA-21-DT-074-07	LA-21-DT-074-08	LA-21-DT-074-09	LA-21-DT-074-10	LA-21-DT-096-1
Y^{89}	52.49	30.97	21.58	43.99	78.91	45.72	39.47	26.39	51.67
Zr^{90}									1706.1
Zr^{91}	36.52	4.82	174.37	101.77	18.57	260.75	226.00	24.99	1614.6
Nb^{93}	0.02	3.69	0.82	0.17	0.47	0.07	0.50	0.43	0.09
Cs^{133}	-	-	0.02	0.14	-	0.01	-	-	-
Ba^{137}	-	4.27	14.30	0.22	0.08	0.02	-	0.07	1.89
La^{139}	0.08	0.01	2.39	25.06	134.85	0.01	74.83	100.97	3.48

Ce^{140}	0.17	0.01	5.98	62.60	283.90	0.05	150.04	176.18	24.40
Pr^{141}	0.04	0.01	0.84	7.73	29.83	0.01	14.31	16.92	5.57
Nd^{146}	0.42	0.14	3.98	31.60	106.07	0.33	49.04	54.38	35.38
Sm^{147}	1.43	0.18	1.93	7.91	18.35	1.94	7.32	5.79	20.39
Eu^{153}	1.54	0.60	1.10	2.07	6.98	1.80	3.46	3.92	7.68
Gd^{157}	6.41	0.67	2.34	14.30	16.95	5.00	7.70	3.24	21.72
Tb^{159}	1.33	0.20	0.46	2.02	2.28	0.94	1.08	0.38	2.63
Dy^{163}	9.64	2.68	2.96	10.12	14.34	6.70	6.36	3.31	12.51

Sample Mean (ppm)	LA-21-DT-096-9	LA-21-DT-096-11	LA-21-DT-096-12	LA-21-DT-096-13	LA-21-DT-096-14	LA-21-DT-096-21	LA-21-DT-096-23	LA-21-DT-096-26	LA-21-DT-096-28
Y^{89}	29.73	46.15	69.96	56.54	57.91	83.33	132.17	106.55	188.46
Zr^{90}	244.02	278.40	141.17	190.14	142.30	695.44	501.92	337.73	469.94
Zr^{91}	243.62	277.60	140.67	189.99	139.40	697.29	508.73	337.76	467.43
Nb^{93}	-	0.01	0.01	0.01	0.04	0.06	1.27	0.05	0.06
Cs^{133}	0.01	-	-	-	-	-	-	-	-
Ba^{137}	-	-	-	-	-	-	-	-	0.18
La^{139}	-	0.01	-	-	-	0.01	-	0.01	0.98
Ce^{140}	0.01	0.02	0.01	0.01	0.01	0.03	0.04	0.17	3.33
Pr^{141}	0.02	0.01	0.01	0.01	0.01	0.01	0.01	0.01	0.37
Nd^{146}	0.32	0.35	0.33	0.26	0.29	0.40	0.37	0.32	1.51
Sm^{147}	2.07	2.13	1.52	1.32	1.50	1.19	1.53	1.33	1.74
Eu^{153}	1.14	1.27	1.08	0.91	0.89	0.87	1.03	1.02	2.25
Gd^{157}	8.92	10.67	6.22	5.49	6.03	4.38	5.89	5.21	7.19
Tb^{159}	1.55	2.05	1.43	1.21	1.25	0.99	1.47	1.42	1.94
Dy^{163}	7.63	11.11	10.98	9.28	9.59	9.50	14.30	12.84	20.08

Sample Mean (ppm)	LA-21-DT-096-37	LA-21-DT-096-38	LA-21-DT-096-39	LA-21-DT-096-40	LA-21-DT-096-41	LA-21-DT-096-42	LA-21-DT-096-43	LA-21-DT-096-44	LA-21-DT-096-45
Y^{89}	69.31	109.11	107.15	126.93	86.00	140.52	114.24	233.48	130.51
Zr^{90}	120.82	778.14	408.38	231.16	169.77	186.68	419.55	1155.0	195.34
Zr^{91}	122.03	770.29	404.26	231.77	169.33	190.73	406.88	1135.1	196.28
Nb^{93}	0.58	0.52	0.05	1.64	0.10	0.04	0.15	0.09	0.23
Cs^{133}	-	0.01	0.02	0.01	0.01	0.01	0.01	0.01	0.01
Ba^{137}	-	0.11	0.24	-	-	0.03	0.11	-	-
La^{139}	0.01	0.47	0.69	0.02	0.04	1.13	0.28	0.04	0.02
Ce^{140}	0.05	2.93	2.79	0.08	0.11	2.21	0.75	0.19	0.09
Pr^{141}	0.01	0.56	0.36	0.02	0.01	0.21	0.08	0.02	0.02
Nd^{146}	0.30	3.22	1.70	0.37	0.45	1.09	0.37	0.37	0.42
Sm^{147}	1.15	3.07	1.98	1.78	1.52	1.72	1.47	1.54	1.73
Eu^{153}	0.94	2.22	2.15	1.28	1.12	1.27	1.15	1.12	1.30
Gd^{157}	4.59	7.40	5.93	7.22	5.24	7.01	6.89	8.44	7.15
Tb^{159}	1.00	1.67	1.42	1.79	1.17	1.82	1.62	2.45	1.78
Dy^{163}	8.28	13.71	12.84	15.83	10.11	16.85	14.65	26.24	15.75

Sample Mean (ppm)	LA-21-DT-096-46	LA-21-DT-096-47	LA-21-DT-096-48	LA-21-DT-096-49	LA-21-DT-096-50	LA-21-DT-096-51	LA-21-DT-096-52	LA-21-DT-096-53	LA-21-DT-096-54
Y^{89}	125.68	161.89	228.04	132.47	94.12	304.62	158.95	112.87	158.95
Zr^{90}	436.13	415.15	1753.4	720.69	146.96	56.52	1094.7	625.73	746.66
Zr^{91}	432.41	415.42	1702.2	722.40	145.62	56.91	1058.3	625.24	736.26
Nb^{93}	0.06	0.05	0.83	0.06	0.05	0.11	0.01	0.06	0.05
Cs^{133}	0.02	0.01	0.01	0.02	0.01	0.01	-	-	-
Ba^{137}	-	-	0.28	-	-	3.92	0.39	-	0.01
La^{139}	-	0.02	0.18	0.25	0.21	979.81	3.46	1.04	0.24

Ce^{140}	0.04	0.08	0.26	0.56	0.45	1907.06	10.39	2.51	0.72
Pr^{141}	0.02	0.01	0.02	0.05	0.05	190.21	1.02	0.21	0.06
Nd^{146}	0.27	0.27	0.22	0.46	0.46	707.38	3.40	0.91	0.39
Sm^{147}	1.43	1.50	1.21	1.39	1.50	109.26	1.40	1.39	1.58
Eu^{153}	1.10	1.21	1.11	1.13	1.17	21.74	3.19	1.03	1.22
Gd^{157}	6.78	8.04	8.47	6.72	5.22	77.42	7.57	7.55	8.75
Tb^{159}	1.68	2.19	2.63	1.86	1.32	9.27	2.19	1.89	2.28
Dy^{163}	15.35	20.30	27.30	16.71	11.25	55.75	20.11	15.71	20.48

Sample Mean (ppm)	LA-21-DT-096-55	LA-21-DT-096-56	LA-21-DT-096-57	LA-21-DT-096-58	LA-21-DT-096-59	LA-21-DT-096-60	LA-21-DT-096J-01	LA-21-DT-096J-02	LA-21-DT-096J-03
Y^{89}	99.02	235.68	50.94	147.17	97.45	41.81	107.32	136.31	132.36
Zr^{90}	121.91	267.01	565.75	160.81	122.68	359.74			
Zr^{91}	122.36	267.40	563.56	159.50	122.36	360.70	146.46	58.25	102.34
Nb^{93}	0.02	0.88	0.01	0.52	0.02	0.25	0.35	1.13	0.26
Cs^{133}	-	-	-	-	-	-	-	0.01	-
Ba^{137}	-	-	-	-	-	-	0.04	0.12	0.02
La^{139}	0.08	0.02	0.03	0.10	0.02	0.02	0.09	1.73	0.28
Ce^{140}	0.25	0.10	0.04	0.32	0.06	0.04	0.42	3.14	0.82
Pr^{141}	0.05	0.01	0.02	0.04	0.02	0.03	0.09	0.37	0.14
Nd^{146}	0.34	0.15	0.26	0.35	0.29	0.37	0.77	1.87	0.99
Sm^{147}	1.21	0.91	1.31	1.53	1.13	1.62	1.89	2.52	2.20
Eu^{153}	1.02	0.87	1.00	1.19	1.05	1.18	1.54	1.83	1.37
Gd^{157}	7.41	8.13	5.94	7.95	5.75	6.30	6.49	9.05	9.26
Tb^{159}	1.76	2.68	1.24	2.06	1.38	1.13	1.58	2.20	2.31
Dy^{163}	14.14	28.94	8.40	19.06	12.38	7.15	13.09	17.50	18.36

Sample Mean (ppm)	LA-21-DT-096J-04	LA-21-DT-096J-05	LA-21-DT-096J-06	LA-21-DT-096J-07	LA-21-DT-096J-08	LA-21-DT-096J-09	LA-21-DT-096J-10
Y^{89}	114.80	213.71	50.74	115.33	189.37	140.09	127.05
Zr^{90}							
Zr^{91}	371.55	50.46	31.40	73.33	76.71	155.84	250.19
Nb^{93}	0.53	0.06	2.55	0.06	0.02	0.18	0.26
Cs^{133}	-	0.02	-	-	-	-	0.01
Ba^{137}	0.10	0.55	0.20	0.10	0.02	0.10	0.23
La^{139}	0.08	267.27	58.42	2.70	0.02	0.02	224.02
Ce^{140}	0.57	528.15	122.57	5.05	0.04	0.06	419.78
Pr^{141}	0.16	53.23	12.25	0.51	0.01	0.01	42.25
Nd^{146}	1.24	184.36	41.43	1.92	0.26	0.34	152.52
Sm^{147}	2.50	26.66	7.87	2.05	1.63	1.58	24.50
Eu^{153}	1.43	4.00	1.64	1.42	1.21	1.29	3.56
Gd^{157}	9.91	22.71	8.28	7.06	9.54	7.57	19.73
Tb^{159}	2.31	3.94	1.32	1.70	2.68	2.10	2.94
Dy^{163}	16.99	29.21	7.73	14.01	23.43	17.51	18.96

Sample Mean (ppm)	LA-21-DT-017-1	LA-21-DT-017-2	LA-21-DT-017-3	LA-21-DT-017-4	LA-21-DT-017-5	LA-21-DT-017-6	LA-21-DT-017-7	LA-21-DT-017-8	LA-21-DT-017-9
Ho^{165}	0.60	0.27	0.27	0.26	0.37	0.38	0.78	0.60	4.42
Er^{166}	1.36	0.79	0.80	0.67	1.08	1.17	2.72	1.81	19.77
Tm^{169}	0.15	0.15	0.12	0.10	0.16	0.21	0.41	0.24	3.55
Yb^{172}	1.07	1.20	0.95	0.85	1.40	1.66	3.60	1.90	29.61
Lu^{175}	0.17	0.25	0.20	0.18	0.28	0.33	0.69	0.34	5.30
Hf^{178}	4.39	11.31	12.35	6.25	16.30	23.94	10.80	1.18	10.45
Hf^{179}									

Ta^{181}	-	0.01	0.01	-	0.01	0.01	0.01	0.01	0.02
Pb^{204}	0.35	0.41	0.21	0.24	0.44	0.55	0.28	0.14	0.47
Pb^{206}	2.53	7.10	6.67	3.42	10.08	16.69	6.00	1.04	4.62
Pb^{207}	0.55	1.45	1.36	0.66	1.93	3.27	1.20	0.23	0.88
Pb^{208}	0.02	0.09	0.05	0.07	0.04	0.09	0.04	0.02	0.05
Th^{232}	0.04	0.28	0.20	0.32	0.09	0.28	0.16	0.05	0.08
U^{238}	0.92	3.17	3.17	1.93	3.60	7.01	2.72	0.40	2.80
Pb Total	0.75	2.10	1.96	1.02	2.90	4.83	1.76	0.32	1.35

Sample Mean (ppm)	LA-21-DT-017-10	LA-21-DT-017-11	LA-21-DT-017-12	LA-21-DT-017-13	LA-21-DT-017-14	LA-21-DT-017-15	LA-21-DT-017-16	LA-21-DT-017-17	LA-21-DT-017-18
Ho^{165}	0.56	2.63	3.64	2.49	1.27	0.59	0.91	0.48	0.44
Er^{166}	1.70	10.58	14.77	9.25	4.31	1.68	2.08	1.15	1.35
Tm^{169}	0.25	1.58	2.29	1.44	0.58	0.22	0.22	0.17	0.20
Yb^{172}	1.94	12.47	18.42	11.16	4.28	1.61	1.62	1.49	1.41
Lu^{175}	0.33	2.00	3.07	1.75	0.68	0.26	0.21	0.26	0.25
Hf^{178}	2.41	1.93	14.16	15.63	2.96	4.47	2.90	15.31	1.47
Hf^{179}									
Ta^{181}	0.01	0.01	0.01	0.01	-	0.01	-	0.01	0.01
Pb^{204}	0.21		0.20	0.41	0.38				
Pb^{206}	1.30	1.61	8.49	9.67	1.88	2.61	1.09	9.81	0.90
Pb^{207}	0.27	0.33	1.73	1.97	0.37	0.54	0.22	2.01	0.20
Pb^{208}	0.02	0.03	0.08	0.09	0.02	0.04	0.02	0.16	0.01
Th^{232}	0.05	0.29	0.20	0.28	0.04	0.04	0.02	0.47	0.03
U^{238}	0.58	0.63	4.15	4.59	0.79	1.15	0.59	3.28	0.40
Pb Total	0.39	0.48	2.49	2.83	0.55	0.78	0.32	2.92	0.28

Sample Mean(ppm)	LA-21-DT-017-19	LA-21-DT-017-20	LA-21-DT-017-22	LA-21-DT-017-23	LA-21-DT-017-24	LA-21-DT-017-25	LA-21-DT-017-26	LA-21-DT-017-27	LA-21-DT-017-28
Ho^{165}	0.64	0.32	1.60	0.42	0.35	0.13	0.29	0.74	0.44
Er^{166}	1.95	0.97	6.31	1.55	1.25	0.43	1.05	2.95	1.39
Tm^{169}	0.30	0.17	1.01	0.27	0.19	0.10	0.17	0.42	0.22
Yb^{172}	2.42	1.72	8.41	2.73	1.73	0.93	1.50	4.13	1.92
Lu^{175}	0.41	0.35	1.38	0.54	0.36	0.20	0.28	0.73	0.34
Hf^{178}	6.70	35.53	5.30	19.26	9.50	17.28	1.91	6.09	3.73
Hf^{179}									
Ta^{181}	0.02	0.01	0.01	0.01	0.01	-	0.01	0.01	0.01
Pb^{204}	0.12	0.22	0.42	0.17	-	-	0.37	0.51	0.60
Pb^{206}	5.71	17.15	3.10	10.77	4.96	12.71	1.21	2.42	2.97
Pb^{207}	1.23	3.41	0.69	2.25	0.96	2.58	0.29	0.50	0.60
Pb^{208}	0.11	0.16	0.03	0.13	0.05	0.16	0.03	0.02	0.19
Th^{232}	0.25	0.62	0.05	0.52	0.16	0.40	0.05	0.10	0.12
U^{238}	1.98	8.48	1.26	5.44	2.60	5.20	0.56	1.32	1.25
Pb Total	1.73	5.00	0.92	3.17	1.44	3.73	0.37	0.71	0.96

Sample Mean(ppm)	LA-21-DT-017-29	LA-21-DT-017-30	LA-21-DT-017-31	LA-21-DT-017-32	LA-21-DT-017-34	LA-21-DT-017-35	LA-21-DT-017-36	LA-21-DT-017-37	LA-21-DT-017-38
Ho^{165}	0.80	0.84	0.32	0.50	0.64	0.50	0.68	1.28	1.12
Er^{166}	3.31	3.79	1.19	2.15	2.40	1.45	2.39	5.43	4.50
Tm^{169}	0.54	0.69	0.19	0.38	0.40	0.17	0.39	0.88	0.76
Yb^{172}	5.07	7.52	1.91	3.84	3.38	1.26	3.27	8.64	6.84
Lu^{175}	0.95	1.56	0.34	0.73	0.62	0.18	0.61	1.72	1.27
Hf^{178}	9.70	93.57	4.61	23.89	10.35	0.77	17.11	17.33	29.68
Hf^{179}									

Ta^{181}	0.01	0.03	0.01	0.02	0.01	0.01	0.01	0.01	0.02
Pb^{204}	0.46	0.44	0.24	0.10	0.25	0.16	0.25	0.09	0.34
Pb^{206}	4.26	36.64	3.68	15.75	6.15	0.66	8.28	7.42	16.88
Pb^{207}	0.90	7.44	0.79	3.08	1.24	0.16	1.70	1.46	3.39
Pb^{208}	0.03	0.16	0.07	0.38	0.12	0.26	0.16	0.04	0.14
Th^{232}	0.16	0.74	0.18	0.66	0.48	3.07	0.90	0.19	0.46
U^{238}	2.20	20.30	1.85	7.22	2.81	1.62	4.93	4.00	7.34
Pb Total	1.25	10.60	1.11	4.71	1.83	0.32	2.48	2.15	4.93

Sample Mean(ppm)	LA-21-DT-017-39	LA-21-DT-017-40	LA-21-DT-017-41	LA-21-DT-017-42	LA-21-DT-017-43	LA-21-DT-017-44	LA-21-DT-017-45	LA-21-DT-017-46	LA-21-DT-017-47
Ho^{165}	0.79	0.72	1.18	1.18	0.39	0.89	0.67	0.28	0.41
Er^{166}	2.92	2.54	4.45	4.35	1.47	3.26	2.41	1.08	1.58
Tm^{169}	0.47	0.39	0.69	0.74	0.23	0.56	0.36	0.22	0.26
Yb^{172}	4.08	3.30	5.96	5.88	2.26	5.09	3.55	2.60	2.58
Lu^{175}	0.74	0.61	1.05	0.99	0.42	0.94	0.69	0.50	0.46
Hf^{178}	7.79	10.67	8.00	9.69	16.04	21.96	15.01	28.01	30.69
Hf^{179}									
Ta^{181}	0.01	0.01	0.02	0.02	0.01	0.01	0.01	0.01	0.01
Pb^{204}	0.07	0.40	0.31	0.35	0.41	0.25	0.23	0.12	0.39
Pb^{206}	5.10	7.72	4.65	3.31	8.53	12.24	5.80	17.46	21.02
Pb^{207}	1.08	1.54	1.14	0.58	1.65	2.46	1.09	3.46	4.15
Pb^{208}	0.10	0.14	0.23	0.09	0.15	0.14	0.09	0.17	0.15
Th^{232}	0.34	0.38	0.14	0.34	0.52	0.31	0.21	0.51	0.36
U^{238}	2.50	3.15	2.30	2.18	4.29	5.88	3.47	7.64	8.58
Pb Total	1.53	2.30	1.51	0.99	2.53	3.61	1.70	5.10	6.10

Sample Mean(ppm)	LA-21-DT-017-48	LA-21-DT-017-49	LA-21-DT-017-50	LA-21-DT-017-51	LA-21-DT-017-52	LA-21-DT-017-53	LA-21-DT-017-54	LA-21-DT-017-55	LA-21-DT-017-56
Ho^{165}	0.14	0.42	0.66	1.07	1.59	0.85	1.55	0.80	0.15
Er^{166}	0.64	1.71	2.33	3.99	6.34	3.14	5.40	3.61	0.61
Tm^{169}	0.13	0.35	0.36	0.63	1.14	0.56	0.85	0.65	0.10
Yb^{172}	1.31	3.67	3.16	5.53	9.76	4.86	7.22	6.76	0.92
Lu^{175}	0.31	0.82	0.56	0.96	1.73	0.90	1.34	1.29	0.18
Hf^{178}	21.13	47.73	11.46	6.58	16.85	13.35	26.18	59.14	6.37
Hf^{179}									
Ta^{181}	0.01	0.02	0.01	0.01	0.02	0.02	0.02	0.03	0.01
Pb^{204}	-	0.24	0.08	0.32	0.07	0.16	0.13	0.24	0.03
Pb^{206}	8.97	23.02	7.16	3.91	7.54	7.59	11.80	36.04	4.34
Pb^{207}	1.82	4.39	1.54	0.82	1.57	1.46	2.33	7.20	0.84
Pb^{208}	0.12	0.47	0.12	0.07	0.07	0.14	3.35	0.42	0.09
Th^{232}	0.19	1.48	0.45	0.12	0.29	0.31	31.79	1.38	0.24
U^{238}	4.74	12.80	3.45	1.59	3.89	3.12	11.57	15.58	1.85
Pb Total	2.64	6.80	2.14	1.17	2.21	2.23	5.12	10.52	1.28

Sample Mean(ppm)	LA-21-DT-017-57	LA-21-DT-017-58	LA-21-DT-017-59	LA-21-DT-017-60	LA-21-DT-017J-01	LA-21-DT-017J-02	LA-21-DT-017J-03	LA-21-DT-017J-04	LA-21-DT-017J-05
Ho^{165}	0.32	0.16	0.92	0.63	0.54	0.54	1.68	0.86	0.55
Er^{166}	1.19	0.58	2.33	1.93	0.85	0.79	3.60	1.80	0.99
Tm^{169}	0.23	0.10	0.27	0.30	0.08	0.07	0.39	0.17	0.09
Yb^{172}	2.25	0.84	2.03	2.65	0.41	0.37	2.27	1.09	0.45
Lu^{175}	0.46	0.16	0.29	0.47	0.05	0.05	0.35	0.16	0.09
Hf^{178}	14.18	5.34	0.46	36.86					
Hf^{179}					1.09	0.23	0.07	0.07	1.17

Ta^{181}	0.01	0.01	-	0.01	0.02	-	-	-	-
Pb^{204}	0.18	0.59	0.45	0.58		0.45	0.55	-	-
Pb^{206}	7.46	2.79	0.25	21.79	0.63	0.26	0.05	0.05	0.48
Pb^{207}	1.47	0.59	0.08	4.41	0.12	0.04	0.02	0.01	0.12
Pb^{208}	0.07	0.05	0.08	0.09	0.14	0.01	-	0.01	0.02
Th^{232}	0.24	0.15	0.25	0.30	0.77	0.01	0.01	-	0.08
U^{238}	3.71	1.31	0.86	8.49	0.72	0.06	0.03	0.02	0.25
Pb Total	2.17	0.84	0.11	6.32					

Sample Mean(ppm)	LA-21-DT-017J-06	LA-21-DT-017J-07	LA-21-DT-017J-08	LA-21-DT-017J-09	LA-21-DT-017J-10	LA-21-DT-021-01	LA-21-DT-021-02	LA-21-DT-021-03	LA-21-DT-021-04
Ho^{165}	0.88	0.27	0.12	1.19	1.19	0.57	0.09	0.11	0.15
Er^{166}	1.74	0.40	0.17	3.31	2.81	2.51	0.35	0.35	0.51
Tm^{169}	0.16	0.03	0.01	0.40	0.38	0.54	0.09	0.07	0.09
Yb^{172}	1.07	0.16	0.06	2.95	2.50	4.34	0.63	0.49	0.64
Lu^{175}	0.12	0.02	0.01	0.45	0.42	0.62	0.11	0.06	0.08
Hf^{178}									
Hf^{179}	0.07	0.11	0.03	0.08	0.12	0.20	1.84	0.20	0.11
Ta^{181}	-	-	-	-	-	0.83	0.55	0.80	0.43
Pb^{204}	-0.22	0.31	0.09	0.60	0.59	0.79	0.91	2.63	1.48
Pb^{206}	0.02	0.02	0.01	0.03	0.04	0.94	2.59	3.02	0.90
Pb^{207}	-	-	-	0.01	0.02	0.28	0.82	2.03	0.54
Pb^{208}	-	-	-	-	-	0.09	0.49	2.32	0.43
Th^{232}	-	-	-	-	-	0.05	0.44	0.11	0.08
U^{238}	0.01	0.02	0.01	0.01	0.02	0.37	1.08	0.78	0.24
Pb Total									

Sample Mean(ppm)	LA-21-DT-021-05	LA-21-DT-021-06	LA-21-DT-021-07	LA-21-DT-021-08	LA-21-DT-021-09	LA-21-DT-021-10	LA-21-DT-049-01	LA-21-DT-049-02	LA-21-DT-049-03
Ho^{165}	0.29	0.17	0.40	2.73	0.66	1.32	1.35	0.88	5.77
Er^{166}	1.07	0.50	1.29	11.39	2.41	3.83	3.40	2.26	14.34
Tm^{169}	0.18	0.09	0.22	2.01	0.37	0.52	0.48	0.25	1.50
Yb^{172}	1.16	0.49	1.22	13.76	2.43	2.83	2.49	1.45	6.39
Lu^{175}	0.12	0.07	0.17	1.90	0.28	0.31	0.23	0.14	0.61
Hf^{178}									
Hf^{179}	1.72	0.95	0.54	0.12	0.03	-	0.49	0.28	0.06
Ta^{181}	0.12	0.24	0.13	0.18	0.10	0.04	0.03	0.10	0.08
Pb^{204}	5.48	1.07	0.98	0.72	0.56	0.48	0.83	0.49	0.83
Pb^{206}	6.69	1.95	0.93	0.42	0.19	0.07	0.86	0.55	0.88
Pb^{207}	5.46	0.89	0.23	0.21	0.10	0.01	0.36	0.18	0.32
Pb^{208}	3.83	0.58	0.10	0.15	0.06	0.01	0.59	0.16	0.89
Th^{232}	0.15	0.19	0.11	0.02	0.01	-	0.02	0.04	0.21
U^{238}	0.75	0.63	0.38	0.11	0.06	0.01	0.30	0.23	0.14
Pb Total									

Sample Mean(ppm)	LA-21-DT-049-04	LA-21-DT-049-05	LA-21-DT-049-06	LA-21-DT-049-07	LA-21-DT-049-08	LA-21-DT-049-09	LA-21-DT-049-10	LA-21-DT-074-01	LA-21-DT-074-02
Ho^{165}	3.61	7.63	1.80	5.28	3.57	0.66	3.68	2.06	1.13
Er^{166}	11.23	19.61	6.38	18.76	12.75	2.11	12.35	5.94	4.93
Tm^{169}	1.45	2.25	0.98	2.70	1.95	0.33	1.83	0.83	0.95
Yb^{172}	8.74	10.81	6.84	17.90	12.52	2.18	11.87	5.41	7.28
Lu^{175}	1.20	1.19	0.92	2.36	1.61	0.30	1.51	0.73	1.12
Hf^{178}									
Hf^{179}	10.09	3.29	3.91	0.98	1.96	5.75	4.45	3.33	0.16

Ta^{181}	0.23	0.06	0.09	0.04	0.12	0.22	0.10	0.17	0.15
Pb^{204}	0.39	0.03	0.64	0.42	0.15	-	-	1.05	0.97
Pb^{206}	6.94	3.48	4.01	1.01	2.79	7.05	2.88	5.12	0.94
Pb^{207}	1.55	0.79	0.89	0.25	0.59	1.43	0.61	1.27	0.53
Pb^{208}	0.66	0.36	0.22	0.06	0.07	0.15	0.11	1.76	0.48
Th^{232}	1.16	0.17	0.26	0.03	0.16	0.45	0.23	0.27	0.06
U^{238}	3.61	1.58	1.60	0.48	1.02	3.57	2.21	1.65	0.23
Pb Total									

Sample Mean(ppm)	LA-21-DT-074-03	LA-21-DT-074-04	LA-21-DT-074-05	LA-21-DT-074-06	LA-21-DT-074-07	LA-21-DT-074-08	LA-21-DT-074-09	LA-21-DT-074-10	LA-21-DT-096-1
Ho^{165}	1.65	0.83	0.67	1.64	2.88	1.44	1.23	0.88	1.93
Er^{166}	3.98	4.11	2.26	4.22	8.63	4.47	4.27	3.16	5.83
Tm^{169}	0.45	0.88	0.40	0.55	1.32	0.75	0.71	0.58	0.88
Yb^{172}	2.82	7.70	3.03	3.40	9.02	5.28	4.66	4.62	6.55
Lu^{175}	0.36	1.13	0.49	0.49	1.21	0.88	0.72	0.71	0.94
Hf^{178}									50.38
Hf^{179}	1.10	0.12	5.03	3.14	0.50	8.44	6.52	0.68	
Ta^{181}	0.03	0.62	0.19	0.07	0.13	0.05	0.18	0.22	0.03
Pb^{204}	0.70	1.04	1.19	0.93	14.73	0.41	0.42	-	0.38
Pb^{206}	1.26	1.09	5.72	5.49	20.14	16.03	6.76	1.71	6.72
Pb^{207}	0.29	0.85	1.76	1.36	10.29	3.38	1.54	0.40	1.14
Pb^{208}	0.09	0.69	1.59	1.59	14.63	0.47	0.87	0.33	0.79
Th^{232}	0.10	0.04	0.63	0.17	0.03	1.37	0.54	0.03	7.26
U^{238}	0.53	0.17	2.63	1.96	1.48	6.86	3.28	0.63	15.57
Pb Total									2.30

Sample Mean(ppm)	LA-21-DT-096-9	LA-21-DT-096-11	LA-21-DT-096-12	LA-21-DT-096-13	LA-21-DT-096-14	LA-21-DT-096-21	LA-21-DT-096-23	LA-21-DT-096-26	LA-21-DT-096-28
Ho^{165}	1.03	1.53	2.29	1.82	1.95	2.33	3.97	3.05	5.64
Er^{166}	2.37	3.35	7.41	5.80	6.08	9.53	15.63	11.37	22.97
Tm^{169}	0.34	0.39	1.07	0.82	0.84	1.63	2.53	1.88	3.96
Yb^{172}	2.46	2.63	7.36	5.75	5.87	12.89	20.68	14.66	32.09
Lu^{175}	0.40	0.39	1.10	0.84	0.87	1.90	2.85	1.90	4.37
Hf^{178}	6.05	7.06	3.48	4.65	3.37	16.90	13.23	8.71	12.29
Hf^{179}									
Ta^{181}	-	0.01	-	0.01	0.01	0.04	0.18	0.04	0.04
Pb^{204}	0.30	0.15			0.05	0.20	0.18	0.27	0.26
Pb^{206}	5.39	6.69	3.86	5.80	5.55	23.90	12.05	10.03	8.32
Pb^{207}	1.09	1.39	0.78	1.15	1.20	5.00	2.42	2.06	1.56
Pb^{208}	0.03	0.18	0.02	0.04	0.04	0.48	0.22	0.22	0.16
Th^{232}	0.10	0.62	0.07	0.12	0.09	1.22	0.70	0.70	1.02
U^{238}	2.20	3.20	1.79	2.30	1.98	8.94	5.82	4.23	6.42
Pb Total	1.56	2.01	1.13	1.67	1.63	7.23	3.60	2.99	2.44

Sample Mean(ppm)	LA-21-DT-096-37	LA-21-DT-096-38	LA-21-DT-096-39	LA-21-DT-096-40	LA-21-DT-096-41	LA-21-DT-096-42	LA-21-DT-096-43	LA-21-DT-096-44	LA-21-DT-096-45
Ho^{165}	2.03	3.02	3.10	3.47	2.41	4.04	3.33	6.95	3.58
Er^{166}	7.62	11.24	12.13	12.15	9.56	15.86	11.97	28.89	13.06
Tm^{169}	1.23	1.78	1.92	1.81	1.59	2.55	1.81	4.84	1.93
Yb^{172}	9.42	13.66	16.26	13.00	12.22	18.97	13.72	38.35	14.08
Lu^{175}	1.27	1.93	2.24	1.60	1.70	2.61	1.79	5.28	1.75
Hf^{178}	3.05	20.37	10.57	5.80	4.37	4.90	10.58	29.20	5.00
Hf^{179}									

Ta^{181}	0.09	0.08	0.03	0.18	0.04	0.02	0.04	0.04	0.05
Pb^{204}	0.07	0.09	0.24	0.10	0.02	-	0.12	0.09	-
Pb^{206}	4.81	18.18	7.18	9.03	4.91	4.69	10.15	41.46	8.67
Pb^{207}	0.99	3.59	1.42	1.88	1.00	0.98	1.98	8.47	1.69
Pb^{208}	0.12	0.34	0.22	0.17	0.08	0.12	0.21	0.56	0.19
Th^{232}	0.36	1.53	1.26	0.50	0.27	0.40	0.83	1.86	0.52
U^{238}	1.98	10.94	6.81	3.50	2.42	2.77	5.65	18.84	3.37
Pb Total	1.44	5.36	2.16	2.67	1.44	1.41	3.01	12.16	2.55

Sample Mean(ppm)	LA-21-DT-096-46	LA-21-DT-096-47	LA-21-DT-096-48	LA-21-DT-096-49	LA-21-DT-096-50	LA-21-DT-096-51	LA-21-DT-096-52	LA-21-DT-096-53	LA-21-DT-096-54
Ho^{165}	3.80	4.69	7.00	3.94	2.70	10.53	4.88	3.43	4.89
Er^{166}	14.49	16.52	26.19	14.69	9.53	31.95	17.27	11.44	17.18
Tm^{169}	2.27	2.45	4.20	2.38	1.47	4.14	2.58	1.70	2.49
Yb^{172}	17.71	17.55	31.99	18.12	10.87	27.96	18.12	12.41	18.39
Lu^{175}	2.47	2.35	4.47	2.70	1.40	3.51	2.42	1.67	2.46
Hf^{178}	11.02	10.69	44.26	18.58	3.90	1.58	27.97	16.15	19.24
Hf^{179}									
Ta^{181}	0.03	0.03	0.12	0.03	0.05	0.01	0.02	0.02	0.01
Pb^{204}	-	0.23	0.32	0.15	0.15	0.80	0.16	0.22	0.22
Pb^{206}	13.41	14.30	32.17	14.05	3.25	32.32	20.36	18.03	20.10
Pb^{207}	2.79	2.85	6.45	2.86	0.65	6.31	4.01	3.61	4.08
Pb^{208}	0.29	0.26	0.48	3.77	0.08	55.18	0.29	0.31	0.28
Th^{232}	0.94	0.70	2.25	12.52	0.23	242.78	1.23	1.01	0.78
U^{238}	6.41	5.96	19.44	6.89	1.69	17.35	14.20	7.82	8.95
Pb Total	4.00	4.21	9.42	6.00	0.98	37.99	5.95	5.37	5.91

Sample Mean(ppm)	LA-21-DT-096-55	LA-21-DT-096-56	LA-21-DT-096-57	LA-21-DT-096-58	LA-21-DT-096-59	LA-21-DT-096-60	LA-21-DT-096J-01	LA-21-DT-096J-02	LA-21-DT-096J-03
Ho^{165}	2.83	7.13	1.55	4.23	2.86	1.26	3.13	3.93	4.30
Er^{166}	8.61	25.87	4.80	14.32	10.39	3.59	10.72	12.61	14.40
Tm^{169}	1.14	3.84	0.65	2.11	1.60	0.48	1.76	1.90	2.15
Yb^{172}	7.67	27.33	4.48	15.10	12.00	3.36	12.50	13.36	15.80
Lu^{175}	0.92	3.51	0.68	1.93	1.57	0.54	1.66	1.67	2.34
Hf^{178}	3.09	6.78	14.96	4.22	3.27	9.29	3.52	1.36	2.30
Hf^{179}									
Ta^{181}	0.01	0.10	0.01	0.07	0.02	0.04	0.06	0.13	0.03
Pb^{204}	0.13	0.28	0.03	0.11		0.55	0.64	0.43	0.43
Pb^{206}	4.01	7.34	15.09	6.10	3.41	10.90	4.47	1.56	4.36
Pb^{207}	0.82	1.50	3.12	1.28	0.64	2.31	0.94	0.31	0.94
Pb^{208}	0.11	0.09	0.07	0.15	0.05	0.09	0.14	0.14	0.12
Th^{232}	0.27	0.22	0.20	0.50	0.22	0.29	0.29	0.19	0.19
U^{238}	1.82	3.30	6.55	2.59	1.68	4.87	2.29	1.00	1.62
Pb Total	1.21	2.14	4.37	1.83	0.99	3.20			

Sample Mean(ppm)	LA-21-DT-096J-04	LA-21-DT-096J-05	LA-21-DT-096J-06	LA-21-DT-096J-07	LA-21-DT-096J-08	LA-21-DT-096J-09	LA-21-DT-096J-10
Ho^{165}	3.70	6.63	1.37	3.36	6.01	4.17	3.95
Er^{166}	11.64	21.70	3.72	11.63	21.23	13.65	12.43
Tm^{169}	1.74	3.31	0.52	1.89	3.35	2.16	1.86
Yb^{172}	12.56	22.90	3.32	13.82	24.42	15.21	13.16
Lu^{175}	1.86	2.99	0.39	1.79	3.46	1.97	1.75
Hf^{178}	8.67	1.18	0.69	1.60	1.76	3.52	5.97
Hf^{179}							

Ta^{181}	0.07	0.02	0.30	0.04	0.01	0.04	0.06
Pb^{204}	0.35	0.38	0.36	0.29	0.33	0.29	0.27
Pb^{206}	11.59	6.15	1.65	3.14	2.26	7.48	7.38
Pb^{207}	2.39	0.91	0.31	0.68	0.46	1.56	1.40
Pb^{208}	0.16	4.91	0.68	0.15	0.06	0.15	2.01
Th^{232}	0.42	81.30	18.58	0.18	0.14	0.19	57.00
U^{238}	5.62	16.02	3.85	1.35	0.94	2.49	10.24
Pb Total							

Appendix IV

Sulphide LA-ICP-MS

Sample ID Mean (ppm)	DT009 Sp1 Chalcopyrite	DT009 Sp2 Pyrrhotite	DT017 SP1 Cobaltite	DT017 Sp 2 pyrite	DT020 Sp1 Arsenopyrite	DT020 Sp2 Pyrite	DT020 Sp3 Chalcopyrite	DT023 Sp1 Chalcopyrite	DT023 Sp2 Pyrrhotite
Li^{7}	-	-	-	-	1.85	-	-	-	0.35
Be^{9}	-	-	-	0.14	-	0.11	-	-	-
B^{11}	-	1.38	396.06	31.02	-	0.32	-	-	1.23
Na^{23}	5.72	5.39	119.82	8.18	18.94	8.23	-	6.95	-
Mg^{24}	0.07	0.08	1.43	1.77	11.76	0.40	0.57	0.08	0.14
Al^{27}	0.44	0.23	0.49	5.33	24.09	2.90	3.86	3.31	-0.22
Si^{29}	462.56	427.78		26107	6501.3		1915.9	805.32	859.60
P^{31}	25.44	21.60	50.85	7.92	144.40	4.54	13.15	13.36	-
S^{33}	302778	264051	963074	430974	365742	236731	259248	315171	245984
S^{34}	356939	321896	828048	586188	313715	336996	331364	396441	196048
K^{39}	-	-	7.33	-	13.44	30.73	3.76	-	4.27
Ca^{43}	-	144.55	295.28	1.96	-	-	-	287.82	-
Sc^{45}	0.02	0.06	0.03	0.21	-	0.01	-	0.02	0.14
Ti^{47}	-	0.08	-	0.15	-	-	-	-	0.22
V^{51}	0.26	0.28	0.98	0.44	0.03	0.25	0.33	0.31	-

Sample ID Mean (ppm)	DT028 Sp1 Arsenopyrite	DT028 Sp2 Chalcopyrite	DT028 Sp3 Pyrrhotite	DT034 Sp3 Pyrrhotite	DT034 Sp2 Chalcopyrite	DT063 Sp1 Cubanite	DT088 Sp1 Pyrrhotite	DT088 Sp2 Chalcopyrite	DT088 Sp3 Pyrite
Li^{7}	0.40	-	0.20	-	1.04	0.44	0.38	0.38	-
Be^{9}	-	0.72	-	-	-	-	0.10	-	-
B^{11}	1.04	9.51	22.77	1.46	22.83	-	0.14	0.74	0.05
Na^{23}	107.86	38.08	56.73	2.21	34.68	5.49	1.20	1.88	2.09
Mg^{24}	6.45	47.23	35.33	0.17	4.59	0.46	1.11	15.24	4.92

Al^{27}	744.00	93.69	293.30	0.87	15.96	12.77	1.61	21.40	81.70
Si^{29}	2555.9	969.22	2589.5	627.65	1972.8	1837.7	52.95	48.84	9.89
P^{31}	-	7.55	7.66	17.72	47.17	2.47	14.13	16.11	12.87
S^{33}	277957	454795	395830	325738	534825	408075	338195	411463	586160
S^{34}	168585	394562	308824	249711	395563	297933	343174	361946	566900
K^{39}	336.65	2.51	23.32	-	3.60	-	-	2.35	7.03
Ca^{43}	-	332.18	903.55	760.38	-	-	-	12.12	6.54
Sc^{45}	0.24	0.03	0.29	0.09	0.20	0.07	-	0.09	-
Ti^{47}	5.22	4.23	6.66	0.27	0.62	1.65	-	2.02	0.69
V^{51}	1.18	0.86	4.30	0.47	0.86	0.70	0.29	1.42	0.53

Sample ID Mean (ppm)	DT098 Sp1 Chalcopyrite	DT098 Sp2 pyrrhotite	DT099 Sp1 pyrrhotite	DT099 Sp2 Pyrite	DT102 Sp1 Pyrrhotite	DT102 Sp2 Chalcopyrite	DT117 Sp1 Galena	DT117 Sp2 pyrite	DT117 Sp3 Sphalerite
Li^{7}	-	0.38	-	1.01	-	-	-	1.35	-
Be^{9}	-	-	-	-	-	-	-	0.25	-
B^{11}	0.84	0.43	3.17	0.16	6.14	5.10	0.07	2.63	9.97
Na^{23}	0.71	1.23	1.54	2.76	30.96	75.04	2.08	9.19	5.32
Mg^{24}	19.38	0.24	3.22	22.88	43.55	15.51	1.56	7.73	4.48
Al^{27}	115.93	10.88	14.03	195.10	285.87	55.40	5.34	4.11	10.90
Si^{29}	135.44	41.55	17.10	74.39	2334.8	664.90	179.98	-	591.73
P^{31}	16.31	-	14.97	3.90	36.61	54.51	12.35	67.65	48.31
S^{33}	482282	523509	436036	595251	563184	437836	107574	711615	526943
S^{34}	389022	320392	402969	477816	446870	412950	102452	696046	569036
K^{39}	-	1.48	6.22	11.96	11.05	2.76	12.80	2.33	-
Ca^{43}	20.48	13.26	1277.94	5.91	732.45	170.75	157.67	451.58	-
Sc^{45}	0.12	0.03	0.03	-	-	-	0.05	-	-

Ti^{47}	-	2.51	-	1.41	10.83	0.52	0.11	0.25	5.31
V^{51}	0.86	0.49	0.28	0.56	0.30	0.53	0.42	0.44	0.16

Sample ID Mean (ppm)	DT117 Sp4 Pyrrhotite	DT117 Sp5 Chalcopyrite	DT118A Sp1 Arsenopyrite	DT118A Sp2 Sphalerite	DT118A Sp3 Pyrite	DT118A Sp4 Chalcopyrite	DT118A Sp5 Pyrrhotite	DT119 Sp1 Pyrrhotite	DT119 Sp2 Chalcopyrite
Li^{7}	-	0.67	-	-	0.15	-	-	1.35	0.32
Be^{9}	-	-	-	0.02	-	0.19	-	0.84	0.01
B^{11}	5.64	-	-	7.36	-	-	7.11	24.47	-
Na^{23}	23.62	16.63	4.66	9.56	25.24	14.36	8.36	162.85	44.40
Mg^{24}	3.40	16.76	1.37	2.40	2.87	4.05	5.36	63.84	12.26
Al^{27}	69.57	35.91	0.70	1.29	2.19	5.84	13.67	195.46	40.42
Si^{29}	1256.6	2360.0	-	2120.7	196.68	943.45	656.37	1539.1	-
P^{31}	27.52	11.22	31.00	25.49	8.01	29.14	32.74	35.90	13.05
S^{33}	409018	549286	284402	384568	581293	509841	390697	354136	668834
S^{34}	378800	436282	240566	407813	510121	463287	325262	218952	631492
K^{39}	6.96	4.51	-	-	-	-	-	19.25	3.01
Ca^{43}	54.00	-	23.86	-	22.47	87.56	459.65	13.94	-
Sc^{45}	-	0.16	-	0.02	-	-	-	0.04	0.33
Ti^{47}	0.62	0.03	-	-	0.12	0.26	0.96	9.76	1.79
V^{51}	0.24	0.68	0.56	0.14	0.53	0.59	0.31	0.87	-

Sample ID Mean (ppm)	DT119 Sp3 Cobaltite	DT017 Line 1 Chalcopyrite	DT017 Line1 Cubanite	DT034 Line 1 Pyrrhotite	DT034 Line 1 Pyrite	DT050B line 1 Chalcopyrite	DT050B Line 1 Troilite	DT050B Line 1 Pyrrhotite	DT063 Line 1 Pyrite
Li^{7}	-	0.09	0.25	0.13	0.06	0.33	-	-	-

Be^{9}	1.47	-	-	0.06	-	0.20	-	-	-
B^{11}	-	12.01	12.61	2.26	1.35	2.83	0.16	-	0.29
Na^{23}	53.08	11.79	15.57	19.93	2.19	8.81	2.81	2.05	397.62
Mg^{24}	4.92	1.58	0.67	9.41	0.11	3.55	0.02	0.01	1.92
Al^{27}	11.97	35.36	13.30	165.89	4.39	151.66	0.09	0.05	11.32
Si^{29}	1731.6	827.07	556.89	370.15	253.17	663.98	-	52.65	2142.6
P^{31}	114.17	21.31	21.34	5.69	4.03	19.93	17.15	9.04	8.32
S^{33}	952370	369754	381628	845244	296413	373744	385686	427043	429540
S^{34}	576730	359589	332364	595440	239597	338548	368684	318504	431955
K^{39}	-	-	-	4.36	1.54	-	-	-	-
Ca^{43}	623.72	-	-	43.36	-	6179.95	111.80	-	228.64
Sc^{45}	0.25	0.51	0.12	0.08	-	0.07	0.08	0.02	0.03
Ti^{47}	-	1.82	1.22	0.47	0.39	0.58	-	1.01	0.24
V^{51}	0.69	0.52	0.28	0.74	0.39	0.37	0.28	0.31	0.30

Sample ID Mean (ppm)	DT063 Line 1 Chalcopyrite	DT069 Line 1 Pyrrhotite	DT-069 Line 1 Troilite	DT-069 line 1 Chalcopyrite
Li^{7}	-	-	-	0.06
Be^{9}	-	-	-	-
B^{11}	-	0.44	1.14	0.59
Na^{23}	8.45	1.88	-	15.13
Mg^{24}	1.67	-	1.32	0.26
Al^{27}	146.19	-	26.96	0.95
Si^{29}	303.82	224.26	149.43	281.87
P^{31}	14.36	14.24	8.66	9.44
S^{33}	384677	409676	272525	376579

S^{34}	391743.72	342935.09	213926.97	372148.00
K^{39}	-	-	-	1.98
Ca^{43}	-	-	64.34	-
Sc^{45}	0.04	0.02	-	-
Ti^{47}	0.20	-	-	0.26
V^{51}	0.37	0.17	0.25	0.16

Sample ID Mean (ppm)	DT009 Sp1 Chalcopyrite	DT009 Sp2 Pyrrhotite	DT017 SP1 Cobaltite	DT017 Sp 2 pyrite	DT020 Sp1 Arsenopyrite	DT020 Sp2 Pyrite	DT020 Sp3 Chalcopyrite	DT023 Sp1 Chalcopyrite	DT023 Sp2 Pyrrhotite
Cr^{53}	-	0.45	17.68	-	34.56	0.34	-	1.34	1.11
Mn^{55}	1.09	1.29	6.14	1.02	-	1.00	0.88	-	1.37
Co^{59}	1.72	217.46	1897073	274.24	147159	1445.49	0.88	1.24	150.17
Ni^{60}	0.99	185.29	82588	46.63	378.20	116.69	0.19	0.83	118.30
Ni^{61}	-	264.71	85188	85.07	613.66	273.56	-	16.19	194.84
Cu^{63}	238923	0.11	7.47	2.09	4.49	10.86	196003	222366	0.55
Cu^{65}	228878	0.05	4.82	1.33	12.78	10.59	179210	223992	0.45
Zn^{66}	310.12	0.32	1.95	0.24	6.07	0.40	56.28	96.87	10.37
Zn^{68}	334.80	-	10.56	-	-	0.88	54.85	97.80	12.05
Ga^{69}	0.26	-	-	-	-	0.01	0.07	0.02	-
As^{75}	-	1.16	4589287	388.43	2225656	34.53	4.64	-	7.26
Se^{77}	152.68	105.41	517.47	148.41	265.82	86.47	134.45	169.24	126.94
Se^{78}	149.83	129.77	449.62	201.40	171.18	115.45	171.32	140.64	187.56
Se^{82}	175.57	133.10	667.59	184.70	397.38	84.78	107.67	189.29	113.68
Rb^{85}	-	-	-	-	-	0.02	-	0.05	-

Sample ID Mean (ppm)	DT028 Sp1 Arsenopyrite	DT028 Sp2 Chalcopyrite	DT028 Sp3 Pyrrhotite	DT034 Sp3 Pyrrhotite	05-016-DT034 Sp2 Chalcopyrite	DT063 Sp1 Cubanite	DT088 Sp1 Pyrrhotite	DT088 Sp2 Chalcopyrite	DT088 Sp3 Pyrite
Cr^{53}	1.46	2.58	2.97	2.67	10.60	3.58	0.92	3.60	1.00
Mn^{55}	-	6.67	9.04	0.59	1.32	1.11	3.88	2.13	1.53
Co^{59}	12807.03	1.00	130.96	83.29	10.14	0.29	0.20	0.18	9184.5
Ni^{60}	127.82	2.22	168.97	5.42	19.54	0.27	249.66	7.93	233.15
Ni^{61}	255.87	9.44	415.99	10.60	44.07	8.12	1284.16	24.01	530.99
Cu^{63}	0.63	284419	32.18	11522	283195	215314	0.78	216178	2.86
Cu^{65}	0.22	281199	8.24	9200.8	299906	234971	1.33	227111	8.59
Zn^{66}	-	74.96	1.78	0.12	88.61	299.89	0.58	123.40	0.07
Zn^{68}	1.55	80.22	-	-	108.79	336.46	-	131.05	-
Ga^{69}	3.54	0.10	0.03	-	0.19	0.28	0.01	0.02	0.03
As^{75}	2345470.66	4.46	26.78	8.82	-	24.64	-	1.07	1687.34
Se^{77}	107.00	161.97	125.66	195.39	298.68	314.33	56.15	41.28	66.97
Se^{78}	45.33	232.56	117.10	224.57	62.51	287.89	42.82	-	78.06
Se^{82}	138.42	186.18	134.82	194.41	368.38	284.62	62.00	48.90	74.57
Rb^{85}	0.37	0.01	0.27	0.02	0.10	-	-	0.07	0.12

Sample ID Mean (ppm)	DT098 Sp1 Chalcopyrite	DT098 Sp2 pyrrhotite	DT099 Sp1 pyrrhotite	DT099 Sp2 Pyrite	DT102 Sp1 Pyrrhotite	DT102 Sp2 Chalcopyrite	DT117 Sp1 Galena	DT117 Sp2 pyrite	DT117 Sp3 Sphalerite
Cr^{53}	-	0.23	6.43	1.95	5.93	-	-	6.41	15.84
Mn^{55}	2.42	2.15	2.84	11.14	3.10	0.27	0.29	2.35	1389.5
Co^{59}	0.73	205.02	32.68	686.60	443.06	3.67	0.11	1109.31	2.64
Ni^{60}	1.86	157.57	103.84	677.03	142.25	0.30	0.14	60.49	0.93
Ni^{61}	-	406.93	395.84	1904.45	274.04	20.54	0.61	155.35	-
Cu^{63}	221836	8.73	1.15	388.61	1.45	269671	1.56	1.54	14.37
Cu^{65}	217514	6.83	0.37	72.63	1.09	260191	1.78	2.73	14.87

Zn^{66}	116.70	1.37	2.29	4.87	0.25	23.04	12.95	1.74	780471
Zn^{68}	128.16	-	0.39	1.84	0.18	24.61	6.97	3.78	817262
Ga^{69}	0.28	-	0.07	0.41	-	0.09	0.07	0.23	0.42
As^{75}	4.82	9.72	11.19	101.19	-	-	0.78	2193.43	13.56
Se^{77}	92.86	70.28	81.04	101.17	26.53	18.40	91.60	11.26	86.44
Se^{78}	113.41	58.48	-	86.99	-	52.95	131.72	33.06	123.42
Se^{82}	99.86	126.89	60.50	109.94	7.37	30.31	84.64	15.54	126.39
Rb^{85}	0.05	0.06	-	0.08	0.11	0.14	0.06	-	0.09

Sample ID Mean (ppm)	DT117 Sp4 Pyrrhotite	DT117 Sp5 Chalcopyrite	DT118A Sp1 Arsenopyrite	DT118A Sp2 Sphalerite	DT118A Sp3 Pyrite	DT118A Sp4 Chalcopyrite	DT118A Sp5 Pyrrhotite	DT119 Sp1 Pyrrhotite	DT119 Sp2 Chalcopyrite
Cr^{53}	5.45	2.75	2.66	-	0.86	1.58	-	-	-
Mn^{55}	3.98	6.32	0.60	1289.51	1.05	2.63	1.10	3.90	4.21
Co^{59}	1.82	0.14	436.13	-	3883.49	-0.01	0.13	462.55	6.58
Ni^{60}	262.00	1.83	110.90	0.67	101.12	2.09	215.84	117.93	0.53
Ni^{61}	726.71	12.19	288.99	-	222.43	-0.09	457.35	342.85	-
Cu^{63}	7.74	220515.48	1.48	218.47	1.34	223514.76	1.39	179.05	158251
Cu^{65}	9.22	219936.32	1.21	221.75	2.34	205152.12	1.47	279.43	149374
Zn^{66}	2.75	186.63	0.31	559726.87	0.48	93.82	0.92	3.38	81.91
Zn^{68}	2.90	220.02	0.19	592430.66	0.26	92.10	2.75	6.32	95.55
Ga^{69}	0.03	0.26	-	0.86	0.09	0.85	0.04	0.36	-
As^{75}	2.05	13.98	2008678.84	389.60	8114.93	20.18	25.29	9.94	41.13
Se^{77}	7.95	2.70	21.20	15.87	7.89	21.31	14.62	156.12	332.57
Se^{78}	-	-	1.08	33.42	6.12	-	-	60.57	112.06
Se^{82}	10.57	-	19.83	62.44	1.28	6.55	0.18	158.97	312.10
Rb^{85}	0.15	-	-	0.06	-	-	-	0.24	0.47

Sample ID Mean (ppm)	DT119 Sp3 Cobaltite	DT017 Line 1 Chalcopyrite	DT017 Line1 Cubanite	DT034 Line 1 Pyrrhotite	DT034 Line 1 Pyrite	DT050B line 1 Chalcopyrite	DT050B Line 1 Troilite	DT050B Line 1 Pyrrhotite	DT063 Line 1 Pyrite
Cr^{53}	21.72	1.22	-	2.13	0.72	2.29	6.15	1.70	1.51
Mn^{55}	-	10.45	2.97	9.14	1.01	13.46	1.83	2.72	4.10
Co^{59}	1450252	0.08	0.10	24414	90.52	58.80	145.55	156.37	1740.5
Ni^{60}	5756.5	1.92	46.09	2.35	3.58	60.16	423.91	410.79	27.35
Ni^{61}	14528	9.93	67.57	2.64	29.30	150.71	1118.2	981.12	73.60
Cu^{63}	75.67	306445	274449	6.57	11545	258445	3.37	2.10	6316.9
Cu^{65}	78.64	314231	260090	5.45	12168	254038	11.35	3.27	5845.0
Zn^{66}	2.62	162.31	158.51	6.64	0.94	70.73	0.99	0.41	214.94
Zn^{68}	-	175.37	185.00	4.81	1.35	67.25	0.16	-	119.74
Ga^{69}	1.69	0.21	0.27	0.21	0.17	0.20	-	0.07	0.47
As^{75}	3610384	4.90	1.95	2571.7	6.82	7.99	3.05	6.48	1.66
Se^{77}	577.77	105.17	105.68	103.46	159.22	121.53	124.71	123.42	295.09
Se^{78}	807.91	120.47	127.71	97.83	148.17	122.11	93.27	65.35	282.64
Se^{82}	831.67	101.66	94.76	100.13	215.26	112.07	100.96	117.99	310.71
Rb^{85}	0.66	-	0.07	0.06	-	-	0.08	0.22	0.01

Sample ID Mean (ppm)	DT063 Line 1 Chalcopyrite	DT069 Line 1 Pyrrhotite	DT-069 Line 1 Troilite	DT-069 line 1 Chalcopyrite
Cr^{53}	0.23	0.71	1.90	1.54
Mn^{55}	0.84	0.66	11.36	0.94
Co^{59}	0.35	194.94	128.38	403.76
Ni^{60}	37.52	279.26	209.94	321.06
Ni^{61}	94.68	717.04	632.89	779.73
Cu^{63}	304158	0.70	0.64	303920
Cu^{65}	295628	0.67	0.68	291799

Zn^{66}	141.73	0.18	0.33	403.30
Zn^{68}	126.79	2.40	0.60	270.39
Ga^{69}	0.18	0.05	-	0.17
As^{75}	2.99	5.35	6.10	3.09
Se^{77}	276.88	205.17	159.25	227.53
Se^{78}	276.55	200.17	169.69	236.40
Se^{82}	284.43	208.06	185.60	238.69
Rb^{85}	-	0.04	0.08	0.01

Sample ID Mean (ppm)	DT009 Sp1 Chalcopyrite	DT009 Sp2 Pyrrhotite	DT017 SP1 Cobaltite	DT017 Sp 2 pyrite	DT020 Sp1 Arsenopyrite	DT020 Sp2 Pyrite	DT020 Sp3 Chalcopyrite	DT023 Sp1 Chalcopyrite	DT023 Sp2 Pyrrhotite
Sr^{88}	-	0.02	-	-	0.45	1.42	-	-	0.12
Y^{89}	-	0.08	2.56	-	4.32	-	-	-	-
Zr^{90}	-	-	-	-	-	0.06	-	-	0.21
Nb^{93}	-	-	1.88	-	4.47	-	-	-	-
Mo^{95}	-	0.29	-	0.81	-	0.77	-	-	-
Ru^{101}	0.23	-	-	-	-	-	-	0.56	-
Rh^{103}	13.51	-	-	-	-	0.01	10.31	13.44	-
Pd^{105}	27.24	-	14.09	-	-	-	30.90	35.69	-
Pd^{106}	3.44	-	9.17	0.42	-	-	-	2.86	0.38
Ag^{107}	11.33	1.00	1.54	1.00	-	15.67	203.49	5.76	0.08
Pd^{108}	3.18	0.12	7.80	-	-	-	-	1.42	0.69
Ag^{109}	9.87	0.41	0.18	2.85	0.37	14.33	183.55	9.52	0.46
Cd^{111}	38.91	0.02	-	0.06	0.28	0.09	2.29	17.24	3.35
Sn^{118}	24.69	-	0.05	0.27	-	0.01	2.57	55.61	0.90
Sn^{120}	23.47	-	-	0.45	5.65	0.25	2.84	45.46	-

Sample ID Mean (ppm)	DT028 Sp1 Arsenopyrite	DT028 Sp2 Chalcopyrite	DT028 Sp3 Pyrrhotite	DT034 Sp3 Pyrrhotite	05-016-DT034 Sp2 Chalcopyrite	DT063 Sp1 Cubanite	DT088 Sp1 Pyrrhotite	DT088 Sp2 Chalcopyrite	DT088 Sp3 Pyrite
Sr^{88}	1.25	0.14	2.36	0.20	0.17	-0.15	-	0.01	0.01
Y^{89}	1.47	-	-	-	0.39	-	0.01	-	-
Zr^{90}	-	0.13	-	-	-	-	0.01	0.03	-
Nb^{93}	0.54	-	-	-	-	-	-	-	-
Mo^{95}	-	-	-	-	-	-	-	0.29	-
Ru^{101}	-	0.28	-	0.30	-	0.54	-	-	-
Rh^{103}	-	16.63	-	1.49	15.28	11.23	-	12.77	-
Pd^{105}	-	48.98	-	3.58	37.83	33.14	-	34.77	-
Pd^{106}	-	0.72	-	0.29	0.20	4.60	0.32	0.68	-
Ag^{107}	-	5.80	0.25	33.06	2.33	129.97	0.45	0.36	0.24
Pd^{108}	-	0.22	-	0.20	-	3.18	-	0.72	0.06
Ag^{109}	0.25	5.68	0.35	34.32	4.10	128.93	0.29	0.16	0.06
Cd^{111}	0.56	8.49	-	2.02	13.95	90.41	0.29	10.10	-
Sn^{118}	1.43	105.88	0.54	0.27	13.97	72.65	1.41	0.87	0.54
Sn^{120}	1.54	90.76	0.11	-	14.87	73.69	0.01	1.58	0.08

Sample ID Mean (ppm)	DT098 Sp1 Chalcopyrite	DT098 Sp2 pyrrhotite	DT099 Sp1 pyrrhotite	DT099 Sp2 Pyrite	DT102 Sp1 Pyrrhotite	DT102 Sp2 Chalcopyrite	DT117 Sp1 Galena	DT117 Sp2 pyrite	DT117 Sp3 Sphalerite
Sr^{88}	-	-	0.02	-	-	0.51	-	0.06	0.40
Y^{89}	-	-	-	0.04	0.08	0.18	-	0.02	-
Zr^{90}	0.03	-	-	0.07	-	0.43	-	-	0.53
Nb^{93}	-	-	-	-	-	-	-	-	-
Mo^{95}	-	-	0.16	-	-	-	-	-	-
Ru^{101}	0.41	-	-	-	-	-	-	-	0.07
Rh^{103}	14.20	0.16	-	-	-	18.69	16.45	-	29.01

Pd^{105}	35.80	0.55	0.51	-	-	39.35	0.13	-	2.31
Pd^{106}	0.53	-	-	-	-	-	0.34	-	818.90
Ag^{107}	207.96	7.95	1.03	3.36	1.45	87.11	3611.9	0.02	1788.4
Pd^{108}	0.14	-	-	-	-	0.24	0.74	-	565.06
Ag^{109}	207.83	4.89	1.07	18.15	1.44	101.31	3878.5	0.09	1927.3
Cd^{111}	21.42	0.80	-	0.60	-	7.32	10.91	1.86	29163
Sn^{118}	52.71	-	1.10	1.11	1.37	-	3.37	2.78	3.89
Sn^{120}	40.18	-	-	269.61	1.44	0.97	2.33	0.32	2.98

Sample ID Mean (ppm)	DT117 Sp4 Pyrrhotite	DT117 Sp5 Chalcopyrite	DT118A Sp1 Arsenopyrite	DT118A Sp2 Sphalerite	DT118A Sp3 Pyrite	DT118A Sp4 Chalcopyrite	DT118A Sp5 Pyrrhotite	DT119 Sp1 Pyrrhotite	DT119 Sp2 Chalcopyrite
Sr^{88}	0.03	0.04	0.05	0.04	0.03	-	1.27	0.83	1.29
Y^{89}	-	0.07	0.64	-	-	-	0.07	-	-
Zr^{90}	0.10	0.14	-	0.08	0.02	-	-	0.76	-
Nb^{93}	-	0.04	0.10	-	-	-	-	-	-
Mo^{95}	0.20	-	-	-	-	-	0.30	-	-
Ru^{101}	0.18	0.18	-	-	-	-	-	0.33	0.85
Rh^{103}	-	17.99	0.04	0.04	-	13.88	-	-	15.36
Pd^{105}	-	27.21	0.24	0.10	-	25.47	0.18	-	25.40
Pd^{106}	-	0.71	1.21	436.63	0.14	0.80	-	-	4.12
Ag^{107}	4.78	51.40	0.13	15.22	0.06	58.36	1.86	1.53	49.95
Pd^{108}	-	0.18	0.18	282.77	0.10	0.41	-	-	0.29
Ag^{109}	4.98	46.62	0.23	12.06	0.04	55.57	1.99	2.52	47.70
Cd^{111}	0.01	7.50	-	16155	-	10.82	-	-	19.65
Sn^{118}	-	15.73	-	1.65	0.01	51.02	8.45	2.53	49.06
Sn^{120}	1.12	18.26	0.55	0.92	1.11	58.60	5.66	1.16	66.34

Sample ID Mean (ppm)	DT119 Sp3 Cobaltite	DT017 Line 1 Chalcopyrite	DT017 Line1 Cubanite	DT034 Line 1 Pyrrhotite	DT034 Line 1 Pyrite	DT050B line 1 Chalcopyrite	DT050B Line 1 Troilite	DT050B Line 1 Pyrrhotite	DT063 Line 1 Pyrite
Sr^{88}	4.24	0.03	0.18	0.08	0.03	0.64	-	-	0.32
Y^{89}	0.59	3.12	-	0.13	-	2.23	-	-	-
Zr^{90}	-	1036.12	-	1.49	-	0.14	-	-	-
Nb^{93}	-	-	-	-	-	0.05	-	-	0.05
Mo^{95}	1.24	0.08	-	-	-	-	0.32	0.49	-
Ru^{101}	-	-	0.37	-	-	-	-	-	-
Rh^{103}	-	15.54	13.42	-	0.64	13.18	-	-	0.16
Pd^{105}	-	35.17	26.45	-	1.09	26.93	-	-	0.81
Pd^{106}	0.79	4.36	4.07	-	-	0.63	-	-	6.40
Ag^{107}	-	16.56	267.60	1.38	36.87	1068.51	1.24	0.29	118.92
Pd^{108}	-	1.65	5.01	-	-	0.21	-	-	3.87
Ag^{109}	1.94	12.64	258.32	1.21	41.92	1075.86	1.74	1.54	130.94
Cd^{111}	1.06	16.44	112.72	0.20	-	9.09	-	-	342.84
Sn^{118}	2.45	40.20	42.68	0.73	-	17.52	0.22	0.52	82.45
Sn^{120}	2.62	39.51	39.25	0.72	-	18.97	0.45	0.21	94.33

Sample ID Mean (ppm)	DT063 Line 1 Chalcopyrite	DT069 Line 1 Pyrrhotite	DT-069 Line 1 Troilite	DT-069 line 1 Chalcopyrite
Sr^{88}	0.04	0.02	0.14	0.66
Y^{89}	-	-	0.10	0.02
Zr^{90}	0.09	-	-	-
Nb^{93}	-	-	-	0.02
Mo^{95}	0.12	-	-	-
Ru^{101}	0.22	-	-	0.24
Rh^{103}	15.50	-	-	12.09

Pd^{105}	32.00	-	-	22.92
Pd^{106}	0.57	-	-	0.80
Ag^{107}	32.24	0.22	-	35.94
Pd^{108}	0.77	-	-	0.73
Ag^{109}	31.69	-	-	35.75
Cd^{111}	17.78	-	-	34.59
Sn^{118}	46.05	0.80	-	63.57
Sn^{120}	48.75	0.41	0.12	59.72

Sample ID Mean (ppm)	DT009 Sp1 Chalcopyrite	DT009 Sp2 Pyrrhotite	DT017 SP1 Cobaltite	DT017 Sp 2 pyrite	DT020 Sp1 Arsenopyrite	DT020 Sp2 Pyrite	DT020 Sp3 Chalcopyrite	DT023 Sp1 Chalcopyrite	DT023 Sp2 Pyrrhotite
Sb^{121}	-	0.09	5.69	0.13	64.97	0.46	0.05	0.07	0.03
Sb^{123}	-	0.02	3.76	-	90.20	0.34	-	0.08	-
Te^{125}	-	-	-	1.00	2.25	-	-	0.59	-
Cs^{133}	-	-	-	-	-	-	-	0.20	-
Ba^{137}	-	-	1.81	-	-	0.10	-	-	-
La^{139}	0.02	-	-	-	-	0.02	-	-	-
Ce^{140}	-	-	-	-	-	0.04	-	-	-
Pr^{141}	0.05	-	-	-	0.06	0.03	-	-	-
Nd^{146}	-	-	-	-	-	0.02	-	-	-
Sm^{147}	-	-	-	-	-	-	-	-	-
Eu^{153}	-	-	-	-	-	-	-	-	-
Gd^{157}	0.12	-	-	-	-	-	-	-	-
Dy^{163}	-	-	-	-	-	-	-	-	-
Er^{166}	-	-	-	-	-	-	0.07	-	-
Yb^{172}	-	-	-	-	-	-	-	-	-

Sample ID Mean (ppm)	DT028 Sp1 Arsenopyrite	DT028 Sp2 Chalcopyrite	DT028 Sp3 Pyrrhotite	DT034 Sp3 Pyrrhotite	05-016-DT034 Sp2 Chalcopyrite	DT063 Sp1 Cubanite	DT088 Sp1 Pyrrhotite	DT088 Sp2 Chalcopyrite	DT088 Sp3 Pyrite
Sb^{121}	6.63	0.08	0.28	0.01	0.33	0.79	0.06	-	0.17
Sb^{123}	6.16	0.19	-	-	-	1.04	-	0.37	0.01
Te^{125}	21.02	-	-	-	0.01	0.53	-	-	0.56
Cs^{133}	0.13	-	0.03	-	0.05	0.26	0.01	-	-
Ba^{137}	16.91	0.69	1.13	-	-	-	-	0.58	0.11
La^{139}	-	-	0.10	0.02	1.00	-	-	-	-
Ce^{140}	-	-	-	0.02	1.75	-	-	0.07	-
Pr^{141}	-	-	-	-	0.71	-	-	-	-
Nd^{146}	-	-	-	-	0.20	-	-	-	-
Sm^{147}	-	-	-	-	-	-	-	-	-
Eu^{153}	-	-	-	0.03	-	-	-	-	-
Gd^{157}	-	-	-	-	-	-	-	-	-
Dy^{163}	-	0.09	-	-	-	-	-	-	-
Er^{166}	-	-	-	-	-	-	-	-	-
Yb^{172}	-	-	-	-	-	-	-	-	-

Sample ID Mean (ppm)	DT098 Sp1 Chalcopyrite	DT098 Sp2 pyrrhotite	DT099 Sp1 pyrrhotite	DT099 Sp2 Pyrite	DT102 Sp1 Pyrrhotite	DT102 Sp2 Chalcopyrite	DT117 Sp1 Galena	DT117 Sp2 pyrite	DT117 Sp3 Sphalerite
Sb^{121}	0.22	0.02	-	0.45	-	0.68	46.28	0.24	11.02
Sb^{123}	0.61	0.57	-	0.51	-	1.16	60.07	-	8.75
Te^{125}	-	-	-	0.50	1.38	1.05	5.69	-	17.13
Cs^{133}	-	0.01	0.01	-	-	-	0.03	-	-
Ba^{137}	0.62	-	0.33	-	-	-	-	-	1.54
La^{139}	0.07	-	-	0.18	0.11	1.20	-	-	-
Ce^{140}	0.04	-	-	0.33	0.47	1.26	-	-	-

Pr^{141}	-	0.01	-	-	-	0.38	-	-	-
Nd^{146}	-	-	-	0.18	-	0.63	-	0.02	-
Sm^{147}	-	-	-	-	-	-	0.34	-	0.05
Eu^{153}	-	-	-	0.05	-	0.17	-	-	-
Gd^{157}	0.13	-	-	0.07	-	-	-	-	-
Dy^{163}	-	-	-	-	-	-	-	-	-
Er^{166}	-	-	-	-	-	-	-	-	-
Yb^{172}	-	-	-	-	-	-	0.01	0.03	-

Sample ID Mean (ppm)	DT117 Sp4 Pyrrhotite	DT117 Sp5 Chalcopyrite	DT118A Sp1 Arsenopyrite	DT118A Sp2 Sphalerite	DT118A Sp3 Pyrite	DT118A Sp4 Chalcopyrite	DT118A Sp5 Pyrrhotite	DT119 Sp1 Pyrrhotite	DT119 Sp2 Chalcopyrite
Sb^{121}	-	2.93	382.15	2.80	0.14	0.79	-	0.33	1.34
Sb^{123}	0.15	3.62	359.14	2.82	0.39	1.03	0.19	0.45	2.03
Te^{125}	-	1.26	0.91	2.66	-	-	-	-	0.01
Cs^{133}	-	-	-	-	-	0.07	-	-	0.11
Ba^{137}	-	-	-	-	-	-	-	0.44	-
La^{139}	-	-	0.05	-	0.01	-	0.07	0.08	-
Ce^{140}	-	-	0.03	0.01	-	-	0.02	0.24	-
Pr^{141}	-	-	-	-	-	-	-	-	-
Nd^{146}	-	0.13	-	-	-	-	-	-	-
Sm^{147}	-	-	0.24	-	0.03	-	0.09	-	-
Eu^{153}	-	0.03	0.03	0.02	-	-	-	-	-
Gd^{157}	-	-	-	-	-	-	-	-	-
Dy^{163}	0.12	-	-	-	-	-	0.05	-	-
Er^{166}	-	-	-	-	-	-	-	-	-
Yb^{172}	0.09	-	-	-	0.02	-	0.07	-	-

Sample ID Mean (ppm)	DT119 Sp3 Cobaltite	DT017 Line 1 Chalcopyrite	DT017 Line1 Cubanite	DT034 Line 1 Pyrrhotite	DT034 Line 1 Pyrite	DT050B line 1 Chalcopyrite	DT050B Line 1 Troilite	DT050B Line 1 Pyrrhotite	DT063 Line 1 Pyrite
Sb^{121}	-	0.09	-	0.84	0.18	1.05	-	-	3.41
Sb^{123}	0.04	0.06	0.11	0.86	-	1.20	-	-	3.40
Te^{125}	34.56	-	-	0.92	0.68	-	-	-	12.67
Cs^{133}	0.13	0.07	0.25	0.03	-	0.04	-	0.01	0.01
Ba^{137}	-	-	-	-	-	0.07	-	-	0.12
La^{139}	0.12	-	-	0.04	-	4.65	0.07	-	0.10
Ce^{140}	0.11	0.01	-	0.11	-	5.43	-	-	0.03
Pr^{141}	-	-	-	0.03	-	1.27	-	-	-
Nd^{146}	-	-	-	0.04	-	2.27	-	-	-
Sm^{147}	-	-	-	0.02	-	0.73	-	-	-
Eu^{153}	-	-	-	-	-	0.02	-	-	0.04
Gd^{157}	-	-	-	0.03	-	0.84	-	-	-
Dy^{163}	-	0.04	-	0.02	-	0.13	-	-	-
Er^{166}	-	0.23	-	-	-	0.04	-	-	-
Yb^{172}	-	0.36	-	-	-	-	-	-	-

Sample ID Mean (ppm)	DT063 Line 1 Chalcopyrite	DT069 Line 1 Pyrrhotite	DT-069 Line 1 Troilite	DT-069 line 1 Chalcopyrite
Sb^{121}	1.53	-	0.02	0.17
Sb^{123}	1.52	-	0.18	0.07
Te^{125}	1.06	-	-	0.19
Cs^{133}	-	-	0.06	-
Ba^{137}	-	-	-	0.15
La^{139}	-	-	-	0.01
Ce^{140}	-	-	-	-

Pr^{141}	-	-	-	-
Nd^{146}	-	-	-	-
Sm^{147}	-	0.09	-	-
Eu^{153}	-	-	-	-
Gd^{157}	-	-	-	0.05
Dy^{163}	-	-	-	-
Er^{166}	-	-	-	-
Yb^{172}	-	-	-	-

Sample ID Mean (ppm)	DT009 Sp1 Chalcopyrite	DT009 Sp2 Pyrrhotite	DT017 SP1 Cobaltite	DT017 Sp 2 pyrite	DT020 Sp1 Arsenopyrite	DT020 Sp2 Pyrite	DT020 Sp3 Chalcopyrite	DT023 Sp1 Chalcopyrite	DT023 Sp2 Pyrrhotite
Hf^{178}	0.22	-	-	0.08	-	-	-	0.70	-
Ta^{181}	-	-	-	-	-	0.21	-	-	-
W^{182}	-	-	-	-	-	20.04	-	-	-
Re^{185}	-	-	-	-	0.24	0.46	-	-	-
Os^{189}	-	-	-	-	-	0.07	-	-	-
Ir^{193}	-	-	-	-	-	-	-	-	-
Pt^{194}	-	0.14	-	-	-	-	-	-	-
Pt^{195}	-	-	-	-	-	-	-	-	-
Au^{197}	0.06	-	0.12	0.02	3.72	-	-	0.20	-
Tl^{205}	0.08	-	0.65	0.19	-	33.62	0.30	0.11	0.03
Pb^{208}	1.95	0.49	21.75	22.40	1.96	23.24	3.53	0.79	0.44
Bi^{209}	2.57	1.20	54.40	53.63	3.24	0.02	1.69	0.82	0.35
Th^{232}	-	-	-	-	-	-	-	-	-
U^{238}	-	-	-	-	0.17	2.18	-	-	-

Sample ID Mean (ppm)	DT028 Sp1 Arsenopyrite	DT028 Sp2 Chalcopyrite	DT028 Sp3 Pyrrhotite	DT034 Sp3 Pyrrhotite	05-016-DT034 Sp2 Chalcopyrite	DT063 Sp1 Cubanite	DT088 Sp1 Pyrrhotite	DT088 Sp2 Chalcopyrite	DT088 Sp3 Pyrite
Hf^{178}	-	-	-	-	-	-	-	-	-
Ta^{181}	-	-	-	-	-	-	-	-	-
W^{182}	1.73	-	-	-	-	-	-	-	-
Re^{185}	0.19	0.04	-	-	-	-	-	-	-
Os^{189}	-	-	-	-	-	-	-	-	-
Ir^{193}	-	-	-	-	-	-	-	-	-
Pt^{194}	-	-	-	-	-	-	-	-	-
Pt^{195}	-	0.16	-	-	0.20	-	-	-	-
Au^{197}	0.15	0.03	0.10	0.12	0.10	0.05	0.02	0.12	0.06
Tl^{205}	0.04	0.29	-	-	0.18	0.28	0.27	0.28	0.06
Pb^{208}	4.47	3.32	0.61	0.22	3.93	1.58	4.01	2.64	6.26
Bi^{209}	6.48	4.03	1.06	0.18	4.24	2.20	3.48	0.56	18.87
Th^{232}	-	-	-	-	-	-	-	-	-
U^{238}	-	0.30	-	-	-	-	-	0.01	-

Sample ID Mean (ppm)	DT098 Sp1 Chalcopyrite	DT098 Sp2 pyrrhotite	DT099 Sp1 pyrrhotite	DT099 Sp2 Pyrite	DT102 Sp1 Pyrrhotite	DT102 Sp2 Chalcopyrite	DT117 Sp1 Galena	DT117 Sp2 pyrite	DT117 Sp3 Sphalerite
Hf^{178}	-	-	0.01	-	-	-	-	-	-
Ta^{181}	-	0.01	-	-	-	-	-	-	-
W^{182}	-	0.01	-	-	-	-	-	-	-
Re^{185}	-	-	-	-	-	-	-	-	-
Os^{189}	-	-	0.35	-	-	-	-	-	0.08
Ir^{193}	-	-	-	-	-	-	-	-	-
Pt^{194}	0.34	-	-	-	-	0.21	-	-	-
Pt^{195}	-	-	-	-	-	-	-	-	-

Au^{197}	0.02	0.04	0.01	-	0.32	0.07	0.14	0.40	2.96
Tl^{205}	0.46	2.90	0.10	0.68	-	0.18	54280	0.53	53358
Pb^{208}	2.25	10.67	0.54	13.45	1.29	9.88		17.30	1176888
Bi^{209}	2.94	5.50	0.04	21.04	3.10	7.30	6012.3	0.61	7372.1
Th^{232}	0.01	-	-	-	-	-	-	-	-
U^{238}	-	-	-	-	-	-	-	0.35	-

Sample ID Mean (ppm)	DT117 Sp4 Pyrrhotite	DT117 Sp5 Chalcopyrite	DT118A Sp1 Arsenopyrite	DT118A Sp2 Sphalerite	DT118A Sp3 Pyrite	DT118A Sp4 Chalcopyrite	DT118A Sp5 Pyrrhotite	DT119 Sp1 Pyrrhotite	DT119 Sp2 Chalcopyrite
Hf^{178}	-	-	-	0.07	-	-	-	-	-
Ta^{181}	-	-	-	-	-	-	-	-	-
W^{182}	-	1.25	0.31	-	-	-	0.31	0.23	-
Re^{185}	-	-	0.14	-	-	-	-	-	0.14
Os^{189}	-	-	0.24	-	-	-	-	-	-
Ir^{193}	-	-	-	-	-	-	-	-	0.64
Pt^{194}	-	-	-	0.45	0.05	-	-	-	-
Pt^{195}	0.07	-	-	-	-	-	-	0.14	-
Au^{197}	0.55	0.73	1.30	12.35	0.10	0.30	-	0.43	1.05
Tl^{205}	0.17	0.48	0.03	0.12	0.01	0.04	-	-	1.03
Pb^{208}	8.16	8.81	24.51	3.19	0.21	1.34	0.81	0.52	21.76
Bi^{209}	0.07	1.96	54.26	0.41	0.17	0.54	0.59	0.26	10.82
Th^{232}	-	-	-	-	-	-	-	-	-
U^{238}	-	-	-	0.04	-	-	-	-	-

Sample ID Mean (ppm)	DT119 Sp3 Cobaltite	DT017 Line 1 Chalcopyrite	DT017 Line1 Cubanite	DT034 Line 1 Pyrrhotite	DT034 Line 1 Pyrite	DT050B line 1 Chalcopyrite	DT050B Line 1 Troilite	DT050B Line 1 Pyrrhotite	DT063 Line 1 Pyrite

Hf^{178}	-	11.90	-	0.04	-	-	-	-	-
Ta^{181}	-	-	-	-	-	-	-	-	-
W^{182}	-	-	-	-	-	-	-	-	0.14
Re^{185}	-	-	-	0.02	-	-	-	-	0.03
Os^{189}	-	-	-	-	-	-	-	-	-
Ir^{193}	-	-	-	-	-	-	-	0.08	-
Pt^{194}	-	-	0.25	-	-	-	-	-	-
Pt^{195}	1.00	-	-	-	-	-	-	0.21	-
Au^{197}	6.46	-	-	1.68	-	0.01	0.05	-	0.28
Tl^{205}	-	0.55	0.13	0.51	0.30	1.48	-	-	0.70
Pb^{208}	3.19	1.92	2.48	8.74	2.61	24.11	0.35	0.12	19.54
Bi^{209}	3.18	3.66	4.19	12.72	4.12	18.51	0.79	0.39	41.14
Th^{232}	-	-	-	0.11	-	-	-	-	0.11
U^{238}	-	3.32	-	0.40	-	0.16	-	-	0.01

Sample ID Mean (ppm)	DT063 Line 1 Chalcopyrite	DT069 Line 1 Pyrrhotite	DT-069 Line 1 Troilite	DT-069 line 1 Chalcopyrite
Hf^{178}	-	-	-	-
Ta^{181}	-	-	-	-
W^{182}	-	-	-	-
Re^{185}	-	-	-	-
Os^{189}	0.08	-	-	-
Ir^{193}	-	-	-	-
Pt^{194}	-	-	-	-
Pt^{195}	-	-	-	-
Au^{197}	0.05	0.01	0.20	0.27
Tl^{205}	0.03	-	-	0.29

Pb^{208}	1.61	0.06	-	3.47
Bi^{209}	2.55	-	-	4.25
Th^{232}	-	-	-	0.03
U^{238}	-	-	-	0.02

Appendix V

Tourmaline LA-ICP-MS

Sample ID Mean (ppm)	DT009 Sp3 Tourmaline	DT017 Sp 3 Tourmaline	DT028 Sp4 Tourmaline	DT034 Sp4 Tourmaline	DT119 Sp4 Tourmaline	DT088 Line 1 tourmaline	DT-088 Tourmaline part 1	DT-088 Tourmaline part 2	DT-088 Tourmaline part 3
Li^{7}	4.97	2.92	5.14	2.97	5.97	5.94	8.57	3.08	7.25
Be^{9}	6.92	7.03	3.57	9.96	-	16.62	14.60	10.15	16.01
B^{11}	71446	75483	40472	41511	141742	46539	47589	45518	46341
Na^{23}	60971	80132	51799	69382	29550	32915	32075	33691	31470
Mg^{24}	22204	47637	22085	25904	35915	53506	57691	55164	41098
Al^{27}	205118	193055	198555	127332	164107	213041	219088	213521	200359
Si^{29}	528562	543874	430753	448610	470182	294973	290519	306150	269702
P^{31}	123.23	83.37	59.26	40.61	76.00	27.05	85.57	54.27	11.32
S^{33}	-	-	-	-	11177	-	5557.6	-	-
S^{34}	4456.57	3350.59	2730.8	2998.8	7152.2	7480.9	8647.7	6735.8	8869.2
K^{39}	79.15	141.94	101.52	48.35	63.07	106.99	108.11	133.67	64.61
Ca^{43}	16922.91	65716.97	14928	25713	11222	21765	26992	20097	15415
Sc^{45}	14.79	42.75	32.06	42.09	25.55	17.04	18.73	20.17	11.47
Ti^{47}	2919.2	2771.3	1487.3	1828.4	2693.1	4033.6	4264.9	4168.3	3169.5
V^{51}	165.83	542.54	388.37	270.66	181.64	660.09	702.72	697.27	554.10

Sample ID Mean (ppm)	DT009 Sp3 Tourmaline	DT017 Sp 3 Tourmaline	DT028 Sp4 Tourmaline	DT034 Sp4 Tourmaline	DT119 Sp4 Tourmaline	DT088 Line 1 tourmaline	DT-088 Tourmaline part 1	DT-088 Tourmaline part 2	DT-088 Tourmaline part 3
Cr^{53}	144.03	214.30	364.33	126.17	39.15	455.54	521.31	540.95	138.12
Mn^{55}	135.25	251.41	222.87	301.14	256.82	896.98	823.82	918.17	915.12
Co^{59}	107.99	102.85	59.00	30.61	42.96	23.40	17.59	21.76	35.12

Ni^{60}	16.86	72.25	22.30	5.53	3.67	8.48	9.28	7.98	10.06
Ni^{61}	-	120.58	90.45	27.62	52.33	28.31	104.71	25.45	53.87
Cu^{63}	0.32	-	0.24	0.17	24.35	1.90	1.42	1.93	3.64
Cu^{65}	-	0.13	0.07	0.32	25.71	1.97	1.24	2.76	4.59
Zn^{66}	28.09	13.67	11.15	27.33	13.77	138.01	125.75	143.87	127.60
Zn^{68}	36.17	23.10	16.73	33.36	14.62	135.66	167.83	116.96	130.73
Ga^{69}	73.03	61.68	63.67	29.95	35.37	92.56	93.37	104.08	75.72
As^{75}	10.39	42.37	12.79	10.06	1735.4	-	-	-	-
Se^{77}	-	23.71	-	-	-	-	-	3.90	7.94
Se^{78}	-	-	-	7.40	-	57.40	178.86	83.28	-
Se^{82}	-	13.32	17.06	-	-	13.62	6.64	9.46	-
Rb^{85}	-	0.22	-	0.31	0.29	0.31	-	-	1.14

Sample ID Mean (ppm)	DT009 Sp3 Tourmaline	DT017 Sp 3 Tourmaline	DT028 Sp4 Tourmaline	DT034 Sp4 Tourmaline	DT119 Sp4 Tourmaline	DT088 Line 1 tourmaline	DT-088 Tourmaline part 1	DT-088 Tourmaline part 2	DT-088 Tourmaline part 3
Sr^{88}	180.01	1930.8	172.36	809.96	457.04	239.33	240.51	276.70	155.92
Y^{89}	22.24	2.83	60.73	5.57	1.74	0.58	1.16	0.94	0.23
Zr^{90}	-	10.98	7.14	6.12	13.21	2.14	1.85	3.42	0.35
Nb^{93}	3.70	6.32	18.00	1.91	0.54	0.41	0.72	0.81	-
Mo^{95}	-	-	-	-	-	0.07	1.52	-	2.92
Ru^{101}	-	-	-	-	-	-	-	-	-
Rh^{103}	-	-	-	-	-	-	-	-	-
Pd^{105}	0.76	-	0.89	0.01	-	-	-	-	-
Pd^{106}	-	-	0.33	-	-	-	-	-	-
Ag^{107}	-	-	-	-	-	0.31	0.94	-	-
Pd^{108}	-	-	-	-	-	-	0.86	-	-
Ag^{109}	-	-	-	-	-	0.44	0.42	0.78	0.38

Cd^{111}	-	-	0.05	-	-	-	-	-	-
Sn^{118}	35.79	3.69	49.35	26.40	28.68	9.49	15.12	8.56	7.95
Sn^{120}	37.40	5.26	39.06	28.51	19.67	7.74	9.58	6.56	7.51

Sample ID Mean (ppm)	DT009 Sp3 Tourmaline	DT017 Sp 3 Tourmaline	DT028 Sp4 Tourmaline	DT034 Sp4 Tourmaline	DT119 Sp4 Tourmaline	DT088 Line 1 tourmaline	DT-088 Tourmaline part 1	DT-088 Tourmaline part 2	DT-088 Tourmaline part 3
Sb^{121}	1.34	2.11	0.15	1.14	-	0.34	0.44	0.08	0.79
Sb^{123}	0.93	2.10	1.91	1.14	0.04	-	0.35	0.17	-
Te^{125}	-	-	-	-	0.02	-	-	-	-
Cs^{133}	0.04	0.13	-	0.59	0.19	0.09	-	0.34	0.10
Ba^{137}	0.40	2.11	0.58	1.39	-	1.75	3.44	1.70	1.70
La^{139}	2.35	0.20	1.83	1.19	-	0.41	0.18	0.71	0.24
Ce^{140}	3.92	0.11	2.86	2.71	0.21	1.09	1.34	1.17	0.71
Pr^{141}	1.53	-	1.38	2.59	-	0.17	0.14	0.27	-
Nd^{146}	1.27	-	0.86	0.52	-	-	-	-	-
Sm^{147}	0.10	-	-	-	-	-	-	-	-
Eu153	0.06	-	-	-	-	0.05	-	0.13	0.11
Gd^{157}	-	-	0.34	-	-	-	-	-	0.62
Dy^{163}	-	-	1.01	-	0.74	-	-	-	-
Er^{166}	0.20	-	2.86	0.57	-	0.18	0.27	0.32	-
Yb^{172}	0.15	-	4.22	0.78	-	-	-	-	-

Sample ID Mean (ppm)	DT009 Sp3 Tourmaline	DT017 Sp 3 Tourmaline	DT028 Sp4 Tourmaline	DT034 Sp4 Tourmaline	DT119 Sp4 Tourmaline	DT088 Line 1 tourmaline	DT-088 Tourmaline part 1	DT-088 Tourmaline part 2	DT-088 Tourmaline part 3
Hf^{178}	0.52	2.80	0.44	0.85	3.21	-	0.53	-	-
Ta^{181}	0.88	-	2.54	-	-	-	-	-	-
W^{182}	3.64	0.92	3.09	-	-	-	-	-	-

Re^{185}	0.10	-	0.43	-	-	0.08	0.37	0.48	-
Os^{189}	-	-	-	-	-	0.01	1.15	0.01	0.01
Ir^{193}	-	-	-	-	-	-	-	-	-
Pt^{194}	-	-	0.01	-	-	-	-	-	-
Pt^{195}	-	-	-	-	-	-	-	-	-
Au^{197}	0.24	0.40	-	0.06	1.23	-	1.13	-	-
Tl^{205}	0.68	-	0.16	0.66	0.19	1.79	2.47	2.53	0.54
Pb^{208}	5.48	0.76	2.54	7.91	9.66	18.61	18.15	22.72	8.63
Bi^{209}	0.03	0.24	0.35	1.12	-	0.01	0.01	0.01	0.18
Th^{232}	0.10	-	0.37	-	-	-	-	-	-
U^{238}	0.08	-	-	0.11	1.85	0.35	0.59	0.21	-

Appendix VI

SEM Data Garnet

Sample ID	DT120A	DT120A	DT-98	DT-98	DT-98	DT-98	DT-98	DT063	DT063	DT063
Drill Hole	17-01	17-01	17-01	17-01	17-01	17-01	17-01	16-04	16-04	16-04
SEM site	SEM4	SEM4	SEM2	SEM2	SEM 4	SEM 4	SEM 4	SEM2	SEM2	SEM2
Analysis ID	Garnet 1	Garnet 2	Garnet 2	Garnet 1	Garnet 1	Garnet 2	Garnet 3	Garnet 2	Garnet 3	Garnet 4
MgO Wt.%	2.35	2.44	1.48	1.39	1.64	1.53	1.47	1.91	1.84	1.86
Al_2O_3 Wt.%	20.40	20.70	20.60	20.75	20.58	20.70	21.06	19.92	20.26	20.18
SiO_2 Wt.%	36.61	36.38	35.50	35.21	35.92	36.52	35.97	35.95	35.84	35.88
CaO Wt.%	4.52	3.65	1.55	2.18	1.73	1.07	1.39	2.67	2.71	2.54
MnO Wt.%	8.83	8.92	0.44	0.38	0.64	-	0.49	0.46	0.68	0.52
TiO_2 Wt.%	-	-	-	-	-	-	-	-	-	-
FeO Wt.%	27.13	28.07	39.91	39.32	40.17	40.46	40.53	38.54	38.28	38.69
Total	99.84	100.17	99.48	99.24	100.68	100.29	100.91	99.45	99.61	99.67

Sample ID	DT063	DT063	DT063	DT088	DT088	DT088	DT088	DT088	DT088	DT099
Drill Hole	16-04	16-04	16-04	17-01	17-01	17-01	17-01	17-01	17-01	17-01
SEM site	SEM2	SEM4	SEM4	SEM4	SEM4	SEM4	SEM5	SEM5	SEM6	SEM 2
Analysis ID	Garnet 1	Garnet 2	Garnet 1	Garnet 2	Garnet 3	Garnet 1	Garnet 2	Garnet	Garnet	Garnet 2
MgO Wt.%	1.92	1.54	1.46	1.98	1.92	1.84	1.87	1.99	1.93	1.53
Al_2O_3 Wt.%	20.17	20.44	20.15	20.68	20.69	20.67	20.79	20.68	20.87	20.49
SiO_2 Wt.%	35.55	35.27	35.34	35.67	35.99	35.67	35.21	36.14	35.95	35.99
CaO Wt.%	2.52	2.28	2.21	2.72	3.00	2.82	2.13	2.24	2.08	2.17
MnO Wt.%	0.47	0.35	0.56	2.31	3.83	4.35	1.55	1.5.0	1.44	2.82
TiO_2 Wt.%	-	-	-	-	-	-	-	-	-	-
FeO Wt.%	38.6	39.11	38.99	35.82	34.53	34.46	37.54	37.58	37.38	37.22
Total	99.24	98.99	98.72	99.18	99.95	99.81	99.09	100.13	99.64	100.22

Sample ID	DT099	DT050B	DT050B	DT050B	DT050B	DT050B	DT050B	DT056	DT056	DT056
Drill Hole	17-01	16-04	16-04	16-04	16-04	16-04	16-04	16-04	16-04	16-04
SEM site	SEM 2	SEM 2	SEM 3	SEM 3	SEM 3	SEM 4	SEM 4	SEM 1	SEM 1	SEM 2
Analysis ID	Garnet	Garnet 1	Garnet 1	Garnet 2	Garnet 3	Garnet 1	Garnet 2	Garnet 1	Garnet 2	Garnet 1

MgO Wt.%	1.79	1.19	1.21	1.51	1.41	1.23	1.22	1.20	1.20	1.30
Al_2O_3 Wt.%	21.06	20.50	20.95	20.93	20.94	20.97	20.69	20.75	21.25	20.72
SiO_2 Wt.%	36.40	36.10	36.20	36.02	36.04	35.96	36.52	35.64	35.93	35.74
CaO Wt.%	2.38	2.35	2.47	2.16	2.20	2.47	2.50	3.77	3.81	1.99
MnO Wt.%	1.86	2.13	2.76	1.87	1.72	1.84	1.71	2.89	4.09	2.16
TiO_2 Wt.%	-	-	-	-	-	-	-	-	-	-
FeO Wt.%	37.57	37.8	36.87	38.36	38.61	37.79	38.40	34.92	34.07	38.33
Total	101.06	100.08	100.47	100.86	100.92	100.27	101.04	99.17	100.35	100.23

Sample ID	DT056	DT056	DT069	DT069	DT069	DT069	DT069	DT069	DT069	DT069
Drill Hole	16-04	16-04	16-04	16-04	16-04	16-04	16-04	16-04	16-04	16-04
SEM site	SEM 2	SEM 2	SEM 1	SEM 1	SEM 2	SEM 2	SEM 2	SEM 3	SEM 3	SEM 3
Analysis ID	Garnet 2	Garnet 3	Garnet 2	Garnet	Garnet 1	Garnet 2	Garnet 3	Garnet 1	Garnet 2	Garnet 3
MgO Wt.%	1.3	1.28	1.36	1.51	0.68	1.34	1.39	1.46	1.26	0.55
Al_2O_3 Wt.%	20.9	20.89	20.64	21.13	20.68	20.89	21.15	20.87	20.72	20.39
SiO_2 Wt.%	35.92	35.61	35.65	35.82	35.79	35.62	36.03	35.64	35.86	35.53
CaO Wt.%	2.12	2.10	1.42	1.18	5.85	2.70	1.21	1.12	2.85	6.46
MnO Wt.%	1.71	1.87	0.43	0.48	3.18	1.00	1.17	1.25	1.13	4.73
TiO_2 Wt.%	0	0	0	0	0	0	0	0	0	0
FeO Wt.%	38.16	38.15	40.52	40.03	34.25	38.94	40.25	40.46	38.58	31.73
Total	100.11	99.91	100.01	100.14	100.43	100.49	101.19	100.80	100.40	99.40

Sample ID	DT069	DT069	DT069	DT017	DT017	DT017	DT017	DT017	DT017	DT017
Drill Hole	16-04	16-04	16-04	19-01	19-01	19-01	19-01	19-01	19-01	19-01
SEM site	SEM 4	SEM 4	SEM 4	SEM 1	SEM 1	SEM 1	SEM 1	SEM 1	SEM 2	SEM 2
Analysis ID	Garnet 1	Garnet 2	Garnet 3	Garnet 1	Garnet 2	Garnet 3	Garnet 4	Garnet 5	Garnet 1	Garnet 2
MgO Wt.%	1.61	1.49	1.47	2.15	1.46	1.35	1.41	2.41	2.25	2.04
Al_2O_3 Wt.%	20.29	20.59	20.71	21.03	20.71	20.58	20.89	21.27	20.91	20.3
SiO_2 Wt.%	35.73	35.32	35.76	36.11	36.03	35.19	36.09	36.37	36.09	35.41
CaO Wt.%	1.55	1.21	1.63	2.96	3.24	2.98	3.29	2.05	2.74	2.80

MnO Wt.%	0.48	0.49	0.76	1.43	2.78	2.91	2.91	0.95	0.36	0.81
TiO_2 Wt.%	-	-	-	-	-	-	-	-	-	-
FeO Wt.%	40.1	40.46	40.62	36.73	36.62	36.69	36.37	38.12	38.41	37.84
Total	99.76	99.56	100.95	100.41	100.84	99.7	100.97	101.16	100.77	99.2

Sample ID	DT017	DT017	DT017	DT017	DT017	DT017	DT017	DT017	DT020	DT020
Drill Hole	19-01	19-01	19-01	19-01	19-01	19-01	19-01	19-01	19-01	19-01
SEM site	SEM 3	SEM 3	SEM 4	SEM 4	SEM 4	SEM 5	SEM 5	SEM 5	SEM 1	SEM 1
Analysis ID	Garnet 1	Garnet 2	Garnet 1	Garnet 2	Garnet 3	Garnet	Garnet 2	Garnet 3	Garnet 1	Garnet 2
MgO Wt.%	2.47	2.52	2.13	2.37	2.26	2.03	1.92	1.64	1.26	1.43
Al_2O_3 Wt.%	21.37	21.06	21.04	20.96	21.08	20.86	21.1	20.66	20.7	20.59
SiO_2 Wt.%	36.34	36.44	36.65	36.03	36.41	35.46	36.83	35.64	35.87	36.13
CaO Wt.%	2.32	2.28	2.73	2.15	2.34	2.94	2.82	2.69	6.6	4.69
MnO Wt.%	-	-	0.9	0.43	0.36	0.67	0.84	0.87	2.42	2.53
TiO_2 Wt.%	-	-	-	-	-	-	-	-	-	-
FeO Wt.%	37.66	37.83	37.54	37.9	38.06	37.3	37.25	38.57	33.65	34.43
Total	100.16	100.13	100.99	99.83	100.52	99.26	100.77	100.06	100.52	99.8

Sample ID	DT020	DT020	DT020	DT020	DT020	DT028	DT028	DT028	DT028	DT009
Drill Hole	19-01	19-01	19-01	19-01	19-01	16-02	16-02	16-02	16-02	16-02
SEM site	SEM 3	SEM 4	SEM 4	SEM 4	SEM 5	SEM 2	SEM 2	SEM 3	SEM 3	SEM 1
Analysis ID	Garnet 2	Garnet	Garnet 2	Garnet 3	Garnet 1	Garnet 1	Garnet 2	Garnet 1	Garnet 2	Garnet 1
MgO Wt.%	1.26	1.49	1.25	1.17	0.81	1.3	1	1.46	1.42	1.68
Al_2O_3 Wt.%	20.63	20.82	20.71	20.82	20.69	21.02	20.66	20.85	20.72	20.9
SiO_2 Wt.%	35.59	35.94	35.73	35.48	35.51	35.49	35.72	35.78	36.27	35.85
CaO Wt.%	5.35	4.74	4.19	5.38	7.92	0.87	1.08	0.77	0.77	0.91
MnO Wt.%	3.53	2.26	4.48	2.32	3.62	1.04	1.77	1.18	1.11	0.87
TiO_2 Wt.%	-	-	-	-	-	-	-	-	-	-
FeO Wt.%	32.85	35.05	33.34	34.32	30.47	40.61	39.89	40.51	40.42	40.29
Total	99.21	100.31	99.7	99.49	99.01	100.33	100.1	100.55	100.7	100.5

Sample ID	DT009	DT009	DT009	DT009	DT009	DT009	DT009	DT009	DT009	DT009
Drill Hole	16-02	16-02	16-02	16-02	16-02	16-02	16-02	16-02	16-02	16-02
SEM site	SEM 1	SEM 1	SEM 2	SEM 2	SEM 3	SEM 3	SEM 3	SEM 3	SEM 4	SEM 4
Analysis ID	Garnet 2	Garnet 3	Garnet 1	Garnet 2	Garnet 1	Garnet 2	Garnet 3	Garnet 4	Garnet 1	Garnet 2
MgO Wt.%	1.72	1.67	1.87	1.81	1.72	1.8	1.8	1.84	1.6	1.66
Al_2O_3 Wt.%	20.56	20.74	20.93	20.19	20.74	20.6	20.78	20.96	20.27	20.54
SiO_2 Wt.%	35.33	35.43	35.57	35.57	35.89	35.94	35.42	35.7	35.14	35.45
CaO Wt.%	0.83	0.95	0.99	0.98	1	0.61	0.97	0.88	0.58	0.86
MnO Wt.%	1.28	0.91	0.79	0.94	1.02	0.92	0.98	0.9	1.04	0.94
TiO_2 Wt.%	0	0	0	0	0	0	0	0	0	0
FeO Wt.%	39.83	40.31	39.79	40.43	40.28	40.2	40.13	40.38	40.38	39.9
Total	99.54	100.01	99.93	99.92	100.65	100.07	100.09	100.65	99	99.35

Sample ID	DT009	DT009	DT009	DT009	DT023	DT023	DT023	DT023	DT023	DT023
Drill Hole	16-02	16-02	16-02	16-02	16-01	16-01	16-01	16-01	16-01	16-01
SEM site	SEM 4	SEM 5	SEM 5	SEM 5	SEM 1	SEM 1	SEM 1	SEM 2	SEM 3	SEM 3
Analysis ID	Garnet 3	Garnet 1	Garnet 2	Garnet 3	Garnet 1	Garnet 2	Garnet 3	Garnet 1	Garnet 1	Garnet 2
MgO Wt.%	1.78	1.69	1.73	1.72	1.39	1.29	1.25	1.62	1.37	1.3
Al_2O_3 Wt.%	20.95	20.29	20.68	20.85	20.62	20.71	20.14	20.83	20.34	20.74
SiO_2 Wt.%	35.86	35.37	35.82	36.13	35.60	35.23	34.98	35.22	35.23	35.66
CaO Wt.%	0.84	1.09	1.05	1.05	0.80	0.71	1.42	0.37	0.61	0.36
MnO Wt.%	1.04	1.15	1.00	0.87	0.56	0.49	0.64	0.45	0.51	0.43
TiO_2 Wt.%	0	0	0	0	0	0	0	0	0	0
FeO Wt.%	40.30	39.67	40.15	40.45	41.12	41.30	40.63	42.31	41.77	41.89
Total	100.77	99.26	100.42	101.08	100.1	99.72	99.05	100.79	99.83	100.37

Sample ID	DT023	DT023	DT023	DT023	DT023	DT023	DT023	DT023	DT023	DT023
Drill Hole	16-01	16-01	16-01	16-01	16-01	16-01	16-01	16-01	16-01	16-01
SEM site	SEM 3	SEM 4	SEM 4	SEM 5	SEM 5	SEM 6	SEM 6	SEM 6	SEM 7	SEM 7
Analysis ID	Garnet 3	Garnet 1	Garnet 2	Garnet 1	Garnet 2	Garnet 1	Garnet 2	Garnet 3	Garnet 1	Garnet 2
MgO Wt.%	1.37	1.50	1.38	1.12	1.34	1.23	1.36	1.36	1.41	1.28
Al_2O_3 Wt.%	20.46	20.80	20.38	20.16	20.16	20.62	20.76	20.04	20.47	20.23
SiO_2 Wt.%	35.53	34.67	34.88	34.79	35.20	35.38	35.48	35.02	35.38	35.24
CaO Wt.%	0.38	0.42	0.56	1.74	0.90	1.12	1.35	1.83	0.46	1.78
MnO Wt.%	0.29	0.67	0.52	1.58	1.16	0.45	0.60	0.54	0.48	0.65
TiO_2 Wt.%	-	-	-	0.36	-	-	-	-	-	-
FeO Wt.%	42.03	41.91	41.41	39.64	40.63	41.23	40.58	40.4	42.04	40.27
Total	100.07	99.97	99.12	99.39	99.38	100.04	100.12	99.2	100.24	99.45

Sample ID	DT023	DT023	DT032	DT032	DT032	DT032	DT006	DT006	DT006	DT006
Drill Hole	16-01	16-01	19-02	19-02	19-02	19-02	16-02	16-02	16-02	16-02
SEM site	SEM 7	SEM 7	SEM 2	SEM 2	SEM 2	SEM 2	SEM 1	SEM 2	SEM 2	SEM 2
Analysis ID	Garnet 3	Garnet 4	Garnet 1	Garnet 2	Garnet 3	Garnet 4	Garnet 1	Garnet 1	Garnet 2	Garnet 3
MgO Wt.%	1.39	1.36	1.63	1.26	1.08	1.56	1.65	1.75	1.55	1.26
Al_2O_3 Wt.%	20.54	20.26	20.57	20.67	20.55	21.14	20.97	20.71	20.45	20.32
SiO_2 Wt.%	35.3	35.27	35.99	35.91	35.62	35.87	36.08	36.00	36.53	36.54
CaO Wt.%	0.60	2.08	1.97	3.12	2.82	1.64	4.20	7.40	9.30	6.44
MnO Wt.%	0.36	0.96	1.13	4.23	4.77	1.16	21.42	17.61	17.83	20.28
TiO_2 Wt.%	-	-	-	-	-	-	-	-	-	-
FeO Wt.%	41.41	40.12	38.77	35.27	34.77	39.21	16.62	15.65	14.6	15.74
Total	99.61	100.06	100.05	100.47	99.61	100.57	100.95	99.12	100.26	100.58

Sample ID	DT005	DT005	DT005	DT005	DT005	DT005	DT024	DT024	DT030	DT030
Drill Hole	19-03	19-03	19-03	19-03	19-03	19-03	16-01	16-01	19-02	19-02
SEM site	SEM 1	SEM 1	SEM 3	SEM 3	SEM 5	SEM 5	SEM 1	SEM 1	SEM 1	SEM 3
Analysis ID	Garnet 1	Garnet 2	Garnet 1	Garnet 2	Garnet 1	Garnet 2	Garnet 1	Garnet 2	Garnet 1	Garnet 1
MgO Wt.%	1.84	1.72	1.91	1.75	1.82	1.88	1.83	1.88	2.22	2.26
Al_2O_3 Wt.%	21.01	20.77	20.70	21.07	21.30	20.81	21.08	21.10	20.73	20.78
SiO_2 Wt.%	36.26	36.10	35.98	35.53	35.85	36.39	36.23	36.28	35.73	36.52
CaO Wt.%	1.07	1.27	0.95	0.61	0.89	1.47	2.14	2.35	2.46	2.42
MnO Wt.%	2.18	2.20	2.14	2.74	2.26	2.05	2.26	2.31	1.30	1.89
TiO_2 Wt.%	-	-	-	-	-	-	-	-	-	-
FeO Wt.%	38.69	37.88	37.63	37.95	38.23	38.26	36.83	36.19	37.77	35.47
Total	101.05	99.95	99.3	99.65	100.35	100.84	100.37	100.12	100.21	99.35

Sample ID	DT030	DT030	DT030	DT030	DT042	DT042	DT042	DT064	DT064	DT064
Drill Hole	19-02	19-02	19-02	19-02	16-04	16-04	16-04	16-04	16-04	16-04
SEM site	SEM 3	SEM 3	SEM 4	SEM 4	SEM 1	SEM 1	SEM 1	SEM 3	SEM 3	SEM 3
Analysis ID	Garnet 2	Garnet 3	Garnet 1	Garnet 2	Garnet 1	Garnet 2	Garnet 3	Garnet 1	Garnet 2	Garnet 3
MgO Wt.%	2.08	2.42	1.90	1.94	2.13	1.96	2.76	1.45	1.68	1.90
Al_2O_3 Wt.%	21.25	20.99	21.18	21.42	20.70	20.73	20.89	20.83	20.68	20.77
SiO_2 Wt.%	36.64	36.33	36.77	36.16	35.55	35.77	36.18	35.75	36.00	36.28
CaO Wt.%	2.13	2.32	3.39	2.08	3.12	3.46	2.16	3.55	2.85	1.48
MnO Wt.%	1.67	1.38	2.45	1.36	15.83	15.51	11.12	2.74	1.57	1.35
TiO_2 Wt.%	-	-	-	-	-	-	-	-	-	-
FeO Wt.%	36.54	36.72	34.94	37.08	22.5	22.17	26.18	35.45	37.27	39.05
Total	100.32	100.17	100.63	100.05	99.83	99.61	99.29	99.76	100.05	100.84

Sample ID	DT054	DT054	DT054	DT054	DT054	DT054	DT054	DT054	DT058	DT058
Drill Hole	16-04	16-04	16-04	16-04	16-04	16-04	16-04	16-04	16-04	16-04
SEM site	SEM 1	SEM 1	SEM 1	SEM 1	SEM 3	SEM 3	SEM 3	SEM 3	SEM 1	SEM 1
Analysis ID	Garnet 1	Garnet 2	Garnet 3	Garnet 4	Garnet 1	Garnet 2	Garnet 3	Garnet 4	Garnet 1	Garnet 2
MgO Wt.%	2.20	2.06	2.12	2.19	1.50	1.76	1.21	1.08	1.50	1.68
Al_2O_3 Wt.%	21.01	20.72	21.43	21.05	20.72	20.79	20.88	20.86	20.68	20.63
SiO_2 Wt.%	36.45	36.52	36.09	36.48	36.18	36.62	36.17	36.23	35.88	35.44
CaO Wt.%	2.73	2.14	2.67	2.72	3.49	2.64	4.11	4.83	6.12	2.59
MnO Wt.%	0.69	1.13	0.67	1.03	1.76	1.26	3.35	3.39	8.70	6.61
TiO_2 Wt.%	-	-	-	-	-	-	-	-	-	-
FeO Wt.%	37.36	38.18	37.82	37.46	36.56	37.45	35.17	33.9	26.74	32.48
Total	100.43	100.74	100.79	100.93	100.22	100.52	100.9	100.3	99.61	99.43

Sample ID	DT058	DT058	DT058	DT058	DT058	DT058	DT053	DT053	DT053	DT053
Drill Hole	16-04	16-04	16-04	16-04	16-04	16-04	16-04	16-04	16-04	16-04
SEM site	SEM 1	SEM 3	SEM 3	SEM 3	SEM 4	SEM 4	SEM 3	SEM 3	SEM 3	SEM 4
Analysis ID	Garnet 3	Garnet 1	Garnet 2	Garnet 3	Garnet 1	Garnet 2	Garnet 1	Garnet 2	Garnet 3	Garnet 1
MgO Wt.%	1.75	1.29	1.41	1.44	1.65	1.60	1.57	1.80	1.96	2.16
Al_2O_3 Wt.%	20.70	20.72	20.91	20.60	20.85	21.05	21.33	20.74	21.00	20.46
SiO_2 Wt.%	35.92	35.35	35.93	35.83	35.91	35.71	35.74	36.11	35.98	35.52
CaO Wt.%	2.74	4.30	2.66	2.60	2.74	2.73	3.42	2.05	2.32	0.75
MnO Wt.%	6.85	5.22	5.17	5.00	2.89	2.62	2.35	1.10	1.32	0.25
TiO_2 Wt.%	-	-	-	-	-	-	-	-	-	-
FeO Wt.%	32.6	32.43	34.47	34.51	36.47	36.85	36.18	39.16	38.37	40.05
Total	100.54	99.31	100.54	99.98	100.5	100.56	100.58	100.96	100.95	99.18

Sample ID	DT053	DT053	DT001	DT001	DT001	DT001	DT001	DT001	DT003	DT003
Drill Hole	16-04	16-04	19-03	19-03	19-03	19-03	19-03	19-03	19-03	19-03
SEM site	SEM 4	SEM 4	SEM 2	SEM 2	SEM 2	SEM 3	SEM 3	SEM 3	SEM 2	SEM 2
Analysis ID	Garnet 2	Garnet 3	Garnet 1	Garnet 2	Garnet 3	Garnet 1	Garnet 2	Garnet 3	Garnet 1	Garnet 2
MgO Wt.%	1.97	1.93	2.06	2.01	1.24	1.67	1.71	1.73	1.8	1.85
Al_2O_3 Wt.%	20.62	20.97	20.22	21.08	20.82	20.51	20.56	20.71	21.34	20.9
SiO_2 Wt.%	35.85	35.81	35.85	35.54	35.25	35.98	35.86	35.61	36.39	35.74
CaO Wt.%	0.55	0.89	1.61	1.82	2.62	1.87	1.31	1.93	2.73	2.75
MnO Wt.%	0.22	0.22	0.98	1.44	2.85	1.26	1.16	1.35	0.38	0.42
TiO_2 Wt.%	-	-	-	-	-	-	-	-	-	-
FeO Wt.%	41.3	40.64	38.39	37.9	36.62	38.04	38.87	38.49	37.63	37.52
Total	100.52	100.44	99.11	99.79	99.41	99.33	99.47	99.82	100.27	99.18

Sample ID	DT003	DT003	DT003	DT003	DT003	DT003	DT003	DT003	DT003	DT035
Drill Hole	19-03	19-03	19-03	19-03	19-03	19-03	19-03	19-03	19-03	19-04
SEM site	SEM 3	SEM 3	SEM 4	SEM 4	SEM 4	SEM 5	SEM 5	SEM 5	SEM 5	SEM 3
Analysis ID	Garnet 1	Garnet 2	Garnet 1	Garnet 2	Garnet 3	Garnet 1	Garnet 2	Garnet 3	Garnet 4	Garnet 1
MgO Wt.%	1.67	1.56	1.87	1.42	1.33	2.57	2.36	1.78	1.48	2.54
Al_2O_3 Wt.%	20.82	20.96	20.75	20.60	20.70	21.12	21.16	21.00	20.98	20.91
SiO_2 Wt.%	35.67	36.1	36.53	35.91	36.02	36.34	36.76	36.28	36.34	36.54
CaO Wt.%	2.09	3.07	2.61	3.19	3.26	2.23	2.33	2.9	2.68	3.08
MnO Wt.%	2.03	2.03	0.76	2.68	2.57	0.31	0.51	1.01	1.78	1.94
TiO_2 Wt.%	-	-	-	-	-	-	-	-	-	-
FeO Wt.%	37.03	36.28	37.6	35.98	35.96	37.87	37.22	37.17	37.6	35.27
Total	99.31	100.01	100.13	99.78	99.85	100.45	100.34	100.14	100.86	100.29

Sample ID	DT035	DT035	DT050A	DT050A	DT050A	DT092	DT092	DT070	DT070	DT070
Drill Hole	19-04	19-04	16-04	16-04	16-04	17-01	17-01	16-04	16-04	16-04
SEM site	SEM 3	SEM 3	SEM 3	SEM 3	SEM 4	SEM 3	SEM 3	SEM 1	SEM 1	SEM 1
Analysis ID	Garnet 2	Garnet 3	Garnet 1	Garnet 2	Garnet 1	Garnet 1	Garnet 2	Garnet 1	Garnet 2	Garnet 3
MgO Wt.%	2.57	2.35	1.76	1.85	1.83	2.18	2.25	1.21	1.26	1.23
Al_2O_3 Wt.%	21.25	20.49	21.06	20.74	21.56	20.87	20.65	20.74	20.97	20.59
SiO_2 Wt.%	36.56	36.59	35.93	36.00	35.77	36.25	36.48	35.49	35.72	36.01
CaO Wt.%	2.82	2.63	2.56	2.13	2.17	2.35	2.81	2.30	1.50	0.99
MnO Wt.%	2.44	2.98	0.76	0.59	0.66	0.32	0.47	0.96	0.85	0.89
TiO_2 Wt.%	-	-	-	-	-	-	-	-	-	-
FeO Wt.%	35.36	35.54	37.31	38.81	38.23	37.88	37.65	38.41	39.15	39.89
Total	101.00	100.59	99.37	100.12	100.22	99.85	100.31	99.11	99.66	99.61

Sample ID	DT070	DT070	DT111	DT111	DT111	DT111	DT113	DT113	DT113	DT113
Drill Hole	16-04	16-04	21-6	21-6	21-6	21-6	21-8	21-8	21-8	21-8
SEM site	SEM 2	SEM 2	SEM 3	SEM 3	SEM 3	SEM 3	SEM 1	SEM 1	SEM 2	SEM 2
Analysis ID	Garnet 1	Garnet 2	Garnet 1	Garnet 2	Garnet 3	Garnet 4	Garnet 1	Garnet 2	Garnet 1	Garnet 2
MgO Wt.%	1.13	1.35	-	-	-	-	0.50	0.29	0.33	0.38
Al_2O_3 Wt.%	20.73	21.01	1.30	0.76	0.95	1.83	20.85	20.46	20.71	20.53
SiO_2 Wt.%	35.87	36.02	30.52	30.08	30.56	31.16	36.55	36.06	36.82	36.55
CaO Wt.%	1.72	1.39	29.20	29.30	29.66	29.90	8.45	8.77	11.50	9.70
MnO Wt.%	1.49	0.53	-	-	-	-	8.61	8.70	6.59	5.87
TiO_2 Wt.%	-	-	37.50	38.41	38.30	37.95	-	-	-	-
FeO Wt.%	39.18	39.66	0.64	0.47	0.39	0.48	25.51	25.29	24.86	27.64
Total	100.12	99.96	99.17	99.02	99.86	101.31	100.47	99.56	100.80	100.66

Sample ID	DT061	DT061	DT061	DT061	DT061	DT061	DT061	DT061	DT061
Drill Hole	16-04	16-04	16-04	16-04	16-04	16-04	16-04	16-04	16-04
SEM site	SEM 2	SEM 2	SEM 2	SEM 2	SEM 4	SEM 4	SEM 4	SEM 4	SEM 4
Analysis ID	Garnet 1	Garnet 2	Garnet 3	Garnet 4	Garnet 1	Garnet 2	Garnet 3	Garnet 4	Garnet 5
MgO Wt.%	1.64	1.28	1.35	1.73	1.77	1.35	1.68	1.31	1.78
Al_2O_3 Wt.%	21.16	20.52	20.79	20.97	20.85	21.13	21.42	20.87	20.89
SiO_2 Wt.%	35.76	36.3	35.93	35.87	36.31	36.43	36.16	36.87	36.47
CaO Wt.%	2.22	3.33	3.76	2.21	2.22	4.45	1.98	4.56	2.03
MnO Wt.%	0.78	1.70	1.72	0.66	0.63	1.46	0.51	2.23	0.65
TiO_2 Wt.%	-	-	-	-	-	-	-	-	-
FeO Wt.%	39.40	36.86	36.35	39.20	38.50	35.41	39.23	34.62	38.38
Total	100.97	100.00	99.90	100.64	100.28	100.24	100.99	100.46	100.20

Appendix VII

SEM Data Staurolite

Sample ID	DT098	DT063	DT063	DT063	DT087	DT087	DT087	DT087
Drill Hole	17-01	16-04	16-04	16-04	17-01	17-01	17-01	17-01
SEM site	SEM2	SEM4	SEM4	SEM4	SEM1	SEM1	SEM1	SEM2
Analysis ID	staur1	Staur1	Staur2	Staur3	Staurolite 2	Staurolite 3	Staurolite 1	Staurolite 2
MgO Wt.%	1.13	1.08	1.12	1.05	1.30	1.45	1.35	1.24
Al_2O_3 Wt.%	54.31	52.11	52.08	52.91	52.64	52.22	52.12	53.48
SiO_2 Wt.%	27.11	25.48	26.52	26.10	26.05	26.34	26.18	27.00
$Ti0_2$ Wt.%	0.48	0.45	0.41	0.39	0.40	0.41	0.52	0.45
MnO Wt.%	-	-	-	-	0.43	0.51	0.48	0.46
FeO Wt.%	16.86	16.54	16.77	16.62	15.42	15.39	15.73	15.53
ZnO Wt.%	-	-	-	-	-	-	-	-
Total	99.89	95.77	96.89	97.08	96.23	96.31	96.39	98.16

Sample ID	DT087	DT087	DT088	DT088	DT088	DT088	DT088	DT088
Drill Hole	17-01	17-01	17-01	17-01	17-01	17-01	17-01	17-01
SEM site	SEM2	SEM3	SEM2	SEM2	SEM3	SEM3	SEM4	SEM5
Analysis ID	Staurolite	Staurolite	Staurolite 2	Staurolite	Staurolite 2	Staurolite	Staurolite	Staurolite
MgO Wt.%	1.42	1.57	1.16	1.20	1.25	1.16	1.29	1.30
Al_2O_3 Wt.%	52.86	52.26	53.66	53.13	53.53	53.11	53.13	53.27
SiO_2 Wt.%	26.23	25.92	26.14	26.19	25.50	26.61	25.83	26.73
$Ti0_2$ Wt.%	0.54	0.42	0.44	0.30	0.45	0.39	0.42	0.51
MnO Wt.%	0.42	0.37	-	-	-	-	-	-
FeO Wt.%	16.00	15.99	15.16	15.40	15.71	15.65	14.36	15.34
ZnO Wt.%	-	-	-	-	-	-	-	-
Total	97.47	96.53	96.56	96.22	96.44	96.92	95.03	97.15

Sample ID	DT088	DT099	DT099	DT099	DT099	DT099	DT099	DT050B
Drill Hole	17-01	17-01	17-01	17-01	17-01	17-01	17-01	16-04
SEM site	SEM6	SEM 1	SEM 1	SEM 2	SEM 3	SEM 3	SEM 3	SEM 1
Analysis ID	Staurolite	Staurolite 2	Staurolite	Staurolite	Staurolite 2	Staurolite 3	Staurolite 1	Staurolite
MgO Wt.%	1.45	1.32	1.14	1.03	1.16	1.29	1.15	1.03
Al_2O_3 Wt.%	52.49	53.13	54.05	54.02	53.40	52.96	53.33	54.15
SiO_2 Wt.%	26.38	26.44	26.37	25.49	25.96	26.75	25.82	25.86
$Ti0_2$ Wt.%	0.56	0.29	0.35	0.49	0.37	0.50	0.47	0.45
MnO Wt.%	-	-	-	-	-	-	-	-
FeO Wt.%	15.74	16.09	16.27	16.12	15.68	16.36	16.18	15.79
ZnO Wt.%	-	-	-	-	-	-	-	-
Total	96.62	97.27	98.18	97.14	96.57	97.87	96.94	97.28

Sample ID	DT050B	DT050B	DT050B	DT050B	DT050B	DT056	DT056	DT056
Drill Hole	16-04	16-04	16-04	16-04	16-04	16-04	16-04	16-04
SEM site	SEM 1	SEM 2	SEM 2	SEM 4	SEM 5	SEM 1	SEM 3	SEM 3
Analysis ID	Staurolite 2	Staurolite	Staurolite 2	staurolite	staurolite	staurolite	Staurolite 1	Staurolite 2
MgO Wt.%	1.04	0.96	1.02	0.97	1.14	0.63	1.16	1.17
Al_2O_3 Wt.%	54.46	54.01	54.25	53.96	53.64	55.57	53.09	53.96
SiO_2 Wt.%	26.73	25.42	26.24	26.38	26.07	23.86	26.5	26.48
$Ti0_2$ Wt.%	0.46	0.38	0.56	0.48	0.45	0.27	0.49	0.37
MnO Wt.%	-	-	-	-	-	-	-	-
FeO Wt.%	16.46	16.23	16.68	16.59	16.89	15.43	16.00	16.03
ZnO Wt.%	-	-	-	-	-	-	-	-
Total	99.14	97.01	98.75	98.38	98.19	95.77	97.24	98.00

Sample ID	DT056	DT056	DT056	DT056	DT-98	DT-98	DT-98	DT028
Drill Hole	16-04	16-04	16-04	16-04	17-01	17-01	17-01	16-02
SEM site	SEM 4	SEM 5	SEM 5	SEM 5	SEM2	SEM 3	SEM 3	SEM 1
Analysis ID	Staurolite	Staurolite 1	Staurolite 2	Staurolite 3	Staurolite	Staurolite 2	Staurolite	Staurolite
MgO Wt.%	0.98	1.33	1.01	1.07	1.14	1.03	1.05	0.85
Al_2O_3 Wt.%	54.57	54.25	54.92	54.18	53.14	54.78	54.60	53.83
SiO_2 Wt.%	26.56	26.49	26.28	26.78	25.53	26.1	25.94	25.57
$Ti0_2$ Wt.%	0.25	0.25	-	0.32	0.42	0.28	0.52	0.36
MnO Wt.%	-	-	-	-	-	-	-	-
FeO Wt.%	16.19	16.67	16.40	16.60	15.65	16.51	16.48	16.14
ZnO Wt.%	-	-	-	-	-	-	-	-
Total	98.56	99.00	98.62	98.96	95.87	98.70	98.59	96.74

Sample ID	DT028	DT023	DT023	DT023	DT023	DT032	DT032	DT032
Drill Hole	16-02	16-01	16-01	16-01	16-01	19-02	19-02	19-02
SEM site	SEM 4	SEM 2	SEM 4	SEM 4	SEM 5	SEM 1	SEM 2	SEM 3
Analysis ID	Staurolite	Staurolite	Staurolite 2	Staurolite	Staurolite	Staurolite	Staurolite	Staurolite
MgO Wt.%	0.84	1.13	0.85	0.85	0.66	1.16	1.26	1.24
Al_2O_3 Wt.%	55.11	54.93	51.18	52.69	53.58	53.52	56.09	52.67
SiO_2 Wt.%	26.39	26.37	24.42	24.74	24.48	25.46	27.38	25.28
$Ti0_2$ Wt.%	0.44	0.27	0.30	0.30	0.28	0.38	0.47	0.39
MnO Wt.%	-	-	-	-	-	-	-	-
FeO Wt.%	16.33	16.21	15.47	16.11	15.21	15.98	16.22	15.86
ZnO Wt.%	-	0.51	0.38	0.56	0.43	-	-	-
Total	99.11	99.43	92.60	95.34	94.63	96.50	101.42	95.45

Sample ID	DT005	DT005	DT005	DT005	DT005	DT024	DT024	DT024
Drill Hole	19-03	19-03	19-03	19-03	19-03	16-01	16-01	16-01
SEM site	SEM 1	SEM 1	SEM 2	SEM 3	SEM 4	SEM 3	SEM 3	SEM 4
Analysis ID	Staurolite 1	Staurolite 2	Staurolite	Staurolite	Staurolite	Staurolite 1	Staurolite 2	Staurolite
MgO Wt.%	1.20	1.29	1.25	1.33	1.26	1.03	1.15	1.09
Al_2O_3 Wt.%	54.29	54.64	53.05	53.02	54.33	53.88	54.12	54.63
SiO_2 Wt.%	25.69	26.47	25.87	26.26	26.89	26.02	26.8	26.21
$Ti0_2$ Wt.%	0.43	0.43	0.37	0.48	0.58	0.50	0.55	0.58
MnO Wt.%	-	-	-	-	-	-	-	-
FeO Wt.%	15.65	15.35	14.6	15.19	15.1	15.08	15.95	15.58
ZnO Wt.%	-	-	-	-	-	-	-	0.55
Total	97.26	98.18	95.13	96.28	98.16	96.51	98.55	98.64

Sample ID	DT030	DT030	DT030	DT030	DT030	DT064	DT064	DT064
Drill Hole	19-02	19-02	19-02	19-02	19-02	16-04	16-04	16-04
SEM site	SEM 1	SEM 2	SEM 3	SEM 4	SEM 4	SEM 2	SEM 2	SEM 3
Analysis ID	Staurolite	Staurolite	Staurolite	Staurolite 1	Staurolite 2	Staurolite 1	Staurolite 2	Staurolite
MgO Wt.%	1.44	1.50	1.67	1.35	1.39	1.14	1.24	1.37
Al_2O_3 Wt.%	53.01	53.54	54.75	54.03	53.48	54.34	53.70	54.25
SiO_2 Wt.%	26.20	25.76	26.60	26.13	26.65	25.68	26.42	26.39
$Ti0_2$ Wt.%	0.38	0.42	0.44	0.49	0.56	0.63	0.37	0.33
MnO Wt.%	-	-	-	-	-	-	-	-
FeO Wt.%	15.70	16.12	15.12	15.61	15.76	15.95	16.10	16.43
ZnO Wt.%	-	-	0.2	-	-	-	-	-
Total	96.74	97.33	98.78	97.63	97.84	97.75	97.83	98.77

Sample ID	DT001	DT001	DT001	DT003	DT003	DT035	DT035	DT050A
Drill Hole	19-03	19-03	19-03	19-03	19-03	19-04	19-04	16-04
SEM site	SEM 1	SEM 1	SEM 3	SEM 1	SEM 1	SEM 3	SEM 3	SEM 1
Analysis ID	Staurolite 1	Staurolite 2	Staurolite	Staurolite 2	Staurolite 1	Staurolite 1	Staurolite 2	Staurolite
MgO Wt.%	1.21	1.08	1.22	1.74	1.33	1.40	1.92	1.14
Al_2O_3 Wt.%	52.36	52.75	55.2	52.95	52.71	54.92	53.31	51.31
SiO_2 Wt.%	24.90	24.55	26.11	26.91	25.90	27.01	26.50	24.20
$Ti0_2$ Wt.%	0.55	0.36	0.53	0.50	0.38	-	0.54	0.36
MnO Wt.%	-	-	-	-	-	-	-	-
FeO Wt.%	15.68	15.14	13.9	15.96	13.57	13.79	14.38	15.15
ZnO Wt.%	-	-	-	-	-	1.64	-	-
Total	94.7	93.89	96.95	98.07	93.89	98.76	96.64	92.16

Sample ID	DT050A	DT050A	DT092	DT092	DT092	DT092	DT092	DT039
Drill Hole	16-04	16-04	17-01	17-01	17-01	17-01	17-01	16-04
SEM site	SEM 5	SEM 5	SEM 2	SEM 2	SEM 3	SEM 4	SEM 5	SEM 1
Analysis ID	Staurolite 1	Staurolite 2	Staurolite 1	Staurolite 2	Staurolite	Staurolite	Staurolite	Staurolite
MgO Wt.%	1.27	1.12	1.32	1.19	1.07	1.20	1.39	1.54
Al_2O_3 Wt.%	58.45	54.20	53.49	53.12	55.32	52.21	52.73	54.13
SiO_2 Wt.%	28.79	26.81	25.91	26.44	26.58	27.03	26.09	26.64
$Ti0_2$ Wt.%	-	-	0.41	-	-	0.36	0.38	0.60
MnO Wt.%	-	-	-	-	-	-	-	0.45
FeO Wt.%	16.39	16.04	15.66	15.73	14.80	15.33	15.20	12.73
ZnO Wt.%	-	-	-	-	0.74	-	0.6	-
Total	104.90	98.17	96.78	96.48	98.53	96.12	96.39	96.09

Sample ID	DT039	DT039	DT070	DT061	DT061	DT061	DT061
Drill Hole	16-04	16-04	16-04	16-04	16-04	16-04	16-04
SEM site	SEM 1	SEM 5	SEM 2	SEM 1	SEM 1	SEM 2	SEM 3
Analysis ID	Staurolite 2	Staurolite	Staurolite	Staurolite 1	Staurolite 2	Staurolite	Staurolite
MgO Wt.%	1.58	1.63	0.40	1.05	1.04	1.23	1.07
Al_2O_3 Wt.%	51.81	54.27	56.57	53.39	53.21	53.65	54.95
SiO_2 Wt.%	26.63	26.81	24.81	25.63	26.21	25.87	25.40
$Ti0_2$ Wt.%	0.45	0.45	0.32	0.29	0.37	0.51	0.49
MnO Wt.%	0.60	0.58	-	-	-	-	-
FeO Wt.%	13.01	13.08	14.94	16.04	16.1	16.32	16.11
ZnO Wt.%	-	-	-	-	-	-	-
Total	94.08	96.82	97.03	96.40	96.93	97.57	98.02

Appendix VIII

SEM Data Biotite

Sample ID	DT120A	DT120A	DT120A	DT120A	DT120A	DT120B	DT120B	DT120B	DT120B
Drill Hole	17-01	17-01	17-01	17-01	17-01	17-01	17-01	17-01	17-01
SEM site	SEM 5	SEM 1	SEM 2	SEM 3	SEM 3	SEM 3	SEM 4	SEM 1	SEM 1
Analysis ID	Biotite 1	Biotite	Biotite	bio 2	bio	bio	biotite	biotite 2	Biotite
Na_2O Wt.%	-	2.13	-	-	-	0.18	0.41	-	-
MgO Wt.%	10.47	7.91	12.24	12.07	11.64	13.45	13.93	12.48	12.57
Al_2O_3Wt.%	16.88	19.67	17.01	17.04	16.34	16.86	16.56	16.22	16.61
SiO_2 Wt.%	34.46	42.84	36.94	36.41	37.09	36.93	37.50	35.67	36.08
K_2O Wt.%	9.26	6.34	9.62	9.42	8.93	9.52	9.41	9.14	9.43
CaO Wt.%	-	3.29	-	-	-	-	-	-	-
TiO_2 Wt.%	1.49	1.42	1.59	1.42	1.56	1.25	1.55	1.35	1.64
FeO Wt.%	20.90	12.50	18.74	18.33	18.97	18.54	17.57	18.32	17.19
Total	93.47	96.12	96.15	94.69	96.32	96.72	96.92	93.19	93.52

Sample ID	DT120B	DT063	DT063	DT063	DT063	DT063	DT063	DT087	DT087
Drill Hole	17-01	16-04	16-04	16-04	16-04	16-04	16-04	17-01	17-01
SEM site	SEM 1	SEM2	SEM2	SEM3	SEM3	SEM4	SEM4	SEM1	SEM1
Analysis ID	Biotite	Bio 1	Bio 2	Bio 1	Bio 2	Biotite 1	Biotite 2	Biotite	Biotite 2
Na_2O Wt.%	-	-	-	0.27	-	0.15	0.37	-	0.37
MgO Wt.%	12.42	6.83	6.83	6.73	6.50	5.97	5.80	8.66	8.73
Al_2O_3 Wt.%	16.14	19.27	18.42	18.7	18.88	18.24	19.26	19.35	19.81
SiO_2 Wt.%	35.99	34.11	33.25	33.65	33.67	33.17	33.71	34.78	35.52
K_2O Wt.%	10.04	9.21	9.58	9.37	9.39	9.40	9.16	9.41	9.43
CaO Wt.%	-	-	-	-	-	-	-	-	-
TiO_2 Wt.%	1.49	1.60	1.43	1.43	1.68	1.78	1.74	1.43	1.47
FeO Wt.%	18.17	24.14	24.89	24.79	25.26	25.94	26.32	21.99	21.83
Total	94.25	95.16	94.39	94.93	95.38	94.64	96.35	95.62	97.16

Sample ID	DT087	DT087	DT088	DT088	DT088	DT088	DT088	DT099	DT099
Drill Hole	17-01	17-01	17-01	17-01	17-01	17-01	17-01	17-01	17-01
SEM site	SEM2	SEM3	SEM3	SEM3	SEM4	SEM5	SEM6	SEM 1	SEM 1
Analysis ID	Biotite 1	Biotite	biotite 2	biotite	Biotite	Biotite	Biotite	Biotite 2	Biotite
Na_2O Wt.%	0.32	0.43	-	-	-	-	-	-	-
MgO Wt.%	8.52	8.71	7.47	7.28	7.17	6.98	6.99	6.52	5.88
Al_2O_3 Wt.%	18.67	19.00	19.05	19.48	18.82	19.77	18.99	20.07	19.01
SiO_2 Wt.%	34.72	34.35	33.24	33.53	32.37	32.63	33.68	34.79	32.87
K_2O Wt.%	9.54	10.16	9.11	10.25	7.96	9.15	9.40	9.06	9.25
CaO Wt.%	-	-	-	-	-	-	-	-	-
TiO_2 Wt.%	1.59	1.31	1.74	1.62	1.45	1.82	1.39	1.55	1.57
FeO Wt.%	22.45	21.86	22.95	22.5	24.59	22.57	23.59	25.08	25.58
Total	95.94	95.81	93.56	94.66	92.36	92.92	94.04	97.06	94.17

Sample ID	DT099	DT050B	DT050B	DT050B	DT050B	DT050B	DT056	DT056	DT056
Drill Hole	17-01	16-04	16-04	16-04	16-04	16-04	16-04	16-04	16-04
SEM site	SEM 3	SEM 1	SEM 2	SEM 4	SEM 5	SEM 5	SEM 3	SEM 4	SEM 5
Analysis ID	Biotite	Biotite	Biotite	Biotite	Biotite 2	Biotite	Biotite 1	Biotite 1	Biotite 1
Na_2O Wt.%	-	-	-	-	-	-	-	-	-
MgO Wt.%	5.97	5.02	5.41	5.34	5.50	5.70	5.75	5.76	5.98
Al_2O_3 Wt.%	18.81	19.36	19.39	19.86	20.01	19.55	19.77	19.41	19.71
SiO_2 Wt.%	32.86	32.60	32.99	34.01	34.07	33.74	33.93	32.91	33.61
K_2O Wt.%	8.77	9.16	9.26	9.36	9.64	9.47	9.3	9.19	9.28
CaO Wt.%	-	-	-	-	-	-	-	-	-
TiO_2 Wt.%	1.93	1.31	1.28	1.66	1.62	1.35	1.70	1.42	0.99
FeO Wt.%	25.26	26.52	26.82	26.45	27.33	25.99	25.32	25.56	25.82
Total	93.60	93.98	95.15	96.68	98.18	95.81	95.78	94.24	95.38

Sample ID	DT056	DT069	DT069	DT-98	DT-98	DT-98	DT020	DT020	DT028
Drill Hole	16-04	16-04	16-04	17-01	17-01	17-01	19-01	19-01	16-02
SEM site	SEM 5	SEM 1	SEM 4	SEM 1	SEM 1	SEM 3	SEM 1	SEM 3	SEM 1
Analysis ID	Biotite 2	Biotite 1	Biotite	Biotite 1	Biotite 2	Biotite	Biotite	Biotite	Biotite
Na_2O Wt.%	-	-	-	-	0.81	-	-	-	-
MgO Wt.%	5.99	5.55	5.51	5.68	5.37	5.83	5.91	6.62	5.51
Al_2O_3 Wt.%	20.03	18.62	18.52	19.11	18.74	19.93	18.74	19.11	19.55
SiO_2 Wt.%	34.01	33.53	34.10	32.91	32.38	33.59	32.04	32.81	33.01
K_2O Wt.%	9.32	9.49	9.52	9.40	10.48	9.38	8.15	8.41	9.47
CaO Wt.%	-	-	-	-	-	-	-	-	-
TiO_2 Wt.%	1.33	2.70	2.67	1.89	1.66	1.74	1.76	1.26	1.75
FeO Wt.%	25.58	27.17	27.24	25.47	25.5	25.47	27.33	25.26	25.95
Total	96.26	97.05	97.56	94.46	94.95	95.94	93.93	93.46	95.25

Sample ID	DT028	DT028	DT009	DT009	DT009	DT023	DT023	DT023	DT023
Drill Hole	16-02	16-02	16-02	16-02	16-02	16-01	16-01	16-01	16-01
SEM site	SEM 3	SEM 4	SEM 1	SEM 2	SEM 2	SEM 1	SEM 1	SEM 2	SEM 4
Analysis ID	Biotite	Biotite	Biotite	Biotite 1	Biotite 2	Biotite 1	Biotite 2	Biotite	Biotite 1
Na_2O Wt.%	-	-	-	-	-	0.21	0.29	-	-
MgO Wt.%	5.02	5.17	6.33	6.23	6.09	5.42	5.20	5.11	4.90
Al_2O_3 Wt.%	19.08	19.73	18.64	19.18	18.28	19.17	19.14	19.26	18.36
SiO_2 Wt.%	32.98	33.67	33.26	33.29	32.18	33.13	33.43	33.38	32.58
K_2O Wt.%	9.89	9.68	9.43	9.32	9.10	9.33	9.39	9.52	9.15
CaO Wt.%	-	-	-	-	-	-	-	-	-
TiO_2 Wt.%	1.83	1.69	1.67	1.53	1.58	1.73	1.76	1.83	1.52
FeO Wt.%	26.49	26.93	26.69	24.30	24.76	26.27	26.34	27.00	27.76
Total	95.29	96.86	96.02	93.85	91.99	95.28	95.55	97.10	94.28

Sample ID	DT023	DT022	DT022	DT022	DT032	DT032	DT032	DT006	DT006
Drill Hole	16-01	16-01	16-01	16-01	19-02	19-02	19-02	16-02	16-02
SEM site	SEM 4	SEM 1	SEM 2	SEM 3	SEM 1	SEM 2	SEM 3	SEM 1	SEM 2
Analysis ID	Biotite 2	Biotite	Biotite	Biotite	Biotite	Biotite	Biotite	Biotite	Biotite
Na_2O Wt.%	0.20	-	-	-	-	-	-	-	-
MgO Wt.%	4.99	10.56	10.48	10.58	6.31	6.97	6.27	12.73	12.48
Al_2O_3 Wt.%	18.65	19.89	19.26	19.71	18.7	20.24	19.09	17.90	18.03
SiO_2 Wt.%	31.36	35.53	35.29	35.67	32.88	34.38	32.44	36.06	35.59
K_2O Wt.%	9.06	9.63	9.75	9.68	9.02	9.33	10.13	9.97	9.97
CaO Wt.%	-	-	-	-	-	-	-	1.31	1.37
TiO_2 Wt.%	1.58	1.60	1.56	1.63	1.53	1.32	1.32	0.53	0.60
FeO Wt.%	26.21	19.20	20.08	19.14	24.39	25.00	24.52	15.64	16.45
Total	92.04	96.41	96.41	96.41	92.83	97.24	93.78	94.15	94.49

Sample ID	DT006	DT088	DT005	DT005	DT005	DT005	DT024	DT024	DT024
Drill Hole	16-02	17-01	19-03	19-03	19-03	19-03	16-01	16-01	16-01
SEM site	SEM 3	SEM 2	SEM 1	SEM 2	SEM 4	SEM 5	SEM 1	SEM 2	SEM 3
Analysis ID	Biotite	Biotite	Biotite	Biotite	Biotite	Biotite	Biotite	Biotite	Biotite
Na_2O Wt.%	-	-	-	-	-	-	-	-	0.45
MgO Wt.%	12.11	7.21	7.23	6.50	7.60	7.33	7.03	7.54	5.46
Al_2O_3 Wt.%	17.44	18.92	19.68	19.71	19.57	19.75	20.35	19.09	17.86
SiO_2 Wt.%	35.56	33.28	33.62	33.35	34.21	34.14	35.21	33.82	31.13
K_2O Wt.%	10.08	9.24	9.32	9.18	9.12	9.20	9.37	8.46	8.92
CaO Wt.%	2.03	-	-	-	-	-	-	-	-
TiO_2 Wt.%	0.76	1.41	1.52	1.74	1.57	1.36	1.96	1.25	1.64
FeO Wt.%	16.93	22.33	23.88	22.91	23.21	23.59	23.54	25.92	25.12
Total	94.92	92.40	95.25	93.39	95.27	95.36	97.46	96.09	90.59

Sample ID	DT024	DT030	DT030	DT030	DT030	DT109	DT109	DT109	DT109
Drill Hole	16-01	19-02	19-02	19-02	19-02	21-06	21-06	21-06	21-06
SEM site	SEM 4	SEM 1	SEM 2	SEM 3	SEM 4	SEM 1	SEM 1	SEM 1	SEM 1
Analysis ID	Biotite	Biotite	Biotite	Biotite	Biotite	Biotite 2	Biotite	Biotite 2	Biotite
Na_2O Wt.%	-	-	0.38	-	-	-	-	-	-
MgO Wt.%	6.59	7.39	8.74	9.16	7.31	15.18	15.34	15.00	14.98
Al_2O_3 Wt.%	19.82	18.84	20.05	20.34	19.48	18.41	18.33	17.71	18.71
SiO_2 Wt.%	34.53	33.84	33.6	31.30	33.85	37.36	37.28	36.56	37.31
K_2O Wt.%	9.99	9.45	7.86	6.56	9.23	10.10	10.12	10.17	10.03
CaO Wt.%	-	-	-	-	-	-	-	-	-
TiO_2 Wt.%	1.82	1.99	1.41	1.60	1.62	1.87	1.58	1.48	1.72
FeO Wt.%	24.4	23.29	24.04	24.58	23.31	12.60	13.30	12.67	13.21
Total	97.13	94.80	96.09	93.55	94.81	95.51	95.95	93.59	95.95

Sample ID	DT064	DT064	DT054	DT054	DT054	DT058	DT058	DT058	DT058
Drill Hole	16-04	16-04	16-04	16-04	16-04	16-04	16-04	16-04	16-04
SEM site	SEM 2	SEM 3	SEM 1	SEM 1	SEM 2	SEM 1	SEM 2	SEM 3	SEM 4
Analysis ID	Biotite	Biotite	Biotite 1	Biotite 2	Biotite	Biotite	Biotite	Biotite	Biotite
Na_2O Wt.%	-	-	-	-	-	-	-	-	-
MgO Wt.%	7.20	7.07	7.82	7.45	8.57	7.35	7.24	6.83	6.53
Al_2O_3 Wt.%	19.75	19.53	19.57	16.99	20.12	17.56	19.13	18.60	19.49
SiO_2 Wt.%	33.93	34.39	34.68	32.12	35.36	32.09	33.31	33.27	33.67
K_2O Wt.%	9.28	9.30	9.21	9.12	9.32	9.00	9.13	9.34	9.45
CaO Wt.%	-	-	-	-	-	-	-	-	-
TiO_2 Wt.%	1.87	1.44	1.35	1.28	1.46	1.79	1.20	1.81	1.68
FeO Wt.%	23.81	25.3	22.77	24.36	22.84	22.83	23.82	24.95	24.70
Total	95.84	97.02	95.40	91.33	97.68	90.63	93.83	94.80	95.51

Sample ID	DT053	DT053	DT001	DT001	DT001	DT003	DT003	DT003	DT035
Drill Hole	16-04	16-04	19-03	19-03	19-03	19-03	19-03	19-03	19-04
SEM site	SEM 1	SEM 2	SEM 1	SEM 2	SEM 4	SEM 1	SEM 6	SEM 6	SEM 1
Analysis ID	Biotite	Biotite	Biotite	Biotite	Biotite	Biotite	Biotite 2	Biotite 1	Biotite
Na_2O Wt.%	-	-	-	-	-	-	-	-	-
MgO Wt.%	6.77	7.37	7.01	7.43	6.94	7.44	7.89	7.57	8.36
Al_2O_3 Wt.%	20.00	19.95	18.58	16.95	19.30	19.18	18.30	19.09	18.52
SiO_2 Wt.%	34.08	33.86	33.1	31.86	31.78	33.81	33.48	33.98	33.08
K_2O Wt.%	9.40	9.39	8.65	8.94	7.98	9.54	9.10	9.19	9.62
CaO Wt.%	-	-	-	-	-	-	-	-	-
TiO_2 Wt.%	1.03	2.12	1.63	1.87	1.35	1.51	1.65	1.85	0.83
FeO Wt.%	24.36	22.26	22.86	23.46	24.54	23.33	24.02	23.04	21.75
Total	95.65	94.95	91.83	90.5	91.89	94.81	94.44	94.71	92.17

Sample ID	DT035	DT035	DT035	DT035	DT050A	DT050A	DT050A	DT050A	DT050A
Drill Hole	19-04	19-04	19-04	19-04	16-04	16-04	16-04	16-04	16-04
SEM site	SEM 2	SEM 2	SEM 3	SEM 4	SEM 1	SEM 2	SEM 3	SEM 4	SEM 5
Analysis ID	Biotite	Biotite 2	Biotite	Biotite	Biotite	Biotite	Biotite	Biotite	Biotite
Na_2O Wt.%	-	-	-	-	-	-	-	-	-
MgO Wt.%	8.06	8.12	7.79	7.51	6.48	6.58	6.25	6.46	6.71
Al_2O_3 Wt.%	17.36	17.56	18.19	19.17	18.99	19.38	19.00	19.08	19.46
SiO_2 Wt.%	30.14	32.06	31.95	33.17	31.86	32.62	32.16	33.94	33.78
K_2O Wt.%	6.39	9.31	9.04	9.09	8.60	8.97	8.74	9.65	9.17
CaO Wt.%	-	-	-	-	-	-	-	-	-
TiO_2 Wt.%	0.61	1.31	1.16	0.79	1.19	1.28	1.30	1.98	1.36
FeO Wt.%	24.78	22.54	22.34	25.80	23.48	24.17	22.85	25.00	24.85
Total	87.34	90.90	90.47	95.53	90.60	93.01	90.30	96.11	95.32

Sample ID	DT092	DT092	DT092	DT092	DT039	DT039	DT039	DT039	DT039
Drill Hole	17-01	17-01	17-01	17-01	16-04	16-04	16-04	16-04	16-04
SEM site	SEM 1	SEM 2	SEM 4	SEM 5	SEM 1	SEM 2	SEM 3	SEM 4	SEM 5
Analysis ID	Biotite	Biotite	Biotite	Biotite	Biotite	Biotite	Biotite	Biotite	Biotite
Na_2O Wt.%	-	-	-	-	-	-	-	-	-
MgO Wt.%	8.16	7.81	7.4	7.18	11.23	10.35	11.13	12.65	9.94
Al_2O_3 Wt.%	19.06	18.43	19.17	19.6	19.24	18.6	19.22	19.11	19.53
SiO_2 Wt.%	34.58	33.4	33.47	32.52	32.74	34.62	34.13	29.82	35.94
K_2O Wt.%	9.55	9.76	9.24	9.40	6.40	9.13	7.87	2.90	9.30
CaO Wt.%	-	-	-	-	-	-	-	-	-
TiO_2 Wt.%	1.63	1.59	1.63	1.69	0.71	1.26	1.24	1.06	1.41
FeO Wt.%	21.34	23.12	22.64	22.10	11.32	17.34	17.82	21.86	18.28
Total	94.31	94.11	93.54	92.49	81.64	91.31	91.42	87.40	94.41

Sample ID	DT070	DT070	DT070	DT070	DT070	DT070	DT070	DT070	DT070
Drill Hole	16-04	16-04	16-04	16-04	16-04	16-04	16-04	16-04	16-04
SEM site	SEM 1	SEM 1	SEM 1	SEM 2	SEM 2	SEM 2	SEM 3	SEM 3	SEM 3
Analysis ID	Biotite 1	Biotite 2	Biotite 3	Biotite 1	Biotite 2	Biotite 3	Biotite 1	Biotite 2	Biotite 3
Na_2O Wt.%	-	-	-	-	-	-	-	-	0.45
MgO Wt.%	5.34	7.78	20.85	7.59	7.57	5.85	21.70	21.95	6.88
Al_2O_3 Wt.%	17.13	16.47	8.42	15.52	17.56	23.34	14.77	15.01	18.77
SiO_2 Wt.%	33.14	33.88	45.32	34.37	32.97	26.14	36.96	36.76	33.94
K_2O Wt.%	9.19	9.65	7.96	9.52	9.51	2.48	9.71	9.55	9.36
CaO Wt.%	-	-	-	-	1.75	-	-	-	-
TiO_2 Wt.%	-	-	0.57	-	-	-	2.17	2.22	1.65
FeO Wt.%	29.42	26.37	11.5	26.60	26.27	34.23	6.39	6.26	24.56
Total	94.22	94.15	94.60	93.60	96.81	92.04	93.16	94.15	95.62

Sample ID	DT076	DT076	DT111	DT111	DT061	DT061	DT061	DT118B	DT034
Drill Hole	19-10	19-10	21-6	21-6	16-04	16-04	16-04	19-10	19-04
SEM site	SEM 1	SEM 3	SEM 1	SEM 1	SEM 1	SEM 2	SEM 3	SEM 3	SEM 1
Analysis ID	Biotite	Biotite	Biotite 1	Biotite 2	Biotite 1	Biotite 1	Biotite 1	Biotite	Biotite
Na_2O Wt.%	-	-	-	-	-	-	-	-	-
MgO Wt.%	8.53	9.05	10.20	10.58	5.21	6.52	6.21	12.93	7.79
Al_2O_3 Wt.%	15.65	16.15	15.27	15.28	19.59	19.35	19.23	18.57	17.9
SiO_2 Wt.%	34.10	35.00	34.88	34.76	33.25	33.65	33.40	37.72	34.52
K_2O Wt.%	9.25	9.34	9.56	9.81	8.94	9.06	9.95	10.15	9.43
CaO Wt.%	-	-	-	-	-	-	-	-	-
TiO_2 Wt.%	2.43	2.39	2.28	2.01	2.13	1.66	1.59	1.58	2.19
FeO Wt.%	23.64	21.58	20.75	20.50	24.60	24.31	24.91	14.97	22.84
Total	93.61	93.51	92.94	92.93	93.72	94.55	95.28	95.93	94.67

Sample ID	DT102	DT102	DT117	DT117	DT117	DT117
Drill Hole	19-04	19-04	19-10	19-10	19-10	19-10
SEM site	SEM 2	SEM 4	SEM 1	SEM 2	SEM 2	SEM 4
Analysis ID	Biotite	Biotite	Biotite	Biotite 1	Biotite 2	Biotite
Na_2O Wt.%	-	-	-	-	-	-
MgO Wt.%	8.93	8.13	8.30	14.85	15.53	9.13
Al_2O_3 Wt.%	19.38	19.24	17.15	15.81	15.40	17.36
SiO_2 Wt.%	34.06	33.51	34.89	33.06	37.07	34.99
K_2O Wt.%	10.66	9.40	9.61	6.66	9.70	9.85
CaO Wt.%	-	-	-	-	-	-
TiO_2 Wt.%	1.44	0.98	3.09	0.95	0.83	2.63
FeO Wt.%	22.51	22.70	21.10	17.79	14.28	19.58
Total	96.99	94.38	94.13	89.65	92.8	94.61

Appendix IX

SEM Data Chlorite

Drill Hole	17-01	17-01	17-01	17-01	17-01	17-01	17-01	17-01	17-01
Sample ID	DT120A	DT120A	DT120A	DT120B	DT120B	DT120B	DT120B	DT120B	DT120B
SEM site	SEM5	SEM 4	SEM 4	SEM 3	SEM 1	SEM 1	SEM 2	SEM 2	SEM 2
Analysis ID	Chlorite	Chlor 2	Chlor 1	Chlorite	Chlorite 2	Chlorite	Chlorite 1	Chlorite 2	Chlorite 3
MgO Wt.%	4.10	15.61	14.62	18.86	19.55	17.28	17.89	17.65	16.98
Al_2O_3 Wt.%	16.59	21.3	20.9	22.3	23.27	21.3	21.57	21.32	21.64
SiO_2 Wt.%	25.66	25.14	24.67	26.93	27.39	25.21	25.11	25.32	25.09
FeO Wt.%	41.58	23.75	25.24	21.58	20.51	21.03	21.28	21.38	22.09
Total	88.65	86.21	85.44	89.87	90.88	84.83	85.85	85.67	85.93

Drill Hole	17-01	17-01	16-04	16-04	16-04	17-01	17-01	17-01	17-01
Sample ID	DT120B	DT120B	DT063	DT063	DT063	DT087	DT087	DT087	DT088
SEM site	SEM 2	SEM2	SEM3	SEM4	SEM4	SEM1	SEM1	SEM3	SEM4
Analysis ID	Chlorite 4	Chlorite 2	Chlor 1	Chlorite 1	Chlorite 2	Chlorite 1	Chlorite 2	Chlorite	Chlorite
MgO Wt.%	17.33	0.62	10.00	9.09	9.17	13.61	13.60	12.69	11.75
Al_2O_3 Wt.%	20.88	12.43	22.30	21.71	22.60	23.18	22.66	22.73	21.77
SiO_2 Wt.%	24.64	27.11	23.60	22.81	22.78	24.75	25.03	23.78	23.73
FeO Wt.%	20.76	46.49	31.91	33.41	33.04	27.61	28.20	28.31	29.92
Total	83.89	88.71	87.81	87.15	87.59	89.16	89.49	87.50	87.17

Drill Hole	17-01	17-01	17-01	17-01	17-01	17-01	17-01	17-01	16-04
Sample ID	DT088	DT088	DT088	DT088	DT099	DT099	DT-119	DT-119	DT050B
SEM site	SEM5	SEM5	SEM1	SEM1	SEM 2	SEM 3	SEM3	SEM3	SEM 2
Analysis ID	Chlorite 2	Chlorite	Chlorite 1	Chlorite 3	Chlorite	Chlorite	chlorite 1	chlorite 2	Chlorite 1
MgO Wt.%	10.99	11.54	2.71	3.86	8.54	8.87	0.62	0.51	7.56
Al_2O_3 Wt.%	22.61	24.12	17.56	15.36	22.03	22.59	21.71	20.31	21.95
SiO_2 Wt.%	23.37	24.87	22.50	24.53	22.43	23.12	23.81	22.32	22.32
FeO Wt.%	29.37	30.78	42.82	44.20	33.35	32.95	40.02	41.08	34.99
Total	86.34	91.32	85.58	88.97	86.35	87.52	87.87	85.73	86.82

Drill Hole	16-04	16-04	16-04	16-04	16-04	16-04	16-04	16-04	16-04
Sample ID	DT050B	DT056	DT056	DT056	DT056	DT056	DT069	DT069	DT069
SEM site	SEM 2	SEM 1	SEM 1	SEM 4	SEM 5	SEM 5	SEM 1	SEM 1	SEM 3
Analysis ID	Chlorite 2	Chlorite 2	Chlorite 1	Chlorite 1	Chlorite 1	Chlorite 2	Chlorite 2	Chlorite	Chlorite
MgO Wt.%	8.00	4.12	3.93	8.29	9.28	8.62	8.44	8.59	4.84
Al_2O_3 Wt.%	22.38	23.74	23.95	22.09	22.38	22.64	22.82	23.7	23.03
SiO_2 Wt.%	23.05	21.55	21.79	22.70	22.78	22.27	23.44	23.6	22.36
FeO Wt.%	34.72	39.66	39.43	33.33	33.19	33.87	35.04	33.9	40.57
Total	88.16	89.07	89.10	86.55	87.62	87.41	89.73	90.07	90.80

Drill Hole	16-04	17-01	19-01	19-01	19-01	19-01	19-01	19-01	19-01
Sample ID	DT069	DT-98	DT017	DT017	DT017	DT017	DT017	DT017	DT017
SEM site	SEM 4	SEM 3	SEM 1	SEM 2	SEM 2	SEM 3	SEM 3	SEM 3	SEM 5
Analysis ID	Chlorite	Chlorite	Chlorite	Chlorite	Chlorite 2	Chlorite 1	Chlorite 2	Chlorite 3	Chlorite
MgO Wt.%	8.31	7.69	12.44	11.87	12.68	1.70	2.00	12.47	7.79
Al_2O_3 Wt.%	22.90	22.59	23.31	23.2	23.24	17.42	18.85	23.85	19.94
SiO_2 Wt.%	23.11	22.91	23.31	23.47	23.65	23.52	24.9	24.04	23.47
FeO Wt.%	35.26	34.46	28.53	28.48	27.18	45.61	44.98	27.42	35.00
Total	89.58	87.65	87.59	87.04	86.76	88.25	90.73	87.78	86.20

Drill Hole	19-01	19-01	19-01	19-01	19-01	16-02	16-02	16-02	16-01
Sample ID	DT020	DT020	DT020	DT020	DT020	DT028	DT009	DT009	DT023
SEM site	SEM 1	SEM 1	SEM 3	SEM 4	SEM 5	SEM 4	SEM 4	SEM 5	SEM 1
Analysis ID	Chlorite	Chlorite 2	Chlorite	Chlorite	Chlorite	Chlorite	Chlorite	Chlorite	Chlorite
MgO Wt.%	8.71	8.19	9.66	8.79	8.45	7.29	7.38	3.53	3.72
Al_2O_3 Wt.%	22.89	21.77	22.76	22.57	21.22	23.17	21.05	21.11	20.59
SiO_2 Wt.%	23.47	22.38	23.82	22.94	22.92	22.42	22.85	21.97	19.78
FeO Wt.%	33.86	33.81	32.48	33.52	33.81	36.14	34.73	41.83	39.15
Total	88.92	86.15	88.72	87.82	86.4	89.01	86.83	88.44	83.60

Drill Hole	16-01	16-01	16-01	16-01	16-01	16-01	16-01	19-02	19-02
Sample ID	DT023	DT023	DT023	DT023	DT023	DT022	DT022	DT032	DT032
SEM site	SEM 4	SEM 4	SEM 5	SEM 6	SEM 7	SEM 1	SEM 3	SEM 1	SEM 2
Analysis ID	Chlorite 2	Chlorite	Chlorite	Chlorite	Chlorite	Chlorite	Chlorite	Chlorite	Chlorite
MgO Wt.%	7.47	6.69	4.27	2.21	3.66	15.99	14.14	9.41	7.63
Al_2O_3 Wt.%	22.41	21.55	23.43	20.41	21.62	23.9	23.4	21.93	21.36
SiO_2 Wt.%	22.53	21.85	21.10	20.89	21.04	24.78	23.86	22.17	21.58
FeO Wt.%	35.97	35.91	38.63	42.7	41.68	24.68	26.80	31.85	33.79
Total	88.38	86.01	87.43	86.20	88.00	89.35	88.20	85.36	84.36

Drill Hole	19-02	19-03	19-03	19-03	19-03	19-03	19-03	19-03	16-01
Sample ID	DT032	DT005	DT005	DT005	DT005	DT005	DT005	DT005	DT024
SEM site	SEM 3	SEM 1	SEM 1	SEM 2	SEM 3	SEM 3	SEM 4	SEM 5	SEM 3
Analysis ID	Chlorite	Chlorite	Chlorite 2	Chlorite	Chlorite	Chlorite 2	Chlorite	Chlorite	Chlorite 1
MgO Wt.%	9.81	10.34	9.76	8.87	10.75	10.74	10.60	8.58	10.26
Al_2O_3 Wt.%	23.44	22.82	23.48	21.59	22.14	21.5	21.15	21.17	23.21
SiO_2 Wt.%	23.38	22.98	23.15	22.72	23.02	23.55	22.64	22.58	23.88
FeO Wt.%	32.00	31.49	33.13	33.08	30.37	31.37	29.70	34.50	32.35
Total	88.63	87.63	89.52	86.26	86.28	87.16	84.09	86.82	89.69

Drill Hole	16-01	16-01	19-02	19-02	19-02	16-04	16-04	16-04	16-04
Sample ID	DT024	DT024	DT030	DT030	DT030	DT042	DT042	DT042	DT064
SEM site	SEM 3	SEM 4	SEM 1	SEM 2	SEM 4	SEM 2	SEM 3	SEM 3	SEM 1
Analysis ID	Chlorite 2	Chlorite	Chlorite	Chlorite	Chlorite	Chlorite	Chlorite 1	Chlorite 2	Chlorite
MgO Wt.%	9.74	8.47	11.69	11.32	11.85	16.04	16.66	17.23	10.75
Al_2O_3 Wt.%	22.87	21.38	23.20	22.13	23.98	21.26	21.41	21.97	23.27
SiO_2 Wt.%	23.18	21.56	24.67	22.88	24.24	23.34	23.13	23.41	23.06
FeO Wt.%	32.97	30.96	30.57	29.31	29.43	21.20	18.86	19.31	31.69
Total	88.76	82.75	90.13	85.64	89.71	81.83	80.43	81.92	88.77

Drill Hole	16-04	16-04	16-04	16-04	16-04	16-04	16-04	16-04	16-04
Sample ID	DT064	DT064	DT054	DT054	DT054	DT054	DT058	DT058	DT053
SEM site	SEM 2	SEM 3	SEM 1	SEM 1	SEM 2	SEM 3	SEM 2	SEM 4	SEM 2
Analysis ID	Chlorite	Chlorite	Chlorite 1	Chlorite 2	Chlorite	Chlorite	Chlorite	Chlorite	Chlorite
MgO Wt.%	9.89	10.49	11.93	11.66	12.73	2.22	10.59	9.85	9.53
Al_2O_3 Wt.%	21.90	23.23	22.50	22.88	24.34	21.79	21.76	21.88	21.98
SiO_2 Wt.%	22.56	22.99	23.57	24.06	25.55	21.81	22.87	23.67	22.17
FeO Wt.%	32.13	32.00	29.26	30.54	27.99	42.55	30.54	32.57	31.70
Total	86.47	88.72	87.25	89.13	90.62	88.37	85.76	87.98	85.37

Drill Hole	16-04	16-04	19-03	19-03	19-03	19-03	19-03	19-03	19-03
Sample ID	DT053	DT053	DT001	DT001	DT001	DT003	DT003	DT003	DT003
SEM site	SEM 3	SEM 4	SEM 1	SEM 2	SEM 4	SEM 1	SEM 2	SEM 2	SEM 2
Analysis ID	Chlorite	Chlorite	Chlorite	Chlorite	Chlorite	Chlorite	Chlorite 1	Chlorite 2	Chlorite 3
MgO Wt.%	7.69	6.12	10.05	7.83	8.13	11.34	5.35	5.48	11.54
Al_2O_3 Wt.%	20.85	20.45	22.61	21.27	21.95	23.27	20.40	19.79	22.60
SiO_2 Wt.%	23.02	21.45	22.17	22.14	21.97	22.61	23.16	23.44	23.14
FeO Wt.%	36.31	36.65	30.75	34.08	34.00	28.84	37.30	37.06	29.48
Total	87.87	84.66	85.57	85.31	86.05	86.06	86.21	85.77	86.76

Drill Hole	19-03	19-03	19-03	19-03	19-03	19-03	19-04	19-04	19-04
Sample ID	DT003	DT003	DT003	DT003	DT003	DT003	DT035	DT035	DT035
SEM site	SEM 3	SEM 4	SEM 4	SEM 4	SEM 5	SEM 6	SEM 2	SEM 2	SEM 4
Analysis ID	Chlorite	Chlorite 1	Chlorite 2	Chlorite 3	Chlorite	Chlorite	Chlorite 1	Chlorite 2	Chlorite 1
MgO Wt.%	5.10	4.78	5.54	5.52	11.90	12.03	2.70	2.93	3.46
Al_2O_3 Wt.%	20.14	22.59	21.69	21.12	23.73	23.09	16.80	19.15	17.85
SiO_2 Wt.%	22.55	23.61	24.64	24.42	23.73	23.46	20.15	23.19	23.58
FeO Wt.%	36.90	37.30	38.51	37.26	28.68	29.76	40.27	40.97	42.45
Total	84.70	88.27	90.38	88.32	88.04	88.33	79.91	86.25	87.33

Drill Hole	19-04	16-04	17-01	17-01	16-04	19-10	19-10	21-8	16-04
Sample ID	DT035	DT050A	DT092	DT092	DT039	DT076	DT076	DT113	DT061
SEM site	SEM 4	SEM 5	SEM 1	SEM 2	SEM 5	SEM 1	SEM 3	SEM 2	SEM 1
Analysis ID	Chlorite 2	Chlorite	Chlorite	Chlorite	Chlorite	Chlorite	Chlorite	Chlorite	Chlorite 1
MgO Wt.%	3.96	10.37	1.52	11.57	13.04	14.38	8.65	2.32	8.20
Al_2O_3 Wt.%	20.47	23.99	16.53	23.08	20.36	19.47	16.57	11.83	22.42
SiO_2 Wt.%	23.87	23.58	24.86	23.22	24.23	26.03	29.08	28.61	22.38
FeO Wt.%	41.82	33.13	43.53	31.02	24.31	26.99	35.78	46.26	33.73
Total	90.12	91.07	86.84	88.88	82.23	86.87	90.84	89.46	86.73

Drill Hole	16-04	16-04	19-10	19-10	19-04	19-04	19-10	19-10	19-10
Sample ID	DT061	DT061	DT118B	DT118B	DT102	DT102	DT117	DT117	DT118A
SEM site	SEM 1	SEM 2	SEM 3	SEM 3	SEM 3	SEM 4	SEM 3	SEM 4	SEM 1
Analysis ID	Chlorite 2	Chlorite	Chlorite 1	Chlorite 2	Chlorite	Chlorite	Chlorite	Chlorite	Chlorite 1
MgO Wt.%	6.99	9.90	11.63	12.29	3.05	12.77	15.24	10.15	12.93
Al_2O_3 Wt.%	22.75	21.50	18.89	19.41	16.76	23.17	16.53	20.95	19.01
SiO_2 Wt.%	22.32	23.47	25.23	26.21	25.76	23.57	26.72	25.54	26.26
FeO Wt.%	34.39	31.48	28.53	27.48	42.64	27.79	24.59	30.54	26.78
Total	86.45	86.34	85.68	86.27	88.20	87.30	83.78	88.27	86.42

Drill Hole	19-10	19-10	19-10
Sample ID	DT118A	DT118A	DT118A
SEM site	SEM 1	SEM 1	SEM 2
Analysis ID	Chlorite 2	Chlorite 3	Chlorite 1
MgO Wt.%	13.74	13.14	12.63
Al_2O_3 Wt.%	19.39	19.87	19.05
SiO_2 Wt.%	26.36	26.13	25.07
FeO Wt.%	26.72	27.60	26.71
Total	87.03	87.64	84.16

Appendix X

SEM Data Muscovite

Drill Hole	17-01	17-01	17-01	17-01	17-01	17-01	17-01	17-01	17-01
Sample ID	DT-119	DT-119	DT-119	DT-119	DT-119	DT099	DT099	DT099	DT099
SEM site	SEM2	SEM2	SEM3	SEM5	SEM6	SEM 1	SEM 2	SEM 3	SEM 3
Analysis ID	muscovite 2	muscovite	musco	musco	musco	Muscovite	Muscovite	Muscovite 2	Muscovite
Na_2O Wt.%	1.43	1.49	1.46	1.29	1.36	0.94	1.05	1.09	1.21
MgO Wt.%	-	-	-	-	-	0.43	-	-	0.28
Al_2O_3 Wt.%	35.03	36.14	35.64	34.76	35.3	35.61	35.59	35.95	35.95
SiO_2 Wt.%	43.54	44.14	44.17	43.21	44.43	44.68	44.03	44.95	44.37
K_2O Wt.%	9.25	9.45	9.51	9.79	9.27	10.78	10.02	9.9	10.78
TiO_2 Wt.%	0.35	0.51	0.42	0.33	0.38	0.38	0.46	0.40	0.39
FeO Wt.%	2.41	2.45	2.21	2.44	2.43	2.19	1.68	1.97	1.97
Total	92.02	94.18	93.41	91.82	93.17	95.00	92.82	94.25	94.95

Drill Hole	16-04	16-04	17-01	16-01	16-01	16-01	16-01	19-02	16-02
Sample ID	DT050B	DT050B	DT-98	DT023	DT022	DT022	DT022	DT032	DT006
SEM site	SEM 1	SEM 5	SEM2	SEM 2	SEM 1	SEM 2	SEM 3	SEM 1	SEM 3
Analysis ID	Muscovite 1	Muscovite	Muscovite	Muscovite	Muscovite	Muscovite	Muscovite	Muscovite	Muscovite
Na_2O Wt.%	0.90	0.83	1.14	0.82	0.65	0.54	-	1.26	-
MgO Wt.%	-	-	-	0.33	0.62	0.51	0.65	-	1.48
Al_2O_3 Wt.%	35.15	35.83	36.13	36.79	34.75	35.16	35.02	34.28	31.24
SiO_2 Wt.%	43.88	44.94	44.66	45.56	44.76	45.33	45.16	43.08	44.50
K_2O Wt.%	10.68	10.12	11.39	10.88	11.46	11.12	11.73	9.57	11.28
TiO_2 Wt.%	0.37	-	0.35	-	0.28	0.51	0.45	-	0.80
FeO Wt.%	2.54	2.05	2.09	2.51	2.44	2.33	2.58	1.86	3.24
Total	93.52	94.32	95.76	96.90	94.96	95.50	95.58	90.05	92.55

Drill Hole	19-03	19-03	19-03	19-03	16-01	16-01	19-02	19-02	16-04
Sample ID	DT005	DT005	DT005	DT005	DT024	DT024	DT030	DT030	DT042
SEM site	SEM 1	SEM 2	SEM 4	SEM 5	SEM 2	SEM 4	SEM 1	SEM 3	SEM 1
Analysis ID	Muscovite	Muscovite	Muscovite	Muscovite	Muscovite	Muscovite	Muscovite	Muscovite	Muscovite

Na_2O Wt.%	1.36	0.87	1.54	1.35	1.09	0.92	0.95	1.04	0.58
MgO Wt.%	-	0.41	-	0.60	-	0.36	0.55	0.48	0.64
Al_2O_3 Wt.%	34.86	35.01	35.80	35.50	36.13	35.24	35.49	35.08	33.59
SiO_2 Wt.%	43.91	44.42	44.29	43.69	44.89	43.68	43.69	43.86	44.10
K_2O Wt.%	8.62	10.07	8.94	9.42	10.79	9.84	9.55	9.54	10.12
TiO_2 Wt.%	0.43	0.32	-	0.45	0.40	0.28	0.33	0.57	0.48
FeO Wt.%	1.62	1.82	1.45	3.13	1.49	1.72	2.40	1.76	2.05
Total	90.81	92.92	92.02	94.15	94.8	92.04	94.02	92.33	91.55

Drill Hole	16-04	16-04	19-03	19-03	19-04	16-04	16-04	17-01	17-01
Sample ID	DT042	DT042	DT001	DT001	DT035	DT050A	DT050A	DT092	DT092
SEM site	SEM 2	SEM 3	SEM 1	SEM 3	SEM 3	SEM 2	SEM 5	SEM 1	SEM 3
Analysis ID	Muscovite	Muscovite	Muscovite	Muscovite	Muscovite	Muscovite	Muscovite	Muscovite	Muscovite
Na_2O Wt.%	0.65	-	1.73	1.51	-	0.89	1.02	-	0.83
MgO Wt.%	0.85	-	-	-	-	-	-	-	-
Al_2O_3 Wt.%	32.9	34.94	34.65	36.12	33.29	34.41	36.18	31.65	35.24
SiO_2 Wt.%	42.11	42.42	43.73	44.25	42.08	42.62	44.76	43.80	44.83
K_2O Wt.%	10.07	10.79	8.81	9.30	10.26	9.85	10.08	8.82	10.05
TiO_2 Wt.%	0.5	-	0.47	-	-	-	-	-	0.29
FeO Wt.%	2.28	0.58	1.60	1.54	1.98	2.00	1.97	3.15	2.43
Total	89.37	88.72	90.99	92.73	87.60	89.76	94.01	87.42	93.67

Drill Hole	17-01	16-04	16-04	16-04	16-04	16-04	19-10	19-10	19-10
Sample ID	DT092	DT039	DT039	DT061	DT061	DT061	DT118B	DT118B	DT118B
SEM site	SEM 5	SEM 1	SEM 2	SEM 1	SEM 4	SEM 4	SEM 1	SEM 1	SEM 1
Analysis ID	Muscovite	Muscovite	Muscovite	Muscovite	Muscovite	Muscovite 2	Muscovite	Muscovite 2	Muscovite 3
Na_2O Wt.%	1.04	0.71	-	1.05	1.79	1.15	-	-	-
MgO Wt.%	-	0.62	0.59	-	-	0.42	1.30	1.79	1.21
Al_2O_3 Wt.%	34.56	34.29	33.58	34.03	33.43	35.35	31.8	30.61	31.13
SiO_2 Wt.%	43.66	44.06	44.20	42.01	45.23	44.7	44.75	44.54	43.09

K_2O Wt.%	9.89	9.84	10.87	9.48	7.51	9.92	10.72	10.95	10.57
TiO_2 Wt.%	0.44	0.40	-	-	-	0.40	1.24	1.27	1.27
FeO Wt.%	2.60	1.60	0.87	2.01	0.95	1.58	2.03	2.14	2.09
Total	92.18	91.52	90.12	88.58	90.06	93.52	91.83	91.30	89.36

Drill Hole	19-10	19-10	16-04	19-04	19-10	19-10
Sample ID	DT118B	DT118B	DT064	DT034	DT117	DT118A
SEM site	SEM 3	SEM 4	SEM 1	SEM 2	SEM 1	SEM 3
Analysis ID	Muscovite	Muscovite	Biotite	Muscovite	Muscovite	Muscovite
Na_2O Wt.%	-	-	1.20	1.23	-	-
MgO Wt.%	1.59	1.92	0.52	0.46	4.10	1.36
Al_2O_3 Wt.%	31.26	31.76	35.21	34.64	19.21	32.12
SiO_2 Wt.%	45.03	46.56	44.66	45.18	45.64	44.17
K_2O Wt.%	10.87	11.92	9.84	9.86	5.43	10.91
TiO_2 Wt.%	0.99	0.43	-	0.52	0.62	1.13
FeO Wt.%	1.96	2.40	2.69	2.78	9.30	1.85
Total	91.68	94.98	94.12	94.67	87.54	91.54

Appendix XI

SEM Data Tourmaline

Sample ID	DT088	DT088	DT088	DT088	DT088	DT088	DT088	DT-119
Drill Hole	17-01	17-01	17-01	17-01	17-01	17-01	17-01	17-01
SEM site	SEM1	SEM1	SEM2	SEM2	SEM5	SEM6	SEM6	SEM1
Analysis ID	Tour 2	Tour 1	Tour 1	Tour 2	Tour	Tour 2	Tour	Tour 1
B_2O_3 Wt.%								
Na_2O Wt.%	1.58	1.15	1.44	1.34	1.69	1.56	1.67	1.79
MgO Wt.%	6.42	5.13	5.26	5.02	5.27	5.29	5.47	5.37
Al_2O_3 Wt.%	32.78	33.62	32.29	32.03	30.96	28.83	29.58	32.99
SiO_2 Wt.%	35.86	35.94	34.35	35.09	35.60	33.22	34.72	35.42
CaO Wt.%	1.33	0.60	1.15	1.39	0.85	1.11	1.31	0.75
TiO_2 Wt.%	0.50	-	0.71	0.66	0.26	0.21	0.78	0.50
FeO Wt.%	7.69	7.82	9.55	10.10	10.71	11.42	10.78	9.24
Total	86.16	84.26	84.76	85.62	85.33	81.79	84.30	86.06

Sample ID	DT-119	DT-119	DT-119	DT-119	DT-119	DT-119	DT-119	DT017
Drill Hole	17-01	17-01	17-01	17-01	17-01	17-01	17-01	19-01
SEM site	SEM1	SEM1	SEM2	SEM3	SEM4	SEM5	SEM6	SEM 2
Analysis ID	Tour 2	Tour 3	Tour	Tour	Tour 1	Tour	Tour	Tourmaline
B_2O_3 Wt.%								
Na_2O Wt.%	1.76	1.75	1.73	1.80	1.68	1.80	1.94	1.77
MgO Wt.%	4.92	4.66	4.55	5.11	5.22	5.04	5.32	5.81
Al_2O_3 Wt.%	33.14	33.49	33.34	32.72	33.02	33.36	32.98	30.92
SiO_2 Wt.%	35.78	35.41	35.02	34.90	35.33	34.70	35.04	35.90
CaO Wt.%	0.68	0.60	0.59	0.75	0.73	0.61	0.57	0.74
TiO_2 Wt.%	0.49	0.54	0.49	0.55	0.58	0.52	0.51	-
FeO Wt.%	9.56	10.13	9.68	9.24	9.15	9.48	9.53	10.88
Total	86.33	86.60	85.39	85.07	85.70	85.51	85.90	86.02

Sample ID	DT017	DT017	DT017	DT020	DT028	DT028	DT028	DT028
Drill Hole	19-01	19-01	19-01	19-01	16-02	16-02	16-02	16-02
SEM site	SEM 3	SEM 3	SEM 4	SEM 4	SEM 2	SEM 2	SEM 3	SEM 4
Analysis ID	Tourmaline 2	Tourmaline	Tourmaline	Tourmaline	tourmaline 2	tourmaline	tourmaline	tourmaline
B_2O_3 Wt.%								
Na_2O Wt.%	1.71	1.59	1.89	1.27	1.81	1.72	1.49	1.44
MgO Wt.%	5.76	5.27	4.12	4.04	3.29	3.83	3.63	3.15
Al_2O_3 Wt.%	31.02	31.93	31.83	32.65	33.06	31.45	32.05	32.58
SiO_2 Wt.%	35.17	35.15	36.18	34.45	35.23	34.54	35.57	35.73
CaO Wt.%	1.30	1.33	0.66	1.18	0.29	0.50	0.49	0.66
TiO_2 Wt.%	0.55	0.42	0.27	0.52	0.39	0.66	-	0.53
FeO Wt.%	10.56	10.67	12.31	11.11	12.08	11.83	12.32	13.00
Total	86.08	86.37	87.26	85.22	88.96	84.54	85.55	87.09

Sample ID	DT009	DT009	DT009	DT009	DT009	DT009	DT009	DT009
Drill Hole	16-02	16-02	16-02	16-02	16-02	16-02	16-02	16-02
SEM site	SEM 1	SEM 1	SEM 2	SEM 2	SEM 3	SEM 3	SEM 4	SEM 5
Analysis ID	Tourmaline 1	Tourmaline 2	Tourmaline 1	Tourmaline 2	Tourmaline 1	Tourmaline 2	Tourmaline	Tourmaline
B_2O_3 Wt.%	26.99	21.22	19.87	12.11	17.38	15.86	11.93	19.47
Na_2O Wt.%	1.62	1.77	1.59	1.74	1.69	1.47	1.65	1.63
MgO Wt.%	2.96	3.17	4.01	3.83	3.98	3.30	4.56	4.51
Al_2O_3 Wt.%	31.6	32.93	32.58	33.17	34.21	31.56	32.64	33.67
SiO_2 Wt.%	32.82	33.92	33.42	34.29	33.26	33.62	33.65	34.43
CaO Wt.%	0.41	-	0.50	0.41	0.85	0.71	0.66	0.64
TiO_2 Wt.%	-	-	0.37	0.48	0.58	-	0.68	0.67
FeO Wt.%	13.97	13.29	10.60	11.12	10.28	13.27	11.01	11.09
Total	110.38	106.3	102.94	97.15	102.22	99.79	96.77	106.1

Sample ID	DT023	DT023	DT022	DT006	DT005	DT005	DT005	DT024
Drill Hole	16-01	16-01	16-01	16-02	19-03	19-03	19-03	16-01
SEM site	SEM 2	SEM 4	SEM 2	SEM 3	SEM 1	SEM 4	SEM 5	SEM 2
Analysis ID	Tourmaline	Tourmaline	Tourmaline	Tourmaline	Tourmaline	Tourmaline	Tourmaline	Tourmaline 1
B_2O_3 Wt.%	14.85	16.39	18.72	11.99	18.81	18.64	25.12	23.22
Na_2O Wt.%	1.59	1.62	1.43	1.16	1.69	1.89	2.03	1.48
MgO Wt.%	3.51	3.83	4.96	7.52	4.87	4.42	5.68	5.21
Al_2O_3 Wt.%	33.70	32.08	33.30	32.52	33.56	32.55	33.24	33.91
SiO_2 Wt.%	34.34	33.35	34.65	35.02	33.8	34.71	34.24	33.76
CaO Wt.%	0.65	0.51	0.55	1.64	0.57	0.0001	0.39	1.40
TiO_2 Wt.%	0.55	0.46	0.47	0.61	0.65	0.69	0.73	0.71
FeO Wt.%	12.33	11.94	10.57	6.86	10.04	10.63	8.83	9.57
Total	101.53	100.17	104.66	97.32	104.00	103.53	110.27	109.27

Sample ID	DT024	DT030	DT058	DT001	DT035	DT035	DT050A	DT092
Drill Hole	16-01	19-02	16-04	19-03	19-04	19-04	16-04	17-01
SEM site	SEM 2	SEM 2	SEM 3	SEM 3	SEM 1	SEM 3	SEM 2	SEM 1
Analysis ID	Tourmaline 2	Tourmaline	Tourmaline	Tourmaline	Tourmaline	Tourmaline	Tourmaline	Tourmaline
B_2O_3 Wt.%	26.96	20.95	17.69	14.11	12.18	3.86	17.44	14.34
Na_2O Wt.%	1.45	1.59	1.84	1.74	1.53	1.39	1.39	1.51
MgO Wt.%	4.71	5.09	4.95	4.25	5.96	5.69	3.39	5.09
Al_2O_3 Wt.%	31.83	30.38	31.18	31.92	31.61	31.4	32.84	32.68
SiO_2 Wt.%	32.85	33.16	33.81	33.46	33.56	33.21	33.47	33.96
CaO Wt.%	1.34	1.17	0.68	0.88	1.17	1.09	0.48	1.20
TiO_2 Wt.%	0.78	0.57	0.53	0.74	0.35	0.38	-	0.67
FeO Wt.%	10.69	11.32	11.44	11.89	8.43	7.89	10.53	10.33
Total	110.60	104.24	102.11	98.99	94.78	84.91	99.55	99.78

Sample ID	DT092	DT061	DT034	DT034	DT009	DT017	DT028	DT034
Drill Hole	17-01	16-04	19-04	19-04	16-02	16-02	16-02	19-04
SEM site	SEM 3	SEM 4	SEM 1	SEM 2	LA Sp3	LA Sp3	LA Sp4	LA Sp4
Analysis ID	Tourmaline	Tourmaline	Tourmaline	Tourmaline	Tourmaline	Tourmaline	Tourmaline	Tourmaline
B_2O_3 Wt.%	-	14.60	14.50	12.65	13.85	15.09	13.59	14.50
Na_2O Wt.%	1.36	1.62	2.11	2.01	1.56	2.14	2.07	2.11
MgO Wt.%	4.84	3.90	6.69	6.73	3.13	5.95	3.83	6.69
Al_2O_3 Wt.%	32.57	31.81	33.49	32.80	33.15	30.62	33.1	33.49
SiO_2 Wt.%	34.66	33.74	35.41	35.74	34.52	34.74	34.42	35.41
CaO Wt.%	1.48	1.23	0.44	0.63	0.29	0.88	0.72	0.44
TiO_2 Wt.%	0.54	0.64	0.37	0.47	0.41	-	0.29	0.37
FeO Wt.%	10.34	12.08	7.13	7.68	12.23	11.08	11.28	7.13
Total	85.79	99.62	100.15	98.71	99.13	100.50	99.29	100.15

Sample ID	DT088	DT119
Drill Hole	17-01	17-01
SEM site	Line 1	Sp4
Analysis ID	Tourmaline	Tourmaline
B_2O_3 Wt.%	15.81	17.69
Na_2O Wt.%	1.55	2.13
MgO Wt.%	5.94	5.38
Al_2O_3 Wt.%	32.70	32.58
SiO_2 Wt.%	33.93	32.41
CaO Wt.%	1.16	0.71
TiO_2 Wt.%	0.66	0.65
FeO Wt.%	8.62	9.14
Total	100.37	100.69

Appendix XII

SEM Data Feldspar

Sample ID	DT120A	DT120B	DT120B	DT120B	DT120B	DT120B	DT063	DT063	DT088
SEM site	SEM3	SEM 1	SEM 1	SEM 2	SEM 2	SEM3	SEM2	SEM3	SEM2
Analysis ID	Feldspar	Feldspar 1	Feldspar 2	Feldspar	Feldspar 2	Feldspar	Feldspar	Feld 1	Feldspar 2
Na_2O Wt. %	6.11	6.67	7.51	7.42	7.62	8.59	1.85	3.29	-
MgO Wt. %	-	-	-	-	-	-	-	-	0.59
Al_2O_3 Wt. %	28.23	26.60	24.90	22.94	25.22	25.53	33.10	31.16	33.45
SiO_2 Wt. %	53.93	56.12	57.99	58.25	57.82	60.06	45.19	47.93	47.46
K_2O Wt. %	-	-	-	2.05	-	-	0.26	-	10.65
CaO Wt. %	11.24	9.39	7.55	6.09	7.67	7.43	17.63	15.35	1.07
FeO Wt. %	-	-	-	0.28	-	-	-	-	2.40
Total	99.52	98.76	97.94	97.02	98.34	101.61	98.03	97.73	95.61

Sample ID	DT088	DT050B	DT056	DT017	DT017	DT020	DT020	DT020	DT020
SEM site	SEM2	SEM 5	SEM 3	SEM 2	SEM 2	SEM 2	SEM 2	SEM 3	SEM 3
Analysis ID	Feldspar	Feldspar	Feldspar	Feldspar 2	Feldspar	Feldspar 1	Feldspar 2	Feldspar	Feldspar 2
Na_2O Wt. %	-	1.79	2.01	2.46	4.61	-	-	-	0.44
MgO Wt. %	-	-	-	-	-	-	-	1.19	-
Al_2O_3 Wt. %	33.09	33.09	34.31	32.39	29.29	36.88	36.01	31.25	36.44
SiO_2 Wt. %	44.64	45.67	46.08	47.57	51.57	45.71	45.92	44.95	42.24
K_2O Wt. %	11.12	-	-	-	2.10	11.00	10.78	10.38	-
CaO Wt. %	-	17.27	17.59	15.59	9.65	0.29	-	-	20.11
FeO Wt. %	3.20	-	-	0.27	0.78	0.46	0.93	1.59	-
Total	92.05	97.82	99.99	98.27	98.00	94.34	93.65	89.37	99.22

Sample ID	DT022	DT022	DT022	DT032	DT006	DT006	DT005	DT005	DT005
SEM site	SEM 1	SEM 2	SEM 2	SEM 3	SEM 1	SEM 2	SEM 2	SEM 2	SEM 3
Analysis ID	Feldspar	Feldspar	Feldspar 2	Feldspar	Feldspar	Feldspar	Feldspar 2	Feldspar	Feldspar
Na_2O Wt. %	0.68	2.11	0.66	7.70	-	0.39	10.49	9.80	9.55
MgO Wt. %	-	-	-	-	-	-	-	-	-
Al_2O_3 Wt. %	35.58	36.51	36.55	25.06	35.69	32.64	24.42	22.33	22.14

SiO_2 Wt. %	43.82	44.27	43.89	58.13	41.28	39.01	65.67	63.02	62.37
K_2O Wt. %	-	7.53	-	-	-	-	0.8	-	-
CaO Wt. %	19.81	0.86	20.41	7.05	20.47	24.83	2.26	3.29	3.31
FeO Wt. %	-	1.58	-	-	-	0.36	-	-	-
Total	99.89	92.87	101.52	97.94	97.45	97.22	103.62	98.45	97.36

Sample ID	DT024	DT024	DT042	DT042	DT042	DT042	DT042	DT109	DT109
SEM site	SEM 1	SEM 2	SEM 1	SEM 1	SEM 2	SEM 3	SEM 3	SEM 1	SEM 1
Analysis ID	Feldspar	Feldspar	Feldspar 2	Feldspar	Feldspar	Feldspar	Feldspar 2	Feldspar 2	Feldspar
Na_2O Wt. %	2.15	4.28	-	1.11	0.63	0.43	-	6.97	8.18
MgO Wt. %	-	-	-	-	-	0.60	-	-	-
Al_2O_3 Wt. %	34.03	30.74	33.15	34.37	34.86	32.05	30.76	26.70	26.07
SiO_2 Wt. %	45.96	51.24	37.47	43.36	41.33	39.28	36.39	57.74	60.13
K_2O Wt. %	1.91	-	-	-	-	-	-	-	-
CaO Wt. %	13.96	13.41	25.50	18.83	19.87	18.87	24.27	8.75	7.09
FeO Wt. %	0.32	-	0.40	-	-	1.77	0.81	-	-
Total	98.33	99.67	96.53	97.67	96.68	93.00	92.23	100.17	101.48

Sample ID	DT109	DT109	DT054	DT054	DT058	DT035	DT035	DT092	DT092
SEM site	SEM 2	SEM 2	SEM 2	SEM 2	SEM 2	SEM 1	SEM 1	SEM 2	SEM 4
Analysis ID	Feldspar	Feldspar 2	Feldspar	Feldspar 2	Feldspar	Feldspar	Feldspar 2	Feldspar	Feldspar
Na_2O Wt. %	6.37	7.31	1.11	1.56	3.53	1.76	0.80	2.27	4.36
MgO Wt. %	-	-	-	-	-	-	0.61	-	-
Al_2O_3 Wt. %	20.26	26.55	35.71	34.92	31.00	28.87	34.69	33.66	30.63
SiO_2 Wt. %	51.56	58.72	44.42	45.21	47.92	46.66	43.05	47.32	50.69
K_2O Wt. %	-	-	-	-	-	9.01	9.97	-	-
CaO Wt. %	5.16	7.68	19.18	18.55	14.65	-	-	17.02	13.78
FeO Wt. %	-	-	-	-	-	3.39	3.23	-	-
Total	83.34	100.27	100.41	100.26	97.10	89.70	92.35	100.28	99.46

Sample ID	DT092	DT092	DT092	DT039	DT039	DT039	DT039	DT039	DT039
SEM site	SEM 4	SEM 5	SEM 5	SEM 1	SEM 2	SEM 2	SEM 2	SEM 3	SEM 3
Analysis ID	Feldspar 2	Feldspar	Feldspar 2	Feldspar	Feldspar 1	Feldspar 2	Feldspar 3	Feldspar 1	Feldspar 2
Na_2O Wt. %	-	2.29	0.79	-	0.98	-	0.77	0.43	0.58
MgO Wt. %	-	-	-	-	-	-	-	-	-
Al_2O_3 Wt. %	27.78	33.14	34.29	31.13	35.51	33.54	35.46	33.47	35.52
SiO_2 Wt. %	38.12	46.14	46.00	37.99	43.79	38.87	43.08	39.79	43.19
K_2O Wt. %	-	-	10.43	-	-	-	-	-	-
CaO Wt. %	24.50	16.78	-	23.29	18.18	24.1	18.46	23.58	18.98
FeO Wt. %	6.41	-	0.90	1.71	-	-	-	-	-
Total	96.80	98.35	92.40	94.12	98.46	96.51	97.76	97.26	98.26

Sample ID	DT039	DT070	DT070	DT111	DT111	DT111	DT111	DT118B	DT118B
SEM site	SEM 4	SEM 1	SEM 2	SEM 1	SEM 1	SEM 2	SEM 3	SEM 1	SEM 1
Analysis ID	Feldspar	Feldspar	Feldspar	Feldspar 1	Feldspar 2	Feldspar	Feldspar	Feldspar 1	Feldspar 2
Na_2O Wt. %	1.60	11.91	12.32	8.91	8.75	9.84	9.73	11.25	0.34
MgO Wt. %	-	-	-	-	-	-	-	-	-
Al_2O_3 Wt. %	31.90	19.43	19.9	23.94	23.21	21.06	24.12	19.68	18.47
SiO_2 Wt. %	43.47	67.26	68.42	61.57	59.47	60.25	63.43	65.64	62.35
K_2O Wt. %	-	-	-	-	-	-	-	0.14	15.95
CaO Wt. %	20.54	0.53	-	4.69	4.91	4.28	4.60	0.48	-
FeO Wt. %	0.30	-	-	-	-	0.28	-	-	-
Total	97.80	99.14	100.65	99.12	96.34	95.72	101.88	97.18	98.05

Sample ID	DT118B	DT118B	DT118B	DT118B	DT118B	DT118B	DT118B	DT102	DT102
SEM site	SEM 1	SEM 2	SEM 2	SEM 3	SEM 3	SEM 3	SEM 4	SEM 1	SEM 1
Analysis ID	Feldspar 3	Feldspar 1	Feldspar 2	Feldspar 1	Feldspar 2	Feldspar 3	Feldspar 1	Feldspar 2	Feldspar 3
Na_2O Wt. %	0.63	-	-	0.30	-	7.83	9.36	-	-
MgO Wt. %	-	-	-	-	-	-	-	-	-
Al_2O_3 Wt. %	18.65	17.94	18.14	18.49	18.60	25.50	23.75	32.48	32.27

SiO_2 Wt. %	62.49	62.55	62.56	63.77	64.29	59.49	62.05	38.20	38.10
K_2O Wt. %	15.47	16.62	15.98	16.95	16.80	0.16	0.23	-	-
CaO Wt. %	-	-	-	-	-	6.94	4.82	25.83	25.68
FeO Wt. %	-	0.41	-	-	-	-	-	2.33	1.16
Total	97.94	97.53	96.69	99.51	99.81	99.92	100.21	98.85	97.21

Sample ID	DT102	DT102	DT102	DT117	DT117	DT118A	DT118A	DT118A
SEM site	SEM 1	SEM 4	SEM 4	SEM 1	SEM 4	SEM 2	SEM 3	SEM 3
Analysis ID	Feldspar 1	Feldspar 1	Feldspar 2	Feldspar	Feldspar	Feldspar	Feldspar 1	Feldspar 2
Na_2O Wt. %	1.71	0.29	4.22	6.76	6.28	7.84	8.43	8.60
MgO Wt. %	-	-	-	-	-	-	-	-
Al_2O_3 Wt. %	34.98	36.79	31.51	26.87	27.44	25.3	24.83	24.58
SiO_2 Wt. %	45.24	42.82	50.55	55.35	55.92	58.91	59.57	59.97
K_2O Wt. %	-	-	-	-	-	-	-	0.18
CaO Wt. %	18.55	20.52	14.23	8.69	9.4	6.90	6.18	5.75
FeO Wt. %	-	-	-	-	-	-	-	-
Total	100.48	100.42	100.51	97.68	99.03	98.95	99.00	99.07

Appendix VIII

SEM Data Pyrite

Sample ID	DT120A	DT063	DT087	DT088	DT028	DT006	DT034
SEM site	SEM5	SEM1	SEM3	SEM1	SEM 4	SEM 1	SEM 2
Analysis ID	pyrite	Pyrite	pyrite	pyrite	Pyrite	Pyrite	Pyrite
S Wt. %	52.90	54.66	55.23	54.15	54.43	56.63	54.28
Fe Wt.%	47.48	48.65	49.21	48.16	46.63	46.98	45.40
Total:	100.38	103.31	104.44	102.31	101.06	103.62	99.68

Sample ID	DT117	DT117	DT117	DT117	DT118A	DT118A	DT118A
SEM site	SEM 1	SEM 2	SEM 3	SEM 4	SEM 1	SEM 2	SEM 3
Analysis ID	Pyrite	Pyrite	Pyrite	Pyrite	Pyrite	Pyrite	Pyrite
S Wt. %	52.66	53.25	53.37	53.80	53.37	53.78	53.23
Fe Wt.%	45.28	45.48	44.98	45.96	46.17	46.09	45.66
Total:	97.94	98.73	98.35	99.76	99.54	99.86	98.89

Appendix XIV

SEM Data Pyrrhotite

Sample ID	DT120A	DT120B	DT-119	DT-119	DT-119	DT050B	DT050B	DT056
SEM site	SEM2	SEM3	SEM3	SEM4	SEM5	SEM 1	SEM 3	SEM 2
Analysis ID	Po	Po	Po	Po	Po	Po	Po	Po
S Wt. %	36.62	38.19	39.66	39.95	39.03	36.15	36.70	36.95
Fe Wt. %	64.15	65.69	61.20	61.25	61.48	60.94	63.74	65.21
Total:	100.77	103.87	100.86	101.20	100.51	101.82	100.43	102.16

Sample ID	DT028	DT009	DT118B	DT118B	DT118B	DT034	DT034	DT102
SEM site	SEM 4	SEM 1	SEM 2	SEM 3	SEM 4	SEM 1	SEM 2	SEM 2
Analysis ID	Pyrrhotite	Pyrrhotite	Pyrrhotite	Pyrrhotite	Pyrrhotite	Pyrrhotite	Pyrrhotite	Pyrrhotite
S Wt. %	38.82	42.78	38.99	39.36	39.58	36.97	37.08	40.31
Fe Wt. %	62.84	64.34	58.12	60.80	60.83	63.27	62.99	60.04
Total:	101.65	107.12	97.12	100.16	100.41	100.25	100.08	100.35

Sample ID	DT102	DT117	DT117	DT117	DT117	DT118A
SEM site	SEM 3	SEM 1	SEM 2	SEM 3	SEM 4	SEM 1
Analysis ID	Pyrrhotite	Pyrrhotite	Pyrrhotite	Pyrrhotite	Pyrrhotite	Pyrrhotite
S Wt. %	39.53	38.85	38.83	38.37	39.42	39.20
Fe Wt. %	60.04	59.29	58.53	58.56	60.77	60.31
Total:	99.57	98.14	97.36	96.93	100.19	99.50

Appendix XV

SEM Data Chalcopyrite

Sample ID	DT063	DT-119	DT-119	DT050B	DT050B	DT056	DT017	DT118B	DT118B
SEM site	SEM1	SEM1	SEM2	SEM 2	SEM 3	SEM 2	SEM 1	SEM 1	SEM 3
Analysis ID	Cp	Cp1	Cp1	Cp	Cp	Cp	Cp	Chalcopyrite	Chalcopyrite
S Wt. %	35.38	34.87	32.25	35.27	35.90	35.50	35.41	34.97	35.88
Fe Wt. %	32.35	31.15	31.28	30.04	32.53	30.39	30.61	30.01	30.46
Cu Wt. %	35.30	34.55	33.83	33.97	33.71	34.57	35.59	33.62	34.77
Total:	103.03	100.57	97.37	99.57	102.13	100.46	101.62	98.60	101.11

Sample ID	DT118B	DT118B	DT034	DT034	DT102	DT117	DT118A	DT118A
SEM site	SEM 3 Chalcopyrite	SEM 4	SEM 1	SEM 2	SEM 2	SEM 4	SEM 1	SEM 2
Analysis ID	2	Chalcopyrite	Chalcopyrite	Chalcopyrite	Chalcopyrite	Chalcopyrite	Chalcopyrite	Chalcopyrite
S Wt. %	35.59	35.34	34.99	35.86	34.78	35.10	35.23	35.21
Fe Wt. %	30.54	30.67	30.22	55.81	29.07	30.11	30.31	30.38
Cu Wt. %	35.01	35.00	35.19	7.88	36.13	34.10	34.22	33.97
Total:	101.14	101.01	100.40	99.55	99.98	99.53	99.76	99.56

Appendix XVI

SEM Data Sphalerite

Sample ID	DT053	DT053	DT118B	DT118B	DT118B	DT118B
SEM site	SEM 2	SEM 2	SEM 1	SEM 1	SEM 2	SEM 3
Analysis ID	Cad Sphal 1	Cad Sphal 2	Sphalerite 1	Sphalerite 2	Sphalerite 1	Sphalerite 1
S Wt.%	32.34	30.61	33.07	32.51	31.71	33.70
Fe Wt.%	10.24	7.88	6.51	6.06	4.98	5.85
Zn Wt.%	41.29	43.30	59.33	59.59	58.05	61.19
Cd Wt.%	16.01	20.35	1.20	1.07	1.24	0.94
Total:	99.87	102.13	100.12	99.22	95.98	101.67

Sample ID	DT118B	DT118B	DT117	DT117	DT117	DT118A
SEM site	SEM 3	SEM 4	SEM 2	SEM 3	SEM 4	SEM 1
Analysis ID	Sphalerite 2	Sphalerite 1	Sphalerite 1	Sphalerite 1	Sphalerite 1	Sphalerite 1
S Wt.%	33.14	33.97	33.18	33.02	33.44	33.53
Fe Wt.%	5.92	6.13	6.58	6.79	6.95	5.97
Zn Wt.%	60.96	61.26	58.71	58.19	58.83	59.31
Cd Wt.%	0.90	1.16	1.14	1.26	1.23	0.95
Total:	100.91	102.52	99.60	99.26	100.46	99.77

Sample ID	DT118A	DT118A	DT118A
SEM site	SEM 2	SEM 2	SEM 3
Analysis ID	Sphalerite 2	Sphalerite 1	Sphalerite 1
S Wt.%	33.45	33.65	33.87
Fe Wt.%	6.62	6.48	6.98
Zn Wt.%	59.68	59.68	58.53
Cd Wt.%	0.88	1.13	1.22
Total:	100.64	100.94	100.61

Appendix XVII

SEM Data Arsenopyrite

Sample ID	DT020	DT035	DT118B	DT118B	DT118B	DT118A	DT118A
SEM site	SEM 2	SEM 4	SEM 2	SEM 3	SEM 4	SEM 1	SEM 3
Analysis ID	Arsenopyrite	Arsenopyrite	Arsenopyrite 1	Arsenopyrite 1	Arsenopyrite	Arsenopyrite	Arsenopyrite
S Wt.%	19.97	22.24	21.07	22.18	21.9	21.23	21.85
Fe Wt. %	34.44	35.81	34.10	36.11	35.87	34.37	34.75
As Wt.%	46.45	46.99	44.15	44.99	46.24	44.87	44.20
Total:	100.87	105.04	99.32	103.27	104.01	100.47	100.80

Appendix XVIII

Geochronology

CA-TIMS U-Pb isotopic data

	Compositional Parameters						Radiogenic Isotope Ratios								Isotopic Ages					
Sample (a)	Th/U (b)	$^{206}Pb^*$ x10^{-13} mol (c)	mol % $^{206}Pb^*$ (c)	Pb^*/Pb_c (c)	Pb_c (pg) (c)	$^{206}Pb/^{204}Pb$ (d)	$^{208}Pb/^{206}Pb$ (e)	$^{207}Pb/^{206}Pb$ (e)	% err (f)	$^{207}Pb/^{235}U$ (e)	% err (f)	$^{206}Pb/^{238}U$ (e)	% err (f)	corr. coef.	$^{207}Pb/^{206}Pb$ (g)	± (f)	$^{207}Pb/^{235}U$ (g)	± (f)	$^{206}Pb/^{238}U$ (g)	± (f)
21-LA-DT-079																				
T-5	0.454	2.4473	99.83%	197	0.34	10808	0.124	0.21928	0.060	17.708315	0.137	0.585969	0.090	0.945	**2974.7**	**0.97**	2974.02	1.32	2973.06	2.14
2-7	0.551	1.5199	99.80%	174	0.25	9390	0.150	0.21915	0.061	17.696643	0.157	0.585930	0.117	0.943	**2973.7**	**0.98**	2973.39	1.51	2972.90	2.79
3-1	0.467	2.4300	99.80%	170	0.40	9341	0.127	0.21911	0.059	17.692733	0.137	0.585897	0.091	0.950	**2973.5**	**0.94**	2973.18	1.32	2972.77	2.17
3-2	0.453	3.8313	99.90%	329	0.32	18103	0.123	0.21918	0.059	17.685815	0.130	0.585498	0.078	0.958	**2973.9**	**0.96**	2972.80	1.25	2971.14	1.86
3-3	0.395	1.3483	99.78%	154	0.24	8588	0.108	0.21919	0.060	17.700014	0.158	0.585924	0.120	0.945	**2974.0**	**0.96**	2973.57	1.52	2972.87	2.85
															weighted mean $^{207}Pb/^{206}Pb$ age = 2973.96 ± 0.42 [2.37] Ma (2s); MSWD = 0.90 (n=5) (h)					
21-LA-DT-103																				
A	0.503	1.4700	99.84%	210	0.20	11443	0.137	0.21998	0.060	17.809961	0.153	0.587455	0.112	0.942	**2979.8**	**0.97**	2979.53	1.47	2979.09	2.66
B	0.412	0.7743	99.75%	133	0.16	7381	0.112	0.21993	0.060	17.806057	0.207	0.587455	0.178	0.962	**2979.5**	**0.97**	2979.32	1.99	2979.10	4.25
C	0.453	1.3012	99.82%	186	0.19	10197	0.123	0.22012	0.059	17.816986	0.160	0.587322	0.122	0.949	**2980.8**	**0.95**	2979.91	1.54	2978.55	2.91
D	0.390	1.5324	99.71%	116	0.36	6474	0.106	0.21994	0.063	17.794746	0.159	0.587051	0.120	0.937	**2979.5**	**1.01**	2978.70	1.53	2977.46	2.86
E	0.389	0.2232	98.94%	31	0.20	1753	0.106	0.22008	0.074	17.817129	0.582	0.587411	0.576	0.992	**2980.6**	**1.18**	2979.91	5.59	2978.91	13.73
															weighted mean $^{207}Pb/^{206}Pb$ age = 2980.02 ± 0.77 [2.37] Ma (2s); MSWD = 1.50 (n=5) (h)					
21-LA-DT-105																				
A	0.415	0.6123	99.51%	68	0.25	3793	0.113	0.21902	0.061	17.671455	0.245	0.585442	0.223	0.970	**2972.8**	**0.99**	2972.02	2.35	2970.92	5.31
B	0.188	2.1528	99.80%	160	0.35	9300	0.051	0.21908	0.059	17.689987	0.140	0.585902	0.095	0.946	**2973.2**	**0.95**	2973.03	1.35	2972.79	2.26
C	0.424	3.1782	99.83%	201	0.44	11126	0.116	0.21912	0.060	17.692244	0.133	0.585851	0.083	0.952	**2973.5**	**0.96**	2973.15	1.28	2972.58	1.98
D	0.356	1.0723	99.80%	168	0.17	9424	0.097	0.21905	0.059	17.674610	0.173	0.585471	0.138	0.951	**2973.0**	**0.96**	2972.19	1.66	2971.03	3.28
E	0.453	5.6846	99.89%	301	0.52	16537	0.123	0.21898	0.059	17.654261	0.127	0.584985	0.074	0.966	**2972.5**	**0.95**	2971.09	1.22	2969.06	1.76
															weighted mean $^{207}Pb/^{206}Pb$ age = 2972.99 ± 0.42 [2.37] Ma (2s); MSWD = 0.73 (n=5) (h)					

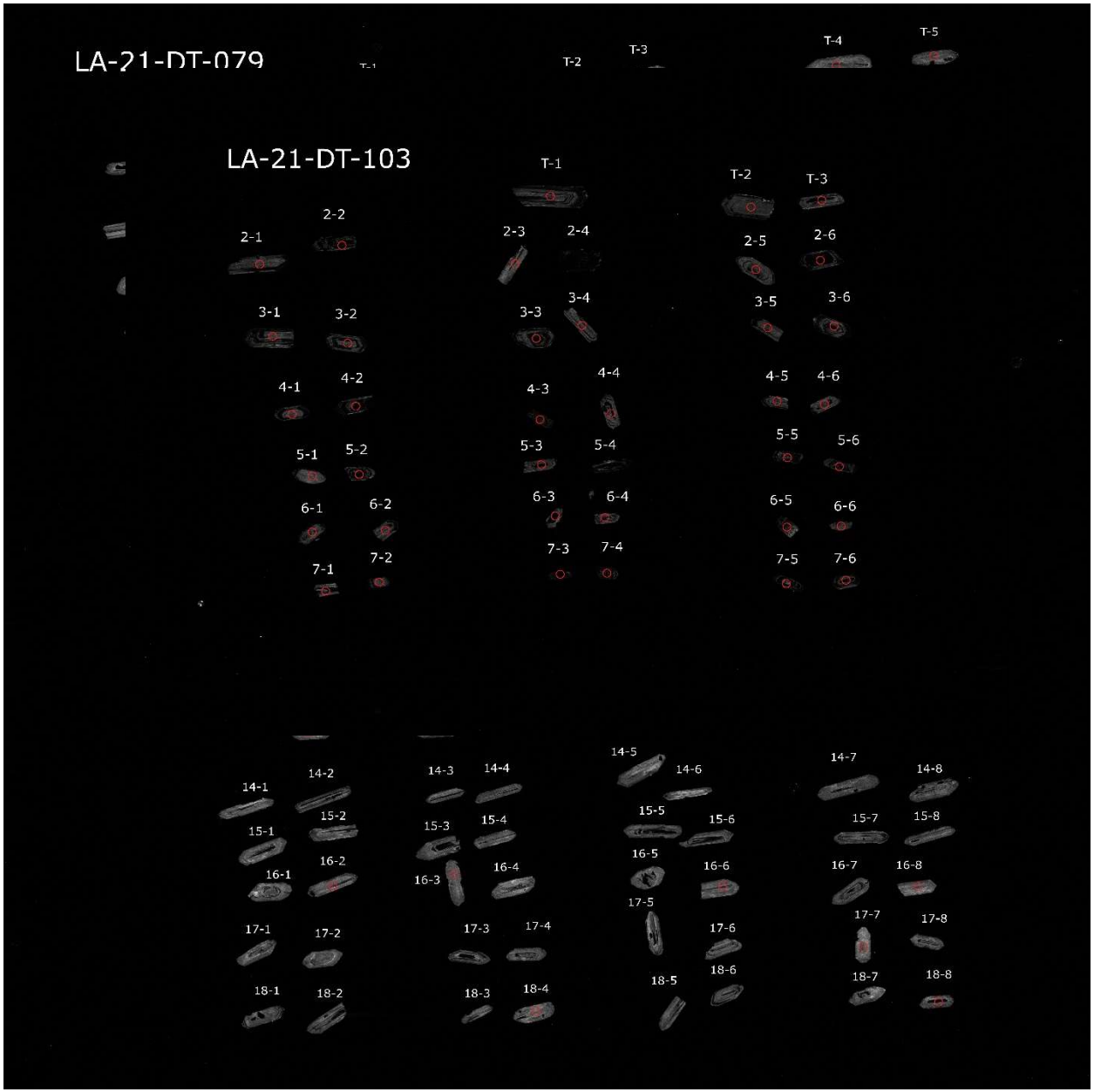
LA-21-DT-079
T-1
T-2
T-3
T-4
T-5
LA-21-DT-103
T-1
T-2
T-3
2-1
2-2
2-3
2-4
2-5
2-6
3-1
3-2
3-3
3-4
3-5
3-6
4-1
4-2
4-3
4-4
4-5
4-6
5-1
5-2
5-3
5-4
5-5
5-6
6-1
6-2
6-3
6-4
6-5
6-6
7-1
7-2
7-3
7-4
7-5
7-6
14-1
14-2
14-3
14-4
14-5
14-6
14-7
14-8
15-1
15-2
15-3
15-4
15-5
15-6
15-7
15-8
16-1
16-2
16-3
16-4
16-5
16-6
16-7
16-8
17-1
17-2
17-3
17-4
17-5
17-6
17-7
17-8
18-1
18-2
18-3
18-4
18-5
18-6
18-7
18-8


LA-21-DT-105

Garnet U/Pb Analysis

LA-21-DT-017

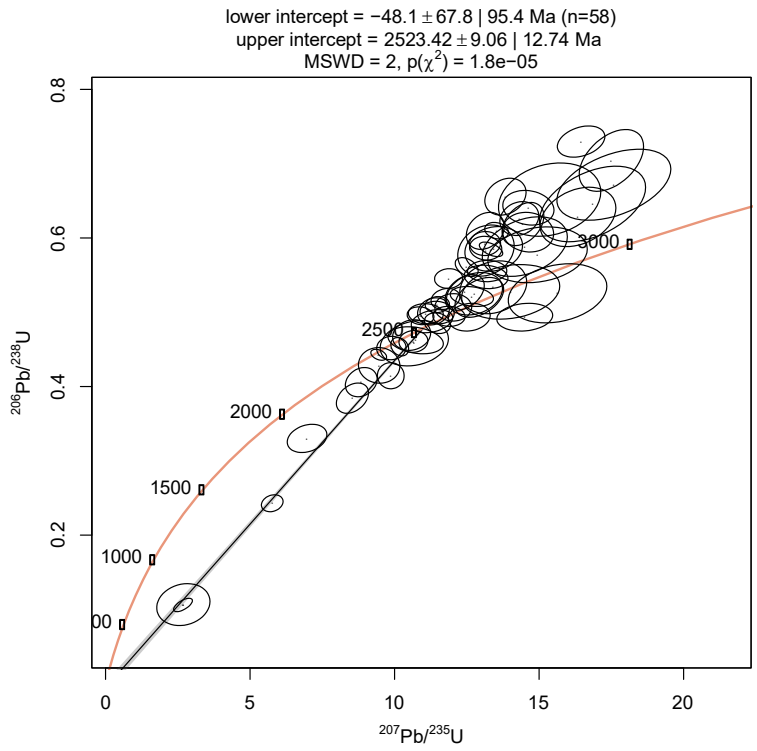

LA-21-DT-096

Inner Core

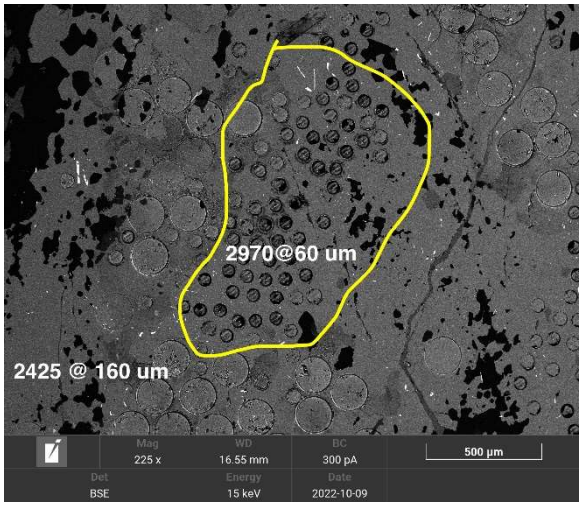

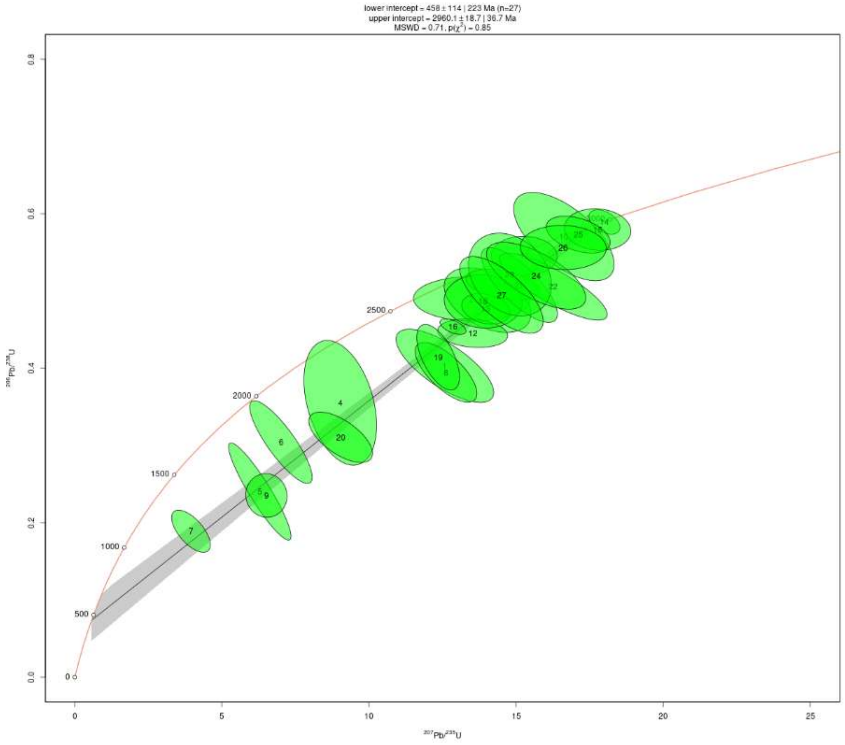

Outer Rim

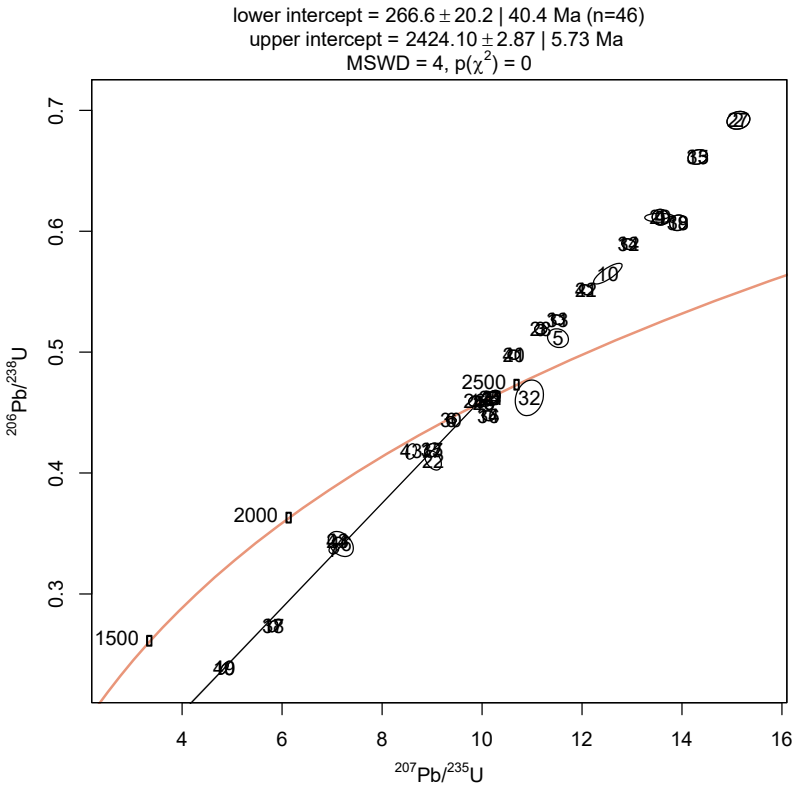
lower intercept = 266.6 ± 20.2 | 40.4 Ma (n=46)
upper intercept = 2424.10 ± 2.87 | 5.73 Ma
MSWD = 4, p(χ²) = 0
206Pb/238U
207Pb/235U
0.3
0.4
0.5
0.6
0.7
4
6
8
10
12
14
16
1500
2000
2500

Appendix XIX

SWIR Data Muscovite

Sample ID	DT-041	DT-024	DT-006	DT-010	DT-067	DT-008
1900 Position	1912.35	1919.35	1916.47	1918.52	1895.88	
1900 Peak Reflectance	0.43	0.34	0.19	0.25	0.15	
1900 Trough Reflectance	0.42	0.34	0.19	0.25	0.15	
1900 Magnitude	0.01	-	-	-	-	-
2200 Position	2202.57	2196.99	2204.31	2198.51	2197.13	2197.45
2200 Peak Reflectance	0.43	0.33	0.18	0.26	0.16	0.09
2200 Trough Reflectance	0.32	0.23	0.11	0.19	0.11	0.06
2200 Magnitude	0.11	0.10	0.07	0.07	0.05	0.03

Sample ID	DT-039	DT-069	DT-061	DT-042	DT-043	DT-043
1900 Position	1911.29		1911.32	1938.93	1911.57	1917.50
1900 Peak Reflectance	0.17		0.29	0.30	0.22	0.22
1900 Trough Reflectance	0.16		0.28	0.21	0.18	0.20
1900 Magnitude	0.01	-	-	0.08	0.03	0.02
2200 Position	2198.57	2198.18	2196.81	2198.81	2200.36	2199.93
2200 Peak Reflectance	0.17	0.87	0.28	0.27	0.19	0.20
2200 Trough Reflectance	0.12	0.68	0.21	0.18	0.10	0.13
2200 Magnitude	0.05	0.19	0.07	0.09	0.09	0.07

Sample ID	DT-032	DT-045	DT-051	DT-022	DT-050	DT-071
1900 Position		1912.21				1926.76
1900 Peak Reflectance		0.28				0.23
1900 Trough Reflectance		0.27				0.22
1900 Magnitude	-	0.01	-	-	-	-
2200 Position	2197.47	2198.87	2197.48	2199.16	2197.83	2197.68
2200 Peak Reflectance	0.43	0.28	0.43	0.18	0.25	0.23
2200 Trough Reflectance	0.29	0.20	0.31	0.14	0.19	0.18
2200 Magnitude	0.14	0.08	0.12	0.03	0.06	0.06

Sample ID	DT-100	DT-100	DT-075	DT-036
1900 Position	1913.89	1912.60	1922.64	1918.55
1900 Peak Reflectance	0.32	0.24	0.41	0.52
1900 Trough Reflectance	0.30	0.20	0.41	0.52
1900 Magnitude	0.02	0.04	-	-
2200 Position	2197.41	2202.81	2198.00	2197.01
2200 Peak Reflectance	0.31	0.22	0.42	0.54
2200 Trough Reflectance	0.20	0.16	0.34	0.42
2200 Magnitude	0.11	0.06	0.08	0.12

Appendix XX

SWIR Data Muscovite with Fe phase

Sample ID	DT-046	DT-041	DT-011	DT-021	DT-021	DT-059
1900 Posistion	1911.32	1917.5	1917.99	1943	1941.17	1907.2
1900 Peak Reflectance	0.206	0.204	0.24	0.153	0.0723	0.1395
1900 Trough Reflectance	0.196	0.195	0.205	0.131	0.0696	0.139
1900 Magnitude	0.01	0.009	0.035	0.022	0.0027	0.0005
2200 Posistion	2200.51	2206.47	2198.71	2200.865	2200.649	2197.337
2200 Peak Reflectance	0.22	0.205	0.249	0.157	0.0709	0.141
2200 Trough Reflectance	0.186	0.167	0.165	0.108	0.0504	0.103
2200 Magnitude	0.034	0.038	0.084	0.049	0.0205	0.038
2250 Posistion	2255	2250.8	2254.14	2251.593	2246.83	2254.03
2250 Peak Reflectance	0.2	0.183	0.208	0.132	0.586	0.122
2250 Trough Reflectance	0.193	0.178	0.207	0.131	0.585	0.121
2250 Magnitude	0.007	0.005	0.001	0.001	0.001	0.001

Sample ID	DT-059	DT-052	DT-004	DT-096	DT-038	DT-002
1900 Posistion		1907.2			1914.921	1920.58
1900 Peak Reflectance		0.105			0.23	0.228
1900 Trough Reflectance		0.105			0.221	0.224
1900 Magnitude	-	-	-	-	0.009	0.004
2200 Posistion	2196.928	2197.976	2198.034	2197.687	2198.871	2196.916
2200 Peak Reflectance	0.124	0.108	0.134	0.15	0.226	0.232
2200 Trough Reflectance	0.097	0.0878	0.0957	0.108	0.162	0.193
2200 Magnitude	0.027	0.0202	0.0383	0.042	0.064	0.039
2250 Posistion	2256.408	2256.09	2256.689	2258.067	2250.579	2255.695
2250 Peak Reflectance	0.113	0.0972	0.119	0.133	0.191	0.215
2250 Trough Reflectance	0.108	0.0965	0.117	0.13	0.188	0.213
2250 Magnitude	0.005	0.0007	0.002	0.003	0.003	0.002

Sample ID	DT-018	DT-069	DT-064	DT-042	DT-025	DT-012
1900 Posistion			1919.55	1916.278	1917.804	1914.036
1900 Peak Reflectance			0.232	0.264	0.268	0.226
1900 Trough Reflectance			0.231	0.179	0.234	0.202
1900 Magnitude	-	-	0.001	0.085	0.034	0.024
2200 Posistion	2200.155	2197.513	2197.56	2198.793	2197.535	2204.993
2200 Peak Reflectance	0.168	0.195	0.245	0.249	0.269	0.225
2200 Trough Reflectance	0.119	0.154	0.212	0.146	0.198	0.142
2200 Magnitude	0.049	0.041	0.033	0.103	0.071	0.083
2250 Posistion	2254.227	2259.355	2258.778	2252.058	2254.919	2251.495
2250 Peak Reflectance	0.139	0.175	0.23	0.181	0.239	0.187
2250 Trough Reflectance	0.131	0.167	0.229	0.173	0.237	0.179
2250 Magnitude	0.008	0.008	0.001	0.008	0.002	0.008

Sample ID	DT-093	DT-029
1900 Posistion		
1900 Peak Reflectance		
1900 Trough Reflectance		
1900 Magnitude	-	-
2200 Posistion	2198.852	2197.875
2200 Peak Reflectance	0.0997	0.235
2200 Trough Reflectance	0.077	0.174
2200 Magnitude	0.0227	0.061
2250 Posistion	2258.26	2255.486
2250 Peak Reflectance	0.0905	0.21
2250 Trough Reflectance	0.0885	0.209
2250 Magnitude	0.002	0.001

Appendix XXI

SWIR Data Kaolinite

Sample ID	DT-014	DT-014
1900 Position	1914.00	1912.00
1900 Peak Reflectance	0.575	0.473
1900 Trough Reflectance	0.397	0.356
1900 Magnitude	0.178	0.117
2200 Position	2207.72	2207.72
2200 Peak Reflectance	0.466	0.386
2200 Trough Reflectance	0.292	0.241
2200 Magnitude	0.174	0.145

Appendix XXII

Thin Section Descriptions

Sample ID: DT001	*Depth: 69.2*	*Location: 19-03*	*Rock Type: Staurolite, Garnet, Biotite schist*	
Mineral	**Abundance**	**Habit**	**Grain Size**	**Comments**
Quartz	30%	Subhedral, recrystalized	100-500 µm	Seriate from 100 to 500 micrometers, shows evidence for dynamic rotational recrystallization as the grain boundaries between quartz are straight and make polygon grains that meet at triple points.
Biotite	20%	Subhedral, platy	100-600 µm	Displays spaced foliation, with foliated layers containing most crystals with their long axis parallel, interspersed with Lamellae of polygon quartz lamellae. Decussate randomly orientated biotite interstitial to staurolite grains
Chlorite	3%	Subhedral, platy	100-600 µm	Appears to replace biotite grains within the biotite rich lamellae. Infills open space within the skeletal staurolite framework
Staurolite	20%	Subhedral to anhedral skeletal textured	0.5-4 mm	Poikiloblastic texture with quartz crystal inclusions. Skeletal very fragmented crystals, openings within the crystals are infilled predominantly with Quartz and minor chlorite
Garnet	10%	Subhedral to anhedral skeletal textured	0.5-5mm	Garnets range from competent unaltered in appearance to skeletal altered grains. Open spaces in skeletal garnet consist of quartz and chalcopyrite infilling

Tourmaline	Trace	Euhedral, triangular prism	50-100 µm	Occur as singular grains within the muscovite quartz schist, most orientated so they are cut looking down the c axis. Zoning present within the grains with a darker green interior and lighter exterior colour
Muscovite	15%	Subhedral, platy shaped	50-300 µm	Occur as in banded lamelle alternating with lamellae of quartz. Crystal laths are orientated parallel within their lamellae, randomly orientated grains interstitial to some quartz grains in the quartz rich lamellae layers.
Chalcopyrite	Trace	Anhedral, rounded blebs and irregular space filling shape	50-100 µm	Space filling in the skeletal garnet crystal
Pyrite	2%	Anhedral, Lath Shaped	5-100 µm	Pyrite laths are about 10 µm in width and can reach lengths up to 100 µm. The grains are orientated parallel to the mica grains in the schists. Within some of the more competent garnet grains the pyrite laths are randomly orientated in the center and become perpendicular as they reach the outer boundary of the crystal.
Zircons	Trace	Subhedral to anhedral, largest grain showing tetragonal bipyramidal shape.	1-20 µm	Very fine grain size, most noticeable by the brown reaction rims formed in biotite around the grains

Overall Comments: Section consists of a schistose rock consisting of lamellae of fine-grained biotite and muscovite interbedded with lamellae of quartz with sparse biotite and muscovite laths interstitial to the quartz grains. Larger porphyritic grains of garnet and staurolite occur surrounded by the mica and quartz lamellae. Section is taken at the contact between two separate beds, a siltstone protolith bed consisting of biotite and quartz lamellae, and a sandstone protolith with predominantly muscovite and quartz lamellae. The mica and quartz lamellae are about 500-1000 µm in width. Possible genesis would be a pelitic protolith siltstone sandstone beds containing detrital zircons, regionally metamorphosed to form garnet, staurolite, and the pelite recrystalized to form biotite muscovite and quartz layers. Later hydrothermal alteration of the rock precipitated tourmaline crystals as well as deposition of pyrite and chalcopyrite as small rectangular laths. The orientation of the pyrite laths is parallel to the sense of shear of the schistose mica quartz lamellae, suggesting deposition post metamorphisms as they infilled along cleavage planes within the micas. Pyrites contained within the open spaces of the garnets on the outer rim of the garnets are parallel and become randomly orientated toward the interior of the garnets. This suggests two possible hydrothermal events, one prior to deformation which deposited the pyrite in a random orientation within the garnets, and one post deformation which followed the foliation planes within the schist and exterior of the garnet. Retrograde metamorphism causes partial replacement of biotite to chlorite as well as alteration of staurolite to chlorite.

Sample ID: DT003	*Depth: 88.1*	*Location:19-03*	*Rock Type: Garnet staurolite mica schist with mineralized garnet quartz chert vein*	
Mineral	**Abundance**	**Habit**	**Grain Size**	**Comments**
Garnet	35%	Subhedral to skeletal	200 µm -10 mm	Coarse grained garnet crystals occur as a garnet quartz chlorite vein. The garnet crystals are fractured, with open space being filled by chlorite and a possible chert mineral, along with chalcopyrite. Pyrrhotite occurs as bands of replacement that postdates the vein.
Chlorite	12%	Subhedral to Anhedral platy and massive texture	200 µm to 1mm	Occurs as both a replacement of platy biotite laths, and as massive vein infilling space between altered garnets in the garnet chert vein. Chlorite vein patches consist of individual small 100 µm crystals that can't always be distinguished that make up patches up to 3-5mm wide.

Quartz	29%	Anhedral	25-500 µm	Quartz grains show evidence of bulging to sub grain rotation recrystallization. Smaller sub grains often separate the larger recrystalized grains and have not yet been incorporated into the larger quartz grains. Occur as space infill within the garnet quartz vein, as well as interstitial to biotite, chlorite laths in the schist
Biotite	8%	Subhedral, platy	200-500 µm	Occurs in orientated lamellae alternating with quartz, as well as interstitial to the quartz lamellae. Often pseudomorphed by chlorite
Staurolite	5%	Anhedral, Skeletal	300-600 µm	Poikiloblastic texture with quartz crystal inclusions. Occurs within the biotite quartz schist.
Chert	3%	anhedral	20 µm	Fills the space between the most fractured garnets within the vein.
Chalcopyrite	4%	anhedral	5 µm to 3mm	infilling matrix to the open space within the garnet vein, no obvious separation of crystal grains. Smaller sized grains are filling the small depressions of the garnets.
Cubanite	1%	Anhedral Exsolution Lamellae	20 µm wide, 200-500 µm long	Occur as exsolution lamellae within coarser grains of chalcopyrite.
Ilmenite	2%	Anhedral	100-200 µm	a few grains present within the chlorite infill matrix of the garnet veins

Pyrite	trace	Euhedral late stage, Anhedral replacement of Pyrrhotite	25-50 µm, 400 µm	Two stages of pyrite present, late-stage euhedral grains associated with the chalcopyrite Vein infill, and fine-grained replacement of pyrrhotite.
Pyrrhotite	1%	Subhedral to Anhedral	50 µm	Occur as linear bands consisting of small ovoid shaped grains, along with subhedral grains occurring alongside chalcopyrite in the garnet veins.
Overall Comments: Sample consists of a biotite staurolite quartz schist rock that has been cut by a 2cm wide garnet quartz vein. The schist portion of the sample is formed by alternating lamellae of biotite and quartz, with interstitial biotite occurring within the quartz lamellae. Biotite is replaced by chlorite with increasing intensity as it approaches the vein. The exterior of the vein consists of quartz containing the smaller 200-400 µm subhedral garnet alongside a matrix of chalcopyrite. The center of the vein consists of the coarse 2-10 mm garnet, these garnets are fractured and, in many cases, skeletal, with open space being filled by chlorite, chert, and sulphides. Probable genesis is likely a protolith siltstone being metamorphosed into a biotite schist with staurolite grains. Hydrothermal fluids infiltrate the schist and precipitate garnet, quartz and later the sulphide and possible oxide minerals. These same fluids also begin to alter the host rock and lead to chloritization of the biotite in the schist. Later cooling caused exsolution of cubanite from the chalcopyrite.				

Sample ID: DT005	*Depth:124.7*	*Location:19-03*	*staurolite, garnet, biotite schist with feldspar vein*	
Mineral	**Abundance**	**Habit**	**Grain Size**	**Comments**
Garnet	25%	Subhedral	1-5 mm	Coarse grained, heavily fractured and replaced by chlorite along fractures.

Staurolite	30%	Subhedral	2-10 mm	Poikiloblastic texture with quartz crystal inclusions. Significant fractures within crystal are filled with chlorite.
Biotite	12%	Subhedral, platy	200 µm-1mm	Occurs as homogenous vein containing the staurolite and garnet porphyroblasts on the exteriors of the feldspar vein. Majority of biotite grains are foliated, with occasional randomly orientated grains
Quartz	15%	Subhedral to Anhedral	50-1000 µm	50 µm grains occur infilling the staurolite and garnet crystals. Larger grains up to 1mm occur in a vein parallel to biotite vein. Biotite laths up to 200 µm occur interstitial to quartz grains.
Chlorite	4%	Anhedral	20-200 µm	Occur within fractures of the garnet and staurolite, possibly replacing them due to hydrothermal alteration
Muscovite	6%	Subhedral, platy	100 µm	Strongly foliated and curved bands of muscovite occur outside the boundaries of the feldspar biotite quartz vein. Representative of a psammite protolith prior to intrusion by veining.
Plagioclase Feldspar	8%	Subhedral to Anhedral, polygonal	50-200 µm	Polygonal shaped feldspar crystals with little visible twinning, biotite, and muscovite interstitial to feldspar grains. Crystal surfaces are sericite altered with a dusty pitted appearance.

Tourmaline	Trace	Euhedral	60 µm	Singular grains of euhedral tourmaline occur within the muscovite schist and feldspar vein.
Chalcopyrite	Trace	Anhedral	10-100 µm	Infills space within the fractures of garnets
Pyrrhotite	Trace	Anhedral	10-40 µm	Appears as possible inclusions within the garnet crystal
Ilmenite	Trace	Anhedral	10-50 µm	Occur as slender laths, especially as inclusions in the staurolite crystals

Overall Comments: Consists of a feldspar, quartz, biotite vein intruding into a muscovite schist. Interior of vein consists of polygonal feldspar grains with occasional interstitial muscovite likely as incorporated wall rock material. Massive biotite occurs proximal to the feldspar interior, followed by quartz on the exterior of the vein boundaries. Garnets and to a lesser degree staurolites are heavily fractured, and the fractures are infilled by chlorite and chalcopyrite. The garnets also seem to have poikilitic pyrite grains present. Likely protolith psammite rock metamorphosed to a muscovite schist with garnet and staurolite phenocrysts. Later intrusion by vein material caused the chloritization of garnet, as well as deposistion of chalcopyrite.

Sample ID: DT006	*Depth:* *515.1*	*Location:16-02*	*Rock Type: Siltstone with minor garnets*	
Mineral	**Abundance**	**Habit**	**Grain Size**	**Comments**
Quartz	32%	Subhedral to anhedral	50-200 µm	Occur as 500 µm lamellae with interstitial muscovite and biotite, separated by lamellae of muscovite and biotite

Muscovite	40%	Subhedral	50-400 µm	Occur as 200-400 µm foliated lamellae interspersed with quartz lamellae, as well as singular grains interstitial to quartz in the quartz rich lamellae
Biotite	15%	Subhedral	30-300 µm	Occur as 200-400 µm foliated lamellae interspersed with quartz lamellae, as well as singular grains interstitial to quartz in the quartz rich lamellae
Plagioclase Feldspar	10%	Anhedral	100-500 µm	very thin 1-5 µm stripes of polysynthetic twinning present on face of mineral, occur within the quartz lamellae as infrequent grains.
Garnet	3%	Subhedral to anhedral	50-500 µm	Occur as two individual crystals showing significant fracturing and fragmentation into small 50 µm pieces. The space between the crystal fragments consists of quartz and biotite.
Tourmaline	Trace	Euhedral to subhedral	20-100 µm	show triangular cross section when slice is orientated looking down the c axis, some crystals are more elongate prisms. Occur as singular crystals interstitial to grains within some muscovite and quartz lamellae
Pyrite	Trace	Subhedral to anhedral	10-150 µm	most occur as small 10-50 µm irregular shaped grains, one larger 150 µm rectangular crystal present

Overall Comments: Sample consists of interspaced lamellae of muscovite and quartz rich lamellae with occasional band of biotite. Small crystals of plagioclase feldspar occur with the quartz grains in the lamellae. Small garnet grains are present and show significant fragmentation into small 50 µm pieces. Trace pyrite and tourmaline crystals are present interstitial to the muscovite and quartz lamellae. Possible sequence of genesis, protolith consisted of small lamellae of siltstone and sandstones, regional metamorphism turned the sandstone into bands of muscovite and quartz with the biotite lamellae formed from the siltstone protolith. Small garnets formed during peak metamorphism. Some hydrothermal fluid flow through the unit caused the alteration and fragmentation of the garnet grain as well as the tourmaline and pyrite crystals.

Sample ID: DT009	*Depth:436.15*	*Location:16-02*	*Rock Type: Pyrrhotite +Chalcopyrite VMS horizon with tourmalinite, massive biotite and small garnets*	
Mineral	**Abundance**	**Habit**	**Grain Size**	**Comments**
Tourmaline	27%	Subhedral to anhedral	20-200 µm	Form massive tourmalinite blebs that consists of intergrowths of smaller tourmaline crystals. Many seems to grow in radiating patterns out from a center point.
Garnet	22%	subhedral	500 µm-1cm	Garnet grains are Poikiloblastic with open space filled by sulphides, tourmaline, and lesser chlorite. Have a red/brown alteration rim along fractures within the garnet.
Pyrrhotite	28%	Anhedral	100-800 µm	Occur as matrix for the sample, individual crystals are hard to distinguish, boundaries between them are straight to rounded. Also occur as space filling within the fractures and pits of the garnet, but not as frequent as chalcopyrite.

Chalcopyrite	6%	Anhedral	50-600 µm	occur as large grains as the sample matrix with Pyrrhotite, as well as frequently infilling the open spaces of the garnet fractures and pits.
Ilmenite	1%	Anhedral	50-100 µm	Occur as subrounded crystals of light grey magnetite that form close to the margins of the sulphides, in contact with either garnet or tourmalinite, or as infilling blebs within the pits of the garnets
Quartz	5%	Anhedral	200-600 µm	Occur as subrounded blebs of quartz within the sulphide matrix, exterior edges of the crystals show rounding, while the interior grain boundaries between quartz are straight and meet at triple points.
Biotite	8%	Subhedral, platy	200-600 µm	occurs as singular subrounded but originally lath shaped grains within the sulphide matrix. As well as massive intergrowths of randomly orientated crystals. The mica is overprinted by tourmaline crystals
Chlorite	1%	subhedral	50 µm	Occurs as infills to some of the pits on the surface of the altered garnet grains.

Overall Comments: Protolith siltstone would have been regionally metamorphosed and consist of garnet crystals in a matrix of biotite and quartz. Early stages of fluid flow through the rock began to break down the garnet crystals and tourmaline crystals grew into open space within garnets as well as overprinting the biotite. Tourmaline crystalized into tourmalinite horizons of radiating crystals of tourmaline. Later hydrothermal fluids continued to fracture the garnets, and biotite and suspended and rounded the fragments of wall rock biotite, garnet, and quartz. Sulphides were then deposited last consisting of Pyrrhotite, chalcopyrite and magnetite.

Sample ID: DT017	*Depth:65*	*Location:19-01*	*Rock Type: Garnet, staurolite, biotite schist, with chalcopyrite*	
Mineral	**Abundance**	**Habit**	**Grain Size**	**Comments**
Garnet	50%	Subhedral	5 mm-2 Cm	Very coarse garnet crystals which have undergone substantial fracturing and pitting, open space in the pits oh the crystal being filled by quartz, chalcopyrite, pyrite, and magnetite. Tourmaline crystals appear to be an overgrowth into the garnets, with tourmaline crystals growing through the garnet in a radiating pattern
Chlorite	10%	Subhedral, lath shaped	50-600 µm	Occurs in a 4mm vein of alternating 500 µm bands of chlorite and an altered feldspar unit. Also occur as individual grains interstitial to quartz grains in a quartz mica schist and infilling open spaces within the fractured coarse garnet crystals

Tourmaline	20%	Euhedral to subhedral	10-200 µm	Occur as radial growths of tourmaline crystals that form blebs of tourmalinite up to 600 µm across, multiple of these radial tourmalinite blebs form a vein adjacent to the fracturing garnet, in some instances filling the larger fractures of the garnet. Some individual tourmaline grains are found in the quartz mica schist
Plagioclase Feldspar	3%	Anhedral	5-30 µm	Occur as patches of very altered fine-grained groundmass that alternates with bands of chlorite
Quartz	8%	Anhedral	20-400 µm	Occur as the main component of the quartz mica schist, with interstitial chlorite and muscovite grains. Also fills the open space pits in the altered and degrading garnet. Show bulging and irregular grain boundaries that suggest only low-grade recrystallization has occurred
Muscovite	2%	Subhedral	20-500 µm	Fine grained crystals occur interstitial to quartz in the schist, as well as one fracture in the garnet that is filled with the medium grained 200-500 µm crystals
Chalcopyrite	5%	Anhedral	50 µm- 3 mm	Fills fractures and open pits in within the garnet as well as filling space between the tourmalinite and chlorite
Ilmenite	1%	Anhedral	50-120 µm	Rounded grains occur within the chalcopyrite matrix as well as filling open space in the open pits of the altered garnet
Cubanite	Trace	Anhedral	10 µm	Form as exsolution lamellae within the chalcopyrite

Cobaltite	1%	Euhedral to subhedral	40-250 µm	Occur as straight edged euhedral to anhedral crystals within a matrix of chalcopyrite in the larger sulphide filled fractures of the garnet
Overall Comments: Sample consists of a few very coarse garnet crystals that are set in a matrix of a quartz feldspar mica schist, possible felsic volcanic protolith. The garnet has been hydrothermally altered leading to open spaces and pits forming as well as large fractures, these fluids crystalized chlorite as well as tourmaline and quartz. Either a separate fluid event or a continuation of these altering hydrothermal fluids then began to crystalize sulphides and ilmenite into the open spaces of the fractured garnet and between tourmaline and quartz crystals.				

Sample ID: DT020	*Depth: 34.4*	*Location:19-01*	*Rock Type: garnet biotite schist*	
Mineral	**Abundance**	**Habit**	**Grain Size**	**Comments**
Garnet	30%	Subhedral- anhedral	50-1500 µm	Subhedral coarser garnets alongside fine anhedral garnet fragments suspended in quartz vein and biotite chlorite vein.
Chlorite	16%	Subhedral	50-600 µm	Fills open spaces in the cracks of the fragmented garnets as well as replacement of biotite in the mica veins. Grain orientation shows a general foliation parallel to the vein direction, with some crystals appearing to have a random orientation
Biotite	20%	Subhedral	50-600 µm	Makes up the bulk of the mica vein, surrounds the interstitial garnet fragment. Small fragments of biotite with random orientation occur suspended in the coarser grained and foliated biotite in the vein.

Quartz	20%	Anhedral	50-400 µm	Quartz vein shows bimodal distribution with quartz grains from 50-100 µm present along the boundaries of the coarse 300-400 µm grains. Shows evidence of low temp bulging recrystallization. Garnet fragments are suspended within the quartz vein along with fragments of the biotite garnet vein.
Tourmaline	Trace	Euhedral, trigonal prism	50-80 µm	Isolated grains cut looking down the C axis, occur suspended within the biotite and chlorite vein.
Alkali Feldspar	3%	Subhedral- anhedral	50-800 µm	Heavily altered grains suspended in a biotite chlorite vein matrix. Best preserved grains are stubby prism shape. Has irregular extinction with some isotropic portions, the rest showing white to yellow birefringence. Appears to be altering to sericite
Plagioclase Feldspar	2%	Subhedral- anhedral	50-800 µm	Heavily altered grains suspended in a biotite chlorite vein matrix. Best preserved grains are stubby prism shape. Has irregular extinction with some isotropic portions, the rest showing white to yellow birefringence. Appears to be altering to sericite
Siderite	5%	Anhedral	100-800 µm	Yellow brown cream coloured. Occurs as a 100 µm veinlet running down the center of the biotite chlorite vein. Widens out to 800 µm as it crosscuts the quartz vein.
Zircon	Trace	euhedral-subhedral	5-50 µm	Small crystals are present within biotite grains, visible due to the damage halos

Chalcopyrite	trace	Anhedral	25-150 µm	Small patch of irregular shaped grains occurring between chlorite and garnet fragments in the quartz vein.
Pyrite	1%	Anhedral	15-250 µm	Disseminated grains throughout the quartz and mica veins
Muscovite	3%	Subhedral	50-500 µm	occurs within the mica vein as foliated coarse grains parallel to the vein direction as well as small randomly orientated fragments
Overall Comments: Sample consists of small garnet fragments suspended in a mica schist and a quartz vein. The mica schist is made up of predominantly biotite, followed by chlorite and some muscovite. The quartz vein shows bimodal sized particles that are suspending fragments of garnet and mica. Siderite occurs as a thin veinlet through the center of the mica vein. Protolith felsic volcanic that is metamorphosed into a biotite schist with coarse garnets.				

Sample ID: DT022	*Depth:401.3*	*Location:16-01*	*Rock Type: Sericite schist with pyrrhotite vein*	
Mineral	**Abundance**	**Habit**	**Grain Size**	**Comments**
Muscovite	30%	Subhedral	50-600 µm	Occurs as lamellae of foliated grains interbedded with quartz lamellae, as well as individual platy grains randomly orientated interstitial to quartz grains.
Quartz	35%	Subhedral- anhedral	100-500 µm	Occur as lamellae 1mm wide interbedded with 500 µm lamellae of muscovite. Shows dynamic recrystallization with smaller grains having been absorbed into the coarser grains and many grains meeting at triple points.

Biotite	15%	Subhedral	100-500 µm	Occur in a biotite rich patch at the interior of a fold hinge present in the muscovite quartz lamellae. Also occur as fragments within the pyrrhotite vein
Chlorite	5%	Subhedral	100-300 µm	Occur as replacement of biotite in the biotite rich portions of the schist. Also occurs as massive groundmass adjacent to the sphalerite vein
Pyrrhotite	12%	Anhedral	400-800 µm	Coarse grains of pyrrhotite can be distinguished based on its anisotropy, each grain has straight to irregular curved grain boundaries.
Plagioclase Feldspar	2%	Anhedral	100-500 µm	Appears as very sericite altered stubby to subrounded prisms. Occur near the biotite rich portions of the sample.
Alkali Feldspar	1%	Anhedral	100-500 µm	Appears as very sericite altered stubby to subrounded prisms. Occur near the biotite rich portions of the sample.
Ilmenite	Trace	Anhedral	50-300 µm	Occur as occasional subrounded grains on the margins of the pyrrhotite veins.
Tourmaline	Trace	Euhedral- trigonal prism	20-100 µm	Singular grains occur sporadically in the muscovite lamellae and biotite rich portions of the sample.

Overall Comments: Sample consists of a muscovite and biotite quartz schist, with some residual feldspars present from the protolith felsic volcanic. The felsic volcanic was regionally metamorphosed into muscovite quartz schist and underwent some tight folding. Later fluid flow through the rock altered the biotite rich portions of the rock to chlorite and crystalized pyrrhotite.

Sample ID: DT023	*Depth: 321.65*	*Location: 16-01*	*Rock Type: Garnet, staurolite, biotite schist with Cp, Po*	
Mineral	**Abundance**	**Habit**	**Grain Size**	**Comments**
Garnet	27%	Subhedral-Anhedral	50 µm to 12mm	Garnets show varying states of alteration and fracturing. Coarser garnets from 8-12 mm appear as fresh unaltered surfaces with fractures through the crystal that contain quartz, chalcopyrite, pyrrhotite, and tourmaline. In some instances, the tourmaline appears to be growing into the garnet in a radial pattern. The smaller garnets 8mm and less show a lighter coloured reaction rim on the exterior of the crystal as well as fractures and pits that are filled by chlorite and sulphides. Garnets are contained within a quartz and mica matrix.
Biotite	10%	Subhedral	40-600 µm	Occur as thin 100 µm semi discontinuous lamellae interstitial to quartz lamellae in the mica schist layers. On the margins with the garnets the biotite forms a thicker layer 200-400 µm wide. Many of the crystals appear to be altered to chlorite.
Chlorite	5%	Subhedral-Anhedral	20-400 µm	Occur as small 20-40 µm anhedral crystals altering the interior of the fractured garnets. Coarser grains appear to be replacing biotite.

Muscovite	10%	Subhedral	100-500 µm	Occurs as interstitial grains between quartz and biotite crystals in the mica quartz schist. A lamellae 1.5 mm wide of muscovite separates the quartz rich vein with garnets from more even quartz and mica schist with less garnets.
Tourmaline	Trace	euhedral to subhedral	20-100 µm	Occur as single grains within the mica lamellae in the quartz schist as well as radial outward growing crystals that appear to grow into the garnet crystals.
Quartz	27%	Subhedral	100-1200 µm	Quartz shows evidence of recrystallization with smaller grains being absorbed into the coarser crystals, as well as straight crystal boundaries meeting at triple points, and some showing bulging crystal boundaries
Feldspar	5%	Subhedral	100-300 µm	Appear nearly indistinguishable from the quartz crystals as they show no signs of twinning, but have a slightly weathered dusty appearance on their exterior
Staurolite	3%	Subhedral-anhedral	50-800 µm	Original crystals would have been up to 2mm in width, now occur as small pieces from a heavily fragmented whole. Space between the fracture's pieces is filled by biotite, muscovite, and tourmaline. All the staurolite occurs in a small portion of the thin section on the margin of a coarse garnet crystal and hosted in a matrix of biotite, muscovite, and chlorite.

Chalcopyrite	8%	Anhedral	20 µm- 2mm	Occurs as small patches infilling the fractures and pits on the garnet crystals, as well as coarser grains forming veinlets in the quartz mica veins.
Pyrrhotite	5%	Anhedral	50-1000 µm	Occurs as small patches infilling the fractures and pits on the garnet crystals, as well as coarser grains forming veinlets in the quartz rich veins.
Zircon	Trace	Subhedral	5-10 µm	Occur as very small crystals most easily identified by the damage halos formed in mica crystals they are hosted within.
Overall Comments: The sample consists of a biotite muscovite quartz schist from a siltstone protolith. Coarse garnets occur within the schist along with some minor staurolite, formed during regional peak metamorphism. A later hydrothermal event altered the garnets and staurolite and crystalized a quartz rich vein along with the chalcopyrite and pyrrhotite. Sulphides appear to be segregated with a chalcopyrite rich series of veinlets in the mica rich schist, and the pyrrhotite occur preferentially in the quartz rich vein.				

Sample ID: DT024	*Depth: 289.9*	*Location:16-01*	*Rock Type: massive biotite, garnet, staurolite, sericite schist*	
Mineral	**Abundance**	**Habit**	**Grain Size**	**Comments**
Biotite	16%	Subhedral, platy	100-600 µm	Occur as thin 100 µm discontinuous lamellae between muscovite lamellae. Also occurs as parallel orientated interstitial crystals between the quartz rich schist and as more randomly orientated coarser grains that fill

				the space between the rounded felspar grains.
Muscovite	21%	Subhedral, platy	100-500 µm	Occur as lamellae 0.5-6mm wide separated by wispy discontinuous lamella of biotite and quartz.
Quartz	30%	Anhedral	100-600	Show bulging grain boundaries with some small grains being recrystalized into the larger ones. Occur as 100-300 µm lamellae with interstitial biotite and muscovite grains.
Staurolite	8%	Euhedral- Subhedral	200 µm- 3mm	Occur as euhedral to fractured subhedral crystals. Fractures are infilled with sulphides, chlorite, or quartz. Hosted in a matrix of foliated muscovite and biotite.
Garnet	3%	Subhedral- anhedral	1-2mm	Occur as fractured and pitted grains infilled by quartz and sulphides. Hosted in a matrix of highly weathered feldspar with interstitial biotite grains
Tourmaline	Trace	Euhedral- Subhedral	20-200 µm	Occur as singular euhedral grains cut looking down the c axis, hosted in the mica schist

Plagioclase Feldspar	14%	Anhedral	300-600 µm	Occur as rounded grains of very altered and weathered feldspar grains, have an irregular pattern of tan brown and translucent colour with undulous and patchy extinction. The rounded grains are suspended in the mica schist. A patch of densely packed rounded grains of feldspar occurs with the garnets, and are separated by interstitial biotite crystals
Chlorite	3%	Subhedral	50-300 µm	Occur as smaller 50-100 µm on the rims of staurolite grains, as well as replacing biotite laths adjacent to sulphide mineralization
Chalcopyrite	4%	Anhedral	200 µm- 2mm	Occur as long jagged edged grains suspended in a mica matrix. Often have smaller rounded to sharp edged pyrrhotite grains in the larger chalcopyrite matrix
Pyrite	Trace	Anhedral	10-50 µm	Occur as small 10-50 µm irregular grains hosted within the rounded feldspar crystals
Pyrrhotite	1%	Subhedral- anhedral	50-200 µm	Occur as rounded to sharp sided grains on the edges of the larger chalcopyrite crystals adjacent to the mica
Ilmenite	Trace	Subhedral, Laths	50-100 µm	10 µm wide, up to 100 µm long laths of light grey colour
Overall Comments: Sample consists predominantly of lamellae of muscovite, biotite, and quartz, with rounded grains of feldspar. Likely a protolith of arkose sandstone that has been regionally metamorphosed to get the schistose mineralogy and texture. A hydrothermal fluid interaction within the rock caused the alteration of staurolite into chlorite as well as recrystallization of some of the biotite crystals into chlorite and deposited the chalcopyrite and pyrrhotite				

Sample ID: DT028	*Depth:433.8*	*Location:16-02*	*Rock Type: Garnet, staurolite, mica schist with tourmalinite spots*	
Mineral	**Abundance**	**Habit**	**Grain Size**	**Comments**
Quartz	40%	Subhedral-anhedral	50-400 µm	Most grains occur within the same size range of 200-300 µm and show bulging grain boundaries, however smaller quartz crystals have been recrystalized into the larger grains, suggesting a recrystallization somewhere between bulging and sub grain rotation. Quartz grains occur in lamellae one to two grains thick separated by discontinuous lamellae of parallel orientated biotite and muscovite. Biotite and muscovite also occur as randomly orientated interstitial grains
Biotite	25%	Subhedral, platy	25-500 µm	Occurs as discontinuous lamellae of parallel foliated grains interfingered with muscovite and occasionally replaced by chlorite. Also occurs as occasional randomly orientated interstitial grains between quartz grains
Muscovite	10%	Subhedral, platy	25-400 µm	Occurs as discontinuous lamellae of parallel foliated grains interfingered with biotite. Also occurs as occasional randomly orientated interstitial grains between quartz grains
Staurolite	8%	Subhedral-anhedral, skeletal	400-1200 µm	Occur as very weathered and pitted grains, the original shape of the mineral is distinguishable but consists only of disconnected grain fragments. Space between grains is infilled by quartz and mica

Garnet	4%	Subhedral	1-3 mm	A few coarse grains occur suspended in the quartz mica schist. The garnets are competent with some rough edges and interior pitting filled by quartz. Tourmaline appears to have grown into the garnets in a radial pattern through the center of the garnet crystals
Tourmaline	8%	euhedral- subhedral	10-400 µm	Occur as singular crystals suspended in the mica schist, to an agglomerate of smaller crystals forming a tourmalinite bleb 200-1000 µm across. Coarser crystals of tourmaline appear to have grown outward in a radial pattern
Chlorite	1%	Subhedral	50-200 µm	Occur as pseudomorph replacement of some biotite grains, as well as small grains on the edges of staurolite
Pyrite	1%	euhedral- subhedral	200-400 µm	Euhedral crystals of late pyrite occur within the mica schist, shows crosscutting relations with the micas in the schist suggesting a late formation
Pyrrhotite	3%	Subhedral-anhedral	50-200 µm	Occurs as semi rounded grains within the mica quartz schist, as well as small irregular shaped space filling crystals between tourmaline grains within the tourmalinite
Chalcopyrite	trace	Anhedral	50-100 µm	occurs alongside the pyrrhotite as small irregular shaped space filling crystals between tourmaline grains within the tourmalinite

Ilmenite	trace	Subhedral	50-300 µm	subrounded to lath shaped grains suspended in the quartz mica schist
Magnetite	trace	Subhedral	50-300 µm	subrounded to lath shaped grains suspended in the quartz mica schist
Overall Comments: Sample consists predominantly of foliated lamellae of quartz, biotite and muscovite derived from the regional metamorphism of a pelite protolith. Metamorphic conditions allowed for the formation of garnet and staurolite. Hydrothermal fluid flow through the rock crystalized tourmaline as well as pyrrhotite and chalcopyrite within the rock, showing signs of intergrowth and open space filling in the garnets. Euhedral pyrite crystals grew within the schists at a late staged event.				

Sample ID: DT030	*Depth: 204.6*	*Location:19-02*	*Rock Type: garnet, staurolite, biotite schist with trace chalcopyrite and pyrite*	
Mineral	**Abundance**	**Habit**	**Grain Size**	**Comments**
Staurolite	20%	Subhedral	600 µm-6mm	Crystals are longer then they are wide, with the average grain being 1-2 mm wide and 4-5mm long. Variable states of alteration is present with some crystals containing only minimal interior pitting while others are nearly completely replaced by quartz with only the occasional staurolite fragment remaining. Chlorite commonly occurs on the rim of the staurolite crystals and within some interior pits.
Garnet	2%	Euhedral-subhedral	200-700 µm	Well developed crystals with distinguishable crystal shape and straight edges. Some pitting present in crystal interior, with open space filled by quartz

Biotite	25%	Subhedral	50-1000 µm	Occurs as foliated discontinuous lamellae separated by quartz grains, occasionally forms 2-3mm thick lamellae with occasional interfingered muscovite and chlorite grains.
Muscovite	5%	Subhedral	100-800 µm	Occurs as occasional interfingered crystals in the larger 2-3mm biotite lamellae, as well as occasional interstitial grains between quartz and feldspars
Chlorite	8%	Subhedral	50-600 µm	Replaces biotite grains showing a well-developed crystal structure. Also occurs on the edges and within the pitted spaces of the staurolite grains and has a randomly orientated structure that is less developed than the biotite pseudomorphs
Quartz	30%	Subhedral	50-600 µm	Most crystals occur in the 200-300 µm range and show evidence of bulging to sub grain rotational recrystallization as there is evidence for smaller grains being recrystallized into larger grains and boundaries are straight to bulging.
Feldspar	8%	Subhedral-anhedral	20-200 µm	Occurs as grains separated by thin discontinuous lamellae of biotite. No twinning is evident, but sericitization of the crystal surfaces distinguishes it from the quartz rich sections of the schist

Pyrite	1%	subhedral	50-400 µm	Irregular shaped fragments of pyrite occur suspended in the mica schist. Occur with chalcopyrite in the same fragments.
Chalcopyrite	1%	Anhedral	50-300 µm	Occur alongside pyrite grains in the biotite schist
Ilmenite	Trace	Subhedral, Tabular	20-200	Occur as thin tabular crystals, 5-20 µm wide but up to 200 µm long. Associated with mica, occurring between grains, and showing parallel foliation
Overall Comments: Sample consists of a foliated biotite quartz schist with regional metamorphic derived staurolite and garnet crystals, likely derived from a pelite protolith. Regional metamorphism caused the pelite to form foliated lamellae of biotite and quartz, in some instances feldspar takes the place of quartz, potentially representing an arkose sandstone lamellae. Hydrothermal fluids infiltrated the sample rock and caused the alteration of staurolite crystals to quartz and chlorite, biotite also recrystalizes to chlorite releasing titanium that forms the ilmenite crystals between the chlorite and biotite crystals. The hydrothermal fluids also precipitated sulphides pyrite and chalcopyrite.				

Sample ID: DT032	*Depth:166.8*	*Location:19-02*	*Rock Type: garnet staurolite schist with Po veinlets*	
Mineral	**Abundance**	**Habit**	**Grain Size**	**Comments**

Staurolite	20%	Subhedral-Anhedral	500 µm-5mm	Crystals are longer then they are wide, with the average grain being 1-2 mm wide and 4-5mm long. Variable states of alteration is present with some crystals containing only minimal interior pitting while others are nearly completely replaced by quartz with only the occasional staurolite fragment remaining. Chlorite commonly occurs on the rim of the staurolite crystals and within some interior pits.
Garnet	4%	Subhedral-Anhedral	1-7 mm	Well developed crystals with distinguishable crystal shape and straight edges. Extensive pitting is present on the crystal interior and edges with open space being infilled by quartz
Biotite	25%	Subhedral	50-600 µm	Occurs as foliated discontinuous lamellae separated by quartz grains, occasionally forms 1mm thick lamellae with occasional interfingered muscovite and chlorite grains. Foliation in the biotite weaves and folds around the staurolite and garnet phenocrysts
Chlorite	5%	Subhedral	50-500 µm	Replaces biotite grains showing a well-developed crystal structure. Also occurs on the edges and within the pitted spaces of the staurolite grains and has a randomly orientated structure that is less developed than the biotite pseudomorphs
Muscovite	10%	Subhedral	100-500 µm	Occurs interfingered with biotite in lamellae of mica separating the quartz lamellae, some are muscovite over biotite rich while others are biotite over muscovite.

Quartz	28%	Subhedral	50-600 µm	Most crystals occur in the 200-300 µm range and show evidence of bulging to sub grain rotational recrystallization as there is evidence for smaller grains being recrystallized into larger grains and boundaries are straight to bulging.
Plagioclase Feldspar	5%	Subhedral- anhedral	20-200 µm	Occurs as grains separated by thin discontinuous lamellae of biotite. No twinning is evident, but sericitization of the crystal surfaces distinguishes it from the quartz rich sections of the schist
Tourmaline	Trace	Euhedral	20-60 µm	A few small crystals are present suspended in the mica schist lamellae
Pyrrhotite	3%	Anhedral	50-600 µm	Occur as tabular shaped with irregular edges, orientated with long side being parallel to the foliation of schist.
Pyrite	trace	Subhedral	20-50 µm	Hosted within the coarser pyrrhotite grains, have some euhedral straight edged faces with other sides that are fragmented and irregular
Chalcopyrite	trace	Anhedral	20-50 µm	rounded blebs of chalcopyrite occur hosted within the coarser pyrrhotite fragments

Overall Comments: Sample consists of a foliated biotite quartz schist with regional metamorphic derived staurolite and garnet crystals, likely derived from a pelite protolith. Regional metamorphism caused the pelite to form foliated lamellae of biotite and quartz, in some instances feldspar takes the place of quartz, potentially representing an arkose sandstone lamellae. Hydrothermal fluids infiltrated the sample rock and caused the alteration of staurolite crystals to quartz and chlorite, as well as recrystalizing some biotite into chlorite. Sulphides crystalized last infiltrating between open space between mica grains and quartz, possibly taking advantage of the mass loss caused by the chloritization.

Sample ID: DT034	*Depth: 165.1*	*Location:19-04*	*Rock Type: Pyrrhotite and chalcopyrite vein 6 cm wide with tourmalinite spots*	
Mineral	**Abundance**	**Habit**	**Grain Size**	**Comments**
Tourmaline	40%	Euhedral-subhedral	5-400 µm	Occur as rounded blebs of tourmalinite consisting of very fine tourmaline crystals intergrown in radial patterns with occasional coarser crystals present. Tourmalinite occasionally contains inclusions of muscovite. Coarser grains of euhedral tourmaline also occur as individual crystals suspended in a pyrrhotite matrix, often showing zoned growth patterns. Also occur growing into quartz along the quartz grain boundaries
Quartz	4%	Subhedral	20-600 µm	Occur on the edges of the pyrrhotite horizon, often as semi rounded fragments of the host rock. Show bulging recrystallization, with irregular bulging grain boundaries with very small quartz crystals occurring on the margins of larger crystals
Muscovite	6%	Subhedral, platy	200 µm-3 mm	Occur as inclusions of fragmentated micaceous plates within the tourmalinite blebs, as well singular crystals suspended in the pyrrhotite matrix. Also occurs interstitial to quartz grains, possibly a relict texture from the siltstone host rock.

Pyrrhotite	40%	Subhedral	200-400 µm	Occurs as the groundmass for the whole sample, grain boundaries are difficult to distinguish except in XPL where the anisotropy of pyrrhotite highlights specific grains. pyrrhotite also occurs as infill on fractures within the tourmalinite and quartz blebs.
Pyrite	4%	Euhedral-subhedral	100-700 µm	Occur as well-formed crystals within the pyrrhotite matrix, often growing around and including the tourmaline crystals. Subhedral shapes occur only as the crystal struggles to form euhedral shapes due to incorporating the many interstitial tourmaline grains
Chalcopyrite	3%	Subhedral-anhedral	50-200 µm	Occurs most commonly as fracture infill within the host rock fragments as well as tourmaline blebs, and occurring closer to the margins of the sulphide horizon
Magnetite	2%	Subhedral-anhedral	20-200 µm	Occur as small semi rounded grains often growing attached to or adjacent to a tourmaline crystal
Overall Comments: Sandstone protolith host rock underwent regional metamorphism into a muscovite quartz schist. Hydrothermal alteration resulted due to fluid flow through the region and began to crystalize tourmaline which grew between crystal grains of quartz and muscovite. Eventual replacement began with tourmaline growing in tourmalinite blebs and replacing the original host rock protolith. The fluid then began to precipitate out chalcopyrite and sphalerite on the margins of the fluid flow pathway, infilling cracks within the host rock fragments. Pyrrhotite became the dominant sulphide and suspended singular crystals of tourmaline within it as it crystalized, along with occasional pyrite and magnetite grains.				

Sample ID: DT035	*Depth:167.1*	*Location:19-04*	*Rock Type: Garnet schist with 2mm pyrite pyrrhotite veinlets*	
Mineral	**Abundance**	**Habit**	**Grain Size**	**Comments**
Biotite	32%	Subhedral	50-600 µm	Foliated crystals showing parallel to near parallel length direction occur as wispy discontinuous lamellae with interstitial quartz and feldspar crystals breaking up the separate lamellae. Often interfingered by muscovite crystals, though the muscovite often appears to show a more random orientation of crystals.
Muscovite	13%	Subhedral	50-600 µm	Occur as interfingering crystals within the biotite lamellae. The crystals due show some parallel foliation to the biotite, however many crystals appear to be growing perpendicular to the general foliation.
Quartz	25%	Subhedral	20-500 µm	Occur as interstitial grains between the biotite and muscovite lamellae, generally as small 20-200 µm crystals. 1 cm wide quartz vein containing pyrite, pyrrhotite and chalcopyrite sulphides consists of coarser 300-500 µm grains.
Alkali Feldspar	13%	Subhedral-anhedral	50-200 µm	Occur as irregular crystals interstitial to biotite and muscovite lamellae. Heavily sericite altered.
Chlorite	5%	Subhedral	50-400 µm	Occur as replacement pseudomorphs of biotite, especially on the margins of altered feldspar and around the quartz vein.

Garnet	3%	Subhedral-anhedral, skeletal	5 mm	Skeletal outline of coarse garnet crystal can be distinguished, now consists of an interconnected network of 200-300 µm garnet crystal fragments with open spaces infilled dominantly by quartz and occasionally muscovite and biotite
Staurolite	trace	Subhedral- anhedral	100-300 µm	A few small crystals irregularly shaped and pitted occurring adjacent to the larger garnet crystal. Open space pits filled by quartz.
Tourmaline	1%	Euhedral- subhedral	50-200 µm	Occur as singular and grouped paired crystals suspended in the mica schist
Pyrrhotite	3%	Subhedral- anhedral	300-800	Form irregular shaped crystals in the quartz vein, often surrounded by chalcopyrite.
Chalcopyrite	1%	Subhedral- anhedral	50-100	Occurs associated with the pyrrhotite, often forming around edges of pyrrhotite crystals and the quartz vein crystals.
Pyrite	3%	Euhedral- subhedral	200-1000µm	Occur as well-developed crystals with straight edges, mostly occurring within the sulphide bearing quartz vein.
Arsenopyrite	1%	Euhedral- subhedral	200-800 µm	Occur as fairly well-developed crystals with straight edges, mostly occurring as coarse phenocrysts in the mica quartz schist

Overall Comments: Host rock consists of wispy discontinuous lamellae of biotite and interfingering muscovite broken up by quartz and highly altered feldspar crystals, possible felsic volcanic tuff protolith that underwent regional metamorphism creating the mica quartz schist with occasional garnet and staurolite. Remobilized sulphides, possibly from the nearby VMS pyrrhotite horizon are present in the form of a sulphide bearing quartz vein which contains crystals of pyrrhotite, pyrite, and chalcopyrite. Arsenopyrite also occurs as coarser grains within the mica schist.

Sample ID: DT039	*Depth:67*	*Location:16-04*	*Rock Type: Meta arkose with minor garnets and staurolite*	
Mineral	**Abundance**	**Habit**	**Grain Size**	**Comments**
Quartz	30%	Subhedral	30-400 µm	Occur as matrix made up of mostly 50-300 µm crystals that show bulging to sub grain rotational recrystallization. Quartz crystals are separated by discontinuous lamellae of biotite and muscovite or singular interstitial mica crystals
Biotite	25%	Subhedral	30-300 µm	Occur as parallel foliated elongate platy crystals, often as wispy discontinuous lamellae, or singular crystals interstitial to quartz
Muscovite	10%	Subhedral	20-200 µm	Occur as parallel foliated elongate platy crystals, often as wispy discontinuous lamellae or singular crystals interstitial to quartz, as well as fine to coarse grains of sericite from alteration of feldspar crystals
Plagioclase Feldspar	25%	Subhedral-anhedral	50-600 µm	Occur predominantly in three 5mm wide lamellae made up of partially rounded plagioclase crystals that have been heavily altered by sericite, in some cases recrystalizing large muscovite crystals. Also occurs as occasional grains in the mica quartz schist

Staurolite	5%	Subhedral	200-600 µm	Well formed crystals with sieve textured pitting filled by quartz. Occurs in the mica quartz schist and not within the feldspar rich layers
Chlorite	3%	Subhedral	50-100 µm	Occur as replacement recrystallization of biotite crystals, often forming an interfingered texture with the remaining biotite
Tourmaline	Trace	Euhedral	10-60 µm	Singular crystals occur suspended in the mica quartz schist, often orientated looking down the c axis. Shows zonation growth rings.
Pyrite	1%	Subhedral	20-300 µm	Tabular to irregular shaped grains occur sporadically throughout the sample
Ilmenite	trace	Subhedral	20-120 µm	Rounded to tabular shaped grains occur sporadically throughout the sample
Overall Comments: Sample consists of alternating layers of mica and quartz rich lamellae, separated by 3-8mm bands of feldspar rich mica schists. Possible protolith consisted of interbedded clay and sandstones separated by occasional layers of arkose sandstone or possibly felsic volcanic tuff. Regional metamorphism led to the formation of the mica quartz schists and crystalized staurolite. Later hydrothermal alteration events through the rock precipitated tourmaline, pyrite and hematite as well as prompting the sericite alteration of the feldspar grains.				

Sample ID: DT042	*Depth:112.4*	*Location:16-04*	*Rock Type: Sericite schist with garnet and staurolite*	
Mineral	**Abundance**	**Habit**	**Grain Size**	**Comments**

Quartz	35%	Subhedral	100-1000 µm	Consists mostly of 100-300 µm of crystals with bulging to straight crystal boundaries. The quartz matrix is separated by discontinuous lamellae of interfingered biotite and muscovite as well as singular interstitial mica grains.
Muscovite	25%	Subhedral	50-500 µm	Occurs as discontinuous lamellae interfingered with biotite all parallel foliated, or as individual grains interstitial to the quartz crystals. Also occurs in several 500-1500 µm lamellae of pure muscovite
Biotite	20%	Subhedral	50-600 µm	Occurs as discontinuous lamellae interfingered with muscovite all parallel foliated, or as individual grains interstitial to the quartz crystals.
Plagioclase Feldspar	12%	Subhedral-anhedral	100-300 µm	Occurs as grains within the quartz mica schist, often having a dusty surface appearance due to sericite alteration, show polysynthetic twinning.
Chlorite	3%	Subhedral	20-700 µm	Occur as recrystallization of biotite grains as well as some coarser radial outgrowths of chlorite adjacent to pyrite grains
Garnet	4%	Euhedral- subhedral	1-3 mm	Occurs as well-developed crystals with straight edges and limited fracturing or pitting. Suspended within the quartz mica schist. Interior pits filled by pyrite and quartz

Pyrite	1%	Subhedral	20-300 µm	Occur as small irregular shaped grains, suspended within the quartz mica schist or infilling open space in a few open space pits in the surface of the garnet
Ilmenite	Trace	Subhedral	20-300 µm	Occur as small irregular shaped grains, suspended within the quartz mica schist or infilling open space in a few open space pits in the surface of the garnet
Overall Comments: Muscovite and biotite quartz schist rock containing a few crystals of garnet. Arkose sandstone protolith which underwent regional metamorphism causing the foliated schists of muscovite biotite with quartz and altered feldspar grains. Later fluid flow caused limited precipitation of pyrite and recrystalizing biotite grains into chlorite.				

Sample ID: DT050A	*Depth:176.4*	*Location: 16-04*	*Rock Type: Large garnets and staurolite in massive bio schist*	
Mineral	**Abundance**	**Habit**	**Grain Size**	**Comments**
Garnet	40%	Euhedral	5mm-4cm	Coarse well-formed garnets with fractured and infilled interiors. Garnets are suspended in a massive biotite vein. Fractures in the interior of the garnet are infilled by pyrrhotite, chalcopyrite, quartz, and fragments of biotite.
Biotite	35%	Euhedral-subhedral	100-800 µm	Occur within a 4 cm wide vein of foliated to massive crystals with most of the crystals being parallel but many overlapping crystals are randomly orientated. Occasional muscovite crystals are interfingered with biotite crystals within the biotite vein. Biotite also occurs as thin wispy discontinuous lamellae in the quartz mica schist host rock to the biotite vein.

Quartz	8%	Subhedral	100-400 µm	Show bulging to polygonal grain boundaries, suggesting partial recrystallization. Occur as partial lamellae separated by the biotite and muscovite lamellae and interstitial grains.
Muscovite	7%	Subhedral	100-900 µm	Occur as interstitial grains separating quartz crystals in the quartz mica schist host rock, as well as occasional crystals growing interfingered with biotite in the coarse biotite vein. Coarse muscovite crystals occur on the margins of the biotite vein
Chlorite	3%	Subhedral-anhedral	50-500 µm	Occurs as a replacement recrystallization of biotite crystals
Staurolite	4%	Subhedral	500-1500 µm	Occur as sieve textured grains with frequent pitting infilled by quartz. Mostly occur within the quartz mica schist host rock, but some less pitted crystals occur suspended in the biotite vein
Tourmaline	Trace	Euhedral	20-50 µm	Occur as small, isolated crystals suspended in the quartz mica schist
Pyrrhotite	3%	Subhedral- anhedral	100-600 µm	Occur as irregular shaped grains infilling large fractures in the interior of the garnets. Associated with smaller crystals of chalcopyrite that grow as irregular blebs within the pyrrhotite

Chalcopyrite	Trace	Subhedral-anhedral	10-300 µm	Occur as small irregular shaped blebs hosted within the fractures of the garnets, grown jointly with pyrrhotite

Overall Comments: Sample is of a foliated to massive biotite vein 3-4 cm's wide that hosts coarse 3cm wide garnet crystals. The interiors of the garnets are fractured and infilled by pyrrhotite and chalcopyrite. The host rock to the vein consists of a biotite muscovite quartz schist showing prominent foliation in the discontinuous mica lamellae. Probably siltstone protolith that underwent regional metamorphism that formed the foliated schist rock. A hydrothermal event precipitated out the vein of biotite and garnets as well as tourmaline crystals in the adjacent schist.

Sample ID: DT050B	*Depth:176.4*	*Location:16-04*	*Rock Type: large garnets and staurolite in massive bio schist*	
Mineral	**Abundance**	**Habit**	**Grain Size**	**Comments**
Quartz	33%	Subhedral-anhedral	50-800 µm	Grains in the quartz mica schist show irregular and bulging grain boundaries with a size range from 50 to 300 µm, whereas the quartz in the quartz vein shows larger grain sizes from 200-800 µm. Quartz dominantly infills the open spaces in the skeletal garnet and staurolite grains, often as well formed polygonal shaped crystals.
Garnet	20%	Subhedral-anhedral	500 µm-2cm	Occur as a large sieve to skeletal textured grain hosted within a cross cutting quartz vein through the host rock schist. The fractures and pits of the garnet are filled by quartz or sulphides, in some instances the sulphides infiltrate into the garnet giving a patchy appearance to the grain appearing almost as inclusions within the garnet

Staurolite	15%	Subhedral-anhedral	400 µm-5mm	Well formed to isolated fragment crystals with sieve textured pitting filled by quartz. Chlorite commonly occurs on the margins on staurolite grains, at times infilling space between two adjacent staurolite grains.
Biotite	15%	Subhedral	20-600 µm	Occur as wispy discontinuous foliated parallel lamellae interfingered with muscovite separated by a quartz grain matrix making up the host rock schist rock. The mica lamellae curve around the staurolite and garnet phenocrysts in the host rock. Can also occur as isolated grains interstitial to the quartz grains.
Muscovite	8%	Subhedral	20-500 µm	Occur as wispy discontinuous foliated parallel lamellae interfingered with biotite separated by a quartz grain matrix making up the host rock schist rock. The mica lamellae curve around the staurolite and garnet phenocrysts in the host rock. Can also occur as isolated grains interstitial to the quartz grains.
Chlorite	3%	Subhedral	50-500 µm	Occur as replacement of biotite, or as a new growth especially adjacent to weathered and altered staurolite.
Plagioclase Feldspar	2%	Anhedral	100-500 µm	Occur as pitted and sericite altered grains with a dusty surface appearance. Occurs within the groundmass of the rock adjacent to quartz and biotite crystals.

Pyrrhotite	3%	Subhedral-anhedral	100-1500 µm	Occur within the quartz vein jointly with chalcopyrite, irregular rounded grain boundaries separate the two phases. Also occur in heavily altered portions of the garnet infilling pits on the surface of the garnet. Pyrrhotite crystals can be distinguished from each other due to anisotropy of grains under cross poles in reflected light and show straight grain boundaries.
Chalcopyrite	1%	Anhedral	50-600 µm	Occur within the quartz vein jointly with pyrrhotite, irregular rounded grain boundaries separate the two phases. Also occur in heavily altered portions of the garnet infilling pits on the surface of the garnet.
Magnetite	Trace	Anhedral	50-100 µm	small irregular grains occurring with pyrrhotite.
Ilmenite	Trace	Anhedral	50 µm	Occur as slender laths often included in garnet grains and between biotite crystals.
Overall Comments: Sample host rock consists of a muscovite biotite quartz schist with phenocrysts of staurolite and garnet, likely a regional metamorphic product from a siltstone protolith. The sample is crosscut by a quart veinlet that follows foliation that precipitates pyrrhotite and chalcopyrite sulphides within the fractures and pits of the garnet crystal.				

Sample ID: DT053	*Depth: 212.2*	*Location: 16-04*	*Rock Type: Garnet Quartz vein in a biotite muscovite schist*	
Mineral	**Abundance**	**Habit**	**Grain Size**	**Comments**
Garnet	30%	Subhedral-anhedral, Skeletal	200 µm-2cm	Occurs as very altered and fractured grains, in many cases completely skeletonized and infilled by quartz and sulphides. Surface of garnets has an etched rough appearance and significant skeletonization makes original grain size difficult to determine

Gahnite	10%	euhedral subhedral	400-800 µm	Green pitted and fractured crystals occurring within the quartz mica schist. Quartz infills the open spaces formed on the gahnite crystals.
Quartz	35%	Subhedral	50 µm-2mm	Within the mica quartz schist, the grains are 50-300 µm in size, show bulging recrystallization with irregular grain boundaries and occur as a groundmass of quartz separated by foliated wispy discontinuous lamellae of biotite and muscovite along with some randomly orientated interstitial mica grains. In the garnet quartz vein the crystals are generally coarser and have more polygonal crystal boundaries
Biotite	13%	Subhedral	20-600 µm	Occur as foliated discontinuous lamellae separated by quartz grains in the mica quartz schist host rock. Occasional muscovite grains occur interfingered with the biotite.
Chlorite	2%	Subhedral	50-300 µm	Occur as replacement recrystallization of biotite grains as well as forming along the fractures and edges of altered garnets.
Pyrrhotite	4%	Subhedral-anhedral	100-500 µm	Occur as infill between fractured garnets and open space in the quartz veins. Separate grains can be determined under cross poles due to the anisotropy of pyrrhotite.
Chalcopyrite	3%	Subhedral-anhedral	50-800 µm	Occur as infill between fractured garnets and open space in the quartz veins, boundary with pyrrhotite is often irregular and rounded.

Sphalerite	2%	Subhedral-anhedral	50-200 µm	Show red internal reflections in transmitted light. Occur as irregular round blebs with the chalcopyrite and pyrrhotite.
Ilmenite	1%	Subhedral- anhedral	20-200 µm	occur as small rounded to tabular grains contained mostly within the garnet crystals
Pyrite	trace	Subhedral	200-500 µm	Three crystals, two 200 µm in size and one 500 µm in size are found in the sample. Show straight crystal edges but have been broken on several sides. Appear to crosscut the pyrrhotite and chalcopyrite
Overall Comments: Sample consists of a quartz vein hosting garnets that have weathered and fractured and been infilled by sulphides pyrrhotite, chalcopyrite and sphalerite. Sulphides within the quartz vein are likely a remobilization from local VMS horizons. Host rock consists of a biotite quartz schist, the product of regional metamorphism from a siltstone protolith rock.				

Sample ID: DT054	*Depth:214.9*	*Location:16-04*	*Rock Type: large garnets in massive biotite, pyrrhotite and chalcopyrite veinlets*	
Mineral	**Abundance**	**Habit**	**Grain Size**	**Comments**
Garnet	30%	Subhedral-anhedral, Skeletal	800 µm- 2 cm	Occurs as very altered and fractured grains, in many cases completely skeletonized and infilled by quartz and sulphides. significant skeletonization makes original grain size difficult to determine. Some variances in crystal appearance are present with the altered interior of the garnets leaving fragments with a rough etched looking surface appearance

Biotite	15%	Subhedral	80-1200 µm	Occur in irregular 2-6mm wide patches of biotite. Shows a general foliation however there is some variation in the foliation between patches and occasional randomly orientated grains. The biotite wraps around the coarse garnet grains and is separated by patches of feldspar and quartz that contain randomly orientated interstitial grains of biotite
Quartz	30%	Subhedral	20-600 µm	100-200 µm polygonal grains occur as infill to the open space created by skeletonization of the garnet grains. 20-200 µm irregular shaped bulging grains occur with the feldspar grains in the matrix of the sample. Small quartz vein adjacent to garnet consists of coarse 400-600 µm crystals, with bulging crystal boundaries.
Chlorite	5%	Subhedral	100-400 µm	Occur as replacement to biotite grains, especially in biotite located adjacent to garnets. Also occasionally occurs within the interior of heavily skeletonized garnet crystals
Plagioclase Feldspar	12%	Subhedral-anhedral	100-300 µm	Feldspar grains show heavy sericitization alteration. Most grains show no twinning, although some appear to have very thin polysynthetic twinning with 1 µm thick lines through them.
Unknown	1%	Anhedral	100-250 µm	Elongate mineral with irregular colour and extinction, shows a dark reaction rim around it when surrounded by biotite.

Pyrrhotite	4%	Anhedral	200-500 µm	Infills open space within the fractured and skeletonized garnet grains, as well as squeezing in between space between biotite grains in the foliated biotite patches.
Chalcopyrite	3%	Anhedral	100-400 µm	Infills open space within the fractured and skeletonized garnet grains, as well as squeezing in between space between biotite grains in the foliated biotite patches. Crystal boundaries between chalcopyrite and pyrrhotite are irregular and rounded.
Overall Comments: Sample consists of several coarse garnet crystals suspended in a vein of patchy biotite and quartz. Fractures within the garnets and open space in the vein are infilled by chalcopyrite and pyrrhotite sulphides. Host rock consists of heavily altered plagioclase feldspar along with quartz grains with interstitial biotite, likely represents a heavily altered felsic volcanic rock. The felsic volcanic underwent regional metamorphism producing coarse garnets, later hydrothermal flow in the rock created a vein of quartz biotite that skeletonized the garnet crystals and deposited the sulphides.				

Sample ID: DT056	*Depth:235.2*	*Location:16-04*	*Rock Type: Garnet staurolite biotite schist with chalcopyrite and pyrrhotite veinlets*	
Mineral	**Abundance**	**Habit**	**Grain Size**	**Comments**
Staurolite	15%	Subhedral- anhedral	200 µm- 1mm	Occur as sieve textured grains with frequent pitting infilled by quartz. Crystals are suspended within the quartz mica schist host rock. Chlorite occurs adjacent to heavily pitted staurolite grains.

Garnet	28%	Subhedral- anhedral	500 µm - 1cm	Coarse garnets occur within a quartz vein that crosscuts the quartz mica schist host rock. The crystals are fractured but mostly whole in their center, become increasingly fragmentated towards their exterior with pitting infilled by chalcopyrite and pyrrhotite. Staurolite grains occur imbedded within the larger garnet crystals.
Quartz	30%	Subhedral	50-800 µm	Quartz occurs as the matrix of the schist containing grains 50-250 µm in size, often with interstitial randomly orientated biotite grains and foliated parallel lamellae of biotite separating the quartz crystals. Quartz also occurs as coarser 300-800 µm crystals in the quartz garnet vein. Quartz crystal boundaries are irregular and bulging
Biotite	12%	Subhedral	20-600 µm	Occur as wispy discontinuous parallel foliated lamellae separated by quartz crystals in the mica quartz schist host rock. Also occur as small randomly orientated interstitial crystals between quartz crystals in the schist
Chlorite	3%	Subhedral-anhedral	50-400 µm	Occur as replacement recrystallization of biotite crystals in the biotite lamellae of the schist. Also occurs infilling fractures and pits of altered garnets and staurolite
Muscovite	1%	Subhedral	10-200 µm	Occurs as occasional interstitial crystal between quartz grains in the schist host rock, as well as very fine-grained crystals of sericite due to sericitization of feldspar crystals.

Plagioclase Feldspar	3%	subhedral	100-500 µm	Occur as heavily altered grains with sericitization and pitting with quartz replacement. No twinning visible, only discernable from the quartz crystals in the schist due to their altered dusty surface appearance
Pyrrhotite	6%	Anhedral	50 µm- 6mm	Occur as small 50-100 µm irregular grains in the mica schist host rock and more predominantly as coarse crystals 200 µm to 6mm in size hosted within the quartz vein or within fractures in the garnets. Individual grains are distinguished only due to their anisotropy under cross poles. Grain boundaries between pyrrhotite are straight edged, whereas with chalcopyrite they are rounded and irregular
Chalcopyrite	2%	Anhedral	50-800 µm	Occur as small, rounded irregular shaped crystals with the pyrrhotite in the quartz veins. Also, as small irregular shaped grains in the mica schist host rock.
Arsenopyrite	Trace	Subhedral	200 µm- 2mm	occurs as platy to irregular shaped grains within the quartz mica schist host rock
Ilmenite	Trace	Subhedral	20-50 µm	Occur as small, rounded blebs often occurring within pits on the surface of staurolite and adjacent to them.
Overall Comments: Sample consists of a host rock staurolite bearing quartz biotite schist that has been crosscut by a garnet quartz vein. Siltstone protolith likely which was regionally metamorphosed into a garnet staurolite bearing biotite schist. A hydrothermal alteration event created the crosscutting quartz vein and precipitated sulphides within the vein and adjacent schist host rock. This hydrothermal alteration then led to the recrystallization of biotite into chlorite as well as chloritization along fractures and pits in the garnet and staurolite.				

Sample ID: DT058	*Depth:244.5*	*Location:16-04*	*Rock Type: Biotite quartz schist with minor garnets and pyrrhotite quartz veinlets*	
Mineral	**Abundance**	**Habit**	**Grain Size**	**Comments**
Biotite	35%	Subhedral	50-600 µm	Occur as discontinuous but parallel foliated lamellae separated by quartz and feldspar grains. Isolated interstitial grains with orientation wavering from foliation occur between quartz grains.
Garnet	10%	Subhedral	600 µm- 4mm	Garnet grains are skeletal with significant fracturing and pitting infilled by quartz and rare chlorite. Foliation in the biotite schist appears to flow around the garnet grains.
Quartz	35%	Subhedral	30-1000 µm	Occur as the matrix of the biotite schist, consisting of 30-300 µm quartz grains with straight to bulging grain boundaries. In the 0.5 to 1mm veinlets the quartz grains are coarser often 400-1000 µm in size
Plagioclase Feldspar	16%	Subhedral-anhedral	20-300 µm	Occur alongside the quartz in the matrix of the biotite schist. Some grains occur with very thin striped polysynthetic twinning or simple twinning. Grains appear to be heavily weathered with irregular boundaries and quartz replacement along with some sericite alteration.
Chlorite	1%	Subhedral-anhedral	20-150 µm	Occur as replacement intergrowths with biotite grains, as well as within some fractures and pits of the altered garnets.

Pyrrhotite	2%	Subhedral-anhedral	50-600 µm	Occur within the quartz veinlets or as small fragments inside the biotite schist up to a few millimeters away from the cross-cutting quartz veinlets. Viewing the grains in cross poles reveals irregular grain boundaries separating individual grains in a larger growth of pyrrhotite inside the quartz veinlet. Shows flame like exsolutions of troilite
Chalcopyrite	1%	Subhedral-anhedral	50-400 µm	Occur within the quartz veinlets or as small fragments inside the biotite schist up to a few millimeters away from the cross-cutting quartz veinlets. Rounded to irregular boundaries with the pyrrhotite. Exsolutions of cubanite present.
Cubanite	trace	Subhedral-anhedral	50-150 µm	occur as straight edged exsolutions within the larger grains of chalcopyrite
Ilmenite	trace	anhedral	40-200 µm	rounded to tabular shaped grains most often occur on the edges of garnet crystals or in the schist adjacent to the garnet.
Overall Comments: Sample consists of a garnet bearing quartz feldspar biotite schist. The presence of significant feldspar in the host rock suggests a possibility of a component of altered felsic volcanic protolith. This protolith underwent regional metamorphism leading to the crystallization of garnet and the foliated orientation to the biotite lamellae. A hydrothermal flow through this rock crystallized veinlets of quartz along with pyrrhotite and chalcopyrite that also crystalized in the vein salvage within the schist host rock.				

Sample ID: DT061	*Depth:263.5*	*Location: 16-04*	*Rock Type: Garnet Biotite staurolite schist with a garnet sericite vein*	
Mineral	**Abundance**	**Habit**	**Grain Size**	**Comments**
Quartz	34%	Subhedral	50-400 µm	Forms the matrix of the biotite schist, consisting of mostly 100-300 µm sized grains with irregular partially recrystallized grain boundaries. Separated by foliated wispy discontinuous lamellae of biotite and muscovite as well as interstitial mica grains. Quartz also fills the open spaces in the pits of the altered garnets and staurolite
Biotite	20%	Subhedral	50-800 µm	Occurs as foliated wispy discontinuous lamellae of biotite with occasional interfingered muscovite. The biotite lamellae curve around the garnet and staurolite phenocrysts and are separated by the quartz grains that make up the matrix of the schist.
Staurolite	20%	Subhedral-anhedral	500 µm-3mm	sieve textured to skeletal grains with the original outline of the crystal discernable based on straight edges of exterior fragments. Open spaces on the staurolite are filled by quartz, and chlorite occurs as replacement of biotite on the margins of the staurolite grains
Garnet	8%	Subhedral-anhedral	400-4mm	Skeletal grains of garnet occur with crystal margins remaining somewhat whole, particularly on one side of the crystal while the interior is fragmented and pitted and infilled by quartz

Muscovite	10%	Subhedral	20-600 µm	Occur interfingered with biotite in the biotite quartz schist, and as the predominant mica in a portion of the sample that is made up of 100-500 µm wide lamellae of muscovite separated by quartz grains. Muscovite lamellae flow and curve around garnet phenocrysts in the schist.
Chlorite	2%	Subhedral	50-200 µm	Occur as replacement to biotite crystals especially along the margins of altered staurolite crystals.
Pyrrhotite	4%	anhedral	10-100 µm	Occur as rounded to irregular shaped grains suspended in the mica schists are occasionally in the interior of staurolite and garnet phenocrysts
Chalcopyrite	1%	anhedral	100-400 µm	Occur as a few rounded to irregular shaped grains suspended in the mica schists are occasionally in the interior of staurolite and garnet phenocrysts
Tourmaline	trace	euhedral	100 µm	Singular isolated crystals are found in the muscovite schist
Ilmenite	1%	subhedral	10-100 µm	Occur as lath shaped inclusions within the staurolite and garnet crystals
Overall Comments: Host rock consists of a muscovite biotite quartz schist with phenocrysts of staurolite and garnet. This host rock likely formed because of the regional metamorphism of a protolith siltstone. Hydrothermal alteration of the rock caused the alteration and breakdown of garnet and staurolite crystals, crystalizing pyrrhotite and chalcopyrite in the schists as well as altering biotite to chlorite.				

Sample ID: DT063	*Depth:283.6*	*Location:16-04*	*Rock Type: Garnet staurolite, biotite schist with trace pyrite*	
Mineral	**Abundance**	**Habit**	**Grain Size**	**Comments**
Biotite	25%	Subhedral	20-600 µm	Occurs as wispy discontinuous lamellae of biotite with interfingered crystals of muscovite. The lamellae are all roughly parallel along foliation and are separated by a matrix of quartz and feldspar grains. Some isolated randomly orientated biotite grains occur interstitial to quartz and feldspar crystals.
Garnet	8%	Subhedral-anhedral	500 µm-4mm	Occur as sieve to skeletal grains hosted in the mica schist host rock. Pits and fractures are infilled by quartz.
Staurolite	5%	Subhedral-anhedral	200-1200 µm	Occur as sieve to skeletal grains hosted in the mica schist host rock. Pits and fractures are infilled by quartz.
Quartz	27%	Subhedral-anhedral	50-900 µm	Occur as smaller 20-300 µm irregular bulging grains in the schist host rock, and as larger 300-900 µm crystals in the quartz vein. Grain boundaries between crystals are irregular and bulging, although extinction colour distinctions show straight edged boundaries within single grains suggesting recrystallization
Plagioclase Feldspar	22%	Subhedral-anhedral	20-200 µm	Occur as larger 400-800 µm rounded grains of feldspar made up of several smaller feldspar crystals. Show alteration with replacement by quartz, as well as a dusty surface appearance due to sericite alteration
Chlorite	3%	Subhedral	50-200 µm	Occur as replacement recrystallization of biotite grains.

Muscovite	5%	Subhedral	10-600 µm	Occurs interfingered with biotite in the mica lamellae of the schist. Some isolated randomly orientated muscovite grains occur interstitial to quartz and feldspar crystals. Muscovite also occurs as sericite alteration of the feldspar grains in the matrix of the schist rock.
Chalcopyrite	4%	Anhedral	50 µm-2mm	Occur infilling space in a quartz vein through the host rock. Small fractures filled with chalcopyrite cut through quartz crystals in the vein suggesting a late precipitation for the sulphides.
Cubanite	1%	Anhedral	10-2000 µm	Occur as exsolution from the chalcopyrite represent a copper loss. Form straight bands through the chalcopyrite crystals, around 10-100 µm wide and up to 2mm long.
Pyrite	Trace	Subhedral	50-100 µm	A few grains occur suspended in the chalcopyrite, the pyrite grains are fractured and infilled by some exsolution with a slightly different colour
Silver	Trace	Anhedral	20 µm	Small crystal of native silver, occurs adjacent to the pyrite grains in the larger chalcopyrite crystals.

Overall Comments: Sample consists of a biotite muscovite quartz feldspar schist with phenocrysts of garnet and staurolite. This is the likely result of regional metamorphism of a felsic volcanic protolith. Post metamorphism saw the intrusion of a cross cutting quartz vein through the schist, late in the formation of the quartz vein chalcopyrite and some pyrite precipitated between quartz grains and in fractures that formed on the quartz grains. Later low temperature alteration led to the exsolution of cubanite from the chalcopyrite as well as alteration of the pyrite grains.

Sample ID: DT064	*Depth:293.5*	*Location:16-04*	*Rock Type: garnet, staurolite, massive biotite schist*	
Mineral	**Abundance**	**Habit**	**Grain Size**	**Comments**
Biotite	35%	Subhedral	50 µm- 3mm	Occurs as wispy discontinuous parallel foliated lamellae separated by a quartz grain matrix. Muscovite is interfingered with biotite in the lamellae and in some instances is the dominant mica. Isolated small grains of biotite occur interstitial to the quartz veins and are randomly orientated. The center of the sample is cut by a massive biotite vein with randomly orientated coarse biotite grains from 500 µm to 3mm in length. Some biotite grains have undergone replacement recrystallization forming chlorite, especially within the biotite vein.
Chlorite	5%	Subhedral	50-800 µm	Occur as replacement recrystallization of biotite grains in the coarse biotite vein, as well as fine grained chlorite forming around the exteriors and within fractures in the altered staurolite.

Garnet	8%	Subhedral	3mm- 10mm	Occur as sieve to skeletal grains hosted in the mica schist host rock. Pits and fractures are infilled by quartz. Small, rounded blebs of ilmenite occur potentially filling pits in the mineral or as inclusions.
Staurolite	10%	Subhedral- anhedral	500 µm- 4mm	Occur as sieve to skeletal grains hosted in the mica schist host rock. Pits and fractures are infilled by quartz. Small, rounded blebs of ilmenite occur potentially filling pits in the mineral or as inclusions. Chlorite occurs along the edges of staurolite, often filling spaces between separate grains or replacing biotite where the biotite meets the staurolite.
Quartz	25%	Subhedral	50-400 µm	Occur as the matrix of the host rock schist, with quartz grains showing mostly straight grain boundaries between each other. Interstitial mica occurs between quartz grains as well as the lamellae of biotite and muscovite. Infills the open spaces of the skeletal to sieve textured staurolite and garnet.
Muscovite	12%	Subhedral	50-500 µm	Occurs as wispy discontinuous parallel foliated lamellae separated by a quartz grain matrix. Biotite is interfingered with the muscovite in the lamellae and in some instances is the dominant mica. Isolated small grains of Muscovite occur interstitial to the quartz veins and are randomly orientated.

Pyrrhotite	3%	Subhedral- anhedral	200-900 µm	Occur as irregular shaped grains hosted within the massive coarse biotite vein as well as smaller linear fragments parallel to foliation hosted in the schist.
Chalcopyrite	1%	Subhedral- anhedral	20-400 µm	Occur within the larger pyrrhotite grains in the massive biotite vein. Often along the edges of the pyrrhotite adjacent to the host rock.
Ilmenite	1%	Subhedral- anhedral	20-300 µm	Occur as small 20-40 µm rounded blebs hosted in the staurolite and garnet phenocrysts. Also, as coarser more rectangular shaped crystals on the margins of the pyrrhotite crystals in the massive biotite vein.
Overall Comments: Sample consists of a muscovite biotite quartz schist, likely the result of regional metamorphism of an interbedded siltstone sandstone protolith. Regional metamorphism also produced the coarse garnet and staurolite phenocrysts. Hydrothermal fluid flow through the rock caused the crystallization of a massive biotite vein through the sample 1 cm wide, along with the precipitation of sulphides pyrrhotite and chalcopyrite. This same hydrothermal alteration caused the recrystallization of biotite as chlorite, and the breakdown of staurolite and garnet.				

Sample ID: DT069	*Depth: 356.9*	*Location:16-04*	*Rock Type: Garnet, biotite schist with Chalcopyrite pyrrhotite veinlets*	
Mineral	**Abundance**	**Habit**	**Grain Size**	**Comments**
Garnet	40%	Subhedral- anhedral	100µm-15mm	Occur as coarse phenocrysts suspended in a matrix of biotite and quartz. Show significant fracturing of grains as well as fragmentation of the exterior of the grains. Open space formed by the fracturing and skeletonization of the grains is infilled by quartz, chlorite, ilmenite, and sulphides pyrrhotite and chalcopyrite
Biotite	15%	Subhedral	50-900 µm	Biotite occurs as foliated laminae interfingered with muscovite grains in the mica schist host rock. These mica laminae within a ground mass of 50-400 µm quartz grains. Fine 50-100 µm laths of biotite occur randomly orientated as interstitial grains to the quartz crystals
Quartz	25%	Subhedral	50 µm- 2mm	Within the mica schist the quartz occurs as grains of 50-400 µm separated by lamellae of muscovite and biotite. Coarser crystals of quartz 500 µm to 2mm in size occur in a quartz vein 5mm across. Quartz grain boundaries are irregular and bulging.
Muscovite	8%	Subhedral	50-800 µm	Muscovite occurs as foliated laminae interfingered with biotite grains in the mica schist host rock. These mica laminae within a ground mass of 50-400 µm quartz grains. Fine 50-100 µm laths of muscovite occur randomly orientated as interstitial grains to the quartz crystals
Chlorite	3%	Subhedral	100-600 µm	Forms on the margins of garnet grains within the quartz vein. Also found filling small open spaces inside the garnet crystals as they are altered.

Chalcopyrite	5%	Subhedral- anhedral	50-1000 µm	Irregular shaped crystals form between quartz grains in the vein and in fractures in the garnets. Smaller crystals of pyrrhotite occur within the coarser grains of chalcopyrite
Pyrrhotite	3%	Subhedral	50-500 µm	Occur as irregular shaped blebs within and alongside the chalcopyrite crystals in the quartz vein.
Ilmenite	1%	Subhedral	10-100 µm	Occur as irregular shaped grains located within the garnet grains, possibly as infills of open pits formed by alteration of the garnet.
Apatite	Trace	Anhedral	400 µm	Occurs in open space of a fracture of garnet, the apatite grows around a crystal of sulphide.
Overall Comments: Sample consists of a biotite muscovite host rock with phenocrysts of garnet that is crosscut by a quartz vein containing chalcopyrite and pyrrhotite. The host rock protolith is likely a sandstone that underwent regional metamorphism resulting in a muscovite biotite schist. Hydrothermal fluid flow through the rock created the quartz vein, while crystalizing chlorite from the altering garnets and precipitating chalcopyrite and pyrrhotite.				

Sample ID: DT076	*Depth:204.9*	*Location:19-10*	*Rock Type: Pyrrhotite chalcopyrite vein in amphibolite basalt*	
Mineral	**Abundance**	**Habit**	**Grain Size**	**Comments**
Amphibole	40%	Subhedral- anhedral	20-600 µm	Occur in a foliated groundmass of fine 20-100 µm crystals intermingled with equally fine grains of quartz. Coarse 200-600 µm grains of amphibole occur as single interstitial grains in the sulphide matrix of the vein, or as smaller crystals occurring in what appear to be fragmented pieces of host rock.
Calcite	10%	Subhedral	100-500 µm	Occur as blebs of multiple calcite crystals intergrown together alongside and around amphibole grains in the sulphide vein
Biotite	4%	Subhedral	20-100 µm	Fine grained biotite occurs as selvage around the exterior of the sulphide vein
Quartz	5%	Subhedral	20-300 µm	Fine grained 20-50 µm quartz within the amphibolite matrix. Coarse 100-300 µm occur as scattered blebs of quartz crystals. Grain boundaries between quartz veins are irregular and bulging.
Chalcopyrite	25%	Anhedral	50 µm-2mm	Chalcopyrite fills around the amphibole and calcite crystals forming a network in a vein 3 cm wide. Individual grains of chalcopyrite are difficult to distinguish. Grain boundaries between chalcopyrite and pyrrhotite are irregular to curved shaped.

Pyrrhotite	15%	Subhedral- anhedral	100-800 µm	Grains of pyrrhotite occur within the larger mass of chalcopyrite in the network textured sulphide vein. The pyrrhotite grains are irregular shaped and are made up of several smaller individual crystals of pyrrhotite
Chlorite	1%	Subhedral	20-100 µm	Occurs as replacement recrystallization of occasional biotite grain
Overall Comments: Sample consists of an amphibolite host rock to a net textured vein of chalcopyrite and pyrrhotite. Protolith likely a basalt that underwent regional metamorphism resulting in a fine-grained amphibolite. Hydrothermal fluid flow through the sample resulted in the formation of a vein of pyrrhotite and chalcopyrite along with calcite and quartz. A reaction selvage around the vein of dark brown fine-grained biotite occurs on the margins of the vein.				

Sample ID: DT087	*Depth:386.6*	*Location:17-01*	*Rock Type: Staurolite biotite schist*	
Mineral	**Abundance**	**Habit**	**Grain Size**	**Comments**
Quartz	40%	Subhedral	40-500 µm	Occur mostly as 40-200 µm grains with irregular bulging grain boundaries. Interstitial biotite grains occur between quartz grains. A few 500 µm quartz veins occur with coarser 300-500 µm quartz grains with polygonal grain boundaries
Biotite	30%	Subhedral	20-600 µm	Occur as parallel foliated wispy discontinuous lamellae occurring interstitial to the quartz grain matrix. In some portions the schist is quartz rich with small isolated interstitial biotite grains, other portions are biotite rich with coarse 300-600 µm biotite crystals surrounding isolated quartz grains.

Staurolite	20%	Subhedral-anhedral	200-1000 µm	Sieve to skeletal porphyroblasts of staurolite occur throughout the schist matrix, larger crystals 400-1000 µm occur within the biotite rich lamellae and smaller 200-400 µm occur in the quartz rich lamellae. Pits and fractures in the staurolite are infilled by quartz.
Chlorite	6%	Subhedral	100-400 µm	Occurs as pseudomorph replacement of biotite grains due to lower temperature alteration
Ilmenite	1%	Anhedral	20-50 µm	Occur as small, rounded grains adjacent to and within altered staurolite grains.
Pyrrhotite	3%	Anhedral	100-400 µm	Irregular shaped grains hosted in the schist, show patchy pyrite that have not completely turned to pyrrhotite during regional metamorphism
Pyrite	trace	Anhedral	20-50 µm	Irregular patchy grains of pyrite occur in the centers of pyrrhotite grains, likely due to the alteration of original pyrite to pyrrhotite due to regional metamorphic conditions
Overall Comments: Sample consists of a biotite quartz schist host rock, the metamorphic result of pelite/siltstone protolith. Regional metamorphism of the protolith resulted in the foliated schist developing with porphyroblastic staurolites growing and the original possibly sedimentary pyrites were altered to a higher temperature pyrrhotite.				

Sample ID: DT088	*Depth:308.6*	*Location:17-01*	*Rock Type: Staurolite garnet biotite schist with quartz tourmaline vein*	
Mineral	**Abundance**	**Habit**	**Grain Size**	**Comments**
Quartz	38%	subhedral-anhedral	100-2000µm	In the biotite quartz schist, the quartz occurs as 100-300µm crystals mostly bordering each other with straight edges and coming to triple point junctions, some have bulging grain boundaries. The quartz grains are often separated by interstitial biotite grains. In the quartz tourmaline vein the quartz grains are much larger from 300 to 2000µm and have irregular bulging grain boundaries
Biotite	25%	Subhedral	50-400µm	Occur as foliated elongate laths in wispy discontinuous lamellae separated by and interstitial to quartz grains
Garnet	8%	subhedral-anhedral	100µm- 1cm	One 1cm garnet phenocrysts occurs within the biotite quartz schist, it has been highly fractured and skeletonized such that it consists of smaller elongate garnet crystals separated by quartz and occasional staurolite crystals. These small crystal grains can be seen to form an original larger crystal.
Staurolite	4%	Subhedral	100-300µm	Occur as small phenocrysts in the biotite quartz schist rock. Often have a few well-formed straight edges with the rest of the crystal being highly pitted and fractured. Pits in the crystal are infilled by quartz
Muscovite	2%	anhedral	10-30µm	Occur as very fine crystals replacing feldspar along the margin of the quartz tourmaline vein

Alkali Feldspar	3%	anhedral	10-100µm	Form masses of highly sericite altered feldspar along the rim between the quartz tourmaline vein and the biotite quartz schist
Chlorite	5%	subhedral-anhedral	50-250µm	Occur as replacement recrystallization of biotite, normally partially recrystalizing larger biotite grains such that the chlorite occurs interfingered with biotite.
Tourmaline	12%	Euhedral-Subhedral	100-1000 µm	Occurs both as isolated singular crystals as well as tightly packed masses of many crystals. Within the quartz tourmaline vein many of the crystals are orientated down the c axis such that you can clearly see the triangular crystal form. The biotite quartz schist also has tourmaline occurring as single crystals as well as clusters of tightly packed crystals. In a few spots in the schist the tourmaline forms radiating patterns with long crystal prisms forming outwards from a singular internal point.
Pyrite	2%	Subhedral	100-600µm	Occur as coarse subhedral crystals in the quartz tourmaline vein. Often the crystals have straight crystalline edges that have been embayed or fractured in spots to imperfect forms.
Ilmenite	1%	Anhedral	10-50µm	Occur as small, rounded pill shaped crystals in the biotite quartz schist

Chalcopyrite	trace	Anhedral	50-200µm	Occur as small space filling irregular crystals interstitial to the quartz tourmaline vein
Pyrrhotite	trace	Anhedral	50-100µm	Occur as small space filling irregular crystals interstitial to the quartz tourmaline vein. Occur with chalcopyrite, often with rounded crystal boundaries between the two infilling the same open space in the vein.

Overall Comments: Sample consists of a biotite quartz schist with phenocrysts of garnet and staurolite. This is likely the regional metamorphic product of a siltstone protolith. This rock was then subjected to hydrothermal quartz tourmaline veining which also produced tourmaline crystals into the surrounding host rock. Pyrite and minor chalcopyrite were introduced along with the quartz tourmaline vein. Later retrograde metamorphism has caused some recrystallization of biotite into chlorite.

Sample ID: DT092	*Depth: 215.6*	*Location:17-01*	*Rock Type: Biotite, Staurolite, Garnet Schist*	
Mineral	**Abundance**	**Habit**	**Grain Size**	**Comments**
Biotite	34%	Subhedral	60-700µm	Occurs primary as wispy discontinuous parallel foliated lamellae. The lamellae wrap around the garnet phenocryst and a pressure shadow is present adjacent to the large garnet where the biotite is randomly orientated. Singular interstitial biotite grains occur within the groundmass of quartz and feldspar grains.
Quartz	30%	Subhedral	50-1000µm	Occurs mostly as finer grained 50-300µm irregular shaped grains with bulging crystal boundaries. Occasional veinlets of quartz occur in the sample where the size of the quartz crystals is larger from 300-1000µm. Quartz infilling the open space of the garnet porphyroblast is polygonal with boundaries meeting at triple points.

Plagioclase Feldspar	7%	Anhedral	50-300µm	Occur as semi rounded and highly sericite altered grains within the quartz matrix in the biotite schist. Dusty spotted surface appearance due to sericite replacement distinguishes it from quartz grains.
Alkali Feldspar	2%	Anhedral	50-300µm	Occur as semi rounded and highly sericite altered grains within the quartz matrix in the biotite schist. Dusty spotted surface appearance due to sericite replacement distinguishes it from quartz grains.
Garnet	12%	Subhedral	10-15mm	Two coarse porphyroblastic garnets occur within the sample. The original euhedral shape of the crystal can be distinguished but is now sieve to skeletal textured with open pits infilled by quartz and occasionally magnetite and staurolite.
Staurolite	6%	Subhedral	100-600µm	Medium grained porphyroblastic crystals of staurolite occur within the biotite schist host rock and as inclusions within garnet. The crystals are pitted and fractured with a sieve texture that is infilled by quartz.
Muscovite	2%	Subhedral	5-400µm	Occurs as very fine 5-20µm grains replacing feldspar from sericite alteration. Occasional muscovite grain occurs interfingered with biotite in the schist.
Tourmaline	trace	Euhedral	20-100µm	Individual crystals occur in the biotite schist, often orientated such that they are cut across the Z axis.

Chlorite	1%	Subhedral	50-200µm	Occurs as replacement of biotite, especially along the margins of the garnet grains.
Magnetite	2%	Subhedral-anhedral	300-500	Occur as roughly square grains, usually one straight edge with other sides being eroded and irregular.
Pyrrhotite	3%	Anhedral	50-400µm	Occur as irregular shaped rough-edged grains suspended in the biotite schist
Pyrite	1%	Subhedral-anhedral	50-800µm	Occur as patchy remnant in some pyrrhotite grains, suggesting original pyrite grains have been replaced by pyrite. One large 800µm grain of pyrite is present in the biotite schist and has a roughly square shaped with one corner eroded out.
Overall Comments: Sample consists of a highly foliated biotite schist with a quartz feldspar matrix and with coarse garnet and staurolite porphyroblasts. Protolith likely a felsic volcanoclastic rather than siltstone due to the feldspar content. Regional metamorphism of this volcanic protolith caused the formation of the foliated biotite veins coarse porphyroblasts.				

Sample ID: DT098	*Depth:100.7*	*Location:17-01*	*Rock Type: Garnet quartz vein*	
Mineral	**Abundance**	**Habit**	**Grain Size**	**Comments**
Quartz	73%	Subhedral-anhedral	50-2000µm	Quartz in the vein occurs mostly as coarse 400-2000µm interlocking crystals with irregular grain boundaries suggestive of bulging recrystallization. Occasionally the quartz grains are separated by a thin wispy biotite veinlet. In the garnet quartz vein the quartz consists of finer grained crystals from 50-400µm in size.

Biotite	6%	Subhedral	50-700µm	Occur as parallel foliated elongate books forming wispy veinlets that run parallel to subparallel through the quartz vein. Possibly infilling fracture space of the quartz vein.
Garnet	8%	Euhedral-Subhedral	20-300µm	Garnet occurs as small 20-300µm crystals tightly packed together in a veinlet 2-5mm wide with a quartz matrix. The garnet vein is parallel to the quartz vein but is separated by veinlets of biotite containing staurolite phenocrysts
Chlorite	3%	Subhedral-anhedral	50-300µm	Occurs primarily as a replacement recrystallization of biotite because of retrograde metamorphism. Also infills open pitted spaces in staurolite crystals as an alteration product.
Staurolite	5%	Subhedral	200µm-3mm	Occur as well-formed crystals, often heavily pitted and fractured. Open space in the pits of the crystal is infilled by chlorite and quartz
Muscovite	2%	Subhedral	50-200µm	Occur in thin wispy veinlets about 200µm wide that run parallel to and within the quartz vein. Occasionally muscovite will also occur interstitial to biotite in the more common biotite veinlets also present within the quartz.

Ilmenite	1%	Subhedral-anhedral	50-200µm	Occur as elongate lath shaped crystals, commonly interstitial between mica grains, especially common adjacent to chlorite that has formed from replacement recrystallization of biotite.
Pyrrhotite	1%	Subhedral-anhedral	100-1000µm	Occurs as irregularly shaped space filling grains between quartz grains in the vein. Often occurs joined with chalcopyrite and has curved to rounded boundaries between the two sulphides
Chalcopyrite	1%	Subhedral-anhedral	100-1000µm	Occurs as irregularly shaped space filling grains between quartz grains in the vein. Often occurs joined with pyrrhotite and has curved to rounded boundaries between the two sulphides
Overall Comments: Sample consists of a quartz vein containing small micaceous veinlets and minor pyrrhotite and chalcopyrite content, alongside and enveloping a garnet quartz vein				

Sample ID: DT099	*Depth:62.3*	*Location:17-01*	*Rock Type: Muscovite biotite staurolite schist*	
Mineral	**Abundance**	**Habit**	**Grain Size**	**Comments**
Quartz	57%	Subhedral-anhedral	50-1000µm	Occur as the matrix of the schist with crystals being separated by biotite or muscovite lamellae and interstitial crystals. Grain boundaries between quartz crystals are irregular and bulging.
Biotite	20%	Subhedral	50-400µm	Occur in foliated wispy discontinuous lamellae within the schist separated by quartz. Occur in sections primarily biotite rich to portions of the samples that are muscovite dominated and contain only sporadic interstitial biotite. Also occurs as isolated individual grains interstitial to the quartz grains.

Staurolite	10%	Subhedral	50-500µm	Occur as highly skeletonized grains with significant fractures and pitting. Original grains were up to 2mm in size but have been broken up into smaller separated pieces but are still contained in the general shape of the original crystal. Open space in the fractures and pits are infilled by quartz and occasionally chlorite. In areas where biotite is adjacent to staurolite crystals it appears to undergo replacement recrystallization to chlorite to a greater degree than away from staurolite
ilmenite	1%	Anhedral	20-200µm	Occur as elongate to rounded pill shaped grains most contained as inclusions within garnet and staurolite but also suspended in the schist matrix.
Chlorite	3%	Subhedral	20-200µm	Occurs interfingered with biotite and appears to be a replacement recrystallization of the original biotite. Occurs most commonly on the margins and rim around staurolite grains.
Muscovite	8%	Subhedral	50-300µm	Occur in foliated wispy discontinuous lamellae within the schist separated by quartz. Occur in sections primarily muscovite rich to portions of the samples that are biotite dominated and contain only sporadic interstitial muscovite

Garnet	1%	Subhedral	3mm	One single coarse garnet phenocryst is present in the schist with the lamellae of biotite and muscovite flowing around the crystal. The Garnet has been skeletonized with significant pitting throughout the interior of the crystal. The open space in the altered garnet is infilled by quartz. elongate to rounded pill shaped ilmenite inclusions are contained within the garnet.
Pyrrhotite	Trace	Anhedral	20-200µm	Occur as sporadic rare grains suspended in the schist. Single grains often contain both chalcopyrite and pyrrhotite together with irregular jagged to rounded boundaries between the two sulphides.
Chalcopyrite	Trace	Anhedral	20-200µm	Occur as sporadic rare grains suspended in the schist. Single grains often contain both chalcopyrite and pyrrhotite together with irregular jagged to rounded boundaries between the two sulphides.
Tourmaline	Trace	Subhedral	20µm	Occur as sporadic rare grains suspended in the schist matric of the sample. A few appear to have grown into a staurolite crystal
Apatite	Trace	Anhedral	30µm	A few isolated crystals of apatite occur sporadically throughout the schist, are difficult to distinguish from quartz but where highlighted during SEM analysis.
Overall Comments: Sample is a schist with alternating lamellae of biotite and muscovite in a matrix of quartz grains with coarse phenocrysts of garnet and staurolite. Likely forms as the product of regional metamorphism from a protolith of interbedded siltstone and sandstones.				

Sample ID: DT102	*Depth:64.7*	*Location:19-04*	*Rock Type: Pyrrhotite massive sulphide in biotite chlorite feldspar schist host rock*	
Mineral	**Abundance**	**Habit**	**Grain Size**	**Comments**
Biotite	15%	Subhedral	100-700µm	Occur as isolated interstitial grains suspended in a pyrrhotite matrix as well as being contained in irregular shaped host rock fragments containing randomly orientated massive biotite with feldspar grains.
Feldspar	10%	anhedral	100-400µm	Occur as rounded shaped crystals as both isolated individual grains in the sulphide matrix or as host rock fragments containing an amalgamation of multiple feldspar grains along with biotite. The feldspars are highly sericitized with a dusty appearance. Possible thin polysynthetic twinning is visible in the grains but difficult to see due to overprinting of sericite
Muscovite	2%	anhedral	10-50µm	Occurs as very small grains replacing feldspar due to sericitization
Chlorite	5%	Subhedral	100-500µm	Occur frequently interfingered with biotite, likely as a replacement recrystallization of the original biotite crystals. Also occur as individual laths in the sulphide matrix. Has a brown to blue interference colour in cross polar transmitted light.
Ilmenite	1%	anhedral	100-400µm	Rounded and irregular crystals of ilmenite occur sporadically in the groundmass of pyrrhotite.

Pyrrhotite	65%	anhedral	200µm-3mm	Massive pyrrhotite makes up the bulk of this sample and is broken up only occasionally by the host rock fragments suspended in the sulphide matrix and the rare inclusion of chalcopyrite and ilmenite. Individual grains of pyrrhotite can only be distinguished in cross polar extinction in reflected light, and show irregular rounded boundaries between crystals to make up the massive sulphide
Chalcopyrite	2%	anhedral	100-200µm	Sporadic irregular shaped crystals occur within the pyrrhotite matrix. Have rounded irregular grain boundaries with the pyrrhotite
Overall Comments: Original host rock consisted of a chlorite feldspar biotite schist likely the metamorphic product of a volcanic tuff. The host rock has been fragmented and destroyed by a horizon of massive pyrrhotite likely formed by sub seafloor replacement. The host rock fragments consist of isolated biotite and chlorite laths to fragments consisting of sericite altered feldspar interstitial to massive biotite. Fragments of the host rock very in size from 100µm up to 4mm at the largest.				

Sample ID: DT109	*Depth:146.9*	*Location:21-6*	*Rock Type: Massive biotite vein contact with feldspathic dike*	
Mineral	**Abundance**	**Habit**	**Grain Size**	**Comments**
Biotite	60%	subhedral	50 µm-2mm	Biotite occurs as shreddy randomly orientated crystals making a massive vein.

Plagioclase feldspar	35%	subhedral	40-600 µm	plagioclase crystals occur together in dike adjacent to the biotite vein, show significant sericite alteration with a dusty surface appearance. Few coarser crystals show polysynthetic twinning of crystals.
Muscovite	5%	anhedral	5-20 µm	Occurs as very fine grains due to sericite breakdown of the plagioclase feldspars
Overall Comments: Sample consists of a fine-grained feldspathic dyke occurring adjacent to a massive hydrothermal biotite vein containing randomly orientated shreddy biotite crystals.				

Sample ID: DT111	*Depth:236.7*	*Location:21-06*	*Rock Type: Garnets within hydrothermally altered basalt/ amphibolite*	
Mineral	**Abundance**	**Habit**	**Grain Size**	**Comments**
Amphibole	60%	anhedral	10-400µm	Very fine 10-100µm sized amphibole makes up most of the sample, occurring as irregular shaped randomly orientated laths occurring in matrix of fine-grained lath shaped plagioclase. Light green blue colour with distinct pleochroism. cross cutting vein causes the formation of a 200-400µm wide amphibole that continues the length of the sample.
Plagioclase Feldspar	24%	Subhedral-anhedral	50-200µm	Occurs as laths interstitial to the amphibole. Have a sericite altered appearance and the polysynthetic twinning only visible in occasional grains.
Biotite	4%	Subhedral	100-200µm	Occur as randomly orientated shreddy grains in 1-3mm blebs in the selvage of the calcite veins.

Garnet	3%	Subhedral-anhedral	1-4mm	500µm garnet fragments making up a 2 by 8mm wide section. Has a red, green mottled colour with pleochroism that matches its colour in cross poles. Appears very altered and may not be garnet, possibly epidote. Occur within a vein of coarser amphibole.
Calcite	5%	Subhedral-anhedral	200-300µm	Occur along the length of a 400 µm wide calcite vein with a 4-5 mm wide vein selvage.
Pyrrhotite	3%	anhedral	5-30µm	Very fine grains of pyrrhotite occur and appear intergrown with amphibole.
Ilmenite	1%	anhedral	10-20 µm	small irregular grains occur sporadically in the matrix of fine-grained feldspar
Overall Comments: Sample consists of a highly altered and metamorphosed basalt, turned into an amphibolite rock. Several instances of cross cutting veins occur within the sample, an early set of coarser amphiboles with possible garnet forming, followed by a later calcite vein that has a vein selvage of biotite and increased plagioclase to amphibole content.				

Sample ID: DT113	*Depth:58*	*Location:21-8*	*Rock Type: Garnet amphibolite*	
Mineral	**Abundance**	**Habit**	**Grain Size**	**Comments**
Amphibole	92%	Subhedral	100-600µm	Roughly polygonal shaped amphibole crystals are tightly packed and overlapping, foliated lengthwise across the whole sample. Light to dark green and tan coloured, on the edges of the thin section clear 56-124 cleavage Is distinguishable.

Garnet	5%	Subhedral-anhedral	500µm-2mm	Garnets show fracturing pitting with calcite infilling open spaces. Garnets are surrounded by the matrix of amphibole crystals, and the amphibole foliation appears to flow around the garnet.
Calcite	2%	anhedral	50-400µm	Calcite veins infill small cracks in the amphibolite matrix, also occurring as the occasional interstitial crystal to amphibole.
Pyrrhotite	1%	anhedral	50-200µm	Occur as occasional long grains fitting in along the foliation planes between amphibole crystals.
Overall Comments: Sample consists almost entirely of amphibole, making it an amphibolite, the regional metamorphic product from a basalt or ultramafic protolith. Hydrothermal alteration caused the formation of garnets in the rock, prior to peak metamorphism that led to the foliation in the amphiboles. Later alteration led to the precipitation of calcite.				

Sample ID: DT117	*Depth:126.5*	*Location:19-10*	*Rock Type: Pyrrhotite, chalcopyrite, sphalerite, galena massive sulphide horizon in a volcaniclastic tuff host rock*	
Mineral	**Abundance**	**Habit**	**Grain Size**	**Comments**
Quartz	25%	subhedral-anhedral	100-800µm	Occur as small irregular shaped crystals alongside feldspar and mica in the schist host rock component of the sample, as well as coarser 300-800µm grains in a quartz vein bleb 1cm wide through the center of the sample. Quartz vein grains are undulous and have irregular intergrown crystal boundaries.

Feldspar	10%	anhedral	50-150µm	Occur as small, rounded grains heavily sericite altered with dusty surface appearance and in some instances almost completely replaced by muscovite. Possible faint thin polysynthetic twinning visible but is difficult to distinguish due to the sericite replacement.
Biotite	12%	subhedral-anhedral	100-400µm	Occur as randomly orientated interstitial grains in a feldspar quartz schist groundmass, as well as a 3mm wide foliated biotite vein consisting entirely of 100-400µm biotite laths.
Muscovite	5%	subhedral-anhedral	10-200µm	Occur as fine-grained sericite replacement of altered feldspars as well as up to 200µm laths of foliated discontinuous wispy crystals interstitial to a quartz feldspar schist.
Chlorite	3%	subhedral-anhedral	50-200µm	Occur as replacement recrystallization of biotite laths, often occurring interfingered with the biotite.
Pyrite	25%	euhedral-subhedral	100-1500µm	Occur as coarse densely packed crystals to isolated individual crystals suspended in a sulphide groundmass consisting of pyrrhotite, chalcopyrite and sphalerite.
Chalcopyrite	5%	anhedral	50-300µm	Occurs as irregular patches in the net textured sulphide groundmass of the rock, with rounded to straight grain boundaries with the pyrrhotite.

Pyrrhotite	8%	anhedral	100-1000µm	Makes up much of the net textured massive sulphide groundmass of the sample. Individual crystals in the massive groundmass can only be distinguished under cross polar extinction in reflected light. Crystal boundaries are rounded and irregular
Sphalerite	5%	anhedral	50-250µm	Occur as irregular patchy crystals in the sulphide groundmass, often filling in space between coarse pyrite grains
Ilmenite	1%	anhedral	50-100µm	Occur as rounded to irregular grains in the sulphide groundmass.
Galena	1%	anhedral	50-100µm	Occur as irregular patchy crystals in the sulphide groundmass, with a creamy light grey colour and distinctive triangular black pits on the crystal surface.
Overall Comments: Host rock consists of feldspar and biotite to muscovite rich schist rock derived as the metamorphic component of a volcaniclastic tuff. Volcanogenic massive sulphide emplacement fragmented the host rock and created a net textured massive sulphide matrix consisting predominantly of coarse pyrite, pyrrhotite, chalcopyrite, sphalerite with minor galena. Later hydrothermal flow through the rock emplaced a quartz biotite vein cross cutting through the sample				

Sample ID: DT118A	*Depth:198.7*	*Location:19-10*	*Rock Type: Chalcopyrite, pyrrhotite sphalerite volcanogenic massive sulphide replacement of volcanic host rock.*	
Mineral	**Abundance**	**Habit**	**Grain Size**	**Comments**
Quartz	25%	Subhedral	200-600µm	Occur as intergrown crystals of quartz, with undulous extinction and irregular bulging grain boundaries. Occur as coarser 400-600µm grains in quartz rich portions of the host rock, and as finer grained 200-300µm grains when in a feldspar rich portion of the host rock.
Chlorite	2%	subhedral- anhedral	50-200µm	Occur as randomly orientated grains interstitial to the feldspar and quartz in the host rock fragments. Have an anomalous berlin blue extinction colour in cross pole transmitted light
Muscovite	3%	subhedral- anhedral	10-50µm	Occur as fine-grained replacement of sericitized feldspar as well as occasional randomly orientated grains interstitial to the quartz and feldspar grains of the host rock matrix
Biotite	2%	subhedral- anhedral	50-200µm	Occur as isolated randomly orientated laths interstitial to quartz and feldspar host rock matrix.
Feldspar	8%	Subhedral- anhedral	50-200µm	Occur as lath to irregular shaped grains, often highly sericitized with fine grained muscovite replacement and a dusty exterior appearance. Occur alongside coarser unaltered quartz in the host rock fragments

Pyrrhotite	10%	Anhedral	1-3mm	Forms an irregular shaped groundmass of massive pyrrhotite with individual grains only distinguishable in cross poles. Rounded irregular boundaries form with chalcopyrite and sphalerite forming the sulphide matrix of the rock. This matrix is then studded with euhedral to subhedral pyrite and Arsenopyrite
Arsenopyrite	5%	Euhedral-Subhedral	200-500µm	Occurs as euhedral to subhedral grains suspended in the groundmass of pyrrhotite, chalcopyrite and sphalerite. Occurs commonly with the pyrite crystals, with occasional grain of arsenopyrite being tightly packed in with the pyrite crystals or occasionally as individual isolated grains
Pyrite	25%	Euhedral-Subhedral	400-1500µm	Occurs as euhedral to subhedral coarse grains suspended in the groundmass of pyrrhotite, chalcopyrite and sphalerite. Can occur as isolated crystals suspended in the groundmass and as tightly packed crystals forming triple point junctions between grains with only slivers of the sulphide matrix interstitial to the coarse pyrite grains
Chalcopyrite	15%	Anhedral	500µm-2mm	Forms the sulphide groundmass of the sample with irregular shaped grains of chalcopyrite occurring jointly with pyrrhotite and sphalerite with rounded crystal boundaries. Well formed grains of pyrite and arsenopyrite are suspended in this sulphide matrix
Sphalerite	5%	Subhedral	200-800µm	Has a light grey colour in reflected light, and a red brown colour in transmitted light due to internal reflections. Very small, rounded blebs of chalcopyrite occur within the sphalerite, likely as a product of chalcopyrite disease. Forms with pyrrhotite and chalcopyrite to form a sulphide groundmass to the rock, often with irregular rounded grain boundaries between the sulphides.

Overall Comments: Massive sulphide horizon consisting of a groundmass of pyrrhotite chalcopyrite and sphalerite forms in a net texture around the quartz feldspar mica rich host rock of which only small fragments survive. The feldspar is heavily sericite altered, in some instances completely replaced by fine grained muscovite. The sulphide groundmass is then studded by euhedral shaped pyrite and arsenopyrite crystals that form as isolated crystals suspended in the matrix as well as tightly packed crystals. Appears to be a exhalative formed massive sulphide replacement of a volcanic rock host that has subsequently undergone amphibolite grade metamorphism causing recrystallization of pyrite and arsenopyrite.

Sample ID: DT118B	*Depth:198.7*	*Location:19-10*	*Rock Type: Pyrite, chalcopyrite, Pyrrhotite vein with Quartz fragments*	
Mineral	**Abundance**	**Habit**	**Grain Size**	**Comments**
Quartz	70%	anhedral	20µm-8mm	Quartz occurs as irregular shaped grains with bulging crystal boundaries and sweeping extinction. Size of the crystals vary from 300µm to 8mm in the quartz vein with much smaller 20-200 µm quartz fragments occurring withing the sulphide vein on the margins of the quartz vein.
Muscovite	6%	subhedral-anhedral	100-200µm	occurs as parallel foliated crystals in a 4-6mm wide lamellae adjacent to the quartz vein. Kink banding of the foliated muscovite occurs in some portions of the lamellae.
Plagioclase Feldspar	2%	anhedral	50-200µm	Heavily sericite altered and fractured grains occur within the sulphide vein. Dusty surface appearance and sericite content distinguishes it from quartz fragments.

Alkali Feldspar	1%	anhedral	50-200µm	Heavily sericite altered and fractured grains occur within the sulphide vein. Dusty surface appearance and sericite content distinguishes it from quartz fragments.
Pyrrhotite	10%	subhedral-anhedral	100-400µm	Occur as significant portion of the 1cm wide sulphide vein, individual grains of pyrrhotite are only distinguishable under cross poles looking for anisotropy. Grain boundaries with chalcopyrite are irregular and rounded.
Pyrite	2%	euhedral-subhedral	50 µm-3mm	Occurs primarily as 50-500 euhedral to subhedral crystals suspended both in the pyrrhotite chalcopyrite vein as well as within quartz fragments in the sulphide vein. One larger 1mm and 3mm grain of pyrite occur in the sulphide vein.
Chalcopyrite	5%	subhedral-anhedral	100 µm-5mm	Occur as smaller 100-300 µm grains in the sulphide vein occurring with pyrrhotite. 5mm wide portion of chalcopyrite may be made up of multiple grains that cannot be distinguished separately
Sphalerite	4%	anhedral	50-600µm	Has a strong red colour in transmitted light and light grey in reflected light. Occurs as small 50-200µm irregular shaped grains in the sulphide vein as well as a 600µm wide grain within the quartz vein, possible chalcopyrite disease present as small grains of chalcopyrite occur within the sphalerite. May be misidentified and really be hematite.

Chlorite	1%	anhedral	50 µm	Occur as small irregular grains in a groundmass of biotite, muscovite and altered feldspar
Overall Comments: Sample consists of a quartz vein fragment on the margins of a sericite host rock at the contact between the sericite schist and a massive sulphide horizon. Massive sulphide is forming a net texture around fragments of quartz, feldspar, and some muscovite.				

Sample ID: DT119	*Depth:300.7*	*Location:17-01*	*Rock Type: Pyrrhotite Chalcopyrite massive sulphide horizon with tourmaline and andalusite*	
Mineral	**Abundance**	**Habit**	**Grain Size**	**Comments**
Tourmaline	35%	Euhedral-subhedral	5-200µm	Occur as massive aggregates of very fine 10-50µm crystals forming irregular shaped tourmaline blebs 2 to 8mm in size. These blebs contain sporadic andalusite and muscovite inclusions. Fractures in the tourmaline blebs are infilled by pyrrhotite and chalcopyrite sulphides. Coarser 100-200µm tourmaline crystals can occasionally be incorporated by the finer grained tourmaline as well as occur as individual crystals suspended in the sulphide matrix
Chlorite	4%	Anhedral	100µm	A 100µm alteration rim of chlorite occurs on the margins of all andalusite grains in the massive sulphide horizon.
Muscovite	2%	Subhedral	50-150µm	Sporadic muscovite fragments are suspended in the sulphide matrix, occur as randomly orientated lath shaped micaceous books

Ilmenite	2%	Anhedral	50-200µm	Occur as irregular shaped crystals infilling space between tourmaline crystals in the sulphide matrix. Have rounded grain boundaries when in contact with the massive sulphide.
andalusite	8%	Subhedral	300µm-5mm	Tan to cream colour with very low birefringence. Chlorite rim has formed around the exterior of the crystals and along the insides of large fractures which are also infilled by pyrrhotite and chalcopyrite Tourmaline crystals up to 50µm have intruded into some andalusite crystals.
Pyrrhotite	30%	Subhedral-anhedral	200-1000µm	Pyrrhotite occurs in a massive sulphide matrix alongside chalcopyrite which it forms irregular rounded boundaries with. Tourmaline and muscovite blebs are suspended in the matrix of pyrrhotite. Individual grains of pyrrhotite are difficult to distinguish but can be seen in cross polar reflected light and show irregular grain boundaries which are straight to rounded in sections
Chalcopyrite	19%	Subhedral-anhedral	200-1000µm	Chalcopyrite occurs in a massive sulphide matrix alongside pyrrhotite which it forms irregular rounded boundaries with. Tourmaline and muscovite blebs are suspended in the matrix chalcopyrite.
Overall Comments: Massive pyrrhotite chalcopyrite sulphide horizon containing fine grained tourmalinite and coarser tourmaline and andalusite phenocrysts. Occasional muscovite crystal likely present as a remnant of the host rock which has been replaced by the deposition of massive sulphide.				

Sample ID: DT120A	*Depth:302.7*	*Location:17-01*	*Rock Type: biotite quartz feldspar schist*	
Mineral	**Abundance**	**Habit**	**Grain Size**	**Comments**
Biotite	32%	Subhedral	50-700µm	50-200µm platy grains occur in wispy discontinuous lamellae throughout the sample, as well as randomly orientated interstitial grains. Coarser 300-700µm biotite crystals occur on the margins of the amphibole feldspar vein.
Plagioclase Feldspar	15%	Subhedral	20-200µm	Fine grained groundmass feldspar occurs with the quartz grains and is broken up by the individual interstitial biotite crystals as well as the foliated biotite lamellae. Hard to distinguish from the quartz due to lack of polysynthetic twinning, however the plagioclase appears with a dusty surface due to sericite alteration.
Quartz	30%	Subhedral	20-200µm	Fine grained groundmass of polygonal to bulging quartz crystals is broken up by the individual interstitial biotite crystals as well as the foliated biotite lamellae. Hard to distinguish from the feldspar due to lack of polysynthetic twinning, however the plagioclase appears with a dusty surface due to sericite alteration.
Garnet	6%	anhedral	6-8mm	Two porphyroblasts of garnet are present hosted in the biotite schist rock. The garnets are heavily fractured and skeletal, with many smaller fragments making up the form of the original coarser garnet grains. Open space in the skeletal garnet grains is infilled by quartz feldspar and chlorite.

Chlorite	4%	Subhedral	50-500µm	Occur as irregular shaped masses adjacent to the garnet crystals, possibly as an alteration product of the garnet. Also form as low temperature replacement of biotite in some of the biotite lamellae.
Amphibole	7%	Subhedral	200-700µm	occur as two parallel linear veins of lath to prism shaped amphibole crystals 500-700µm wide with a feldspar rich vein selvage.
Magnetite	4%	subhedral	50-400µm	Roughly rectangular laths with occasional rounded edges. Occasionally occur with rounded pyrrhotite grains as inclusions within the magnetite grains. Occur as disseminated grains in the in the biotite schist host rock.
Pyrrhotite	2%	Anhedral	50-200µm	Small anhedral rounded crystals of pyrrhotite are sporadically disseminated throughout the biotite schist host rock.
Overall Comments: Sample consists of a biotite quartz feldspar schist host rock with porphryblasts of garnet and a cross cutting vein alteration of amphibole biotite and feldspar. Possible felsic volcanic protolith underwent regional metamorphism that caused the growth of the garnet and led to the foliated biotite felspar and quartz. Hydrothermal flow through the rock created a vein selvage with an alteration assemblage of amphibole.				

Sample ID: DT120B	*Depth:302.7*	*Location:17-01*	*Rock Type: biotite and chlorite quartz feldspar schist*	
Mineral	**Abundance**	**Habit**	**Grain Size**	**Comments**
Biotite	25%	Subhedral	50-700µm	50-200µm platy grains occur in wispy discontinuous lamellae throughout the biotite schist beds, as well as randomly orientated interstitial grains between quartz grains. Coarser 300-700µm biotite crystals occur in a hydrothermal veinlet cross cutting through the sample.
Plagioclase Feldspar	15%	Subhedral	20-200µm	Fine grained groundmass feldspar occurs with the quartz grains and is broken up by the individual interstitial biotite crystals as well as the foliated biotite lamellae. Hard to distinguish from the quartz due to lack of polysynthetic twinning, however the plagioclase appears with a dusty surface due to sericite alteration.
Quartz	30%	Subhedral	20-200µm	Fine grained groundmass of polygonal to bulging quartz crystals is broken up by the individual interstitial biotite crystals as well as the foliated biotite lamellae. Hard to distinguish from the feldspar due to lack of polysynthetic twinning, however the plagioclase appears with a dusty surface due to sericite alteration.
Chlorite	15%	Subhedral	100-500µm	Occur as both lath like shards as well as amorphous blebs in a matrix of feldspar and quartz grains.
Amphibole	8%	Subhedral	200-700µm	Occur within the chlorite schist as irregular prismatic to lath shaped crystals of various colours and assumed compositions. Occur as bands throughout the chlorite schist possibly due to hydrothermal flow veins through the host rock.

Magnetite	5%	subhedral	50-400µm	Roughly rectangular laths with occasional rounded edges. Often occur with rounded pyrrhotite grains as inclusions within the magnetite grains. Occur as disseminated grains in the in the biotite schist host rock.
Pyrrhotite	2%	Anhedral	50-200µm	Small anhedral rounded crystals of pyrrhotite are sporadically disseminated throughout the biotite schist host rock.
Overall Comments: Sample host rock consists of a biotite quartz feldspar schist interbedded with a chlorite schist with a platy amphibole content. Likely the product of regional metamorphism of a volcaniclastic sediment with beds of felsic to more intermediate composition.				